

JUNE 2019

**AJNR**

VOLUME 40 • PP 927-1081

# AJNR

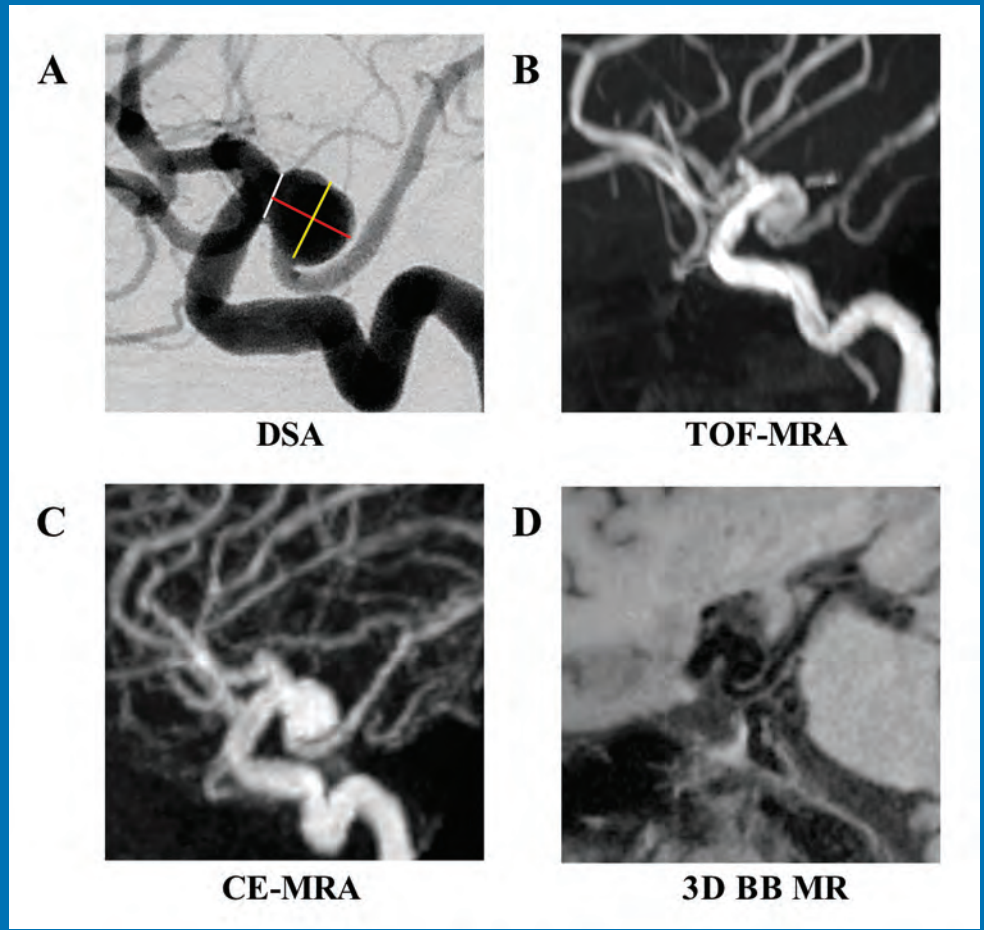
## AMERICAN JOURNAL OF NEURORADIOLOGY

JUNE 2019  
VOLUME 40  
NUMBER 6  
WWW.AJNR.ORG

THE JOURNAL OF DIAGNOSTIC AND  
INTERVENTIONAL NEURORADIOLOGY

Black-blood imaging of saccular aneurysms  
Dynamic enhanced MRI for parotid neoplasms  
AI segmentation of acute ischemic lesions

Official Journal ASNR • ASFNR • ASHNR • ASPNR • ASSR





# ONE AND DONE

## INDICATIONS FOR USE:

The WEB Aneurysm Embolization System is indicated for use at the middle cerebral artery (MCA) bifurcation, internal carotid artery (ICA) terminus, anterior communicating artery (AComm) complex, or basilar artery apex for the endovascular treatment of adult patients with saccular, wide neck bifurcation intracranial aneurysms with dome diameter from 3 mm to 10 mm and either neck size 4 mm or greater or the dome-to-neck ratio is greater than 1 and less than 2.

The WEB Aneurysm Embolization System is contraindicated for patients with known bacterial infection that may interfere with or negatively affect the implantation procedure and patients with known hypersensitivity to nickel. For complete indications, contraindications, potential complications, warnings, precautions, and instructions, see instructions for use (IFU provided with the device).

The VIA® Catheter is intended for the introduction of non-liquid interventional devices (such as stents/\_ow diverters) and infusion of diagnostic (such as contrast media) or non-liquid therapeutic agents into the neuro, peripheral, and coronary vasculature. The VIA Catheter is contraindicated for use with liquid embolic materials, such as n-butyl 2-cyanoacrylate or ethylene vinyl alcohol & DMSO (dimethyl sulfoxide). The VIA Catheter is contraindicated for use in the pediatric population (<22 yrs of age).

Caution: Federal law restricts these devices to sale by or on the order of a physician.

# WEB<sup>®</sup>

*Aneurysm Embolization System*

MicroVention<sup>®</sup> delivers the first intrasaccular solution for wide neck bifurcation aneurysms.

The **world leader**  
and **first**  
**PMA - approved**  
**device** in an  
important new  
category of  
intrasaccular  
flow disruptors.

The WEB<sup>®</sup> System is a safe  
and effective single-device  
solution for treating wide  
neck bifurcation aneurysms.



SL Device



SLS Device

Contact a MicroVention sales associate to learn more  
about integrating the WEB<sup>®</sup> device into your practice.



**MicroVention Worldwide  
Innovation Center**

35 Enterprise  
Aliso Viejo, CA 92656 USA

MicroVention UK Limited

MicroVention Europe, S.A.R.L.

MicroVention Deutschland GmbH

[microvention.com](http://microvention.com)

PH +1.714.247.8000

PH +44 (0) 191 258 6777

PH +33 (1) 39 21 77 46

PH +49 211 210 798-0

# NAVIGATE, BIFURCATE, CONSOLIDATE

CERENOVUS  
SPECTRA™  
family of coils

PROWLER®  
microcatheter



PULSERIDER®  
aneurysm neck reconstruction device

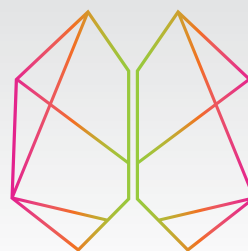


## #THINKCERENOVUS

**Important information:** Prior to use, refer to the instructions for use supplied with this device for indications, contraindications, side effects, warnings, and precautions.

**Caution:** US Law restricts this device to sale by or on the order of a physician

©CERENOVUS 2019. All rights reserved.



## CERENOVUS

PART OF THE *Johnson & Johnson* FAMILY OF COMPANIES

# Bending expectations of conformability and stability.

## **Enhanced conformability**

The hybrid cell structure is designed to enhance stent opening and conformability in bifurcations and tight curves.

## **Ease of use**

All sizes of the Neuroform Atlas Stent are deliverable through Excelsior® SL-10® and Excelsior XT-17™ Microcatheters.

## **Higher deployment accuracy**

The Neuroform Atlas Stent is designed to have very low foreshortening, which enables very high deployment accuracy.



## **Neuroform Atlas®** STENT SYSTEM



THE FOUNDATION OF THE ASNR



# Thank You

To Our P3 Program Partners For Their Support Of  
The ASNR 57th Annual Meeting And The Foundation of The ASNR Symposium 2019

## Sustaining Partner



## Collaborating Partners



## Affiliate Partners





# Simplify the MOC Process



# Manage your CME Credits Online

## CMEgateway.org

### Available to Members of Participating Societies

American Board of Radiology (ABR)  
American College of Radiology (ACR)  
American Roentgen Ray Society (ARRS)  
American Society of Neuroradiology (ASNR)  
Commission on Accreditation of Medical  
Physics Educational Programs, Inc. (CAMPEP)  
Radiological Society of North America (RSNA)  
Society of Interventional Radiology (SIR)  
SNM  
The Society for Pediatric Radiology (SPR)

### It's Easy and Free!

Log on to CME Gateway to:

- View or print reports of your CME credits from multiple societies from a single access point.
- Print an aggregated report or certificate from each participating organization.
- Link to SAMs and other tools to help with maintenance of certification.

### American Board of Radiology (ABR) participation!

By activating ABR in your organizational profile, your MOC-fulfilling CME and SAM credits can be transferred to your own personalized database on the ABR Web site.

### Sign Up Today!

go to [CMEgateway.org](http://CMEgateway.org)

# AJNR *go green*

***AJNR* urges American Society of Neuroradiology members to reduce their environmental footprint by voluntarily suspending their print subscription.**

The savings in paper, printing, transportation, and postage directly fund new electronic enhancements and expanded content.

The digital edition of *AJNR* presents the print version in its entirety, along with extra features including:

- Publication Preview
- Case Collection
- Podcasts
- The *AJNR* News Digest
- The *AJNR* Blog

It also reaches subscribers much faster than print. An electronic table of contents will be sent directly to your mailbox to notify you as soon as it publishes.

Readers can search, reference, and bookmark current and archived content 24 hours a day on [www.ajnr.org](http://www.ajnr.org).

ASNR members who wish to opt out of print can do so by using the *AJNR* Go Green link on the *AJNR* Website (<http://www.ajnr.org/content/subscriber-help-and-services>). Just type your name in the email form to stop print and spare our ecosystem.

## Neuroform Atlas® Stent System

See package insert for complete indications, contraindications, warnings and instructions for use.

**Humanitarian Device.** Authorized by Federal law for use with neurovascular embolic coils in patients who are ≥ 18 years of age for the treatment of wide neck, intracranial, saccular aneurysms arising from a parent vessel with a diameter of 2 mm and ≤ 4.5 mm that are not amenable to treatment with surgical clipping. Wide neck aneurysms are defined as having a neck ≥ 4 mm or a dome-to-neck ratio < 2. The effectiveness of this device for this use has not been demonstrated.

### INDICATIONS FOR USE

The Neuroform Atlas® Stent System is indicated for use with neurovascular embolic coils in patients who are ≥ 18 years of age for the treatment of wide neck, intracranial, saccular aneurysms arising from a parent vessel with a diameter of 2 mm and ≤ 4.5 mm that are not amenable to treatment with surgical clipping. Wide neck aneurysms are defined as having a neck ≥ 4 mm or a dome-to-neck ratio of < 2.

### CONTRAINDICATIONS

Patients in whom antiplatelet and/or anticoagulation therapy is contraindicated.

### POTENTIAL ADVERSE EVENTS

The potential adverse events listed below, as well as others, may be associated with the use of the Neuroform Atlas® Stent System or with the procedure:  
Allergic reaction to nitinol metal and medications, Aneurysm perforation or rupture, Coil herniation through stent into parent vessel, Death, Embolus, Headache, Hemorrhage, In-stent stenosis, Infection, Ischemia, Neurological deficit/intracranial sequelae, Pseudoaneurysm, Stent fracture, Stent migration/embolization, Stent misplacement, Stent thrombosis, Stroke, Transient ischemic attack, Vasospasm, Vessel occlusion or closure, Vessel perforation/rupture, Vessel dissection, Vessel trauma or damage, Vessel thrombosis, Visual impairment, and other procedural complications including but not limited to anesthetic and contrast media risks, hypotension, hypertension, access site complications.

### WARNINGS

- Contents supplied STERILE using an ethylene oxide (EO) process. Do not use if sterile barrier is damaged. If damage is found, call your Stryker Neurovascular representative.
- For single use only. Do not reuse, reprocess or resterilize. Reuse, reprocessing or resterilization may compromise the structural integrity of the device and/or lead to device failure which, in turn, may result in patient injury, illness or death. Reuse, reprocessing or resterilization may also create a risk of contamination of the device and/or cause patient infection or cross-infection, including, but not limited to, the transmission of infectious diseases) from one patient to another. Contamination of the device may lead to injury, illness or death of the patient.
- After use, dispose of product and packaging in accordance with hospital, administrative and/or local government policy.
- This device should only be used by physicians who have received appropriate training in interventional neuroradiology or interventional radiology and practical training on the use of this device as established by Stryker Neurovascular.
- Select a stent size (length) to maintain a minimum of 4 mm on each side of the aneurysm neck along the parent vessel. An incorrectly sized stent may result in damage to the vessel or stent migration. Therefore, the stent is not designed to treat an aneurysm with a neck greater than 22 mm in length.
- If excessive resistance is encountered during the use of the Neuroform Atlas® Stent System or any of its components at any time during the procedure, discontinue use of the stent system. Continuing to move the stent system against resistance may result in damage to the vessel or a system component.
- Persons allergic to nickel titanium (Nitinol) may suffer an allergic response to this stent implant.
- Purge the system carefully to avoid the accidental introduction of air into the stent system.
- Confirm there are no air bubbles trapped anywhere in the stent system.

### CAUTIONS / PRECAUTIONS

- Federal Law (USA) restricts this device to sale by or on the order of a physician.
- Use the Neuroform Atlas Stent System prior to the "Use By" date printed on the package.
- Carefully inspect the stent package and Neuroform Atlas Stent System prior to use to verify that neither has been damaged during shipment. Do not use kinked or damaged components; contact your Stryker Neurovascular representative.
- The stent delivery microcatheter and the Neuroform Atlas Stent delivery wire should not be used to recapture the stent.
- Exercise caution when crossing the deployed stent with adjunctive devices.
- After deployment, the stent may foreshorten from up to 6.3%.
- The max OD of the coiling microcatheter should not exceed the max OD of the stent delivery microcatheter.
- Standard interventional devices with distal tips > 1.8 mm may not be able to pass through the interstices of the stent.
- Safety of the Neuroform Atlas Stent System in patients below the age of 18 has not been established.
- In cases where multiple aneurysms are to be treated, start at the most distal aneurysm first.

### MAGNETIC RESONANCE IMAGING (MRI)

#### Safety Information Magnetic Resonance Conditional

Non-clinical testing and analysis have demonstrated that the Neuroform Atlas Stent is MR Conditional, when tested with a second stent, and adjacent to a Stryker Neurovascular coil system. A patient with the Neuroform Atlas Stent can be safely scanned immediately after placement of this implant, under the following conditions:  
• Static magnetic field of 1.5 and 3.0 Tesla  
• Maximum spatial gradient field up to 2500 Gauss/cm (25 Tesla/m)  
• Maximum MRI system reported whole body averaged specific absorption rate of 2 W/kg (Normal Operating Mode) and head averaged specific absorption rate of 3.2 W/kg.

Under the scan conditions defined above, the Neuroform Atlas Stent is expected to produce a maximum temperature of 4°C after 15 minutes of continuous scanning. The Neuroform Atlas Stent should not migrate in this MRI environment.

In non-clinical testing, the image artifact caused by the device extends approximately 2 mm from the Neuroform Atlas Stent when imaged with a spin echo pulse sequence and 3 Tesla MRI system. The artifact may obscure the device lumen. It may be necessary to optimize MRI imaging parameters for the presence of this implant.

## Excelsior® XT-17™ Microcatheter

See package insert for complete indications, contraindications, warnings and instructions for use.

### INTENDED USE / INDICATIONS FOR USE

Stryker Neurovascular's Excelsior XT-17 Microcatheters are intended to assist in the delivery of diagnostic agents, such as contrast media, and therapeutic agents, such as occlusion coils, into the peripheral, coronary and neuro vasculature.

### CONTRAINDICATIONS

None known.

### POTENTIAL ADVERSE EVENTS

Potential adverse events associated with the use of microcatheters or with the endovascular procedures include, but are not limited to: access site complications, allergic reaction, aneurysm perforation, aneurysm rupture, death, embolism (air, foreign body, plate, thrombus), hematoma, hemorrhage, infection, ischemia, neurological deficits, pseudoaneurysm, stroke, transient ischemic attack, vasospasm, vessel dissection, vessel occlusion, vessel perforation, vessel rupture, vessel thrombosis

### WARNINGS

- The accessories are not intended for use inside the human body.
- Limited testing has been performed with solutions such as contrast media, saline and suspended embolic particles. The use of these microcatheters for delivery of solutions other than the types that have been tested for compatibility is not recommended. Do not use with glue or glue mixtures.
- Carefully inspect all devices prior to use. Verify shape, size and condition are suitable for the specific procedure.
- Exchange microcatheters frequently during lengthy procedures that require extensive guidewire manipulation or multiple guidewire exchanges.
- Never advance or withdraw an intravascular device against resistance until the cause of the resistance is determined by fluoroscopy. Movement of the microcatheter or guidewire against resistance could dislodge a clot, perforate a vessel wall, or damage microcatheter and guidewire. In severe cases, tip separation of the microcatheter or guidewire may occur.
- Contents supplied STERILE using an ethylene oxide (EO) process. Do not use if sterile barrier is damaged. If damage is found, call your Stryker Neurovascular representative.
- For single use only. Do not reuse, reprocess or resterilize. Reuse, reprocessing or resterilization may compromise the structural integrity of the device and/or lead to device failure which, in turn, may result in patient injury, illness or death of the patient.
- After use, dispose of product and packaging in accordance with hospital, administrative and/or local government policy.
- These devices are intended for use only by physicians trained in performing endovascular procedures.
- Inspect product before use for any bends, kinks or damage. Do not use a microcatheter that has been damaged. Damaged microcatheters may rupture causing vessel trauma or tip detachment during steering maneuvers.
- The shaping mandrel is not intended for use inside the human body.
- Discontinue use of microcatheter for infusion if increased resistance is noted. Resistance indicates possible blockage. Remove and replace blocked microcatheter immediately. DO NOT attempt to clear blockage by over-pressurization. Doing so may cause the microcatheter to rupture, resulting in vascular damage or patient injury.
- Do not exceed 2,070 kPa (300 psi) infusion pressure. Excessive pressure could dislodge a clot, causing thromboemboli, or could result in a ruptured microcatheter or severed tip, causing vessel injury.

### CAUTIONS / PRECAUTIONS

- To reduce the probability of coating damage in tortuous vasculature, use a guide catheter with a minimum internal diameter as specified in Table 1 above, and is recommended for use with Stryker Neurovascular hydrophilically coated microcatheters.
- To control the proper introduction, movement, positioning and removal of the microcatheter within the vascular system, users should employ standard clinical angiographic and fluoroscopic practices and techniques throughout the interventional procedure.
- Exercise care in handling of the microcatheter during a procedure to reduce the possibility of accidental breakage, bending or kinking.
- Use the product prior to the "Use By" date printed on the label.
- Limited testing indicates that Excelsior XT-17 Microcatheter is compatible with Dimethyl Sulfoxide (DMSO). The compatibility of Excelsior XT-17 Microcatheter with individual agents suspended in DMSO has not been established.
- Federal Law (USA) restricts this device to sale by or on the order of a physician.
- Wet dispenser coil or packaging tray and hydrophilically coated outer shaft of microcatheters prior to removal from packaging tray. Once the microcatheter has been wetted, do not allow to dry.
- The packaging mandrel is not intended for reuse. The packaging mandrel is not intended for use inside the human body.
- Check that all fittings are secure so that air is not introduced into guide catheter or microcatheter during continuous flush.
- In order to achieve optimal performance of Stryker Neurovascular Microcatheters and to maintain the lubricity of the Hydroflon® Coating surface, it is critical that a continuous flow of appropriate flush solution be maintained between the Stryker Neurovascular Microcatheter and guide catheter, and the microcatheter and any intraluminal device. In addition, flushing aids in preventing contrast crystal formation and/or clotting on both the intraluminal device and inside the guide catheter and/or the microcatheter lumen.
- Do not position microcatheter closer than 2.54 cm (1 in) from the steam source. Damage to the microcatheter may result.
- Excessive tightening of a hemostatic valve onto the microcatheter shaft may result in damage to the microcatheter. Removing the peel away introducer without a guidewire inserted in the microcatheter lumen might result in damage to the microcatheter shaft.
- To facilitate microcatheter handling, the proximal portion of the microcatheter does not have the hydrophilic surface. Greater resistance may be encountered when this section of the microcatheter is advanced into the RHV.

## Excelsior® SL-10® Microcatheter

See package insert for complete indications, contraindications, warnings and instructions for use.

### INTENDED USE / INDICATIONS FOR USE

Stryker Neurovascular's Excelsior SL-10 Microcatheter is intended to assist in the delivery of diagnostic agents, such as contrast media, and therapeutic agents, such as occlusion coils, into the peripheral, coronary, and neurovasculature.

### CONTRAINDICATIONS

None known.

### POTENTIAL ADVERSE EVENTS

Potential adverse events associated with the use of microcatheters or with the endovascular procedures include, but are not limited to: access site complications, allergic reaction, aneurysm perforation, aneurysm rupture, death, embolism (air, foreign body, plate, thrombus), hematoma, hemorrhage, infection, ischemia, neurological deficits, pseudoaneurysm, stroke, transient ischemic attack, vessel dissection, vessel occlusion, vessel perforation, vessel rupture, vessel thrombosis.

### WARNINGS

- Contents supplied STERILE using an ethylene oxide (EO) process. Do not use if sterile barrier is damaged. If damage is found, call your Stryker Neurovascular representative.
- For single patient use only. Do not reuse, reprocess or resterilize. Reuse, reprocessing or resterilization may compromise the structural integrity of the device and/or lead to device failure which, in turn, may result in patient injury, illness or death. Reuse, reprocessing or resterilization may also create a risk of contamination of the device and/or cause patient infection or cross-infection, including, but not limited to, the transmission of infectious diseases) from one patient to another. Contamination of the device may lead to injury, illness or death of the patient.
- After use, dispose of product and packaging in accordance with hospital, administrative and/or local government policy.
- These devices are intended for use only by physicians trained in performing endovascular procedures.
- Limited testing has been performed with solutions such as contrast media, saline and suspended embolic particles. The use of these catheters for delivery of solutions other than the types that have been tested for compatibility is not recommended. Do not use with glue or glue mixtures.
- The accessories are not intended for use inside the human body.
- Carefully inspect all devices prior to use. Verify shape, size and condition are suitable for the specific procedure.
- Exchange microcatheters frequently during lengthy procedures that require extensive guidewire manipulation or multiple guidewire exchanges.
- Never advance or withdraw an intravascular device against resistance until the cause of the resistance is determined by fluoroscopy. Movement of the microcatheter or guidewire against resistance could dislodge a clot, perforate a vessel wall, or damage microcatheter and guidewire. In severe cases, tip separation of the microcatheter or guidewire may occur.
- Inspect product before use for any bends, kinks or damage. Do not use a microcatheter that has been damaged. Damaged microcatheters may rupture causing vessel trauma or tip detachment during steering maneuvers.
- Shaping mandrel is not intended for use inside the human body.
- Discontinue use of microcatheter for infusion if increased resistance is noted. Resistance indicates possible blockage. Remove and replace blocked microcatheter immediately. DO NOT attempt to clear blockage by over-pressurization. Doing so may cause the microcatheter to rupture, resulting in vascular damage or patient injury.
- Do not exceed 2,070 kPa (300 psi) infusion pressure. Excessive pressure could dislodge a clot, causing thromboemboli, or could result in a ruptured microcatheter or severed tip, causing vessel injury.

### CAUTIONS / PRECAUTIONS

- Federal Law (USA) restricts this device to sale by or on the order of a physician.
- To facilitate microcatheter handling, the proximal portion of the microcatheter does not have the hydrophilic surface. Greater resistance may be encountered when this section of the microcatheter is advanced into the RHV.
- Exercise care in handling of the microcatheter during a procedure to reduce the possibility of accidental breakage, bending or kinking.
- To reduce the probability of coating damage in tortuous vasculature, use a guide catheter with a minimum internal diameter that is 1.02 mm (0.038 in) and is recommended for use with Stryker Neurovascular hydrophilically coated microcatheters.
- To control the proper introduction, movement, positioning and removal of the microcatheter within the vascular system, users should employ standard clinical angiographic and fluoroscopic practices and techniques throughout the interventional procedure.
- Flush dispenser coil of hydrophilically coated microcatheters prior to removal from dispenser coil. Once the microcatheter has been wetted, do not allow to dry. Do not reinsert the microcatheter into dispenser coil.
- Do not position microcatheter closer than 2.54 cm (1 in) from the steam source. Damage to the microcatheter may result.
- Check that all fittings are secure so that air is not introduced into guide catheter or microcatheter during continuous flush.
- In order to achieve optimal performance of Stryker Neurovascular Microcatheters and to maintain the lubricity of the Hydroflon® Coating surface, it is critical that a continuous flow of appropriate flush solution be maintained between the Stryker Neurovascular Microcatheter and guide catheter, and the microcatheter and any intraluminal device. In addition, flushing aids in preventing contrast crystal formation and/or clotting on both the intraluminal device and inside the guide catheter and/or the microcatheter lumen.
- Excessive tightening of a hemostatic valve onto the microcatheter shaft may result in damage to the microcatheter.



**Stryker Neurovascular**  
47900 Bayside Parkway  
Fremont, CA 94538

**strykerneurovascular.com**

Date of Release: FEB/2019

EX\_EN\_US

Copyright © 2019 Stryker

AP002413 v1.0 | Page 2 of 2

## Wingspan® Stent System with Gateway® PTA Balloon Catheter

### RX ONLY

See package insert for complete indications, contraindications, warnings and instructions for use.

**Humanitarian Device.** Authorized by Federal law for use in improving cerebral artery lumen diameter in patients 22 to 80 years old with recurrent (2 or more) strokes refractory to a comprehensive regimen of medical therapy and due to atherosclerotic disease of intracranial vessels with 70-95% stenosis that are accessible to the system. The most recent stroke must have occurred more than 7 days prior to treatment with the Wingspan Stent System. Patients are eligible for treatment with the Wingspan Stent System if their Modified Rankin Score (mRS) is 3 or less at the time of treatment. The effectiveness of this device for this use has not been demonstrated.

### INTENDED USE / INDICATIONS FOR USE

The Wingspan Stent System with Gateway PTA Balloon Catheter is Authorized by Federal law for use in improving cerebral artery lumen diameter in patients 22 to 80 years old with recurrent (2 or more) strokes refractory to a comprehensive regimen of medical therapy and due to atherosclerotic disease of intracranial vessels with 70-95% stenosis that are accessible to the system. The most recent stroke must have occurred more than 7 days prior to treatment with the Wingspan Stent System. Patients are eligible for treatment with the Wingspan Stent System if their Modified Rankin Score (mRS) is 3 or less at the time of treatment.

### CONTRAINDICATIONS

- Patients in whom antiplatelet and/or anticoagulation therapy is contraindicated.
- Lesions that are highly calcified or otherwise could prevent access or appropriate expansion of the Stent.
- For the treatment of stroke with an onset of symptoms within 7 days of less of treatment.
- For the treatment of transient ischemic attacks.

### OBSERVED ADVERSE EVENTS

A clinical study was conducted on 45 patients with intracranial atherosclerotic disease at 12 international sites. Data are presented for 44 patients. 39 days are data on 42 patients who have reached the 6-month follow-up visit. The following adverse events observed in the clinical study: Infection, TIA, Stroke, Hematoma, Vasospasm, Hemorrhage, Event, Hypertension, Peripheral vascular diseases, Neurological symptoms, Pain, AMI, Angina, Arrhythmia, Creatinine increase, Hematuria, Hypoglycemia/Hyperglycemia, Asymptomatic Thromboembolic Event, Bradycardia (25 mm), Broken middle-foot left/R-fracture, Cholelithiasis, Chronic antral gastritis, Death, Elevated bilirubin, GOT, GPT, Fever, Histiis hernia, Hypertension, New distal in-stent stenosis.

Pulmonary edema, Respiratory failure, Seizure, Syncope.

### POTENTIAL ADVERSE EVENTS

Potential adverse events that were not observed in the clinical study, but that may be associated with the use of the Wingspan Stent System with Gateway PTA Balloon catheter or with the procedure include: aneurysm, cerebral ischemia, coagulopathy, drug reaction to contrast or antiplatelet medication, emboli (air, tissue, or thrombotic), tissue), hypotension, intimal dissection, ischemia/infarct, restenosis, pseudoaneurysm, stent migration, stent misplacement, stent occlusion, stent thrombosis, stroke, transient ischemic attack, vessel dissection, vessel perforation, vessel rupture, vessel spasm, vessel thrombosis, vessel trauma requiring surgical repair or intervention.

### WARNINGS

Contents supplied STERILE using an ethylene oxide (EO) process. Do not use if sterile barrier is damaged. If damage is found, call your Stryker Neurovascular representative. For single use only. Do not reuse, reprocess or resterilize. Reuse, reprocessing or resterilization may compromise the structural integrity of the device and/or lead to device failure which, in turn, may result in patient injury, illness or death. Reuse, reprocessing or resterilization may also create a risk of contamination of the device and/or cause patient infection or cross-infection, including, but not limited to, the transmission of infectious diseases) from one patient to another. Contamination of the device may lead to injury, illness or death of the patient. After use, dispose of product and packaging in accordance with hospital, administrative and/or local government policy. The Wingspan Stent System is not designed or intended for contrast injections or injections other than hyperosmolar saline. If excessive resistance is encountered during the use of the Wingspan Stent System or with the Gateway PTA Balloon Catheter at any time during the procedure, discontinue use of the System. Movement of the System against resistance may result in damage to the vessel, or a System component. In animal evaluations, the severity of vessel stenosis/neointimal thickness appears to be correlated with the degree of trauma inflicted on the arterial walls by Stent placement or Stent radial expansion. Experience with stent implants indicates that there is a risk of restenosis. Subsequent restenosis may require repeat dilation of the vessel segment containing the stent. The risks and long-term outcome following repeat dilation of endothelialized stents is unknown at present. If the stent is implanted adjacent to or contacting other implanted metal, such as another stent or embolic coil, the metals should be of similar composition to avoid galvanic corrosion potential.

The safety and probable benefits of the Wingspan Stent System with Gateway PTA Balloon Catheter have not been established for treatment of patients with any of the following:

- New or unstable symptoms within 24 hours of treatment;
- Evidence on brain imaging study of subacute or acute ischemia in the vascular territory of the target lesion;
- A recent stroke of a size that would place the patient at risk for intracranial hemorrhage;
- Thrombolytic therapy within 24 hours prior to treatment with the device;
- The cause of the target stenosis is not atherosclerotic;
- The normal diameter of the target vessel is not between 2.00 and 4.50 mm;
- A target lesion length greater than 14 mm;
- Severe calcification at the target lesion;
- A minimum lumen diameter of the target vessel of less than 2 mm after pre-dilation;
- Greater than 50% stenosis proximal or distal to the target intracranial lesion;
- A previous intracerebral or intracranial hemorrhage or a recent hemorrhagic infarction

### CAUTIONS / PRECAUTIONS

#### General Precautions

- The Wingspan Stent System and the Gateway PTA Balloon Catheter are provided STERILE for single use only. Do not resterilize. Store in a cool, dry place.
- Use the Wingspan Stent System and Gateway PTA Balloon Catheter prior to the "Use By" date printed on the package.
- Select a Stent size (length and diameter) that extends a minimum of 3 mm on both sides of the lesion.

#### Preparation Precautions

- Carefully inspect the sterile package and Wingspan Stent System prior to use to verify that neither has been damaged during shipment. Do not use kinked or damaged components.
- Typical antiplatelet and anticoagulation regimen used for interventional intracranial procedures is an important adjunct to Stent treatment. Patients should be advised to take their prescribed medications after the Stent is implanted and should be counseled on the risk of not complying with medical therapy. In-stent thrombosis may occur during the procedure if proper antiplatelet and anticoagulation therapy is not administered.
- Do not steam shape the tip of the Wingspan Stent System because it could damage the Stent or Delivery System.
- Do not use the Wingspan Stent System with antiplatelet and anti-clotting therapy (dose, type, and timing) regimen and intra-procedural anti-clotting agents is required to minimize potential post procedure complications.

#### PROCEDURE PRECAUTIONS

- Implanting a Stent may lead to dissection of the vessel distal or proximal to the Stent and may cause other complications (vasospasm/acute closure) of the vessel requiring additional intervention (i.e., further dilation, placement of stents).
- Do not deploy the Stent if it is not properly positioned in the vessel.
- Placement of the Stent may compromise side branch patency.
- Follow the Wingspan Stent System preparation and use instructions carefully.
- Previous studies have shown that some metal stents may be incompatible with MRI scanning. The Wingspan Stent has been shown to be MRI compatible in MRI systems operating at field strengths of 3.0 Tesla or lower. MRI laboratory evaluation demonstrated that no significant image distortion or heating was created by the presence of the Stents at scanning sequences commonly used during MRI procedures.
- Do not use the Wingspan Stent System or the Gateway PTA Balloon Catheter for repositioning or recapturing the Stent.
- Exercise caution when crossing the deployed Stent with guidewires or other devices.
- In tortuous vessels, a stiff guidewire may cause bending within the Wingspan® Stent System or the Gateway® Balloon Catheter during deployment. In such cases, use only soft guidewires.
- After deployment, the Stent may foreshorten up to 2.4% in 2.5 mm Stents and up to 7.1% in 4.5 mm Stents.
- Start retrieval methods (use of additional wires, snares and/or forceps) may result in additional trauma to the vasculature and/or the vascular access site. Complications may include bleeding, hematoma, or pseudoaneurysm.



**Stryker Neurovascular**  
47900 Bayside Parkway  
Fremont, CA 94538

**strykerneurovascular.com**

Date of Release: MAR/2019

EX\_EN\_US

Copyright © 2019 Stryker

AP002469 v3.0 | Page 2 of 2

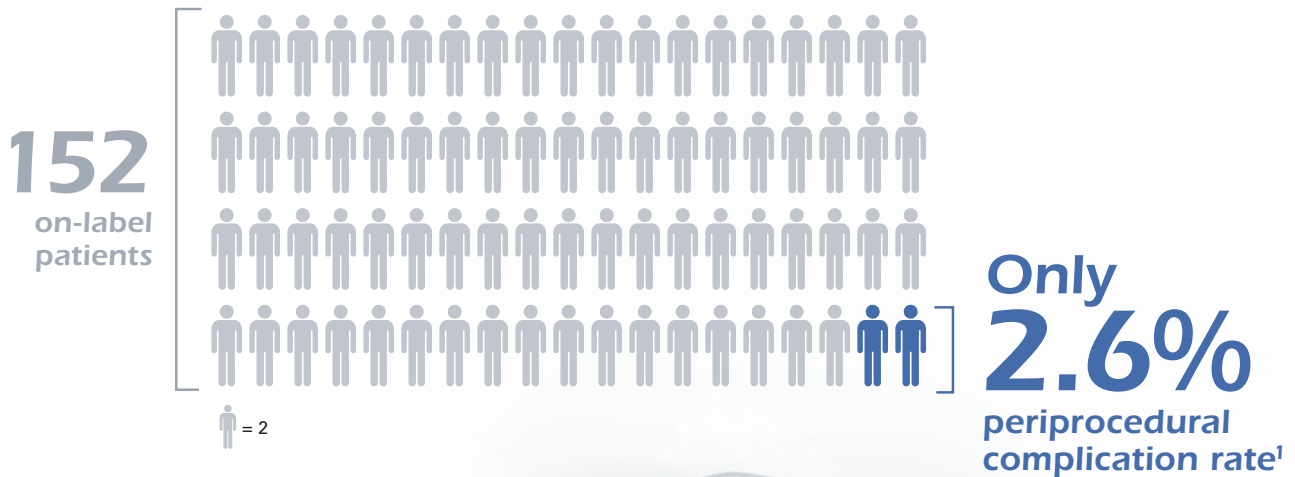
# WEAVE TRIAL

Wingspan StEnt System Post MArket SurVEillance Study

powered by

Wingspan Stent System and  
Gateway PTA Balloon Catheter

## Demonstrated positive results for ICAD treatment



Wingspan Stent System with Gateway PTA Balloon Catheter is authorized under a Humanitarian Device Exemption (HDE). IRB approval is required prior to use.

1. Alexander MJ, et al. *Stroke*. doi: 10.1161/STROKEAHA.118.023996. [Published online ahead of print February 28, 2019.]

**Wingspan**<sup>®</sup>  
STENT SYSTEM

**Gateway**<sup>®</sup>  
PTA BALLOON CATHETER

# AJNR

## AMERICAN JOURNAL OF NEURORADIOLOGY

JUNE 2019  
VOLUME 40  
NUMBER 6  
WWW.AJNR.ORG

Publication Preview at [www.ajnr.org](http://www.ajnr.org) features articles released in advance of print. Visit [www.ajnrblog.org](http://www.ajnrblog.org) to comment on AJNR content and chat with colleagues and AJNR's News Digest at <http://ajnrdigest.org> to read the stories behind the latest research in neuroimaging.

927 **PERSPECTIVES** *A. Elgendy*

### REVIEW ARTICLE

-   928 **Texture Analysis in Cerebral Gliomas: A Review of the Literature** **ADULT BRAIN**  
*N. Soni, et al.*

### SOCIAL MEDIA VIGNETTE

- 935 **The Continued Rise in Professional Use of Social Media at Scientific Meetings: An Analysis of Twitter Use during the ASNR 2018 Annual Meeting** *G. D'Anna, et al.*

### GENERAL CONTENTS

-     938 **Ensemble of Convolutional Neural Networks Improves Automated Segmentation of Acute Ischemic Lesions Using Multiparametric Diffusion-Weighted MRI** **ADULT BRAIN**  
*S. Winzeck, et al.*
-   946 **A Novel Collateral Imaging Method Derived from Time-Resolved Dynamic Contrast-Enhanced MR Angiography in Acute Ischemic Stroke: A Pilot Study** **ADULT BRAIN**  
*H.G. Roh, et al.*
-   954 **Diagnostic Accuracy of High-Resolution Black-Blood MRI in the Evaluation of Intracranial Large-Vessel Arterial Occlusions** **ADULT BRAIN**  
*A.S. Al-Smadi, et al.*
-     960 **Surveillance of Unruptured Intracranial Saccular Aneurysms Using Noncontrast 3D-Black-Blood MRI: Comparison of 3D-TOF and Contrast-Enhanced MRA with 3D-DSA** **ADULT BRAIN**  
**INTERVENTIONAL**  
*C. Zhu, et al.*
-  967 **Baseline and Evolutionary Radiologic Features in Sporadic, Hemorrhagic Brain Cavernous Malformations** **ADULT BRAIN**  
*K.D. Flemming, et al.*
-  973 **The Occipital Emissary Vein: A Possible Marker for Pseudotumor Cerebri** **ADULT BRAIN**  
*A. Hedjoudje, et al.*
-   979 **Association between Tumor Acidity and Hypervascularity in Human Gliomas Using pH-Weighted Amine Chemical Exchange Saturation Transfer Echo-Planar Imaging and Dynamic Susceptibility Contrast Perfusion MRI at 3T** **ADULT BRAIN**  
**FUNCTIONAL**  
*Y.-L. Wang, et al.*
-  987 **Quantitative Susceptibility Mapping of Time-Dependent Susceptibility Changes in Multiple Sclerosis Lesions** **ADULT BRAIN**  
*S. Zhang, et al.*

-    994 **Susceptibility-Weighted MR Imaging Hypointense Rim in Progressive Multifocal Leukoencephalopathy: The End Point of Neuroinflammation and a Potential Outcome Predictor** *M.M. Thurnher, et al.* **ADULT BRAIN**
-   1001 **Thrombectomy with Conscious Sedation Compared with General Anesthesia: A DEFUSE 3 Analysis** *C.J. Powers, et al.* **INTERVENTIONAL**
-    1006 **First-Line Sofia Aspiration Thrombectomy Approach within the Endovascular Treatment of Ischemic Stroke Multicentric Registry: Efficacy, Safety, and Predictive Factors of Success** *G. Marnat, et al.* **INTERVENTIONAL**
- 1013 **Current Hospital Demographics of Subarachnoid Hemorrhage Based on CT Angiography and 3D Rotational Angiography in a Neurosurgical Center** *S.B.T. van Rooij, et al.* **INTERVENTIONAL ADULT BRAIN**
-  1018 **Histologic and Biomolecular Similarities in Healing between Aneurysms and Cutaneous Skin Wounds** *J.R. Ayers-Ringler, et al.* **INTERVENTIONAL**
-  1022 **An Ultrasonographic Multiparametric Carotid Plaque Risk Index Associated with Cerebrovascular Symptomatology: A Study Comparing Color Doppler Imaging and Contrast-Enhanced Ultrasonography** *V. Rafailidis, et al.* **EXTRACRANIAL VASCULAR**
-  1029 **Dynamic Contrast-Enhanced MRI to Differentiate Parotid Neoplasms Using Golden-Angle Radial Sparse Parallel Imaging** *J.L. Mogen, et al.* **HEAD & NECK**
- 1037 **Localization of Parotid Gland Tumors in Relation to the Intraparotid Facial Nerve on 3D Double-Echo Steady-State with Water Excitation Sequence** *H. Fujii, et al.* **HEAD & NECK**
- 1043 **Evaluating the Utility of a Postprocessing Algorithm for MRI Evaluation of Optic Neuritis** *L. Stunkel, et al.* **HEAD & NECK**
-  1049 **A Scoring System for Prediction of Cervical Lymph Node Metastasis in Patients with Head and Neck Squamous Cell Carcinoma** *M.S. Chung, et al.* **HEAD & NECK**
-  1055 **Readout-Segmented Echo-Planar DWI for the Detection of Cholesteatomas: Correlation with Surgical Validation** *N. Fischer, et al.* **HEAD & NECK**
-   1060 **Radiologic and Pathologic Features of the Transmantle Sign in Focal Cortical Dysplasia: The T1 Signal Is Useful for Differentiating Subtypes** *Y. Kimura, et al.* **PEDIATRICS**
- 1067 **Radiation Dose and Image Quality in Pediatric Neck CT** *S.V. Tipnis, et al.* **PEDIATRICS**
-   1074 **Deep Learning-Based Automatic Segmentation of Lumbosacral Nerves on CT for Spinal Intervention: A Translational Study** *G. Fan, et al.* **SPINE**

## ONLINE FEATURES

### LETTERS

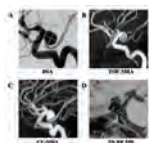
- E26 **Vessel Wall Imaging of Unruptured Intracranial Aneurysms: Ready for Prime Time? Not so Fast!** *V.T. Lehman, et al.*
- E30 **Patients with High-Grade Gliomas and Café-au-Lait Macules: Is Neurofibromatosis Type 1 the Only Diagnosis?** *L. Guerrini-Rousseau, et al.*
- E32 **Reply** *N. Kadom, et al.*

### E33 ERRATUM

## BOOK REVIEWS

*R.M. Quencer, Section Editor*

Please visit [www.ajnrblog.org](http://www.ajnrblog.org) to read and comment on Book Reviews.



Right posterior communicating artery aneurysm on DSA (A), TOF-MRA (B), CE-MRA (C), and 3D-black-blood MR imaging (D). 3D black-blood MR imaging achieved better accuracy for aneurysm size measurements compared with 3D-TOF, using 3D rotational angiography as a criterion standard.

 Indicates Editor's Choices selection

 Indicates Fellows' Journal Club selection

 Indicates open access to non-subscribers at [www.ajnr.org](http://www.ajnr.org)

 Indicates article with supplemental on-line table

 Indicates article with supplemental on-line photo

 Indicates article with supplemental on-line video

 Evidence-Based Medicine Level 1

 Evidence-Based Medicine Level 2

### Official Journal:

American Society of Neuroradiology  
 American Society of Functional Neuroradiology  
 American Society of Head and Neck Radiology  
 American Society of Pediatric Neuroradiology  
 American Society of Spine Radiology

### EDITOR-IN-CHIEF

#### Jeffrey S. Ross, MD

Professor of Radiology, Department of Radiology,  
 Mayo Clinic College of Medicine, Phoenix, AZ

### SENIOR EDITORS

#### Harry J. Cloft, MD, PhD

Professor of Radiology and Neurosurgery,  
 Department of Radiology, Mayo Clinic College of  
 Medicine, Rochester, MN

#### Thierry A.G.M. Huisman, MD

Radiologist-in-Chief, Texas Children's Hospital,  
 Houston, TX

#### Yvonne W. Lui, MD

Associate Professor of Radiology,  
 Chief of Neuroradiology,  
 New York University School of Medicine,  
 New York, NY

#### C.D. Phillips, MD, FACR

Professor of Radiology, Weill Cornell Medical  
 College, Director of Head and Neck Imaging,  
 New York-Presbyterian Hospital, New York, NY

#### Lubdhra M. Shah, MD

Associate Professor of Radiology and Director of  
 Spine Imaging, University of Utah Department of  
 Radiology and Imaging Sciences, Salt Lake City, UT

#### Charles M. Strother, MD

Professor of Radiology, Emeritus, University of  
 Wisconsin, Madison, WI

### STATISTICAL SENIOR EDITOR

#### Bryan A. Comstock, MS

Senior Biostatistician,  
 Department of Biostatistics,  
 University of Washington, Seattle, WA

### ARTIFICIAL INTELLIGENCE DEPUTY EDITOR

#### Christopher G. Filippi, MD

Professor and Vice Chair of Biomedical and  
 Translational Science,  
 Donald and Barbara Zucker School of Medicine at  
 Hofstra/Northwell,  
 Lenox Hill Hospital and Greenwich Village  
 Healthplex, New York, NY

### EDITORIAL BOARD

Ashley H. Aiken, Atlanta, GA  
 Lea M. Alhilali, Phoenix, AZ  
 Kubilay Aydin, Istanbul, Turkey  
 John D. Barr, Dallas, TX  
 Ari Blitz, Baltimore, MD  
 Barton F. Branstetter IV, Pittsburgh, PA  
 Jonathan L. Brisman, Lake Success, NY  
 Keith Cauley, Danville, PA  
 James Y. Chen, San Diego, CA  
 Asim F. Choudhri, Memphis, TN  
 Daniel Chow, Irvine, CA  
 J. Matthew Debnam, Houston, TX  
 Seena Dehkharghani, New York, NY  
 Yonghong Ding, Rochester, MN  
 Clifford J. Eskey, Hanover, NH  
 Saeed Fakhran, Phoenix, AZ  
 Massimo Filippi, Milan, Italy  
 Reza Forghani, Montreal, Quebec, Canada  
 Nils D. Forkert, Calgary, Alberta, Canada  
 Wende N. Gibbs, Los Angeles, CA  
 Christine M. Glastonbury, San Francisco, CA  
 John L. Go, Los Angeles, CA  
 Philipp Göllitz, Erlangen, Germany  
 Allison Grayev, Madison, WI  
 Brent Griffith, Detroit, MI  
 Ajay Gupta, New York, NY  
 Rakesh Kumar Gupta, Haryana, India  
 Lotfi Hacein-Bey, Sacramento, CA  
 Christopher P. Hess, San Francisco, CA  
 Andrei Holodny, New York, NY  
 Benjamin Huang, Chapel Hill, NC  
 Mahesh V. Jayaraman, Providence, RI  
 Valerie Jewells, Chapel Hill, NC  
 Christof Karmonik, Houston, TX  
 Timothy J. Kaufmann, Rochester, MN  
 Hillary R. Kelly, Boston, MA  
 Toshibumi Kinoshita, Akita, Japan  
 Kenneth F. Layton, Dallas, TX  
 Alexander Lerner, Los Angeles, CA  
 Michael Lev, Boston, MA  
 Karl-Olof Lovblad, Geneva, Switzerland  
 Franklin A. Marden, Chicago, IL  
 Joseph C. McGowan, Merion Station, PA  
 Stephan Meckel, Freiburg, Germany  
 Christopher J. Moran, St. Louis, MO  
 Takahisa Mori, Kamakura City, Japan  
 Suresh Mukherji, Ann Arbor, MI  
 Alexander J. Nemeth, Chicago, IL  
 Renato Hoffmann Nunes, Sao Paulo, Brazil  
 Sasan Partovi, Cleveland, OH  
 Laurent Pierot, Reims, France  
 Jay J. Pillai, Baltimore, MD  
 Whitney B. Pope, Los Angeles, CA  
 Joana Ramalho, Lisbon, Portugal  
 Otto Rapalino, Boston, MA

Álex Rovira-Cañellas, Barcelona, Spain  
 Paul M. Ruggieri, Cleveland, OH  
 Amit M. Saindane, Atlanta, GA  
 Erin Simon Schwartz, Philadelphia, PA  
 Maksim Shapiro, New York, NY  
 Timothy Shepherd, New York, NY  
 Mark S. Shiroishi, Los Angeles, CA  
 Bruno P. Soares, Baltimore, MD  
 Maria Vittoria Spampinato, Charleston, SC  
 Khin Khin Tha, Sapporo, Hokkaido, Japan  
 Krishnamoorthy Thamburaj, Hershey, PA  
 Cheng Hong Toh, Taipei, Taiwan  
 Aquilla S. Turk, Greenville, SC  
 Anja G. van der Kolk, Utrecht, the Netherlands  
 Willem Jan van Rooij, Tilburg, Netherlands  
 Arastoo Vossough, Philadelphia, PA  
 Elysa Widjaja, Toronto, Ontario, Canada  
 Max Wintermark, Stanford, CA  
 Ronald L. Wolf, Philadelphia, PA  
 Kei Yamada, Kyoto, Japan  
 Carlos Zamora, Chapel Hill, NC  
 Vahe M. Zohrabian, New Haven, CT

### EDITORIAL FELLOW

Alireza Radmanesh, New York, NY

### SPECIAL CONSULTANTS TO THE EDITOR

#### AJNR Blog Editor

Neil Lall, Denver, CO

#### Case of the Month Editor

Nicholas Stence, Aurora, CO

#### Case of the Week Editors

Juan Pablo Cruz, Santiago, Chile  
 Sapna Rawal, Toronto, Ontario, Canada

#### Classic Case Editor

Sandy Cheng-Yu Chen, Taipei, Taiwan

#### Health Care and Socioeconomics Editor

Pina C. Sanelli, New York, NY

#### Physics Editor

Greg Zaharchuk, Stanford, CA

#### Podcast Editor

Wende N. Gibbs, Los Angeles, CA

#### Twitter Editor

Jennifer McCarty, Houston, TX

Founding Editor  
 Juan M. Taveras

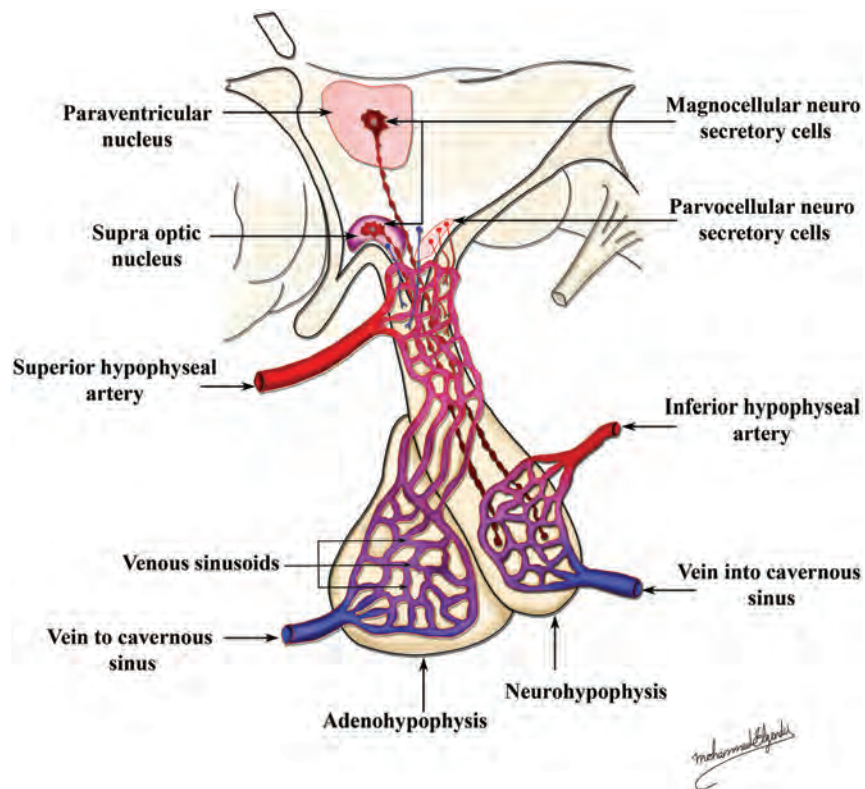
Editors Emeriti  
 Mauricio Castillo, Robert I. Grossman,  
 Michael S. Huckman, Robert M. Quencer

Managing Editor  
 Karen Halm

Assistant Managing Editor  
 Laura Wilhelm

Communications Coordinator  
 Rebecca Artz

Executive Director, ASNIR  
 Mary Beth Hepp



Title: Pituitary Gland. This image was created using Adobe Photoshop. My reference was the neuroanatomy textbook by Alvin Burt (Burt AM. *Textbook of Neuroanatomy*. Philadelphia: Saunders; 1993). This image was part of a print poster about tween brain that I presented at the ASNR meeting in Chicago in 2015.

Azza Elgandy, MD, Research Fellow, Children's Hospital of University of Pittsburgh Medical Center, Pittsburgh, Pennsylvania

# Texture Analysis in Cerebral Gliomas: A Review of the Literature

 N. Soni,  S. Priya, and  G. Bathla



## ABSTRACT

**SUMMARY:** Texture analysis is a continuously evolving, noninvasive radiomics technique to quantify macroscopic tissue heterogeneity indirectly linked to microscopic tissue heterogeneity beyond human visual perception. In recent years, systemic oncologic applications of texture analysis have been increasingly explored. Here we discuss the basic concepts and methodologies of texture analysis, along with a review of various MR imaging texture analysis applications in glioma imaging. We also discuss MR imaging texture analysis limitations and the technical challenges that impede its widespread clinical implementation. With continued advancement in computational processing, MR imaging texture analysis could potentially develop into a valuable clinical tool in routine oncologic imaging.

**ABBREVIATIONS:** AUC = area under the curve; CE = contrast-enhanced; GLCM = gray-level co-occurrence matrix; GLRLM = gray-level run-length matrix; HGG = high-grade glioma; IDH = isocitrate dehydrogenase; IDM = inverse difference moment; LGG = low-grade glioma; MRTA = MR imaging texture analysis; PCNSL = primary central nervous system lymphoma; PCA = principal component analysis; SVM = support vector machine; TA = texture analysis

**G**liomas are central nervous system tumors of glial origin, with glioblastoma being the most common and aggressive subtype, having a median survival of 14.5 months and 10% survival at 5 years.<sup>1</sup> Despite advanced imaging, accurate noninvasive prediction of glioma grade, survival, molecular status, and treatment response remains challenging. Brain biopsy remains the reference standard for histologic and genetic classification, but it is invasive and costly.<sup>2</sup> Additionally, the inherently high molecular heterogeneity in gliomas may decrease the accuracy and prognostic value of stereotactic biopsy diagnosis. Moreover, despite stereotactic biopsy, the pathologic diagnosis may remain inconclusive in about 7%–15% of patients.<sup>3,4</sup> This scenario necessitates preoperative identification of imaging surrogates to accurately assess global tumor heterogeneity and predict glioma grade, genetic milieu, and survival.<sup>5</sup>

Even though multiparametric MR imaging features show significant agreement in terms of morphologic features, some of which are strongly associated with poor survival, the accuracy of

these imaging variables to predict genetic heterogeneity and prognosis is rather limited.<sup>6,7</sup> Similarly, advanced MR imaging techniques such as diffusion, perfusion, and MR spectroscopy have also been beneficial, but with modest success.<sup>8</sup> Texture analysis (TA) is a noninvasive method to quantify macroscopic tissue heterogeneity indirectly linked to microscopic tissue heterogeneity. Recently, MR imaging texture analysis (MRTA)-based studies have shown promise in predicting glioma grade, survival, molecular status, and response assessment. However, despite the continued work, consensus on the clinical role of MRTA remains elusive. Here we review the basic concepts behind MRTA, its applications in glioma imaging, its limitations, current challenges, and potential future directions.

## MRTA: Concepts and Methodology

Texture, according to Merriam-Webster.com, is defined as “something composed of closely interwoven elements,” just as the structure formed by threads of a fabric identifies its character.<sup>9</sup> Similarly, an image texture is a representation of pixel intensities, their distribution, and their interrelationships, which may or may not be discernible to the human eye. TA noninvasively measures tumor heterogeneity (through parameters like kurtosis, entropy, and pixel distribution that potentially correlate with cellular density, angiogenesis, and necrosis) and may better predict tumor biology.<sup>10,11</sup>

The workflow of MRTA is represented in the Figure.

Acquisition parameters such as magnet strength, spatial resolution, signal-to-noise ratio, and different pulse sequences may

Received February 9, 2019; accepted after revision April 22.

From the Department of Radiology, University of Iowa Hospitals and Clinics, Iowa City, Iowa.

Sarv Priya and Neetu Soni share equal first authorship.

Please address correspondence to Sarv Priya, MD, Department of Radiology, 3978 JPP, University of Iowa Hospitals and Clinics, Iowa City, IA, 52242; e-mail: sarv-priya@uiowa.edu; @sarvpriya1985

 Indicates open access to non-subscribers at [www.ajnr.org](http://www.ajnr.org)

 Indicates article with supplemental on-line tables.

<http://dx.doi.org/10.3174/ajnr.A6075>



**FIGURE.** The workflow of MRTA.

influence MRTA features.<sup>12</sup> Most interesting, however, variations in these parameters can provide supplementary texture information, an added advantage of MR imaging over other imaging modalities.<sup>13</sup> Postacquisition, an image undergoes preprocessing, which generally involves segmentation, image interpolation, intensity normalization, gray-level reduction, magnetic field inhomogeneity correction, and filtration. Performance of all these steps except segmentation is not a requirement for TA but helps enhance texture features and maintains uniformity and standardization.

Preprocessing steps can be performed on both open-source and commercially available software. The first step, segmentation, involves drawing an ROI manually or automatically either on a single 2D slice (or multiple slices) or a 3D-VOI.<sup>14</sup> Next, to improve matrix resolution, interpolation is applied for which images are remapped to isotropic spacing to standardize the TA in all 3 directions. Furthermore, interpolation transforms the image into a higher matrix size and improves texture classification.<sup>15</sup>

Different MR imaging sequences have various ranges of intensities for the same image. This feature is addressed through intensity normalization, which extends the gray-level distribution of each MR image to the whole value range (0–255). It enhances the contrast between the tumor and background tissues and is achieved by either remapping the brightness to minimum or maximum value in the histogram, using mean  $\pm$  3 SD, or by using the histogram range between the first and the 99th percentile of the gray-scale image.

The undesirable effect of magnetic susceptibility on image texture can also be modified by use of the filtration process.<sup>16</sup> Filtration can also be applied to derive new maps that individually extract and enhance subtle features otherwise lost while analyzing the original conventional image—that is, it converts an image into different anatomic scales varying from 2 mm (fine features), 3–5 mm (medium features), and 6 mm (coarse features). Furthermore, gray-level reduction is essential in the computation of gray-level matrices because TA can be computed on 16, 32, 64, 128, or 256 levels and actual MR imaging ranges up to 1024 levels.<sup>16</sup> Because increasing the number of gray levels makes them computationally extensive without an added advantage, gray-level matrices are therefore computed at 5 or 6 bits per pixel.<sup>17</sup>

Feature extraction is the next step and includes agnostic and semantic features. Semantic features include shape, necrosis, vascularity, location, and speculation, and these can be quantified as well. Hundreds of features can be computed from available MRTA software.<sup>18</sup> To overcome the issue of redundancy and overfitting that may be seen with multiple extracted features, several classifier models—Fischer coefficient, principal component analysis (PCA), linear/nonlinear discriminant analysis, regression models, support vector machine (SVM) with recursive feature elimination, artificial neural network, and random forest classifiers—are used as well as application of statistical methods to reduce the false discovery rate. These models extract the features that have the best discriminative power.<sup>19</sup> Alternately, unsuper-

vised deep learning models can also be used to agnostically generate discriminating texture features. This obviates generating thousands of random texture features and subsequent optimal feature selection as described above.

### Types of TA

At present, statistical-, structural-, transform-, and spectral-based TAs are the most common agnostic methods used. Statistical-based TA depends on the pixel values, distribution, and spatial interrelationship in the defined ROI.<sup>20</sup>

First-order statistical TA is a histogram representation of image intensities in a predefined ROI and calculates mean, median, percentile, SD, skewness entropy, uniformity, and kurtosis. Mean is a measure of central tendency (average brightness), SD depicts dispersion from the mean, skewness reflects asymmetry of the histogram, kurtosis depicts the pointedness of the histogram (visual contrast), and entropy reflects the irregularity of the image-intensity distribution. The more heterogeneous the tumor, the higher the entropy is.<sup>20</sup>

Second-order or higher order statistical TA quantifies the image pattern on the basis of the spatial relationship or co-occurrence of the pixel value. It consists of several methods, including the 2 most common ones: gray-level co-occurrence matrix (GLCM) and gray-level run-length matrix (GLRLM). The GLCM measures the frequency of pixel pair distribution at a predefined distance,<sup>21</sup> usually measured in 4 directions (0°, 45°, 90°, and 135°) for 2D and in 13 directions for 3D.<sup>14</sup> GLCM features include homogeneity, inverse difference moment (IDM), dissimilarity, correlation, energy, and entropy. GLRLM observes the run of a specific pixel value over a chosen direction and consists of gray-level nonuniformity, run-length nonuniformity, short-run emphasis, and long-run emphasis. Both GLCM and GLRLM are calculated in different directions and averaged to make them rotationally invariant. GLCM may be measured over different pixel distances (for example, from 1 to 5), and similarly, GLRLM is computed over different run lengths to compute different texture features from the same ROI. GLCM and GLRLM over short distance and run provide fine texture, and over longer distance and run provide coarse texture. Different texture features can also be calculated in statistical methods by application of filters such as bandpass or nonorthogonal wavelet transform, which allow extraction of fine ( $\leq$  2 mm), medium (3–5 mm), and coarse texture ( $>$  6 mm) using different filter values.<sup>22</sup>

Local binary patterns have high discriminative power and calculate the pixel value by comparing it with neighboring pixels and then assigning a binary value. Other higher order statistics include busyness, coarseness, and contrast, which calculate the spatial relationship among  $\geq$  3 gray-level pixel values.<sup>16</sup>

Structural (model-based) methods such as fractal analysis provide information about the self-symmetry of the objects. These are computationally extensive and less preferred. Spectral methods include wavelet, Gabor, and Fourier transforms and are based on transforming the spatial information of the image into spatial frequencies.<sup>22</sup>

In general, the first- and second-order statistical methods are used most commonly. First-order statistical methods provide global information, and second-order statistical methods provide

additional information regarding the transition among pixel values. An important consideration is that 2 different tumors may have similar distribution of intensities but may differ in their spatial interrelationship; thus, histogram TA may be limited in such a setting. Second-order statistical TA may be preferable, especially for markedly heterogeneous tumors.<sup>23,24</sup>

### **MRTA Applications in Glioma Imaging**

MRTA applications in gliomas are an active area of research, and multiple reports have shown promising results (On-line Tables 1–4). For the sake of simplicity, we have condensed various studies into 4 broad categories: MRTA for glioma grading, predicting survival, glioma radiogenomics, and a miscellaneous category of studies differentiating gliomas from other CNS tumors and assessing treatment changes.

### **Glioma Grading**

The World Health Organization classifies gliomas as low grade (I and II) and high grade (III and IV).<sup>25</sup> Pretherapy determination of glioma grade can help optimize treatment strategy, predicting therapeutic response, prognosis, and survival.<sup>10,26</sup> On-line Table 1 summarizes prior studies evaluating MRTA for glioma grading.<sup>2,10,27–32</sup> Some of these are briefly discussed below. In general, most studies used either ADC maps, T1-contrast-enhanced (CE) MR imaging, or a multiparametric technique along with a transform statistical (filtration-histogram) technique or purely statistical (first- or second-order) TA. Despite variabilities in TA software, entropy values of the ADC maps consistently showed promising results for differentiating low-grade gliomas (LGGs) from high-grade gliomas (HGGs). Skogen et al<sup>29</sup> performed histogram-based TA in 95 patients using CE-MR images and found SD parameters at a fine texture highly significant (area under the curve [AUC], 0.910) in distinguishing LGGs from HGGs. Tian et al<sup>30</sup> performed multiparametric TA in 153 patients (grades II–IV) using an SVM classifier model. They reported 98% accuracy of MRTA features for glioma grading. They also observed that while multiparametric TA performed better in comparison with single-sequence TA, T1-CE was the best single sequence. Xie et al<sup>31</sup> observed that entropy (AUC = 0.885) and IDM (AUC = 0.901) of model-free and a dynamic contrast-enhanced MR imaging-based model were able to differentiate grade III from grade IV and grade II from grade III gliomas.

### **Glioma Survival Analysis**

Prior studies have used features such as age, extent of resection, degree of necrosis, Karnofsky scores, and enhancing tumor size as prognostic predictors.<sup>33</sup> On-line Table 2 summarizes MRTA studies predicting survival in gliomas.<sup>34–44</sup> As mentioned above, these studies also had considerable heterogeneity in terms of methodologies and classifier models. Most interesting, most studies found CE-MR imaging sequences to be the most useful for predicting survival. Yang et al,<sup>36</sup> for example, noted that even though several texture parameters predicted 12-month survival, CE-MR imaging sequences were the most accurate. They also mentioned that single-image features or MR images may not suffice because different combinations of image features and sequences are predictive for different tasks. Another multiparamet-

ric study by Kickingreder et al<sup>40</sup> in 119 patients using supervised PCA predicted progression-free and overall survival after extracting 11 second-order texture features. The MRTA features outperformed clinical and radiologic risk models in predicting prognosis. Another multiparametric MRTA study by Upadhya et al<sup>35</sup> in 40 patients extracted the top 5 texture features from CE-MR images with an accuracy of 83% in predicting 15-month survival. Liu et al<sup>44</sup> ( $n = 119$ ) also noted the best survival prediction on CE-MR imaging sequences (AUC, 0.791; accuracy, 80.7%). They also discovered that texture features derived from CE-MR imaging were comparable with features derived from a combination of multiple sequences.

### **Glioma Radiogenomics**

The 2016 World Health Organization classification update of gliomas incorporates genetic information for diagnosis. Radiogenomics refers to the relationship between imaging phenotypes and genomics that might allow improved decision-making and consequently improved patient outcomes.<sup>5</sup> Established glioma biomarkers include *isocitrate dehydrogenase (IDH)*, 1p/19q-codeletion, and methylguanine methyltransferase status. Immunohistochemistry combined with genome sequencing is a standard method for identifying glioma mutations.<sup>45,46</sup> Many studies have correlated multiparametric imaging features with glioma mutations and, to date, have shown greater success for *IDH* status compared with other mutations. Currently, standard glioblastoma therapy does not include mutation-specific treatment based on molecular status.<sup>47</sup>

Multiple ongoing clinical trials are, however, evaluating targeted treatments in gliomas.<sup>1</sup> On-line Table 3 summarizes the recently published MRTA studies on glioma radiogenomics.<sup>48–55</sup> Using SVM-recursive feature elimination, Zhang et al<sup>48</sup> ( $n = 152$ ) extracted the top 15 texture features from CE-MR imaging and T2WI with 82% accuracy for predicting *IDH* status. Hsieh et al<sup>49</sup> ( $n = 39$ ) also reported similar results in predicting *IDH* status by extracting 14 GLCM textural features on CE-MR imaging. Han et al<sup>55</sup> also showed that the joint variable derived from T1WI, T2WI, and CE-MR imaging histograms and GLCM features can be used for precise detection of *IDH1*-mutated gliomas. TA using  $B_0$  and fractional anisotropy maps has also shown a high accuracy of 95% in predicting *IDH* status.<sup>50</sup> Bahrami et al<sup>51</sup> reported greater FLAIR tissue heterogeneity and lower edge contrast in *IDH* wild-type compared with *IDH* mutants. Jakola et al<sup>53</sup> also reported greater accuracy for predicting *IDH* mutation using 3D-FLAIR. *IDH*-mutant 1p/19q-codeleted gliomas also have shown similar results compared with an 1p/19q-intact group and an unmethylated group. Shofty et al<sup>52</sup> used retrospective data from various MR imaging scanners with variable parameters. Despite the considerable data heterogeneity, they successfully predicted 1p/19q codeletion and discriminated LGGs on the basis of 1p/19q-codeletion status with an accuracy of 87% by extracting the top 39 texture features, mostly from CE-MR imaging and T2WI. Li et al<sup>56–58</sup> accurately predicted alpha thalassemia mental-retardation syndrome, epidermal growth factor receptor, and p53 status in patients with LGG on T2WI. In general, the second-order TA on CE-MR imaging and FLAIR images mostly contributed to the high accuracy for predicting genomic status.

### Miscellaneous Applications

Glioblastoma imaging features may overlap primary central nervous system lymphomas (PCNSLs) and metastases, rendering a noninvasive distinction truly challenging.<sup>59</sup> Recent MRTA studies, however, have shown promising results in differentiating glioblastomas from PCNSLs and metastases (On-line Table 4).<sup>59-63,66</sup> Kunitatsu et al<sup>60,61</sup> differentiated glioblastomas from PCNSLs with 75% accuracy by selecting the top 4 best-performing texture features from CE-MR images. Xiao et al<sup>62</sup> found skewness and kurtosis to be the best first-order features on CE-MR imaging in a similar population. Suh et al<sup>59</sup> reported 90% accuracy of radiomics-based machine learning algorithms compared with visual analysis by 3 readers in differentiating PCNSLs from glioblastomas. Similarly, Alcaide-Leon et al<sup>63</sup> showed superiority of the SVM classifier over human evaluation. Overall, better results were found using CE-MR imaging and machine-classification models. Dynamic histogram analysis is a novel technique using histogram-based texture parameter analysis on a time-series of dynamic susceptibility contrast MR imaging. Dynamic texture parameter analysis is a further extension of dynamic histogram analysis that analyzes a larger set of time-dependent texture maps from dynamic susceptibility contrast-enhanced series.<sup>64,65</sup> By using dynamic texture parameter analysis, Verma et al<sup>66</sup> extracted texture features from the earliest contrast phase of dynamic susceptibility contrast-enhanced perfusion maps and differentiated glioblastomas from PCNSLs. Skogen et al<sup>67</sup> used MRTA on DTI-derived fractional anisotropy and ADC maps and reported significantly higher heterogeneity in peritumoral edema of glioblastomas compared with metastases.

Assessment of the therapeutic response based solely on Response Assessment in Neuro-Oncology criteria, which are based solely on the 2D size and enhancement, may be challenging.<sup>43</sup> Recently, Ismail et al<sup>68</sup> ( $n = 105$ ) extracted the 2 most discriminative 3D shape features of the enhancing tumor on CE-MR imaging, FLAIR, and T2WI and noted that 3D shape features could distinguish pseudoprogression from true progression. TA may provide useful prognostic information regarding progression and survival in such a patient population. Grossmann et al<sup>41</sup> found that “information correlation,” a GLCM parameter, had a significantly higher score in patients on bevacizumab surviving beyond 3 months. Bahrami et al<sup>43</sup> reported that lower edge contrast of the FLAIR signal of gliomas correlated with poor survival after bevacizumab.

Despite the heterogeneity of the data and software, most studies demonstrate the robustness of the MRTA and its clinical transferability for diagnostic use. Second-order statistical TA showed promising results in most studies. Entropy also appears to be a key feature. Quite possibly, multisequence-based MRTA may have higher accuracy. However, it may be time-consuming, and not all advanced sequences are widely available. Performing MRTA on commonly available CE-MR imaging as well as T2-weighted/FLAIR sequences may be optimal for standardization, given the wide availability and promise shown in early studies. In studies involving LGGs, it may be better to perform MRTA on T2-weighted/FLAIR sequences because they better identify the tumor. On the other hand, CE-MR imaging appears to be the single

best sequence in glioblastoma, as mentioned in a study by Liu et al.<sup>44</sup>

### Challenges and Future Directions

Despite the advantages, widespread clinical implementation of MRTA is still limited, mostly due to nonuniformity and lack of standardization and quantification processes. The real challenge lies in the reproducibility and repeatability of these studies. Multiple studies used indigenous MRTA software, likely with varying algorithms. Thus, studies differ not only in image acquisition but also MRTA methodologies.

The other important aspect is use of a cancer imaging data base, which may suffice for conventional multiparametric assessment but nevertheless has considerable heterogeneity in sequences, protocols, and vendors. This is not confined just to the cancer data base but is a practical consideration for any multicenter study.

The impact of acquisition parameters on MRTA has been addressed in multiple studies. Ford et al,<sup>69</sup> using a digital 3D phantom, concluded that multiple texture features vary considerably between T1-weighted images (spin-echo, gradient echo, gradient recalled-echo, and inversion recovery) and T1 maps. They also noted that TR/TE variations on T1WI and T2WI affect texture features. Another phantom-based study by Buch et al<sup>12</sup> assessed the effect of magnet strength, flip angles, number of excitations, and different scanner platforms and concluded that some texture features are more robust (for example, except for histogram-related median, entropy, and GLCM contrast, all other histogram, GLCM, GLRLM, gray-level gradient matrix, and Law features did not show a significant difference from flip angles) and some are more susceptible to acquisition parameters (all Law features were significantly different for different magnetic strengths). Yang et al<sup>70</sup> found that different reconstruction algorithms, noise levels, and parallel imaging acceleration factors can influence texture parameters. Texture features are also affected by a number of coil elements, coil arrangement, and  $k$ -space sampling.<sup>71</sup> Rapid  $k$ -space sampling techniques can reduce SNR, thus affecting TA, especially histogram intensity-based features.<sup>12,71,72</sup> The inclusion of preprocessing steps may also affect texture features. Mayerhoefer et al<sup>15</sup> found zero-filling interpolation to be the most optimal with an interpolation factor of 4 to improve texture performance. Both Waugh et al<sup>72</sup> and Mayerhoefer et al<sup>13</sup> found spatial resolution to be the most important factor affecting MRTA and that variability in TR/TE, sampling bandwidth, and number of excitations is not significant at higher resolution. However, Molina et al<sup>73</sup> found that several GLCM and GLRLM texture features computed on 3D segmentation of brain gliomas were not robust over different spatial resolution/matrix size and gray-level ranges. They found only entropy to be the most robust feature. For intensity normalization, Collewet et al<sup>74</sup> found mean  $\pm$  3 SDs to be the most optimal strategy. Partial volume artifacts can be corrected by iterative optimal thresholding algorithms.<sup>12</sup>

In terms of analysis, the choice between analyzing multiple-versus-few sequences for MRTA also needs to be addressed. Spin-echo sequences are often acquired routinely in suspected brain tumor while advanced imaging may not be routinely performed, especially on the index scan. TA-based conventional sequences

seem more practical in terms of generalizability, with T1-CE-based TA being the most optimal.

3D-TA appears more accurate than 2D, given the high spatial resolution of the acquired data. Similarly, results based on a VOI analysis appear more reliable than those based on a single slice (also a prominent limitation of multiple prior studies).<sup>75</sup> However, more studies are needed to further establish better accuracy of 3D-MRTA and justify the additional time and effort.<sup>14</sup>

All these factors re-emphasize the need for standardization of MR imaging protocols, including uniform postprocessing techniques, to allow a more valid, multiple-institution comparison of MRTA results.

Challenges in processing include the inhomogeneity of MRTA software, which may be commercial, open-source, or developed in-house. The superiority of one over the other remains speculative at best.<sup>76</sup> Future studies should assess the comparability and accuracy of results across multiple types of software, especially in terms of clinical outcomes, survival, and radiomic parameters, to help with standardization. Finally, adequate training of radiologists is also required for consistent evaluation and implementation in routine workflow.

Another factor is the problem of the “huge data” that need sorting to prevent redundancy. Several classifier models exist to accurately predict the optimal texture feature. However, there is no consensus as to whether one is superior to the others. Artificial intelligence may be helpful in this case, both in feature selection and building prediction models.

Additionally, even though MRTA has shown potential in neuroimaging, certain valid criticisms of this technique should also be acknowledged. One major criticism of MRTA is that it is not hypothesis-driven. In some ways, MRTA is essentially correlating different mathematic computations with various imaging and clinical parameters to see what is statistically significant. This is, however, problematic for 2 main reasons: First, there is no intuitive reason why mathematic variables would make physiologic sense. Whether these significant relationships are merely chance findings secondary to overfitting (see next paragraph) or reflect as-yet unexplored physiologic correlates currently remains unclear. Most interesting, some prior studies have shown correlations between CT texture parameters and histologic markers such as CD34 and Ki-67, findings that may support some tissue-level basis for texture parameters.<sup>11</sup> These, however, remain to be fully determined and validated.

The other major limitation is the problem of overfitting, which can occur when the number of independent parameters being analyzed is larger than the number of data points/sample size. Generally, it is recommended that the sample size be 5–10 times the number of analyzed variables, which is often not the case, especially with studies using a smaller sample size. This issue could be addressed through either larger datasets or analysis of only a few preselected robust variables. Another way to avoid overfitting is to split the data into 3 mutually exclusive sets, one each for training, testing, and finally validation.

Finally, the role of MRTA should also be evaluated in the context of deep learning and neural networks. Even though unsupervised deep learning can self-identify features for itself and does not need manual input (thereby reducing interobserver bias in

ROI selection) and feature selection,<sup>76</sup> deep learning methods require higher processing powers and considerable high-quality ground truth data. The insatiable appetite of deep learning for large quantities of labeled training data (which are both expensive and difficult to produce) is another limitation of the deep learning approach.<sup>77</sup> MRTA, on the other hand, is less data-hungry. Additionally, the internal algorithm feature vectors in unsupervised deep learning may not always be apparent (black box), while TA features can be explained more easily. However, ROI selection bias among observers can influence MRTA results and should be addressed prospectively.<sup>75</sup> However, the 2 techniques may be complementary in terms of optimal feature selection (in deep learning) and ease of use for wider applicability (for MRTA), thereby providing optimal output without substantial changes to the clinical workflow.

## CONCLUSIONS

MRTA has shown promising results in various glioma-related applications. The inclusion of tumor heterogeneity as a radiology-reporting variable appears to break with the notion of radiology being only diagnostic or qualitative and brings the shift toward prognostic value as an imaging biomarker for precision/personalized medicine. However, before widespread clinical applicability, prospective validation of accuracy, selection of robust sequences, interinstitutional congruity of results, and selection of the best possible technique need to be addressed. Last, development of automated segmentation tools with incorporation of machine learning is essential to expedite feature extraction and analysis, thus saving time and additional burden on the radiologist.

## REFERENCES

1. Auffinger B, Thaci B, Nigam P, et al. **New therapeutic approaches for malignant glioma: in search of the Rosetta stone.** *F1000 Med Rep* 2012;4:18 CrossRef Medline
2. Kang Y, Choi SH, Kim YJ, et al. **Gliomas: histogram analysis of apparent diffusion coefficient maps with standard- or high-b-value diffusion-weighted MR imaging—correlation with tumor grade.** *Radiology* 2011;261:882–90 CrossRef Medline
3. Gulsen S. **Achieving higher diagnostic results in stereotactic brain biopsy by simple and novel technique.** *Open Access Maced J Med Sci* 2015;3:99–104 CrossRef Medline
4. Akay A, Rüksen M, Islekel S. **Magnetic resonance imaging-guided stereotactic biopsy: a review of 83 cases with outcomes.** *Asian J Neurosurg* 2019;14:90–95 CrossRef Medline
5. Mazurowski MA. **Radiogenomics: what it is and why it is important.** *J Am Coll Radiol* 2015;12:862–66 CrossRef Medline
6. Law M, Yang S, Wang H, et al. **Glioma grading: sensitivity, specificity, and predictive values of perfusion MR imaging and proton MR spectroscopic imaging compared with conventional MR imaging.** *AJNR Am J Neuroradiol* 2003;24:1989–98 Medline
7. Gutman DA, Cooper LA, Hwang SN, et al. **MR imaging predictors of molecular profile and survival: multi-institutional study of the TCGA glioblastoma data set.** *Radiology* 2013;267:560–69 CrossRef Medline
8. Naveed MA, Goyal P, Malhotra A, et al. **Grading of oligodendroglial tumors of the brain with apparent diffusion coefficient, magnetic resonance spectroscopy, and dynamic susceptibility contrast imaging.** *Neuroradiol J* 2018;31:379–85 CrossRef Medline
9. Texture. Merriam-Webster.com. <https://www.merriam-webster.com/dictionary/texture>. Accessed January 10, 2019
10. Raja R, Sinha N, Saini J, et al. **Assessment of tissue heterogeneity**

- using diffusion tensor and diffusion kurtosis imaging for grading gliomas. *Neuroradiology* 2016;58:1217–31 CrossRef Medline
11. Miles KA, Ganeshan B, Hayball MP. CT texture analysis using the filtration-histogram method: what do the measurements mean? *Cancer Imaging* 2013;13:400–06 CrossRef Medline
  12. Buch K, Kuno H, Qureshi MM, et al. Quantitative variations in texture analysis features dependent on MRI scanning parameters: a phantom model. *J Appl Clin Med Phys* 2018;19:253–64 CrossRef Medline
  13. Mayerhoefer ME, Szomolanyi P, Jirak D, et al. Effects of MRI acquisition parameter variations and protocol heterogeneity on the results of texture analysis and pattern discrimination: an application-oriented study. *Med Phys* 2009;36:1236–43 CrossRef Medline
  14. Depeursinge A, Foncubierta-Rodriguez A, Van De Ville D, et al. Three-dimensional solid texture analysis in biomedical imaging: review and opportunities. *Med Image Anal* 2014;18:176–96 CrossRef Medline
  15. Mayerhoefer ME, Szomolanyi P, Jirak D, et al. Effects of magnetic resonance image interpolation on the results of texture-based pattern classification: a phantom study. *Invest Radiol* 2009;44:405–11 CrossRef Medline
  16. Larroza A, Bodí V, Moratal D. Texture analysis in magnetic resonance imaging: review and considerations for future applications. In: Constantinides C, ed. *Assessment of Cellular and Organ Function and Dysfunction using Direct and Derived MRI Methodologies*. Rijeka: IntechOpen; 2016
  17. Szczypiński PM, Klepaczko A. MaZda: a framework for biomedical image texture analysis and data exploration. In: Depeursinge A, Al-Kadi OS, Mitchell JR, eds. *Biomedical Texture Analysis*. Amsterdam: Elsevier; 2017:315–47
  18. Schaer R, Cid YD, Alkım E, et al. *Web-Based Tools for Exploring the Potential of Quantitative Imaging Biomarkers on Radiology*. Waltham: Academic Press; 2017
  19. Di Cataldo S, Ficarra E. Mining textural knowledge in biological images: applications, methods and trends. *Comput Struct Biotechnol J* 2017;15:56–67 CrossRef Medline
  20. Kolosváry M, Kellermayer M, Merkely B, et al. Cardiac computed tomography radiomics: a comprehensive review on radiomic techniques. *J Thorac Imaging* 2018;33:26–34 CrossRef Medline
  21. Bashir U, Siddique MM, McLean E, et al. Imaging heterogeneity in lung cancer: techniques, applications, and challenges. *AJR Am J Roentgenol* 2016;207:534–43 CrossRef Medline
  22. Davnall F, Yip CS, Ljungqvist G, et al. Assessment of tumor heterogeneity: an emerging imaging tool for clinical practice? *Insights Imaging* 2012;3:573–89 CrossRef Medline
  23. Lubner MG, Smith AD, Sandrasegaran K, et al. CT texture analysis: definitions, applications, biologic correlates, and challenges. *Radiographics* 2017;37:1483–503 CrossRef Medline
  24. Depeursinge A, Fageot J, Al-Kadi OS. Fundamentals of texture processing for biomedical image analysis: a general definition and problem formulation. *Biomedical Texture Analysis*. Amsterdam: Elsevier; 2017:1–27
  25. Louis DN, Perry A, Reifenberger G, et al. The 2016 World Health Organization Classification of Tumors of the Central Nervous System: a summary. *Acta Neuropathol* 2016;131:803–20 CrossRef Medline
  26. Chand P, Amit S, Gupta R, et al. Errors, limitations, and pitfalls in the diagnosis of central and peripheral nervous system lesions in intraoperative cytology and frozen sections. *J Cytol* 2016;33:93–97 CrossRef Medline
  27. Ryu YJ, Choi SH, Park SJ, et al. Glioma: application of whole-tumor texture analysis of diffusion-weighted imaging for the evaluation of tumor heterogeneity. *PLoS One* 2014;9:e108335 CrossRef Medline
  28. Kinoshita M, Sakai M, Arita H, et al. Introduction of high throughput magnetic resonance T2-weighted image texture analysis for WHO grade 2 and 3 gliomas. *PLoS One* 2016;11:e0164268 CrossRef Medline
  29. Skogen K, Schulz A, Dormagen JB, et al. Diagnostic performance of texture analysis on MRI in grading cerebral gliomas. *Eur J Radiol* 2016;85:824–29 CrossRef Medline
  30. Tian Q, Yan LF, Zhang X, et al. Radiomics strategy for glioma grading using texture features from multiparametric MRI. *J Magn Reson Imaging* 2018;48:1518–28 CrossRef Medline
  31. Xie T, Chen X, Fang J, et al. Textural features of dynamic contrast-enhanced MRI derived model-free and model-based parameter maps in glioma grading. *J Magn Reson Imaging* 2018;47:1099–111 CrossRef Medline
  32. Qi XX, Shi DF, Ren SX, et al. Histogram analysis of diffusion kurtosis imaging derived maps may distinguish between low and high grade gliomas before surgery. *Eur Radiol* 2018;28:1748–55 CrossRef Medline
  33. Mazurowski MA, Zhang J, Peters KB, et al. Computer-extracted MR imaging features are associated with survival in glioblastoma patients. *J Neurooncol* 2014;120:483–88 CrossRef Medline
  34. Brynolfsson P, Nilsson D, Henriksson R, et al. ADC texture: an imaging biomarker for high-grade glioma? *Med Phys* 2014;41:101903 CrossRef Medline
  35. Upadhya T, Morvan Y, Stindel E, et al. A framework for multimodal imaging-based prognostic model building: preliminary study on multimodal MRI in glioblastoma multiforme. *IRBM* 2015;36:345–50 CrossRef
  36. Yang D, Rao G, Martinez J, et al. Evaluation of tumor-derived MRI-texture features for discrimination of molecular subtypes and prediction of 12-month survival status in glioblastoma. *Med Phys* 2015;42:6725–35 CrossRef Medline
  37. Chaddad A, Tanougast C. Extracted magnetic resonance texture features discriminate between phenotypes and are associated with overall survival in glioblastoma multiforme patients. *Med Biol Eng Comput* 2016;54:1707–18 CrossRef Medline
  38. Lee J, Jain R, Khalil K, et al. Texture feature ratios from relative CBV maps of perfusion MRI are associated with patient survival in glioblastoma. *AJNR Am J Neuroradiol* 2016;37:37–43 CrossRef Medline
  39. Molina D, Pérez-Beteta J, Luque B, et al. Tumour heterogeneity in glioblastoma assessed by MRI texture analysis: a potential marker of survival. *Br J Radiol* 2016;89:20160242 CrossRef Medline
  40. Kickingereder P, Burth S, Wick A, et al. Radiomic profiling of glioblastoma: identifying an imaging predictor of patient survival with improved performance over established clinical and radiologic risk models. *Radiology* 2016;280:880–89 CrossRef Medline
  41. Grossmann P, Narayan V, Chang K, et al. Quantitative imaging biomarkers for risk stratification of patients with recurrent glioblastoma treated with bevacizumab. *Neuro Oncol* 2017;19:1688–97 CrossRef Medline
  42. Chaddad A, Daniel P, Desrosiers C, et al. Novel radiomic features based on joint intensity matrices for predicting glioblastoma patient survival time. *IEEE J Biomed Health Inform* 2019;23:795–804 CrossRef Medline
  43. Bahrami N, Piccioni D, Karunamuni R, et al. Edge contrast of the FLAIR hyperintense region predicts survival in patients with high-grade gliomas following treatment with bevacizumab. *AJNR Am J Neuroradiol* 2018;39:1017–24 CrossRef Medline
  44. Liu Y, Zhang X, Feng N, et al. The effect of glioblastoma heterogeneity on survival stratification: a multimodal MR imaging texture analysis. *Acta Radiol* 2018;59:1239–46 CrossRef Medline
  45. Combs SE, Rieken S, Wick W, et al. Prognostic significance of IDH-1 and MGMT in patients with glioblastoma: one step forward, and one step back? *Radiat Oncol* 2011;6:115 CrossRef Medline
  46. Xia L, Wu B, Fu Z, et al. Prognostic role of IDH mutations in gliomas: a meta-analysis of 55 observational studies. *Oncotarget* 2015;6:17354–65 CrossRef Medline
  47. Chow D, Chang P, Weinberg BD, et al. Imaging genetic heterogeneity in glioblastoma and other glial tumors: review of current methods and future directions. *AJR Am J Roentgenol* 2018;210:30–38 CrossRef Medline
  48. Zhang X, Tian Q, Wu YX, et al. IDH mutation assessment of glioma

- using texture features of multimodal MR images. *Proceedings of SPIE* 2017;10134 CrossRef
49. Hsieh KL, Chen CY, Lo CM. Radiomic model for predicting mutations in the isocitrate dehydrogenase gene in glioblastomas. *Oncotarget* 2017;8:45888–97 CrossRef Medline
  50. Eichinger P, Alberts E, Delbridge C, et al. Diffusion tensor image features predict IDH genotype in newly diagnosed WHO grade II/III gliomas. *Sci Rep* 2017;7:13396 CrossRef Medline
  51. Bahrami N, Hartman SJ, Chang YH, et al. Molecular classification of patients with grade II/III glioma using quantitative MRI characteristics. *J Neurooncol* 2018;139:633–42 CrossRef Medline
  52. Shofty B, Artzi M, Ben Bashat D, et al. MRI radiomics analysis of molecular alterations in low-grade gliomas. *Int J Comput Assist Radiol Surg* 2018;13:563–71 CrossRef Medline
  53. Jakola AS, Zhang YH, Skjulsvik AJ, et al. Quantitative texture analysis in the prediction of IDH status in low-grade gliomas. *Clin Neurol Neurosurg* 2018;164:114–20 CrossRef Medline
  54. Rui W, Ren Y, Wang Y, et al. MR textural analysis on T2 FLAIR images for the prediction of true oligodendroglioma by the 2016 WHO genetic classification. *J Magn Reson Imaging* 2018;48:74–83 CrossRef Medline
  55. Han L, Wang S, Miao Y, et al. MRI texture analysis based on 3D tumor measurement reflects the IDH1 mutations in gliomas: a preliminary study. *Eur J Radiol* 2019;112:169–79 CrossRef Medline
  56. Li Y, Liu X, Qian Z, et al. Genotype prediction of ATRX mutation in lower-grade gliomas using an MRI radiomics signature. *Eur Radiol* 2018;28:2960–68 CrossRef Medline
  57. Li Y, Liu X, Xu K, et al. MRI features can predict EGFR expression in lower grade gliomas: a voxel-based radiomic analysis. *Eur Radiol* 2018;28:356–62 CrossRef Medline
  58. Li Y, Qian Z, Xu K, et al. MRI features predict p53 status in lower-grade gliomas via a machine-learning approach. *Neuroimage Clin* 2017;17:306–11 CrossRef Medline
  59. Suh HB, Choi YS, Bae S, et al. Primary central nervous system lymphoma and atypical glioblastoma: differentiation using radiomics approach. *Eur Radiol* 2018;28:3832–39 CrossRef Medline
  60. Kunimatsu A, Kunimatsu N, Yasaka K, et al. Machine learning-based texture analysis of contrast-enhanced MR imaging to differentiate between glioblastoma and primary central nervous system lymphoma. *Magn Reson Med Sci* 2019;18:44–52 CrossRef Medline
  61. Kunimatsu A, Kunimatsu N, Kamiya K, et al. Comparison between glioblastoma and primary central nervous system lymphoma using MR image-based texture analysis. *Magn Reson Med Sci* 2018;17:50–57 CrossRef Medline
  62. Xiao DD, Yan PF, Wang YX, et al. Glioblastoma and primary central nervous system lymphoma: preoperative differentiation by using MRI-based 3D texture analysis. *Clin Neurol Neurosurg* 2018;173:84–90 CrossRef Medline
  63. Alcaide-Leon P, Dufort P, Geraldo AF, et al. Differentiation of enhancing glioma and primary central nervous system lymphoma by texture-based machine learning. *AJNR Am J Neuroradiol* 2017;38:1145–50 CrossRef Medline
  64. Slotboom J, Schaer R, Ozdoba C, et al. A novel method for analyzing DSCE-images with an application to tumor grading. *Invest Radiol* 2008;43:843–53 CrossRef Medline
  65. Verma RK, Slotboom J, Heldner MR, et al. Characterization of microcirculation in multiple sclerosis lesions by dynamic texture parameter analysis (DTPA). *PLoS One* 2013;8:e67610 CrossRef Medline
  66. Verma RK, Wiest R, Locher C, et al. Differentiating enhancing multiple sclerosis lesions, glioblastoma, and lymphoma with dynamic texture parameters analysis (DTPA): a feasibility study. *Med Phys* 2017;44:4000–08 CrossRef Medline
  67. Skogen K, Schulz A, Helseth E, et al. Texture analysis on diffusion tensor imaging: discriminating glioblastoma from single brain metastasis. *Acta Radiol* 2019;60:356–66 CrossRef Medline
  68. Ismail M, Hill V, Stasevych V, et al. Shape features of the lesion habitat to differentiate brain tumor progression from pseudoprogression on routine multiparametric MRI: a multisite study. *AJNR Am J Neuroradiol* 2018;39:2187–93 CrossRef Medline
  69. Ford J, Dogan N, Young L, et al. Quantitative radiomics: impact of pulse sequence parameter selection on MRI-based textural features of the brain. *Contrast Media Mol Imaging* 2018;2018:1729071 CrossRef Medline
  70. Yang F, Dogan N, Stoyanova R, et al. Evaluation of radiomic texture feature error due to MRI acquisition and reconstruction: a simulation study utilizing ground truth. *Phys Med* 2018;50:26–36 CrossRef Medline
  71. Schad LR. Problems in texture analysis with magnetic resonance imaging. *Dialogues Clin Neurosci* 2004;6:235–42 Medline
  72. Waugh SA, Lerski RA, Bidaut L, et al. The influence of field strength and different clinical breast MRI protocols on the outcome of texture analysis using foam phantoms. *Med Phys* 2011;38:5058–66 CrossRef Medline
  73. Molina D, Pérez-Beteta J, Martínez-González A, et al. Lack of robustness of textural measures obtained from 3D brain tumor MRIs impose a need for standardization. *PLoS One* 2017;12:e0178843 CrossRef Medline
  74. Collewet G, Strzelecki M, Mariette F. Influence of MRI acquisition protocols and image intensity normalization methods on texture classification. *Magn Reson Imaging* 2004;22:81–91 CrossRef Medline
  75. Hainc N, Stippich C, Stieltjes B, et al. Experimental texture analysis in glioblastoma: a methodological study. *Invest Radiol* 2017;52:367–73 CrossRef Medline
  76. Varghese BA, Cen SY, Hwang DH, et al. Texture analysis of imaging: what radiologists need to know. *AJR Am J Roentgenol* 2019;212:520–28 CrossRef Medline
  77. Suzuki K. Overview of deep learning in medical imaging. *Radiol Phys Technol* 2017;10:257–73 CrossRef Medline

# The Continued Rise in Professional Use of Social Media at Scientific Meetings: An Analysis of Twitter Use during the ASNR 2018 Annual Meeting

G. D'Anna, M.M. Chen, J.L. McCarty, A. Radmanesh, and A.L. Kotsenas

## ABSTRACT

**SUMMARY:** Professional use of social media continues to increase. We analyzed Twitter use of our own American Society of Neuroradiology (ASNR) 2018 annual meeting, reviewing all Twitter posts (3020 tweets from 523 participants) containing the hashtag #ASNR18 from May 21, 2018, to June 12, 2018, extracting the transcripts from Symplur. Then, each tweet was categorized by the role of user, type of tweet, and topic. The dominant user category was neuroradiologist/radiologist (63%). The keynote address, “The Radiology Renaissance: Shaping the Future of Healthcare,” presented by Andy DeLao @Cancergeek was the most frequently tweeted topic (10%). Comment on a session was the major type of tweet. When we compared the data with a similar analysis in 2014, our data analysis showed a growth in the use of Twitter in only 4 years.

**ABBREVIATIONS:** ASNR = American Society of Neuroradiology; RT = retweet

Use of social media in the general population continues to grow, with a median of 53% of the global population using at least 1 social media platform.<sup>1-3</sup> Use of social media has also increased during scientific and medical meetings.<sup>4-9</sup> In 2015, an analysis of social media used during the 52nd Annual Meeting of the American Society of Neuroradiology (ASNR) was made,<sup>10</sup> with the recording and categorization of all tweets. Four years later, we aimed to repeat a similar analysis of the 56th Annual Meeting of the American Society of Neuroradiology (June 2–7, 2018), which was held in Vancouver, British Columbia, Canada, the using hashtag #ASNR18.

We collected all Twitter posts (Twitter.com, San Francisco, California) containing #ASNR18 from May 21, 2018 (10 days before the start of the meeting), to June 12, 2018 (5 days after the end of the meeting), extracting the transcripts from Symplur (<https://www.symplur.com/>). Each tweet was categorized by role of user, type of tweet, and topic. We collected 3020 tweets by 523 participants as well as separately collected retweets, 1870 (61.9%).

During the days of the meeting, an average of 453 tweets were posted each day by a total of 523 participants (versus an average of 65 tweets by a total number of 50 participants in 2014). #ASNR18 generated 8.124 million impressions compared with 415,102 in 2014. An average of 6 tweets per participant were posted on Twitter in the days observed (8 in 2014). The top 3 categories of Twitter accounts using #ASNR18, neuroradiology societies, influencers (nonphysician or scientific professionals involved in health care), and neuroradiologists, generated 521 tweets (17%); in 2014, neuroradiologists generated 54% of tweets ( $n = 223$ ).

The major category of user (Table 1) was neuroradiologist/radiologist (63% of participants). The second largest category was professional societies (14%), which was a new category compared with 2014. A few tweets were posted by members of the patient community ( $n = 7$ ).

English was largely the language of choice, with only 3 tweets in other languages (2 in Portuguese and 1 in Spanish). Regarding the type of tweet (Table 2), the most common was a comment on a session (people commenting on a specific presentation “live”), followed by a simple update of personal status, not directly related to a specific session.

With regard to the most popular topics (Table 3), the keynote address “The Radiology Renaissance: Shaping the Future of Healthcare” presented by Andy DeLao (@Cancergeek) was the topic most tweeted (10%). Factors that could have contributed to this were the sheer number of followers of the presenter, as well as the topics covered within the keynote, including artificial intelligence, future of neuroradiology, and patient-centered care. Other popular tweeted topics included the value of neuroradiologists’

Received March 10, 2019; accepted after revision April 4.

From the Neuroradiology Unit (G.D.A.), Azienda Socio Sanitaria Territoriale Monza Ospedale San Gerardo, Monza, Italy; Department of Radiology (M.M.C.), University of Texas MD Anderson Cancer Center, Houston, Texas; Department of Diagnostic and Interventional Imaging (J.L.M.), University of Texas Health Sciences Center at Houston, Houston, Texas; Department of Radiology (A.R.), New York University School of Medicine, New York, New York; and Department of Radiology (A.L.K.), Mayo Clinic, Rochester, Minnesota.

Please address correspondence to Gennaro D'Anna, MD, Neuroradiology Unit, ASST Monza Ospedale San Gerardo, Via Pergolesi 33, 20900, Monza, Italy; e-mail: [gennaro.danna@gmail.com](mailto:gennaro.danna@gmail.com); @Januarium

<http://dx.doi.org/10.3174/ajnr.A6064>

work and reporting (6%), health care economics and politics (5%), and head and neck radiology (5%).

The tweet content most frequently reposted or “retweeted” was regarding the incidence of depression and burnout in the radiological population, which was retweeted 36 times.

Based on the total number of tweets, we found consistent growth from year to year. J. McCarty in a post on ajnrblog.org in 2016<sup>11</sup> summarized these data, with dramatic growth between 2014 and 2015 (393 versus 2388), and smaller incremental growth between 2015 and 2016 (2388 versus 2589). With no published data about ASNR17, we instead compared the recent session with ASNR16 (2589 versus 3020 tweets).

We found an exponential growth in increased numbers of ra-

diologists/neuroradiologists that participated in tweeting (96, compared with 20 in 2014). Additionally, radiology professional societies engaged in tweets, a new category of participants compared with 2014 (11, compared with zero in 2014).

Most interesting is the evaluation of the topics (Table 3): We labeled each tweet not only as type of tweet or role of the user but also by topic of the tweet.

On the basis of the number of tweets, we found that Twitter participants gave greater importance to health care economics, the value of the report, and taking care of the patients, with all these topics accounting for 7.65% of original tweets and 12.88% of all tweets (including retweets [RTs]).

Twitter has also improved the visibility of specific projects. For example, “Common Data Elements,” a joint ASNR/RSNA project, gained visibility with 19 original tweets and 68 RTs (87 in total, 2.88%) visible to a larger audience.

In 2015, the use of Twitter during the ASNR Annual Meeting was described as “in infancy.”<sup>10</sup> Four years later, the use of Twitter at the Annual Meeting of the ASNR has increased substantially. We now have a large audience, with a neuroradiologic community familiar with Twitter use during meetings.<sup>4,12,13</sup> This started with a social media strategy by the event organizer who encouraged discussion, provided helpful information about times and specific locations of lectures, “Twitter Takeovers” in which neuroradiologists tweeted from the ASNR account during sessions,

and much more. Having a social media strategy plays an important role in improving the visibility of neuroradiology as a subspecialty in the radiology social universe. Through the use of Twitter, the ASNR can facilitate networking, stimulate discussion on topics important to the specialty, and provide educational material for radiologists and residents.

**Table 1: Role of user**

Role	ASNR14	ASNR18
Radiologists	20	96
Radiology departments	7	10
Radiology societies		11
Radiology journals	3	2
Social media professionals	4	4
Vendors	11	6
Other physicians	5	3
Other	1	13
Host city	1	2
Patients		7

**Table 2: Type of tweet**

Type of Tweet	Tot (%) / Orig (%) #ASNR14	Tot (%) / Orig (%) #ASNR18
Commentary on session	202 (49%) / 124 (60.5%)	1830 (61%) / 626 (54%)
Meeting announcements	6 (1.5%) / 3 (1.5%)	69 (2%) / 24 (2%)
Tweetup	61 (14.8%) / 33 (16.1%)	40 (1%) / 14 (1%)
Status update	39 (9.5%) / 26 (12.7%)	619 (20%) / 266 (23%)
Meeting logistics	1 (<1%) / 1 (<1%)	31 (1%) / 19 (2%)
Vendor promotions	9 (2.2%) / 8 (3.9%)	15 (<1%) / 9 (<1%)
Others	6 (1.5%) / 5 (2.4%)	86 (3%) / 60 (5%)

**Note:**—Tot indicates the total number of tweets, including RTs; Orig, only the original tweets.

**Table 3: Topics**

Category	Original	% Tot	RT	% Tot RT	% RT	Total	% Tot
Other	345	30.00%	369	19.73%	51.68%	714	23.64%
Imaging	327	28.44%	614	32.81%	65.24%	941	31.15%
Keynote	117	10.17%	178	9.52%	60.34%	295	9.77%
Health care and politics	61	5.30%	91	4.87%	59.87%	152	5.03%
Value of radiology	45	3.91%	134	7.17%	74.86%	179	5.93%
Social media	39	3.39%	74	3.96%	65.49%	113	3.74%
Location	36	3.13%	25	1.34%	40.98%	61	2.02%
AI, ML, DL	32	2.78%	18	0.96%	36.00%	50	1.66%
Awards	28	2.43%	52	2.78%	65.00%	80	2.65%
PFCC	22	1.91%	36	1.93%	62.07%	58	1.92%
CDE	19	1.65%	68	3.64%	78.16%	87	2.88%
Mentorship	18	1.57%	19	1.02%	51.35%	37	1.23%
Education	17	1.48%	48	2.57%	73.85%	65	2.15%
Tweetup	13	1.13%	26	1.39%	66.67%	39	1.29%
FASNR	9	0.78%	6	0.32%	40.00%	15	0.50%
Symposium	8	0.70%	20	1.07%	71.43%	28	0.93%
Irad	6	0.52%	17	0.91%	73.91%	23	0.76%
COTW	4	0.35%	30	1.60%	88.24%	34	1.13%
Dose	3	0.26%	9	0.48%	75.00%	12	0.40%
Burnout	1	0.09%	36	1.93%	97.30%	37	1.23%
Total	1150		1870			3020	

**Note:**—RT indicates retweets; AI, artificial intelligence; ML, machine learning; DL, deep learning; PFCC, patient and family centered care; FASNR, foundation of American Society of Neuroradiology; Irad, interventional radiology; COTW, case of the week; Tot, type of tweet.

A parallel virtual meeting audience, the “Twitterverse,” is primed to discuss specific radiology-related topics; this audience includes practicing radiologists/neuroradiologists, radiology educators and especially radiology residents, fellows or medical students, and young people interested in our discipline, who can find inspiration for daily work or topics to study and research by following the meeting on Twitter.

Moreover, a unique advantage of this social network is to reach a worldwide audience (as an example, one of the authors followed the entire meeting from Italy); this advantage is an important aspect of social media use that ASNR has effectively promoted so well in recent years. This has expanded the influence of the society outside of North America, taking the leadership in Twitter neuroradiology community. Now the society offers increased social media content, and many neuroradiologists know that neuroradiology-related news, annual meeting logistics, and articles important in the specialty of neuroradiology will be highlighted on the ASNR social media channels. This strategy positions ASNR as global leader in neuroradiology.

Our analysis shows that Twitter use by neuroradiologists and the neuroradiology community has increased substantially during the past 4 years, allowing a larger engaged community to share meeting content with users both at the meeting and following remotely.

Disclosures: Melissa M. Chen—UNRELATED: Travel/Accommodations/Meeting Expenses Unrelated to Activities Listed: ASNR, Comments: travel expenses as the ASNR RVS Update Committee Advisor to the American Medical Association/Specialty Society RVS Update Committee meeting (3 times a year).

## REFERENCES

1. Kohli MD, Daye D, Towbin AJ, et al. **Social media tools for department and practice communication and branding in the digital age.** *Radiographics* 2018;38:1773–85 CrossRef Medline
2. Social Media Fact Sheet. 2018. <https://www.pewinternet.org/fact-sheet/social-media>. Accessed December 23, 2018
3. Social network adoption varies widely by country. Pew Research Center. 2018. <http://www.pewglobal.org/2018/06/19/3-social-network-adoption-varies-widely-by-country/>. Accessed December 23, 2018
4. Radmanesh A, Fitzgerald RT. **Social media and the neuroradiologist: a brief introduction.** *AJNR Am J Neuroradiol.* 2015;36:30–31 CrossRef Medline
5. Hawkins CM, Duszak R, Rawson J V. **Social media in radiology: early trends in Twitter microblogging at radiology’s largest international meeting.** *J Am Coll Radiol* 2014;11:387–90 CrossRef Medline
6. Tanoue MT, Chatterjee D, Nguyen HL, et al. **Tweeting the meeting.** *Circ Cardiovasc Qual Outcomes* 2018;11:e005018 CrossRef Medline
7. Wadhwa V, Brandis A, Madassery K, et al. **#TwittIR: understanding and establishing a Twitter ecosystem for interventional radiologists and their practices.** *J Am Coll Radiol* 2018;15:218–23 CrossRef Medline
8. Hage AN, Chick JF, Jeffers B, et al. **#InterventionalRadiology.** *J Vasc Interv Radiol* 2018;29:669–75 CrossRef Medline
9. Wadhwa V, Latimer E, Chatterjee K, et al. **Maximizing the tweet engagement rate in academia: analysis of the AJNR Twitter feed.** *AJNR Am J Neuroradiol* 2017;38:1866–68 CrossRef Medline
10. Radmanesh A, Kotsenas AL. **Social media and scientific meetings: an analysis of Twitter use at the annual meeting of the American Society of Neuroradiology.** *AJNR Am J Neuroradiol* 2016;37:25–27 CrossRef Medline
11. McCarty J. ASNR 2016 Meeting Social Media Recap. *ajnrblog*. <http://www.ajnrblog.org/2016/06/14/asnr-2016-social-media-recap/>. 2016. Accessed December 30, 2018
12. Lall N. Tips and Tools for Social Media Use. *ajnrblog*. <http://www.ajnrblog.org/2016/05/24/tips-tools-social-media-use/>. 2016. Accessed December 23, 2018
13. Kalia V, Ortiz DA, Patel AK, et al. **Leveraging Twitter to maximize the radiology meeting experience.** *J Am Coll Radiol* 2018;15:177–83 CrossRef Medline

# Ensemble of Convolutional Neural Networks Improves Automated Segmentation of Acute Ischemic Lesions Using Multiparametric Diffusion-Weighted MRI

S. Winzeck, S.J.T. Mocking, R. Bezerra, M.J.R.J. Bouts, E.C. McIntosh, I. Diwan, P. Garg, A. Chutinet, W.T. Kimberly, W.A. Copen, P.W. Schaefer, H. Ay, A.B. Singhal, K. Kamnitsas, B. Glocker, A.G. Sorensen, and O. Wu



## ABSTRACT

**BACKGROUND AND PURPOSE:** Accurate automated infarct segmentation is needed for acute ischemic stroke studies relying on infarct volumes as an imaging phenotype or biomarker that require large numbers of subjects. This study investigated whether an ensemble of convolutional neural networks trained on multiparametric DWI maps outperforms single networks trained on solo DWI parametric maps.

**MATERIALS AND METHODS:** Convolutional neural networks were trained on combinations of DWI, ADC, and low b-value-weighted images from 116 subjects. The performances of the networks (measured by the Dice score, sensitivity, and precision) were compared with one another and with ensembles of 5 networks. To assess the generalizability of the approach, we applied the best-performing model to an independent Evaluation Cohort of 151 subjects. Agreement between manual and automated segmentations for identifying patients with large lesion volumes was calculated across multiple thresholds (21, 31, 51, and 70 cm<sup>3</sup>).

**RESULTS:** An ensemble of convolutional neural networks trained on DWI, ADC, and low b-value-weighted images produced the most accurate acute infarct segmentation over individual networks ( $P < .001$ ). Automated volumes correlated with manually measured volumes (Spearman  $\rho = 0.91$ ,  $P < .001$ ) for the independent cohort. For the task of identifying patients with large lesion volumes, agreement between manual outlines and automated outlines was high (Cohen  $\kappa$ , 0.86–0.90;  $P < .001$ ).

**CONCLUSIONS:** Acute infarcts are more accurately segmented using ensembles of convolutional neural networks trained with multiparametric maps than by using a single model trained with a solo map. Automated lesion segmentation has high agreement with manual techniques for identifying patients with large lesion volumes.

**ABBREVIATIONS:** ALV = automatically segmented lesion volume; CNN = convolutional neural network; E2 = ensemble of CNNs using DWI and ADC; E3 = ensemble of CNNs using DWI, ADC, and LOWB; IQR = interquartile range; LKW = last known to be well; LOWB = low b-value diffusion-weighted image ( $b_0$ ); MLV = manually segmented lesion volume

Accurate acute infarct segmentation on DWI is important for many aspects of the management of patients with ischemic stroke such as deciding whether to triage the patient to an inten-

sive care unit, monitoring brain swelling, aiding prognosis, assessing the risk of complications, and predicting functional outcome. Robust automated segmentation of acute infarcts also has great potential for use in clinical trials in which precise volume measurements are needed to assess differences between groups or to monitor lesion growth. Various automated algorithms for segmenting tissue have been presented.<sup>1–3</sup> However, many of these methods focus only on using a solo diffusion parametric map, such as isotropic high-b-value DWI<sup>1</sup> or an ADC image.<sup>2</sup> There have been studies that combined DWI and ADC maps,<sup>4–6</sup> but these did not include the non-diffusion-weighted low-b-value images ( $b = 0$  s/mm<sup>2</sup>, LOWB), which can potentially be used to measure early vasogenic edema. Another study has proposed us-

Received October 1, 2018; accepted after revision April 19, 2019.

From the Department of Radiology (S.W., S.J.T.M., R.B., M.J.R.J.B., E.C.M., I.D., P.G., H.A., A.G.S., O.W.), Athinoula A. Martinos Center for Biomedical Imaging, Massachusetts General Hospital, Charlestown, Massachusetts; Division of Anaesthesia (S.W.), Department of Medicine, University of Cambridge, Cambridge, UK; Departments of Neurology (A.C., W.T.K., H.A., A.B.S.) and Radiology (W.A.C., P.W.S.), Massachusetts General Hospital, Boston, Massachusetts; Department of Medicine (A.C.), Faculty of Medicine, Chulalongkorn University, King Chulalongkorn Memorial Hospital, Thai Red Cross Society, Bangkok, Thailand; and Department of Computing (K.K., B.G.), Imperial College London, London, UK.

This work was supported by the National Institutes of Health-National Institute of Neurological Disorders and Stroke R01NS059775, R01NS063925, R01NS082285, P50NS051343, R01NS086905, R01NS051412, R21NS077442, R21NS085574, U01NS069208, U01NS086729, U01NS095869; and the National Institutes of Health-National Institute of Biomedical Imaging and Bioengineering, P41EB015896, and 1S10RR019307.

Please address correspondence to Ona Wu, PhD, Athinoula A Martinos Center for Biomedical Imaging, 149 13th St, CNY 2301, Charlestown, MA 02129; e-mail: ona@nmr.mgh.harvard.edu

Indicates open access to non-subscribers at [www.ajnr.org](http://www.ajnr.org)

Indicates article with supplemental on-line appendix and tables.

Indicates article with supplemental on-line photos.

<http://dx.doi.org/10.3174/ajnr.A6077>

ing multiple b-values, up to 2000 s/mm<sup>2</sup> (which are typically not acquired in the acute setting), but whether the data were acquired in the acute or subacute stage was not reported, and the effects of using combinations of parameters were not investigated.<sup>7</sup>

We hypothesize that a multimodal approach can improve the performance of automated segmentation algorithms. Indeed, most radiologists use other sequences in addition to DWI when assessing the extent of acute infarction. We tested this hypothesis by comparing the accuracy of fully automated acute infarct segmentation algorithms that use solo diffusion parametric maps with the performance of algorithms that combine multiple parametric maps. We also posit that ensemble models that aggregate segmentation results from multiple algorithms will surpass single algorithms. The superior accuracy of ensemble algorithms has been shown for tumor applications,<sup>8</sup> but not yet for acute infarct segmentation. Finally, we assessed the generalizability of our approach by evaluating its performance on an independent cohort. We also tested the clinical utility of automated approaches for triaging patients with large infarct volumes who might not benefit from endovascular treatment.<sup>9,10</sup>

## MATERIALS AND METHODS

### Subjects

All analyses were performed retrospectively under Partners Human Research Committee review board approval. MR imaging from patients with acute ischemic stroke admitted at a single academic medical center between 2005 and 2007, imaged within 12 hours of when the patient was last known to be well (LKW), and who did not receive either thrombolysis before MR imaging or experimental therapy were used for training the convolutional neural networks (CNNs).<sup>11</sup> An independent cohort<sup>12,13</sup> consisting of nonoverlapping patients admitted to the same center between 1996 and 2012 for whom imaging was performed within 24 hours of LKW and for whom follow-up MR imaging datasets were available was used for the evaluation group. Both cohorts were drawn from separate repositories for which manual outlines were available that had been drawn several years ago for a study of early-stage stroke patterns<sup>11</sup> or for studies predicting lesion expansion.<sup>12,13</sup>

### MR Imaging

Diffusion-weighted MR imaging was acquired on 1.5T scanners (GE Genesis SIGNA, SIGNA Excite, SIGNA HDx, SIGNA HDxt; GE Healthcare, Milwaukee, Wisconsin) with the following parameters for most subjects: b-value = 1000 s/mm<sup>2</sup>, TR = 5000 ms, TE = 88.9 ms, FOV = 220 mm, 23 5-mm thick-slices and 1-mm gap, and 6 diffusion directions (see the On-line Appendix and On-line Table 1 for details). Diffusion-weighted MR imaging were corrected for eddy current distortions before calculation of isotropic trace DWI maps (geometric mean of the high-b-value acquisitions) and ADC maps (slope of the linear regression fit of the log of the DWI and LOWB images using techniques described previously).<sup>14</sup> Manual outlines had been drawn for prior studies<sup>11-13</sup> using the program Display (McConnell Brain Imaging Centre, Montreal, Canada) by a neuroscientist with 15 years of experience (reader 1: O.W., Training Cohort) and a neuroradiology fellow with 4 years of experience (reader 2: R.B., Evaluation Cohort) interpreting stroke MR imaging. The readers were blinded to the results of the automated segmentation

algorithm. No a priori thresholds were used for manual segmentation, but concomitant ADC and LOWB maps were referenced to avoid inclusion of susceptibility artifacts and chronic lesions with elevated ADC values. Tissue was considered an acute infarct if it exhibited hyperintensity on DWI, with hypointensity on the ADC or abnormal T2 prolongation on LOWB. To assess interrater agreement, we randomly selected 10 subjects from the Evaluation Cohort and outlines drawn by reader 1, and 2-way intraclass correlation was calculated.

A neuroradiologist with 12 years of experience (W.A.C.) assigned each patient to 1 of the following categories based on lesion location: brain stem, cerebellum, supratentorial/cortical, or supratentorial/subcortical. The “supratentorial/cortical” designation was used if any portion of  $\geq 1$  infarct involved the cortex. Patients with both supra- and infratentorial lesions or lesions involving both the brain stem and cerebellum were assigned to a fifth category, “multiple.”

### Image Preprocessing

DWI, ADC, and LOWB images were resampled to an isotropic voxel size of 1 mm<sup>3</sup>. The LOWB brain mask was computed using the Brain Extraction Tool (FSL, Version 5.0.9; (<http://fsl.fmrib.ox.ac.uk/fsl/fslwiki/BET>)).<sup>15,16</sup> Mean and SD were calculated from intensities within the brain mask limited to the 1 to 99 percentile range to normalize values to a mean of 0 and SD of 1.0.

### CNN Training

CNNs were trained to classify voxels as lesion or non-lesion on a NVIDIA Tesla K40 GPU (NVIDIA, Santa Clara, California) using the DeepMedic (Version 0.7.0; (<https://biomedica.doc.ic.ac.uk/software/deepmedic/>)) framework with 2 pathways (see the original publication<sup>17</sup> and the On-line Appendix). On-line Fig 1 shows the architecture. DeepMedic is a 3D-CNN that operates on multiresolution pathways to allow efficient and accurate supervised segmentation. This framework was chosen over other approaches because it performed best in the Ischemic Stroke Lesion Segmentation Challenge (ISLES) 2015 study.<sup>18</sup> Additional studies have also shown that DeepMedic had better or comparable performance compared with other neural network architectures (On-line Appendix). Separate CNNs were trained on single or different combinations of diffusion parametric maps (DWI, ADC, and LOWB individually, and DWI+ADC, ADC+LOWB, DWI+LOWB, DWI+ADC+LOWB). To generate ensemble segmentations, we averaged voxelwise the class posteriors from the softmax layers of 5 independent CNNs.

The results of all models were resampled back to the original image resolution, thresholded at 50%, and masked with the resampled brain masks created at the normalization step. Performance within the training data was assessed via 5-fold cross-validation. For subjects in each fold, lesion segmentations were generated using a CNN that was trained on data from the other 4 folds. Training a single CNN with DWI+ADC+LOWB maps on the full Training Cohort of 116 subjects required approximately 16 hours. Applying the trained CNN to an individual subject to segment the lesion took on average 35 seconds. With sequential evaluation of 5 CNNs, merging their output, and resampling, we estimate that a full segmentation would require <5 minutes.

## Performance Evaluation

Binarized segmentation performances were assessed with the Dice score (measure of overlap between automated and manual lesion segmentations), precision, and sensitivity metrics. Dice score, precision, and sensitivity were computed as follows: Dice =  $2TP / (2 \times TP + FP + FN)$ ; Precision =  $TP / (TP + FP)$ ; Sensitivity =  $TP / (TP + FN)$  for which TP = true-positive, FP = false-positive, and FN = false-negative. All metrics range from 0% to 100%, with higher values indicating better performances.

To evaluate the generalizability of the approach, we retrained the best performing network on the full Training Cohort and applied it to the independent cohort. The Evaluation Cohort was also segmented with an approach that has been used in clinical trials.<sup>19</sup> In brief, the technique combined thresholding of ADC ( $<615 \times 10^{-6} \text{ mm}^2/\text{s}$ ), DWI, and exponential attenuation maps with morphologic operations (opening with a 2-voxel structural element). ADC images were first masked with a LOWB brain mask before thresholding. We evaluated the algorithm on images that had been resampled to 1-mm resolution for processing and on images that were segmented at their original resolution. Segmented outputs from all algorithms were evaluated at 1-mm resolution to reduce potential confounds from different MR imaging acquisition resolutions. Effects of lesion volume and location on performance were investigated using univariable and multivariable regression analysis as a function of the manually segmented lesion volumes (MLVs). We also compared algorithm accuracy between very small MLVs of  $<1 \text{ cm}^3$  (group I-A) and larger MLVs  $\geq 1 \text{ cm}^3$  (group I-B).

To assess the accuracy of using automatically segmented lesion volumes (ALVs) in place of MLVs for identifying patients who have lesion volumes that are too large to likely benefit from endovascular treatment, we explored the agreement between ALV and MLV for MLV  $<21 \text{ cm}^3$  (group II-A) versus  $\geq 21 \text{ cm}^3$  (group II-B), MLV  $<31 \text{ cm}^3$  (group III-A) versus  $\geq 31 \text{ cm}^3$  (group III-B), MLV  $<51 \text{ cm}^3$  (group IV-A) versus  $\geq 51 \text{ cm}^3$  (group IV-B), and MLV  $<70 \text{ cm}^3$  (group V-A) versus  $\geq 70 \text{ cm}^3$  (group V-B) to determine potential misclassification rates of patients with large lesions using automated algorithms compared with manual volumes. The thresholds (21, 31, 51, and  $70 \text{ cm}^3$ ) were selected on the basis of values that had been used for enrollment in prospective endovascular clinical trials of expanded-window interventions.<sup>9,10</sup> To be eligible for endovascular treatment using the DWI or CTP Assessment with Clinical Mismatch in the Triage of Wake-Up and Late Presenting Strokes Undergoing Neurointervention With Trevo (DAWN) trial criteria,<sup>10</sup> patients had to meet the inclusion and exclusion criteria of 1 of the following 3 groups: group A, 80 years of age or older, NIHSS score  $\geq 10$ , and infarct volume of  $<21 \text{ cm}^3$ ; group B, younger than 80 years of age, NIHSS score  $\geq 10$ , and infarct volume of  $<31 \text{ cm}^3$ ; group C, younger than 80 years of age, NIHSS score  $\geq 20$ , and infarct volume of  $<51 \text{ cm}^3$ . For the MR imaging cohort, the infarct volume was measured on DWI. Similarly, to be eligible for late window endovascular treatment using the Endovascular Therapy Following Imaging Evaluation for Ischemic Stroke 3 (DEFUSE) 3 MR imaging criteria,<sup>9</sup> patients had to exhibit an infarct volume on DWI of  $<70 \text{ cm}^3$ . Although there may be other volume thresholds that

**Table 1: Demographics for training and Evaluation Cohorts<sup>a</sup>**

Characteristic	Training (n = 116)	Evaluation (n = 151)	P Value
Age (yr)	67.9 $\pm$ 17.2	65.2 $\pm$ 15.5	0.11
Male sex	57 (49.1%)	104 (68.9%)	.002
NIHSS score	7 (3–15.75) <sup>b</sup>	6 (3–13) <sup>c</sup>	.53
Time to MRI (h)	5.0 (2.9–6.8)	6.2 (3.8–8.3)	.002
Manual lesion volumes (cm <sup>3</sup> )	9.0 (1.5–28.4)	10.6 (2.0–32.4)	.60

<sup>a</sup> Differences as a factor of the Training Cohort are shown. Data are shown as median (IQR), mean  $\pm$  SD, or No. (%).

<sup>b</sup> n = 112.

<sup>c</sup> n = 115.

might be useful for patient selection,<sup>20</sup> we focused on thresholds that were used in positive prospective clinical trials.

**Statistical Analysis.** Differences between model performance metrics were tested by 2-way ANOVA followed by post hoc paired Wilcoxon signed rank tests. Correlations were assessed via the Spearman correlation coefficient ( $\rho$ ). Univariate analysis was performed with the Wilcoxon 2-sample rank sum test for continuous variables or the 2-sided Fisher exact test for categorical variables. Cohen  $\kappa$  assessed agreement between MLV, and ALV statistical tests were conducted with JMP Pro 14.0 (SAS Institute, Cary, North Carolina). P values  $< .05$  were considered significant. Figures of MR imaging data were generated using FSLeaves (Version 0.27; <https://fsl.fmrib.ox.ac.uk/fsl/fslwiki/FSLeaves>).

## RESULTS

Subject demographics for training (n = 116) and Evaluation Cohort (n = 151) are shown in Table 1. Although there were imbalances in sex and time to MR imaging likely due to different inclusion and exclusion criteria of the 2 cohorts (ie, patients for whom follow-up MR imaging is ordered clinically who made up the Evaluation Cohort tend to have more severe conditions), there was no statistical difference in the distribution of MLVs. The median volume of the 10 subjects randomly selected from the Evaluation Cohort for intraclass correlation coefficient analysis was  $9.7 \text{ cm}^3$  (interquartile range [IQR] =  $2.7\text{--}32.6 \text{ cm}^3$ ), ranging from  $1.2$  to  $94.4 \text{ cm}^3$ . The intraclass correlation coefficient for the 2 readers was excellent (intraclass correlation coefficient = 1.00,  $P < .001$ ).

### Effect of Selection of Diffusion Parametric Maps on CNN Performance

Significant differences ( $P < .001$ ) were found among all performance metrics (Dice, precision, sensitivity) across all models (Table 2). Precision could not be calculated for cases in which models could not detect a lesion.

### Individual Diffusion Maps

The CNN trained on DWI yielded significantly higher Dice scores compared with the CNN trained on ADC ( $P < .001$ ) or LOWB ( $P < .001$ ) maps (On-line Fig 2 and Table 2). Findings for the CNN precision (DWI versus ADC,  $P < .001$ , versus LOWB,  $P < .001$ ) and sensitivity (DWI versus ADC,  $P < .001$ , versus LOWB,  $P < .001$ ) were analogous to those for the Dice score. Of the networks trained with a single parametric map, the CNN models that used the DWI parametric map performed best, followed by the model based on the ADC map, with the LOWB-based model having the worst scores.

**Table 2: Comparison of performance metrics of segmentations for different CNN models<sup>a</sup>**

Model	Dice	Precision	Sensitivity
LOWB	6.5 (0.3–20.9)	5.7 (0.3–32.7)	8.5 (0.3–28.5)
ADC <sup>b</sup>	56.4 (27.1–75.4)	59.4 (22.3–78.4)	58.2 (32.7–78.9)
DWI	72.3 (46.2–82.5)	73.0 (38.3–88.1)	84.0 (62.4–90.8)
ADC+LOWB	76.5 (51.9–86.1)	78.1 (47.2–88.8)	79.2 (66.6–89.7)
DWI+LOWB	76.7 (58.4–85.4)	79.4 (52.0–89.8)	83.0 (64.8–90.6)
DWI+ADC	79.0 (57.1–86.4)	79.0 (62.1–90.5)	82.6 (68.4–91.4)
DWI+ADC+LOWB	78.9 (56.2–86.2)	77.4 (55.0–89.8)	83.4 (71.3–91.8)
E2 (DWI+ADC)	82.0 (62.9–88.1)	82.0 (65.1–92.6) <sup>b</sup>	84.1 (71.0–92.6)
E3 (DWI+ADC+LOWB)	82.2 (64.9–88.9)	83.2 (67.7–93.3)	83.9 (71.9–92.4)

<sup>a</sup> All metrics are denoted in percentages as median (IQR). Of the nonensemble models, significant differences in Dice, precision, and sensitivity were found ( $P < .001$ ). The ensemble models, E2 and E3, were superior to all other models ( $P < .001$ ).

<sup>b</sup> Excludes 1 subject with an automatically segmented lesion volume of zero because precision is undefined in this circumstance.

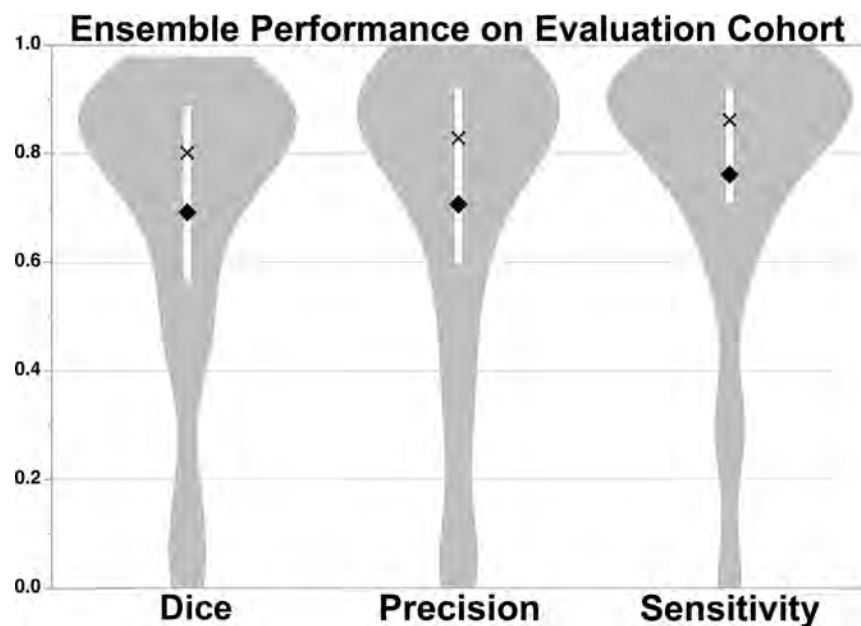


**FIG 1.** Median Dice (80.2% [IQR, 56.6%–88.9%]), precision (82.9% [IQR, 59.7%–92.2%]), and sensitivity (86.2% [IQR, 71.1%–92.3%]) scores of the DWI+ADC+LOWB ensemble on the Evaluation Cohort. The white bar within the violin plot shows the IQR, mean is a diamond, and median is an X.

### Combinations of 2 Diffusion Maps

Including additional diffusion parametric maps as training data improved segmentation results. When we trained CNNs on 2 parametric maps (On-line Fig 2B and Table 2), all 3 CNNs that used combinations of 2 maps yielded higher Dice scores than all single-map CNNs (DWI+ADC versus LOWB, versus ADC, versus DWI,  $P < .001$ ; DWI+LOWB versus LOWB, versus ADC, versus DWI,  $P < .001$ ; ADC+LOWB versus LOWB, versus ADC, versus DWI,  $P < .001$ ). DWI+ADC had the highest Dice score compared with the other combinations (ADC+LOWB,  $P < .001$ ; DWI+LOWB,  $P = .03$ ). Similarly, all CNNs trained with combinations of 2 parametric maps had higher precision than CNNs trained with 1 map (DWI+ADC versus LOWB, versus ADC, versus DWI,  $P < .001$ ; DWI+LOWB versus LOWB, versus ADC, versus DWI,  $P < .001$ ; ADC+LOWB versus LOWB, versus ADC, versus DWI,  $P < .001$ ). However, there was no significant difference in precision between the combinations (DWI+ADC versus DWI+LOWB,  $P = .67$ ; DWI+LOWB versus ADC+LOWB,  $P = .28$ ), except for DWI+ADC versus ADC+LOWB,  $P = .03$ . DWI+ADC similarly outperformed the individual parametric

maps (LOWB,  $P < .001$ ; ADC,  $P < .001$ ) except for DWI ( $P = .28$ ) in terms of sensitivity. ADC+LOWB outperformed the individual LOWB ( $P < .001$ ) and ADC ( $P < .001$ ) models, but not DWI ( $P = .24$ ). Similar results were found for the DWI+LOWB model compared with the individual parametric maps (LOWB,  $P < .001$ ; ADC,  $P < .001$ ; DWI,  $P = .83$ ). DWI+ADC was comparable sensitivity with that of DWI+LOWB ( $P = .11$ ) and had improved sensitivity with respect to ADC+LOWB ( $P < .001$ ). DWI+LOWB and ADC+LOWB were equally sensitive ( $P = .06$ ).

### Combination of 3 Diffusion Maps

The CNN model that combined all 3 parametric maps had a significantly greater Dice score (versus the LOWB, ADC, DWI,  $P < .001$ ; DWI+LOWB,  $P = .01$ ; ADC+LOWB,  $P < .001$ ) compared with all other combinations with the exception of DWI+ADC ( $P = .49$ ). Precision results showed improvement against models using individual maps (versus LOWB, ADC, DWI,  $P < .001$ ) but not against the other combinations (DWI+ADC,  $P = .47$ ; DWI+LOWB,  $P = .69$ ; ADC+LOWB,  $P = .19$ ). Similar results were found for sensitivity (versus LOWB, ADC,  $P < .001$ ; DWI,  $P = .008$ ; DWI+ADC,  $P = .10$ ; DWI+LOWB,  $P = .007$ ; ADC+LOWB,  $P < .001$ ).

### Ensemble of CNNs

Five CNNs were trained, each using either DWI+ADC or DWI+ADC+LOWB, the

2 best-performing models. The Dice performances of each of the 5 individual CNNs were slightly different using DWI+ADC (On-line Table 2 and On-line Fig 3, ANOVA  $P = .02$ , with differences between CNN 2 and CNN 3,  $P = .04$ ; and CNN 4 and CNN 5,  $P = .04$ ) but were similar to one another using DWI+ADC+LOWB (On-line Table 3 and On-line Fig 4, ANOVA  $P = .60$ ). Aggregating results of the individual CNNs to create ensembles (E2: DWI+ADC CNNs, E3: DWI+ADC+LOWB CNNs) significantly improved the Dice performance over individual CNNs ( $P < .001$ ). Both ensembles yielded results similar to one another in terms of Dice ( $P = .66$ ) and precision ( $P = .62$ ), but both surpassed the other CNNs (Table 2,  $P < .001$ ). E3 and E2 had similar sensitivity to one another ( $P = .46$ ) and to the DWI+ADC+LOWB model (versus E2,  $P = .58$ ; versus E3,  $P = .12$ ), but outperformed the others ( $P < .01$ , Table 2).

### Validation on the Independent Cohort

E3 was used for the evaluation studies to assess the generalizability of the approach because E3 tended to perform better than E2.

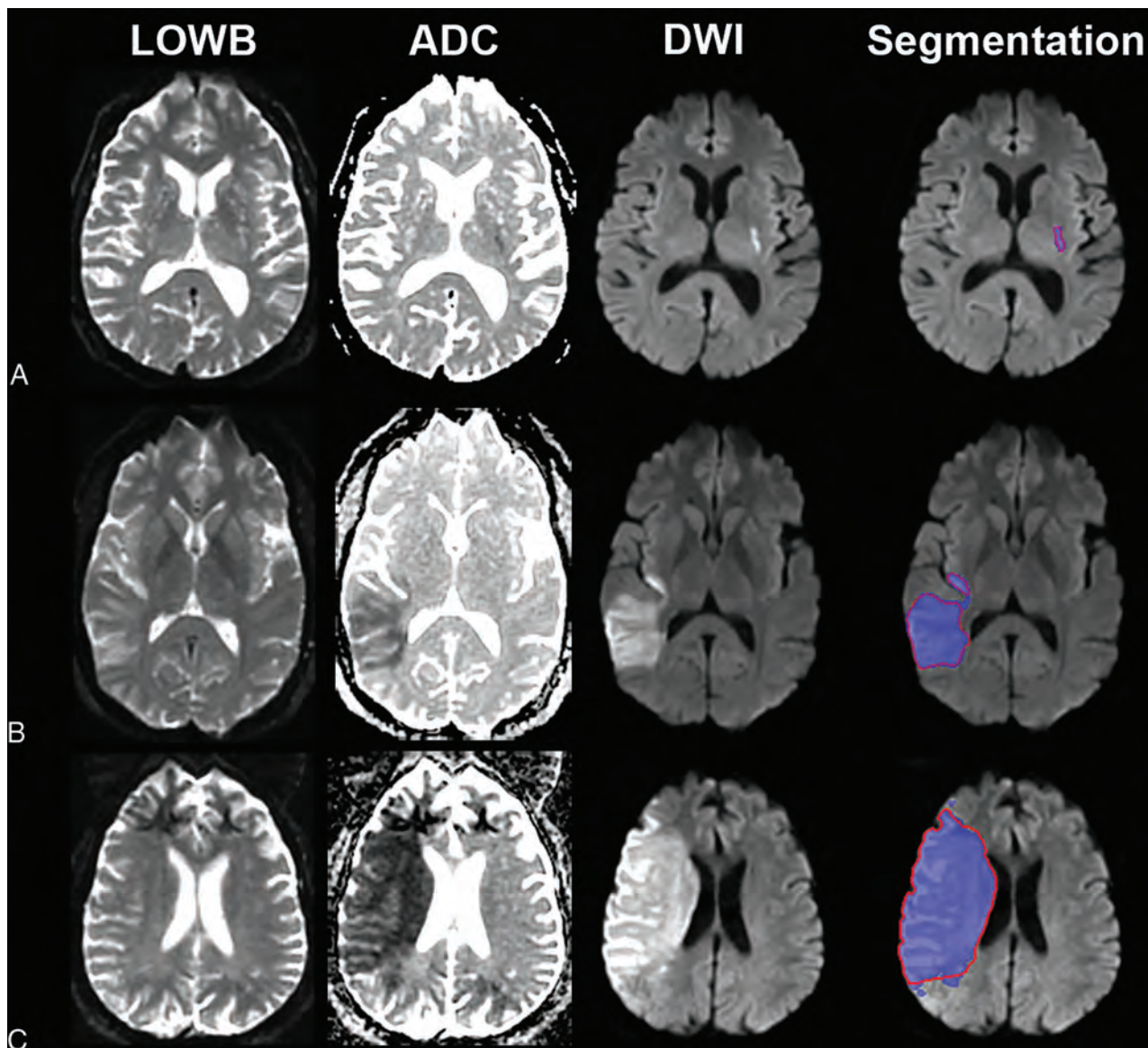


**FIG 2.** Sample segmentation results of the ensemble of DWI+ADC+LOWB (blue regions) on sample subjects along with manual outlines (red outlines). A, A small lesion example from a 70-year-old man with an admission NIHSS score of 1, imaged approximately 9 hours from LKW: MLV = 0.96 cm<sup>3</sup>, ALV = 1.07 cm<sup>3</sup>, Dice = 89.4%. B, Medium lesion sample from a 38-year-old woman with an admission NIHSS score of 4, imaged approximately 10 hours from LKW: MLV = 54.3 cm<sup>3</sup>, ALV = 57.9 cm<sup>3</sup>, Dice = 95.7%. C, A large lesion example from a 62-year-old man with an undocumented admission NIHSS score, imaged approximately 10 hours from LKW: MLV = 229.0 cm<sup>3</sup>, ALV = 208.7 cm<sup>3</sup>, Dice = 94.0%.

Figure 1 shows the results of applying the E3 to the Evaluation Cohort. Dice ( $P = .59$ ), precision ( $P = .35$ ), and sensitivity ( $P = .66$ ) were not significantly different from the results for the Training Cohort. In contrast, the thresholding approach performed significantly worse compared with E3 across all measures ( $P < .001$ ), achieving only a Dice score of 13.3 (2.3–41.6), precision of 7.5 (1.2–34.2), and sensitivity of 60.7 (39.5–72.2) for data analyzed in the original resolution and for data analyzed at 1-mm isotropic resolution (Dice: 11.6 [2.2–34.7], precision: 6.5 [1.1–28.0], sensitivity: 59.4 [37.6–72.2]). We therefore focused the remainder of our analyses on E3 results. Examples of segmentation on subjects from the Evaluation Cohort using E3 are provided in Fig 2 (see On-line Fig 5 for probability maps). Regression analysis showed that Dice scores ( $P < .001$ ), precision ( $P < .001$ ), and sensitivity ( $P = .01$ ) improved with larger lesion volumes. The

independent Evaluation Cohort consisted of strokes involving primarily supratentorial/cortical ( $n = 104$ , 69%) locations and supratentorial/subcortical ( $n = 30$ , 20%) regions. There were significant differences in MLV, ALV, Dice, precision, and sensitivity as a function of location (On-line Table 4). Univariable regression showed that lesion location affected Dice scores ( $P = .002$ ), precision ( $P = .01$ ), and sensitivity ( $P < .001$ ). However, multivariable analysis including lesion volume ( $P < .001$ ), showed that lesion location was no longer significantly associated with the Dice score ( $P = .06$ ) or precision ( $P = .17$ ). Notably, sensitivity was still associated with location ( $P < .001$ ) but not volume ( $P = .09$ ) in multivariable analysis.

ALV correlated significantly with MLV ( $\rho = 0.91$ ,  $P < .001$ ) and NIHSS score ( $\rho = 0.55$ ,  $P < .001$ ), comparable with MLV correlation with NIHSS score ( $\rho = 0.46$ ,  $P < .001$ ). Subgroup

**Table 3: Dependency of automated segmentation performance on MLV<sup>a</sup>**

Group	Thresholds	Dice	Precision <sup>b</sup>	Sensitivity	Correlation
I-A	MLV < 1 cm <sup>3</sup> (n = 22)	31.0 (0–50.0)	29.6 (3.4–54.9)	57.5 (0–90.0)	$\rho = 0.09, P = .68$
I-B	MLV $\geq$ 1 cm <sup>3</sup> (n = 129)	83.5 <sup>c</sup> (71.2–89.3)	84.9 <sup>c</sup> (70.3–92.9)	87.6 <sup>d</sup> (75.8–92.9)	$\rho = 0.90, P < .001$
II-A	MLV < 21 cm <sup>3</sup> (n = 100)	71.2 (45.8–84.8)	71.6 (38.7–84.9)	81.3 (59.8–92.5)	$\rho = 0.79, P < .001$
II-B	MLV $\geq$ 21 cm <sup>3</sup> (n = 51)	89.4 <sup>c</sup> (85.4–92.5)	92.3 <sup>c</sup> (85.6–96.1)	89.3 <sup>e</sup> (83.0–92.2)	$\rho = 0.97, P < .001$
III-A	MLV < 31 cm <sup>3</sup> (n = 113)	73.6 (48.0–85.8)	77.2 (46.3–85.7)	82.5 (62.8–92.1)	$\rho = 0.83, P < .001$
III-B	MLV $\geq$ 31 cm <sup>3</sup> (n = 38)	90.6 <sup>c</sup> (87.3–93.2)	94.7 <sup>c</sup> (88.4–96.8)	89.4 <sup>e</sup> (82.8–93.6)	$\rho = 0.96, P < .001$
IV-A	MLV < 51 cm <sup>3</sup> (n = 124)	75.0 (48.9–86.8)	78.1 (49.2–86.5)	83.3 (65.2–92.5)	$\rho = 0.87, P < .001$
IV-B	MLV $\geq$ 51 cm <sup>3</sup> (n = 27)	91.5 <sup>c</sup> (89.1–93.6)	95.9 <sup>c</sup> (92.2–97.5)	89.2 (83.5–92.2)	$\rho = 0.92, P < .001$
V-A	MLV < 70 cm <sup>3</sup> (n = 131)	77.2 (51.5–87.0)	79.9 (54.2–87.0)	84.0 (67.8–92.6)	$\rho = 0.88, P < .001$
V-B	MLV $\geq$ 70 cm <sup>3</sup> (n = 20)	91.8 <sup>c</sup> (89.4–93.9)	96.0 (93.0–96.9)	89.6 (85.0–92.0)	$\rho = 0.83, P < .001$

<sup>a</sup> Performance metrics are in median (IQR) and percentages. Results of E3 applied to the Evaluation Cohort are shown as a function of different volume thresholds.

<sup>b</sup> Excludes 2 subjects in group A with automatically segmented lesion volumes of zero because precision is undefined in this circumstance.

<sup>c</sup>  $P < .001$ .

<sup>d</sup>  $P < .01$ .

<sup>e</sup>  $P < .05$  group A versus group B, where Group A is the group meeting the threshold criteria and Group B is the group not meeting the threshold criteria.

analysis based on MLV (Table 3) showed that the automated method performed significantly worse on small volumes (<1 cm<sup>3</sup>) compared with large volumes for all metrics (group I-A versus group I-B,  $P < .01$ ). Misclassification rates across all thresholds were low—21 cm<sup>3</sup>: 9/151 (6.0%),  $\kappa = 0.87, P < .001$ ; 31 cm<sup>3</sup>: 6/151 (4.0%),  $\kappa = 0.90, P < .001$ ; 51 cm<sup>3</sup>: 6/151 (4.0%),  $\kappa = 0.86, P < .001$ ; and 70 cm<sup>3</sup>: 4/151 (2.6%),  $\kappa = 0.89, P < .001$ . There were 3 subjects for whom the differences in ALV and MLV were >50 cm<sup>3</sup>; these cases had poor skull stripping as a result of scanner inhomogeneities (On-line Fig 6). If we excluded these 3 subjects, the median (IQR) differences in the misclassified cases for each threshold were the following—21 cm<sup>3</sup>: 18.7 cm<sup>3</sup> (8.9–25.2 cm<sup>3</sup>); 31 cm<sup>3</sup>: 7.4 cm<sup>3</sup> (1.7–16.8 cm<sup>3</sup>); 51 cm<sup>3</sup>: 8.8 cm<sup>3</sup> (8.0–14.6 cm<sup>3</sup>); 70 cm<sup>3</sup>: 5.3 cm<sup>3</sup> (3.7–6.9 cm<sup>3</sup>).

## DISCUSSION

We have shown that an ensemble of CNNs trained with multiparametric diffusion maps improves automated segmentation of acute infarcts over methods that use solo maps. Among the individual parameter models, CNNs trained on DWI performed best. However, a model trained on only DWI may incorrectly classify regions with susceptibility artifacts that appear as DWI hyperintensities or wrongly include subacute T2-shinethrough regions.<sup>21</sup> Networks trained on only ADC images provided a fair performance because reduced ADC values represent cytotoxic edema that manifests in hyperacute stroke,<sup>22</sup> but may undersegment later-stage strokes when ADC pseudonormalizes.<sup>21</sup> CNNs exclusively trained on LOWB performed poorly, likely because our data consisted of mainly patients with early-phase stroke (median, 6 hours from LKW) before vasogenic edema is evident on LOWB.<sup>23</sup>

Combining DWI and ADC improved segmentation, consistent with “standard practice” by expert outliners who typically refer to the ADC image to confirm that the DWI hyperintensity coincides with reduced diffusivity to minimize inclusion of artifacts. Combining LOWB with either ADC or DWI increased the Dice score, suggesting that LOWB provides complementary information. Although inclusion of LOWB with DWI+ADC did not result in statistically significant improved performance, a tendency toward more accurate segmentation was observed in the ensemble models.

We have also shown that our model performs comparably with

humans as reflected by both high Dice scores and correlation between ALV and MLV. Indeed, the Dice scores of the E3 algorithm results were comparable with the Dice scores between human readers in our subcohort of 10 patients with outlines from both readers. The time for automated segmentation currently is approximately 5 minutes, which may be similar to times required by an experienced human reader, but we expect that with optimization and faster GPUs, the time for segmentation can be further reduced. Furthermore, the primary benefits of our automated approach are that the results will be reproducible, unbiased, and scalable (eg, clinical trials that compare lesion volumes for thousands of subjects).

ALV and MLV were closely correlated, but segmentation of small lesion volumes (<1 cm<sup>3</sup>) is more difficult because they are harder to detect and small variation from the ground truth leads to greater aberrations of performance metrics. Small-lesion segmentation could possibly be improved by customizing specific CNNs tailored to detecting lesions by volume size. Nevertheless, we have shown that our automated approach performed comparably with manual lesions delineated by our human experts with regard to patient-selection tasks. The cases of disagreement typically occurred when there were image artifacts that led to poor brain extraction, which, in turn, might have led to poor normalization, resulting in oversegmentation. A second reason for this failure might be that the networks have not previously seen context outside the brain during training because it is excluded in most cases in which the masks are correctly computed. We did not manually fix the brain masks because we wanted to evaluate a fully-automated approach. Refining the automated brain extraction step will likely further improve our algorithms.

There were several limitations to this study. One is the retrospective nature of our analysis, which resulted in variable MR imaging acquisition protocols that changed across the years with clinical practice. However, this is also a strength because our approach will likely be more generalizable to real-world clinical situations and not dependent on a specific MR imaging protocol, which is often used in clinical trials. This may also explain why the thresholding approach performed poorly on our data compared with other studies for which MR imaging acquisition was harmonized as part of a trial.<sup>19</sup> Another potential limitation is that a different reader created the manual outlines used for the Evalua-

tion Cohort from the Training Cohort. However, the accurate segmentation results in both cohorts suggest that the model is not overfitted to 1 particular reader. Another benefit of an automated approach is that it is reproducible and not dependent on the expertise of the reader.

To evaluate the impact of different diffusion maps on segmentation performance, we kept the CNN architecture constant throughout all experiments. In addition to changing the combinations of inputs, we chose to build an ensemble from several CNNs because ensemble learning is known to boost the performances of single-classifier algorithms.<sup>8,24</sup> DeepMedic samples randomly from the Training Cohort (ie, both the selected subjects and extracted samples differ in each training epoch). Although DeepMedic is very robust in its performance, the variation in sampling inherently results in slightly different models, even when trained with the same architecture. Merging the segmentations of several models reduces false-positives and improves overall performance. Although strong single networks are desired and necessary to create a high-performing ensemble, our CNNs may come with bias specific to DeepMedic. Building an ensemble of different CNN architectures might further enhance the performance. Future investigation will need to analyze the benefits of merging more diverse networks to cancel out each other's inherent biases.<sup>8</sup> This diversity of models could be achieved by changing the hyperparameters of DeepMedic using completely different architectures or training on a different dataset.

## CONCLUSIONS

Ensembles of CNNs trained on multiparametric diffusion MR imaging improved automated segmentation of acute infarcts in comparison with individual CNNs trained on solo diffusion maps, producing results that are comparable with manual lesions drawn by experts.

## ACKNOWLEDGMENTS

We gratefully acknowledge the support of NVIDIA Corporation with the donation of the NVIDIA Tesla K40 GPU used for this research.

Disclosures: Steven Mocking—RELATED: Grant: National Institutes of Health, Comments: R01NS059775, R01NS063925; UNRELATED: Employment: Alphabet (Google); Stock/Stock Options: NVIDIA, Comments: as part of index funds only. Mark Bouts—RELATED: Grant: National Institutes of Health, Comments: grant No: R01NS059775.\* Elissa McIntosh—RELATED: Grant: National Institutes of Health, Comments: R01NS059775, R01NS063925.\* Hakan Ay—UNRELATED: Royalties: UpToDate, Comments: authorship royalties. Konstantinos Kamnitsas—UNRELATED: Consultancy: Kheiron Medical, Comments: I consulted for them in the summer of 2017; Employment: Microsoft Research Cambridge, Comments: I interned there in 2017 and 2018. Ben Glocker—UNRELATED: Consultancy: Kheiron Medical Technologies; Grants/Grants Pending: European Research Council.\* Ona Wu—RELATED: Grant: National Institutes of Health, Comments: R01NS38477, R01NS059775, R01NS063925, R01NS082285, P50NS051343, R01NS086905, U01 NS069208; National Institutes of Health—National Institute of Biomedical Imaging and Bioengineering, P41EB015896, 1S10RR019307\*; Provision of Writing Assistance, Medicines, Equipment, or Administrative Support: NVIDIA, Comments: NVIDIA Corporation donated a NVIDIA Tesla K40 GPU used for this research and a Titan XP (which was not used for the current study)\*; UNRELATED: Consultancy: Penumbra, Comments: consultant on unrelated topics; Royalties: delay-compensated calculation of tissue blood flow, US Patent 7,512,435, March 31, 2009, Comments: We received royalties and licensing fees from the following companies: GE Healthcare, Siemens, Olea Medical, Imaging Biometrics Ltd.\* Aneesh Singhal—UNRELATED: Consultancy: Biogen, Omnix, Boston Clinical Research Institute, Comments: Advisory Board; Expert Testimony: various law firms, Comments: individual cases; Grants/Grants Pending: Dana Foundation and National

Institutes of Health, Comments: Clinical trial of VNS in stroke and U10 NS086729, U10INS095869, R01NS105875, U01 NS109028, R01DC012584\*; Royalties: UpToDate, Comments: book chapters; Other: American Academy of Neurology and MedLink, Comments: educational programs and book chapters. W. Taylor Kimberly—UNRELATED: Board Membership: Biogen, Comments: Scientific Advisory Board\*; Grants/Grants Pending: Biogen (CHARM trial), National Institutes of Health, American Heart Association, Remedy Pharmaceuticals (GAMES-RP trial)\*; Travel/Accommodations/Meeting Expenses Unrelated to Activities Listed: Biogen, Comments: travel to CHARM trial investigator meeting to give training presentations to site Principal Investigators. A. Gregory Sorensen—RELATED: Grant: National Institutes of Health, Comments: R01NS38477; UNRELATED: Board membership: Siemens Healthineers. \*Money paid to the institution.

## REFERENCES

- Chen L, Bentley P, Rueckert D. **Fully automatic acute ischemic lesion segmentation in DWI using convolutional neural networks.** *Neuroimage Clin* 2017;15:633–43 CrossRef Medline
- Straka M, Albers GW, Bammer R. **Real-time diffusion-perfusion mismatch analysis in acute stroke.** *J Magn Reson Imaging* 2010;32:1024–37 CrossRef Medline
- Jacobs MA, Mitsias P, Soltanian-Zadeh H, et al. **Multiparametric MRI tissue characterization in clinical stroke with correlation to clinical outcome: Part 2.** *Stroke* 2001;32:950–57 CrossRef Medline
- Hevia-Montiel N, Jimenez-Alaniz JR, Medina-Banuelos V, et al. **Robust nonparametric segmentation of infarct lesion from diffusion-weighted MR images.** *Conf Proc IEEE Eng Med Biol Soc* 2007;2007:2102–05 Medline
- Tsai JZ, Peng SJ, Chen YW, et al. **Automatic detection and quantification of acute cerebral infarct by fuzzy clustering and histographic characterization on diffusion weighted MR imaging and apparent diffusion coefficient map.** *Biomed Res Int* 2014;2014:963032 CrossRef Medline
- Zhang R, Zhao L, Lou W, et al. **Automatic segmentation of acute ischemic stroke from DWI using 3-D fully convolutional DenseNets.** *IEEE Trans Med Imaging*. 2018;37:2149–60 CrossRef Medline
- Mujumdar S, Varma R, Kishore LT. **A novel framework for segmentation of stroke lesions in diffusion weighted MRI using multiple b-value data.** In: *Proceedings of the Conference of the International Association for Pattern Recognition*, Tsukuba, Japan. November 11–15, 2012:3762–65
- Kamnitsas K, Bai W, Ferrante E, et al. **Ensembles of multiple models and architectures for robust brain tumour segmentation.** In: Crimini A, Bakas S, Kuijff H, et al, eds. *Brainlesion: Glioma, Multiple Sclerosis, Stroke and Traumatic Brain Injuries*. Cham: Springer-Verlag; 2018:450–62
- Albers GW, Marks MP, Kemp S, et al; DEFUSE 3 Investigators. **Thrombectomy for stroke at 6 to 16 hours with selection by perfusion imaging.** *N Engl J Med* 2018;378:708–18 CrossRef Medline
- Nogueira RG, Jadhav AP, Haussen DC, et al; DAWN Trial Investigators. **Thrombectomy 6 to 24 hours after stroke with a mismatch between deficit and infarct.** *N Engl J Med* 2018;378:11–21 CrossRef Medline
- Wu O, Schwamm LH, Garg P, et al. **Using MRI as the witness: multimodal MRI-based determination of acute stroke onset.** *Stroke* 2010;41:E273
- Wu O, McIntosh E, Bezerra R, et al. **Prediction of lesion expansion in patients using acute MRI.** *Stroke* 2012;43:A3319
- Wu O, Koroshetz WJ, Ostergaard L, et al. **Predicting tissue outcome in acute human cerebral ischemia using combined diffusion- and perfusion-weighted MR imaging.** *Stroke* 2001;32:933–42 CrossRef Medline
- Sorensen AG, Wu O, Copen WA, et al. **Human acute cerebral ischemia: detection of changes in water diffusion anisotropy by using MR imaging.** *Radiology* 1999;212:785–92 CrossRef Medline
- Smith SM. **Fast robust automated brain extraction.** *Hum Brain Mapp* 2002;17:143–55 CrossRef Medline
- Jenkinson M, Beckmann CF, Behrens TE, et al. **FSL.** *Neuroimage* 2012;62:782–90 CrossRef Medline
- Kamnitsas K, Ledig C, Newcombe VF, et al. **Efficient multi-scale 3D CNN with fully connected CRF for accurate brain lesion segmentation.** *Med Image Anal* 2017;36:61–78 CrossRef Medline

18. Maier O, Menze BH, von der Gablentz J, et al. **ISLES 2015: a public evaluation benchmark for ischemic stroke lesion segmentation from multispectral MRI.** *Med Image Anal* 2017;35:250–69 CrossRef Medline
19. Lansberg MG, Lee J, Christensen S, et al. **RAPID automated patient selection for reperfusion therapy: a pooled analysis of the Echoplanar Imaging Thrombolytic Evaluation Trial (EPITHET) and the Diffusion and Perfusion Imaging Evaluation for Understanding Stroke Evolution (DEFUSE) study.** *Stroke* 2011;42:1608–14 CrossRef Medline
20. Leslie-Mazwi TM, Hirsch JA, Falcone GJ, et al. **Endovascular stroke treatment outcomes after patient selection based on magnetic resonance imaging and clinical criteria.** *JAMA Neurol* 2016;73:43–49 CrossRef Medline
21. Dijkhuizen RM, Knollema S, van der Worp HB, et al. **Dynamics of cerebral tissue injury and perfusion after temporary hypoxia-ischemia in the rat: evidence for region-specific sensitivity and delayed damage.** *Stroke* 1998;29:695–704 CrossRef Medline
22. Jiang Q, Chopp M, Zhang ZG, et al. **The temporal evolution of MRI tissue signatures after transient middle cerebral artery occlusion in rat.** *J Neurol Sci* 1997;145:15–23 CrossRef Medline
23. Schwamm LH, Wu O, Song SS, et al; MR WITNESS Investigators. **Intravenous thrombolysis in unwitnessed stroke onset: MR WITNESS trial results.** *Ann Neurol* 2018;83:980–93 CrossRef Medline
24. Breiman L. Random Forests. In: Schapire RE, ed. *Machine Learning*. the Netherlands: Kluwer Academic Publishers; 2001;5–32

# A Novel Collateral Imaging Method Derived from Time-Resolved Dynamic Contrast-Enhanced MR Angiography in Acute Ischemic Stroke: A Pilot Study

H.G. Roh, E.Y. Kim, I.S. Kim, H.J. Lee, J.J. Park, S.B. Lee, J.W. Choi, Y.S. Jeon, M. Park, S.U. Kim, and H.J. Kim



## ABSTRACT

**BACKGROUND AND PURPOSE:** Assessment of the collateral status has been emphasized for appropriate treatment decisions in patients with acute ischemic stroke. The purpose of this study was to introduce a multiphase MRA collateral imaging method (collateral map) derived from time-resolved dynamic contrast-enhanced MRA and to verify the value of the multiphase MRA collateral map in acute ischemic stroke by comparing it with the multiphase collateral imaging method (MRP collateral map) derived from dynamic susceptibility contrast-enhanced MR perfusion.

**MATERIALS AND METHODS:** From a prospectively maintained registry of acute ischemic stroke, MR imaging data of patients with acute ischemic stroke caused by steno-occlusive lesions of the unilateral ICA and/or the M1 segment of the MCA were analyzed. We generated collateral maps using dynamic signals from dynamic contrast-enhanced MRA and DSC-MRP using a Matlab-based in-house program and graded the collateral scores of the multiphase MRA collateral map and the MRP collateral map independently. Interobserver reliabilities and intermethod agreement between both collateral maps for collateral grading were tested.

**RESULTS:** Seventy-one paired multiphase MRA and MRP collateral maps from 67 patients were analyzed. The interobserver reliabilities for collateral grading using multiphase MRA or MRP collateral maps were excellent (weighted  $\kappa = 0.964$  and  $0.956$ , respectively). The agreement between both collateral maps was also excellent (weighted  $\kappa = 0.884$ ; 95% confidence interval,  $0.819-0.949$ ).

**CONCLUSIONS:** We demonstrated that the dynamic signals of dynamic contrast-enhanced MRA could be used to generate multiphase collateral images and showed the possibility of the multiphase MRA collateral map as a useful collateral imaging method in acute ischemic stroke.

**ABBREVIATIONS:** AIS = acute ischemic stroke; DCE-MRA = dynamic contrast-enhanced MRA; DSC-MRP = dynamic susceptibility contrast-enhanced MR perfusion; mMRA = multiphase MRA; MRP = MR perfusion

The cerebral collaterals are alternative vascular channels for maintaining blood perfusion to the ischemic brain distal to an arterial occlusion. The collateral status varies among patients with

acute ischemic stroke (AIS) and determines the final infarct size and clinical outcome.<sup>1</sup> Prior studies of endovascular treatment showed that better collaterals are associated with less infarct growth and better functional outcome, whereas poor collaterals are linked to hemorrhagic complications and poor recanalization rates.<sup>2-4</sup> In terms of endovascular treatment in patients beyond 5 hours from onset, it was suggested that a better collateral status could extend the time window.<sup>5-9</sup> Therefore, assessment of the collateral status has been emphasized for appropriate treatment decisions in patients with AIS.

The imaging methods for collateral assessment have progressed from single-phase to multiphase imaging.<sup>10-13</sup> The arterial scoring method based on single-phase CTA had a critical limitation of underestimating the leptomeningeal collaterals with a longer transit time due to early triggering of a static acquisition.<sup>10</sup> A method based on multiphase CTA overcame this limitation but still has problems, including radiation exposure, use of iodine contrast media, and imperfect prediction of infarct volume. An-

Received March 4, 2019; accepted April 12.

From the Departments of Radiology (H.G.R., J.W.C.), Neurology (J.J.P.), and Neurosurgery (Y.S.J.), Konkuk University Medical Center, Konkuk University School of Medicine, Seoul, Korea; Department of Radiology (E.Y.K.), Gachon University Gil Medical Center, Incheon, Korea; Siemens Healthineers Ltd (I.S.K.), Seoul, Korea; Departments of Neurosurgery (H.J.L., S.U.K.), Neurology (S.B.L.), and Radiology (H.J.K.), Daejeon St. Mary's Hospital, The Catholic University of Korea, Daejeon, Korea; and Department of Radiology (M.P.), Gangnam Severance Hospital, Yonsei University College of Medicine, Seoul, Korea.

This study was supported by the National Research Foundation of Korea as the subject No. NRF-2017RIA2B1008020.

Please address correspondence to Hyun Jeong Kim, MD, PhD, Department of Radiology, Daejeon St. Mary's Hospital, Medical School, The Catholic University of Korea, 64 Daeheung-Ro, Jung-Gu, Daejeon, 34943, Korea; e-mail: mskendy@cmcdj.or.kr

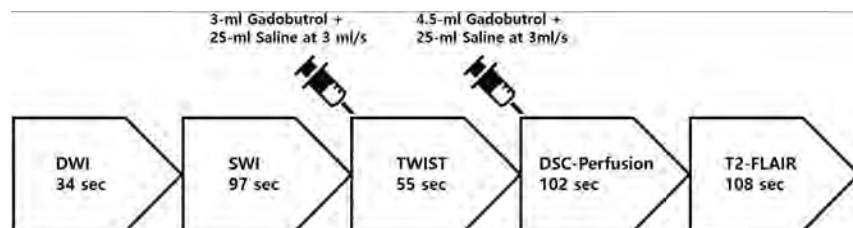
Indicates open access to non-subscribers at [www.ajnr.org](http://www.ajnr.org)

<http://dx.doi.org/10.3174/ajnr.A6068>

**Table 1: Acute stroke MRI acquisition parameters**

Parameter	Acute Stroke MRI				
	SS EPI-DWI	SWI	DCE-MRA (TWIST)	DSC-MRP	T2-FLAIR
TR/TE (ms)	4800/71	28/20	2.62/0.95	1600/30	9000/95
TI (ms)					2500
Turbo factor					21
Flip angle		15°	21°	90°	150°
Bandwidth (Hz/pixel)	1672	120	780	1446	206
Slice thickness/gap (mm)	5/2	2/0	1.2/0	5/2	5/2
FOV (mm)	240 × 240	240 × 195	400 × 300	240 × 240	240 × 217
Matrix size (mm)	130 × 130	384 × 156	320 × 182	128 × 128	256 × 174
B-value (s/mm <sup>2</sup> )	0, 1000				
Measurements	1	1	30	60	1
GRAPPA	2	2	3 × 2		2
Temporal resolution (sec)			1.6	1.6	
Dynamic reconstruction mode			Forward share		
K-space sampling (center/periphery) (%)			15/20		

**Note:**—SS indicates single-shot; TWIST, time-resolved imaging with stochastic trajectories; GRAPPA, generalized autocalibrating partially parallel acquisition.

**FIG 1.** MR imaging protocol for AIS diagnosis.

other multiphase collateral imaging method (collateral flow map) derived from dynamic susceptibility contrast-enhanced MR perfusion (DSC-MRP) was introduced, and the study showed that the collateral flow map had prognostic value in AIS with a major artery occlusion.<sup>12</sup> However, DSC-MRP does not provide angiographic information, which is an indispensable imaging parameter for endovascular treatment. Dynamic contrast-enhanced MRA (DCE-MRA) is also an angiographic imaging method, and like DSC-MRP, it detects intracranial dynamic signals according to the flow of MR imaging contrast media. We developed a new multiphase collateral imaging method, (the mMRA collateral map), using the dynamic signals of DCE-MRA. This study was conducted to verify the value of the mMRA collateral map as a collateral imaging method by comparing it with the multiphase collateral imaging method derived from DSC-MRP (MRP collateral map).

## MATERIALS AND METHODS

### Patients

We analyzed MR imaging data of patients with AIS from a prospectively maintained registry. The MR imaging data of consecutive patients from September 2015 to March 2017 at 2 university medical centers were analyzed retrospectively. Inclusion criteria for this study were as follows: 1) patients who presented with symptoms consistent with AIS within 8 hours of symptom onset; 2) patients older than 18 years of age; 3) patients who underwent brain MR imaging, including DWI, DSC-MRP, and DCE-MRA, at admission; and 4) patients with occlusion or severe stenosis ( $\geq 70\%$ ) of the unilateral ICA and/or M1 segment of the MCA (M1 MCA) and the associated symptoms. Exclusion criteria were as follows: 1) patients with occlusion or severe stenosis of the

contralateral ICA and/or MCA; 2) patients with intracranial hemorrhage on admission MR imaging; 3) patients with previous major stroke with a residual disability (modified Rankin Scale score,  $\geq 2$ ); 4) patients with other brain lesions, such as neoplasm, infection, or demyelination, and so forth; 5) patients unable to undergo MR imaging; and 6) patients with poor-quality MR imaging due to

various artifacts. Institutional review boards of Konkuk University Medical Center and Daejeon St. Mary's Hospital approved this study. All participants provided informed consent.

### Imaging Protocol and Postprocessing to Generate the Collateral Map

All MR imaging examinations were performed on a 3T Magnetom Skyra MR system (Siemens, Erlangen, Germany) with a 20-channel head/neck coil. The routine MR imaging protocol for AIS included DWI, SWI, DCE-MRA, DSC-MRP, and FLAIR. The acquisition parameters are summarized in Table 1. DCE-MRA was performed by the repetitive acquisition of coronal 3D imaging slabs extending from the aortic arch to the cranial vertex, including the whole brain, with a temporal resolution of 1.6 seconds per dynamic acquisition. 3D rotational arteriography was reconstructed with a dataset of an arterial time point of DCE-MRA to interpret the arterial status. The total acquisition time for the MR imaging was 6 minutes 36 seconds, and the total amount of contrast medium was 7.5 mL of gadobutrol (Gadovist; Bayer Schering Pharma, Berlin, Germany) (Fig 1).

We developed a Matlab-based program (MathWorks, Natick, Massachusetts) to produce an mMRA collateral map and an MRP collateral map (Fig 2). The sequential postprocessing steps are as follows: 1) opening and reading DICOM source images of DCE-MRA and DSC-MRP; 2) cropping all DICOM images of DCE-MRA to obtain only the brain region by removing the cervical and aortic arch areas, which are not necessary for the mMRA collateral map; 3) storing all acquired DCE-MRA or DSC-MRP image data in a 4D matrix; 4) creating MIP images for each time point that represent the bolus passage for each phase after subtraction of the

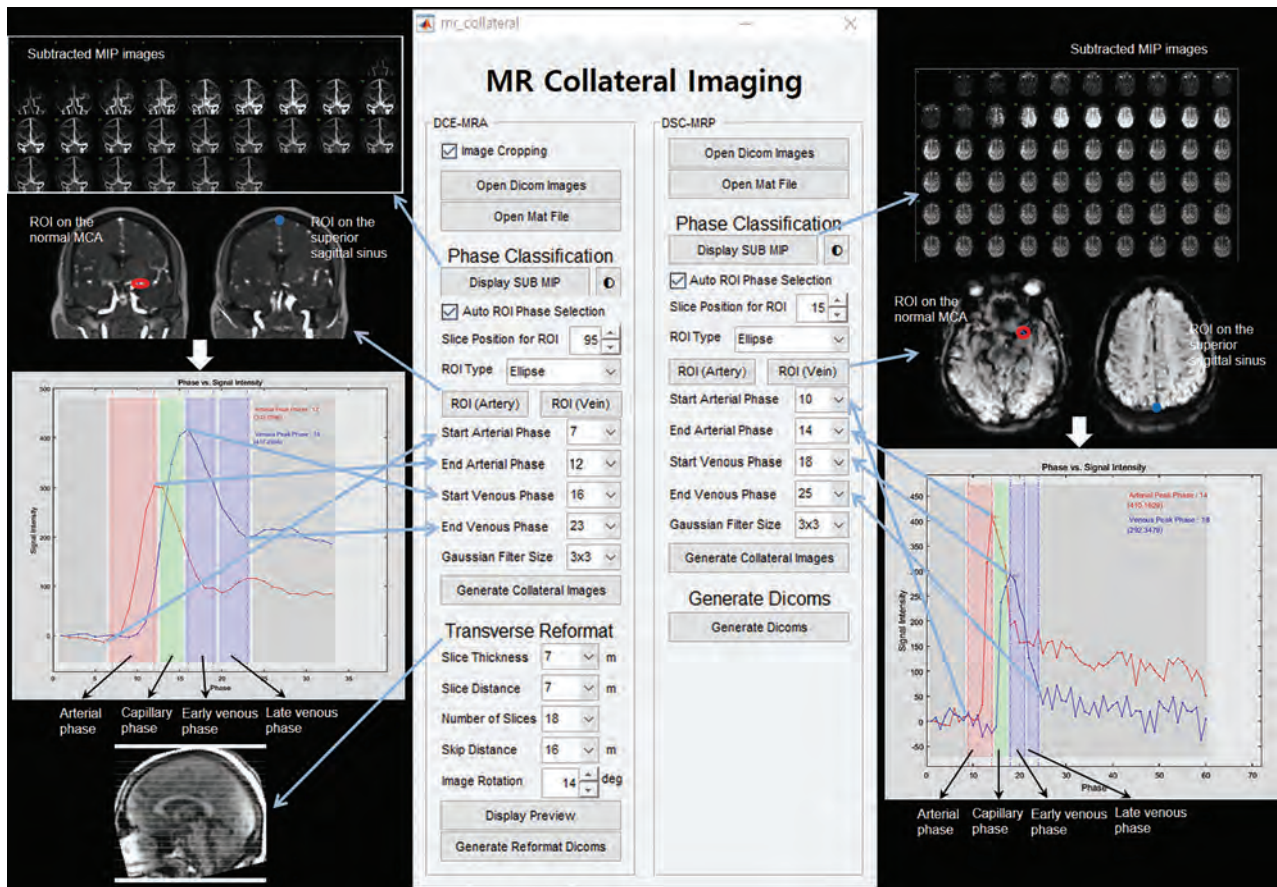


**FIG 2.** Postprocessing sequences for the mMRA collateral map (left) and the MRP collateral map (right). After being loaded and stored in a 4D matrix of DICOM source images of DCE-MRA and DSC-MRP for approximately 1 minute, subtracted MIP images with both the time and spatial information are displayed. We apply ROIs on the MCA in nonischemic hemisphere and superior sagittal sinus. Arterial and venous signal intensity–time curves are generated by plotting signal changes in the ROIs, and 4 phases (arterial phase = from the beginning of arrival of the contrast in the MCA to the arterial bolus peak; capillary phase = from just past the arterial bolus peak to just before the venous bolus peak in the superior sagittal sinus; early venous phase = first half of the venous phase from the venous bolus peak to the starting point of the venous plateau; late venous phase = second half of the venous phase) of collateral maps are determined according to the signal intensity–time curves automatically. In mMRA collateral maps, an axial reformatting process for the original coronal images is added before generating the collateral map.

first phase noncontrast image from each subsequent time-series image to eliminate the background signal; 5) obtaining arterial and venous signal intensity–time curves for ROIs on the MCA in nonischemic hemisphere and the superior sagittal sinus by plotting signal changes in the ROIs; 6) separating the 4D image sets from DCE-MRA and DSC-MRP into the following 4 phases according to bolus passage status, which were plotted on the signal intensity–time curve (arterial phase = from the beginning of arrival of the contrast in the MCA to the arterial bolus peak; capillary phase = from just past the arterial bolus peak to just before the venous bolus peak in the superior sagittal sinus; early venous phase = first half of the venous phase from the venous bolus peak to the starting point of the venous plateau; late venous phase = second half of the venous phase); and 7) reformatting the 4D image sets from DCE-MRA and DSC-MRP into averaged 4-phase axial image sets (collateral map) with the desired reconstruction parameters (slice range covering the whole brain, slice thickness ranging from 7 to 15 mm, slice distance, and number of slices) (Figs 3 and 4). For coronally acquired DCE-MRA data, additional reconstruction processing was needed to obtain the axial images parallel to the anterior/posterior commis-

sure line. The postprocessing times from loading of source images of DCE-MRA and DSC-MRP to generating the mMRA collateral map and MRP collateral map were approximately 5 and 2 minutes, respectively.

### Collateral Grading and Statistical Analysis

We developed a preliminary collateral grading system with a 6-point scale for collateral maps to define the collateral-perfusion status and severity of ischemia in the MCA territory by comparison with the unaffected cerebral hemisphere. The collateral grading system was defined as follows: 5 = excellent, 4 = good, 3 = intermediate to good, 2 = intermediate to poor, 1 = poor, 0 = very poor (Table 2). This grading system was made by modifications of 2 previously reported grading systems by Tan et al<sup>14</sup> and Menon et al.<sup>7</sup> To make the collateral grading easy and straightforward, we adopted the criterion of one-half of the MCA territory at each phase. Additionally, one-half of the MCA territory is widely considered the threshold above which a poor outcome is highly probable.<sup>15</sup>

In visually undetermined, borderline cases with a collateral-perfusion delay of approximately one-half of the MCA territory,

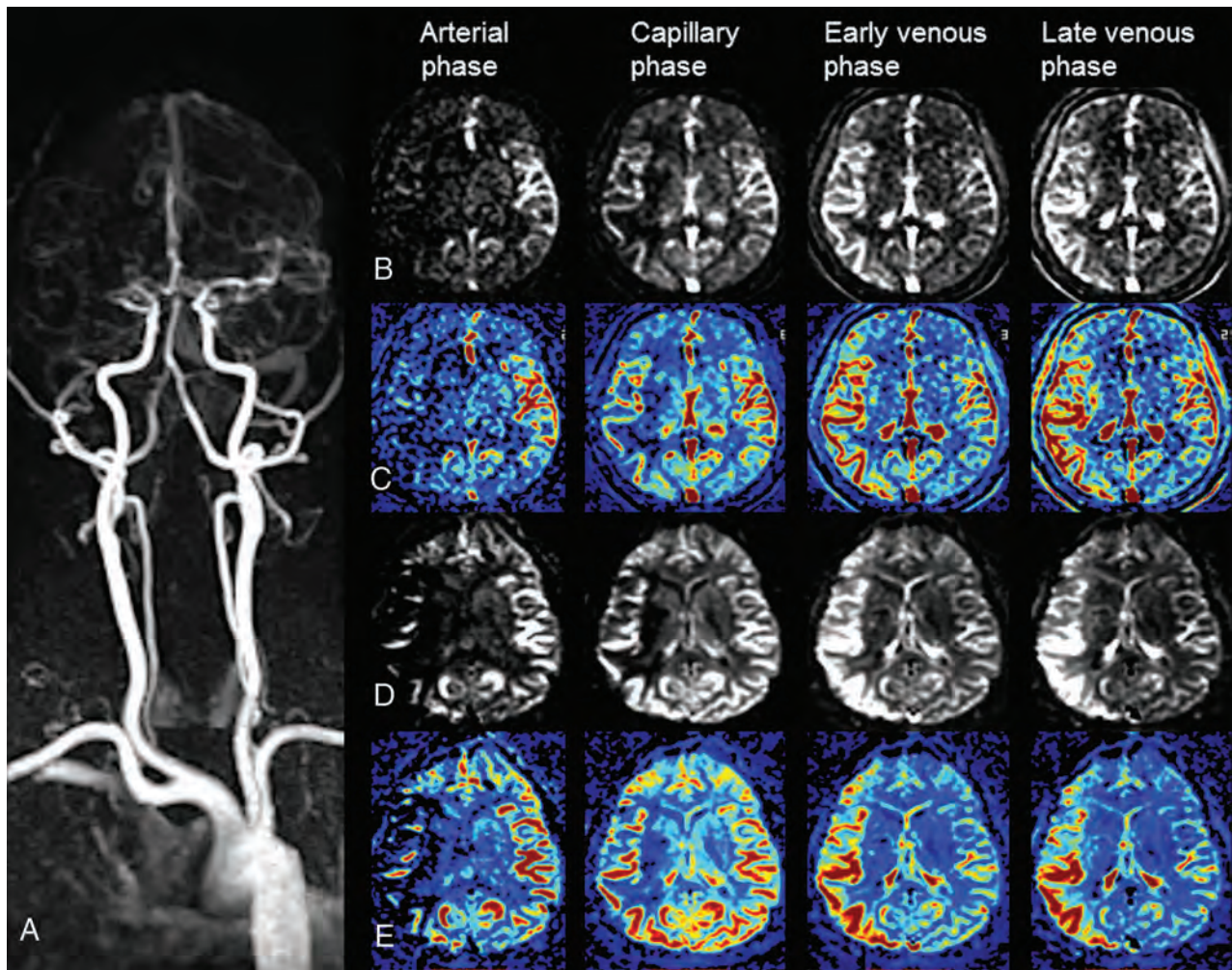


**FIG 3.** mMRA and MRP collateral maps at 2 hours 18 minutes and 2 hours 21 minutes after symptom onset in a 61-year-old woman with occlusion of the right MCA. The 3-month mRS score of the patient was 2. A, DCE-MRA shows occlusion of the right M1 MCA. Gray-scale (B) and color-coded (C) mMRA collateral maps. On the mMRA collateral maps, the collateral-perfusion delay involves more than one-half of the MCA territory, including the subcortical structures in the capillary phase and no collateral-perfusion delay in the early venous phase. The collateral score is 3 (intermediate to good). Gray-scale (D) and color-coded (E) MRP collateral maps. The MRP collateral map shows the same collateral score as the mMRA collateral map.

the collateral score was decided by counting the number of regions with a collateral-perfusion delay similar to that of ASPECTS.<sup>16</sup> The differentiation of 3 subcortical structures (eg, caudate, lentiform nucleus, and internal capsule) might be arbitrary or limited with the resolution of the collateral map, and subcortical structures are less influenced by collateral circulation; therefore, we divided the MCA territory into 8 areas: M1, M2, M3, M4, M5, M6, the insular ribbon, and the subcortical structures (Fig 5). For example, a collateral-perfusion delay greater than one-half of the MCA territory means that the collateral-perfusion delay involves  $>4$  of the 8 regions in the MCA territory. Two experienced neuroradiologists (H.J.K. and H.G.R. with 15 years and 17 years of experience, respectively) independently graded the collateral scores of the mMRA and MRP collateral maps in a blinded fashion on 2 separate occasions 1 week apart. Both neuroradiologists were also blinded to all clinical and other imaging data. To assess the intermethod agreement between the mMRA collateral map and the MRP collateral map, we determined the final scores by consensus. The functional outcome of patients was

assessed at day 90 with mRS. A favorable outcome was defined as an mRS of  $\leq 2$ , or an mRS equal to the prestroke mRS if the prestroke mRS was  $>2$ , at day 90.

Statistical analysis was performed using SPSS Statistics, Version 21 (IBM, Armonk, New York). The interobserver reliabilities for collateral grading of both collateral maps and the intermethod agreement between the mMRA and the MRP collateral maps were measured by the Cohen weighted  $\kappa$ . Coefficients were interpreted as follows:  $\kappa = 0.21$ – $0.40$ , fair agreement;  $\kappa = 0.41$ – $0.60$ , moderate agreement;  $\kappa = 0.61$ – $0.80$ , substantial agreement;  $\kappa = 0.81$ – $1.0$ , almost perfect agreement.

## RESULTS

Sixty-seven patients, including 34 women and 33 men, with a mean age of  $69.7 \pm 11.5$  years (range, 38–93 years), met the inclusion criteria. All patients presented with AIS. Thirteen patients (19.4%) presented with occlusion of the extracranial ICA, 7 patients (10.4%) presented with severe stenosis of the extracranial ICA, 4 patients (6.0%) presented with occlusion of the intracra-

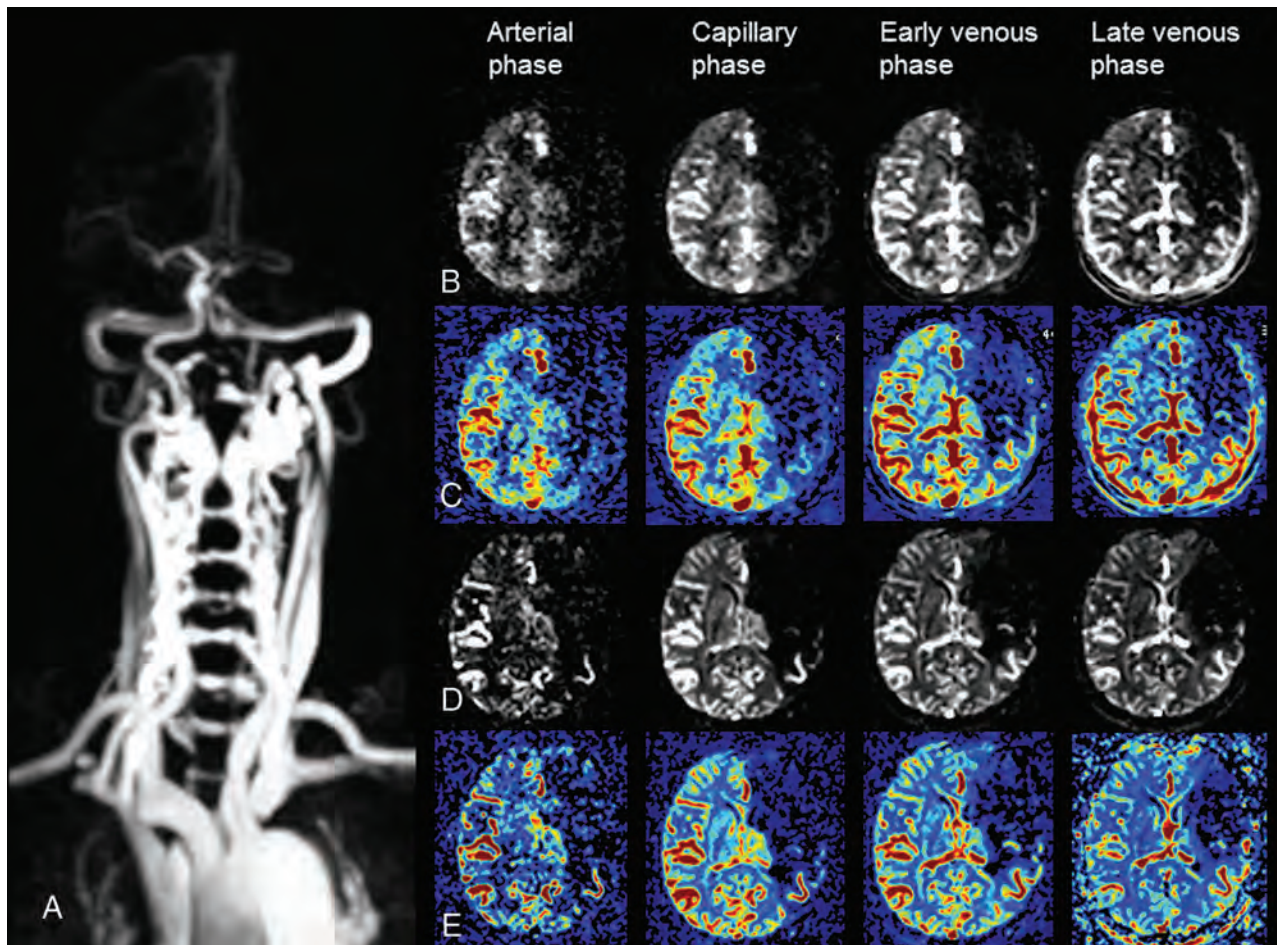


**FIG 4.** mMRA and MRP collateral maps at 5 hours 44 minutes and 5 hours 47 minutes after symptom onset in a 72-year-old man with occlusion of the left ICA and MCA. This patient died 27 days after admission. *A*, DCE-MRA shows occlusion of the left proximal ICA and MCA. Gray-scale (*B*) and color-coded (*C*) mMRA collateral maps. On the mMRA collateral maps, the collateral-perfusion delay involves more than one-half of the MCA territory, including the subcortical structures in the capillary phase, and persists until the late venous phase. The collateral score is 0 (very poor). Gray-scale (*D*) and color-coded (*E*) MRP collateral maps. The MRP collateral map shows the same collateral score as the mMRA collateral map.

**Table 2: Collateral grading system for analysis of the collateral map**

Score	Description of Collateral Status
5 (Excellent)	No or small <sup>a</sup> collateral-perfusion delay in the MCA territory in the capillary phase regardless of the collateral status in the arterial phase
4 (Good)	Collateral-perfusion delay equal to or less than one-half of MCA territory in the capillary phase and no or small delay in the early venous phase
3 (Intermediate to good)	1) Collateral-perfusion delay equal to or less than one-half of the MCA territory in the capillary phase and equal or less than one-half in the early venous phase 2) Collateral-perfusion delay more than one-half of the MCA territory in the capillary phase and no or small delay in the early venous phase
2 (Intermediate to poor)	Collateral-perfusion delay more than one-half of the MCA territory in the capillary phase and equal to or less than one-half in the early venous phase
1 (Poor)	Collateral-perfusion delay more than one-half of the MCA territory in the early venous phase and equal to or less than one-half in the late venous phase
0 (Very poor)	Collateral-perfusion delay/defect more than one-half of the MCA territory in the late venous phase regardless of perfusion status at previous phases

<sup>a</sup>“Small” indicates an area <1 of 8 MCA regions (Fig 5).

nial ICA, 2 patients (3.0%) presented with severe stenosis of the intracranial ICA, 15 patients (22.4%) presented with occlusion of the ICA and M1 MCA, 1 patient (1.5%) presented with severe stenosis of the ICA and M1 MCA, 23 patients (34.3%) presented with occlusion of the M1 MCA, and 2 patients (3.0%) presented with severe stenosis of the M1 MCA. After good recovery (mRS 0

or 1) from the initial stroke during the study period, 4 of 67 patients had a recurrent stroke ( $n = 2$ ) or TIA ( $n = 2$ ) due to occlusion of the left MCA ( $n = 1$ ), severe in-stent restenoses at the left distal ICA ( $n = 1$ ) and right MCA ( $n = 1$ ), and persistent severe stenosis of the proximal left ICA ( $n = 1$ ), respectively. Finally, 71 paired mMRA collateral maps and MRP collateral maps of 67

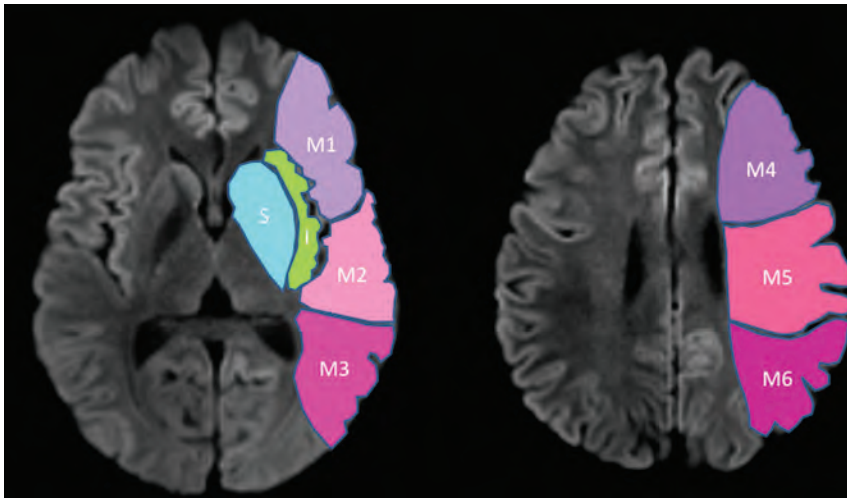


**FIG 5.** Eight topographic regions of the MCA territory for MR collateral imaging (collateral map). I = insular ribbon; S = subcortical structures (basal ganglia and internal capsule); M1, M2, and M3 are the anterior, lateral, and posterior MCA territories, respectively, at the basal ganglia level; M4, M5, and M6 are the anterior, lateral, and posterior MCA territories, respectively, at the supraganglionic level.

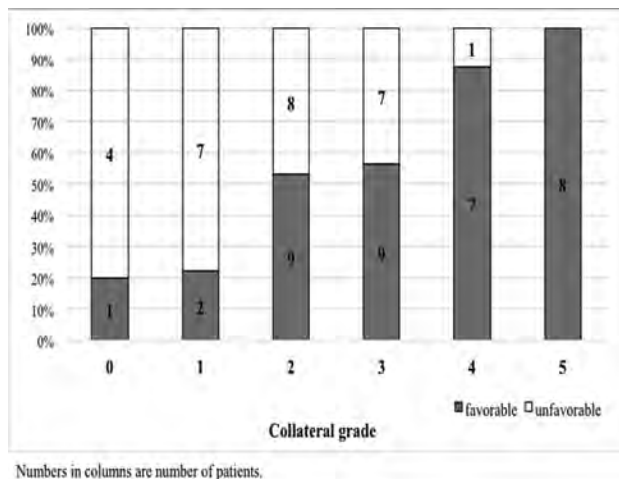


**FIG 6.** A 100% stacked column chart of the functional outcomes and collateral grades of patients.

patients were generated successfully and compared. The interobserver reliability for collateral grading of the mMRA collateral map (weighted  $\kappa = 0.964$ ; 95% confidence interval, 0.929–0.999) and of the MRP collateral map (weighted  $\kappa = 0.956$ ; 95% confidence interval, 0.919–0.993) was almost perfect. The agreement between both collateral maps was also excellent (weighted  $\kappa = 0.884$ ; 95% confidence interval, 0.819–0.949) (Figs 3 and 4). Among 63 patients, excepting 4 patients with recurrent stroke or TIA, excellent collateral grade was found in 8 patients (12.7%); good collateral grade, in 8 (12.7%); intermediate to good collateral grade, in 16 (25.4%); intermediate to poor collateral grade, in 17 (27.0%); poor collateral grade, in 9 (14.3%); and very poor collateral grade, in 5 (7.9%). The functional outcome of the patients was demonstrated in Fig 6.

## DISCUSSION

We demonstrated that the dynamic signals of DCE-MRA could be used to generate multiphase collateral images, called the mMRA

collateral map, and showed good agreement between the mMRA collateral map and the MRP collateral map for the grading of collateral status. Kim et al reported that multiphase collateral images derived from DSC-MRP, a similar concept to our MRP collateral map, could provide information about collateral circulation and had prognostic value in 134 patients with AIS.<sup>12</sup> Their collateral flow map consisted of early, mid-, and late phases divided according to reference time point and representing the midpoint of the midphase on the signal intensity–time curve, and the 3 phases were correlated with arterial, capillary, and venous phases on DSA, respectively. They showed good correlation between MRP- and DSA-based collateral grades. DCE-MRA is an angiographic imaging method, but the dynamic signals are essentially similar to those of DSC-MRP, which are produced by MR imaging contrast media during passage from the cerebral arteries to the dural sinuses. Therefore, we evaluated the value of the mMRA collateral map as a collateral imaging method by comparing it with the MRP collateral map.

Several studies have shown that a large ischemic core and poor collaterals among imaging parameters were strong predictors of an unfavorable response to endovascular treatment and poor functional outcome, and excluding patients with a large ischemic core and poor collateral circulation may avoid futile and dangerous recanalization therapy.<sup>2,5,6,8,9,17,18</sup> Conversely, good collateral circulation can limit ischemic core expansion and prolong the time that penumbral tissue-at-risk remains salvageable until reperfusion therapy, and some studies have suggested that the time window for endovascular treatment can be successfully extended in patients with good collaterals.<sup>2,5,6,8,9,17,18</sup> Therefore, a quick and accurate estimation of the collateral status is essential for endovascular treatment in patients with AIS. Multiphase CTA was recently used in the Endovascular Treatment for Small Core and Anterior Circulation Proximal Occlusion with Emphasis on Minimizing CT to Recanalization Times (ESCAPE) trial and was shown to help determine the clinical outcome.<sup>3,11</sup> The multiphase CTA technique is quick and easy to use without complex postprocessing and acquires temporal information at 3 time points.<sup>11</sup> However, the MR imaging–based collateral map has several fundamental advantages over multiphase CTA, in addition to the avoidance of radiation and iodine contrast media<sup>19</sup>: 1) The phases of the MR imaging–based collateral map are not fixed and can be individualized after obtaining time-intensity curves and delay correction. Therefore, the MR imaging–based collateral map may overcome intrinsic patient factors and problems due to scan timing and may reflect each phase more precisely. 2) MRP and MRA permit repeat scanning if the first scan is deemed inappropriate. 3) The MR imaging–based collateral map can provide more detailed information about the tissue-level, brain parenchymal collateral perfusion in addition to cortical artery information.

collateral map, and showed good agreement between the mMRA collateral map and the MRP collateral map for the grading of collateral status. Kim et al reported that multiphase collateral images derived from DSC-MRP, a similar concept to our MRP collateral map, could provide information about collateral circulation and had prognostic value in 134 patients with AIS.<sup>12</sup> Their collateral flow map consisted of early, mid-, and late phases divided according to reference time point and representing the midpoint of the midphase on the signal intensity–time curve, and the 3 phases were correlated with arterial, capillary, and venous phases on DSA, respectively. They showed good correlation between MRP- and DSA-based collateral grades. DCE-MRA is an angiographic imaging method, but the dynamic signals are essentially similar to those of DSC-MRP, which are produced by MR imaging contrast media during passage from the cerebral arteries to the dural sinuses. Therefore, we evaluated the value of the mMRA collateral map as a collateral imaging method by comparing it with the MRP collateral map.

Previous studies have shown that half-dose single-phase contrast-enhanced MRA and perfusion did not negatively affect either the image quality or the quantitative analysis of perfusion data.<sup>20,21</sup> Another study showed that time-resolved DCE-MRA with a low dose (2–3 mL) of gadobutrol could provide good image quality with a signal-to-noise ratio comparable with that of conventional single-phase 3D high-resolution contrast-enhanced MRA with a standard dose.<sup>22</sup> Therefore, we could adopt a low-dose protocol for DCE-MRA, and the remaining contrast media could be used for DSC-MRP. We succeeded in generating mMRA and MRP collateral maps in all patients. Additional angiographic imaging is not necessary in the stroke MR imaging protocol when the mMRA collateral map is applied as collateral imaging, unlike the MRP collateral map, which shortens the imaging time while also requiring a minimal dose of contrast media.

We used a self-developed collateral grading system because there was no established grading method for 4-phase collateral imaging. Our grading system was largely based on that of multiphase CTA according to the perfusion lag and its extent. The differences were that we used the criterion of one-half of the MCA territory at each grading score, and we included parenchymal collateral perfusion as well as cortical arteries in comparison with the healthy contralateral MCA territory. Because an infarct volume of more than one-half of the MCA territory has been widely considered the threshold for poor outcome of acute MCA stroke, we thought that the one-half-area criterion could be optimal for visual assessment while avoiding ambiguous terms, such as “some,” “a few,” or “periphery,” used in the existing grading systems.<sup>11,12,23</sup> In borderline cases with collateral-perfusion delay in approximately one-half of the MCA territory, the 8-region MCA diagram was used to resolve the ambiguity in collateral grading. We divided the venous phase into early venous phase and late venous phase because we observed that patients with a larger area of collateral-perfusion delay/defect in the late venous phase tended to have a large ischemic core and a worse prognosis than patients with a smaller area. We considered that validation of the clinical meaning of early and late venous phases was necessary in the application of the collateral map to patients with AIS.

Our study has several limitations. First, the clinical efficacy of the mMRA collateral map as a collateral imaging method was not evaluated. We showed a chart with a tendency for an increasing proportion of patients with favorable outcome as increasing collateral grade, but the numbers in these data are too small to evaluate statistically. Although the DSC-MRP-based collateral imaging has been evaluated clinically, the evaluation was a retrospective observational study at a single medical center.<sup>12</sup> Further clinical studies are necessary to validate the clinical usefulness of the mMRA collateral map and the grading method. We are pursuing a prospective clinical study for this validation. Second, 5 additional minutes were needed for postprocessing to generate an mMRA collateral map. Therefore, the total imaging time was 11 minutes 36 seconds for the MR imaging acquisition and postprocessing in this study. Although this was an acceptable time for acute stroke imaging, further effort should be made to shorten the imaging time.

## CONCLUSIONS

We introduced a new collateral imaging method derived from time-resolved DCE-MRA and showed that this method can provide collateral information, like the collateral imaging method derived from DSC-MRP. Future validation of the clinical usefulness of the mMRA collateral map and large clinical studies are needed.

Disclosures: Hyun Jeong Kim—RELATED: Grant: National Research Foundation of Korea. Comments: This study was supported by National Research Foundation of Korea, subject No. 2017RIA2B1008020. \*\*Money paid to the institution.

## REFERENCES

- Liebeskind DS. **Collateral circulation.** *Stroke* 2003;34:2279–84 CrossRef Medline
- Liebeskind DS, Tomsick TA, Foster LD, et al; IMS III Investigators. **Collaterals at angiography and outcomes in the Interventional Management of Stroke (IMS) III trial.** *Stroke* 2014;45:759–64 CrossRef Medline
- Goyal M, Demchuk AM, Menon BK, et al; ESCAPE Trial Investigators. **Randomized assessment of rapid endovascular treatment of ischemic stroke.** *N Engl J Med* 2015;372:1019–30 CrossRef Medline
- Bang OY, Saver JL, Buck BH, et al; UCLA Collateral Investigators. **Impact of collateral flow on tissue fate in acute ischaemic stroke.** *J Neurol Neurosurg Psychiatry* 2008;79:625–29 Medline
- Ribo M, Flores A, Rubiera M, et al. **Extending the time window for endovascular procedures according to collateral pial circulation.** *Stroke* 2011;42:3465–69 CrossRef Medline
- Hwang YH, Kang DH, Kim YW, et al. **Impact of time-to-reperfusion on outcome in patients with poor collaterals.** *AJNR Am J Neuroradiol* 2015;36:495–500 CrossRef Medline
- Menon BK, Qazi E, Nambiar V, et al; Interventional Management of Stroke III Investigators. **Differential effect of baseline computed tomographic angiography collaterals on clinical outcome in patients enrolled in the Interventional Management of Stroke III Trial.** *Stroke* 2015;46:1239–44 CrossRef Medline
- Hill MD, Demchuk AM, Goyal M, et al; IMS3 Investigators. **Alberta Stroke Program early computed tomography score to select patients for endovascular treatment: Interventional Management of Stroke (IMS)-III trial.** *Stroke* 2014;45:444–49 CrossRef Medline
- Bang OY, Saver JL, Kim SJ, et al. **Collateral flow predicts response to endovascular therapy for acute ischemic stroke.** *Stroke* 2011;42:693–99 CrossRef Medline
- Menon BK, Smith EE, Modi J, et al. **Regional leptomeningeal score on CT angiography predicts clinical and imaging outcomes in patients with acute anterior circulation occlusions.** *AJNR Am J Neuroradiol* 2011;32:1640–45 CrossRef Medline
- Menon BK, d’Este CD, Qazi EM, et al. **Multiphase CT angiography: a new tool for the imaging triage of patients with acute ischemic stroke.** *Radiology* 2015;275:510–20 CrossRef Medline
- Kim SJ, Son JP, Ryoo S, et al. **A novel magnetic resonance imaging approach to collateral flow imaging in ischemic stroke.** *Ann Neurol* 2014;76:356–69 CrossRef Medline
- Parthasarathy R, Sohn SI, Jeerakathil T, et al. **A combined arterial and venous grading scale to predict outcome in anterior circulation ischemic stroke.** *J Neuroimaging* 2015;25:969–77 CrossRef Medline
- Tan JC, Dillon WP, Liu S, et al. **Systematic comparison of perfusion-CT and CT-angiography in acute stroke patients.** *Ann Neurol* 2007;61:533–43 CrossRef Medline
- Souza LC, Yoo AJ, Chaudhry ZA, et al. **Malignant CTA collateral profile is highly specific for large admission DWI infarct core and poor outcome in acute stroke.** *AJNR Am J Neuroradiol* 2012;33:1331–36 CrossRef Medline
- Barber PA, Demchuk AM, Zhang J, et al. **Validity and reliability of a**

- quantitative computed tomography score in predicting outcome of hyperacute stroke before thrombolytic therapy: ASPECTS Study Group—Alberta Stroke Programme Early CT Score.** *Lancet* 2000;355:1670–74 CrossRef Medline
17. Bang OY, Saver JL, Kim SJ, et al; UCLA-Samsung Stroke Collaborators. **Collateral flow averts hemorrhagic transformation after endovascular therapy for acute ischemic stroke.** *Stroke* 2011;42:2235–39 CrossRef Medline
  18. Leng X, Fang H, Leung TW, et al. **Impact of collateral status on successful revascularization in endovascular treatment: a systematic review and meta-analysis.** *Cerebrovasc Dis* 2016;41:27–34 CrossRef Medline
  19. Aviv RI, Parsons M, Bivard A, et al. **Multiphase CT angiography: a poor man's perfusion CT?** *Radiology* 2015;277:922–94 CrossRef Medline
  20. Nael K, Meshksar A, Ellingson B, et al. **Combined low-dose contrast-enhanced MR angiography and perfusion for acute ischemic stroke at 3T: a more efficient stroke protocol.** *AJNR Am J Neuroradiol* 2014;35:1078–84 CrossRef Medline
  21. Manka C, Träber F, Gieseke J, et al. **Three-dimensional dynamic susceptibility-weighted perfusion MR imaging at 3.0 T: feasibility and contrast agent dose.** *Radiology* 2005;234:869–77 CrossRef Medline
  22. Bak SH, Roh HG, Moon WJ, et al. **Appropriate minimal dose of gadobutrol for 3D time-resolved MRA of the supra-aortic arteries: comparison with conventional single-phase high-resolution 3D contrast-enhanced MRA.** *AJNR Am J Neuroradiol* 2017;38:1383–90 CrossRef Medline
  23. Higashida RT, Furlan AJ, Roberts H, et al; Technology Assessment Committee of the American Society of Interventional and Therapeutic Neuroradiology, Technology Assessment Committee of the Society of Interventional Radiology. **Trial design and reporting standards for intra-arterial cerebral thrombolysis for acute ischemic stroke.** *Stroke* 2003;34:e109–37 Medline

# Diagnostic Accuracy of High-Resolution Black-Blood MRI in the Evaluation of Intracranial Large-Vessel Arterial Occlusions

 A.S. Al-Smadi,  R.N. Abdalla,  A.H. Elmokadem,  A. Shaibani,  M.C. Hurley,  M.B. Potts,  B.S. Jahromi,  T.J. Carroll, and  S.A. Ansari



## ABSTRACT

**BACKGROUND AND PURPOSE:** 3D high-resolution black-blood MRI or MR vessel wall imaging allows evaluation of the intracranial arterial wall and extraluminal pathology. We investigated the diagnostic accuracy and reliability of black-blood MRI for the intraluminal detection of large-vessel arterial occlusions.

**MATERIALS AND METHODS:** We retrospectively identified patients with intracranial arterial occlusions, confirmed by CTA or DSA, who also underwent 3D black-blood MRI with nonenhanced and contrast-enhanced T1 sampling perfection with application-optimized contrasts by using different flip angle evolution (T1 SPACE) sequences. Black-blood MRI findings were evaluated by 2 independent and blinded neuroradiologists. Large-vessel intracranial arterial segments were graded on a 3-point scale (grades 0–2) for intraluminal baseline T1 hyperintensity and contrast enhancement. Vessel segments were considered positive for arterial occlusion if focal weak (grade 1) or strong (grade 2) T1-hyperintense signal and/or enhancement replaced the normal intraluminal black-blood signal.

**RESULTS:** Thirty-one patients with 38 intracranial arterial occlusions were studied. The median time interval between black-blood MRI and CTA/DSA reference standard studies was 2 days (range, 0–20 days). Interobserver agreement was good for T1 hyperintensity ( $\kappa = 0.63$ ) and excellent for contrast enhancement ( $\kappa = 0.89$ ). High sensitivity (100%) and specificity (99.8%) for intracranial arterial occlusion diagnosis was observed with either intraluminal T1 hyperintensity or contrast-enhancement imaging criteria on black-blood MRI. Strong grade 2 intraluminal enhancement was maintained in >80% of occlusions irrespective of location or chronicity. Relatively increased strong grade 2 intraluminal T1 hyperintensity was noted in chronic/incidental versus acute/subacute occlusions (45.5% versus 12.5%,  $P = .04$ ).

**CONCLUSIONS:** Black-blood MRI with or without contrast has high diagnostic accuracy and reliability in evaluating intracranial large-vessel arterial occlusions with near-equivalency to DSA and CTA.

**ABBREVIATIONS:** BBMRI = black-blood MRI; MR VWI = MR vessel wall imaging; SPACE = sampling perfection with application-optimized contrasts by using different flip angle evolution

**A**cute ischemic stroke secondary to intracranial large-vessel thromboembolic occlusion has substantial morbidity and mortality. Emergent intervention in large-vessel occlusions with

intravenous thrombolysis and/or endovascular thrombectomy has been shown to dramatically improve clinical outcomes.<sup>1</sup> However, even delayed diagnosis of complete intracranial arterial occlusions and differentiation from intracranial vessel wall pathologies impact medical and surgical management. Currently, neurovascular imaging is performed using various imaging modalities, including CTA, MRA, and DSA, but the limited assessment of the arterial wall cannot reliably differentiate in situ pathologies such as intracranial atherosclerosis, dissection, vasculitis, or steno-occlusive vasculopathy. Due to the superior contrast and high spatial resolution of 3D black-blood MR imaging (BBMRI) or MR vessel wall imaging (MR VWI), the extraluminal vessel wall can be clearly distinguished from the

Received January 31, 2019; accepted after revision April 10.

From the Departments of Radiology (A.S.A.-S., R.N.A., A.H.E., A.S., M.C.H., M.B.P., B.S.J., S.A.A.), Neurology (S.A.A.), and Neurological Surgery (A.S., M.C.H., M.B.P., B.S.J., S.A.A.), Northwestern University, Feinberg School of Medicine, Chicago, Illinois; Department of Radiology (T.J.C.), University of Chicago, Chicago, Illinois; Department of Radiology (R.N.A.), Ain Shams University, Cairo, Egypt; and Department of Radiology (A.H.E.), Mansoura University, Mansoura, Egypt.

This work was supported by the following grants: American Heart Association 13GRNT17340018 and 14GRNT20380798 (Principal Investigators: S.A. Ansari and T.J. Carroll); National Institutes of Health/National Heart, Lung, and Blood Institute 1R21HL130969 (Principal Investigator: S.A. Ansari); and National Institutes of Health/National Heart, Lung, and Blood Institute 1R01NS093908 (Principal Investigator: T.J. Carroll).

Please address correspondence to Sameer A. Ansari, MD, PhD, Departments of Radiology, Neurology, and Neurological Surgery, Northwestern University, Feinberg School of Medicine, 676 N St Clair St, Suite 800, Chicago, IL 60611-2927; e-mail: s-ansari@northwestern.edu

 Indicates open access to non-subscribers at [www.ajnr.org](http://www.ajnr.org)

 Indicates article with supplemental on-line table.

<http://dx.doi.org/10.3174/ajnr.A6065>

intraluminal black-blood compartment, allowing improved diagnosis and delineation of intravascular thromboembolic occlusions and their related blood products.<sup>2</sup>

3D-TOF-MRA is considered the most common MRA technique for evaluating intracranial steno-occlusive disease in acute ischemic stroke, often as an adjunct to MR diffusion-weighted imaging.<sup>3,4</sup> However, 3D-TOF-MRA has been shown to be insensitive due to poor flow enhancement from in-plane dephasing or slow-flow artifacts,<sup>5</sup> leading to false-positive results either by upgrading the stenosis severity or a false diagnosis of a vascular occlusion.<sup>6</sup> Although the T1 spin-echo sequence can accurately identify subacute hemorrhage or thrombus as signal hyperintensity on conventional MR imaging due to the presence of methemoglobin,<sup>7</sup> it has major limitations in the detection of intra-arterial thrombosis, including lower resolution, flow artifacts from inadequate double inversion recovery flow-suppression techniques, and chronologic variance of signal intensity, depending on the stage of thrombus evolution (oxy-/deoxy-hemoglobin, intra-/extracellular methemoglobin, and hemosiderin). Conversely, BBMRI using the T1 sampling perfection with application-optimized contrasts by using different flip angle evolution (SPACE; Siemens, Erlangen, Germany) sequences with intravoxel phase dispersion provides excellent intravascular black-blood flow suppression with intravoxel dephasing for assessment of static thrombus independent of its age (through the presence of intravascular T1-isointense/hyperintense signal or contrast enhancement). In addition, 3D isotropic BBMRI facilitates multiplanar and curved reconstructions to better evaluate the tortuous intracranial arteries.<sup>8</sup> Our study aimed to assess the accuracy and reliability of BBMRI in diagnosing intracranial large-vessel arterial occlusions.

## MATERIALS AND METHODS

### *Patient and Imaging Studies*

Institutional review board approval at Northwestern University was obtained for a retrospective medical record and PACS imaging review of patients with suspected diagnosis of stroke and intracranial thromboembolic occlusions. From October 2014 to June 2018, we identified 199 BBMRI studies and included patients with documented large-vessel arterial occlusions on CTA and/or DSA, performed within 30 days of the BBMRI study. All large-vessel arterial occlusions reported on CTA and/or DSA were reviewed and confirmed by a separate interventional neuroradiologist, and whenever discrepancy was found between CTA and DSA, DSA was used as the reference standard. Patients were excluded if they received any intervention (IV/IA tPA thrombolysis and/or mechanical thrombectomy) between BBMRI and reference CTA/DSA. Imaging exclusion criteria were notable for patient motion artifacts rendering the study nondiagnostic, limited BBMRI scan volumes excluding the ROI/vessel occlusion site, or imaging without the availability of both pre- and post-contrast-enhanced T1 SPACE sequences.

We studied patient demographics, clinical presentations, vessel occlusion sites, ischemic strokes, and age of ischemic strokes using sequence-specific MR imaging findings (DWI, ADC, FLAIR, and unenhanced T1- and T2-weighted images) to classify strokes in the affected arterial territory as acute/subacute or

chronic.<sup>9</sup> Arterial occlusions were classified as acute/subacute (<3 weeks) if the patient presented with acute/subacute infarcts in the downstream vascular territory. Chronic/incidental (>3 weeks) occlusions were defined if there were no infarcts or chronic infarcts in the downstream vascular territory, the patient presented with acute/subacute infarcts in a different vascular territory, or if previous angiographic studies (>3 weeks before BBMRI) reported an occlusion.

### **BBMRI Protocol**

BBMRI sequences were acquired on a 3T MR imaging scanner (Magnetom Skyra; Siemens) in a clinical setup with a 20-channel head coil. In all cases, a standardized MR imaging stroke protocol was performed, including axial T1 spin-echo, T2 fast spin-echo, DWI, FLAIR, gradient recalled-echo or SWI sequences, TOF-MRA, and DSC brain perfusion imaging. Additionally, 3D variable flip angle TSE BBMRI (T1 SPACE) imaging was performed with the following parameters: FOV = 165 mm, TR/TE = 800/22 ms, integrated parallel acquisition technique factor = 2, number in z-direction = 104 slices, bandwidth = 372 Hz/pixel, turbo factor = 30, scan time = ~ 8 minutes, imaging matrix = 320 × 352, voxel volume = 0.5 × 0.5 × 0.6 mm. A single-dose (1 mmol/mL) of gadobutrol, a gadolinium-based T1-shortening contrast agent (Gadavist; Bayer Schering Pharma, Berlin, Germany), was injected, and the scan was repeated 9 minutes after contrast administration. Radial *k*-space view ordering was used to optimize T1-weighted contrast. Images were generated and transferred to a PACS for direct visualization on the workstation.

### **BBMRI Analysis**

BBMRI (T1 SPACE) images were separately evaluated by 2 independent neuroradiologists on a de-identified PACS workstation. Both observers were blinded to patient demographics, imaging indications, other MR imaging sequences, and other angiographic studies (MRA/CTA/DSA). Qualitative image analyses of the intraluminal arterial hyperintensity and contrast enhancement were performed on the PACS workstation. Intraluminal T1 hyperintensity was graded on a 3-point scale: 0, none; 1, weak visualization/hyperintense signal less than that of the intraorbital fat; or 2, strong visualization/hyperintense signal equal to or more than that of the intraorbital fat. Intraluminal enhancement was graded on a 3-point scale: 0, none or signal equal to that of the pre-contrast image; 1, weak enhancement with signal greater than that of the pre-contrast image, but less than that of the pituitary stalk; 2, strong enhancement with signal greater than that of the pre-contrast image, equal to or greater than that of the pituitary stalk.

Normal vessels were defined as exhibiting preserved intraluminal black-blood properties with no intraluminal signal intensity or enhancement (Fig 1). Arterial occlusion was defined as a focal area of intraluminal T1-hyperintense signal or enhancement graded as 1 or 2, completely replacing the normal intraluminal black-blood signal on nonenhanced and/or contrast-enhanced T1 SPACE images, respectively (Figs 2 and 3). Both readers were asked to assess a total of 19 intracranial arterial segments in the anterior circulation, including the bilateral supraclinoid internal carotid arteries (ICA); middle cerebral artery (MCA) M1–M2

(superior/inferior) segments; anterior cerebral artery (ACA) A1–A2 segments; and the posterior circulation, including the posterior cerebral artery (PCA) P1 segments, or posterior communicating arteries if more dominant; P2 segments; the vertebral artery (VA) V4 segments; and the basilar artery (BA). Aplastic vessel segments not visualized on CTA or DSA imaging were excluded from BBMRI analysis.

### Statistical Analysis

The diagnostic performance of BBMRI was expressed as sensitivity and specificity of intraluminal T1 hyperintensity or contrast enhancement in diagnosing arterial occlusions versus controls, which were defined as normal major intracranial segments by reference standard angiographic studies (CTA and/or DSA). Interobserver agreement for BBMRI intraluminal arterial hyperintensity and contrast enhancement was assessed using the Cohen  $\kappa$  coefficient. The Cohen  $\kappa$  coefficient varies between 0 and 1, with 0 representing no agreement and 1 representing complete agreement.  $\kappa$  values of  $>0.8$ ,  $>0.6-0.8$ ,  $>0.4-0.6$ , and  $\leq 0.4$  indicated excellent, good, fair, and poor agreement, respectively. Subgroup analyses comparing anterior and posterior circulations and acute/subacute versus chronic/incidental occlusions were performed using Mann-Whitney and Fisher exact tests for continuous and categorical variables, respectively. In case of disagreement, images were reviewed by a third neuroradiologist for consensus grading

of intraluminal T1 hyperintensity and contrast enhancement, and utilized for subgroup analyses. A 2-tailed  $P$  value  $< .05$  was considered statistically significant. Statistical analysis was performed using SPSS statistical software (Version 23.0; IBM, Armonk, New York).

### RESULTS

Thirty-one patients (14 male [45%], 17 female [55%]; mean age, 62 years; range, 34–79 years) presented with ischemic stroke symptoms and 38 intracranial large-vessel arterial occlusions that were identified and included in the study. The median time between the reference scan (CTA/DSA) confirming large-vessel occlusions and the BBMRI scan was 2 days (range, 0–20 days). A total of 571/589 major intracranial vessel segments in 31 patients were included in the study (6 aplastic segments and 12 normal segments not visualized in the limited BBMRI scan volumes were excluded).

A single arterial occlusion was present in 25/31 patients, 2 occlusions in 5/31 patients, and 3 occlusions in a single patient, providing 38 occlusions and 533 patent segments for independent evaluation by the blinded observers. Arterial occlusions were distributed relatively equally between the anterior and posterior intracranial circulations (58% versus 42%): ACA ( $n = 4$ ) and MCA ( $n = 18$ ) versus the PCA ( $n = 4$ ), VA ( $n = 10$ ), and BA ( $n = 2$ ). Acute/subacute DWI infarcts were observed in 22 patients with 29 occlusions, but only downstream in the vascular distributions of 16/29 occlusions characterized as acute/subacute occlusions, and the remaining 13 were considered chronic/incidental occlusions. Chronic infarcts were noted on T1/T2/FLAIR-weighted images downstream of 3 occlusions in 3 patients, and no infarcts were seen in 6 patients with 6 occlusions, providing a total of 16 acute/subacute occlusions and 22 chronic/incidental occlusions for analysis.

Both observers successfully identified all intracranial large-vessel arterial occlusions on BBMRI by either weak (grade 1) or strong (grade 2) visualization of intraluminal T1 hyperintensity and/or contrast enhancement with no false-negative results (Online Table). Only a single case of a false-positive basilar artery occlusion was reported by both observers on pre- and post-contrast BBMRI and confirmed by CTA, yet deemed to be a severe, long-segment atherosclerotic stenosis with slow stringlike flow

rather than an occlusion on DSA. By combining grades 1 and 2 for intraluminal T1 hyperintensity and/or contrast enhancement, we observed excellent sensitivity (100%) and specificity (99.8%) with either pre- or post-contrast-enhanced BBMRI, providing near-equivalent diagnostic power and accuracy in the diagnosis of intracranial large-vessel arterial occlusions in comparison with the reference standards of CTA and DSA.

Good interobserver agreement for intraluminal T1 hyperintensity (unweighted  $\kappa = 0.63$ ) and excellent interobserver agreement for intraluminal

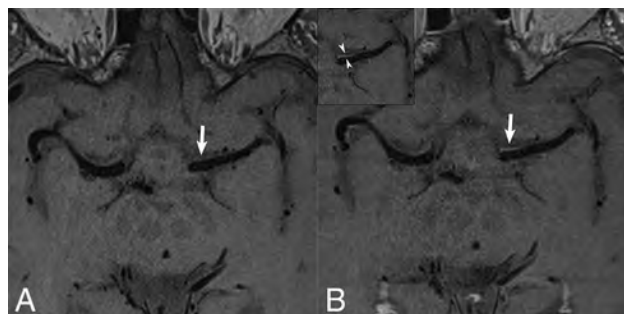


**FIG 1.** High-resolution axial pre- (A) and post contrast (B) BBMRI demonstrates patent bilateral MCAs with normal intraluminal hypointensity (black-blood) due to flow-suppression techniques. Normal thin vessel wall or marginal periarterial enhancement (arrows) is observed on post-contrast versus pre-contrast imaging, best delineated in the inset (arrowheads).



**FIG 2.** A 39-year-old patient who presented with left-sided hemiplegia. MR DWI axial (A) shows restricted diffusion (arrow) in the periventricular white matter, consistent with an acute infarct. Axial pre-contrast (B) BBMRI demonstrates a focus of grade 2/strong intraluminal T1 hyperintensity (thick arrow) in the distal M1 segment proximal to the MCA bifurcation, compared with the normal retroglobal orbital fat (thin arrow), suspicious for an acute/subacute occlusion. DSA anteroposterior image (C) confirms the M1 right MCA occlusion (black arrowhead), after supply to a prominent anterior temporal branch.

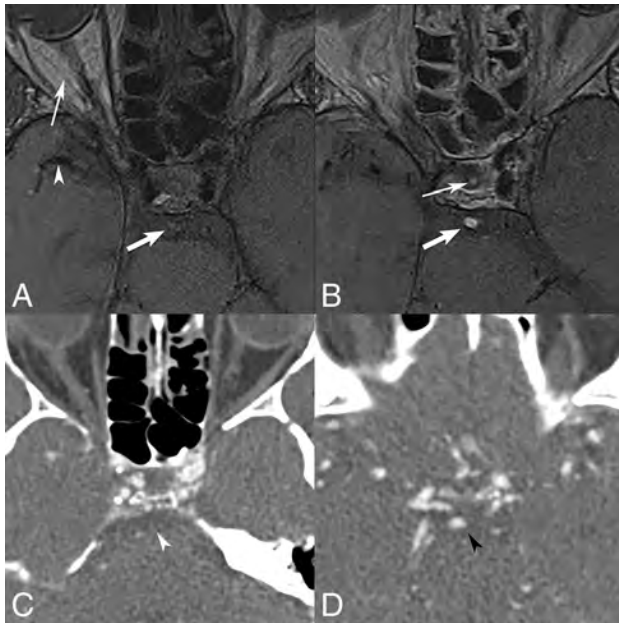


**FIG 3.** A 63-year-old patient who presented with nausea, vomiting, and double vision secondary to multiple posterior circulation strokes. Axial pre-contrast BBMRI (A) shows a focus of grade 1/weak intraluminal T1 hyperintensity in the basilar artery (*thick arrow*), replacing the normal intra-arterial black-blood signal of the M1 segment (*arrowhead*), but less intense than in the orbital fat (*thin arrow*). Axial post-contrast BBMRI (B) shows grade 2/strong intraluminal contrast enhancement (*thick arrow*) of the basilar artery thrombus, compared with the normal avidly enhancing signal of the infundibular stalk (*thin arrow*). CTA (C and D) at the level of pons and the circle of Willis confirms occlusion of the basilar artery (*white arrowhead*) with distal basilar tip reconstitution (*black arrowhead*) from the anterior circulation via the posterior communicating artery.

contrast enhancement (unweighted  $\kappa = 0.89$ ) were noted, consistent with reliable BBMRI findings in the diagnosis of intraluminal arterial signal abnormality and enhancement. In fact, there was near complete agreement between observers on the presence of strong (grade 2) intraluminal enhancement in 33/38 (87%) confirmed arterial occlusions with disagreement of grade 1 versus grade 2 enhancement in only a single segment.

On subgroup analyses of anterior versus posterior circulation occlusions (Table 1) and acute/subacute versus chronic/incidental occlusions (Table 2), there were no statistical differences in baseline demographics or time between BBMRI and reference scans. Posterior circulation occlusions had a higher percentage of chronic/incidental occlusions than anterior circulation occlusions (81.2% versus 40.9%,  $P = .02$ ). Both anterior and posterior circulation occlusions maintained a high degree of contrast enhancement (>80% of occlusions with strong grade 2 enhancement), relatively lower degrees of T1 hyperintensity (22.7% and 43.7% with strong grade 2 hyperintensity, respectively), and no statistical differences in BBMRI findings between the groups.

Chronic/incidental occlusions had a predilection for the posterior circulation (59.1%), whereas most acute/subacute occlusions (81.2%) were identified in the anterior circulation ( $P = .02$ ). Both acute/subacute and chronic/incidental occlusions continued to demonstrate a high degree of contrast enhancement (>80% of occlusions with a strong grade 2 enhancement) and no statistical differences. However, chronic/incidental occlu-

**Table 1: Subgroup analysis of anterior versus posterior circulation occlusions**

	Anterior (n = 22)	Posterior (n = 16)	P Value
Mean age (range) (yr)	59.3 (34–77)	63.1 (39–79)	.24
Male (%)	40.9	62.5	.32
Median time between BBMRI and CTA/DSA days (range) (day)	3 (0–18)	1 (0–20)	.62
Occlusion chronicity (%)			.02
Acute/subacute	59.1	18.8	
Chronic/incidental	40.9	81.2	
Hyperintensity (%)			.29
Grade 1	77.3	56.2	
Grade 2	22.7	43.7	
Enhancement (%)			.99
Grade 1	18.2	12.5	
Grade 2	81.8	87.5	

**Table 2: Subgroup analysis of acute/subacute versus chronic/incidental occlusions**

	Acute/ Subacute (n = 16)	Chronic/ Incidental (n = 22)	P Value
Mean age (range) (yr)	58.1 (34–77)	62.9 (37–79)	.16
Male (%)	50%	50%	.99
Median time between BBMRI and CTA/DSA (range) (day)	3 (0–18)	1 (0–20)	.8
Occlusion site (%)			.02 <sup>a</sup>
Anterior	81.2	40.9	
Posterior	18.8	59.1	
Hyperintensity (%)			.04 <sup>a</sup>
Grade 1	87.5	54.5	
Grade 2	12.5	45.5	
Enhancement (%)			.99
Grade 1	12.5	18.2	
Grade 2	87.5	81.8	

<sup>a</sup> Significant.

sions exhibited statistically higher grades of T1 hyperintensity on pre-contrast BBMRI compared with acute/subacute occlusions (45.5% versus 12.5% with strong grade 2 hyperintensity,  $P = .04$ ).

## DISCUSSION

High-resolution BBMRI or VWI is increasingly used in clinical practice for the evaluation of intracranial vessel wall pathology.<sup>8,10</sup> Multiple studies have described VWI findings in various intracranial steno-occlusive diseases, including accuracy and reliability measurements in direct comparison with conventional vascular imaging techniques (CTA, MRA, and DSA).<sup>10–15</sup> BBMRI has been shown to characterize intracranial stenoses with high sensitivity (89%–93%) and specificity (53%–98%) and excellent interobserver agreement,<sup>10,14,15</sup> but there have been few independent studies of BBMRI findings to diagnose or differentiate large-vessel arterial occlusions.

Hui et al<sup>12</sup> reported 10 patients with DSA-confirmed acute/subacute large-vessel occlusions who underwent BBMRI, but they emphasized vessel wall enhancement patterns rather than intraluminal thrombus characteristics for insight into underlying pathologies. Recently, Bai et al<sup>14</sup> evaluated 60 patients with 80 suspected MCA intracranial atherosclerotic disease lesions with TOF-MRA, BBMRI, and CTA as the reference standard identifying 15 arterial occlusions. In this small subset, they also noted a

very high sensitivity (100%) and specificity (95%–97%) in detecting occlusions with VWI, using either source or minimum-intensity black-blood luminal angiography techniques, whereas TOF-MRA overestimated the pathology with significantly lower specificity (85%). In a larger series of 62 patients with acute stroke with MR imaging negative for the susceptibility vessel sign and BBMRI, Baik et al<sup>13</sup> reported contrast-enhancement patterns of intracranial stenoses and occlusions, identifying strong, round, and concentric enhancement in 15/20 (75%) patients with suspected acute arterial occlusions compared with 4.7% with severe intracranial stenoses. These findings correlate well with the 87.5% strong grade 2 enhancement of acute/subacute occlusions seen in our study. In a separate study, Kim et al<sup>16</sup> also studied 20 chronic unilateral MCA occlusions with high-resolution BBMRI and described 2 distinct “plugged” or “vanishing” patterns as either heterogeneous intraluminal signal in 13/20 patients or an absence of vascular structures in 7/20 patients, with shrunken MCA or collateral vessels, respectively. These latter findings suggest a stenocclusive vasculopathy/Moyamoya pathology rather than thromboembolic occlusions, but the authors did not comment on intraluminal hyperintensity or contrast-enhancement patterns.

Prior literature has suggested that acute, symptomatic, intracranial atherosclerotic disease plaques may be associated with higher degrees of eccentric (extraluminal) contrast enhancement compared with chronic or asymptomatic plaques.<sup>17</sup> In contrast, we noted persisting strong intraluminal enhancement of chronic/incidental arterial occlusions, hypothesized to be secondary to gadolinium leakage or superimposed inflammation of organized fibrin and platelet-rich thrombus. Methemoglobin is produced in the early stages (>7 days) of thrombus formation and requires time for accumulation. This feature may account for the lower grades of intraluminal T1 hyperintensity in acute/subacute occlusions that presented with early subacute infarcts (<7 days). Methemoglobin also has the strongest paramagnetic properties for shortening T1 relaxation times and can persist for several weeks to months,<sup>18</sup> potentially explaining the statistically higher grades of intraluminal T1 hyperintensity seen in chronic/incidental occlusions. In fact, 4 patients in our cohort underwent 3-, 6-, 9-, or 18-month follow-up BBMRI scans (data not shown), respectively, with persisting T1 hyperintensity on precontrast BBMRI in all 4 patients and strong grade 2 enhancement on post-contrast BBMRI in 3/4 patients. Another mechanism for chronic intraluminal T1 hyperintensity may be related to slow flow adjacent to the arterial occlusion site, resulting in impaired intravoxel dispersion and loss of the normal black-blood signal, independent of thrombus chronicity. Although we observed a higher percentage of posterior circulation occlusions diagnosed as chronic/incidental occlusions, this may be explained by the redundant supply of bilateral vertebral arteries with a predilection for silent occlusions (no vertebral artery occlusions presented with acute infarcts on DWI).

In our study, we independently evaluated the accuracy of both pre- and post-contrast BBMRI in diagnosing acute/subacute and chronic/incidental arterial occlusions in all major cerebral arteries, regardless of the underlying etiology, and in a large patient cohort. BBMRI identifies intracranial arterial occlusions with excellent sensitivity and specificity (100% and

99.8%, respectively) compared with CTA and DSA. High accuracy was sustained across anterior versus posterior circulation locations and acute/subacute versus chronic/incidental occlusions. Although there was higher interobserver agreement with >80% strong grade 2 intraluminal enhancement on post-contrast BBMRI, all occlusions were also successfully identified as grade 1 or 2 intraluminal T1 hyperintensity, consistent with equal and independent accuracy on pre-contrast BBMRI. These findings suggest that even noncontrast BBMRI may be superior to 3D-TOF-MRA sequences, which have a lower reported sensitivity (88%–100%) and specificity (85%–97%) for detecting intracranial occlusions in comparison with the criterion standard CTA and DSA modalities.<sup>15,19</sup>

Our study had the limitations of a retrospective analysis with its inherent challenges. There could have been inadvertent observer recall bias from prior clinical experience, though we attempted to mitigate this by blinding the observers to patient names and clinical history, allowing significant time intervals since MR imaging, and assessing their agreement. Our classification of arterial occlusion chronicity has the potential for error; therefore, we used an objective paradigm based on their clinical history, MR imaging findings, and prior angiographic studies. The sample size was small, yet to our knowledge, this is the largest series specifically focusing on the utility of BBMRI in the detection of intracranial large-vessel arterial occlusions. Finally, CTA was used as the reference standard when DSA was not available; however, studies have shown 100% sensitivity and specificity for CTA in detecting large-vessel arterial occlusions.<sup>20</sup>

## CONCLUSIONS

3D high-resolution BBMRI provides an adjunctive MR imaging-based mechanism to confidently diagnose large-vessel arterial occlusions in the setting of conventional low-resolution MR imaging and nonspecific MRA findings. BBMRI with or without contrast provides high accuracy in the diagnosis of acute/subacute as well as chronic/incidental occlusions, with near-equivalent sensitivity and specificity to CTA and DSA.

## ACKNOWLEDGMENTS

We thank Saadia Sattar, MSc, who contributed to the statistical analysis of this study.

Disclosures: Timothy J. Carroll—*RELATED: Grant:* National Institutes of Health, *Comments:* National Institutes of Health/National Institute of Neurological Disorders and Stroke 1R01NS093908\*; *UNRELATED: Grants/Grants Pending:* National Institutes of Health.\* Sameer A. Ansari—*RELATED: Grant:* American Heart Association 13GRNT17340018 and 14GRNT20380798 (Principal Investigators: S.A. Ansari and T.J. Carroll); National Institutes of Health/National Heart, Lung, and Blood Institute 1R21HL130969 (Principal Investigator: S.A. Ansari); and National Institutes of Health/National Institute of Neurological Disorders and Stroke 1R01NS093908 (Principal Investigator: T.J. Carroll).\* \*Money paid to the institution.

## REFERENCES

1. Goyal M, Menon BK, van Zwam WH, et al; HERMES collaborators. **Endovascular thrombectomy after large-vessel ischaemic stroke: a meta-analysis of individual patient data from five randomised trials.** *Lancet* 2016;387:1723–31 CrossRef Medline
2. Ciesienki KL, Caravan P. **Molecular MRI of thrombosis.** *Curr Cardiovasc Imaging Rep* 2010;4:77–84 Medline

3. Korogi Y, Takahashi M, Mabuchi N, et al. **Intracranial vascular stenosis and occlusion: diagnostic accuracy of three-dimensional, Fourier transform, time-of-flight MR angiography.** *Radiology* 1994; 193:187–93 CrossRef Medline
4. Ishimaru H, Ochi M, Morikawa M, et al. **Accuracy of pre- and post-contrast 3D time-of-flight MR angiography in patients with acute ischemic stroke: correlation with catheter angiography.** *AJNR Am J Neuroradiol* 2007;28:923–26 Medline
5. Axel L. **Blood flow effects in magnetic resonance imaging.** *Magn Reson Annu* 1986;237–44
6. Stock KW, Wetzel S, Kirsch E, et al. **Anatomic evaluation of the circle of Willis: MR angiography versus intraarterial digital subtraction angiography.** *AJNR Am J Neuroradiol* 1996;17:1495–99 Medline
7. Ginat DT, Meyers SP. **Intracranial lesions with high signal intensity on T1-weighted MR images: differential diagnosis.** *Radiographics* 2012;32:499–516 CrossRef Medline
8. Mandell DM, Mossa-Basha M, Qiao Y, et al; Vessel Wall Imaging Study Group of the American Society of Neuroradiology. **Intracranial vessel wall MRI: principles and expert consensus recommendations of the American Society of Neuroradiology.** *AJNR Am J Neuroradiol* 2017;38:218–29 CrossRef Medline
9. Allen LM, Hasso AN, Handwerker J, et al. **Sequence-specific MR imaging findings that are useful in dating ischemic stroke.** *Radiographics* 2012;32: 1285–97 CrossRef Medline
10. Lee NJ, Chung MS, Jung SC, et al. **Comparison of high-resolution MR imaging and digital subtraction angiography for the characterization and diagnosis of intracranial artery disease.** *AJNR Am J Neuroradiol* 2016;37:2245–50 CrossRef Medline
11. Kim JM, Jung KH, Sohn CH, et al. **High-resolution MR technique can distinguish moyamoya disease from atherosclerotic occlusion.** *Neurology* 2013;80:775–76 CrossRef Medline
12. Hui FK, Zhu X, Jones SE, et al. **Early experience in high-resolution MRI for large vessel occlusions.** *J Neurointerv Surg* 2015;7:509–16 CrossRef Medline
13. Baik SH, Kwak HS, Hwang SB, et al. **Three-dimensional black blood contrast enhanced magnetic resonance imaging in patients with acute ischemic stroke and negative susceptibility vessel sign.** *Eur J Radiol* 2018;102:188–94 CrossRef Medline
14. Bai X, Lv P, Liu K, et al. **3D black-blood luminal angiography derived from high-resolution MR vessel wall imaging in detecting MCA stenosis: a preliminary study.** *AJNR Am J Neuroradiol* 2018;39: 1827–32 CrossRef Medline
15. Liu Q, Huang J, Degnan AJ, et al. **Comparison of high-resolution MRI with CT angiography and digital subtraction angiography for the evaluation of middle cerebral artery atherosclerotic steno-occlusive disease.** *Int J Cardiovasc Imaging* 2013;29:1491–98 CrossRef Medline
16. Kim SM, Ryu CW, Jahng GH, et al. **Two different morphologies of chronic unilateral middle cerebral artery occlusion: evaluation using high-resolution MRI.** *J Neuroimaging* 2014;24:460–66 CrossRef Medline
17. Vakil P, Vranic J, Hurley MC, et al. **T1 gadolinium enhancement of intracranial atherosclerotic plaques associated with symptomatic ischemic presentations.** *AJNR Am J Neuroradiol* 2013;34:2252–58 CrossRef Medline
18. Moody AR. **Magnetic resonance direct thrombus imaging.** *J Thromb Haemost* 2003;1:1403–09 CrossRef Medline
19. Degnan AJ, Gallagher G, Teng Z, et al. **MR angiography and imaging for the evaluation of middle cerebral artery atherosclerotic disease.** *AJNR Am J Neuroradiol* 2012;33:1427–35 CrossRef Medline
20. Nguyen-Huynh MN, Wintermark M, English J, et al., **How accurate is CT angiography in evaluating intracranial atherosclerotic disease?** *Stroke* 2008;39:1184–88 CrossRef Medline

# Surveillance of Unruptured Intracranial Saccular Aneurysms Using Noncontrast 3D-Black-Blood MRI: Comparison of 3D-TOF and Contrast-Enhanced MRA with 3D-DSA

C. Zhu, X. Wang, L. Eisenmenger, B. Tian, Q. Liu, A.J. Degnan, C. Hess, D. Saloner, and J. Lu



## ABSTRACT

**BACKGROUND AND PURPOSE:** Patients with unruptured intracranial aneurysms routinely undergo surveillance imaging to monitor growth. Angiography is the criterion standard for aneurysm diagnosis, but it is invasive. This study aimed to evaluate the accuracy and reproducibility of a 3D noncontrast black-blood MR imaging technique for unruptured intracranial aneurysm measurement in comparison with 3D-TOF and contrast-enhanced MRA, using 3D rotational angiography as a reference standard.

**MATERIALS AND METHODS:** Sixty-four patients ( $57.3 \pm 10.9$  years of age, 41 women) with 68 saccular unruptured intracranial aneurysms were recruited. Patients underwent 3T MR imaging with 3D-TOF-MRA, 3D black-blood MR imaging, and contrast-enhanced MRA, and they underwent 3D rotational angiography within 2 weeks. The neck, width, and height of the unruptured intracranial aneurysms were measured by 2 radiologists independently on 3D rotational angiography and 3 MR imaging sequences. The accuracy and reproducibility were evaluated by Bland-Altman plots, the coefficient of variance, and the intraclass correlation coefficient.

**RESULTS:** 3D black-blood MR imaging demonstrates the best agreement with DSA, with the smallest limits of agreement and measurement error (coefficients of variance range, 5.87%–7.04%). 3D-TOF-MRA had the largest limits of agreement and measurement error (coefficients of variance range, 12.73%–15.78%). The average coefficient of variance was 6.26% for 3D black-blood MR imaging, 7.03% for contrast-enhanced MRA, and 15.54% for TOF-MRA. No bias was found among 3 MR imaging sequences compared with 3D rotational angiography. All 3 MR imaging sequences had excellent interreader agreement (intraclass correlation coefficient,  $>0.95$ ). 3D black-blood MR imaging performed the best for patients with intraluminal thrombus ( $n = 10$ ).

**CONCLUSIONS:** 3D black-blood MR imaging achieves better accuracy for aneurysm size measurements compared with 3D-TOF, using 3D rotational angiography as a criterion standard. This noncontrast technique is promising for surveillance of unruptured intracranial aneurysms.

**ABBREVIATIONS:** BB = black-blood; CE = contrast-enhanced; CV = coefficient of variance; 3DRA = 3D rotational angiography; IA = intracranial aneurysm; ICC = intraclass correlation coefficient; LOA = limit of agreement; SPACE = spatial and chemical-shift encoded excitation; UIA = unruptured intracranial aneurysm

Intracranial aneurysms (IAs) are common, with approximately 3% of adults having an unruptured IA (UIA).<sup>1</sup> UIAs are associ-

ated with morbidity and mortality due to the risk of rupture and the resultant subarachnoid hemorrhage.<sup>2</sup> Of patients surviving ruptured IAs, 30% will experience high morbidity due to associated intraparenchymal hemorrhage from late-onset complications such as vasospasm leading to cerebral infarction. Only approximately one-third of patients with subarachnoid hemorrhage related to IA rupture will fully return to their prior jobs,<sup>3,4</sup> but diagnosis of IAs before rupture may improve patient outcomes.<sup>5</sup>

Clinical management of UIAs is based largely on aneurysm size and other features such as location, shape, and sac-to-neck

Received February 22, 2019; accepted after revision April 15.

From the Department of Radiology and Biomedical Imaging (C.Z., L.E., C.H., D.S.), University of California, San Francisco, San Francisco, California; Department of Radiology (X.W., B.T., Q.L., J.L.), Changhai Hospital, Shanghai, China; Department of Radiology (X.W.), General Hospital of Northern Military Command, Liaoning, China; and Department of Radiology (A.J.D.), Children's Hospital of Philadelphia, Philadelphia, Pennsylvania.

Chengcheng Zhu and Xinrui Wang contributed equally to this work.

This work was supported by the National Natural Science Foundation of China (No. 81670396, No. 31470910), and the National Institutes of Health, grant K99HL136883.

The sponsoring organizations had no involvement in the study design, data collection, data analysis, data interpretation, writing of the article, or the decision to submit for publication.

Please address correspondence to Jianping Lu, MD, Department of Radiology, Changhai Hospital, Shanghai, China; e-mail: cjr.lu Jianping@vip.163.com

Indicates open access to non-subscribers at [www.ajnr.org](http://www.ajnr.org)

Indicates article with supplemental on-line table.

Indicates article with supplemental on-line photo.

<http://dx.doi.org/10.3174/ajnr.A6080>

ratio, with saccular aneurysms being the most common type.<sup>6-9</sup> Because intervention-associated risks may exceed the low rupture rates for smaller UIAs,<sup>5</sup> most of those small aneurysms are followed with surveillance instead of immediate treatment. In addition, more incidental UIAs have been found on widely used non-invasive imaging techniques. Usually, incidental UIAs that are regular in shape and <7 mm are followed up to assess changes with time that may modify clinical decision-making,<sup>10</sup> but how to best diagnose and monitor UIAs remains uncertain.

Although 3D rotational angiography (3DRA) is the criterion standard for diagnosing IAs as well as evaluating IA morphology measurements,<sup>11</sup> both MR imaging and CTA have become increasingly important in evaluating UIAs. This change is largely because both MR imaging and CTA are less invasive than 3DRA, reducing the risks of IA screening and monitoring of known UIAs.<sup>12-14</sup> However, unlike MR imaging, both 3DRA and CTA expose patients to ionizing radiation and iodinated contrast media. MR imaging is an option that removes the uncertain risks of repeat radiation and contrast media exposure.

Vascular MR imaging has substantially improved with the development of techniques enabling the diagnosis, visualization, and assessment of intracranial aneurysms with high accuracy.<sup>15</sup> Numerous studies have assessed the value of both flow-based (TOF) and contrast-enhanced (CE) MRA techniques.<sup>5</sup> Fewer studies have evaluated 3D noncontrast black-blood (BB) MR imaging in aneurysm characterization, though early data have shown promise<sup>15</sup> with the use of high-isotropic resolution (up to 0.5 mm) to visualize the aneurysm geometry and wall.<sup>16</sup> 3D-BB MR imaging, however, has not been validated against 3DRA for aneurysm size measurements or compared with other clinical MRA techniques. This study aimed to compare black-blood MR imaging with 3D-TOF/CE-MRA for aneurysm size measurements using 3DRA as a reference standard. We hypothesized that 3D noncontrast BB MR imaging can be used to measure aneurysm size accurately.

## MATERIALS AND METHODS

### Study Population

This study was approved by the institutional review board of Changhai Hospital. Informed consent was obtained from all patients. A total of 69 consecutive patients with confirmed saccular IAs were recruited between January 2016 and March 2018. All patients underwent 3T MR imaging and 3DRA within 2 weeks.

### Imaging Protocol

**MR Imaging.** MR imaging was performed on a 3T whole-body MR imaging system (Magnetom Skyra; Siemens, Erlangen, Germany) using a 20-channel head coil. 3D-TOF-MRA, 3D-BB MR imaging, and CE-MRA were performed successively. The unenhanced 3D-TOF-MRA was performed with TR = 21 ms, TE = 3.4 ms, flip angle = 20°, FOV = 180 × 200 mm<sup>2</sup>, matrix = 330 × 384, in-plane resolution = 0.5 × 0.5 mm<sup>2</sup>, slice thickness = 0.7 mm, 144 slices, and total acquisition time of 4 minutes 56 seconds. The 3D-BB MR imaging (spatial and chemical-shift encoded excitation [SPACE]) was performed with TR = 900 ms, TE = 5.6 ms, FOV = 160 × 160, matrix = 320 × 320, slice thickness = 0.5 mm, echo-train length = 60, 280 slices, and total acquisition time of 8

minutes 16 seconds. CE-MRA was then performed at the first pass of intravenous injection of Gd-DTPA at a dose of 0.1 mmol/kg, using a FLASH 3D spoiled gradient-echo sequence with TR = 3.66 ms, TE = 1.44 ms, FOV = 182 × 224 mm<sup>2</sup>, flip angle = 20°, matrix = 320 × 320, in plane resolution = 0.6 × 0.7 mm<sup>2</sup>, slice thickness = 0.7 mm, 120 slices, and total acquisition time of 1 minute 24 seconds.

**3DRA.** 3DRA was performed on the Artis zee Biplane angiographic system (VC14; Siemens). A 5-second DSA acquisition protocol was performed with contrast injection at a rate of 3 mL/s of Ultravist (iopromide; Bayer HealthCare, Berlin, Germany). During the 5-second acquisition after a delay of 1 second, a 200° rotation of the C-arm was performed to obtain 133 frames. The parameters were as follows: FOV = 320 × 320 mm<sup>2</sup>, matrix = 1024 × 1024.

### Image Analysis

Image analysis was performed independently by 2 radiologists (X.W. and B.T. with 5 and 9 years of experience) who were blinded to patients' clinical data. All measurements were conducted on the postprocessing workstation (syngo X Workspace; Siemens). Measurement of 3DRA was performed on volume-rendered reconstruction, and measurements of TOF-MRA and CE-MRA were performed on MIP reconstructions. The MIP images were imported to the workstation, and the image viewer automatically set a default window/level for the best display. In addition, 2 observers were also allowed to adjust the window/level and projection angles to best display the aneurysm and the parent vessel. Measurement of 3D-BB MR imaging was performed on MPR images.

For each IA, we measured the following parameters: 1) height: the maximum distance from the neck center to the dome of the aneurysm; 2) width: the longest diameter of an aneurysm perpendicular to the height; and 3) neck: the minimum width of the aneurysm at its junction with the parent vessel (Fig 1). Measurements were performed by the 2 readers (X.W. and B.T.) separately, with an interval of 2 weeks between different modalities. One reader performed the second measurement (X.W.) 2 weeks later using the same method to evaluate the intrareader variability. All these measurements were performed only for the luminal geometry, for which DSA could be used as a reference standard. If the aneurysms had intraluminal thrombus, the images were evaluated separately for the true aneurysm geometry.

### Statistical Analysis

Normality assumptions were assessed using the Shapiro-Wilk test. Continuous variables were expressed as either mean ± SD or median (interquartile range). Categorical variables were summarized by count (percentage). Comparisons of aneurysm height, width, and neck diameter among different imaging modalities were analyzed using the Kruskal-Wallis test. Measurement differences between MR imaging modalities and DSA as well as intra- and interreader variabilities were assessed using the Bland-Altman analysis. Bias was assessed as the mean of the pair differences, and the 95% limits of agreement (LOA) were defined as bias ± 1.96 × SD. Measurement error was quantified by the coefficient of variance (CV = SD / mean × 100%). Agreement between

measurements was summarized by the intraclass correlation coefficient (ICC) with a 2-way mixed model. An ICC value >0.80 indicated excellent agreement. On the basis of the measurement errors of each MR imaging sequence, the sample sizes needed to detect 5%, 10%, and 20% changes in aneurysm size growth in longitudinal studies were calculated by using 0.9 power and .05 significance as described in a previous publication.<sup>17</sup> Statistical analyses were performed using SPSS, Version 24.0 (IBM, Ar-

monk, New York) and MedCalc for Windows, Version 9.4.2.0 (MedCalc Software, Mariakerke, Belgium).

## RESULTS

Of the 69 recruited patients, 5 were excluded for the following reasons: 1) an interval of >2 weeks between MR imaging and DSA ( $n = 2$ ); 2) a ruptured aneurysm ( $n = 1$ ); and 3) insufficient image quality due to motion artifacts on 3D-BB MR imaging ( $n = 2$ ). The remaining 64 patients ( $57.3 \pm 10.9$  years of age, 41 women) with 68 saccular UIAs were included. UIAs were located in the internal carotid artery ( $n = 32$ ), middle cerebral artery ( $n = 12$ ), anterior communicating artery ( $n = 10$ ), posterior communicating artery and posterior cerebral artery ( $n = 8$ ), and vertebral-basilar artery ( $n = 6$ ). The average interval between MR imaging and DSA was  $2.2 \pm 1.6$  days (range, 1–9 days). Mild flow artifacts were observed in 3 UIAs with aneurysm diameters of >15 mm on 3D-BB MR imaging. These artifacts did not affect the measurement accuracy.

### Agreement between MR Imaging Sequences and DSA

As shown in Table 1, there was no significant difference in aneurysm height, width, and neck diameter among TOF/CE-MRA, 3D-BB MR imaging, and DSA ( $P > .05$ ). Agreement of the quantitative measurements between MR imaging modalities and DSA is summarized in Table 2. Bland-Altman plots for each measurement are shown in Fig 2 and the On-line Figure. Measurements between MR imaging modalities and DSA showed excellent agreement with ICCs of >0.96. Measurement on TOF-MRA showed the largest variance (overall CV, 15.54%) and higher LOA compared with measurements on CE-MRA (overall CV, 7.03%) and 3D-BB MR imaging (overall CV, 6.26%). Based on the measurement errors of each MR image, the calculated sample sizes in future longitudinal studies to detect 5%, 10%, and 20% change in aneurysm growth are shown in Table 3. Compared with 3D-TOF, the use of CE-MRA or 3D-BB MR imaging reduces the sample size

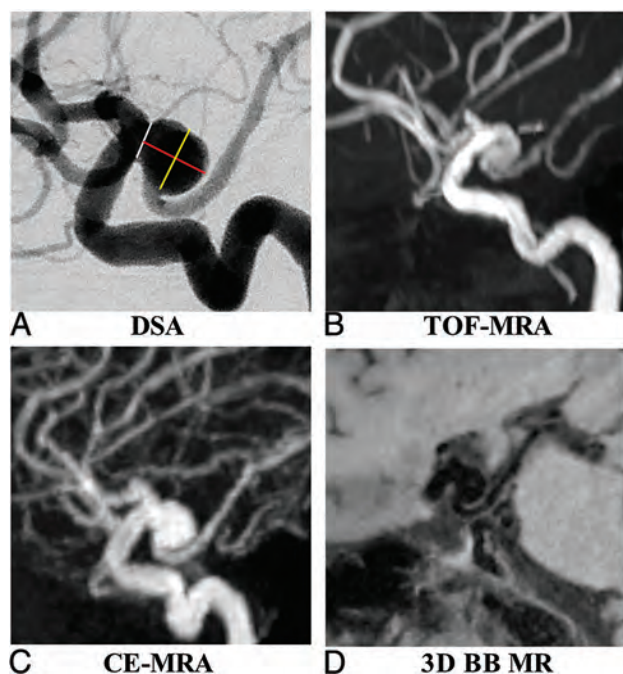


**FIG 1.** A 61-year-old woman with a right posterior communicating artery aneurysm on DSA (A), TOF-MRA (B), CE-MRA (C), and 3D-BB MR imaging (D). Aneurysm height (red line), width (yellow line), and neck (white line) measurements are demonstrated in A.

**Table 1: Comparison of aneurysm height, width, and neck measurements among MR and DSA imaging modalities<sup>a</sup>**

	TOF-MRA	CE-MRA	3D-BB MRI	3DRA	P Value
Height (mm)	7.7 (5.5–11.1)	8.0 (6.0–12.8)	7.8 (5.4–12.6)	7.7 (5.5–12.6)	.918
Width (mm)	7.5 (5.8–11.5)	8.4 (5.8–14.0)	7.8 (5.5–13.9)	8.1 (5.9–13.3)	.957
Neck (mm)	6.8 (5.3–10.4)	6.7 (5.2–10.6)	7.0 (4.8–10.2)	6.9 (4.6–9.8)	.774

<sup>a</sup>Data are median (interquartile range).

**Table 2: Comparison of MRI techniques with DSA for aneurysm measurements**

	Mean (mm)	SD	CV (100%)	Bias	LOA	ICC
Height						
TOF-MRA	9.21	1.50	15.43	−0.55	(−3.49–2.39)	0.96 (0.93–0.98)
CE-MRA	9.90	0.62	6.32	0.14	(−1.08–1.36)	0.98 (0.97–0.99)
3D-BB MRI	9.73	0.59	6.04	−0.03	(−1.19–1.13)	0.99 (0.99–0.99)
Width						
TOF-MRA	9.53	1.56	15.78	−0.33	(−2.73–3.39)	0.96 (0.94–0.97)
CE-MRA	10.12	0.61	6.18	0.26	(−0.94–1.46)	0.99 (0.98–0.99)
3D-BB MRI	9.96	0.58	5.87	0.10	(−1.04–1.24)	0.99 (0.99–0.99)
Neck						
TOF-MRA	8.00	0.98	12.73	0.31	(−1.61–2.23)	0.96 (0.93–0.98)
CE-MRA	8.08	0.68	8.81	0.39	(−0.94–1.72)	0.97 (0.95–0.99)
3D-BB MRI	7.71	0.54	7.04	0.02	(−1.04–1.08)	0.98 (0.98–0.99)
Overall						
TOF-MRA	8.91	1.41	15.54	−0.19	(−2.95–2.57)	0.96 (0.95–0.97)
CE-MRA	9.37	0.64	7.03	0.26	(−0.99–1.51)	0.98 (0.98–0.99)
3D-BB MRI	9.14	0.57	6.26	0.03	(−1.08–1.15)	0.99 (0.99–0.99)

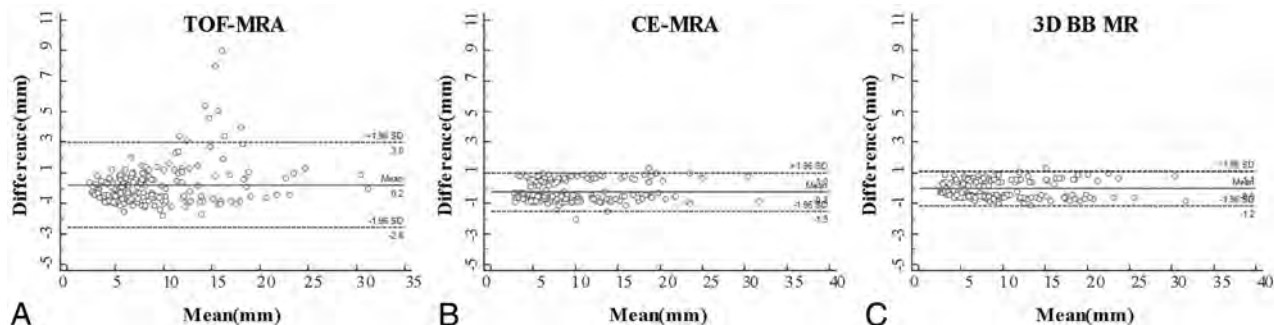


**FIG 2.** Bland-Altman plots of aneurysm measurements of TOF-MRA (A), CE-MRA (B), and 3D-BB MR imaging (C) versus 3DRA as the reference standard. Solid horizontal lines define the reference standard, and upper and lower dashed lines define the LOA.

**Table 3: Sample size calculation using different MRI sequences to detect aneurysm growth**

Aneurysm Growth	TOF-MRA (CV = 15.54%)	CE-MRA (CV = 7.03%)	SPACE (CV = 6.26%)
5%	406	84	66
10%	102	21	17
20%	26	6	5

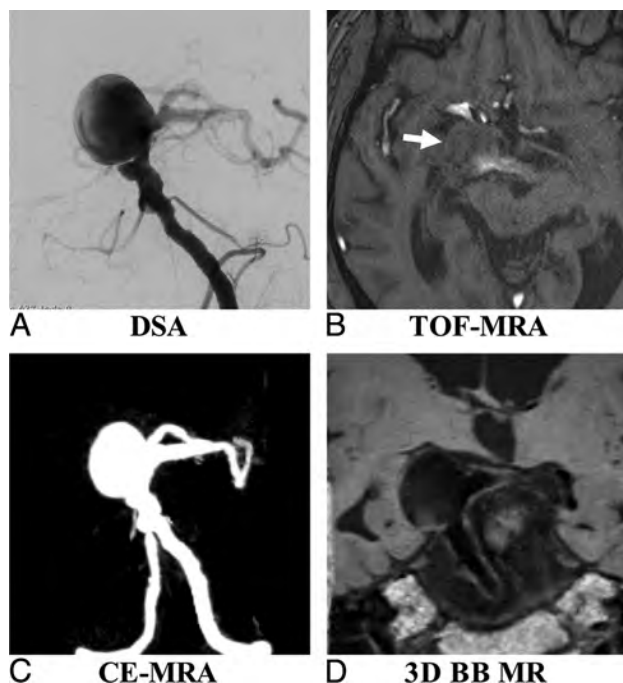


**FIG 3.** A 53-year-old man with multiple basilar artery aneurysms on DSA (A). The aneurysm shows isointensity on TOF-MRA (B) because of the slow flow (arrow). The aneurysm sac and neck were integrally visualized on CE-MRA (C) and 3D-BB MR imaging (D).

by 79% and 84%, respectively. Comparisons of MR imaging modalities with DSA for aneurysm measurements by locations are summarized in On-line Table. The measurement errors did not vary significantly across locations.

Sample patient images are shown in Figs 3 and 4. Figure 3 shows that TOF is limited as a means of displaying the aneurysm geometry due to severe flow artifacts, while DSA, CE-MRA, and SPACE characterize the geometry nicely. Figure 4 shows an aneurysm with intraluminal thrombus. 3D-BB MR imaging can clearly show the entire aneurysm structure including both the lumen and the thrombus.

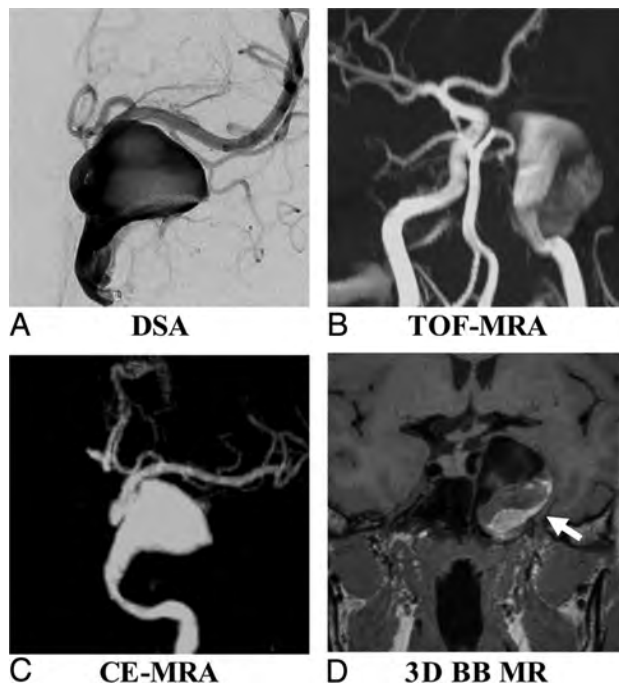


**FIG 4.** A 63-year-old woman with a right middle cerebral artery aneurysm on DSA (A). 3D-BB SPACE (D) can clearly visualize the sac and intraluminal thrombus of the aneurysm, which is superior to DSA (A), TOF-MRA (B), and CE-MRA (C).

#### **Intra- and Interreader Agreement**

Intra- and interreader agreement is shown in Table 4. There were no significant mean differences between readers ( $P > .05$ ). The overall intra- and interreader measurements showed excellent agreement, with ICCs of  $>0.97$ .

#### **Aneurysms with Intraluminal Thrombus**

Ten aneurysms were found with intraluminal thrombus: 3 aneurysms located in the middle cerebral artery, 2 located in the internal carotid artery, 2 located in the anterior communicating artery, 2 located in the posterior communicating artery, and 1 located in the basilar artery. Aneurysm sizes ranged from 8.0 to 28.2 mm. 3D-BB MR imaging gave the best evaluation of aneurysm dimensions, with clear delineation of both the lumen and thrombus (Fig 3). The median thickness of the intraluminal thrombus was 2.8 mm (IQR, 0.8–4.4 mm).

**Table 4: Intra- and interreader agreement for aneurysm measurements**

	CV (100%)	Bias	LOA	ICC
<b>Intrareader agreement</b>				
Height				
TOF-MRA	7.02	0.19	(-0.87-1.25)	0.99 (0.98-0.99)
CE-MRA	6.71	0.14	(-1.09-1.37)	0.99 (0.98-0.99)
3D-BB MRI	6.37	-0.08	(-1.18-1.02)	0.99 (0.98-0.99)
3DRA	6.87	0.14	(-1.04-1.32)	0.99 (0.98-0.99)
Width				
TOF-MRA	6.94	0.06	(-0.99-1.12)	0.99 (0.98-0.99)
CE-MRA	6.45	0.10	(-1.13-1.33)	0.99 (0.98-0.99)
3D-BB MRI	6.31	0.18	(-0.92-1.28)	0.99 (0.98-0.99)
3DRA	6.25	0.11	(-1.00-1.23)	0.99 (0.98-0.99)
Neck				
TOF-MRA	7.29	0.18	(-1.04-1.39)	0.98 (0.98-0.99)
CE-MRA	7.05	0.13	(-0.93-1.19)	0.99 (0.98-0.99)
3D-BB MRI	6.72	0.14	(-0.90-1.18)	0.99 (0.98-0.99)
3DRA	6.98	-0.08	(-1.17-1.02)	0.99 (0.98-0.99)
Overall				
TOF-MRA	7.08	0.14	(-0.78-1.06)	0.99 (0.98-0.99)
CE-MRA	6.78	0.12	(-1.06-1.30)	0.99 (0.98-0.99)
3D-BB MRI	6.51	0.08	(-0.96-1.12)	0.99 (0.98-0.99)
3DRA	6.75	0.06	(-1.04-1.16)	0.99 (0.98-0.99)
<b>Interreader agreement</b>				
Height				
TOF-MRA	8.12	0.02	(-1.45-1.49)	0.98 (0.98-0.99)
CE-MRA	8.19	0.23	(-1.33-1.80)	0.98 (0.98-0.99)
3D-BB MRI	8.03	0.03	(-1.50-1.56)	0.98 (0.98-0.99)
3DRA	7.87	-0.07	(-1.58-1.44)	0.98 (0.98-0.99)
Width				
TOF-MRA	8.03	-0.03	(-1.50-1.44)	0.98 (0.98-0.99)
CE-MRA	7.55	0.17	(-1.30-1.64)	0.99 (0.98-0.99)
3D-BB MRI	8.37	0.03	(-1.61-1.67)	0.98 (0.98-0.99)
3DRA	7.15	-0.13	(-1.54-1.28)	0.99 (0.98-0.99)
Neck				
TOF-MRA	8.96	0.18	(-0.74-1.10)	0.97 (0.95-0.98)
CE-MRA	8.81	0.07	(-0.81-1.07)	0.98 (0.97-0.99)
3D-BB MRI	8.95	0.14	(-0.72-1.00)	0.98 (0.97-0.99)
3DRA	8.82	0.10	(-0.82-0.98)	0.98 (0.97-0.99)
Overall				
TOF-MRA	8.44	0.06	(-0.78-1.06)	0.98 (0.98-0.99)
CE-MRA	8.16	0.16	(-0.74-0.98)	0.98 (0.98-0.99)
3D-BB MRI	8.43	0.07	(-0.63-0.93)	0.98 (0.98-0.99)
3DRA	8.15	-0.03	(-0.72-1.00)	0.98 (0.98-0.99)

## DISCUSSION

In this study, measurements obtained on 3D-BB MR imaging were in close agreement with 3DRA measurements and had a better accuracy than 3D-TOF with less than half the TOF measurement error. The sample size needed to measure aneurysm size change in longitudinal studies would be reduced by 84% using 3D-BB MR imaging compared with using 3D-TOF. Our results support the use of noncontrast 3D-BB MR imaging for intracranial aneurysm surveillance. Despite previous studies evaluating the use of BB MR imaging sequences in the characterization of IAs, this is the first study to validate 3D-BB MR imaging against the criterion standard 3DRA for aneurysm morphology measurements. In addition, this is the first study to compare 3D-BB MR imaging with 3D-TOF and CE-MRA for IA measurement accuracy.

Although 3DRA remains the criterion standard in aneurysm evaluation and treatment planning with high spatial resolution and excellent hemodynamic temporal resolution,<sup>11</sup> DSA is inva-

sive with procedural risks such as arterial dissection, hematomas, stroke, and even death that are more important than the small theoretic risks of radiation and contrast exposure.<sup>18</sup> Alternatively, CTA is a fast, noninvasive imaging test that is often used in first-line aneurysm assessment. CTA has widespread availability and has been shown to be of benefit in not only aneurysm detection<sup>19-23</sup> but also presurgical planning.<sup>24</sup> Despite the advantages of CTA, like DSA, CTA uses radiation and iodinated contrast, reducing its adoption in UIA screening and monitoring.<sup>12</sup> MR imaging does not have these issues.<sup>25</sup> Other disadvantages of CTA include the fact that despite the development of improved techniques in the region of the skull base,<sup>26,27</sup> MR imaging lacks the attenuation and streak artifacts occasionally encountered in CTA.<sup>28</sup> MR imaging can play a major role in UIA detection, monitoring, and treatment planning.<sup>29</sup>

3D-TOF and CE-MRA are commonly used methods for UIA evaluation. 3D-TOF-MRA is a popular method because it does not require a contrast agent<sup>10,30,31</sup>; however, it has flow artifacts and can confuse T1-weighted hyperintense thrombus within an aneurysm with flow-related enhancement.<sup>32,33</sup> Bright thrombus can mimic flowing lumen, and isointense thrombus is difficult to distinguish from surrounding brain tissue.<sup>15</sup> TOF-MRA can also make detection of IAs difficult in the setting of T1 hyperintense intraparenchymal or subarachnoid hemorrhage.<sup>34-36</sup> Our study observed that while still similar to 3DRA, 3D-TOF-

MRA had the least accuracy of the MR imaging-based methods tested, in accordance with previous literature.

CE-MRA is an accurate method for UIA evaluation because it is not flow-dependent.<sup>37</sup> CE-MRA was shown to be superior to 3D-TOF-MRA for assessment of sac shape, visualizing an aneurysm neck, calculating of the sac/neck ratio, and identifying branches originating from the sac and/or neck,<sup>5</sup> especially for large aneurysms (>13 mm), when flow artifacts were commonly present. Despite these advantages of CE-MRA, its limitations include the use of gadolinium-based contrast media, dependence on timing of contrast administration that may lead to venous contamination, and radiofrequency power deposition at high field strengths.<sup>38</sup> Recent concerns regarding gadolinium deposition in the brain parenchyma, while uncertain and controversial, call into question its widespread use in repeat imaging for surveillance.<sup>39</sup>

When we compared it with other imaging modalities, 3D-BB

MR imaging has clear advantages. First, it is an accurate method for UIA measurements as evidenced in the superior agreement of this study with DSA, which was comparable with CE-MRA. Although our CE-MRA protocol had better resolution (around 0.7 mm isotropic) than most routine clinical protocols (0.9–1.1 mm),<sup>5</sup> 3D-BB MR imaging had an even higher resolution (0.5 mm isotropic), which may explain its slightly improved accuracy. 3D-BB MR imaging has also been used for intracranial stenosis quantification<sup>11</sup> and extracranial carotid plaque imaging<sup>40</sup> in studies showing excellent agreement with DSA. Our study extends these observations in showing that 3D-BB MR imaging provides accurate assessment of aneurysms. The high accuracy of 3D-BB MR imaging is favorable for future longitudinal studies, which can reduce sample size more significantly than with 3D-TOF and reduce the cost of the clinical trial. Accurate quantification of aneurysm growth is important because fast-growing aneurysms have a much higher risk of rupture.<sup>41,42</sup>

Second, as a noncontrast acquisition, 3D-BB MR imaging is ideal for repeat, routine surveillance of UIAs compared with contrast techniques including CE-MRA and CTA. It can also be repeated if the first acquisition fails due to patient motion or other issues. Third, 3D-BB SPACE is insensitive to flow artifacts, which is superior to 3D-TOF (Figs 3 and 4). The 3D fast-spin-echo BB sequence is inherently blood-suppressed.<sup>43</sup> Although in large aneurysms, flow artifacts can still occur, several additional techniques, including improved motion-sensitized driven-equilibrium<sup>44</sup> and delay alternating with nutation for tailored excitation (DANTE)<sup>45</sup> may be used to optimize blood suppression. Previous work comparing 3D-TOF and BB techniques showed significant advantages to BB imaging in cases of large aneurysms or slow blood flow.<sup>36,46</sup> In 1 study, the authors found 3 patients in whom the aneurysm was not demonstrated on 3D-TOF due to the presence of local hematoma, but by performing a BB sequence, they found that all of the IAs were subsequently identified without the need for contrast.<sup>15</sup>

Last, 3D-BB MR imaging can also visualize intraluminal thrombus and the vessel wall, which is a unique advantage in comparison with angiographic methods. Because vessel wall features and postcontrast enhancement have been studied as potential markers of aneurysm rupture,<sup>25,47</sup> this ability could become increasingly important in aneurysm characterization and monitoring.

### Limitations

There are some limitations to this study. First, we evaluated only saccular aneurysms with fusiform aneurysms excluded. Second, our current 3D-BB MR imaging sequence has a scan time of approximately 9 minutes, greater than the time it takes for either CE-MRA (2–3 minutes) or TOF (~5 minutes). It is possible that a lower resolution (0.6–0.7 mm isotropic) can achieve sufficient accuracy with a significantly reduced scan time. Advanced acceleration techniques, including compressed sensing, may potentially reduce the scan time significantly with similar image quality.<sup>48</sup> Future studies are needed to determine the minimum spatial resolution necessary and apply new acceleration techniques clinically. Third, the image-reconstruction methods were not the same across imaging modalities. We used the reconstruction

methods that were conventionally used in clinical routine,<sup>15,49,50</sup> and also note that the influence of reconstruction methods for aneurysm measurements has been rarely studied. However, we believe the differences caused by reconstruction methods were much less than the differences caused by imaging techniques, as shown in our data.

Despite these limitations, we believe that they are offset by the improved IA measurements compared with the other MR imaging techniques as well as the ability of 3D-BB MR imaging to characterize the vessel wall without the use of gadolinium-based contrast, supporting the use of noncontrast BB MR imaging to replace CE-MRA in monitoring IAs.

### CONCLUSIONS

3D-BB MR imaging achieves superior accuracy for intracranial aneurysm size measurements over 3D-TOF using 3DRA as the criterion standard, though all MR imaging measurements did not significantly differ from those with 3DRA. This noncontrast technique is promising for clinical surveillance of patients with unruptured intracranial aneurysms.

Disclosures: Christopher Hess—UNRELATED: Expert Testimony: various medicolegal firms; Grants/Grants Pending: National Institutes of Health\*; Travel/Accommodations/Meeting Expenses Unrelated to Activities Listed: Korean Society of Radiology, MRI Garmisch Symposium, Comments: Korean Society of Radiology; travel costs to lecture and participate in Korean Congress of Radiology 2018 and 18th MRI International MRI Symposium Garmisch-Partenkirchen. \*Money paid to individual.

### REFERENCES

1. Wiebers DO, Whisnant JP, Huston J 3rd, et al; International Study of Unruptured Intracranial Aneurysms Investigators. **Unruptured intracranial aneurysms: natural history, clinical outcome, and risks of surgical and endovascular treatment.** *Lancet* 2003;362:103–10 CrossRef Medline
2. Fogelholm R, Hernesniemi J, Vapalahti M. **Impact of early surgery on outcome after aneurysmal subarachnoid hemorrhage: a population-based study.** *Stroke* 1993;24:1649–54 CrossRef Medline
3. Passier PE, Visser-Meily JM, Rinkel GJ, et al. **Life satisfaction and return to work after aneurysmal subarachnoid hemorrhage.** *J Stroke Cerebrovasc Dis* 2011;20:324–29 CrossRef Medline
4. Rinkel GJ, Algra A. **Long-term outcomes of patients with aneurysmal subarachnoid haemorrhage.** *Lancet Neurol* 2011;10:349–56 CrossRef Medline
5. Cirillo M, Scomazzoni F, Cirillo L, et al. **Comparison of 3D TOF-MRA and 3D CE-MRA at 3T for imaging of intracranial aneurysms.** *Eur J Radiol* 2013;82:e853–59 CrossRef Medline
6. Komotar RJ, Starke RM, Connolly ES. **The natural course of unruptured cerebral aneurysms.** *Neurosurgery* 2012;71:N7–9 CrossRef Medline
7. Backes D, Vergouwen MD, Tiel Groenestege AT, et al. **PHASES score for prediction of intracranial aneurysm growth.** *Stroke* 2015;46:1221–26 CrossRef Medline
8. Gibbs GF, Huston J 3rd, Bernstein MA, et al. **Improved image quality of intracranial aneurysms: 3.0-T versus 1.5-T time-of-flight MR angiography.** *AJNR Am J Neuroradiol* 2004;25:84–87 Medline
9. Nael K, Villablanca JP, Mossaz L, et al. **3T contrast-enhanced MR angiography in evaluation of suspected intracranial aneurysm: comparison with MDCT angiography.** *AJR Am J Roentgenol* 2008;190:389–95 CrossRef Medline
10. Anzalone N, Scomazzoni F, Cirillo M, et al. **Follow-up of coiled cerebral aneurysms at 3T: comparison of 3D time-of-flight MR angiography and contrast-enhanced MR angiography.** *AJNR Am J Neuroradiol* 2008;29:1530–36 CrossRef Medline
11. Park JE, Jung SC, Lee SH, et al. **Comparison of 3D magnetic reso-**

- nance imaging and digital subtraction angiography for intracranial artery stenosis. *Eur Radiol* 2017;27:4737–46 CrossRef Medline
12. van der Schaaf IC, Velthuis BK, Wermer MJ, et al; ASTRA Study Group. **New detected aneurysms on follow-up screening in patients with previously clipped intracranial aneurysms: comparison with DSA or CTA at the time of SAH.** *Stroke* 2005;36:1753–58 CrossRef Medline
  13. Wermer MJ, Buskens E, van der Schaaf IC, et al. **Yield of screening for new aneurysms after treatment for subarachnoid hemorrhage.** *Neurology* 2004;62:369–75 CrossRef Medline
  14. Wermer MJ, van der Schaaf IC, Velthuis BK, et al. **Yield of short-term follow-up CT/MR angiography for small aneurysms detected at screening.** *Stroke* 2006;37:414–18 CrossRef Medline
  15. Stivaros SM, Harris JN, Adams W, et al. **Does black blood MRA have a role in the assessment of intracerebral aneurysms?** *Eur Radiol* 2009;19:184–92 CrossRef Medline
  16. Zhu C, Haraldsson H, Tian B, et al. **High resolution imaging of the intracranial vessel wall at 3 and 7 T using 3D fast spin echo MRI.** *MAGMA* 2016;29:559–70 CrossRef Medline
  17. Zhang X, Zhu C, Peng W, et al. **Scan-rescan reproducibility of high resolution magnetic resonance imaging of atherosclerotic plaque in the middle cerebral artery.** *PLoS One* 2015;10:e0134913 CrossRef Medline
  18. Kaufmann TJ, Huston J 3rd, Mandrekar JN, et al. **Complications of diagnostic cerebral angiography: evaluation of 19,826 consecutive patients.** *Radiology* 2007;243:812–19 CrossRef Medline
  19. Tipper G, U-King-Im JM, Price SJ, et al. **Detection and evaluation of intracranial aneurysms with 16-row multislice CT angiography.** *Clin Radiol* 2005;60:565–72 CrossRef Medline
  20. Chen CY, Hsieh SC, Choi WM, et al. **Computed tomography angiography in detection and characterization of ruptured anterior cerebral artery aneurysms at uncommon location for emergent surgical clipping.** *Clin Imaging* 2006;30:87–93 CrossRef Medline
  21. Carstairs SD, Tanen DA, Duncan TD, et al. **Computed tomographic angiography for the evaluation of aneurysmal subarachnoid hemorrhage.** *Acad Emerg Med* 2006;13:486–92 CrossRef Medline
  22. Uysal E, Yanbuloglu B, Erturk M, et al. **Spiral CT angiography in diagnosis of cerebral aneurysms of cases with acute subarachnoid hemorrhage.** *Diagn Interv Radiol* 2005;11:77–82 Medline
  23. Goddard AJ, Tan G, Becker J. **Computed tomography angiography for the detection and characterization of intra-cranial aneurysms: current status.** *Clin Radiol* 2005;60:1221–36 CrossRef Medline
  24. Suzuki Y, Nakajima M, Ikeda H, et al. **Preoperative evaluation of the venous system for potential interference in the clipping of cerebral aneurysm.** *Surg Neurol* 2004;61:357–64; discussion 364 CrossRef Medline
  25. Edjlali M, Gentic JC, Régent-Rodriguez C, et al. **Does aneurysmal wall enhancement on vessel wall MRI help to distinguish stable from unstable intracranial aneurysms?** *Stroke* 2014;45:3704–06 CrossRef Medline
  26. Tomandl BF, Hammen T, Klotz E, et al. **Bone-subtraction CT angiography for the evaluation of intracranial aneurysms.** *AJNR Am J Neuroradiol* 2006;27:55–59 Medline
  27. Sakamoto S, Kiura Y, Shibukawa M, et al. **Subtracted 3D CT angiography for evaluation of internal carotid artery aneurysms: comparison with conventional digital subtraction angiography.** *AJNR Am J Neuroradiol* 2006;27:1332–37 Medline
  28. Kouskouras C, Charitanti A, Giavroglou C, et al. **Intracranial aneurysms: evaluation using CTA and MRA: correlation with DSA and intraoperative findings.** *Neuroradiology* 2004;46:842–50 CrossRef Medline
  29. Vaphiades MS, Horton JA. **MRA or CTA, that's the question.** *Surv Ophthalmol* 2005;50:406–10 CrossRef Medline
  30. Kahära V. **Postprocedural monitoring of cerebral aneurysms.** *Acta Radiol* 2006;47:320–27 CrossRef Medline
  31. Okahara M, Kiyosue H, Hori Y, et al. **Three-dimensional time-of-flight MR angiography for evaluation of intracranial aneurysms after endosaccular packing with Guglielmi detachable coils: comparison with 3D digital subtraction angiography.** *Eur Radiol* 2004;14:1162–68 Medline
  32. Moody AR, Pollock JG, O'Connor AR, et al. **Lower-limb deep venous thrombosis: direct MR imaging of the thrombus.** *Radiology* 1998;209:349–55 CrossRef Medline
  33. Derdeyn CP, Graves VB, Turski PA, et al. **MR angiography of saccular aneurysms after treatment with Guglielmi detachable coils: preliminary experience.** *AJNR Am J Neuroradiol* 1997;18:279–86 Medline
  34. Jäger HR, Ellamushi H, Moore EA, et al. **Contrast-enhanced MR angiography of intracranial giant aneurysms.** *AJNR Am J Neuroradiol* 2000;21:1900–07 Medline
  35. Evans AL, Coley SC, Wilkinson ID, et al. **First-line investigation of acute intracerebral hemorrhage using dynamic magnetic resonance angiography.** *Acta Radiol* 2005;46:625–30 CrossRef Medline
  36. Thomas B, Sunaert S, Thamburaj K, et al. **Spurious absence of signal on 3D time-of-flight MR angiograms on 1 and 3 Tesla magnets in cerebral arteries associated with a giant ophthalmic segment aneurysm: the need for alternative techniques.** *JBR-BTR* 2005;88:241–44 Medline
  37. Okumura A, Araki Y, Nishimura Y, et al. **The clinical utility of contrast-enhanced 3D MR angiography for cerebrovascular disease.** *Neurol Res* 2001;23:767–71 CrossRef Medline
  38. Bernstein MA, Huston J 3rd, Lin C, et al. **High-resolution intracranial and cervical MRA at 3.0T: technical considerations and initial experience.** *Magn Reson Med* 2001;46:955–62 CrossRef Medline
  39. McDonald RJ, McDonald JS, Kallmes DF, et al. **Intracranial gadolinium deposition after contrast-enhanced MR imaging.** *Radiology* 2015;275:772–82 CrossRef Medline
  40. Zhao H, Wang J, Liu X, et al. **Assessment of carotid artery atherosclerotic disease by using three-dimensional fast black-blood MR imaging: comparison with DSA.** *Radiology* 2015;274:508–16 CrossRef Medline
  41. Mehan WA Jr, Romero JM, Hirsch JA, et al. **Unruptured intracranial aneurysms conservatively followed with serial CT angiography: could morphology and growth predict rupture?** *J Neurointerv Surg* 2014;6:761–66 CrossRef Medline
  42. Villablanca JP, Duckwiler GR, Jahan R, et al. **Natural history of asymptomatic unruptured cerebral aneurysms evaluated at CT angiography: growth and rupture incidence and correlation with epidemiologic risk factors.** *Radiology* 2013;269:258–65 CrossRef Medline
  43. Zhu C, Sadat U, Patterson AJ, et al. **3D high-resolution contrast enhanced MRI of carotid atheroma: a technical update.** *Magn Reson Imaging* 2014;32:594–97 CrossRef Medline
  44. Zhu C, Graves MJ, Yuan J, et al. **Optimization of improved motion-sensitized driven-equilibrium (iMSDE) blood suppression for carotid artery wall imaging.** *J Cardiovasc Magn Reson* 2014;16:61 CrossRef Medline
  45. Viessmann O, Li L, Benjamin P, et al. **T2-weighted intracranial vessel wall imaging at 7 Tesla using a DANTE-prepared variable flip angle turbo spin echo readout (DANTE-SPACE).** *Magn Reson Med* 2017;77:655–63 CrossRef Medline
  46. Naganawa S, Ito T, Shimada H, et al. **Cerebral black blood MR angiography with the interleaved multi-slab three-dimensional fast spin echo sequence.** *Radiat Med* 1997;15:385–88 Medline
  47. Wang X, Zhu C, Leng Y, et al. **Intracranial aneurysm wall enhancement associated with aneurysm rupture: a systematic review and meta-analysis.** *Acad Radiol* 2018 Jun 13. [Epub ahead of print] CrossRef Medline
  48. Zhu C, Tian B, Chen L, et al. **Accelerated whole brain intracranial vessel wall imaging using black blood fast spin echo with compressed sensing (CS-SPACE).** *MAGMA* 2018;31:457–67 CrossRef Medline
  49. van Rooij WJ, Sprengers ME, de Gast AN, et al. **3D rotational angiography: the new gold standard in the detection of additional intracranial aneurysms.** *AJNR Am J Neuroradiol* 2008;29:976–79 CrossRef Medline
  50. HaiFeng L, YongSheng X, YangQin X, et al. **Diagnostic value of 3D time-of-flight magnetic resonance angiography for detecting intracranial aneurysm: a meta-analysis.** *Neuroradiology* 2017;59:1083–92 CrossRef Medline

# Baseline and Evolutionary Radiologic Features in Sporadic, Hemorrhagic Brain Cavernous Malformations

K.D. Flemming, S. Kumar, G. Lanzino, and W. Brinjikji



## ABSTRACT

**BACKGROUND AND PURPOSE:** Much has been written about the initial radiologic features of cavernous malformations, but less known are the radiologic natural history and evolution of the lesions, particularly when they initially present with hemorrhage. We aimed to describe the typical evolution of a sporadic, hemorrhagic brain cavernous malformation with time.

**MATERIALS AND METHODS:** From our institutional review board–approved cavernous malformation registry, we assessed initial clinical and radiologic features and the subsequent MR imaging evolution of 51 patients with sporadic, hemorrhagic brain cavernous malformations (with follow-up brain MRIs available for review).

**RESULTS:** The initial MR imaging demonstrated mostly Zabramski type I lesions (94.2%) with T1 hyperintensity (94.2%) and associated edema (76.5%). Eight patients (15.6%) rebled in the first year with lesions characterized by new T1 hyperintensity (100%), edema (61.5%), and growth (median, 4 mm). By 90 days, most lesions had changed from Zabramski type I to type II or III (65.2%). While 76.5% had edema associated with the acute hemorrhage, none had persistent edema beyond 90 days unless rebleeding occurred. Across time, the frequency of T1 hyperintensity decreased from 94.2% at baseline to 73.9%, 57.1%, and 50.0% at <90, 91–365, and >365 days. DWI intensity at baseline and <90, 91–365, and >365 days was hypointense at 53.1%, 56.5%, 70.1%, and 81.2%, respectively.

**CONCLUSIONS:** Hemorrhagic cavernous malformation demonstrates a characteristic pattern of evolution on follow-up imaging. Knowing this evolution helps to analyze the timing of imaging in relation to the clinical presentation and may help distinguish true cavernous malformation hemorrhagic evolution from mimics and guide appropriate timing of interval-imaging follow-up after symptomatic bleeds in untreated patients.

**ABBREVIATIONS:** CM = cavernous malformation; DVA = developmental venous anomaly

Cavernous malformations (CMs) are angiographically occult vascular malformations that appear in the brain, spinal cord, and rarely nerve roots. Pathologically, they comprise endothelial-lined caverns containing defective tight junctions that predispose these lesions to hemorrhage.<sup>1</sup>

A typical CM has a reticulated appearance on T2 MR imaging, often likened to mulberries or popcorn. This appearance reflects the underlying pathology in which the caverns may be

filled with blood, thrombosis, and calcification.<sup>2–7</sup> However, after an acute hemorrhagic episode, the appearance of a CM is less distinctive and can be difficult to diagnose initially.<sup>8</sup> While many clinical natural history studies exist,<sup>9–12</sup> few reports have detailed the radiographic evolution of hemorrhagic CM lesions.

We aimed to describe the initial clinical and radiologic features of patients with sporadic, hemorrhagic CMs of the brain. We further aimed to describe the typical evolution of these lesions in patients with multiple MRIs across time.

## MATERIALS AND METHODS

### Patient Population and Study Design

Our institution has maintained an institutional review board–approved prospective cavernous malformation registry since 2014. Demographic and clinical data are collected at the initial visit and then every 1 or 2 years. Data include clinical presentation features and comorbidities. For this study, we included patients with the following: 1) an initial clinical presentation with hemor-

Received February 11, 2019; accepted after revision April 21.

From the Departments of Neurology (K.D.F., S.K.), Neurosurgery (G.L.), and Neuroradiology (W.B.), Mayo Clinic, Rochester, Minnesota.

This publication work was supported by grant No. UL1 TR002377 from the National Center for Advancing Translational Sciences.

The contents are solely the responsibility of the authors and do not necessarily represent the official views of the National Institutes of Health.

Please address correspondence to Kelly Flemming, MD, Mayo Clinic, 200 First St SW, Rochester, MN 55905; e-mail: Flemming.Kelly@mayo.edu

Indicates open access to non-subscribers at www.ajnr.org

<http://dx.doi.org/10.3174/ajnr.A6076>

rhagic CM on MR imaging associated with symptoms as defined per standard guidelines,<sup>13</sup> 2) a presumed sporadic form of CM, and 3) follow-up MR imaging from at least 1 time point following discovery of the lesion.

### MR Imaging Studies

The initial diagnostic MR imaging of the brain in each patient was reviewed in detail, and the location and size of the CM on T2 sequences were recorded. The number of CMs recorded was based on hemosiderin-sensitive sequences (gradient recalled-echo or SWI) when available. If a hemosiderin sequence was not available, the total number of CMs was counted from a standard T2 sequence. We only included patients with multiple CMs if the CMs were clustered around a developmental venous anomaly (DVA). Cavernous malformations were based on Zabramski typing.<sup>14</sup> We recorded the presence of high T1 signal, perilesional high T1 signal,<sup>15</sup> edema, and gadolinium enhancement. Increased T1 signal was considered mild, moderate, or severe if <one-third, one-third to two-thirds, or all of the lesion demonstrated increased T1 signal. Edema, measured on FLAIR sequences, was considered mild, moderate, or significant if <one-third, one-third to two-thirds, or the entire lesion was surrounded by edema on FLAIR sequences, respectively. Characteristics (hypointense, mixed, hyperintense) on DWI and ADC imaging were also collected. Follow-up MR images were reviewed in a similar manner.

### Outcomes

The primary outcome of this study was the temporal evolution of hemorrhagic cavernous malformations. Outcomes of interest were changes in the Zabramski classification, the presence of persistent edema, change in T1 hyperintensity, and the appearance on DWI/ADC. Patients had subsequent MRIs per clinical practice at varying time frames after the initial hemorrhage. We chose to group the subsequent MRIs into those performed <90 days after the hemorrhage, 91–365 days after the initial hemorrhage, and >365 days after hemorrhage. If a patient's follow-up MR imaging demonstrated rebleeding, we noted it but did not include those patients in the data regarding size change, persistent enhancement, persistent T1 hyperintensity, and edema.

### Statistical Analysis

We used descriptive statistics with means, medians, and frequencies for the initial clinical and radiologic features. All statistical analyses were performed using JMP 13.0 (SAS Institute, Cary, North Carolina).

## RESULTS

### Patient Population

We identified 54 of 196 patients in our registry with sporadic brain CMs who had presented with a symptomatic hemorrhage; 51 underwent at least 1 follow-up MR imaging of the brain. The demographics, clinical presentation, and initial MR imaging data for this cohort are presented in Table 1. The median age at presentation was 38.3 years (range, 17.7–70.5 years). Most patients (72.0%) presented with a focal neurologic deficit.

**Table 1: Demographics of patients with sporadic, brain CMs (n = 51)**

Clinical Information	
Sex	31 (60.8%) male
Age at diagnosis (yr)	Median, 38.3 (range, 17.7–70.5)
Race	45 (90.0%) Caucasian
Clinical presentation (No.) (%)	Focal neurologic deficit, 37 (72.6%) Seizure, 4 (7.8%) Headache, 8 (15.6%) Spell, not seizure, 1 (2.0%) Other, 1 (2.0%)
Initial MRI scan brain (No.)	
Symptom onset to first MRI (day)	Median, 4 (range, 0–30)
>1 CM <sup>a</sup>	3 (5.88%)
Size (mm)	Median, 12.7 (range, 4.7–34.7)
Brain stem location	31 (60.8%)
Location	Cortical, 12 (23.5%) Supratentorial, subcortical, 6 (11.8%) Posterior fossa, 32 (62.7%) Intraventricular, 1 (2.0%)
Zabramski lesion type	Type I, 48 (94.2%) Type II, 3 (5.8%)
DVA	21/42 <sup>b</sup> (50.0%)
T1 hyperintensity	48 (94.1%)
Enhancement with Gd	7/42 <sup>b</sup> (16.7%)
Edema	39 (76.5%)
DWI intensity	Low, 26/49 <sup>b</sup> (53.1%) Mixed, 21/49 <sup>b</sup> (42.9%) High, 2/49 <sup>b</sup> (4.0%)
ADC map intensity	Low, 19/42 <sup>b</sup> (45.2%) Mixed, 23/42 <sup>b</sup> (54.8%) High, 0
Perilesional high T1 signal	17/51 (33.3%)

<sup>a</sup> These patients had multiple CMs bordering a DVA; thus, they were considered sporadic lesions.

<sup>b</sup> Nine patients did not have gadolinium sequences, 3 did not have DWI, and 9 did not have ADC imaging.

### Baseline MR Imaging

The initial, diagnostic MR imaging of the brain was performed 4 days after initial symptoms (range, 0–30 days). The average size at presentation was 12.7 mm (range, 4.7–34.7 mm). The initial, diagnostic MR imaging demonstrated type I lesions with high T1 signal intensity in nearly all patients (94.2%). Thirty-nine (76.5%) had associated edema. Seventeen (33.3%) had high perilesional T1 signal. The DWI and ADC intensity was low or mixed signal in most patients at baseline.

### Follow-Up MR Imaging

While all 51 patients had at least 2 consecutive MR imaging scans, 35 (68.7%) had ≥3 MR imaging scans for review. In the first year, 8 (15.7%) patients had a rebleed. Of these, all lesions showed new areas of T1 hyperintensity and 8 (61.5%) demonstrated edema, and there was an average 4-mm increase in size (range, 0–15 mm) with the new clinical hemorrhage. The median time from the first-to-last MR imaging available for review was 341 days (range, 27–3022 days).

Twenty-eight patients had repeat MR imaging within the first 90 days following the initial brain hemorrhage (Table 2). Five had a recurrent, symptomatic hemorrhage as the indication for the follow-up MR imaging. Within the first 90 days, it was common

**Table 2: Evolution of MRI changes on follow-up imaging at specific time intervals<sup>a</sup>**

	≤90 Days	91–365 Days	>365 Days
No.	28	24	23
Time to follow-up MRI (day)	Median, 46 (range, 12–90)	Median, 159.5 (range, 92–365)	Median, 1136 (range, 382–3022)
Follow-up MRI demonstrated rebleed (No.)	5	3	6
T1 hyperintensity	17/23 (73.9%)	12/21 (57.1%)	8/16 (50%)
T1 hyperintensity (moderate to significant)	9/17 (52.9%)	6/12 (50%)	1/8 (12.5%)
Enhancement with gadolinium	6/22 (27.3%)	7/20 (35%)	9/16 (56.2%)
Degree of enhancement (moderate to significant)	2/6 (33.3%)	1/7 (14.3%)	2/9 (22.2%)
Edema	2/23 (8.7%)	0	0
Degree of edema (moderate to significant)	1/2 (50%)	—	—
DWI low intensity	13/23 (56.5%)	12/17 (70.1%)	13/16 (81.2%)
ADC low intensity	14/19 (73.7%)	12/16 (75.0%)	8/13 (61.5%)
Change to Zabramski type II or III lesion	15/23 (65.2%)	17/21 (80.9%)	16/16 (100%)
Average size change (compared with original MRI) (mm)	Median, 1.4 (range, -6.5 to +1.7)	Median, 2.05 (range, -24.7 to +1.1)	Median, -3.3 (range, -9.7 to +8.9)

**Note:**— indicates no data.

<sup>a</sup> Denominators noted are based on the availability of the particular MRI sequence.

**Table 3: Evolution of MRI changes on follow-up brain imaging <1 year versus >1 year<sup>a</sup>**

	≤365 Days	>365 Days
No.	37	23
Median time to MRI (day)	101 (range, 5–263)	1136 (range, 382–3022)
No. with recurrent hemorrhage	8	6
T1 hyperintensity	19/32 (59.4%)	8/16 (50.0%)
T1 hyperintensity (moderate to significant)	10/19 (56.2%)	1/9 (11.1%)
Enhancement with gadolinium	8/31 (25.8%)	9/16 (56.2%)
Edema	2/32 (6.2%)	0
DWI low intensity	20/29 (68.9%)	13/16 (81.2%)
ADC low intensity	19/28 (67.9%)	8/13 (61.5%)
Change to Zabramski type II or III lesions	27/32 (84.4%)	16/16 (100%)
Average size change (mm) (range)	Median, -1.4 (-24.7 to +1.1)	Median, -3.3 (-9.7 to +8.9)

<sup>a</sup> Denominators noted are based on the availability of the particular MRI sequence.

(73.9%) to have persistent T1 hyperintensity, but most lesions had changed from Zabramski type I to type II or III (65.2%). The average decrease in size was 1.4 mm (range, -1.65 to +1.7 mm). While 76.5% had edema associated with the acute hemorrhage on the initial MR imaging, only 2 patients (8.7%) had persistent edema by 90 days if they had not rebleed.

Between 91 and 365 days, 24 patients underwent MR imaging, and 3 of these had a recurrent bleed. Twenty-three patients had MRIs >365 days after the initial bleed. Six patients had a hemorrhage in this time frame. The median time to MR imaging of >365 days was 1136 days (range, 382–3022 days). With time, the frequency of increased T1 hyperintensity decreased from 94.1% at baseline to 73.9%, 57.1%, and 50.0% at <90, 91–365, and >365 days. With time, 100% of the hemorrhagic lesions that did not rebleed evolved to type II or III lesions, and no patient had persistent edema beyond 90 days.

DWI intensity at baseline and <90, 91–365, and >365 days was low at 53.1%, 56.5%, 70.1%, and 81.2%, respectively. The ADC map intensity was low in 45.2%, 73.7%, 75.0%, and 61.5% at baseline and <90, 91–365, and >365 days. Gadolinium enhancement, often mild, within the lesion was variable throughout the course with 16.7%, 27.3%, 35.0%, and 56.2% at baseline and <90, 91–365, and >365 days, respectively.

Table 3 takes data from Table 2 and divides it into patients with MRI imaging at <1 year and >1 year. If a patient had an MR imaging in both the <90- and 91- to 365-day time frame, the first

MR imaging was used in the analysis. In Figs 1 and 2, we show patient examples of the typical evolution of a CM hemorrhage with time. Figure 3 shows the evolutionary features in graphic form.

## DISCUSSION

We found that the 1-year symptomatic rebleed risk was similar to that previously reported in the literature<sup>9,10,12,16</sup> and was associated with new areas of T1 hyperintensity, edema, and growth. We found that a typical, sporadic, brain hemorrhagic CM decreases in size and evolves to a type II or III lesion if it

does not rebleed. Among lesions that did not rebleed, edema resolved within 90 days in all cases. On DWI, about half of the lesions had low signal intensity on the initial presentation, and 80% had low signal intensity at >365 days. ADC map intensity was generally low in more than half of patients. While T1 signal evolved from high-to-low intensity, almost half of patients continued to demonstrate some degree of hyperintensity. Recognizing the distinguishing features of a hemorrhagic CM at presentation and its evolution with time is useful in distinguishing these lesions from other non-CM pathologies with similar initial clinical and radiologic characteristics such as tumors and other vascular malformations. In addition, understanding the evolution of an untreated hemorrhagic CM is important in assessing the need and ideal interval for future scheduled radiologic follow-ups in the absence of new clinical events. On the basis of our experience, we recommend a follow-up MR imaging within 3 months after the original bleed. After an initial baseline study, further imaging follow-up is recommended if any new clinical event is suspicious for an interval bleed, in patients with CM growth of >5 mm, and in those patients with risk factors (eg, older age, history of systemic cancer) of a CM mimic.

Prior studies have described CM evolution but typically in patients with and without hemorrhage (mixture of types), and the number of patients was small.<sup>8,14,16–20</sup> Moreover, few series have

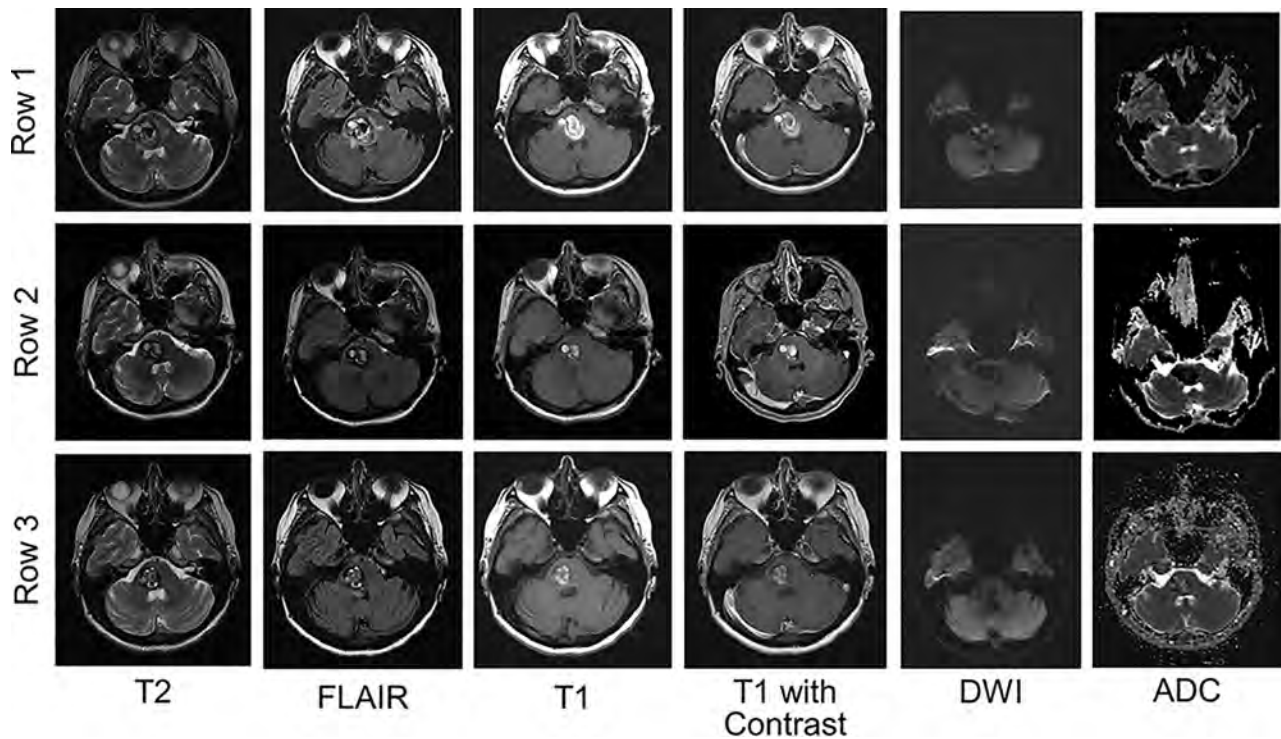


**FIG 1.** Typical evolution of a hemorrhagic CM on MR imaging with time. *Row 1*, A hemorrhagic CM in the pons at the time of acute focal symptoms. MR imaging demonstrates subacute hemorrhage with increased T1 and T2 signal, with surrounding edema on FLAIR. In this patient, there was no enhancement of the lesion. DWI and ADC maps demonstrate low signal intensity. *Rows 2 and 3*, The evolution of the lesion 1 and 8 months later, respectively. The edema is reduced by 1 month and absent at 8 months. The lesion decreases in size, but there remains an increased T1 signal. DWI remains low signal intensity throughout. The ADC map demonstrates low or mixed intensity by 8 months.

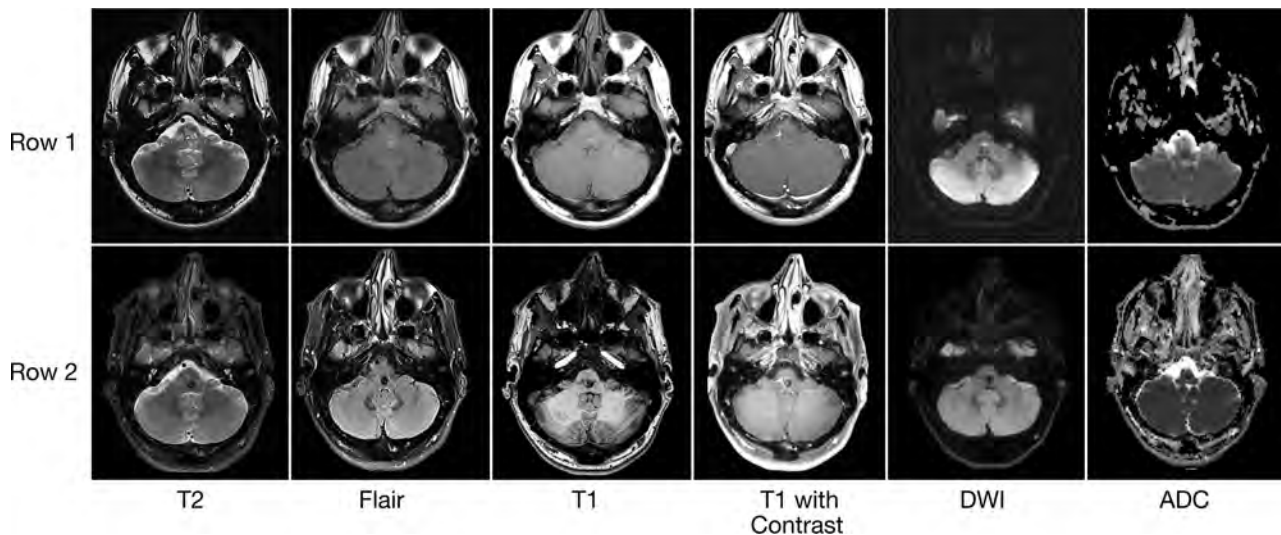


**FIG 2.** Radiologic evolution of hemorrhagic cavernous malformations. *Row 1*, An acute hemorrhage into a medullary cavernous malformation with surrounding FLAIR hyperintensity. There is a small developmental venous anomaly on contrast imaging. A follow-up MR imaging (*row 2*) was performed 3 months later. The cavernous malformation has evolved from a Zabramski type I to type III lesion. There is no persistent edema, and the ADC and DWI demonstrate hypointensity.

reported modern MR imaging sequences. Willinsky et al<sup>8</sup> followed 30 patients with initial hemorrhage due to a CM. Seven of these patients had follow-up MR imaging demonstrating a re-bleed ( $n = 1$ ), regression (decrease in size by 20%;  $n = 5$ ), and stability ( $n = 1$ ). Similarly, they found edema and mass effect to be strictly associated with Zabramski type I lesions or an acute-to-subacute hemorrhage. Other studies, while limited in the number

of symptomatic hemorrhages, have suggested a decrease in size and a predictable evolution from Zabramski type I to II and II to III.<sup>16,19,20</sup> Kazawa and Shibamoto<sup>18</sup> assessed DWI characteristics in patients with CMs (with or without bleeding) and showed that most CMs demonstrate low-intensity signal. This study did not look at the evolution of these characteristics.

Decreases in edema and enhancement of CMs with time make

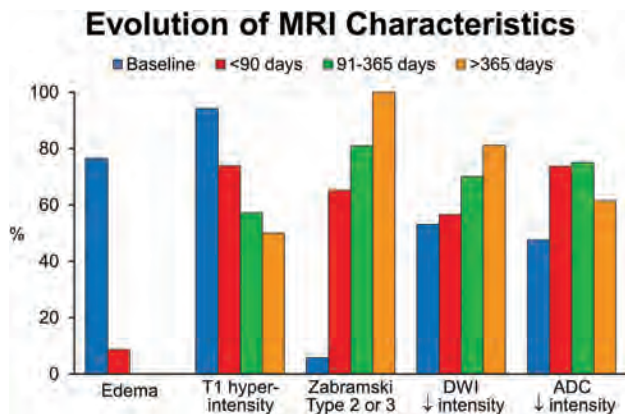


**FIG 3.** Overview of the evolutionary MR imaging changes of hemorrhagic CM with time. This graphic display shows the percentage of patients with particular MR imaging characteristics at baseline and  $\leq 90$  days, 91–365 days, and  $> 365$  days.

sense because the hemorrhagic cavity retracts and disruption in the blood-brain barrier abates. Likewise, one might expect a typical evolution of hemorrhage to isointensity on T1 with time. However, that is not the case in at least half of patients from our study. This finding may be due to the persistent slow flow or thrombosis within the caverns or ongoing asymptomatic, intralésional hemorrhage. Incomplete reabsorption of blood within the boundaries (“intracapsular” blood) of the CM is a peculiar feature of CMs, probably related to their pathogenesis and morphologic structure. Dammann et al<sup>16</sup> reported that about 19% of 199 patients followed had radiographic evidence of hemorrhage. The article did not specify whether those with or without prior hemorrhage were among the 19%.

These lesions also have an interesting evolution on DWI and ADC. In 50% of cases, lesions were hypointense on both ADC and DWI. ADC maps represent the true diffusion signal, and one would expect a lesion that is hypointense on ADC to be bright on DWI. However, this feature was not found in many cases due to a T2 blackout effect. T2 blackout effect is a phenomenon whereby lesions with actual diffusion restriction on ADC appear dark on DWI due to the presence of very low T2 signal, and it is the reverse of T2 shine through. Most interesting, the T2 blackout effect increased with time because  $> 80\%$  of lesions had low signal on DWI at  $> 365$  days, likely related to deposition of hemosiderin in the CM.

### Limitations

Our current study is limited by tertiary care referral bias, inconsistent timing of follow-up MR imaging, and small numbers. Our study was a convenience sample of already completed MR imaging scans, often at facilities outside our institution. Thus, there was no standard imaging protocol. In addition, while some patients went on to have surgery and pathologically proved etiology, others had presumptive cavernous malformations. However, this is the largest series to report specifically on the evolution of Zabramski type I CM lesions and, to our knowledge, the first to detail temporal changes in DWI and ADC MR imaging sequences in a large series.

### CONCLUSIONS

Hemorrhagic CM demonstrates a characteristic pattern of evolution on follow-up imaging studies. Knowing this evolution is helpful to analyze the timing of imaging in relation to clinical presentation, distinguish true CM hemorrhagic evolution from that of CM mimics, and guide the appropriate timing of interval imaging follow-up after a symptomatic bleed in untreated patients. On the basis of these findings, we recommend that the first follow-up MR imaging be performed within 3 months after a presenting hemorrhagic episode. If patients have further symptoms or demonstrate significant growth, further repeat MR imaging studies may be indicated thereafter.

Disclosures: Giuseppe Lanzino—UNRELATED; Board Membership: Superior Medical Editing.

### REFERENCES

- Labauge P, Brunereau L, Levy C, et al. **The natural history of familial cerebral cavernomas: a retrospective MRI study of 40 patients.** *Neuroradiology* 2000;42:327–32 CrossRef Medline
- Bien S, Friedburg H, Harders A, et al. **Intracerebral cavernous angiomas in magnetic resonance imaging.** *Acta Radiol Suppl* 1986;369:79–81 Medline
- Kim DS, Park YG, Choi JU, et al. **An analysis of the natural history of cavernous malformations.** *Surg Neurol* 1997;48:9–17; discussion 17–18 CrossRef Medline
- Lehnhardt FG, von Smekal U, Rückriem B, et al. **Value of gradient-echo magnetic resonance imaging in the diagnosis of familial cerebral cavernous malformation.** *Arch Neurol* 2005;62:653–58 CrossRef Medline
- Rapacki TF, Brantley MJ, Furlow TW Jr, et al. **Heterogeneity of cerebral cavernous hemangiomas diagnosed by MR imaging.** *J Comput Assist Tomogr* 1990;14:18–25 CrossRef Medline
- Rigamonti D, Drayer BP, Johnson PC, et al. **The MRI appearance of cavernous malformations (angiomas).** *J Neurosurg* 1987;67:518–24 CrossRef Medline
- Cortés Velaa JJ, Concepcion Aramendia L, Ballenilla Marco F, et al. **Cerebral cavernous malformations: spectrum of neuroradiological findings.** *Radiologia* 2012;54:401–09 CrossRef Medline
- Willinsky R, Harper W, Wallace MC, et al. **Follow-up MR of intracranial cavernomas: the relationship between haemorrhagic events and morphology.** *Interv Neuroradiol* 1996;2:127–35 CrossRef Medline
- Horne MA, Flemming KD, Su IC, et al; Cerebral Cavernous Malformations Individual Patient Data Meta-Analysis Collaborators. **Clinical course of untreated cerebral cavernous malformations: a meta-analysis of individual patient data.** *Lancet Neurol* 2016;15:166–73 CrossRef Medline
- Flemming KD, Link MJ, Christianson TJ, et al. **Prospective hemorrhage risk of intracerebral cavernous malformations.** *Neurology* 2012;78:632–36 CrossRef Medline
- Taslimi S, Modabbernia A, Amin-Hanjani S, et al. **Natural history of cavernous malformation: systematic review and meta-analysis of 25 studies.** *Neurology* 2016;86:1984–91 CrossRef Medline
- Al-Shahi Salman R, Hall JM, Horne MA, et al; Scottish Audit of Intracranial Vascular Malformations (SAIVMs) collaborators. **Untreated clinical course of cerebral cavernous malformations: a prospective, population-based cohort study.** *Lancet Neurol* 2012;11:217–24 CrossRef Medline
- Al-Shahi Salman R, Berg MJ, Morrison L, et al. **Hemorrhage from cavernous malformations of the brain: definition and reporting standards—Angioma Alliance Scientific Advisory Board.** *Stroke* 2008;39:3222–30 CrossRef Medline
- Zabramski JM, Wascher TM, Spetzler RF, et al. **The natural history of**

- familial cavernous malformations: results of an ongoing study.** *J Neurosurg* 1994;80:422–32 Medline
15. Yun TJ, Na DG, Kwon BJ, et al. **A T1 hyperintense perilesional signal aids in the differentiation of a cavernous angioma from other hemorrhagic masses.** *AJNR Am J Neuroradiol* 2008;29:494–500 CrossRef Medline
16. Dammann P, Jabbarli R, Wittek P, et al. **Solitary sporadic cerebral cavernous malformations: risk factors of first or recurrent symptomatic hemorrhage and associated functional impairment.** *World Neurosurg* 2016;91:73–80 CrossRef Medline
17. Yoon PH, Kim DI, Jeon P, et al. **Cerebral cavernous malformations: serial magnetic resonance imaging findings in patients with and without gamma knife surgery.** *Neurol Med Chir (Tokyo)* 1998;38(Suppl):255–61 CrossRef Medline
18. Kazawa N, Shibamoto Y. **The MRI imaging of cerebral cavernous malformation with practical use of diffusion weighted image.** *Int Journal of Radiology* 2015;2:24–28 CrossRef
19. Clatterbuck RE, Moriarity JL, Elmaci I, et al. **Dynamic nature of cavernous malformations: a prospective magnetic resonance imaging study with volumetric analysis.** *J Neurosurg* 2000;93:981–86 CrossRef Medline
20. Sigal R, Krief O, Houtteville JP, et al. **Occult cerebrovascular malformations: follow-up with MR imaging.** *Radiology* 1990;176:815–19 CrossRef Medline

# The Occipital Emissary Vein: A Possible Marker for Pseudotumor Cerebri

 A. Hedjoudje,  A. Piveteau,  C. Gonzalez-Campo,  A. Moghekar,  P. Gailloud, and  D. San Millán



## ABSTRACT

**BACKGROUND AND PURPOSE:** Transverse sinus stenosis can lead to pseudotumor cerebri syndrome by elevating the cerebral venous pressure. The occipital emissary vein is an inconstant emissary vein that connects the torcular herophili with the suboccipital veins of the external vertebral plexus. This retrospective study compares the prevalence and size of the occipital emissary vein in patients with pseudotumor cerebri syndrome with those in healthy control subjects to determine whether the occipital emissary vein could represent a marker of pseudotumor cerebri syndrome.

**MATERIALS AND METHODS:** The cranial venous system of 46 adult patients with pseudotumor cerebri syndrome (group 1) was studied on CT venography images and compared with a group of 92 consecutive adult patients without pseudotumor cerebri syndrome who underwent venous assessment with gadolinium-enhanced 3D-T1 MPRAGE sequences (group 2). The presence of an occipital emissary vein was assessed, and its proximal (intraosseous) and distal (extracranial) maximum diameters were measured and compared between the 2 groups. Seventeen patients who underwent transverse sinus stent placement had their occipital emissary vein diameters measured before and after stent placement.

**RESULTS:** Thirty of 46 (65%) patients in group 1 versus 29/92 (31.5%) patients in group 2 had an occipital emissary vein ( $P < .001$ ). The average proximal and distal occipital emissary vein maximum diameters were significantly larger in group 1 (2.3 versus 1.6 mm,  $P < .005$  and 3.3 versus 2.3 mm,  $P < .001$ ). The average maximum diameters of the occipital emissary vein for patients who underwent transverse sinus stent placement were larger before stent placement than after stent placement: 2.6 versus 1.8 mm proximally ( $P < .06$ ) and 3.7 versus 2.6 mm distally ( $P < .005$ ).

**CONCLUSIONS:** Occipital emissary veins are more frequent and larger in patients with pseudotumor cerebri syndrome than in healthy subjects, a finding consistent with their role as collateral venous pathway in transverse sinus stenosis. A prominent occipital emissary vein is an imaging sign that should raise the suspicion of pseudotumor cerebri syndrome.

**ABBREVIATIONS:** OEV = occipital emissary vein; MDCT = multidetector row CT; PTCS = pseudotumor cerebri syndrome; SCTV = subtracted CT venography

Emissary veins of the skull base and posterior fossa play an important role in directing cerebral venous blood toward cervical outflow pathways.<sup>1,2</sup> Emissary veins include the anterior, posterior, and lateral condylar emissary veins, the mastoid emissary vein, and the occipital emissary vein (OEV).<sup>1</sup> The OEV is located at or close to the midline of the occipital squama and

connects the torcular herophili or distal superior sagittal sinus to the suboccipital veins that drain into the vertebral artery venous plexus, the deep cervical vein, or both (Fig 1).<sup>3</sup> The OEV, when present, may connect with the diploic veins of the occipital and parietal bones. Due to its proximal location, the OEV is the only emissary vein of the skull base/posterior fossa that can provide a derivation pathway for the transverse sinus (Fig 2). The reported prevalence of the OEV is highly variable, ranging from 0.46% to 58.33%.<sup>3-12</sup> The OEV, however, has received little attention in the anatomic, surgical, and radiologic literature. Enlarged OEVs have been described in craniosynostosis, increased intracranial pressure, and transverse sinus or sigmoid sinus thrombosis.<sup>13-15</sup>

Pseudotumor cerebri syndrome (PTCS), also known as idiopathic or benign intracranial hypertension, is characterized by increased intracranial pressure, which may lead to complete loss

Received March 12, 2019; accepted after revision April 3.

From the Neuroradiology Unit (A.H., C.G.-C., D.S.M.), Service of Diagnostic and Interventional Imaging, Sion Hospital, Sion, Valais, Switzerland; Department of Interventional Neuroradiology (A.H., P.G.) and Cerebral Fluid Center (A.M.), Department of Neurology, The Johns Hopkins Hospital, Baltimore, Maryland; Imaging Department (A.H.), University Hospital of Rouen, Rouen, France; and Imaging Department (A.P.), University Hospital of Geneva, Geneva, Switzerland.

Please address correspondence to Abderrahmane Hedjoudje, MD, 720 Rutland Ave, Baltimore, MD 21205; e-mail: a.hedjoudje@gmail.com

 Indicates article with supplemental on-line table

<http://dx.doi.org/10.3174/ajnr.A6061>

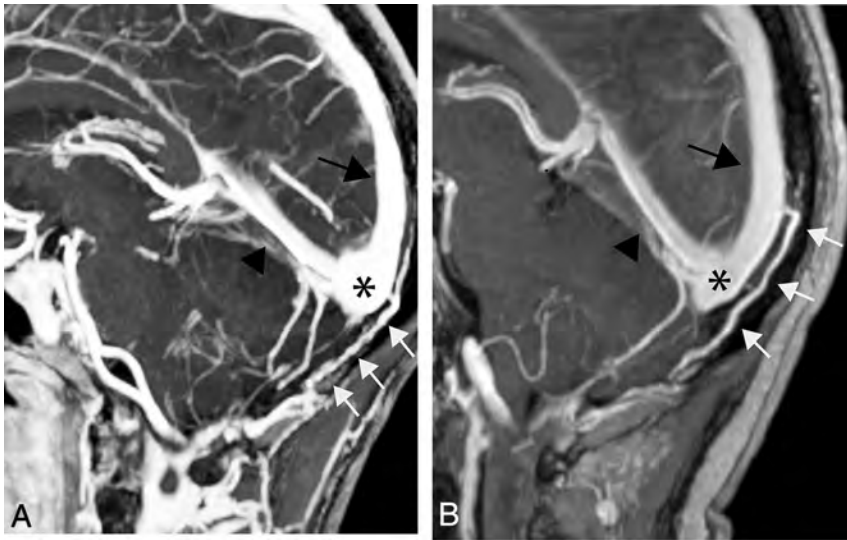


**FIG 1.** MR imaging of the craniocervical region in healthy subjects: gadolinium-enhanced 3D-T1 MPRAGE sagittal acquisitions, thick MIP reconstructions (FOV = 232 × 256 mm<sup>2</sup>, matrix = 232 × 256, slice thickness = 1 mm, slices per slab = 160–208, TR/TE = 2200/2.09–4.68 ms, bandwidth = 140–240 Hz/pixel.) Parallel acquisition was performed in the generalized autocalibrating partially parallel acquisition mode, with reference line phase encoding. *A*, Classic OEV origin from the torcular herophili (asterisk). The OEV courses intraosseously within the occipital squama (arrows) and exists the skull proximal to the foramen magnum to join the suboccipital veins. *B*, An OEV originating from the distal superior sagittal sinus. The black arrow indicates the superior sagittal sinus; the black arrowhead, the straight sinus.

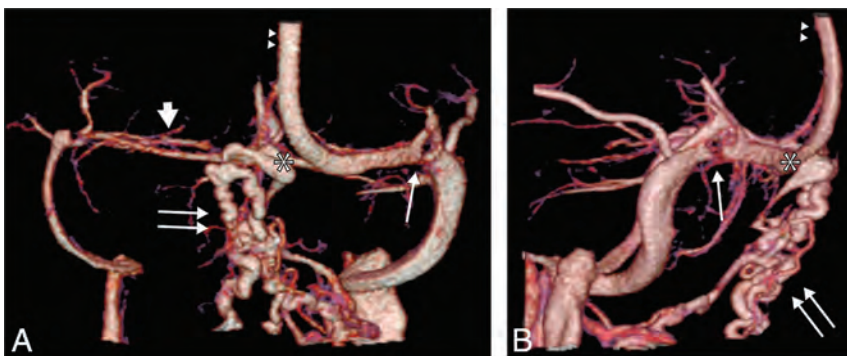


**FIG 2.** Venous phase of an SCTV obtained with a 320–detector row MDCT in a patient with pseudotumor cerebri syndrome. Posterior (*A*) and right lateral (*B*) projections. A dilated OEV (double arrows) originates from the torcular herophili (asterisk), consisting of several intraosseous and extracranial veins with various exit zones from the occipital squama. A hypoplastic transverse sinus is documented on the right side (thick arrow), and a severe transverse sinus intrinsic stenosis from an arachnoid granulation is seen on the left side (thin arrow). The double arrowheads indicate the superior sagittal sinus.

of vision and disabilities due to intractable headaches or pulsatile tinnitus.<sup>16–20</sup>

Dural sinus venous outflow obstruction may be observed in up to 93% of patients with PTCS and plays an important role in the syndrome pathophysiology.<sup>21,22</sup> Transverse sinus stenosis is the most sensitive sign of PTCS on MR imaging.<sup>23</sup> Stenosis may be primary (intrinsic), principally due to thrombosis or arachnoid granulation with or without brain herniation,<sup>24</sup> or secondary (extrinsic), mainly in relation to increased CSF pressure.<sup>25</sup> PTCS may also be observed in dural arteriovenous fistulas due to arteriovenous shunting and venous restrictive disease.<sup>26</sup> The cranial venous system should therefore be studied in detail in all patients with PTCS to rule out an intrinsic/extrinsic stenosis or an arteriovenous shunt and as a preplanning technique when considering

dural venous sinus stent placement. Dural sinus stent placement is being used increasingly to treat PTCS that is refractory to medical management as an alternative to ventricular shunting, and has also been used in patients with PTCS with severe pulsatile tinnitus or malignant PTCS with rapidly evolving vision loss.<sup>27,28</sup>

PTCS imaging findings include an enlarged “empty sella,”<sup>29</sup> optic nerve abnormalities (papilledema and tortuous optic nerves), dilated subarachnoid spaces around cranial nerves (optic nerve sheaths, the Meckel cave, an oculomotor nerve within the lateral wall of the longitudinal sternal stabilization system, Dorello canal, and so forth),<sup>29–31</sup> and venous outflow restriction. Prominent OEVs may be commonly observed during clinical routine in patients with PTCS with transverse sinus stenosis and not in healthy individuals. The OEVs in patients with PTCS and transverse sinus stenosis may be increased in size because they serve as a venous collateral. The purpose of our study was to evaluate the prevalence and size of the OEV in patients with PTCS and in healthy controls and to determine whether the OEV could represent a marker of venous PTCS.

## MATERIALS AND METHODS

This was a retrospective case-control study. Informed consent for imaging and dural venous sinus stent placement was obtained from all patients with PTCS. In addition, all patients had given consent to being included in an institutional review board–approved data base at Johns Hopkins Hospital, authorizing analysis of data obtained during routine diagnostic and interventional clinical activity.

The cranial venous system of 46 adult patients with PTCS (group 1) was studied on subtracted CT venography (SCTV) images obtained on a 320–detector row multidetector row CT (MDCT) scanner (Aquilion ONE CT scanner; Toshiba Medical Systems, Tokyo, Japan). All patients satisfied the modified Dandy criteria for PTCS, were not pregnant, and were not on medications or had medical conditions associated with intracranial hypertension. None of these patients had undergone shunt or bariatric surgery. Technical parameters were as follow: 0.5-mm detector width, 0.25-mm reconstruction interval, 512 × 512 matrix, 160-mm FOV, 0.75-second scan rotation time, 80-kV tube voltage, and 150- to 280-mA tube current. A native head CT volume scan was obtained and used as a mask for subtraction. There-

**Table 1: Characteristics of patients with PTCS and the control group**

	PTCS (n = 46)	Control (n = 92)	P Value
Age (mean) (yr)	35.6 ± 9.9	41.1 ± 12.3	.01
Female/male	40:6	62:30	.01
CSF opening pressure (mean) (range) (cm H <sub>2</sub> O)	34 ± 9 (22–65) (n = 44/46)		
Patients treated with stenting	29/46		
Prestenting pressure gradient (mean) (range) (mm Hg)	9 (6–15) (n = 29/46)		
Poststenting pressure gradient (No.) (range) (mm Hg)	1 (0–2) (n = 29/46)		

after, 50 mL of nonionic contrast material (iopamidol, Isovue 370; Bracco, Princeton, New Jersey) was injected intravenously at a flow rate of 6 mL/s followed by a saline flush. The dynamic volume CT angiography followed with 5 volume scans in the arterial phase at 15–25 seconds and 7 volume scans in the venous phase at 30–45 seconds postinjection. Poststenting follow-up imaging was acquired 6 months after the procedure.

A group of 92 adult patients who underwent MR imaging for routine medical studies (1.5T, Aera; Siemens Erlangen, Germany) with gadolinium-enhanced 3D-T1 MPRAGE sequences was used as controls (group 2). Inclusion criteria were adults between 18 and 60 years of age and the availability of gadolinium-enhanced 3D-T1 MPRAGE images. Excluded were patients with clinical and/or radiologic evidence of PTCS, intracranial venous thrombosis, dural sinus stenosis, intracranial arteriovenous shunts, posterior fossa surgery, posterior fossa tumor and evidence of increased intracranial pressure. MR imaging parameters were as follows: 232 × 256 mm FOV, 232 × 256 matrix, 1-mm slice thickness, 160–208 slices per slab, TR/TE = 2200/2.09–4.68 ms, 140- to 240-Hz/pixel bandwidth. A parallel acquisition was conducted in the generalized autocalibrating partially parallel acquisition mode with reference line phase encoding; 0.1 mmol/kg of gadolinium (gadoterate meglumine, Dotarem; Guerbet, Aulnay-sous-Bois, France; or gadobenate dimeglumine, MultiHance; Bracco Diagnostics, Princeton, New Jersey) was injected in each patient. When available, CT images (64–detector row MDCT, Optima MR450w with GEM Suite; GE Healthcare, Milwaukee, Wisconsin) in patients from group 2 were studied (bone algorithm reconstructions).

### Image Analysis

Consensual analysis of the imaging data was performed by 2 senior radiology residents (A.H., A.P.) and a senior, board-certified neuroradiologist (D.S.M.). SCTV for group 1 and gadolinium 3D-T1 MPRAGE MR imaging of group 2 were evaluated for the presence of an OEV. When an OEV was visible, maximum diameters were measured at its proximal osseous segment in the occipital squama and extracranially immediately in front of the OEV foramen. For the control group, the presence of the osseous canal corresponding to the OEV was also assessed on CT (64–detector row MDCT) when available.

For patients who underwent transverse sinus stent placement and for whom a follow-up SCTV was available, the size of the OEV was measured in the same location before and after the procedure. Follow-up SCTV was performed within 2 days poststenting.

### Statistical Analysis

The number of patients was restricted to those available in our center (monocentric study). To increase the statistical power, we recruited 2 controls for each patient. The 2:1 ratio would also compensate for the smaller frequency of visible veins in the control group to improve the statistical power of the comparison of vein sizes between groups. No pairing was performed because it would

have reduced the number of subjects and would prevent any comparison on pairing variables. With 46 patients and 92 controls, a 2-sided type I error rate set at 0.05, an expected proportion of controls with a visible vein equal to 30%, and an expected proportion of patients with a visible vein equal to 65%, the statistical power would be to 45%.

Data are presented as median and range for continuous variables and as a percentage for frequency data. Statistical analysis of frequency data was performed using a Fisher exact test. Continuous variables were compared using a Student *t* test. A *P* value ≤ .05 was considered statistically significant. Statistical analysis was performed using the Statistical Toolbox in Matlab (MathWorks, Natick, Massachusetts).

### RESULTS

Patient demographics are summarized in Table 1. Patients with PTCS and control subjects were similar in overall profile. Patients with PTCS had a slightly greater preponderance of women.

Forty-six patients were included in the PTCS group (87% were women with an average age of 36 years), and MR imaging studies from 92 consecutive patients meeting the selection criteria were included in the control group (67% were women with an average age of 41 years). No patient was further excluded from analysis after inclusion.

An OEV was observed in 30 of the 46 patients in group 1 (65.2%) and 29 of the 92 patients in group 2 (31.5%) (*P* < .0003). The prevalence of an OEV for men and women was similar in groups 1 and 2.

The average diameter of the OEV in its osseous segment (proximal) was 2.3 mm (range, 1–7 mm) in group 1 and 1.6 mm (range, 0.5–3 mm) in group 2 (*P* < .0049). Extracranially, at the exit of the OEV foramen, the average OEV diameter was 3.3 mm in group 1 (range, 1.8–10 mm) and 2.3 mm (range, 1–7 mm) in group 2 (*P* < .0001). The average proximal and distal OEV maximum diameters were therefore both significantly larger in group 1. OEV characteristics are summarized in Table 2.

In group one, 29 of the 46 patients (63%) underwent transverse sinus stent placement; 17 had a poststenting control CT venography at the time of review (Fig 3). Poststent placement reduction in the size of the OEV was observed in 9/17 cases (53%). In 2 cases, the reduction was only visible in the extracranial portion, and in 1 case, the OEV was no longer visible. The average maximum diameters of the OEV before and after stent placement were, respectively, 2.6 versus 1.8 mm proximally (intraosseous segment, *P* < .06) and 3.7 versus 2.6 mm distally (extracranial

**Table 2: Comparison of OEV characteristics of patients with PTCS and the control group**

	Group 1 (PTCS) (n = 46)	Group 2 (Control) (n = 92)	P Value
Prevalence of OEV (No.)	65.2% (30)	31.5% (29)	<.0003
Male	4/6 (66.6%)	9/30 (30.0%)	
Female	24/40 (60.0%)	20/62 (32.2%)	
Osseous segment diameter (mean) (range) (mm)	2.3 (1–7)	1.6 (0.5–3)	<.0049
Extracranial segment diameter (mean) (range) (mm)	3.3 (1.8–10)	2.3 (1–7)	<.0001

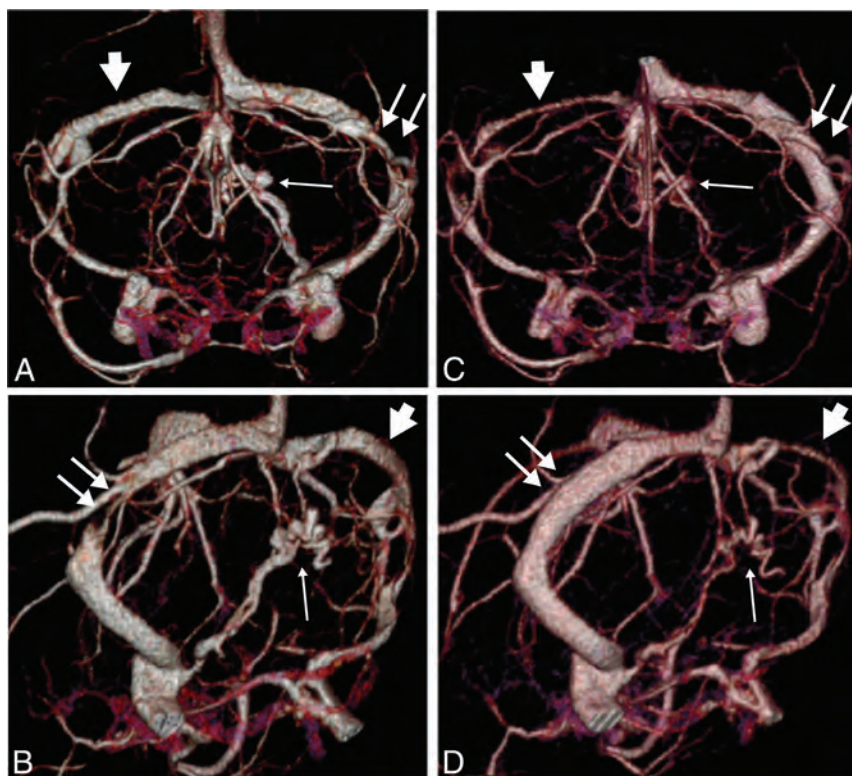


**FIG 3.** Venous phase of an SCTV with a 320–detector row MDCT in a patient with pseudotumor cerebri syndrome before (A and B) and after (C and D) left transverse sinus stent placement, anterior Towne projections (A and C), and left posterior oblique projections (B and D). There is a marked reduction of the OEV (small arrow) after stent placement in the left transverse sinus (double arrows), which has recovered its normal caliber. Note the size reduction of the right transverse sinus (arrowhead) proximal to an intrinsic stenosis after stent placement due to preferential drainage of the superior sagittal sinus into the stented transverse sinus.

**Table 3: Comparison of OEV characteristics of patients with PTCS before and after transverse sinus stenting**

	Before Stenting (n = 17)	After Stenting (n = 17)	P Value
Osseous segment diameter (mean) (range) (mm)	2.6 (1.5–4)	1.8 (1–2.1)	<.06
Extracranial segment diameter (mean) (range) (mm)	3.7 (2–7)	2.6 (1–3.25)	<.0045

portion,  $P < .0045$ ). OEV characteristics results before and after stent placement are summarized in Table 3.

The exit point of the OEV was, in both groups, always located between the external occipital protuberance and the foramen magnum. Multiple OEVs were found in 3.2% of cases in group 2, two OEVs on 2 occasions and a triple OEV once. On 1 occasion, the OEV took its origin from the distal superior sagittal sinus and not the torcular herophili (Fig 1B).

At the time of data collection for group 1, a sufficient number of SCTVs of healthy patients that could be used as a healthy con-

trol population for group 2 were not available. Thus, group 2 was based on MR imaging data using gadolinium-enhanced 3D-T1 MPRAGE. Gadolinium-enhanced 3D-T1 MPRAGE provides very good depiction of diploic veins and was thought to reliably demonstrate the prevalence of an OEV.<sup>32</sup> In group two, 75% of patients had CT data available. One hundred percent of OEVs observed on MR imaging were visible on CT. In 4 patients (4.3%), an OEV canal was visible on CT but no visible OEV was found on MR imaging, which could be due to the OEV having become atretic with time. MR imaging could therefore be less sensitive than CT for detecting OEVs in a small percentage of patients, though in these cases, the OEV may not be functional (atretic).

## DISCUSSION

Venous outflow obstruction is increasingly recognized as an etiology of PTCS, and transverse sinus stenosis is considered a sensitive sign of the condition.<sup>23</sup> The observation of very prominent OEVs in patients with PTCS led us to investigate the size and prevalence of OEVs in these patients and in healthy controls.

The OEV has received little attention in the literature. The few anatomic studies available were conducted on dry skulls. OEV foramina prevalence varied significantly among studies, ranging from as low as 0.46% up to 58% (Online Table). In our study, an OEV was present in 65% of patients with PTCS and 30% of control subjects. In terms of OEV prevalence, 1 study presented results similar to those in our PTCS group (group 1),<sup>11</sup> and another showed results similar to those in our control group (group 2).<sup>12</sup> Overall, a higher OEV prevalence was found in both groups compared with the prevalence previously reported in the anatomic literature. This

prevalence is surprising considering that even the smallest bone foramina should be detectable on dry skulls. On the other hand, occipital squama foramina may account not only for OEVs but also exit zones of regional diploic veins, potentially leading to OEV prevalence overestimation on dry skull specimens.

When we considered discrepancies in size measurements obtained on CT and MR imaging,<sup>33</sup> OEVs were significantly larger in patients with PTCS (group 1), all of whom had transverse sinus stenosis, than in control subjects without venous outflow obstruction (group 2). Surprisingly, however, the prevalence of OEV in

patients with PTCS was significantly higher than in control subjects (65.2% versus 31.5%). OEVs missed by the imaging protocol in group 2 consisting of gadolinium 3D-T1 MPRAGE and dry CT (in most cases) could explain this discrepancy, though both techniques successfully detected OEVs as small as 0.5 mm. Alternatively, venous hypertension (demonstrated by intravenous pressure measurements in all patients with PTCS) may recanalize atretic OEVs or render more conspicuous very small OEVs that would otherwise be undetectable in normal conditions.

The OEV is the only potential venous collateral pathway of the posterior fossa in cases of transverse sinus or proximal sigmoid sinus stenosis aside from the parietal emissary veins of Santorini, which were not studied here. Other posterior fossa emissary veins such as the mastoid or posterior condylar emissary veins<sup>1</sup> are located downstream from the transverse sinus stenosis generally encountered in PTCS. Although the size of OEVs significantly increases in PTCS, it did not represent a functionally efficient derivation pathway because all our patients were clinically symptomatic. The ability of the OEV to represent a successful collateral pathway is likely limited by its intraosseous portion, which probably restricts the degree of OEV dilation. Indeed, OEV diameters were, in all cases, larger extracranially than in the osseous portion. The role of the OEV as a collateral venous pathway is, however, supported by its regression in 53% of the stented patients with PTCS.

The OEV anatomy in group 2 was otherwise consistent with classic descriptions. Its origin was from the distal superior sagittal sinus on 1 occasion (1%), and multiple OEVs were observed in 3 healthy subjects (2 double OEVs, 1 triple OEV).

There are limitations to this study. First, the retrospective nature of the analysis and lack of blinding could limit the generalization of our findings. Different imaging modalities were used to compare a group of patients with PTCS (SCTV) with a control group of healthy individuals (MR imaging). The study design sizes of OEVs obtained through CT and MR imaging measurements could, therefore, be partly explained by differences in size rendering between the 2 techniques, especially given the small size of the evaluated anatomic structures (several millimeters). The sensitivity of MR imaging in detecting the OEV was also likely lower than in CT (4.3% of OEV canals on CT did not contain an OEV on MR imaging), possibly due to atretic OEVs. This likelihood could explain the higher prevalence of OEVs in the PTCS group than in the control group. Indeed, elevated venous pressure in dural sinuses proximal to the transverse sinus stenosis could lead to recanalization of an atretic OEV.

## CONCLUSIONS

The OEV diameter in patients with PTCS is larger than in healthy subjects, a finding consistent with its role as a collateral venous pathway in transverse sinus stenosis. An OEV is more frequent in patients with PTCS than in healthy subjects, even though the prevalence of OEVs in the latter group was found to be higher than previously reported in the literature. A prominent OEV on CT should prompt the radiologist to look for other signs of PTCS and suggest a CT- or MR imaging-based venous study. Prominent occipital emissary veins may be a valuable secondary sign prompting further investigation.

Disclosures: Abhay Moghekar—UNRELATED: Consultancy: Orbees Inc, Putnam Associates, Comments: Market research about hydrocephalus, market research about stroke; Expert testimony: Koskoff and Beider DeLuca & Weizenbaum Ltd, Comments: Medicolegal consultancy; Payment for development of educational presentations: NEJM-Knowledge Plus, Comments: Developed neurology online questions; Travel/accommodations/meeting expenses unrelated to activities listed: Spinal CSF Leak Foundation, Comments: Travel and accommodation reimbursed for guest lecture. Philippe Gailloud—UNRELATED: Consultancy: Cerenovus; Grants/grants pending: Siemens\*; Patents (planned, pending or issued): Artventive; Stock/stock options: Artventive. \*Money paid to institution.

## REFERENCES

- San Millán Ruíz D, Gailloud P, Rüfenacht DA, et al. **The craniocervical venous system in relation to cerebral venous drainage.** *AJNR Am J Neuroradiol* 2002;23:1500–08 Medline
- Pekçevik Y, Pekçevik R. **Why should we report posterior fossa emissary veins?** *Diagn Interv Radiol* 2014;20:78–81 CrossRef Medline
- Boyd GI. **The emissary foramina of the cranium in man and the anthropoids.** *J Anat* 1930;65:108–21 Medline
- Sharma PK, Malhotra VK, Tewari SP. **Emissary occipital foramen.** *Anat Anz* 1986;162:297–98 Medline
- Premsagar IC, Lakhtakia PK, Bisaria KK. **Occipital emissary foramen in Indian skulls.** *J Anat* 1990;173:187–88 Medline
- Gözil R, Kadioglu D, Calgüner E. **Occipital emissary foramen in skulls from central Anatolia.** *Acta Anat (Basel)* 1995;153:325–26 CrossRef Medline
- Louis RG Jr, Loukas M, Wartmann CT, et al. **Clinical anatomy of the mastoid and occipital emissary veins in a large series.** *Surg Radiol Anat* 2009;31:139–44 CrossRef Medline
- Akram Hossain SM, Lutfor Rahman MK. **Occipital emissary foramen in Bangladeshi skulls.** *Pak J Med Sci* 2001;17:156–58
- Murlimanju BV, Prabhu LV, Pai MM, et al. **Occipital emissary foramina in human skulls: an anatomical investigation with reference to surgical anatomy of emissary veins.** *Turk Neurosurg* 2011;21:36–38 Medline
- Singhal S, Ravindranath R. **Occipital emissary foramina in South Indian modern human skulls.** *ISRN Anat* 2013;2013:727489 CrossRef Medline
- Subashri A, Thenmozhi MS. **Occipital emissary foramina in human adult skull and their clinical implications.** *Research Journal of Pharmacy and Technology* 2016;9:716 CrossRef
- Kabilamurthi S. **Occipital emissary foramen? A morphometric analysis.** *Int J Sci Res* 2017;6:1853–54
- Hayward R. **Venous hypertension and craniosynostosis.** *Childs Nerv Syst* 2005;21:880–88 CrossRef Medline
- Chynn KY. **Occipital emissary vein enlargement: a sign of increased intracranial pressure.** *Radiology* 1963;81:242–47 CrossRef Medline
- Salem M, Dolati P, Fusco MR, et al. **Abnormal large central occipital emissary vein: a case report and review of literature.** *Cureus* 2016;8:e60 CrossRef Medline
- Durcan FJ, Corbett JJ, Wall M. **The incidence of pseudotumor cerebri: population studies in Iowa and Louisiana.** *Arch Neurol* 1988;45:875–77 CrossRef Medline
- Wall M, George D. **Idiopathic intracranial hypertension: a prospective study of 50 patients.** *Brain* 1991;114(Pt 1A):155–80 Medline
- Friedman DI, Jacobson DM. **Diagnostic criteria for idiopathic intracranial hypertension.** *Neurology* 2002;59:1492–95 CrossRef Medline
- Lansley JA, Tucker W, Eriksen MR, et al. **Sigmoid sinus diverticulum, dehiscence, and venous sinus stenosis: potential causes of pulsatile tinnitus in patients with idiopathic intracranial hypertension?** *AJNR Am J Neuroradiol* 2017;38:1783–88 CrossRef Medline
- Kastanioudakis I, Konitsiotis S, Asproudis I, et al. **Venous pulsatile tinnitus due to pseudotumor cerebri syndrome in a young morbid obese female.** *Hippokratia* 2013;17:383 Medline
- Kumpe DA, Bennett JL, Seinfeld J, et al. **Dural sinus stent placement for idiopathic intracranial hypertension.** *J Neurosurg* 2012;116:538–48 CrossRef Medline
- Farb RI, Vanek I, Scott JN, et al. **Idiopathic intracranial hyper-**

- tension: the prevalence and morphology of sinovenous stenosis.** *Neurology* 2003;60:1418–24 CrossRef Medline
23. Morris PP, Black DF, Port J, et al. **Transverse sinus stenosis is the most sensitive MR imaging correlate of idiopathic intracranial hypertension.** *AJNR Am J Neuroradiol* 2017;38:471–77 CrossRef Medline
  24. Malekzadehlashkariani S, Wanke I, Rüfenacht DA, et al. **Brain herniations into arachnoid granulations: about 68 cases in 38 patients and review of the literature.** *Neuroradiology* 2016;58:443–57 CrossRef Medline
  25. Morris PP, Lachman N, Black DF, et al. **Increased curvature of the tentorium cerebelli in idiopathic intracranial hypertension.** *AJNR Am J Neuroradiol* 2017;38:1789–93 CrossRef Medline
  26. Cognard C, Casasco A, Toevi M, et al. **Dural arteriovenous fistulas as a cause of intracranial hypertension due to impairment of cranial venous outflow.** *J Neurol Neurosurg Psychiatry* 1998;65:308–16 CrossRef Medline
  27. Ahmed RM, Wilkinson M, Parker GD, et al. **Transverse sinus stenting for idiopathic intracranial hypertension: a review of 52 patients and of model predictions.** *AJNR Am J Neuroradiol* 2011;32:1408–14 CrossRef Medline
  28. Elder BD, Goodwin CR, Kosztowski TA, et al. **Venous sinus stenting is a valuable treatment for fulminant idiopathic intracranial hypertension.** *J Clin Neurosci* 2015;22:685–89 CrossRef Medline
  29. Bialer OY, Rueda MP, Bruce BB, et al. **Meningoceles in idiopathic intracranial hypertension.** *AJR Am J Roentgenol* 2014;202:608–13 CrossRef Medline
  30. San Millán D, Kohler R. **Enlarged CSF spaces in pseudotumor cerebri.** *AJR Am J Roentgenol* 2014;203:W457–58 CrossRef Medline
  31. Degnan AJ, Levy LM. **Pseudotumor cerebri: brief review of clinical syndrome and imaging findings.** *AJNR Am J Neuroradiol* 2011;32:1986–93 CrossRef Medline
  32. Jivraj K, Bhargava R, Aronyk K, et al. **Diploic venous anatomy studied in-vivo by MRI.** *Clin Anat* 2009;22:296–301 CrossRef Medline
  33. Khandelwal N, Agarwal A, Kochhar R, et al. **Comparison of CT venography with MR venography in cerebral sinovenous thrombosis.** *AJR Am J Roentgenol* 2006;187:1637–43 CrossRef Medline

# Association between Tumor Acidity and Hypervascularity in Human Gliomas Using pH-Weighted Amine Chemical Exchange Saturation Transfer Echo-Planar Imaging and Dynamic Susceptibility Contrast Perfusion MRI at 3T

Y.-L. Wang, J. Yao, A. Chakhoyan, C. Raymond, N. Salamon, L.M. Liao, P.L. Nghiemphu, A. Lai, W.B. Pope, N. Nguyen, M. Ji, T.F. Cloughesy, and B.M. Ellingson



## ABSTRACT

**BACKGROUND AND PURPOSE:** Acidification of the tumor microenvironment from abnormal metabolism along with angiogenesis to meet metabolic demands are both hallmarks of malignant brain tumors; however, the interdependency of tumor acidity and vascularity has not been explored. Therefore, our aim was to investigate the association between pH-sensitive amine chemical exchange saturation transfer echoplanar imaging (CEST-EPI) and relative cerebral blood volume (CBV) measurements obtained from dynamic susceptibility contrast (DSC) perfusion MRI in patients with gliomas.

**MATERIALS AND METHODS:** In this retrospective study, 90 patients with histologically confirmed gliomas were scanned between 2015 and 2018 (median age, 50.3 years; male/female ratio = 59:31). pH-weighting was obtained using chemical exchange saturation transfer echo-planar imaging estimation of the magnetization transfer ratio asymmetry at 3 ppm, and CBV was estimated using DSC-MR imaging. The voxelwise correlation and patient-wise median value correlation between the magnetization transfer ratio asymmetry at 3 ppm and CBV within T2-hyperintense lesions and contrast-enhancing lesions were evaluated using the Pearson correlation analysis.

**RESULTS:** General colocalization of elevated perfusion and high acidity was observed in tumors, with local intratumor heterogeneity. For patient-wise analysis, median CBV and magnetization transfer ratio asymmetry at 3 ppm within T2-hyperintense lesions were significantly correlated ( $R = 0.3180, P = .002$ ), but not in areas of contrast enhancement ( $P = .52$ ). The positive correlation in T2-hyperintense lesions remained within high-grade gliomas ( $R = 0.4128, P = .001$ ) and in *isocitrate dehydrogenase* wild-type gliomas ( $R = 0.4300, P = .002$ ), but not in World Health Organization II or in *isocitrate dehydrogenase* mutant tumors. Both magnetization transfer ratio asymmetry at 3 ppm and the voxelwise correlation between magnetization transfer ratio asymmetry and CBV were higher in high-grade gliomas compared with low-grade gliomas in T2-hyperintense tumors (magnetization transfer ratio asymmetry,  $P = .02$ ; Pearson correlation,  $P = .01$ ). The same trend held when comparing *isocitrate dehydrogenase* wild-type gliomas and *isocitrate dehydrogenase* mutant gliomas (magnetization transfer ratio asymmetry,  $P = .04$ ; Pearson correlation,  $P = .01$ ).

**CONCLUSIONS:** A positive linear correlation between CBV and acidity in areas of T2-hyperintense, nonenhancing tumor, but not enhancing tumor, was observed across patients. Local heterogeneity was observed within individual tumors.

**ABBREVIATIONS:** CEST-EPI = chemical exchange saturation transfer echo-planar imaging; *IDH* = *isocitrate dehydrogenase*; *IDH*<sup>MUT</sup> = *IDH* mutant; *IDH*<sup>WT</sup> = *IDH* wild-type; LGG = low-grade glioma; HGG = high-grade glioma; *MTR*<sub>asym</sub> = magnetization transfer ratio asymmetry; SAGE = spin and gradient-echo; WHO = World Health Organization; *MGMT* = *O*-6-methylguanine-DNA methyltransferase

Primary central nervous system tumors occur in approximately 21 per 100,000 population, with gliomas representing 27% of all

primary brain tumors and 81% of malignant brain tumors.<sup>1</sup> Five-year survival rates for patients diagnosed with gliomas range from

Received October 22, 2018; accepted after revision April 10, 2019.

From the UCLA Brain Tumor Imaging Laboratory (Y.-L.W., J.Y., A.C., C.R., B.M.E.), Center for Computer Vision and Imaging Biomarkers, Department of Radiological Sciences (J.Y., A.C., C.R., N.S., W.B.P., B.M.E.), Physics and Biology in Medicine (B.M.E.), Department of Neurology (P.L.N., A.L., N.N., M.J., T.F.C.), Department of Psychiatry and Biobehavioral Sciences (B.M.E.), UCLA Brain Research Institute (L.M.L., A.L., B.M.E.), and Department of Neurosurgery (L.M.L.), David Geffen School of Medicine, University of California, Los Angeles, Los Angeles, California; Department of Radiology (Y.-L.W.), People's Liberation Army General Hospital, Beijing, China; and Department of Bioengineering (J.Y., B.M.E.), Henry Samueli School of Engineering and Applied Science, University of California, Los Angeles, Los Angeles, California.

Y.L. Wang and J. Yao contributed equally to this work.

This work was supported by the American Cancer Society Research Scholar Grant (RSG-15-003-01-CCE) (B.M. Ellingson); Art of the Brain (T.F. Cloughesy); UCLA Specialized Program of Research Excellence in Brain Cancer (National Institutes of Health/National Cancer Institute IP50CA211015-01A1) (B.M. Ellingson, L.M. Liao, P.L. Nghiemphu, A. Lai, W.B. Pope, T.F. Cloughesy); and National Institutes of Health/National Cancer Institute, 1R21CA223757-01 (B.M. Ellingson).

Please address correspondence to Benjamin M. Ellingson, PhD, Departments of Radiological Sciences and Psychiatry, David Geffen School of Medicine, University of California, Los Angeles, 924 Westwood Blvd., Suite 615, Los Angeles, CA 90024; e-mail: bellingson@mednet.ucla.edu

Indicates open access to non-subscribers at [www.ajnr.org](http://www.ajnr.org)

Indicates article with supplemental on-line photos.

<http://dx.doi.org/10.3174/ajnr.A6063>

## Patient demographics

	All Patients	WHO II	WHO III	WHO IV
No. of patients				
Total	90	24	26	40
Presurgery	43 (47.8%)	15 (62.5%)	15 (57.7%)	13 (32.5%)
Postsurgery, pretreatment	15 (16.7%)	5 (20.8%)	3 (12.0%)	7 (17.5%)
On treatment (radiation, chemotherapy, and so forth)	32 (35.6%)	4 (16.7%)	8 (32.0%) (2 on bevacizumab)	20 (50.0%) (2 on bevacizumab)
Age (yr)				
Mean	50.3	44	46.3	56.8
Range	15 (pediatric)–90	22–90	15 (pediatric)–70	19–81
Sex				
Male	59 (65.6%)	10 (41.7%)	17 (65.4%)	32 (80.0%)
Female	31 (35.4%)	14 (58.3%)	9 (34.6%)	8 (20.0%)
IDH status				
Wild-type	51 (56.7%)	2 (8.3%)	11 (42.3%)	38 (95.0%)
Mutant	39 (43.3%)	22 (91.7%)	15 (57.7%)	2 (5.0%)
MGMT-promoter methylation status				
Unmethylated	27 (30.0%)	1 (4.2%)	6 (23.1%)	20 (50.0%)
Methylated	17 (18.9%)	4 (16.7%)	1 (3.8%)	12 (30.0%)
NA	46 (51.1%)	19 (79.2%)	19 (73.1%)	8 (20.0%)
Histology				
Astrocytoma	25 (27.8%)	10 (41.7%)	15 (57.7%)	NA
Oligoastrocytoma	11 (12.2%)	2 (8.3%)	9 (34.6%)	NA
Oligodendroglioma	14 (15.6%)	12 (50.0%)	2 (7.7%)	NA

**Note:**—NA indicates not applicable.

<sup>a</sup>Data are number and percentage unless otherwise indicated.

5.5% for glioblastoma to >80% in World Health Organization (WHO) grade II oligodendrogliomas,<sup>1</sup> illustrating the wide disparity in survival depending on the level of malignancy and the need for noninvasive techniques for early delineation of malignant transformation.

Metabolic reprogramming is a critical characteristic of cancer. Tumor cells often inefficiently shunt glucose, glutamine, and other substrates down the glycolytic pathway, regardless of the presence of oxygen.<sup>2</sup> This feature results in acidification of the tumor microenvironment through lactic acid accumulation and inefficient elimination of metabolic by-products<sup>3</sup> at a rate proportional to the degree of aggressiveness<sup>4,5</sup> and invasion.<sup>6,7</sup> In addition to increased metabolic activity, tumor angiogenesis is critical for malignant transformation,<sup>8–10</sup> either through neovascularization or cooption of existing vasculature.<sup>11,12</sup> As tumors grow larger and growth rates are accelerated by this increased vascularity, regions of the tumor can become hypoxic as metabolic demands outpace nutrient delivery.<sup>13</sup> This decreased oxygen tension increases the acidity of interstitial space through carboxylic acid buildup and further increases the rate of lactic acid accumulation from glycolysis. Thus, we hypothesized that gliomas with a high degree of perfusion may also have a high level of acidity.

In the current study, we used a fast pH-weighted molecular MR imaging technique using amine chemical exchange saturation transfer echo-planar imaging (CEST-EPI)<sup>14</sup> and compared it with DSC-perfusion MR imaging to examine the association between tumor acidity and vascularity in patients with histologically confirmed gliomas with various levels of malignancy.

## MATERIALS AND METHODS

### Patients

A total of 90 histologically confirmed gliomas (WHO II,  $n = 24$ ; WHO III,  $n = 26$ ; WHO IV,  $n = 40$ ) were included in this retro-

spective study at either initial diagnosis ( $n = 43$ ), following an operation ( $n = 15$ ), or during active treatment with radiation and/or chemotherapy ( $n = 32$ ). All scans were obtained between April 2015 and August 2018. All patients provided informed, written consent to participate in advanced imaging and our research data base according to the guidelines approved by the institutional review board (University of California, Los Angeles), in compliance with the Health Insurance Portability and Accountability Act. All diagnoses were determined histopathologically after surgical resection or biopsy, according to the 2016 WHO classification of CNS tumors,<sup>15</sup> by neuropathologists who were blinded to the MR imaging data. *Isocitrate dehydrogenase 1 (IDH1 R132H)* mutation status was available for all 90 patients (51 *IDH* mutant [*IDH*<sup>MUT</sup>] and 39 *IDH* wild-type [*IDH*<sup>WT</sup>] tumors), determined by genomic sequencing analysis using the polymerase chain reaction *IDH1* mutation-detection kit and immunohistochemistry according to manufacturer's instructions. Briefly, tumor DNA was isolated from the frozen or formalin-fixed tissue using DNeasy Blood and Tissue Kit (Qiagen). A 236-bp fragment that included codon 132 was amplified using the primers 5'-GCGTCAAATGTGCCACTATC-3' and 5'-GCAAAATCACAT-TATTGCCAAC-3' to generate a 236 bp fragment. PCR products were sequenced by BigDye Terminator v1.1 (Applied Biosystems), and sequences were determined via a 3730 sequencer (Applied Biosystems). The *O*-6-methylguanine-DNA methyltransferase (*MGMT*) promoter methylation status, determined from formalin-fixed paraffin-embedded tissue samples, was available in 44 of 90 cases. Additional patient information is in the Table.

### Anatomic MR Imaging

In addition to CEST-EPI before contrast administration and DSC-perfusion MR imaging, all patients underwent anatomic imaging according to the international standardized brain

tumor imaging protocol,<sup>16</sup> including T2-weighted FLAIR images, T2-weighted turbo spin-echo images, and diffusion-weighted images with 3-mm slice thickness and no interslice gap, and parameter-matched, 1-mm isotropic 3D-T1-weighted MPRAGE scans before and following injection of 0.01 mg/kg of Gd-DTPA, and DSC-MR imaging. All anatomic images were registered to postcontrast T1-weighted images for subsequent analyses.

### **pH-Weighted Amine CEST-EPI**

Amine CEST-EPI was obtained with either a single-echo CEST-EPI sequence<sup>14</sup> or a multiecho CEST spin and gradient-echo (SAGE) EPI sequence<sup>17</sup> using the 2 gradient echoes. MR imaging acquisition parameters included the following: FOV = 240–256 × 217–256 mm, matrix size = 128 × 116–128, slice thickness = 4 mm with no interslice gap, 25 consecutive slices, excitation pulse flip angle = 90°, TE = 27 ms for single-echo CEST-EPI and 14.0 and 34.1 ms for the 2 gradient-echoes using CEST-SAGE-EPI, bandwidth = 1628 Hz, and generalized autocalibrating partially parallel acquisition factor = 2–3. Off-resonance saturation was applied using a pulse train of 3 × 100 ms Gaussian pulses with a peak amplitude of 6 microtesla. A total of 29 off-resonance or z-spectral points were sampled at frequency offsets of –3.5 to –2.5 ppm, –0.3 to +0.3 ppm, and +2.5 to +3.5 ppm, all in increments of 0.1 ppm. A reference scan ( $S_0$ ) was obtained with the same acquisition parameters, without the saturation pulses. Total scan time for CEST-EPI was approximately 7 minutes 30 seconds, benchmarked on a 3T Magnetom Prisma MR imaging scanner (Versions VE11A–C; Siemens, Erlangen, Germany).

Clinical postprocessing of CEST-EPI consisted of affine motion correction (MCFLIRT; FSL, <https://fsl.fmrib.ox.ac.uk/fsl/fslwiki/MCFLIRT>) and  $B_0$  correction via a z-spectra-based K-means clustering and Lorentzian fitting algorithm.<sup>18</sup> An integral of the width of 0.4 ppm was then obtained around both the –3.0 and +3.0 ppm (–3.2 to –2.8 and +2.8 to +3.2 ppm, respectively) spectral points of the inhomogeneity-corrected data. These data points were combined with the  $S_0$  image to calculate the asymmetry in the magnetization transfer ratio ( $MTR_{asym}$ ) at 3.0 ppm as defined by equation  $MTR_{asym}(\omega) = \frac{S(-\omega) - S(\omega)}{S_0}$ , where  $\omega$  is the offset frequency of interest (3.0 ppm). For data from the CEST-SAGE-EPI acquisition, the average  $MTR_{asym}$  at 3.0 ppm calculated from the first (TE = 14.0 ms) and second (TE = 34.1 ms) gradient-echoes was averaged to increase the SNR of the resulting  $MTR_{asym}$  images. All resulting maps were registered to high-resolution postcontrast T1-weighted images for subsequent analyses.

### **DSC-Perfusion MR Imaging**

For DSC-MR imaging, a total dose of 0.1 mmol/kg of Gd-DTPA (Magnevist; Bayer HealthCare Pharmaceuticals, Wayne, New Jersey) was administered, 0.025 mmol/kg for the preload dosage to mitigate T1-based leakage contamination and the remaining 0.075 mmol/kg for dynamic bolus administration. A 2-minute gap was placed between the preload dose and the start of baseline DSC-MR imaging. DSC-MR imaging was acquired with a TE/TR = 21–23/1250–1293 ms, flip angle = 60°, matrix size = 128 ×

128, slice thickness = 5 mm with no interslice gap, number of baseline acquisitions before contrast agent injection = 10–25, and number of timepoints = 120. The total scan time for DSC-MR imaging was approximately 1.5 minutes.

All DSC-MR imaging acquisitions completely covered the spatial extent of contrast-enhancing and nonenhancing tumors. Calculation of CBV was performed by first motion-correcting the dynamic time-series using FSL (MCFLIRT). Next, CBV maps were calculated using a bidirectional contrast agent leakage-correction algorithm to model contrast flux into and out of the vasculature. Last, normalized CBV was computed by dividing the CBV map by the average CBV value within a 5-mm sphere in contralateral, normal-appearing white matter. Last, final CBV maps were aligned to the corresponding postcontrast T1-weighted images for subsequent analyses.

### **Data Analysis and Statistics**

In patients with high-grade gliomas, contrast-enhancing tumor ROIs, defined on contrast-enhancing T1-weighted subtraction maps, were segmented using a semiautomatic procedure as previously described,<sup>19</sup> and the Analysis of Functional Neuro Images (AFNI; <http://afni.nimh.nih.gov/>) software. Additional, semiautomatically defined ROIs including T2-hyperintense lesions consistent with peritumoral edema and/or nonenhancing tumor, including contrast enhancement but not central necrosis, along with areas of obvious central necrosis, were also delineated and examined in all patients. Briefly, the semiautomatic segmentation procedure consists of the following: 1) manually defining the general region of lesion occurrence, 2) thresholding T2/FLAIR images or T1-weighted subtraction map images using an empiric threshold to best define the extent of abnormality, and then 3) manually editing the resulting masks to exclude any nontumor tissue. Two raters performed the segmentation independently and cross-checked each other's segmentation. A neuroradiologist with 13 years of clinical experience performed the final evaluation and minor corrections of ROIs.

In all ROIs, the median estimates of CBV and  $MTR_{asym}$  at 3 ppm were calculated and used for subsequent analyses. For voxelwise correlation, the  $MTR_{asym}$  at 3 ppm and CBV values of all voxels in different ROIs were analyzed using the Pearson correlation. For ROI-wise analysis, the linear correlation between the median  $MTR_{asym}$  at 3 ppm and CBV values across all patients within different ROIs was analyzed using the Pearson correlation coefficient. We conducted the analysis in all patients and in subgroups of patients, including different treatment cohorts and across grades. Additionally, a nonparametric Kruskal-Wallis test and a Dunn test for multiple comparisons were used to compare pH- and perfusion-weighted MR imaging measurements and correlation coefficients across tumor grades. Normality was assessed using a Shapiro-Wilk test. A nonparametric Mann-Whitney  $U$  test was used to compare measurements within tumors on the basis of *MGMT* promoter methylation status and *IDH* mutation status. All statistical tests were performed using GraphPad Prism software, v6.0H (GraphPad Software, San Diego, California). Significance was set at  $P < .05$ .

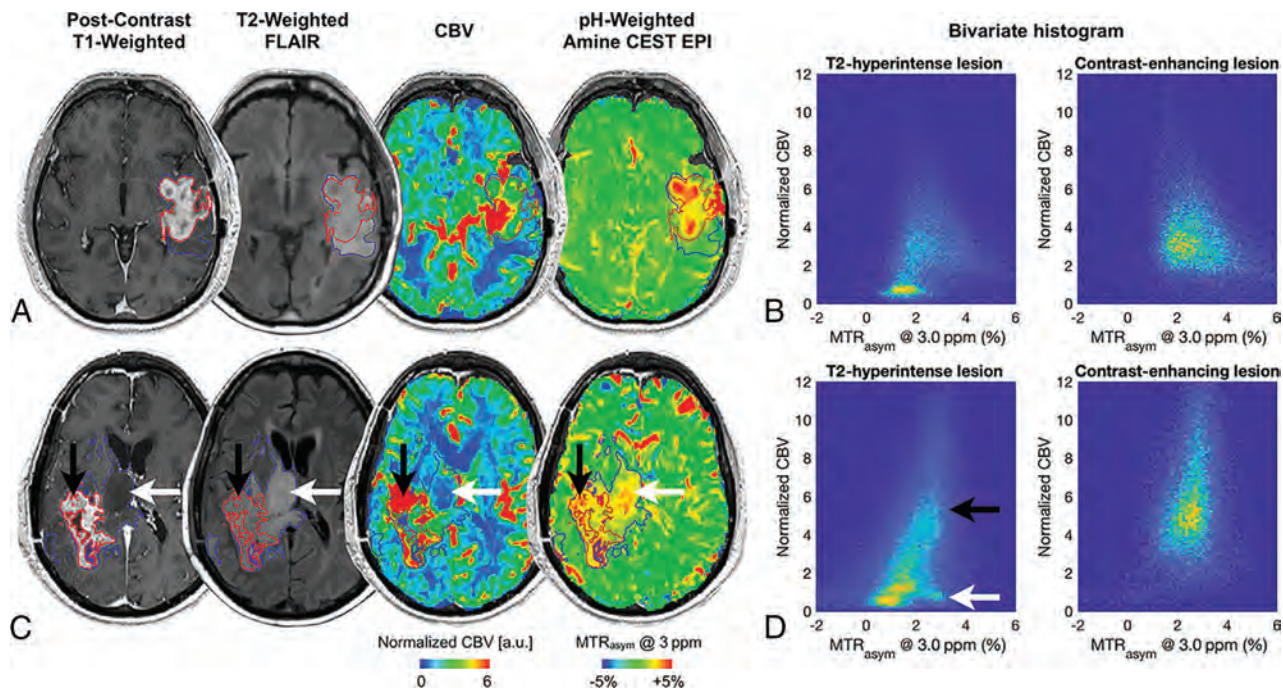


**FIG 1.** Postcontrast T1-weighted images, T2-weighted FLAIR images, CBV, and pH-weighted MR images of a 68-year-old male patient (A) with a recurrent *IDH*<sup>WT</sup>, *MGMT*-unmethylated anaplastic (WHO III) oligodendroglioma and a 68-year-old male patient (C) with a recurrent *IDH*<sup>WT</sup>, *MGMT*-unmethylated glioblastoma. Note the high vascularity and acidity within the areas of contrast enhancement and high acidity extending into the areas of T2 hyperintensity. B and D, The bivariate histogram of pH-weighted  $MTR_{asym}$  and CBV of all voxels within the T2-hyperintense lesion and contrast-enhancing lesion of the corresponding patient. The lesion ROIs are outlined in red (contrast-enhancing lesion) and blue (T2-hyperintense lesion) in the MR images. In the patient in C, the white arrow indicates a nonenhancing part of the lesion, which demonstrates low CBV with elevated acidity, while the black arrow indicates an enhancing lesion with both high CBV and high  $MTR_{asym}$  contrast.

## RESULTS

### Correlation between CBV and $MTR_{asym}$ at 3 ppm

A total of 50 of 90 patients had contrast-enhancing lesions in the current study that could be evaluated. Although regions of elevated vascularity appear generally colocalized to areas of increased acidity, local intratumor heterogeneity is frequently observed (Fig 1). The observation is consistent with the finding that both CBV and  $MTR_{asym}$  at 3 ppm are more elevated in contrast-enhancing regions ( $MTR_{asym}$  median = 2.276%, CBV median = 1.910) compared with T2-hyperintense regions ( $MTR_{asym}$  median = 1.667%, CBV median = 1.095; Mann-Whitney *U* test,  $P < .0001$  for  $MTR_{asym}$ ,  $P < .0001$  for CBV). When we examined the correlation between median CBV and  $MTR_{asym}$  at 3 ppm across the entire patient cohort, no statistically significant linear association was observed in areas of contrast enhancement (Pearson correlation  $R = 0.0925$ ,  $P = .5231$ ). In areas of T2 hyperintensity, however, a statistically significant positive association was observed between median CBV and  $MTR_{asym}$  at 3 ppm (Fig 2A;  $R = 0.3180$ ,  $P = .0023$ ), suggesting that patients with nonenhancing tumor demonstrating a high blood volume (possibly due to responsive vessel dilation, vessel cooption, or angiogenesis) may also have higher acidity. These same trends were observed when considering all patients not on active therapy (ie, pre- or postsurgery and before radiation and/or chemotherapy), with no correlation found between CBV and  $MTR_{asym}$  at 3 ppm in contrast-enhancing tumor ( $R = 0.2097$ ,  $P = .3369$ ), but a significant correlation was seen within T2-hyperintense regions (On-line Fig 1A;  $R = 0.2875$ ,  $P = .0287$ ). For patients on active therapy, this

significant correlation no longer existed (On-line Fig 1B;  $R = 0.2638$ ,  $P = .1446$ ), indicating a change of perfusion/metabolism pattern in these patients.

Consistent with the patient-wise observation that T2-hyperintense lesions exhibit a more significant median CBV–median  $MTR_{asym}$  correlation than contrast-enhancing lesions, the voxel-wise analysis in different ROIs across all patients showed that the *P* value of the Pearson correlation was lower in T2-hyperintense lesions (median =  $5.55 \times 10^{-122}$ ) compared with contrast-enhancing lesions (median =  $3.68 \times 10^{-26}$ ,  $P = .0003$ ). However, the correlation coefficient *R* was not significantly different in the 2 ROIs (Mann-Whitney,  $P = .3344$ ), indicating the heterogeneity within individual tumors.

### CBV and $MTR_{asym}$ at 3 ppm across Tumor Grades

In the particular cohort of patients that we examined, which included both treated and treatment-naïve tumors, no significant association was observed between CBV and tumor grade within contrast-enhancing tumor (On-line Fig 1C; Kruskal-Wallis,  $P = .7408$ ) or T2-hyperintense lesions (On-line Fig 1D; Kruskal-Wallis,  $P = .0815$ ). The  $MTR_{asym}$  at 3 ppm within contrast-enhancing tumor did not vary significantly among tumor grades (On-line Fig 2A; Kruskal-Wallis,  $P = .0895$ ); however, it did show a higher  $MTR_{asym}$  at 3 ppm in high-grade gliomas (HGGs, WHO III and IV) compared with low-grade gliomas (LGGs, WHO II) (On-line Fig 2C; Mann-Whitney,  $P = .0365$ ; HGG = 2.351%, LGG = 1.665%). Likewise, the  $MTR_{asym}$  at 3 ppm within areas of T2 hyperintensity was not significantly different among tu-

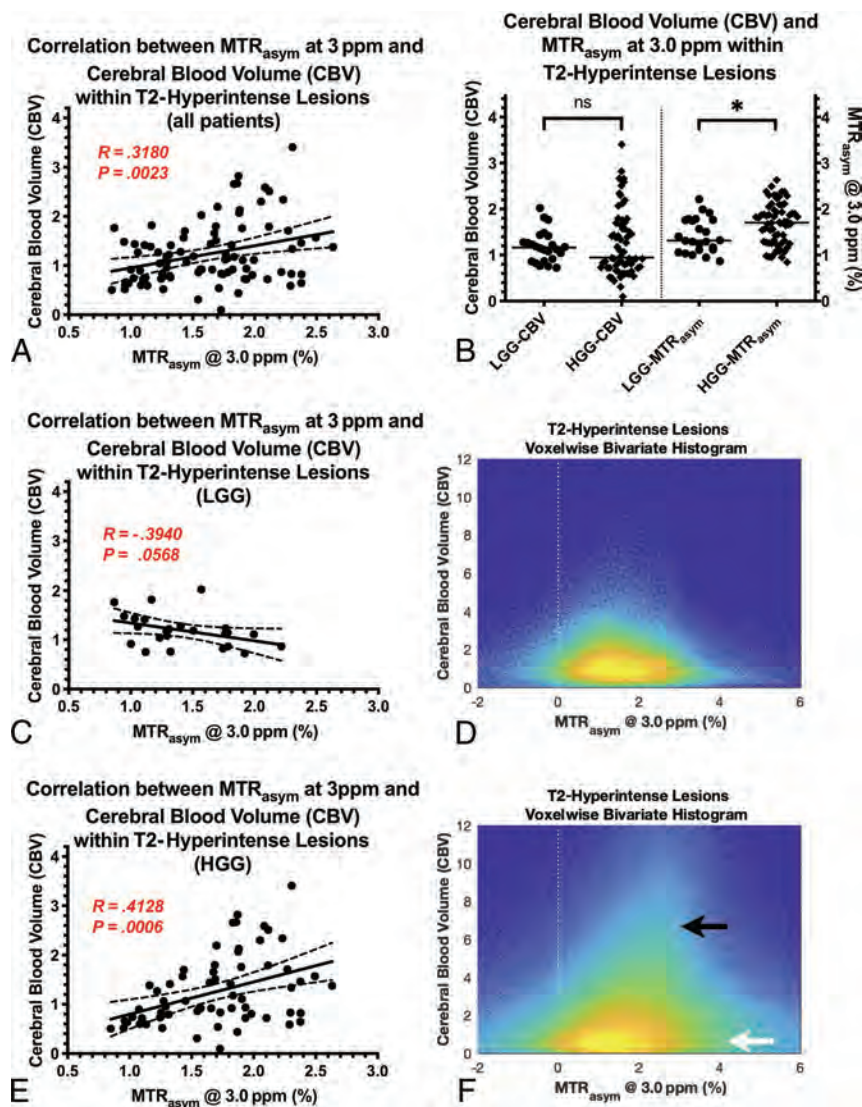


**FIG 2.** A, Association between CBV and tumor acidity within T2-hyperintense lesion areas in all patients, both treatment-naïve and those on active treatment. B, Cerebral blood volume and  $MTR_{asym}$  at 3 ppm, a measure of tumor acidity, within T2-hyperintense lesions compared between low-grade and high-grade gliomas. The median value of CBV is 1.163 in LGGs and 0.9470 in HGGs. The median value of  $MTR_{asym}$  at 3 ppm is 1.316% in LGGs and 1.706% in HGGs ( $P = .0176$ ). C and E, The correlation between CBV and tumor acidity in LGGs and HGGs, respectively. D and F, The bivariate histograms of pH-weighted  $MTR_{asym}$  and CBV of all voxels within T2-hyperintense lesions across patients in LGGs and HGGs, respectively. Note that in HGGs, in all voxel analyses (F), there is a high correlation component (black arrow) and a low correlation component (white arrow). The bivariate histograms were plotted with the logarithmic scale for better visualization.

mor grades (On-line Fig 2B; Kruskal-Wallis,  $P = .0532$ ), but it did demonstrate increasing acidity within HGGs (Fig 2B; Mann-Whitney,  $P = .0176$ ; HGG = 1.706%, LGG = 1.316%).

We also analyzed the patient-wise correlation of CBV and  $MTR_{asym}$  in T2-hyperintense lesions in different WHO tumor grades. The correlation was significant within HGGs (Fig 2E;  $R = 0.4128$ ,  $P = .0006$ ), but not within WHO grade II tumors (Fig 2C;  $R = -0.3940$ ,  $P = .0568$ ). However, the correlation changed from a negative correlation in grade II to a positive correlation in high grades. The bivariate histograms of all voxels across all patients in the corresponding cohort were plotted in Fig 2D, -F.

As for the difference in the Pearson correlation of voxelwise CBV and  $MTR_{asym}$  across tumor grade, we observed significantly

different  $R$  values across the grades in T2-hyperintense lesions (On-line Fig 2E; Kruskal-Wallis,  $P = .0329$ ) but not in contrast-enhancing lesions (On-line Fig 2D; Kruskal-Wallis,  $P = .3338$ ). The Pearson correlation coefficient  $R$  was significantly higher in HGGs than in LGGs in T2-hyperintense lesions (On-line Fig 2F; Mann-Whitney,  $P = .0088$ ; HGG = 0.0842, LGG =  $-0.0288$ ), but not in contrast-enhancing lesions (On-line Fig 2E; Mann-Whitney  $U$  test,  $P = .4817$ ).

### CBV and $MTR_{asym}$ at 3 ppm in MGMT-Methylated and IDH Mutant Gliomas

In 44 patients with *MGMT* promoter methylation status available, no difference in CBV was observed in contrast-enhancing tumor (On-line Fig 3A; Mann-Whitney,  $P = .8085$ ) or T2-hyperintense disease (On-line Fig 3B; Mann-Whitney,  $P = .5038$ ). Similarly, no difference in the  $MTR_{asym}$  at 3 ppm was observed in contrast-enhancing tumor (On-line Fig 3A; Mann-Whitney,  $P = .3234$ ) or T2-hyperintense lesions (On-line Fig 3B; Mann-Whitney,  $P = .8301$ ).

Measures of CBV within contrast-enhancing tumor were higher in  $IDH^{WT}$  tumors compared with  $IDH^{MUT}$  tumors (On-line Fig 3C; Mann-Whitney,  $P = .0134$ ;  $IDH^{WT} = 1.993$ ,  $IDH^{MUT} = 1.081$ ), but there was not a difference in CBV within T2-hyperintense tumor regions (Fig 3A; Mann-Whitney,  $P = .6892$ ). Measurements of  $MTR_{asym}$  at 3 ppm in contrast-enhancing tumor was not significantly higher in  $IDH^{WT}$  compared with  $IDH^{MUT}$  tumors (On-line Fig 3C; Mann-Whitney,  $P = .5896$ ). However, the difference became significant

in T2-hyperintense lesions (Fig 3A; Mann-Whitney,  $P = .0368$ ;  $IDH^{WT} = 1.722\%$ ,  $IDH^{MUT} = 1.538\%$ ). The voxelwise Pearson correlation coefficient  $R$  was significantly higher in  $IDH^{WT}$  gliomas compared with  $IDH^{MUT}$  gliomas in T2-hyperintense lesions (Fig 3B; Mann-Whitney,  $P = .0076$ ;  $IDH^{WT} = 0.0941$ ,  $IDH^{MUT} = -0.00187$ ), but not in contrast-enhancing lesions (On-line Fig 3D; Mann-Whitney,  $P = .7599$ ).

### DISCUSSION

The high metabolic demand of growing tumor could result in increased intracellular acidity. Altered vascularity and blood flow within tumors can lead to local regions of hypoxia.<sup>20</sup> This lack of oxygen, in turn, can increase glycolysis and result in accumulation

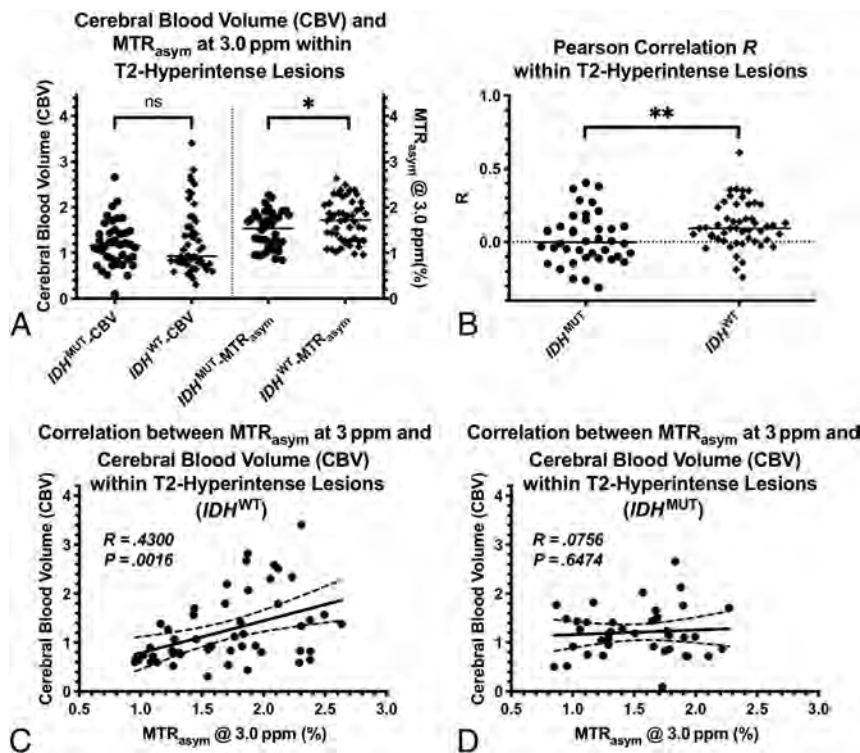


**FIG 3.** A, Measurements of CBV and  $MTR_{asy}$  at 3 ppm within T2-hyperintense lesions for  $IDH^{MUT}$  and  $IDH^{WT}$  gliomas are compared. The median value of CBV is 1.163 in  $IDH^{MUT}$  and 0.9298 in  $IDH^{WT}$ . The median value of  $MTR_{asy}$  at 3 ppm is 1.538% in  $IDH^{MUT}$  and 1.722% in  $IDH^{WT}$  ( $P = .0368$ ). B, The Pearson correlation  $R$  values between CBV  $MTR_{asy}$  at 3 ppm in T2-hyperintense lesions for  $IDH^{MUT}$  and  $IDH^{WT}$  are compared. The median value of  $R$  is  $-0.001871$  in  $IDH^{MUT}$  and  $0.09405$  in  $IDH^{WT}$  ( $P = .0076$ ). C and D, The patient-wise correlation between CBV and  $MTR_{asy}$  at 3 ppm in T2-hyperintense lesions for  $IDH^{WT}$  and  $IDH^{MUT}$  tumors, respectively.

of carboxylic acid and lactic acid within the extracellular space.<sup>3,21</sup> Acidification of the tumor microenvironment can result in vascular endothelial growth factor<sup>22</sup> and platelet-derived endothelial cell growth factor<sup>23</sup> expression, resulting in further angiogenesis and altered blood flow. This positive feedback loop can lead to additional decreased oxygen tension, increased glycolysis, increased acidification, and eventual tumor invasion and alterations of the tumor genome.

Consistent with this well-characterized process, we observed overall higher acidity and vascularity, as quantified by amine CEST-EPI and DSC-perfusion MR imaging, in contrast-enhancing tumors compared with T2-hyperintense lesions. However, within individual tumors, heterogeneous distribution of high-perfusion areas and high-acidity areas was frequently observed. Regions of high perfusion do not necessarily colocalize with regions of high acidity. For example, in Fig 1C, the arrow indicates a nonenhancing tumor region that exhibits high acidity but normal perfusion, which could indicate the existence of active tumor at the stage in which vessel cooption or angiogenesis has not occurred yet. The black arrow indicates a more traditional case in which the contrast-enhancing tumor is both highly perfused and highly acidic, suggesting that amine CEST-EPI as a pH-sensitive imaging technique is able to provide complementary information about tumor metabolism and microenvironment to current standard imaging protocols.

When examining the median values only within tumor regions across the entire patient cohort, we observed a significant correlation between acidity and vascularity within T2-hyperintense, nonenhancing tumor. Because this may have been due to the mixture of both treatment-naïve and treated gliomas included in our patient cohort and because we observed substantially higher levels of acidity in areas of necrosis known to have poor blood flow and hypoxia,<sup>24-26</sup> we isolated only patients who were not on active therapy. Results from this subset of patients ( $n = 58$  of 90) showed the same trends, with no apparent relationship between blood volume and acidity in areas of contrast enhancement, but a significant, positive correlation in areas of T2 hyperintensity. Most interesting, when we examined the correlation within different tumor grades or different  $IDH$ -mutation statuses, the results were different. For high-grade gliomas (WHO III and IV) and  $IDH$ -wild type gliomas, the correlation between perfusion and acidity was positive, consistent with the hypothesis of a vicious cycle between tissue acidosis and altered blood flow due to the increasing metabolic demand of malignant tumor.

However, in grade II gliomas and in  $IDH$  mutant gliomas, the correlation between perfusion and acidity was lost, indicating a possible different metabolic signature.

High-resolution microscopy work from Helmlinger et al<sup>27</sup> in solid tumors has shown an apparent lack of correlation between areas of interstitial pH and  $pO_2$ , suggesting that areas of angiogenesis may not necessarily be spatially colocalized to regions of acidity. Thus, results from the current study showed that tumor acidity, oxygen consumption, and neovascularity are complex processes and potentially spatially heterogeneous, which is consistent with this known genetic, histopathologic, proteomic, and metabolic spatial heterogeneity.<sup>28,29</sup> To better interpret the radiologic findings and to develop a full picture of the complex relationship between perfusion and acidity in gliomas, additional histopathologic studies will be needed, for example, the tissue evaluation of proliferation, cell density, vessel density, and glycolytic pathway biomarkers.

The current study also observed a lower level of acidity in  $IDH^{MUT}$  compared with  $IDH^{WT}$  gliomas. This is consistent with recent observations by Paech et al<sup>30</sup> using relaxation-compensated multipool CEST at 7T, and the work by Jiang et al<sup>31</sup> using amide proton transfer imaging, as well as  $IDH^{MUT}$  gliomas being known as less aggressive and having inhibition of the conversion of isocitrate to alpha-ketoglutarate, resulting in a buildup of 2-hydroxyglutarate, inhibiting oxidative phosphorylation and altering the ability of  $IDH^{MUT}$  tumor cells to effectively use glycolysis.<sup>32</sup>

The current study also observed higher CBV in contrast-enhancing tumors in  $IDH^{WT}$  compared with  $IDH^{MUT}$  tumors, which is consistent with a previous report.<sup>33</sup> Uniquely, we found that the correlation between voxelwise CBV and  $MTR_{asym}$  in T2-hyperintense regions is significantly higher in  $IDH^{WT}$  compared with  $IDH^{MUT}$  tumors. Because the distribution of  $IDH$  status is related to grade, we were not able to rule out the difference being more related to the genetic phenotype of glioma or the aggressiveness. However, our result does reveal that there are different patterns of perfusion/acidity distribution in gliomas, the heterogeneity of which may be related to genetic alternations and patient prognosis. We believe that further investigation of the corresponding histology features will clarify the potential role of combining perfusion and acidity imaging in the clinical setting of the management of patients with brain tumors.

With its unique contrast, CEST MR imaging has been shown to have great potential for various clinical applications.<sup>17,34,35</sup> However, there is no standard sequence and postprocessing protocol for it yet, which may limit its use by clinicians. Apart from pH,  $MTR_{asym}$  at 3.0 ppm may also be affected by several other factors, including amine proton concentration, tissue relaxivities, and field inhomogeneity.<sup>14</sup> In the current study, we have corrected only for  $B_0$  inhomogeneity, but not the effect of T2 and amine concentration, the increase in which would amplify the  $MTR_{asym}$  contrast enhancement under the condition of tissue acidity. We will continue to work on improving the CEST technique. This includes correcting for the confounding factors, exploring CEST metrics other than the asymmetric analysis, and accelerating the acquisition time.

One conceived limitation of our current study was the inhomogeneity in the patient population because we included both treatment-naïve and treated tumors. It is possible that some of the treated tumors may have undergone malignant transformation by the time of the MR imaging examination, leading to miscategorization because tumor grade was mostly based on pathologic findings at initial diagnosis. However, we propose that the mixture of both treated and untreated tumors allowed us to better generalize across all patient populations in a way that is consistent with clinical practice, suggesting that amine CEST-EPI may be useful as a clinical tool under a variety of treatment conditions.

## CONCLUSIONS

Patients with both untreated and treated gliomas have spatially colocalized, regional, altered vascularity and acidity. Examination of median measurements within tumor regions across a large number of patients demonstrated a positive linear association between blood volume and tumor acidity in areas of T2-hyperintense, nonenhancing tumor; however, areas of contrast enhancement were more complex and did not show a strong relationship. Future studies aimed at therapeutically altering either vascularity, hypoxia, or acidity in patients with gliomas may reveal more information about the intricate interplay among these tumor characteristics.

Disclosures: Linda M. Liau—UNRELATED: Grants/Grants Pending: Northwest Biotherapeutics\*; Stock/Stock Options: Actuate Therapeutics.\* Albert Lai—UNRELATED: Consultancy: Merck, Comments: Advisory Board; Payment for Development of Educational Presentations: AbbVie, Comments: Society for NeuroOncology Annual

Meeting lecture. Whitney B. Pope—RELATED: Consulting Fee or Honorarium: Bracco, Guerbet. Timothy F. Cloughesy—UNRELATED: Board Membership: Global Coalition for Adaptive Research, 501c3 for sponsoring clinical trials. No payment to author; Consultancy: VBI, VBL, Deciphera Pharmaceuticals, Agios Pharmaceuticals, Tocagen, Merck, Celgene, Puma, AbbVie, Eli Lilly and Company; Stock/Stock Options: Notable Labs. Benjamin M. Ellingson—UNRELATED: Consultancy: MedQIA, Agios Pharmaceuticals, Imaging Endpoints, Hoffman-La Roche/Genentech, Insys Therapeutics, OmniOx, Nativis, Siemens, Janssen Pharmaceutica, Medicenna, Novogen/Kazia; Grants/Grants Pending: Agios Pharmaceuticals, Roche, Janssen Pharmaceutica, Siemens. \*Money paid to the institution.

## REFERENCES

- Ostrom QT, Gittleman H, Liao P, et al. **CBTRUS Statistical Report: primary brain and other central nervous system tumors diagnosed in the United States in 2010–2014.** *Neuro Oncol* 2017;19:v1–88 CrossRef Medline
- Warburg OH, Dickens F, Kaiser Wilhelm Institute for Biology. *The Metabolism of Tumours: Investigations from the Kaiser Wilhelm Institute for Biology, Berlin-Dahlem.* London: Arnold Constable & Co; 1930
- Gatenby RA, Gillies RJ. **Why do cancers have high aerobic glycolysis?** *Nat Rev Cancer* 2004;4:891–99 CrossRef Medline
- Morita T, Nagaki T, Fukuda I, et al. **Clastogenicity of low pH to various cultured mammalian cells.** *Mut Res* 1992;268:297–305 CrossRef Medline
- Gatenby RA, Vincent TL. **An evolutionary model of carcinogenesis.** *Cancer Res* 2003;63:6212–20 Medline
- Martinez-Zaguilan R, Seftor EA, Seftor RE, et al. **Acidic pH enhances the invasive behavior of human melanoma cells.** *Clin Exp Metastasis* 1996;14:176–86 CrossRef Medline
- Turner GA. **Increased release of tumour cells by collagenase at acid pH: a possible mechanism for metastasis.** *Experientia* 1979;35:1657–58 CrossRef Medline
- Russell SM, Elliott R, Forshaw D, et al. **Glioma vascularity correlates with reduced patient survival and increased malignancy.** *Surg Neurol* 2009;72:242–46; discussion 246–47 CrossRef Medline
- Leon SP, Folkert RD, Black PM. **Microvessel density is a prognostic indicator for patients with astroglial brain tumors.** *Cancer* 1996;77:362–72 CrossRef Medline
- Wesseling P, van der Laak JA, Link M, et al. **Quantitative analysis of microvascular changes in diffuse astrocytic neoplasms with increasing grade of malignancy.** *Hum Pathol* 1998;29:352–58 CrossRef Medline
- Jain RK, di Tomaso E, Duda DG, et al. **Angiogenesis in brain tumors.** *Nat Rev Neurosci* 2007;8:610–22 Medline
- Plate KH, Mennel HD. **Vascular morphology and angiogenesis in glial tumors.** *Exp Toxicol Pathol* 1995;47:89–94 CrossRef Medline
- Rampling R, Cruickshank G, Lewis AD, et al. **Direct measurement of pO<sub>2</sub> distribution and bioreductive enzymes in human malignant brain tumors.** *Int J Radiat Oncol Biol Phys* 1994;29:427–31 CrossRef Medline
- Harris RJ, Cloughesy TF, Liau LM, et al. **Simulation, phantom validation, and clinical evaluation of fast pH-weighted molecular imaging using amine chemical exchange saturation transfer echo planar imaging (CEST-EPI) in glioma at 3 T.** *NMR Biomed* 2016;29:1563–76 CrossRef Medline
- Louis DN, Perry A, Reifenberger G, et al. **The 2016 World Health Organization Classification of Tumors of the Central Nervous System: a summary.** *Acta Neuropathol* 2016;131:803–20 CrossRef Medline
- Ellingson BM, Bendszus M, Boxerman J, et al; Jumpstarting Brain Tumor Drug Development Coalition Imaging Standardization Steering Committee. **Consensus recommendations for a standardized brain tumor imaging protocol in clinical trials.** *Neuro Oncol* 2015;17:1188–98 CrossRef Medline
- Harris RJ, Yao J, Chakhoyan A, et al. **Simultaneous pH-sensitive and oxygen-sensitive MRI of human gliomas at 3 T using multi-echo amine proton chemical exchange saturation transfer spin-and-gra-**

- dient echo echo-planar imaging (CEST-SAGE-EPI). *Magn Reson Med* 2018;80:1962–78 CrossRef Medline
18. Yao J, Ruan D, Raymond C, et al. **Improving B0 correction for pH-weighted amine proton chemical exchange saturation transfer (CEST) imaging by use of K-means clustering and Lorentzian estimation.** *Tomography* 2018;4:123–37 CrossRef Medline
  19. Ellingson BM, Kim HJ, Woodworth DC, et al. **Recurrent glioblastoma treated with bevacizumab: contrast-enhanced T1-weighted subtraction maps improve tumor delineation and aid prediction of survival in a multicenter clinical trial.** *Radiology* 2014;271:200–10 CrossRef Medline
  20. Raghunand N, Gatenby RA, Gillies RJ. **Microenvironmental and cellular consequences of altered blood flow in tumours.** *Br J Radiol* 2003;76(Spec No 1):S11–22 CrossRef Medline
  21. Helmlinger G, Schell A, Dellian M, et al. **Acid production in glycolysis-impaired tumors provides new insights into tumor metabolism.** *Clin Cancer Res* 2002;8:1284–91 Medline
  22. Shi Q, Le X, Wang B, et al. **Regulation of vascular endothelial growth factor expression by acidosis in human cancer cells.** *Oncogene* 2001;20:3751–56 CrossRef Medline
  23. Griffiths L, Dachs GU, Bicknell R, et al. **The influence of oxygen tension and pH on the expression of platelet-derived endothelial cell growth factor/thymidine phosphorylase in human breast tumor cells grown in vitro and in vivo.** *Cancer Res* 1997;57:570–72 Medline
  24. Ellingson BM, Wen PY, Cloughesy TF. **Evidence and context of use for contrast enhancement as a surrogate of disease burden and treatment response in malignant glioma.** *Neuro Oncol* 2018;20:457–71 CrossRef Medline
  25. da Ponte KF, Berro DH, Collet S, et al. **In vivo relationship between hypoxia and angiogenesis in human glioblastoma: a multimodal imaging study.** *J Nucl Med* 2017;58:1574–79 CrossRef Medline
  26. Flynn JR, Wang L, Gillespie DL, et al. **Hypoxia-regulated protein expression, patient characteristics, and preoperative imaging as predictors of survival in adults with glioblastoma multiforme.** *Cancer* 2008;113:1032–42 CrossRef Medline
  27. Helmlinger G, Yuan F, Dellian M, et al. **Interstitial pH and pO<sub>2</sub> gradients in solid tumors in vivo: high-resolution measurements reveal a lack of correlation.** *Nat Med* 1997;3:177–82 CrossRef Medline
  28. Patel AP, Tirosh I, Trombetta JJ, et al. **Single-cell RNA-seq highlights intratumoral heterogeneity in primary glioblastoma.** *Science* 2014;344:1396–401 CrossRef Medline
  29. Sottoriva A, Spiteri I, Piccirillo SGM, et al. **Intratumor heterogeneity in human glioblastoma reflects cancer evolutionary dynamics.** *Proc Natl Acad Sci U S A* 2013;110:4009–14 CrossRef Medline
  30. Paech D, Windschuh J, Oberhollenzer J, et al. **Assessing the predictability of IDH mutation and MGMT methylation status in glioma patients using relaxation-compensated multi-pool CEST MRI at 7.0 Tesla.** *Neuro Oncol* 2018;20:1661–71 CrossRef Medline
  31. Jiang S, Zou T, Eberhart CG, et al. **Predicting IDH mutation status in grade II gliomas using amide proton transfer-weighted (APT<sub>w</sub>) MRI.** *Magn Reson Med* 2017;78:1100–09 CrossRef Medline
  32. Borodovsky A, Seltzer MJ, Riggins GJ. **Altered cancer cell metabolism in gliomas with mutant IDH1 or IDH2.** *Curr Opin Oncol* 2012;24:83–89 CrossRef Medline
  33. Kickingereder P, Sahn F, Radbruch A, et al. **IDH mutation status is associated with a distinct hypoxia/angiogenesis transcriptome signature which is non-invasively predictable with rCBV imaging in human glioma.** *Sci Rep* 2015;5:16238 CrossRef Medline
  34. Tietze A, Blicher J, Mikkelsen IK, et al. **Assessment of ischemic penumbra in patients with hyperacute stroke using amide proton transfer (APT) chemical exchange saturation transfer (CEST) MRI.** *NMR Biomed* 2014;27:163–74 CrossRef Medline
  35. Xu X, Yadav NN, Knutsson L, et al. **Dynamic glucose-enhanced (DGE) MRI: translation to human scanning and first results in glioma patients.** *Tomography* 2015;1:105–14 CrossRef Medline

# Quantitative Susceptibility Mapping of Time-Dependent Susceptibility Changes in Multiple Sclerosis Lesions

S. Zhang, T.D. Nguyen, S.M. Hurtado Rúa, U.W. Kaunzner, S. Pandya, I. Kovanlikaya, P. Spincemille, Y. Wang, and S.A. Gauthier



## ABSTRACT

**BACKGROUND AND PURPOSE:** MR imaging studies have demonstrated that magnetic susceptibility in multiple sclerosis lesions is dependent on lesion age. The objective of this study was to use quantitative susceptibility mapping to determine whether lesions with a hyperintense rim, indicative of iron-laden inflammatory cells (rim+), follow a unique time-dependent trajectory of susceptibility change compared with those without (rim-).

**MATERIALS AND METHODS:** We studied patients with MS with at least 1 new gadolinium-enhancing lesion and at least 3 longitudinal quantitative susceptibility mapping scans obtained between 1.1 and 6.1 years. Lesions were classified as rim+ if a hyperintense rim appeared on quantitative susceptibility mapping at any time. A multilevel growth curve model compared longitudinal susceptibility among rim+ and rim- lesions.

**RESULTS:** Thirty-two new gadolinium-enhancing lesions from 19 patients with MS were included, and 16 lesions (50%) were identified as rim+. Quantitative susceptibility mapping rim+ lesions were larger than rim- lesions with gadolinium enhancement ( $P < .001$ ). Among all lesions, susceptibility increased sharply after enhancement to a peak between 1 and 2 years followed by a decrease. The overall susceptibility curve height for rim- lesions was 4.27 parts per billion lower than that for rim+ lesions ( $P = .01$ ). Rim- lesions demonstrated a higher linear slope relative to rim+ lesions ( $P = .023$ ) but faster cubic decay relative to rim+ lesions ( $P = .005$ ). Rim- lesions started decaying approximately 2 years earlier compared with rim+ lesions.

**CONCLUSIONS:** There was a marked difference in the susceptibility temporal trajectory between rim+ and rim- lesions during the first 6 years of lesion formation. Most rim+ lesions retain iron for years after the initial lesion appearance.

**ABBREVIATIONS:** Gd = gadolinium; Gd+ = Gd-enhancing; GRE = gradient recalled-echo; QSM = quantitative susceptibility mapping; ppb = parts per billion; rim+ = rim positive; rim- = rim negative

Quantitative susceptibility mapping (QSM)<sup>1</sup> provides efficient in vivo quantification of susceptibility changes related to iron deposition and helps identify lesions with iron-laden in-

flammatory cells.<sup>2</sup> It has been widely used in studying multiple sclerosis and can demonstrate the retention of iron among a subset of chronic lesions.<sup>3-5</sup> Enhancing MS lesions identified on post-gadolinium (Gd) T1WI in the routine MR imaging surveillance are representative of the breakdown of the blood-brain barrier and acute disease activity.<sup>6</sup> As the BBB closes, lesions transition to the chronic stage. However, a subset of lesions may retain a rim of iron-enriched inflammatory cells with ongoing damage. Chronic active MS lesions, characterized by a hyperintense rim on QSM, have been shown to contain iron-enriched, activated microglia and macrophages on histopathology<sup>5</sup> and have been linked to greater tissue damage on in vivo MR imaging.<sup>7,8</sup> Identifying lesions likely to retain chronic inflammation would be useful for potential therapeutic targeting. Accordingly, it would be valuable to study MS lesion-evolution trajectories from the time of enhancement to the chronic lesion stage.

QSM is a phase-based magnetic field deconvolution technique that overcomes blooming artifacts and provides accurate quanti-

Received January 29, 2019; accepted after revision April 17.

From the Departments of Radiology (S.Z., T.D.N., S.P., I.K., P.S., Y.W., S.A.G.) and Neurology (U.W.K., S.A.G.) and Feil Family Brain and Mind Research Institute (S.A.G.), Weill Cornell Medicine, New York, New York; Department of Radiology (S.Z.), Tongji Hospital, Tongji Medical College, Huazhong University of Science and Technology, Wuhan, China; Department of Mathematics and Statistics (S.M.H.R.), College of Science and Health Professions, Cleveland State University, Cleveland, Ohio; and Department of Biomedical Engineering (Y.W.), Cornell University, Ithaca, New York.

This work was supported, in part, by grants from the National Institutes of Health (R01NS090464, R01NS104283, R01NS105144, S10 OD021782), the National Multiple Sclerosis Society (RG-1602-07671), and grant ULI TR000456-06 from the Weill Cornell Clinical and Translational Science Center.

Please address correspondence to Susan A. Gauthier, DO, MPH, Department of Neurology, Weill Cornell Medical College, 1305 York Ave, Suite Y217, NY, NY 10021; e-mail: sag2015@med.cornell.edu

Indicates open access to non-subscribers at www.ajnr.org

<http://dx.doi.org/10.3174/ajnr.A6071>

fication and localization of the magnetic sources.<sup>1,9,10</sup> Previous QSM studies demonstrated that MS lesion susceptibility increases as the acute, enhancing MS lesion transitions to the nonenhancing stage, reaches a peak in the chronic active stage, and eventually decays away in the final stage of a glia scar.<sup>11-14</sup> Although these studies identified a unique time-dependent trajectory in susceptibility on QSM, they are limited given the cross-sectional design or short longitudinal follow-up. In addition, a number of recent gradient recalled-echo (GRE) imaging studies have identified a unique subpopulation of chronic MS lesions with a hypointense rim on the phase image or a hyperintense rim on QSM. These studies have used histopathologic validation<sup>7,15-17</sup> and, more recently, PET imaging<sup>18</sup> to validate that these lesions have persistent inflammation represented by iron-laden microglia and macrophages. Initial detection and the expected life span of lesions with a hyperintense rim appearance on QSM (rim+) as well as the time-dependent susceptibility changes among these lesions compared with those without a rim (rim-) have yet to be explored, to our knowledge.

The aim of this study was to assess longitudinal tissue-susceptibility changes in new Gd-enhancing lesions for up to 6 years after the first identification and to determine whether lesion trajectories depend on the development of a hyperintense rim on QSM.

## MATERIALS AND METHODS

### Patient Selection

This was a retrospective study of a cohort of 19 patients with relapsing-remitting MS selected from an ongoing, prospective MS MR imaging and clinical data base for which annual MR imaging scans (including QSM) were collected during 6 years. Patients were selected for this study if they met the following inclusion criteria: 1) They had at least 1 new Gd-enhancing (Gd+) MS lesion on routine annual MR imaging, 2) had at least 3 longitudinal QSM scans (including at the time of Gd+ lesion detection), 3) had at least 1 MR imaging performed >1 year after Gd+ lesion detection, and 4) had prior MR imaging to ensure that Gd+ lesions were newly formed lesions and not re-enhancement of older lesions. MR images were acquired on 2 different imaging platforms during the 6 years (GE Healthcare and Siemens, details below). Clinical data collected for patients included the following: age, sex, Expanded Disability Status Scale scores, disease duration, and treatment duration. This study was approved by Weill Cornell Medicine institutional review board, and written informed consent was obtained from each subject.

### MR Imaging Protocol and Image Processing

Brain MRIs (from 2011 to 2018) were performed on 3T MR imaging scanners (Signa HDxt, GE Healthcare, Milwaukee, Wisconsin, with a product 8-channel head coil; Magnetom Skyra, Siemens, Erlangen, Germany with a product 20-channel head/neck coil). The scanning protocol consisted of standard 3D-T1WI, 2D-T2WI, and 3D-T2-weighted FLAIR sequences for anatomic structure, multiecho 3D-GRE imaging for QSM, and gadolinium-enhanced 3D-T1WI to detect blood-brain barrier disruption. The acquisition parameters for multiecho GRE were the following: FOV = 24 cm, TR = 49–58 ms, TE1/ΔTE = 4.5–6.7/4.1–4.8 ms, last TE = 47.7 ms, acquisition

matrix = 320–416 × 205–320, readout bandwidth = 244–260 Hz/pixel, axial slice thickness = 3 mm, flip angle = 15°–20°, acceleration factor = 2, number of averages = 1. The scan time was around 4 minutes and 30 seconds (48 slices), varying slightly with brain superior-inferior dimensions.

This QSM imaging protocol was harmonized for both scanner manufacturers and was demonstrated to be reproducible across manufacturers.<sup>19,20</sup> QSM was reconstructed from complex GRE images using a fully automated morphology-enabled dipole inversion (MEDI+0) method zero-referenced to the ventricular CSF.<sup>21</sup> All the conventional images (T1WI, T1WI+Gd, T2WI, T2-weighted FLAIR) and the follow-up QSM images were coregistered to the baseline GRE magnitude images using the FMRIB Linear Image Registration Tool (FLIRT; <http://www.fmrib.ox.ac.uk/fsl/fslwiki/FLIRT>).<sup>22</sup>

### Lesion Susceptibility and Volume Measurements

New Gd+ MS lesions were identified on T1WI+Gd images and visually classified on QSM as rim+ or rim-<sup>8</sup> by 2 independent reviewers (S.Z., a neuroradiologist with 7 years of experience; S.A.G., an MS neurologist with 16 years of experience).<sup>8</sup> A lesion was designated as rim+ if QSM was hyperintense at the edge of the lesion at any of the longitudinal time points. In addition, at each time point, newly identified Gd+ lesions were dated as zero years. Lesions were also classified as either “nodular” or “shell” enhancing to estimate the stage of lesion enhancement (ie, early or late stage, respectively).<sup>12,23</sup> In case of a rare (4 lesions) disagreement, a third neuroradiologist (I.K., with 22 years of experience) determined the lesion type. ROI analysis was performed using ITK-SNAP software (Version 3.6.0; <http://www.itksnap.org/>) to obtain regional volume and QSM measurements within the identified lesions. To assess a change in lesion volume, we drew lesion ROIs on raw T2-weighted FLAIR images, which had isotropic 1-mm high-resolution images, at all time points. To assess longitudinal susceptibility change, we first created ROIs on coregistered T2-weighted FLAIR images and then overlaid them on the QSM images at initial lesion detection. When necessary, these ROIs were manually edited to better match lesion geometry on QSM and removal of the central veins (vessel-like structures with hyperintense QSM appearance). The edited ROIs were overlaid onto QSM images from all other subsequent time points. The susceptibility value of the adjacent normal-appearing white matter was subtracted from the lesion susceptibility to offset the influence of local fiber orientation.

### Statistical Analysis

A regression model with orthogonal time polynomials was used to analyze the longitudinal evolution of lesion volumes for rim+ and rim- lesions at the lesion level while adjusting for multiple lesions per patient. The final model included a third-order orthogonal polynomial, the fixed conditional effect was lesion group, and patient was the random effect.

A multilevel growth curve model with orthogonal time polynomials was used to analyze the longitudinal evolution of QSM values for rim+ and rim- lesions while adjusting for patient-level covariates (fixed effects: individual lesion volume, patient age, Expanded Disability Status Scale score, disease duration, and

treatment duration) and multiple lesions per patient (random effects). An eighth-order orthogonal polynomial model was necessary to capture the upward and downward evolution of QSM values within lesion groups. Orthogonal polynomials are transformations that make the original time terms independent. They allow a precise and robust evaluation of QSM longitudinal differences. Our orthogonal polynomial was defined on the basis of the lesion-age octiles (8 quantiles). This approach accounts for the sample lesion age distribution. The statistical analysis was performed using R statistical and computing software (2017; <http://www.r-project.org/>).

## RESULTS

### Patient and Lesion Characteristics

Nineteen patients with relapsing-remitting MS (15 women and 4 men,  $36.3 \pm 6.4$  years of age) met the inclusion criteria with a total of 32 new T1WI+Gd lesions: 9 nodular-enhancing (28%, susceptibility,  $6.87 \pm 5.80$  parts per billion [ppb]) and 23 shell-enhancing (72%,  $12.10 \pm 8.95$  ppb) lesions. Central veins were found in 10 (31%) lesions. Patients had a mean disease duration of  $4.8 \pm 3.2$  years and an Expanded Disability Status Scale score of  $1.4 \pm 1.7$ . The average time from initial MR imaging to the last MR imaging was  $3.6 \pm 1.4$  years (range, 1.1–6.1 years). Patients were treated with various disease-modifying therapies, and at the time of lesion identification, the cohort was on therapy for a mean duration of  $3.5 \pm 3.0$  years.

### Lesions with a Hyperintense Rim on QSM

Among the 32 new Gd+ lesions, 16 lesions (50%) were identified as QSM rim+, and evidence of the rim was seen at the time of enhancement for most (81%) of these lesions. Qualitatively, rim+ lesions were visualized on QSM scans longer than rim- lesions (Figs 1–3), and once identified, the hyperintense rim was consistently found on all subsequent scans in 14 (88%) of the rim+ lesions (Figs 2 and 3). Although susceptibility values were lowest at the time of Gd-enhancement, subtle evidence of a rim could be seen in 13 (81%) lesions at that time. The longitudinal evolution of lesion volume, adjusting for multiple lesions per patient and conditioning on lesion group, is presented in Fig 4. Fitted volumes derived from the regression model demonstrated that rim+ lesions ( $1042.45 \text{ mm}^3$ ) were significantly larger than rim- lesions ( $322.34 \text{ mm}^3$ ) at the time of Gd-enhancement ( $P < .001$ ). Following the start of a decline in volume after Gd-enhancement, rim+ lesions remained larger than rim- lesions and maintained a significant difference at lesion ages 0.5, 2, and 4 years (all  $P < .001$ ) (Fig 4).

### Time-Dependent Susceptibility Change in QSM Rim+ and Rim- Lesions

The final model for the longitudinal lesion evolution of QSM values included T2-weighted FLAIR lesion volume and Expanded Disability Status Scale scores at baseline as patient-level fixed effects (all  $P$  values  $< .05$ ). All lesions demonstrated a continued increase in susceptibility until a peak between 1 and 2 years, which was followed by a reduction during the subsequent years. There was a significant effect of lesion group (rim+ versus rim-) on the intercept term, indicating lower overall QSM values for the rim-

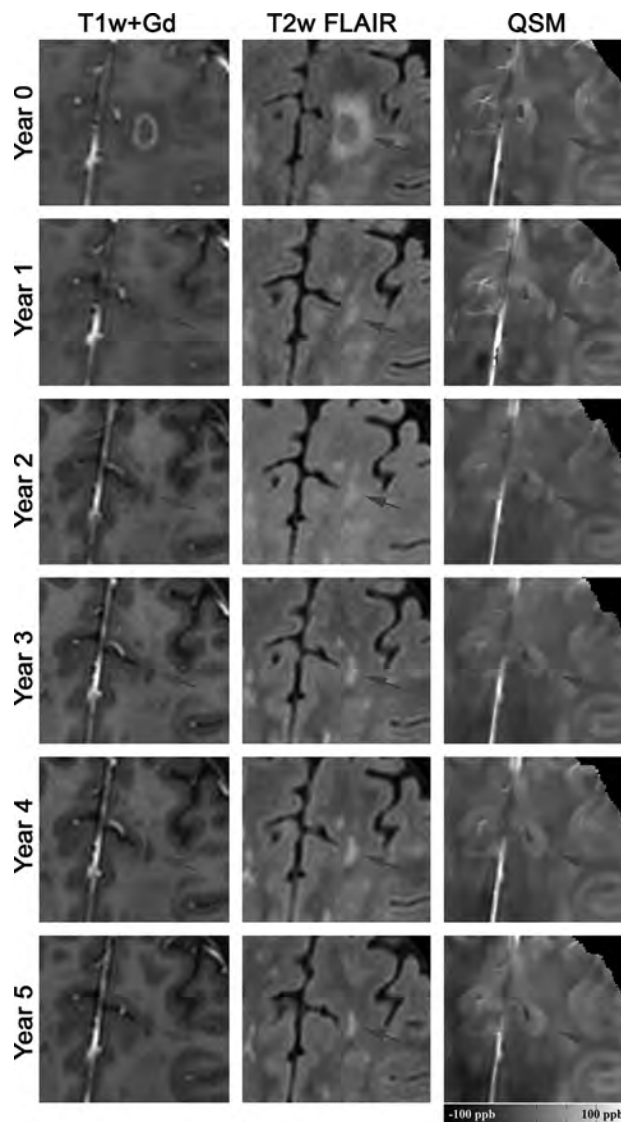


**FIG 1.** Longitudinal QSM and T2-weighted FLAIR images of a new Gd-enhancing MS lesion without a QSM rim appearance (rim-). At baseline, the enhancing lesion was isointense on QSM (mean lesion susceptibility =  $-3.31$  ppb), became most hyperintense at 1 year ( $22.50$  ppb), and gradually disappeared in subsequent years ( $-1.18$  ppb at year 5).

lesions relative to the rim+ (estimate =  $-4.27$ , SE = 1.62,  $P = .01$ ) (Fig. 5). There was also a significant effect of lesion group on the slope and cubic terms, indicating a faster linear growth rate for rim- lesions relative to rim+ lesions (estimate = 8.42, SE = 3.66,  $P = .023$ ) as well as significantly faster cubic decay for rim- lesions relative to rim+ lesions (estimate =  $-10.64$ , SE = 3.75,  $P = .005$ ). All other effects of lesion group conditioning on time decay were not significantly different between the 2 groups. When considering lesion-volume change, as opposed to baseline lesion volume, as a covariate in the model, a significant association was found between QSM change and volume change ( $P = .002$ ) (for every  $1\text{-mm}^3$  decrease in volume, there was 0.014-ppb reduction in QSM). The relationship between susceptibility and volume change was similar among rim+ and rim- lesions ( $P > .27$ ).

The Table summarizes the model-fitted mean susceptibilities along with their 95% confidence intervals. The estimated suscep-

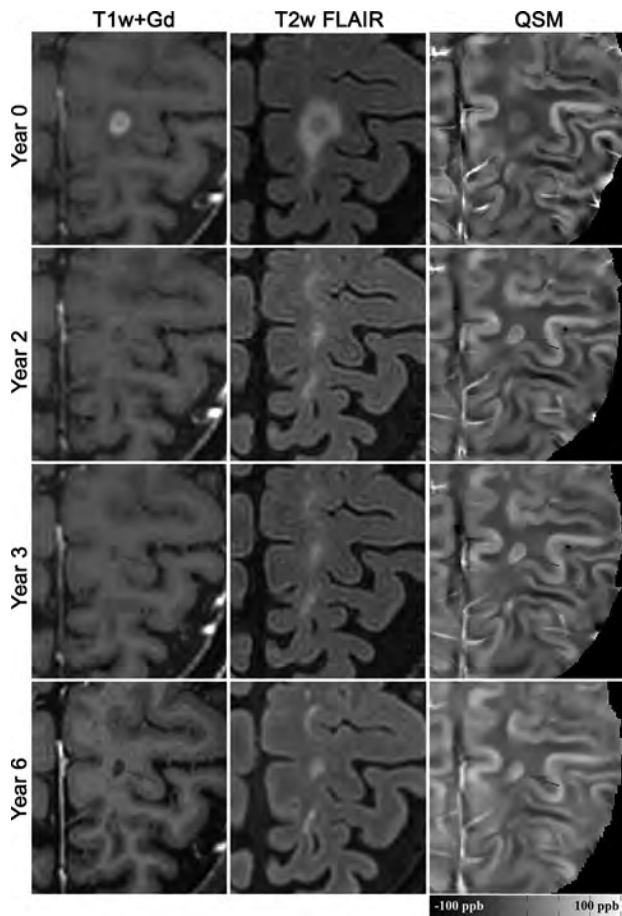


**FIG 2.** Longitudinal QSM and T2-weighted FLAIR images of a new Gd-enhancing MS lesion with a QSM rim appearance (rim+). This lesion was slightly hyperintense on QSM at the time of Gd-enhancement (mean lesion susceptibility = 12.74 ppb), became most hyperintense at 3 years (34.28 ppb), and remained hyperintense at 6 years (25.15 ppb).

tibility means for rim- lesions demonstrated a decay after 1.5 years with 95% confidence, while the estimated means for rim+ lesions remained persistently elevated from lesions 0.5–4 years of age. A decline in susceptibility is found in rim+ lesions only after the fourth year.

## DISCUSSION

The current study is the longest longitudinal lesion-based susceptibility study examining the time-dependent susceptibility changes quantified on QSM. Our study indicates that QSM rim+ lesions have a unique time-dependent trajectory. Compared with QSM rim- lesions, rim+ lesions start with a higher susceptibility and larger volume and, most important, retain a high-susceptibility value for a number of years after initial detection. This study provides further insight into a distinct subgroup of MS lesions, those that retain a rim of iron-laden inflammatory cells and have the potential for continued tissue damage.<sup>7,8,17</sup>

QSM provides a noninvasive way to quantify the susceptibility change in MS lesions. The susceptibility increase observed in our study is consistent with previous studies in which a jump in lesion susceptibility occurs as an enhancing lesion evolves to the chronic, nonenhancing state.<sup>11–14</sup> The initial rise in susceptibility, occurring within weeks, in active lesions may be related to myelin

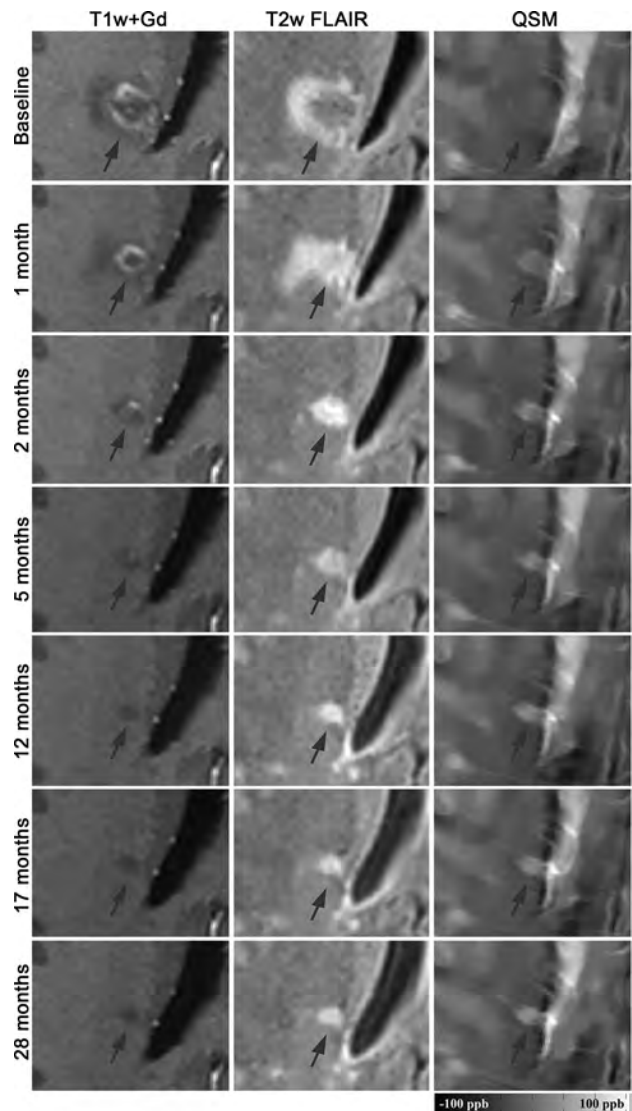


**FIG 3.** Longitudinal QSM and T2-weighted FLAIR images of a new Gd-enhancing MS lesion with a QSM rim appearance (rim+). This lesion was isointense on QSM at baseline and demonstrated an increase in susceptibility and rim appearance on subsequent QSM scans. The lesion susceptibility increased continually from  $-0.34$  ppb at baseline to 26.35 ppb at 28 months. Gd-enhancement remained in this lesion until month 2.

digestion,<sup>24</sup> and the subsequent increase, which occurs for months, is more likely related to removal of the myelin debris within macrophages<sup>25</sup> and the release of iron.<sup>12</sup> A subset of chronic MS lesions, identified as chronic active or slowly expanding lesions, has been described as having a hypocellular lesion center and a rim of activated proinflammatory microglia and macrophages.<sup>17,26,27</sup> These lesions demonstrate evidence of active demyelination and axonal destruction at their rim and are thought to contribute to long-term, ongoing tissue damage in MS.<sup>8,17,26–28</sup> A number of studies have demonstrated that most microglia and macrophages found at the rim of chronic active MS lesions contain iron.<sup>7,15,17,29–32</sup> The source of the released iron is presumed to be derived from damaged myelin and dying oligodendrocytes in acute lesions<sup>31</sup> and functions to promote polarization of microglia and macrophage cells to a proinflammatory state.<sup>30</sup> Our data suggest that the development of rim+ lesions

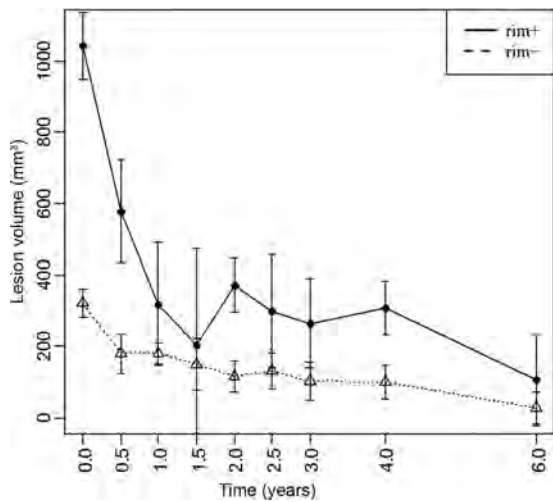


**FIG 4.** Longitudinal lesion-volume evolution changes among QSM rim+ and rim- lesions. Rim+ lesions were statistically larger at Gd-enhancement (time = 0), 0.5, 2, and 4 years (all  $P < .0001$ ).

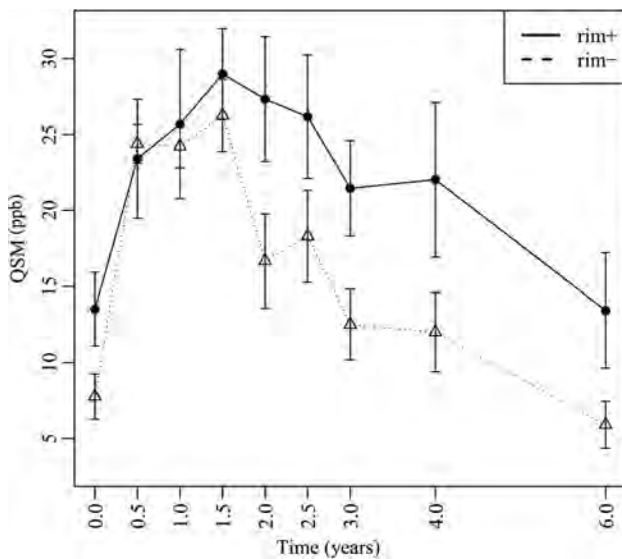


**FIG 5.** Longitudinal lesion age-dependent susceptibility time course of QSM rim+ and rim- MS lesions. Rim+ lesions demonstrate a higher peak QSM value and significantly slower decay rate compared with rim- (see text).

**The mean susceptibility of rim+ and rim- lesions derived from the regression model**

Time (yr)	Rim+			Rim-		
	No. of Lesions	Mean (ppb)	95% CI	No. of Lesions	Mean (ppb)	95% CI
0	16	13.51	11.09–15.93	16	7.77	6.27–9.26
0.5	10	23.40	19.47–27.33	9	24.39	23.11–25.67
1	7	25.69	20.78–30.60	11	24.22	22.79–25.64
1.5	5	28.99	26.00–31.98	5	26.25	23.86–28.63
2	6	27.33	23.22–31.44	7	16.66	13.57–19.76
2.5	8	26.17	22.10–30.25	10	18.29	15.27–21.31
3	7	21.45	18.31–24.59	9	12.50	10.19–14.81
4	8	22.02	16.92–27.12	10	12.00	9.40–14.61
6	5	13.42	9.64–17.21	6	5.90	4.36–7.45

may be related to a higher level of iron release, given the higher susceptibility peak among these lesions, and that the extent of iron release potentially contributes to the development of chronic in-

flammation. In addition, we found that rim+ lesions were much larger at the time of Gd-enhancement, a finding that supports the concept of a larger inflammatory event leading to more demyelination and iron release. Studying the physiologic mechanisms driving iron release within the acute lesion could identify therapeutic targets aimed at decreasing the occurrence of chronic active MS lesions.

The reduction of susceptibility in both rim+ and rim- lesions was related to volume loss; however, the relationship was similar and suggests that pathologic differences may explain our observed differences in the decay rate. The relatively abrupt reduction in susceptibility found among the QSM rim- lesions would be consistent with either loss of iron from the lesion or, more likely, a higher potential for remyelination among these lesions.<sup>5</sup> Remyelination occurring in rim- lesions would be consistent with histologic observations indicating that iron-enriched microglia and macrophages are not found at the rim of remyelinated or shadow plaques<sup>17</sup> and in vivo MR imaging studies demonstrating less tissue damage in lesions without a QSM rim.<sup>7,8</sup>

The slow decay of susceptibility in rim+ lesions and retention of the hyperintense rim suggest that these lesions retain iron for a number of years; thus, they have the potential for ongoing damage across a more extended period.<sup>17</sup> Although iron is retained, there is an eventual reduction in susceptibility, which suggests that most of these lesions have a life span of only a few years before iron loss and probable transition to a chronic inactive state or glia scar.<sup>25</sup> Histologically, chronic active lesions have been found to be associated with longer disease duration and to predominantly occur in progressive disease, in which new Gd+ lesions are infrequently found.<sup>27</sup> However, given the aforementioned MR imaging GRE studies, these lesions can occur frequently within the relapsing phase of the disease, and consistent with others,<sup>7</sup> we found that lesions that become chronic active lesions can show subtle evidence of a rim at the Gd+ stage. These combined observations suggest that QSM rim+ lesions could serve as an early-stage imaging biomarker for disease prognosis, and this possibility warrants further exploration.

QSM has been shown to provide a high level of diagnostic accuracy in predicting Gd+ lesions.<sup>13</sup> In this study, most lesions were shell-enhancing, which are thought to be slightly older enhancing lesions and tend to demonstrate a slightly higher susceptibility.<sup>12</sup> Most important, the average susceptibility at the time of enhancement of all lesions (nodular and shell enhancing) was comparable with that of the previous work<sup>12</sup> and below the cutoff value of 13.5 ppb for predicting Gd+ MS lesions.<sup>13</sup> Furthermore, GRE imaging is being explored to improve the diagnostic accuracy of MS based on the identification of a central vein or central vein sign. Most interesting, we found that only one-third of lesions had a central vein on QSM, which is lower than previously suggested, using a combined T2-weighted FLAIR and T2\* sequence,<sup>33</sup> and this finding suggests that more research is required to assess the frequency of the central vein sign in MS lesions.

There are limitations in this study. Our lesion sample size is relatively small, and more important, not all lesions were measured at each time point or followed through to all 6 years. We will continue to identify Gd+ lesions from our ongoing data base to expand on our observations and provide more data to each lesion-

age year. This expansion will allow further exploration into the effect of individual lesion size as well as patient-specific covariates such as disease duration, disability status, and treatment effect. As mentioned above, very early changes in susceptibility are likely due to a number of pathophysiologic mechanisms at play: Imaging the early-stage lesions with frequent and short-interval QSM with the addition of myelin imaging<sup>34</sup> would allow a more detailed analysis of the early rise in susceptibility. Similarly, a serial MR imaging study with both QSM and myelin imaging during the decay stage can evaluate the loss of iron versus remyelination in rim – lesions. Last, our study focused on white matter MS lesions and excluded cortical gray matter lesions, which are known to occur quite frequently in MS and require ultra-high-field imaging for depiction.<sup>35</sup> Most interesting, a high-field 7T study using QSM identified cortical lesions as having a much lower susceptibility compared with white matter lesions, suggesting less iron in cortical lesions compared with white matter lesions.<sup>36</sup> Thus, as we move forward with 7T QSM MR imaging, we intend to explore and compare the time-dependent susceptibility changes among smaller regions within the lesion (ie, regions of tissue enhancement) as well as lesions located within the cortex.

## CONCLUSIONS

We identified unique trajectories of lesion time-dependent change in susceptibility among different subtypes of MS lesions. These observations are consistent with the iron-laden inflammatory cells present within the rim of a select subset of chronic lesions retaining iron for a number of years and slowly transitioning to an inactive state. This study supports the use of serial QSM to provide information regarding the current state of inflammation within chronic MS lesions.

Disclosures: Sandra M. Hurtado-Rúa—RELATED: Grant: National Institutes of Health, Comments: R01-NS104283–01A1.\* Pascal Spincemaille—UNRELATED: Patents (Planned, Pending or Issued): Cornell University, Comments: P.S. is an inventor on a patent describing methods (QSM) used in this work\*; Stock/Stock Options: Medimagemetric LLC. Yi Wang—RELATED: Grant: National Institutes of Health R01NS090464, R01NS095562\*; UNRELATED: Patents (Planned, Pending or Issued): Cornell University, Comments: QSM technology patents\*; Stock/Stock Options: Medimagemetric LLC, Comments: Cornell spinoff company. Susan A. Gauthier—RELATED: Grant: R01NS104283, R01NS105144\*; UNRELATED: Consultancy: one-time Celgene Advisory Board; Grants/Grants Pending: Genzyme, Mallinckrodt.\* Thanh D. Nguyen—RELATED: Grant: National Multiple Sclerosis Society, National Institutes of Health.\* \*Money paid to the institution.

## REFERENCES

- de Rochefort L, Liu T, Kressler B, et al. **Quantitative susceptibility map reconstruction from MR phase data using Bayesian regularization: validation and application to brain imaging.** *Magn Reson Med* 2010;63:194–206 CrossRef Medline
- Wang Y, Spincemaille P, Liu Z, et al. **Clinical quantitative susceptibility mapping (QSM): biometal imaging and its emerging roles in patient care.** *J Magn Reson Imaging* 2017;46:951–71 CrossRef Medline
- Langkammer C, Liu T, Khalil M, et al. **Quantitative susceptibility mapping in multiple sclerosis.** *Radiology* 2013;267:551–59 CrossRef Medline
- Stuber C, Pitt D, Wang Y. **Iron in multiple sclerosis and its noninvasive imaging with quantitative susceptibility mapping.** *Int J Mol Sci* 2016;17 CrossRef Medline
- Wisniewski C, Ramanan S, Olesik J, et al. **Quantitative susceptibility mapping (QSM) of white matter multiple sclerosis lesions: interpreting positive susceptibility and the presence of iron.** *Magn Reson Med* 2015;74:564–70 CrossRef Medline
- Filippi M, Rocca MA, Ciccarelli O, et al; MAGNIMS Study Group. **MRI criteria for the diagnosis of multiple sclerosis: MAGNIMS consensus guidelines.** *Lancet Neurol* 2016;15:292–303 CrossRef Medline
- Absinta M, Sati P, Schindler M, et al. **Persistent 7-Tesla phase rim predicts poor outcome in new multiple sclerosis patient lesions.** *J Clin Invest* 2016;126:2597–609 CrossRef Medline
- Yao Y, Nguyen TD, Pandya S, et al. **Combining quantitative susceptibility mapping with automatic zero reference (QSM0) and myelin water fraction imaging to quantify iron-related myelin damage in chronic active MS lesions.** *AJNR Am J Neuroradiol* 2018;39:303–10 CrossRef Medline
- Li JQ, Chang SX, Liu T, et al. **Reducing the object orientation dependence of susceptibility effects in gradient echo MRI through quantitative susceptibility mapping.** *Magn Reson Med* 2012;68:1563–69 CrossRef Medline
- Zhou D, Liu T, Spincemaille P, et al. **Background field removal by solving the Laplacian boundary value problem.** *NMR Biomed* 2014; 27:312–19 CrossRef Medline
- Zhang Y, Gauthier SA, Gupta A, et al. **Longitudinal change in magnetic susceptibility of new enhanced multiple sclerosis (MS) lesions measured on serial quantitative susceptibility mapping (QSM).** *J Magn Reson Imaging* 2016;44:426–32 CrossRef Medline
- Zhang Y, Gauthier SA, Gupta A, et al. **Quantitative susceptibility mapping and R2\* measured changes during white matter lesion development in multiple sclerosis: myelin breakdown, myelin debris degradation and removal, and iron accumulation.** *AJNR Am J Neuroradiol* 2016;37:1629–35 CrossRef Medline
- Zhang S, Nguyen TD, Zhao Y, et al. **Diagnostic accuracy of semiautomatic lesion detection plus quantitative susceptibility mapping in the identification of new and enhancing multiple sclerosis lesions.** *Neuroimage Clin* 2018;18:143–48 CrossRef Medline
- Chen W, Gauthier SA, Gupta A, et al. **Quantitative susceptibility mapping of multiple sclerosis lesions at various ages.** *Radiology* 2014;271:183–92 CrossRef Medline
- Bagnato F, Hametner S, Yao B, et al. **Tracking iron in multiple sclerosis: a combined imaging and histopathological study at 7 Tesla.** *Brain* 2011;134(Pt 12):3602–15 CrossRef Medline
- Yao B, Ikonomidou VN, Cantor FK, et al. **Heterogeneity of multiple sclerosis white matter lesions detected with T2\*-weighted imaging at 7.0 Tesla.** *J Neuroimaging* 2015;25:799–806 CrossRef Medline
- Dal-Bianco A, Grabner G, Kronnerwetter C, et al. **Slow expansion of multiple sclerosis iron rim lesions: pathology and 7 T magnetic resonance imaging.** *Acta Neuropathol* 2017;133:25–42 CrossRef Medline
- Kaunzner UW, Kang Y, Zhang S, et al. **Quantitative susceptibility mapping identifies inflammation in a subset of chronic multiple sclerosis lesions.** *Brain* 2019;142:133–45 CrossRef Medline
- Deh K, Kawaji K, Bulk M, et al. **Multicenter reproducibility of quantitative susceptibility mapping in a gadolinium phantom using MEDI+0 automatic zero referencing.** *Magn Reson Med* 2019;81: 1229–36 CrossRef Medline
- Deh K, Nguyen TD, Eskreis-Winkler S, et al. **Reproducibility of quantitative susceptibility mapping in the brain at two field strengths from two vendors.** *J Magn Reson Imaging* 2015;42:1592–600 CrossRef Medline
- Liu Z, Spincemaille P, Yao Y, et al. **MEDI+0: morphology enabled dipole inversion with automatic uniform cerebrospinal fluid zero reference for quantitative susceptibility mapping.** *Magn Reson Med* 2018;79:2795–803 CrossRef Medline
- Jenkinson M, Bannister P, Brady M, et al. **Improved optimization for the robust and accurate linear registration and motion correction of brain images.** *Neuroimage* 2002;17:825–41 CrossRef Medline
- Gaitán MI, Shea CD, Evangelou IE, et al. **Evolution of the blood-brain barrier in newly forming multiple sclerosis lesions.** *Ann Neurol* 2011;70:22–29 CrossRef Medline
- Deh K, Ponath GD, Molvi Z, et al. **Magnetic susceptibility increases**

- as diamagnetic molecules breakdown: myelin digestion during multiple sclerosis lesion formation contributes to increase on QSM. *J Magn Reson Imaging* 2018;48:1281–87 CrossRef Medline
25. Kuhlmann T, Ludwin S, Prat A, et al. **An updated histological classification system for multiple sclerosis lesions.** *Acta Neuropathol* 2017;133:13–24 CrossRef Medline
  26. Frischer JM, Bramow S, Dal-Bianco A, et al. **The relation between inflammation and neurodegeneration in multiple sclerosis brains.** *Brain* 2009;132:1175–89 CrossRef Medline
  27. Prineas JW, Kwon EE, Cho ES, et al. **Immunopathology of secondary-progressive multiple sclerosis.** *Ann Neurol* 2001;50:646–57 CrossRef Medline
  28. Singh S, Dallenga T, Winkler A, et al. **Relationship of acute axonal damage, Wallerian degeneration, and clinical disability in multiple sclerosis.** *J Neuroinflammation* 2017;14:57 CrossRef Medline
  29. Stephenson E, Nathoo N, Mahjoub Y, et al. **Iron in multiple sclerosis: roles in neurodegeneration and repair.** *Nat Rev Neurol* 2014;10:459–68 CrossRef Medline
  30. Mehta V, Pei W, Yang G, et al. **Iron is a sensitive biomarker for inflammation in multiple sclerosis lesions.** *PLoS One* 2013;8:e57573 CrossRef Medline
  31. Hametner S, Wimmer I, Haider L, et al. **Iron and neurodegeneration in the multiple sclerosis brain.** *Ann Neurol* 2013;74:848–61 CrossRef Medline
  32. Lassmann H. **The pathologic substrate of magnetic resonance alterations in multiple sclerosis.** *Neuroimaging Clin N Am* 2008;18:563–76 CrossRef Medline
  33. Maggi P, Absinta M, Grammatico M, et al. **Central vein sign differentiates multiple sclerosis from central nervous system inflammatory vasculopathies.** *Ann Neurol* 2018;83:283–94 CrossRef Medline
  34. Nguyen TD, Deh K, Monohan E, et al. **Feasibility and reproducibility of whole brain myelin water mapping in 4 minutes using fast acquisition with spiral trajectory and adiabatic T2prep (FAST-T2) at 3 Tesla.** *Magn Reson Med* 2016;76:456–65 CrossRef Medline
  35. Magliozzi R, Reynolds R, Calabrese M. **MRI of cortical lesions and its use in studying their role in MS pathogenesis and disease course.** *Brain Pathol* 2018;28:735–42 CrossRef Medline
  36. Bian W, Tranvinh E, Tourdias T, et al. **In vivo 7T MR quantitative susceptibility mapping reveals opposite susceptibility contrast between cortical and white matter lesions in multiple sclerosis.** *AJNR Am J Neuroradiol* 2016;37:1808–15 CrossRef Medline

# Susceptibility-Weighted MR Imaging Hypointense Rim in Progressive Multifocal Leukoencephalopathy: The End Point of Neuroinflammation and a Potential Outcome Predictor

M.M Thurnher, J. Boban, A. Rieger, and E. Gelpi



## ABSTRACT

**BACKGROUND AND PURPOSE:** Progressive multifocal leukoencephalopathy (PML) represents a life-threatening demyelinating disorder of the brain caused by reactivation of a rare opportunistic infection with *JC Polyomavirus*. The aims of this study were to describe the incidence of a susceptibility-weighted imaging hypointense rim in patients with multifocal leukoencephalopathy and to explore the histologic correlates and prognostic value of the rim with regard to the clinical outcome.

**MATERIALS AND METHODS:** This retrospective study included 18 patients with a definite diagnosis of progressive multifocal leukoencephalopathy. Ten patients were HIV-positive, 3 patients had natalizumab-associated progressive multifocal leukoencephalopathy, 1 patient had multiple myeloma, 3 patients had a history of lymphoma, and 1 was diagnosed with acute myeloid leukemia. Patients were divided into short- (up to 12 months) and long-term (>12 months) survivors. A total of 93 initial and follow-up MR imaging examinations were reviewed. On SWI, the presence and development of a hypointense rim at the periphery of the progressive multifocal leukoencephalopathy lesions were noted. A postmortem histologic examination was performed in 2 patients: A rim formed in one, and in one, there was no rim.

**RESULTS:** A total of 73 progressive multifocal leukoencephalopathy lesions were observed. In 13 (72.2%) patients, a well-defined thin, linear, hypointense rim at the periphery of the lesion toward the cortical side was present, while in 5 (27.8%) patients, it was completely absent. All 11 long-term survivors and 2 short-term survivors presented with a prominent SWI-hypointense rim, while 5/7 short-term survivors did not have this rim.

**CONCLUSIONS:** The thin, uniformly linear, gyriform SWI-hypointense rim in the parasial U-fibers in patients with definite progressive multifocal leukoencephalopathy might represent an end-point stage of the neuroinflammatory process in long-term survivors.

**ABBREVIATIONS:** *JCV* = *JC Polyomavirus*; PML = progressive multifocal leukoencephalopathy

Progressive multifocal leukoencephalopathy (PML) is an infectious demyelinating disease of the central nervous system, caused by reactivation and replication of the *JC Polyomavirus* (*JCV*).<sup>1</sup> Although PML was traditionally associated with HIV/AIDS, a shift toward patients on immunomodulation therapy has been observed in the past decade.<sup>2</sup> Furthermore, PML has also

been reported in patients with immune deficits associated with hematologic disorders.<sup>3,4</sup> The MR imaging features of PML include single or multiple T2-weighted and FLAIR-hyperintense white matter lesions.<sup>5,6</sup> Lesion borders are usually sharply demarcated toward the gray matter and blurred toward the deep white matter or ventricles, with absent or only faint contrast enhancement.<sup>7</sup> On diffusion-weighted imaging, a high-signal-intensity rim of restricted diffusion that represents active demyelination has been described.<sup>8</sup> To date, no specific features on conventional MR images have been identified as predictive of patient survival.<sup>9</sup>

Recently, the presence of a dark rim adjacent to the cortex or in the deep cortical layers on susceptibility-weighted imaging was reported in 2 patients with PML.<sup>10</sup> Data based on quantitative susceptibility mapping of the lesions suggested a paramagnetic (blood product or nonheme iron deposits) effect.<sup>11</sup> However, the mechanism that led to the susceptibility change remains unclear, because no histologic correlation was performed. SWI is a recently introduced MR imaging technique that has been used to

Received March 5, 2019; accepted after revision April 9.

From the Departments of Biomedical Imaging and Image-Guided Therapy (M.M.T., J.B.) and Dermatology (A.R.) and Institute of Neurology (E.G.), University Hospital Vienna, Medical University of Vienna, Vienna, Austria; and Neurological Tissue Bank of the Biobanc-Hospital Clinic-Institut d'Investigacions Biomediques August Pi i Sunyer (E.G.), Barcelona, Spain. Dr Boban's permanent address is University of Novi Sad, Faculty of Medicine, Novi Sad, Serbia.

Please address correspondence to Majda M. Thurnher, MD, University Hospital Vienna, Department of Biomedical Imaging and Image-Guided Therapy, Medical University of Vienna, Waehringer Guertel 18–20, A-1090 Vienna, Austria; e-mail: majda.thurnher@meduniwien.ac.at

Indicates article with supplemental on-line table.

Indicates article with supplemental on-line photo.

<http://dx.doi.org/10.3174/ajnr.A6072>

evaluate hemorrhage, quantify brain iron content, and identify brain calcifications.<sup>12</sup>

The aims of this retrospective study were to describe the incidence of an SWI-hypointense rim in patients with PML, to elucidate the histologic correlate of this rim, and to explore the prognostic value of the observed SWI features with regard to the clinical outcome.

## MATERIALS AND METHODS

### Study Population

A total of 18 consecutive patients with a definite diagnosis of PML (13 male and 5 female patients), with an average age of 50.56 years (range, 26–75 years) who underwent MR imaging of the brain at our institution from September 2009 to December 2018 were included in this institutional review board (Ethics Committee of the Medical University Vienna)-approved, retrospective study. Patients with no SWI in any of the MR imaging examinations were excluded. Ten (55.6%) patients were HIV-positive, 3 (16.7%) had natalizumab-associated PML, 1 patient (5.6%) had multiple myeloma, 3 patients (16.7%) had lymphoma, and 1 patient (5.6%) had acute myeloid leukemia and bone marrow transplantation. Of the 3 patients with lymphoma, 1 patient had large-cell lymphoma, 1 patient had small-cell B-cell lymphoma in remission, 1 patient was being treated with rituximab, and 1 patient had non-Hodgkin lymphoma. In 1 patient, herpes simplex virus type 2 encephalitis was also diagnosed, and 5 patients had a chronic coinfection with the hepatitis C virus. The diagnosis of definite PML in all patients was established on the basis of clinical data, imaging findings, and detection of DNA copies of the JCV in the CSF using the polymerase chain reaction, according to the American Academy of Neurology criteria (American Academy of Neurology guidelines).<sup>13</sup>

For HIV-positive patients, we included the following clinical data: current and nadir CD4 count, plasma viral load, duration of the HIV infection; neurologic signs and symptoms at the PML onset; and duration of antiretroviral therapy. In 2 HIV-negative patients, the neurologic signs and symptoms and the time range between the onset of PML and the underlying disease were noted. For natalizumab-associated PML, we included the following clinical data: the year of the diagnosis of multiple sclerosis and the duration of natalizumab therapy.

Patients were classified as long- or short-term survivors, with a survival time of up to 12 months for short-term survivors and longer than 12 months for long-term survivors.

### MR Imaging Protocol

Ninety-one MR imaging examinations were performed in 18 patients on different clinical MR imaging scanners (Avanto, Siemens, Erlangen, Germany, 1.5T; Tim Trio, Siemens, 3T; Ingenia, Philips Healthcare, Best, the Netherlands, 1.5T; Achieva, Philips Healthcare, 3T). The MR imaging protocol included the following sequences: axial FLAIR, coronal T2-weighted, axial T1-weighted, and axial diffusion-weighted MR imaging in all patients. Postcontrast T1WI was performed in all patients (82/91 examinations). SWI was performed in all patients (74/91 examinations). Susceptibility-weighted imaging was performed with the following parameters: FOV = 230 × 190 × 130 mm (ante-

rior-posterior × right-left × height-feet), voxel size = 0.6 × 0.6 × 1 mm, reconstruction matrix = 960, TE/TR = 7.12/31 ms, flip angle = 17° with no water or fat suppression used (3T MR imaging unit, Tim Trio). Parameters for the SWI sequence on the 1.5T MR imaging unit (Avanto) were the following: FOV = 230 × 186 × 150 mm, voxel size = 0.85 × 1 × 2 mm, reconstruction matrix = 576, TE/TR = 12/35 ms, flip angle = 20° with no water or fat suppression.

### Image Analysis

Overall, 91 MR imaging examinations were analyzed, with a mean of 4.17 follow-up imaging studies per patient (range, 0–11 studies).

All imaging studies were analyzed independently on a digital workstation by 2 readers and in a final consensus read (M.M.T., J.B.). The morphologic findings of lesions were described, including the lesion location, the size and number, and lesion features on pre- (T2WI, FLAIR, T1WI, DWI) and postcontrast T1WI. On SWI, the presence or absence of a hypointense rim at the periphery of the PML lesions was noted. The development of this rim with time was estimated, compared with prior images, and expressed in weeks. In addition, the correlation of the onset of an SWI-hypointense rim, DWI abnormalities, and the presence of contrast enhancement was explored.

### Neuropathology

A postmortem neuropathologic examination was performed in 2 patients (patients 2 and 16 in the On-line Table). Formalin-fixed and paraffin-embedded tissue blocks from multiple brain areas, including a whole, representative hemispheric section, were processed for conventional histologic and immunohistochemical stains. Five- $\mu$ m-thick sections were stained with hematoxylin-eosin, as well as Klüver-Barrera (Luxol fast blue and Nuclear fast red) for the labeling of myelin sheaths, and, in selected areas, with Prussian blue for the detection of iron. Immunohistochemistry was applied for the detection of the JCV and for the evaluation of astroglia (glial fibrillary acidic protein, GFAP; Dako, Glostrup, Denmark) and microglia (HLA-DR; Dako).

### Statistical Analysis

Descriptive statistics were used for various findings on MR imaging. For categorical data, we used frequencies and percentages, while for continuous data, range and median values were used. Survival was estimated using Kaplan-Meier estimates. The results are presented in a pictorial-review format.

## RESULTS

### Clinical Data

All patients fulfilled the American Academy of Neurology criteria for definite PML. Among HIV-positive subjects, the median duration of HIV infection before the onset of PML was 5.88 years (range, 0–23 years), the mean nadir CD4+ was 89 cells/mL (range, 15–199 cells/mL), the mean current CD4+ T-cell count (at the onset of PML) was 120.4 cells/mL (range, 15–292 cells/mL), and the mean viral load at the time of PML diagnosis and before combination antiretroviral therapy (cART) initiation was 3.83 IU/mL (range, 2.59–6.04 IU/mL) and it was 1.29 IU/mL (below the

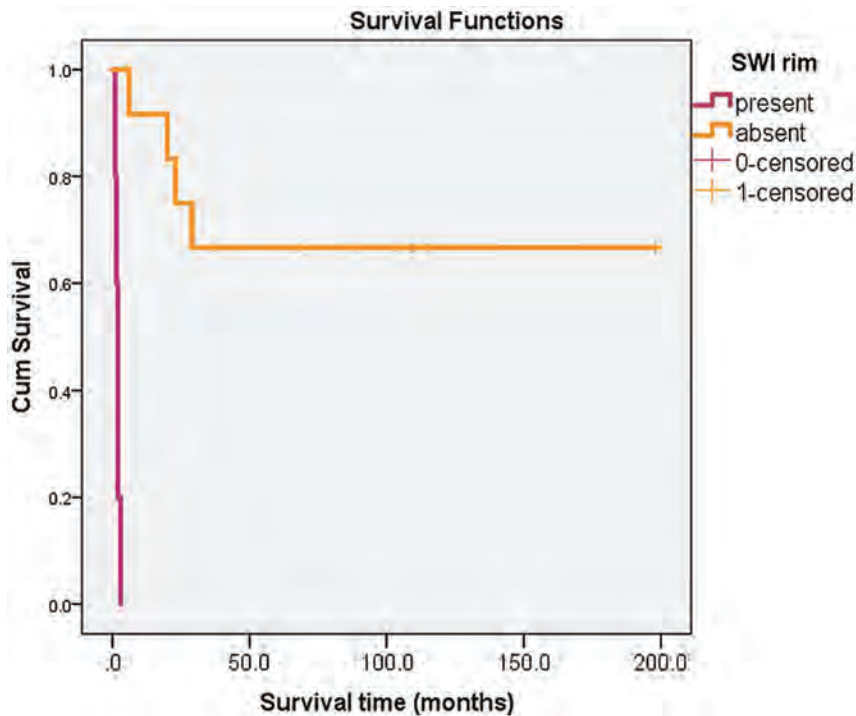


**FIG 1.** Kaplan-Meier survival analysis, with differences in survival and outcome between patients with (in purple) and without (in orange) an SWI-hypointense rim.

detection level) after cART initiation. In 4 (40%) patients, PML was the initial manifestation of the HIV infection/AIDS.

Neurologic symptoms at presentation are listed in the On-line Table.

Three patients (18.75%) were receiving HAART before the PML diagnosis (median duration of cART was 5.33 years; range, 3–9 years). In all patients, DNA copies of the *JCV* were detected in the CSF. One patient presented with B-cell chronic lymphocytic leukemia. In 1 patient with acute myeloid leukemia and bone marrow transplantation, the diagnosis of PML was made 3 months after the bone marrow transplantation. One patient was under immunomodulatory therapy for multiple myeloma. Of the 3 patients with natalizumab PML, all had relapsing-remitting MS diagnosed 5–12 years (mean, 8.3 years) before the onset of PML. The duration of natalizumab therapy was 3.6 years (4 years, 3 years, 3 years, respectively).

Seven patients were classified as short-term survivors, with a mean survival time of 2.93 months (range, 1–6 months). The cause of death was PML in 5 patients, and 1 patient died due to a non-PML cause (lung embolism). One short-term survivor (with a defined SWI-hypointense rim) has survived 5 months and is alive and stable at the moment. In 11 patients classified as long-term survivors, the mean survival time was 81.82 months (range, 20–198 months).

The results of the survival analysis clearly demonstrate differences in survival and outcome between patients with (in purple) and without (in orange) an SWI-hypointense rim (Fig 1).

### MR Imaging Findings

A total of 73 PML lesions were observed in 18 patients, involving the frontal (31/42.4%), parietal (9/12.3%), temporal (5/6.8%),

and occipital (6/8.2%) lobes, and the insular region (4/5.5%), the external capsule (1/1.4%), the internal capsule (2/2.8%), the thalamus (1/1.4%), the corpus callosum (1/1.4%), the pons (1/1.4%), and the cerebellum (9/12.3%). All lesions had typical MR imaging features—that is, high signal on T2WI/FLAIR and marked low signal on T1WI. Only 2 of 18 patients (11.1%) showed a peripheral rim of restricted diffusion on DWI with corresponding low ADC values.

Contrast enhancement was present in 10/18 (55.6%) patients. According to the enhancement pattern, patients were divided into 4 groups: 1) “No enhancement” was seen in 8/18 (44.4%) patients (2 patients with lymphoma, 2 with MS, 1 patient with multiple myeloma, and 3 HIV-positive patients); 2) “faint enhancement” was detected in 5/18 (27.8%) patients (3 HIV-positive patients, 1 patient with MS, and 1 patient with lymphoma); 3) an “inflammatory pattern” was seen in 2/18 (11.2%) pa-

tients (1 HIV-positive patient, 1 patient with acute myeloid leukemia and bone marrow transplantation); and 4) an “immune reconstitution inflammatory syndrome pattern” was present in 1 of 18 (5.6%) patients (an HIV-positive patient).

### SWI Findings

SWI findings were available for all 18 patients. On SWI, a well-defined thin, linear, hypointense rim at the periphery of the lesion, located toward the cortical side (Fig 2), was present in 13/18 patients (72.2%), while in 5 patients (27.8%), the rim was completely absent (Fig 3). Of 16 patients in whom SWI was performed within the first 2 months after the PML diagnosis, the presence of an SWI-hypointense rim was detected in 11 patients, with the mean time to formation of 2.8 weeks (range, 1–8 weeks). In 1 patient, the first signs of an SWI-hypointense rim were observed 13 weeks after the initial MR imaging examination, but the follow-up examination was not performed within the first 2 months. In addition, in 1 patient, the first SWI data were available 6 years after the diagnosis, with a positive SWI-hypointense rim (burn-out lesion). The SWI-hypointense rim gradually increased in thickness with time, spreading continuously along the juxtacortical white matter following the gyral architecture.

### Correlation of SWI and Contrast Enhancement and DWI Findings

At the time of the first appearance of the SWI dark rim, only 4 patients had contrast enhancement. However, this contrast enhancement was not located at the SWI-hypointense rim, but either on the peripheral rim of the PML lesion toward the ventricle or closer to the center of the PML lesion (faint or dotted enhancement). Contrast enhancement was not observed in the region of

the SWI-hypointense rim in any of the examinations in which postcontrast T1WI was available for analysis.

In 2 patients (patients 8 and 12) in whom a DWI-hyperintense rim was present, SWI did not show a dark rim. In 1 patient (patient 12) in whom follow-up was available, 3 weeks after the initial examination, the DWI rim disappeared and the SWI rim was detected (Fig 4).

### Neuropathologic Findings

A neuropathologic examination was performed in 2 patients, (patients 2 and 16 in the On-line Table); in 1 patient, an SWI rim was

present (patient 2), but no SWI rim was detected in the second patient (patient 16). Patient 2, with a survival time of 6 months, died of multiorgan dysfunction syndrome, and in patient 16, the cause of death was PML.

In patient 2 (On-line Figure A1), gross examination showed multiple white matter lesions in both hemispheres, some of which were softened and yellowish and were most pronounced at the frontal regions with an already necrotic aspect. Histology showed features of an extensive inflammatory demyelinating pathology with prominent loosening of white matter, loss of myelin sheaths with relatively preserved axons, abundant macrophages, and perivascular lymphocytic infiltrates. No parenchymal bleeding was observed.

In patient 16 (On-line Figure B1), gross examination showed multiple and partly confluent and softened white matter lesions mainly in the left-brain hemisphere, extending from the frontal to the parietotemporal regions, with relative preservation of the overlying cortex. Histology confirmed the inflammatory and demyelinating nature of the lesion (On-line Figure B5). No parenchymal bleeding was detected.

In patient 2 with the faint SWI rim, the number of PML-infected cells was much lower than in the patient without an SWI rim (On-line Figure A5 and B5). In addition, there was much more prominent astrogliosis and microglial activation in the deep cortical layers and at the cortical-subcortical junction, including the U-fibers (On-line Figure A6 and A7). This feature was observed not only in areas overlying PML lesions but also in areas without focal lesions, but with diffuse white matter pallor and moderate gliosis. In both cases, a Prussian blue stain was performed for the detection of iron deposits. In patient 2,

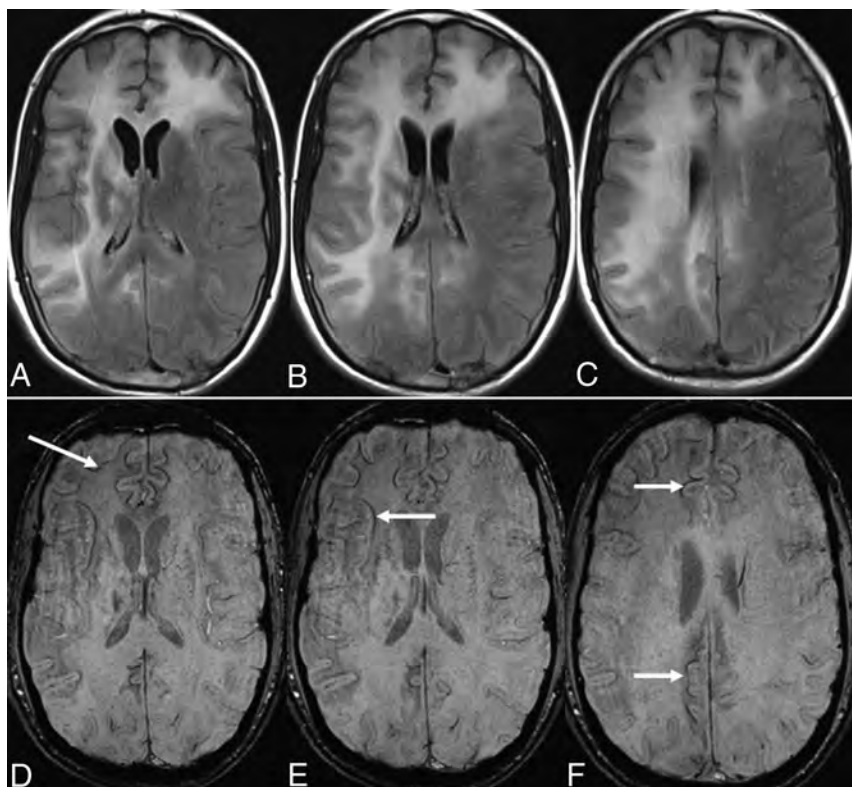


**FIG 2.** On axial FLAIR images (A–C), multifocal PML lesions are observed in both frontal lobes, the capsula interna and externa, and the right parietal lobe. A linear, relatively thin hypointense rim is observed on the cortical side of the lesions on axial SWI (D–F) in a long-term survivor (9 years, still alive).

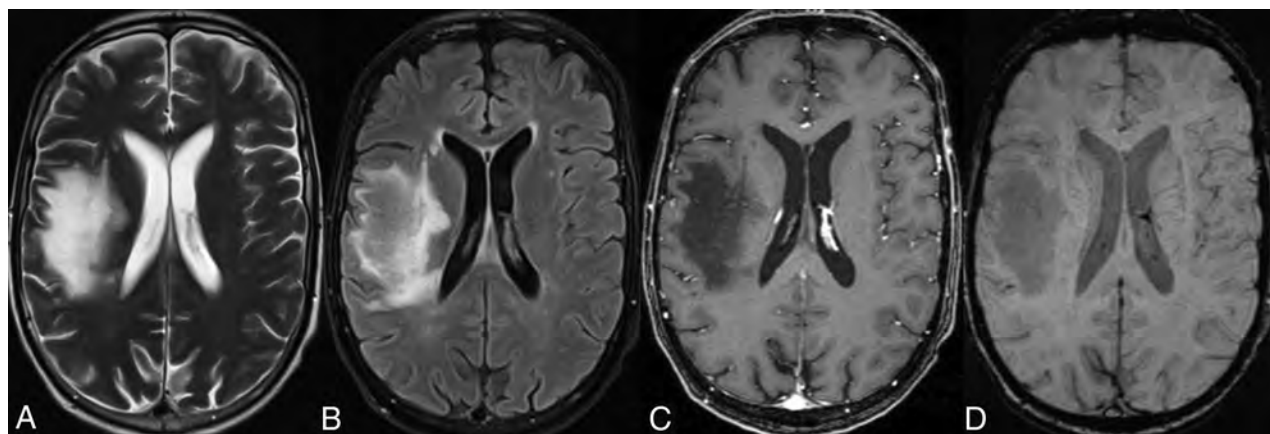


**FIG 3.** A typical T2-weighted (A) and FLAIR (B) hyperintense PML lesion is observed in the frontoparietal corona radiata on the right side. On the postcontrast T1-weighted axial image (C), only a faint enhancement pattern is observed. On the axial SWI (D), there are no signs of a gyriform hypointense rim. The patient was classified as a short-term survivor (11 weeks).

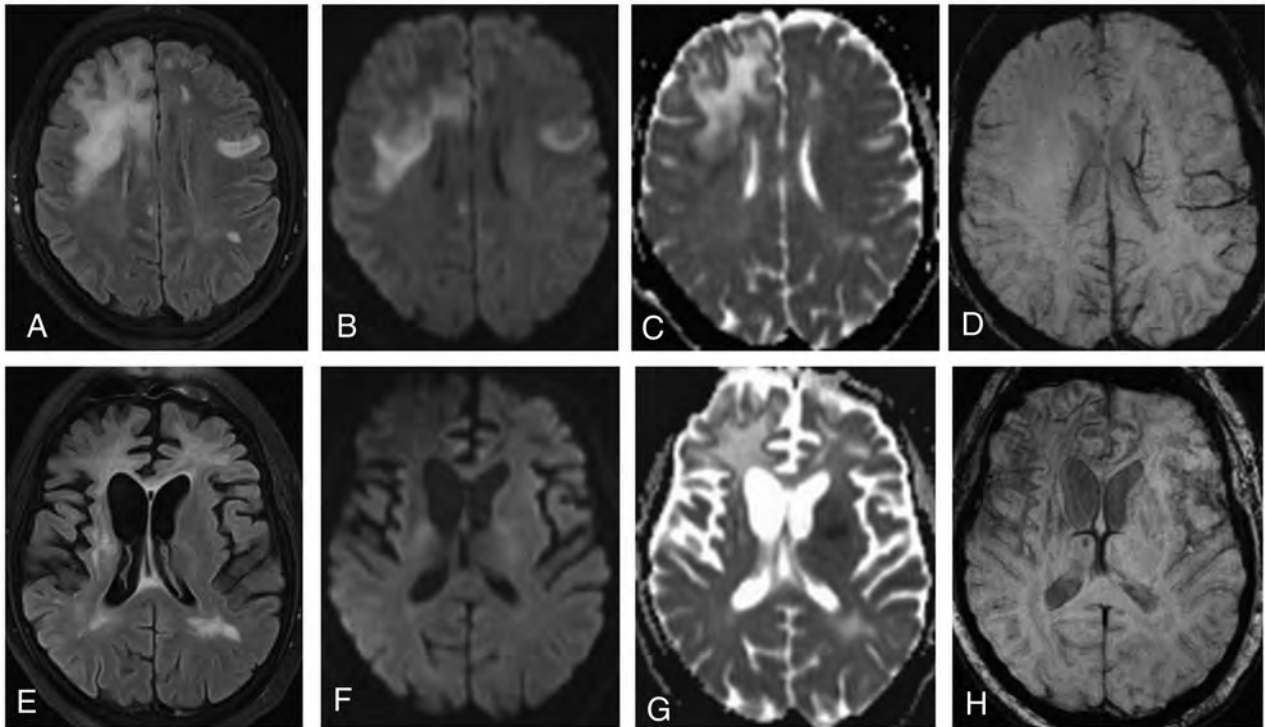


**FIG 4.** On an axial FLAIR image (A), bilateral high-signal-intensity lesions are detected. DWI clearly demonstrates a high-signal-intensity rim at the periphery of the lesion in the right frontal lobe on trace DWI (B), with low ADC values (C) indicating restricted diffusion. On SWI (D), no abnormalities are seen. On follow-up MR imaging (3 months later), atrophic changes with dilation of the ventricles are observed in both hemispheres (more prominent in the right) (E). On DWI/ADC (F and G), no hyperintense rim is present. On SWI (H), a dark rim is clearly visible.

abundant blue pigment was observed within actively demyelinating lesions (On-line Figure A3, triple asterisks). In the surrounding areas, diffuse homogeneous cytoplasmic staining of pericapillary cells was also observed (On-line Figure A3, double asterisks). In contrast, around vessels with moderate chronic gliosis, there was glial pigment and non-Prussian blue pigment alternating with Prussian blue pigment (On-line Figure A3, asterisk). In patient 16, fewer perivascular Prussian blue-positive areas were detected.

## DISCUSSION

PML represents a life-threatening demyelinating disease of the brain as a result of infection with the *JCV*.<sup>14</sup> Since the AIDS epidemic, PML was reported exclusively in association with HIV, but more recently, there has been a shift toward other immunosuppressive conditions, including patients on immune-suppression therapy and patients with long-standing autoimmune inflammatory or hematologic malignancies.<sup>15,16</sup> In addition, several case reports on immunocompetent patients developing PML have also been published.<sup>17,18</sup>

A relatively thin, uniformly linear SWI-hypointense rim was observed in 13 of 18 patients with PML in our study. The rim exclusively affected the U-fibers, following the cortical architecture, and did not correlate with other MR imaging findings. No signs of susceptibility changes were detected in the center of the PML lesions or on the side toward the deep white matter and the ventricle. In addition, infratentorial PML lesions showed no SWI-hypointense rim formation. Eleven of 13 patients in whom the SWI-hypointense rim was present were long-term survivors,

whereas in 5 of 7 short-term survivors, there was no SWI-hypointense rim detected. One of our short-term survivors died due to a non-PML cause, and the SWI-hypointense rim in this particular patient could not be seen in correlation with the short survival (patient 2 in the On-line Table). One short-term survivor is still alive (patient 17 in the On-line Table), and because the cutoff point of 12 months has not yet been reached, this patient was classified as a short-term survivor, though a positive clinical outcome is highly likely at the moment.

The detection of the linear hypointense rim in the region of the U-fibers on SWI sequences has only recently been described and was postulated to be a specific finding in PML lesions.<sup>10</sup> Later, the same group reported the presence of such a rim in patients with chronic cerebral infarction and after encephalitis.<sup>19</sup> The etiology of this rim was unresolved and was not fully explained. Carra-Dalliere et al<sup>11</sup> suggested that an SWI-hypointense rim in patients with PML could be a consequence of paramagnetic material deposits, based on quantitative susceptibility mapping. In both studies, no histologic correlation of SWI findings was available.

Several morphologic phenomena occur at the edges of a PML lesion and beneath juxtacortical areas, mainly primary oligodendroglial dysfunction by *JCV* infection and consequent myelin degeneration, microglial activation, astroglial proliferation, and axonal impairment. Axonal damage can produce retrograde neuronal degeneration and lead to progressive cortical atrophy. It is known that PML also involves the U-fibers. Chronically activated glial cells and microglia/macrophages may contain high levels of iron and pigment within their cytoplasm. In addition, blood-

brain barrier disruption caused by PML may lead to leakage of heme products into the perivascular space. Although diffuse homogeneous cytoplasmic staining of cells reflects the presence of ferritin, hemosiderin shows the typical granular particles in lysosomes. We found severe reactive changes at the corticosubcortical boundary surrounding the PML lesions, which were more prominent in the patient with a longer survival. We also observed a higher, but not exclusive, ferritin and hemosiderin content within the lesions in the patient with a longer survival than in the patient with a shorter survival, which was more abundant around small vessels and capillaries in the deep cortical layers and at the juxtacortical border.

A similar but less prominent SWI-hypointense rim was observed in the deep cortical layers of the precentral gyrus in patients with amyotrophic lateral sclerosis. On histopathologic studies, intracellular deposits of iron (in the form of ferritin) were confirmed in reactive microglial cells, located in the middle and deep layers of the motor cortex, in areas that were affected by neuronal loss and axonal degeneration.<sup>20</sup> Kim et al<sup>21</sup> recently reported ferritin accumulation in proliferated microglial cells in severely demyelinated U-fibers in patients with adult-onset leukoencephalopathy, with axonal spheroids and pigmented glia, as well as treelike SWI hypointensities in the subcortical white matter. In recently published studies by van Duijn et al<sup>22</sup> and Bulk et al,<sup>23</sup> a bandlike T2\*-hypointense cortical rim was observed on 7T in a subset of patients with Alzheimer disease, which was believed to be derived from increased myelin-associated, nonheme iron in the middle layers of the cortex and Baillarger lines and was also found in disintegrated axons and microglial cells.

One possible explanation for the specific location of iron deposition in our patients with PML and in the above-mentioned disorders is the fact that subcortical U-fibers have a greater iron content than both cerebral gray and white matter, due to the high density of iron-rich oligodendrocytes, and are considered slow metabolic fibers with a slow myelin turnover. In addition, the region of U-fibers has long medullary arterioles and venules in a gyriform distribution.<sup>24</sup>

The other important question to address is the cause of iron deposition in PML. In 1981, Konijn et al<sup>25</sup> had already suggested that ferritin accumulation could be a nonspecific, acute-phase reactant in response to inflammation. It seems that accumulating iron in proliferated microglial cells is not a specific finding in any of the above-mentioned neurodegenerative diseases, but rather a pattern in progressive and long-standing neuroinflammation. The fact that siderin- and ferritin-laden macrophages were seen in the perivascular region, especially around the small capillaries at the gray-white matter interface, indicates the possibility of inflammation-induced blood-brain barrier disturbance, with extravasation of blood cells and subsequent perivascular deposition of iron and iron end products. If an SWI dark rim does, indeed, represent an effective chronic neuroinflammatory response to a brain injury, it should then be present in PML long-term survivors and could be considered a sign of end-stage inflammation. The absence of an SWI dark rim in our short-term survivors favors this hypothesis.

In a recently published study, a T1WI-hyperintense cortical signal on MR imaging has been reported in 61.2% of patients with

PML.<sup>26</sup> A hyperintense cortical signal was detected adjacent to subcortical PML lesions on precontrast T1-weighted MR images and resembled the SWI-hypointense rim seen in our patients. In addition, atrophy of the cortical area affected was reported in 96.7% of cases with hyperintense cortical signal. SWI was available in 15 of 49 patients in that particular study, and none of them had any SWI abnormality. On histology, hyperintense cortical signal areas were associated with striking *JCV*-associated demyelination of the cortical and subcortical U-fibers, heavy macrophage infiltration, and a pronounced reactive gliosis in the deep cortical layers.<sup>26</sup> There were neither microhemorrhages nor iron deposits in the postmortem histologic sections of our 2 patients with PML in whom histologic analysis was obtained.

The characteristic MR imaging finding suggestive of inflammation is the presence of contrast enhancement in a given lesion. In general, in HIV-related PML, enhancement is observed in only up to 15%. This is different for natalizumab-associated PML, in which enhancement will be present in 43% of cases.<sup>27</sup> In a recently described form of PML, called “inflammatory PML,” prominent enhancement along the perivascular spaces was observed.<sup>28</sup> These lesions show perivascular cuffing and inflammatory plasma cell infiltrates.<sup>29</sup> It was suggested that this PML form represents the fulminant, active, lytic infection of white matter cells caused directly by the *JCV*.

In our study, we could not establish a relationship between the presence of contrast enhancement and SWI-hypointense rim formation. In 2 of our short-term survivors, MR imaging findings were consistent with an inflammatory PML pattern, and neither of them developed an SWI-hypointense rim. Therefore, it seems likely that the SWI rim indicates a transitory BBB disturbance, rather than fulminant infection of oligodendrocytes, as seen in inflammatory PML.

The fact that, in 2 patients (patients 8 and 12 in the On-line Table), the presence of the peripheral rim of restricted diffusion was only present initially (as long as the SWI rim was not detected) and disappeared later with the formation of the SWI rim further confirms the hypothesis that the SWI rim represents the end-stage of neuroinflammation. Further prospective studies with a clearly defined time period for the follow-up MR imaging examination may deliver data that will indicate the time range needed for an SWI rim to develop in long-term survivors.

One limitation of our study is the relatively small number of patients, which does not allow an estimation of the real incidence of an SWI dark rim in patients with PML. Ideally, prospective data should be collected from several institutions. Another limitation is the rather limited histopathologic data of only 2 patients. However, the patient with a dark SWI rim died soon after the PML diagnosis from a non-PML-related disease; thus, the changes observed on histology most probably reflect findings in long-term survivors.

## CONCLUSIONS

The formation of a thin, uniformly linear, gyriform SWI-hypointense rim in the region of the paralesional U-fibers in patients with PML seems to represent an end-point stage of the neuroinflammatory process in long-term survivors. Its morphologic correlate could be related to the chronic gli-inflammatory reaction, with

increased iron content in microglia, oligodendroglia, and astroglia, and is attributable to BBB leakage along the perivascular spaces.

## ACKNOWLEDGMENTS

We are grateful to Mrs Irene Ebner of the Institute of Neurology of the Medical University of Vienna for the excellent technical neuropathologic work-up.

Disclosures: Majda M. Thurnher—UNRELATED: Royalties: Amirsys. Armin Rieger—UNRELATED: Payment for Lectures Including Service in Speakers Bureaus: MSD, Gilead Sciences, GlaxoSmithKline, Comments: presentations in several ad boards; Travel/Accommodations/Meeting Expenses Unrelated to Activities Listed: Gilead Sciences, MSD, GlaxoSmithKline, Comments: invitations to join several HIV/AIDS congresses.\* \*Money paid to the institution.

## REFERENCES

1. Fournier A, Martin-Blondel G, Lechapt-Zalcman E, et al. Immune reconstitution inflammatory syndrome unmasking or worsening AIDS-related progressive multifocal leukoencephalopathy: a literature review. *Front Immunol* 2017;8:577 CrossRef Medline
2. Carson KR, Focosi D, Major EQ, et al. Monoclonal antibody-associated progressive multifocal leukoencephalopathy in patients with rituximab, natalizumab, and efalizumab: a review from the Research on Adverse Drug Events and Reports (RADAR) project. *Lancet Oncol* 2009;10:816–24 CrossRef Medline
3. Gocmen R, Acar NP, Cagdas D, et al. Progressive multifocal leukoencephalopathy in a patient with lymphoma and presumptive hyper IgE syndrome. *J Neurovirol* 2017;23:632–36 CrossRef Medline
4. Al-Tawfiq JA, Banda RW, Daabil RA, et al. Progressive multifocal leukoencephalopathy (PML) in a patient with lymphoma treated with rituximab: a case report and literature review. *J Infect Public Health* 2015;8:493–97 CrossRef Medline
5. Thurnher MM, Donovan Post MJ. Neuroimaging in the brain in HIV-1-infected patients. *Neuroimaging Clin N Am* 2008;18:93–117, viii CrossRef Medline
6. Tan CS, Korálnik IJ. Progressive multifocal leukoencephalopathy and other disorders caused by JC virus: clinical features and pathogenesis. *Lancet Neurol* 2010;9:425–37 CrossRef Medline
7. Thurnher MM, Post MJ, Rieger A, et al. Initial and follow-up MR imaging findings in AIDS-related progressive multifocal leukoencephalopathy treated with highly active antiretroviral therapy. *AJNR Am J Neuroradiol* 2001;22:977–84 Medline
8. Narvid J, Rehani B, Talbot JF. Diagnostic performance of brain MRI in immune reconstitution inflammatory syndrome. *J Neuroimaging* 2016;26:303–08 CrossRef Medline
9. Post MJ, Thurnher MM, Clifford DB, et al. CNS-immune reconstitution inflammatory syndrome in the setting of HIV infection, Part I: overview and discussion of progressive multifocal leukoencephalopathy-immune reconstitution inflammatory syndrome and cryptococcal-immune reconstitution inflammatory syndrome. *AJNR Am J Neuroradiol* 2013;34:1297–307 CrossRef Medline
10. Miyagawa M, Maeda M, Umino M, et al. Low signal intensity in U-fiber identified by susceptibility-weighted imaging in two cases of progressive multifocal leukoencephalopathy. *J Neurol Sci* 2014; 344:198–202 CrossRef Medline
11. Carra-Dalliere C, Menjot de Champfleür N, Ayrignac X, et al. Quantitative susceptibility mapping suggests a paramagnetic effect in PML. *Neurology* 2015;84:1501–02 CrossRef Medline
12. Liu C, Li W, Tong KA, et al. Susceptibility-weighted imaging and quantitative susceptibility mapping in the brain. *J Magn Reson Imaging* 2015;42:23–41 CrossRef Medline
13. Berger JR, Aksamit AJ, Clifford DB, et al. PML diagnostic criteria: consensus statement from the AAN Neuroinfectious Disease Section. *Neurology* 2013;80:1430–38 CrossRef Medline
14. Pontillo G, Cocozza S, Lanzillo R, et al. Brain susceptibility changes in a patient with natalizumab-related progressive multifocal leukoencephalopathy: a longitudinal quantitative susceptibility mapping and relaxometry study. *Front Neurol* 2017;8: 294 CrossRef Medline
15. Davis MJ, Khan A, Royal W 3rd. Progressive multifocal leukoencephalopathy as the first manifestation of occult sarcoidosis: report and review of the literature. *Neurologist* 2013;19:26–29 CrossRef Medline
16. Sholten P, Krait P, Jacobs B. Posterior fossa progressive multifocal leukoencephalopathy: first presentation of an unknown autoimmune disease. *BMJ Case Rep* 2017;2017 CrossRef Medline
17. Grewal J, Dalal P, Bowman M, et al. Progressive multifocal leukoencephalopathy in a patient without apparent immunosuppression. *J Neurovirol* 2016;22:686–87 CrossRef Medline
18. Van de Kolk NM, Arts P, van Uden IW, et al. Progressive multifocal leukoencephalopathy in an immunocompetent patient. *Ann Clin Transl Neurol* 2016;3:226–32 CrossRef Medline
19. Umino M, Maeda M, Ii Y, et al. Low-signal-intensity rim on susceptibility-weighted imaging is not a specific finding to progressive multifocal leukoencephalopathy. *J Neurol Sci* 2016;362:155–59 CrossRef Medline
20. Kwan JY, Jeong SY, Van Gelderen P, et al. Iron accumulation in deep cortical layers accounts for MRI signal abnormalities in ALS: correlating 7 Tesla MRI and pathology. *PLoS One* 2012;7:e35241 CrossRef Medline
21. Kim M, Lee H, Cho HJ, et al. Pathologic correlation of paramagnetic white matter lesions in adult-onset leukoencephalopathy with axonal spheroids and pigmented glia. *J Neuropathol Exp Neurol* 2017; 76:924–28 CrossRef Medline
22. van Duijn S, Bulk M, van Duinen SG, et al. Cortical iron reflects severity of Alzheimer's disease. *J Alzheimers Dis* 2017;60:1533–45 CrossRef Medline
23. Bulk M, Abelmoula WM, Nabuurs RJA, et al. Post-mortem MRI and histology demonstrate differential iron accumulation and cortical myelin organization in early and late onset Alzheimer's disease. *Neurobiol Aging* 2018;62:231–42 CrossRef Medline
24. Birkel C, Carassiti D, Hussain F, et al. Assessment of ferritin content in multiple sclerosis brains using temperature-induced R<sub>2</sub> changes. *Magn Reson Med* 2018;79:1609–15 CrossRef Medline
25. Konijn AM, Carmel N, Levy R, et al. Ferritin synthesis in inflammation, II: mechanism of increased ferritin synthesis. *Br J Haematol* 1981;49:361–70 CrossRef Medline
26. Khoury MN, Alsop DC, Agnihotri SP, et al. Hyperintense cortical signal on magnetic resonance imaging reflects focal leukocortical encephalitis and seizure risk in progressive multifocal leukoencephalopathy. *Ann Neurol* 2014;75:659–69 CrossRef Medline
27. Brew BJ, Davies NWS, Cinque P, et al. Progressive multifocal leukoencephalopathy and other forms of JC virus disease. *Nat Rev Neurol* 2010;6:667–79 CrossRef Medline
28. Wattjes MP, Wijburg MT, Vennegoor A, et al; Dutch-Belgian Natalizumab-associated PML study group. MRI characteristics of early PML-IRIS after natalizumab treatment in patients with MS. *J Neurol Neurosurg Psychiatry* 2016;87:879–84 CrossRef Medline
29. Wattjes MP, Wijburg MT, van Eijk J, et al; Dutch-Belgian Natalizumab-associated PML study group. Inflammatory natalizumab-associated PML: baseline characteristics, lesion evolution and relation with PML-IRIS. *J Neurol Neurosurg Psychiatry* 2018;89:535–41 CrossRef Medline

# Thrombectomy with Conscious Sedation Compared with General Anesthesia: A DEFUSE 3 Analysis

C.J. Powers, D. Dornbos III, M. Mlynash, D. Gulati, M. Torbey, S.M. Nimjee, M.G. Lansberg, G.W. Albers, and M.P. Marks



## ABSTRACT

**BACKGROUND AND PURPOSE:** The optimal patient sedation during mechanical thrombectomy for ischemic stroke in the extended time window is unknown. The purpose of this study was to assess the impact of patient sedation on outcome in patients undergoing thrombectomy 6–16 hours from stroke onset.

**MATERIALS AND METHODS:** Endovascular Therapy Following Imaging Evaluation for Ischemic Stroke 3 (DEFUSE 3) was a multicenter, randomized, open-label trial of thrombectomy for ICA and M1 occlusions in patients 6–16 hours from stroke onset. Subjects underwent thrombectomy with either general anesthesia or conscious sedation at the discretion of the treating institution.

**RESULTS:** Of the 92 patients who were randomized to intervention, 26 (28%) underwent thrombectomy with general anesthesia and 66 (72%) underwent thrombectomy with conscious sedation. Baseline clinical and imaging characteristics were similar among all groups. Functional independence at 90 days was 23% for general anesthesia, 53% for conscious sedation, and 17% for medical management ( $P = .009$  for general anesthesia versus conscious sedation). Conscious sedation was associated with a shorter time from arrival in the angiosuite to femoral puncture (median, 14 versus 18 minutes;  $P = 0.05$ ) and a shorter time from femoral puncture to reperfusion (median, 36 versus 48 minutes;  $P = .004$ ). Sixty-six patients were treated at sites that exclusively used general anesthesia ( $n = 14$ ) or conscious sedation ( $n = 52$ ). For these patients, functional independence at 90 days was significantly higher in the conscious sedation subgroup (58%) compared with the general anesthesia subgroup (21%) ( $P = .03$ ).

**CONCLUSIONS:** Patients who underwent thrombectomy with conscious sedation in the extended time window experienced a higher likelihood of functional independence at 90 days, a lower NIHSS score at 24 hours, and a shorter time from femoral puncture to reperfusion compared with those who had general anesthesia. This effect remained robust in institutions that only treated patients with a single anesthesia technique.

**ABBREVIATIONS:** CS = conscious sedation; GA = general anesthesia; IQR = interquartile range

There is controversy regarding optimal anesthesia management during thrombectomy. Currently studied options include general anesthesia (GA), conscious sedation (CS), or local

anesthetic only. In their meta-analysis of 22 studies (3 randomized controlled trials and 19 observational studies) including 4716 patients, Brinjikji et al<sup>1</sup> reported higher odds of death and respiratory complications and lower odds of good functional outcomes after thrombectomy for patients who had GA. In contrast, 3 small randomized studies have not shown a difference in outcomes between GA and conscious sedation, though all these studies were performed using thrombectomy within the early time window (<6 hours).<sup>2–4</sup> The 2018 American Heart Association Guidelines for the early management of ischemic stroke recommend the selection of GA or conscious sedation based on individual patient risk factors, technical aspects of the procedure, and other clinical characteristics.<sup>5</sup> These guidelines are also based solely on studies of endovascular therapy in the early time window.

The Endovascular Therapy Following Imaging Evaluation for

Received January 29, 2019; accepted after revision April 1.

From the Departments of Neurological Surgery (C.J.P., D.D., S.M.N.) and Neurology (D.G.), Ohio State University Wexner Medical Center, Columbus, Ohio; Departments of Neurology and Neurological Science (M.M., M.G.L., G.W.A.) and Diagnostic Radiology (M.P.M.), Stanford University School of Medicine, Stanford, California; and Department of Neurology (M.T.), University of New Mexico, Albuquerque, New Mexico.

This research was supported financially by the National Institute of Neurologic Disorders and Stroke.

Please address correspondence to Ciarán J. Powers, MD, PhD, N1022 Doan Hall, 410 West 10th Ave, Columbus, OH 43220; e-mail: [ciaran.powers@osumc.edu](mailto:ciaran.powers@osumc.edu)

Indicates open access to non-subscribers at [www.ajnr.org](http://www.ajnr.org)

Indicates article with supplemental on-line table.

<http://dx.doi.org/10.3174/ajnr.A6059>

Ischemic Stroke 3 (DEFUSE 3) study showed that mechanical thrombectomy for ischemic stroke, between 6 and 16 hours from last known well, plus standard medical therapy resulted in better functional outcome than medical therapy alone for patients with internal carotid artery or proximal middle cerebral artery (M1) occlusion and a target mismatch profile on perfusion imaging.<sup>6</sup> The use of general anesthesia as opposed to conscious sedation during mechanical thrombectomy was at the discretion of the treating interventionalist.

In this substudy of the DEFUSE 3 trial, we explored the impact of anesthesia management on patient outcome after mechanical thrombectomy in the extended time window.

## MATERIALS AND METHODS

DEFUSE 3 was a multicenter, randomized, open-label, blinded end point trial of thrombectomy for ICA and M1 occlusions in patients who could be treated during an extended time window, 6–16 hours after they were last known well, and who had a favorable ratio between penumbra and core infarct. The local institutional review boards at each site approved the study, and informed consent was obtained from each patient's legal next of kin. Patients were eligible if they had an infarct volume of <70 mL, a ratio of volume of ischemic tissue to initial infarct volume of  $\geq 1.8$ , and an absolute volume of potentially reversible ischemia of  $\geq 15$  mL. Furthermore, patients had an occlusion of the cervical or intracranial internal carotid artery or the proximal middle cerebral artery on noninvasive vascular imaging. Patients with basilar artery occlusions were not included in this study. Ninety-two patients were randomized to the endovascular therapy group, and 90, to the medical therapy group.

The use of GA as opposed to CS during thrombectomy was at the discretion of the treating providers. The treating center recorded whether GA or CS was used and the reasons for choosing the method of sedation on the primary case report forms. The reasons for choosing GA over CS included routine preference for GA during thrombectomy, interventionalist preference, inability of patients to protect their airways, and excessive patient motion. Assignment of anesthesia choice was based on what was actually performed, not intention-to-treat.

The primary outcome in this analysis of the DEFUSE 3 study was functional independence (mRS score of 0–2) at 90 days, comparing GA with CS. Other outcomes included the odds ratio of functional independence at 90 days, median mRS scores at 90 days, NIHSS score at 24 hours and discharge, revascularization efficacy (TICI score), and procedural measures, including median times from symptom onset to imaging, imaging to arrival in the angi suite, arrival to femoral puncture, and puncture to reperfusion.

### Statistical Analysis

Continuous variables were compared using the Mann-Whitney *U* test for 2 groups or the Kruskal-Wallis test for 3 groups. We compared frequencies using the  $\chi^2$  test. Exact statistics were used when expected cell frequencies in a  $2 \times 2$  table were <5. We used logistic regression or ordinal logistic regression for the multivariable analysis with binary or ordinal outcome measures. Results of the ordinal logistic regression analyses were accepted only if the

proportionality test result was not significant. Significance was defined at  $\alpha < .05$ , and all tests were 2-sided. The multivariable regression analysis was adjusted for age, NIHSS score, serum glucose level, and time from last known well to randomization. Statistical analysis was performed with the SAS 9.4 (SAS Institute, Cary, North Carolina).

## RESULTS

Ninety-two patients were randomized to intervention, with 26 (28%) undergoing thrombectomy using GA and 66 (72%) undergoing thrombectomy with CS. There were only 4 patients with CS before GA (15% of 26 GA cases). Their rate of mRS 0–2 was not different from that in other patients with GA: 1/4 (25%) versus 5/22 (23%) ( $P = 1.0$ ). If we had assigned them to the CS group, then the rates of mRS 0–2 for CS versus pure GA would be 36/70 (51%) versus 5/22 (23%) ( $P = .02$ ). This is not meaningfully different compared with the rates of good outcome based on what was actually performed (53% versus 23%).

There were no significant differences among the GA, CS, and medical management (90 patients) groups in age, sex, median NIHSS score, affected hemisphere, or treatment with intravenous tPA (On-line Table). There were also no significant differences among the 3 groups in the imaging characteristics, including volume of ischemic core, volume of hypoperfusion lesion, occlusion site, or ASPECTS score on baseline CT (On-line Table). There were no differences in rates of good collaterals using the Modified Tan scale for the 131 patients who underwent CTA. There were no differences in the first blood pressures on arrival.

Additionally, there were no differences between the GA and CS groups in the history of atrial fibrillation, diabetes mellitus, hypercholesterolemia, myocardial infarction, or prior stroke (On-line Table). There was no difference in the baseline mRS 0–2 among these groups either (On-line Table).

The primary outcome of functional independence, defined as mRS 0–2 at 90 days, was 23% for GA, 53% for CS, and 17% for medical management (Table). The adjusted common odds ratio of functional independence based on multivariable regression analysis comparing GA versus CS was 0.27 (95% Confidence Interval = 0.09–0.75) ( $P = .01$ ). The median mRS score at 90 days was 3.5 (interquartile range [IQR] = 3–5) for thrombectomy with GA, 2 (IQR = 1–4) for thrombectomy with CS, and 4 (IQR = 3–6) with medical management ( $P < .001$  comparing all 3 groups;  $P = .05$  for GA versus CS; and  $P = .22$  for GA versus medical management) (Table and Figure). Additionally, the NIHSS score at 24 hours (median, 15.5 versus 8;  $P = .03$ ) and at discharge (median, 8 versus 4;  $P = .13$ ) was lower with CS than with GA, though the latter difference was not significant. In addition, the length of stay for patients treated with CS was shorter than for those treated with GA (mean, 5.93 versus 8.02 days;  $P = .03$ ), though there were no differences in discharge destination.

Sixty-six patients were enrolled by sites that performed >1 thrombectomy and exclusively used GA ( $n = 14$ ) or CS ( $n = 52$ ). While there was no difference in the ordinal mRS scores at 90 days for these patients, functional independence was significantly higher in the CS subgroup (58%) than in the GA subgroup (21%) ( $P = .033$ ).

**Table: Outcome measures for patients in DEFUSE 3**

Outcome Measures	Thrombectomy with GA (n = 26)	Thrombectomy with CS (n = 66)	Med Therapy (n = 90)	P GA vs CS	P GA vs Med	P CS vs Med
Primary outcome: functional independence at 90 days (No.) (%)	6 (23)	35 (53)	15 (17)	.01	.56	<.001
Median score on modified Rankin Scale at 90 days (IQR)	3.5 (3–5)	2 (1–4)	4 (3–6)	.047	.22	<.001
NIHSS score at 24 hr (IQR)	15.5 (6–20)	8 (4–13)	16 (11–21)	.03	.31	<.001
NIHSS score at discharge or at days 5–7 (IQR)	8 (4–12)	4 (2–11)	15 (7–21)	.13	.01	<.001
Safety outcomes (No.) (%)						
Death at 90 days	5 (19)	8 (12)	23 (26)	.51	.51	.04
Symptomatic intracranial hemorrhage	1 (4)	5 (8)	4 (4)	.67	1.0	.5
Early neurologic deterioration	2 (8)	6 (9)	12 (13)	1.0	.52	.41
Parenchymal hematoma type 2	3 (12)	5 (8)	3 (3)	.68	.13	.28
Imaging outcomes						
Median infarct volume at 24 hr (IQR) (mL)	39.6 (21.1–132.3)	33.6 (13.8–71.3)	41.0 (25.4–106.2)	.37	.83	.12
Median infarct growth at 24 hr (IQR) (mL)	26.9 (12.9–104.8)	22.3 (7.5–55.6)	32.8 (18.3–74.8)	.35	.75	.04
Reperfusion >90% at 24 hr (No.)/(total No.) (%)	16/21 (76)	43/54 (80)	12/68 (18)	.76	<.001	<.001
Complete recanalization at 24 hr (No.)/(total No.) (%)	17/23 (74)	48/60 (80)	14/77 (18)	.56	<.001	<.001
Reperfusion >90% and/or complete recanalization at 24 hr (No.)/(total No.) (%)	17/24 (71)	48/61 (79)	14/80 (18)	.44	<.001	<.001
TICI score of 2b or 3 (No.)/(total No.) (%)	18/26 (69)	52/66 (79)	NA	.33	NA	NA
Length of stay at enrolling hospital (days)	8.02 (5.35–12.18)	5.93 (3.31–8.85)	8.94 (6.17–14.03)	.03	.33	<.001
Discharge destination				.36	.83	.48
Home	3 (12)	13 (20)	14 (16)	.39	.76	.53
Acute care facility	2 (8)	6 (9)	4 (4)			
Skilled nursing facility	7 (27)	11 (17)	18 (20)			
Acute rehab unit	10 (38)	26 (39)	35 (39)			
Death	3 (12)	2 (3)	9 (10)			
Other	1 (4)	8 (12)	10 (11)			

**Note:**—Med indicates medical management; rehab, rehabilitation.

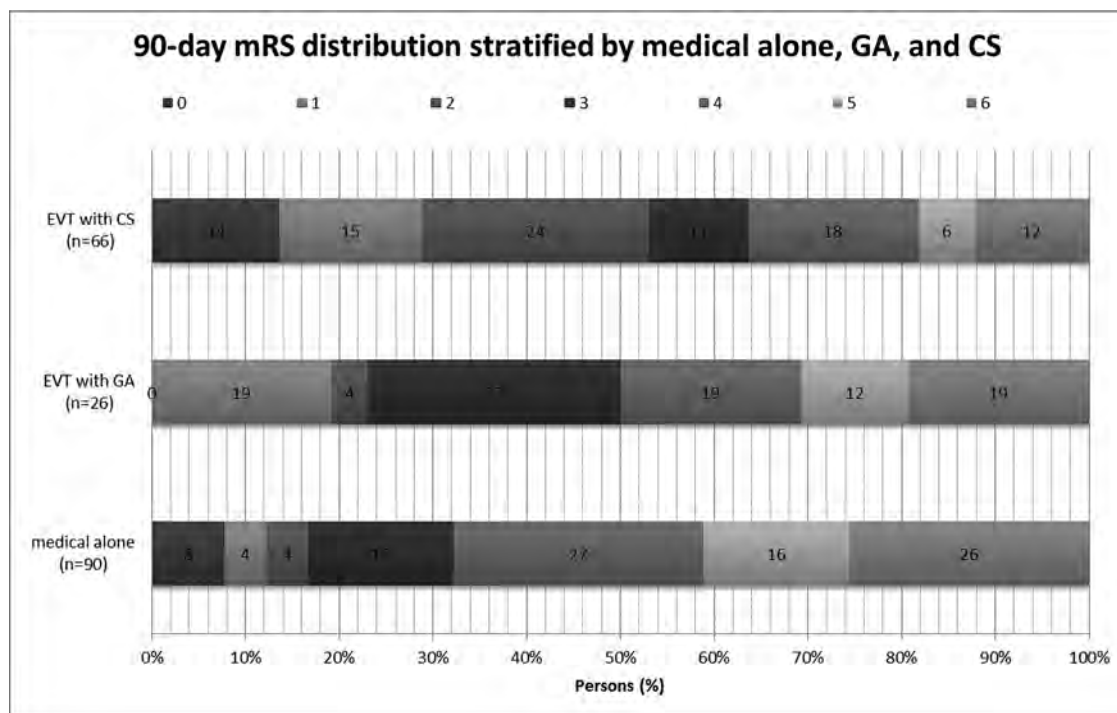


**FIGURE.** Ninety-day modified Rankin Scale scores for patients in DEFUSE 3 stratified by endovascular therapy (EVT) with conscious sedation, EVT with general anesthesia, and medical therapy alone.

There were no significant differences in the time from onset of symptoms to qualifying imaging among the 3 groups (On-line Table). For the patients who underwent thrombectomy, there were no significant differences between GA and CS for time to arrival in the angi suite or from femoral puncture to the first clot removal attempt. However, CS was associated with a shorter time from arrival in the angi suite to femoral puncture (median, 14 versus 18 minutes;  $P = .05$ ) and a shorter time from femoral puncture to reperfusion (TICI 2b or 3 as assessed by the core lab) (median, 35 versus 42 minutes;  $P = .03$ ).

There were no significant differences in symptomatic intracranial hemorrhage, early neurologic deterioration, or type 2 parenchymal hematoma among the 3 groups (Table). While there was no difference in the death rates at 90 days between GA and CS, there was a significantly lower mortality in CS versus medical management, with an odds ratio of 0.40 (95% CI, 0.17–0.97;  $P = .04$ ), but not when comparing GA with medical management (OR = 0.69; 95% CI, 0.23–2.1;  $P = .54$ ). There were no differences in infarct volume or infarct growth at 24 hours among the 3 groups. Both GA and CS were associated with higher reperfusion rates compared with medical therapy, without significant differences between the 2 thrombectomy groups.

Regarding relevant serious adverse events, patients undergoing GA had 1 episode of aspiration pneumonia, 1 episode of respiratory arrest, and 1 episode of respiratory failure. Patients undergoing CS had 1 episode of pneumonia and 1 episode of respiratory failure.

## DISCUSSION

In this analysis of the DEFUSE 3 study, the benefit of mechanical thrombectomy performed during the extended time window, between 6 and 16 hours from last known well, for patients with ICA or M1 occlusions and a target mismatch profile on perfusion imaging was apparent in patients who underwent CS but not in those who underwent GA. Specifically, functional independence at 90 days was observed in 53% of patients treated with CS, but in only 23% of those treated with GA and 17% treated by medical management. CS was associated with a slightly shorter time from arrival in the angi suite to femoral puncture and from femoral puncture to reperfusion. Patients undergoing CS were also noted to have an improved NIHSS score at 24 hours and to some extent on discharge, which could have contributed to the shorter length of stay. Of note, while the median initial NIHSS score was 3 points higher in the GA group, this was not statistically significant.

Because GA versus CS was not randomized, it is possible that patients who underwent thrombectomy with GA were more clinically unstable than those with CS and thus more likely to have a poor outcome. To address this potential bias, we performed an adjusted analysis to account for differences in baseline predictors of clinical outcome. In addition, we noted that many sites typically chose to use either GA or CS as a matter of institutional preference. For sites that routinely used GA, presumably there would be no tendency for less stable patients to receive GA. Therefore, we also analyzed the patients treated at sites that appeared to exclusively use GA or CS. For these 66 patients, the functional outcome was significantly higher in the CS subgroup (58%) than the GA subgroup (21%), indicating that this difference is not sin-

gularly attributable to a selection bias in which patients with more comorbidities, higher stroke burden, and worsened overall medical status received GA rather than CS.

These results are consistent with post hoc analyses of other thrombectomy trials. Analysis of the Interventional Management of Stroke III (IMS III) trial showed worsened neurologic outcomes and increased mortality after thrombectomy for patients who underwent GA.<sup>7</sup> Post hoc analysis of the Multicenter Randomized Clinical Trial of Endovascular Treatment for Acute Ischemic Stroke in the Netherlands (MR CLEAN) study showed improved neurologic outcome at 3 months after thrombectomy for patients who did not undergo GA.<sup>8</sup> Because these were both post hoc analyses, it remains unclear whether these results were due to a patient selection bias.

The DEFUSE 3 results contrast with results from randomized, single-center trials. The Sedation Versus General Anesthesia for Endovascular Therapy in Acute Stroke—Impact on Neurological Outcome (AnStroke) study randomized 90 patients to CS or GA and found no difference in neurologic outcome after 3 months or any differences in blood pressure decline, blood glucose level, PaCO<sub>2</sub>, time intervals, degree of recanalization, NIHSS score at 24 hours, infarct volume, or hospital mortality.<sup>2</sup> In The Sedation vs Intubation for Endovascular Stroke Treatment Trial (SIESTA), 150 patients were randomized to CS or GA, and more patients were functionally independent after 3 months if they had undergone GA, but there was no change in mortality.<sup>3</sup> The General Or Local Anaesthesia in Intra Arterial Therapy (GOLIATH) study randomized 128 patients to CS or GA and showed no difference in infarct growth, with a trend toward better clinical outcome in the GA arm, though this could have been due to the significant difference in successful reperfusion in the GA arm compared with the CS arm (76.9% versus 60.3%,  $P = .04$ ).<sup>4</sup> All 3 of these prospective randomized studies were limited by a small number of patients.

There are a number of potential mechanisms through which GA may contribute to worse outcomes following mechanical thrombectomy. GA requires orotracheal intubation, and this additional step may result in a delay in the therapeutic intervention of mechanical thrombectomy. Hypotension and hyperventilation during GA may result in the loss of pial collaterals maintaining the ischemic penumbra. In addition, orotracheal intubation may place the patient at risk for aspiration. Proponents of GA during mechanical thrombectomy cite the decreased patient motion that allows better imaging quality and a lower risk of device-related complications such as vessel perforation, dissection, or subarachnoid hemorrhage. However, it is unclear that better imaging is important for ICA or M1 occlusion, where the anatomy is more consistent compared with other vessels such as the distal middle cerebral artery. Complications such as perforation and subarachnoid hemorrhage have not been significantly different between patients undergoing GA and CS in prior studies<sup>2-3</sup> or in this study. As a post hoc analysis, the results of this study are limited by the potential for unrecognized selection bias. Specifically, the interventionalist may have chosen GA over CS for patients who seemed more clinically unstable and therefore were more likely to have a worse outcome. We attempted to address this limitation by performing adjusted analyses and analyzing patients who were

treated at sites that used only GA or CS for their thrombectomy cases, and the observed difference remained robust in this patient cohort as well. There remains a need for further research on the topic of GA versus CS in the extended time window for mechanical thrombectomy. It will be important that future studies control for the duration of the procedure because this may be longer with GA and confound the results.

## CONCLUSIONS

Patients who underwent thrombectomy with conscious sedation in the extended time window experienced a higher likelihood of functional independence at 90 days, a lower NIHSS score at 24 hours, and a shorter time from femoral puncture to reperfusion compared with those who had general anesthesia. This effect remains robust in institutions that only treated patients with a single anesthesia technique.

Disclosures: Michel Torbey—*RELATED: Grant:* National Institute of Neurological Disorders and Stroke.\* Shahid M. Nimjee—*UNRELATED: Board Membership:* Medtronic, *Comments:* Acute Ischemic Stroke Medical Advisory Board. Maarten G. Lansberg—*RELATED: Grant:* National Institute of Neurological Disorders and Stroke.\* Gregory W. Albers—*UNRELATED: Equity and Consulting:* iSchemaView, *Consulting:* Medtronic; Michael P. Marks—*RELATED: Grant:* National Institutes of Health—National Institute of Neurological Disorders and Stroke\*; *UNRELATED: Stock/Stock Options:* ThrombixMedical. \*Money paid to the institution.

## REFERENCES

1. Brinjikji W, Pasternak J, Murad MH, et al. **Anesthesia-related outcomes for endovascular stroke revascularization: a systematic review and meta-analysis.** *Stroke* 2017;48:2784–91 CrossRef Medline
2. Löwhagen Hendén P, Rentzos A, Karlsson JE, et al. **General anesthesia versus conscious sedation for endovascular treatment of acute ischemic stroke: the AnStroke Trial (Anesthesia During Stroke).** *Stroke* 2017;48:1601–07 CrossRef Medline
3. Schönenberger S, Uhlmann L, Hacke W, et al. **Effect of conscious sedation vs general anesthesia on early neurological improvement among patients with ischemic stroke undergoing endovascular thrombectomy: a randomized clinical trial.** *JAMA* 2016;316:1986–96 CrossRef Medline
4. Simonsen CZ, Yoo AJ, Sorensen LH, et al. **Effect of general anesthesia and conscious sedation during endovascular therapy on infarct growth and clinical outcomes in acute ischemic stroke: a randomized clinical trial.** *JAMA Neurol* 2018;75:470–77 CrossRef Medline
5. Powers WJ, Rabinstein AA, Ackerson T, et al; American Heart Association Stroke Council. **2018 Guidelines for the Early Management of Patients with Acute Ischemic Stroke: A Guideline for Healthcare Professionals From the American Heart Association/American Stroke Association.** *Stroke* 2018;49:e46–110 CrossRef Medline
6. Albers GW, Marks MP, Kemp S, et al; DEFUSE 3 Investigators. **Thrombectomy for stroke at 6 to 16 hours with selection by perfusion imaging.** *N Engl J Med* 2018;378:708–18 CrossRef Medline
7. Abou-Chebl A, Yeatts SD, Yan B, et al. **Impact of general anesthesia on safety and outcomes in the endovascular arm of Interventional Management of Stroke (IMS) III trial.** *Stroke* 2015;46:2142–48 CrossRef Medline
8. Berkhemer OA, van den Berg LA, Fransen PS, et al; MR CLEAN investigators. **The effect of anesthetic management during intra-arterial therapy for acute stroke in MR CLEAN.** *Neurology* 2016;87:656–64 CrossRef Medline

# First-Line Sofia Aspiration Thrombectomy Approach within the Endovascular Treatment of Ischemic Stroke Multicentric Registry: Efficacy, Safety, and Predictive Factors of Success

G. Marnat, X. Barreau, L. Detraz, R. Bourcier, B. Gory, A. Sgreccia, F. Gariel, J. Berge, P. Menegon, M. Kyheng, J. Labreuche, A. Consoli, R. Blanc, and B. Lapergue, on behalf of the ETIS Investigators



## ABSTRACT

**BACKGROUND AND PURPOSE:** After publications on the effectiveness of mechanical thrombectomy by stent retrievers in acute ischemic stroke with large-vessel occlusion, alternative endovascular approaches have been proposed using first-line aspiration catheters. Several devices are currently available to perform A Direct Aspiration First Pass Technique. The Sofia catheter aspiration has been widely used by interventionalists, but data are scarce about its efficacy and safety. Our aim was to report our multicenter thrombectomy experience with first-line Sofia catheter aspiration and to identify independent prognostic factors of clinical and procedural outcomes.

**MATERIALS AND METHODS:** We performed a retrospective analysis of the prospectively maintained Endovascular Treatment of Ischemic Stroke multicentric registry. Data from consecutive patients who benefited from thrombectomy with a first-line Sofia approach between January 2013 and April 2018 were studied. We excluded other first-line approaches (stent retriever or combined aspiration and stent retriever) and extracranial occlusions. Baseline characteristics, procedural data, and angiographic and clinical outcomes were analyzed.

**RESULTS:** During the study period, 296 patients were treated. Mean age and initial NIHSS score were, respectively, 69.5 years and 16. Successful reperfusion, defined by the modified TICl 2b/3, was obtained in 86.1% ( $n = 255$ ; 95% CI, 81.7%–89.9%). Complete reperfusion (modified TICl 3) was obtained in 41.2% ( $n = 122$ ; 95% CI, 35.5%–47.1%). A first-pass effect was achieved in 24.2% ( $n = 71$ ; 95% CI, 19.4%–29.6%). A rescue stent retriever approach was required in 29.7% ( $n = 88$ ; 95% CI, 24.6%–35.3%). The complication rate was 9.5% ( $n = 28$ ; 95% CI, 6.4%–13.5%). Forty-three percent ( $n = 122$ ; 95% CI, 37.1%–48.9%) of patients presented with a favorable 3-month outcome ( $mRS \leq 2$ ). Older age, MI-occlusion topography, and intravenous thrombolysis use prior to thrombectomy were independent predictors of the first-pass effect.

**CONCLUSIONS:** The first-line contact aspiration approach appeared safe and efficient with Sofia catheters. These devices achieved very high reperfusion rates with a low requirement for stent retriever rescue therapy, especially for MI occlusions.

**ABBREVIATIONS:** ADAPT = A Direct Aspiration First Pass Technique; DAC = distal aspiration catheter; ETIS = Endovascular Treatment of Ischemic Stroke; FPE = first-pass effect; IQR = interquartile range; IVT = intravenous thrombolysis; mTICl = modified TICl; PH = parenchymal hematoma

After publication of the major trials reporting the efficacy of mechanical thrombectomy for large-vessel occlusion strokes,<sup>1</sup> the principal concern is now to optimize recanalization rates. Recent advances in thrombectomy devices progressively enabled major improvement. In addition to stent retrievers, contact aspi-

ration has greatly modified the endovascular approach and is now considered a routine technique. Since the A Direct Aspiration First Pass Technique (ADAPT) was described,<sup>2,3</sup> various distal aspiration catheter (DAC) technologies have been developed. ADAPT consists of contact thrombus suction through a large-diameter catheter. This is a seductive first-line approach because it appears effective, safe, fast, and cost-effective.<sup>4</sup> With recent publications of the Contact Aspiration Versus Stent Retriever for

Received January 9, 2019; accepted after revision April 18.

From the Interventional and Diagnostic Neuroradiology Department (G.M., X.B., F.G., J.B., P.M.), Bordeaux University Hospital, Bordeaux, France; Interventional and Diagnostic Neuroradiology Department (L.D., R.B.), Nantes University Hospital, Nantes, France; Department of Diagnostic and Therapeutic Neuroradiology (B.G.), University Hospital of Nancy, Nancy, France; Institut National de la Santé et de la Recherche Médicale U1254 (B.G.), IADI F-54000, Nancy, France; Department of Radiology (A.S.), Ospedali Riuniti, Siena, Italy; Université Lille (M.K., J.L.), Centre Hospitalier Universitaire Lille, Lille, France; Department of Neuroradiology (A.C.), Foch Hospital, Suresnes, France; Interventional Neuroradiology Department (R.B.), Fondation Ophtalmologique Rothschild, Paris, France; and Department of Neurology (B.L.), Stroke Center, Foch Hospital, Suresnes, France; ETIS Collaborators are in the On-line Appendix.

Financial support was provided by MicroVention (Tustin, California).

The funders had no role in the design and conduct of the study; collection, management, analysis, and interpretation of the data; preparation, review, or approval of the manuscript; or decision to submit the manuscript for publication.

Please address correspondence to Gaultier Marnat, MD, Interventional and Diagnostic Neuroradiology Department, Bordeaux University Hospital, Hôpital Pellegrin, Place Amélie Raba-Léon, 33000 Bordeaux, France; e-mail: gaultier.marnat@chu-bordeaux.fr

 Indicates article with supplemental on-line appendix and tables.

 Indicates article with supplemental on-line photo.

<http://dx.doi.org/10.3174/ajnr.A6074>

Successful Revascularization (ASTER) and Aspiration thrombectomy versus stent retriever thrombectomy as first-line approach for large vessel occlusion (COMPASS) trials, ADAPT can now be considered a first-line option in the thrombectomy strategy.<sup>5,6</sup> In case of aspiration failure, the endovascular technique can then be converted to a combined aspiration + stent retriever approach.<sup>7</sup> These DACs must have specific characteristics such as navigability, torqueability, visibility, kink resistance, and aspiration capacity to obtain higher performance levels.

Sofia (soft torqueable catheter optimized for intracranial access; MicroVention, Tustin, California) is a DAC with a specific hybrid design. Its braid and coil construction combines different softness segments with a distal inner lumen of 0.055–0.070 inches, respectively, in 5F and 6F Plus versions. Despite previous publications,<sup>8–11</sup> the safety and efficacy of this DAC in a large population with first-line Sofia use are yet to be reported.

Recanalization is a strong predictor of favorable outcome. Especially, the recently described first-pass effect (FPE), defined as a complete recanalization after 1 pass of mechanical thrombectomy, has been related to substantial improvement in clinical outcome compared with final good recanalization results after numerous passes.<sup>12</sup> However, in the North American Solitaire Stent-Retriever Acute Stroke registry study,<sup>12</sup> most patients were treated with a first-line stent retriever strategy. Data regarding the FPE under the ADAPT strategy are still underreported to date.

We present here the largest multicentric experience to date of the first-line ADAPT strategy using Sofia 6F Plus or 5F catheters. We aimed to study the clinical and angiographic effectiveness with specific attention to predictive factors of the first-pass effect.

## MATERIALS AND METHODS

### Study Design and Population

We performed a retrospective analysis of our prospectively maintained, multicentric Endovascular Treatment of Ischemic Stroke (ETIS) data base. ETIS is a prospective registry collecting data from patients benefiting from mechanical thrombectomy in 4 major French comprehensive stroke centers. Local ethics committees approved this study.

Consecutive patients from January 2013 to April 2018, presenting with acute ischemic stroke due to large-vessel occlusion strokes of the anterior or posterior circulation treated by mechanical thrombectomy using first-line ADAPT with a Sofia catheter were analyzed. We excluded patients treated first-line by another DAC, stent retrievers combined with distal aspiration, or stent retrievers alone. Extracranial occlusions were also excluded.

### Treatment Protocol

The indication for treatment was left to the discretion of each operator according to local protocol. Intravenous thrombolysis treatment (IVT) was administered in association with mechanical thrombectomy in patients treated within 4.5 hours of stroke onset in the absence of contraindications. Endovascular treatment was performed with the patient under local anesthesia alone, conscious sedation, or general anesthesia depending on the patient's condition and each contributing center's anesthesia protocol.

For all selected cases, the operator's decision was to perform distal aspiration through a Sofia catheter as the first intention.

Sofia catheter choice was made according to operator's discretion, local protocols, catheter availability, and occlusion topography to fit with the ADAPT strategy as a first-line treatment option. First, an 8F or 9F guide catheter was placed into the cervical internal carotid artery. Then, a Sofia 6F Plus or 5F was advanced over a microwire to the occlusion site with or without microcatheter support, depending on cervical and intracranial ICA tortuosity. The use of a balloon-guide catheter was left to the interventionist's discretion. A 3-minute aspiration period, using either a dedicated pump or manual depression through a vacuum syringe, was applied before DAC removal. In the case of failure or partial efficacy, this maneuver could be repeated. In case of ADAPT failure or insufficient recanalization, the choice to convert to another endovascular technique (distal aspiration combined with stent retrievers or stent retrievers alone) was left to the operator's discretion. Complementary endovascular treatments, such as cervical or intracranial angioplasty and/or stent placement, were performed depending on stroke etiology and severity and angiographically detected underlying lesions.

### Data Collection and Outcome Evaluation

Age, sex, medical history, previous medication, stroke severity using the NIHSS score, stroke etiology, imaging technique, ASPECTS, IVT, and angiographic (arterial occlusion topography, degree of revascularization assessed by the modified TICI [mTICI] score) data were recorded.

Clinical outcome was assessed by the mRS 3 months after stroke. Favorable outcome was defined by an mRS  $\leq 2$ . Angiographic reperfusion was rated using the mTICI score. Successful revascularization was defined by mTICI  $\geq 2b$ . Near-complete and excellent reperfusion was defined, respectively, by mTICI of 2c/3 and 3. The FPE was defined as an mTICI 3 after a single aspiration maneuver.

Safety criteria were also recorded, including procedural complications (dissection, embolism in a new territory, and intracranial arterial perforation), intracranial hemorrhage, and mortality. Procedural times were analyzed.

### Statistical Analysis

Categorical variables were expressed as frequencies and percentages. Quantitative variables were expressed as means or medians (interquartile range, [IQR]) for non-normal distribution. The normality of distributions was assessed graphically and using the Shapiro-Wilk test.

Associations of baseline characteristics (patient and treatment characteristics) with outcomes (favorable outcome, successful and excellent reperfusion, FPE) were first investigated in center-adjusted analyses using generalized linear mixed models by including center as a random effect. To assess the independent predictors of each outcome, we entered all patient and treatment characteristics with a  $P < .20$  in center-adjusted analyses into a backward-stepwise multivariable generalized linear mixed model using a removal criterion of  $P > .05$ . Before developing the multivariable prognostic models, we examined the log-linearity assumption for continuous characteristics using restricted cubic spline functions as well as the absence of collinearity between candidate predictors by calculating the variance inflation factors. To avoid case deletion in analyses due to missing data on baseline

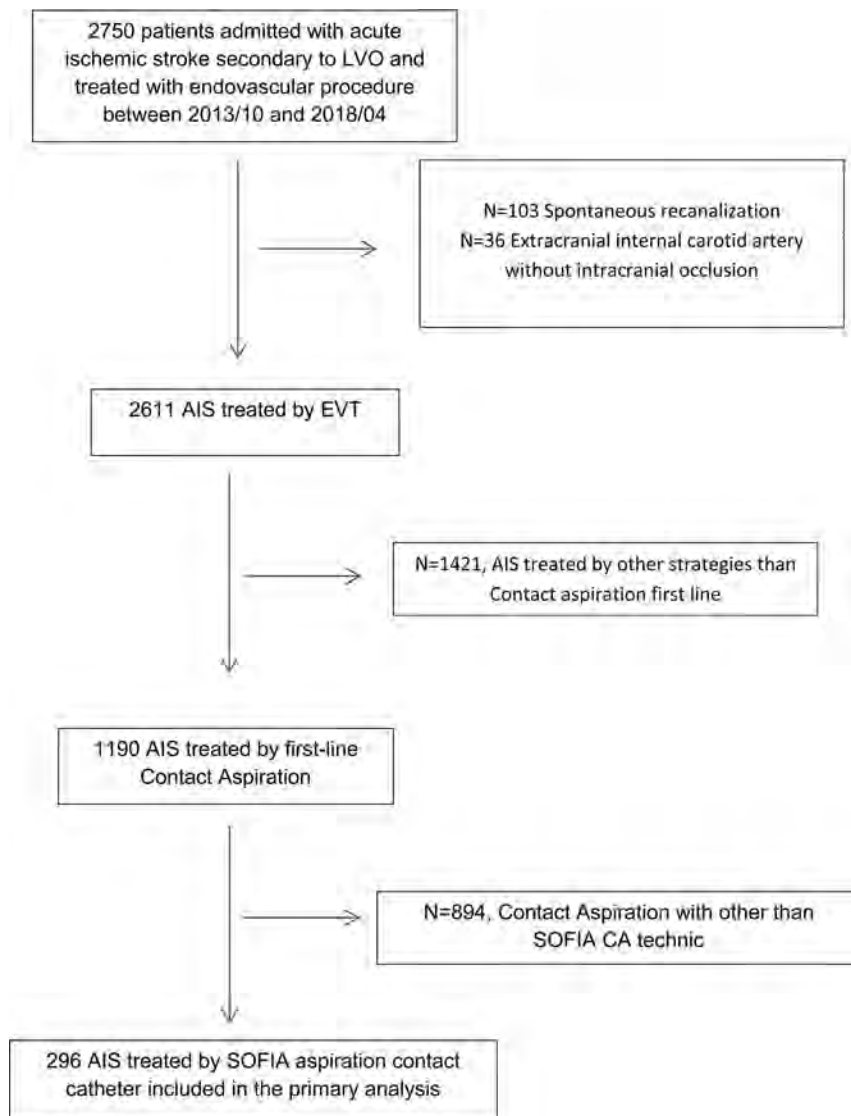


**FIGURE.** Flowchart of the Sofia-Contact Aspiration, First-Line Technique Registry. AIS indicates acute ischemic stroke; LVO, large vessel occlusion; EVT, endovascular treatment; CA, contact aspiration.

characteristics and outcomes, we imputed missing data by multiple imputations using a regression-switching approach (chained equations with  $m = 10$ ). The imputation procedure was performed under the missing at random assumption using all baseline characteristics and study outcomes with a predictive mean matching method for continuous variables and a multinomial or binary logistic regression model for categorical variables. Estimates obtained in the different imputed datasets were combined using the Rubin rules. Finally, we examined the performance of the final prognostic models in terms of discrimination by calculating the C-statistics in each imputed dataset and by reporting the median and range values.

Statistical testing was performed at the 2-tailed  $\alpha$  level of .05. Data were analyzed using the SAS software package, Release 9.4 (SAS Institute, Cary, North Carolina).

## RESULTS

### Population and Participating Centers

From October 2013 to April 2018, we treated 2750 patients with an arterial large-vessel occlusion by mechanical thrombectomy at

4 comprehensive stroke centers. Of these, 296 (10.8%) who had undergone endovascular treatment with the Sofia aspiration catheter as a first-line approach were included in the present study (center A: 73 patients; B: 103 patients, C: 92 patients, D: 28 patients) (Figure).

The main patient and treatment characteristics are reported in Table 1. Overall, the mean age was  $69.5 \pm 13.8$  years; 50.7% ( $n = 150$ ) were men, and the median admission NIHSS score was 16 (IQR, 11–21). Intravenous tPA before endovascular treatment was administered in 48.3% ( $n = 142$ ) of patients. The median time from symptom onset to arterial puncture was 242 minutes (IQR, 186–324 minutes). Most patients were treated with a 6F Sofia catheter ( $n = 226$ , 76.3%), and the remaining 70 (23.7%) were treated with a 5F catheter.

### Effectiveness and Safety Outcomes

The main safety and effectiveness outcomes are summarized in Table 2. Thrombectomy was effective in 86.1% ( $n = 255$ ; 95% CI, 81.7%–89.9%) of patients (successful reperfusion, mTICI 2b–3) with a median number of passes of 2 (IQR, 1–3) and a median time of 40 minutes (IQR, 24–65 minutes) from groin puncture. Excellent reperfusion (mTICI 3) was achieved in 41.2% of patients ( $n = 122$ ; 95% CI, 35.5%–47.1%). The first-pass effect was achieved in 24.2% ( $n = 71$ , 95% CI, 19.4–29.6%). Rescue therapy was required in 29.7% ( $n = 88$ ; 95% CI, 24.6%–35.3%).

Procedural complications occurred in 9.5% ( $n = 28$ ; 95% CI, 6.4%–13.5%) of patients. These included 14 (4.7%) new-territory embolisms, 4 (1.4%) vessel perforations, 4 (1.4%) extracranial carotid dissections, and 6 (2.0%) vasospasms. Intracranial hemorrhage within 24 hours occurred in 44.6% ( $n = 115$ ; 95% CI, 38.4%–50.9%). Among these, there were 31 (12.0%) parenchymal hematomas (PH-1 and PH-2) and 16 (6.2%) symptomatic intracranial hemorrhages. At 90 days, 43% of patients ( $n = 122$ ; 95% CI, 37.1%–48.9%) were functionally independent (mRS 0–2) and 22.9% had died ( $n = 65$ ; 95% CI, 18.1%–28.2%) (See the On-line Figure for the overall distribution of 90-day mRS). Results according to anterior or posterior occlusion topography are presented in On-line Tables 1 and 2.

Among patients treated with the ADAPT approach alone without the need for rescue therapy, successful reperfusion was obtained in 91.8% ( $n = 191$ ; 95% CI, 87.2%–95.2%); 50.5% ( $n = 100$ ; 95% CI, 43.3%–57.7%) had a 90-day favorable outcome. In this subgroup of patients, the mortality rate was 20.2% ( $n = 40$ ; 95% CI, 14.8%–

**Table 1: Baseline characteristics (n = 296)<sup>a</sup>**

Characteristics	No.	Values
Baseline demographics and medical history		
Age (mean) (yr)	296	69.5 ± 13.8
Men	296	150 (50.7)
Hypertension	288	158 (54.9)
Diabetes	285	50 (17.4)
Dyslipidemia	284	93 (32.7)
Current smoking	272	70 (25.7)
Previous stroke or TIA	286	43 (15.0)
Previous CAD	285	50 (17.5)
Antithrombotic medications	291	120 (41.2)
Antiplatelet	291	69 (23.7)
Anticoagulant	291	34 (11.7)
Current stroke event		
Systolic BP (mean) (mm Hg)	245	148 ± 28
Diastolic BP (mean) (mm Hg)	245	82 ± 19
Blood glucose (median) (IQR) (mmol/L)	229	6.4 (5.7–8.0)
Admission NIHSS score (median) (IQR)	290	16 (11–21)
ASPECTS (median) (IQR)	278	7 (6–9)
Prestroke mRS ≥1	291	64 (22.0)
Site of occlusion		
M1 MCA	296	124 (41.9)
M2 MCA		40 (13.5)
T-car		54 (18.2)
Tandem		39 (13.2)
Vertebrobasilar		39 (13.2)
Stroke etiology		
Large-artery atherosclerosis	295	44 (14.9)
Cardioembolic		127 (43.1)
Dissection		11 (3.7)
Others		113 (38.3)
Intravenous rtPA	294	142 (48.3)
General anesthesia	291	71 (24.4)
Procedural times (median) (IQR) (min)		
Onset to imaging	279	113 (84–180)
Admission to imaging	248	25 (16–41.5)
Imaging to groin puncture	262	107 (69–151)
Imaging to recanalization	279	157 (118–205)
Onset to puncture	276	242 (186–324)
Puncture to recanalization	287	40 (25–65.5)
Balloon-guide catheter	296	23 (7.8)
Mode of admission		
Mothership	295	121 (41.0)
Drip and ship		174 (59.0)
Sofia catheter		
5F	296	70 (23.7)
6F		226 (76.3)

**Note:**—BP indicates blood pressure; CAD, coronary artery disease; T-car, occlusion of carotid terminus; Mothership, comprehensive stroke centers with on-site interventional neuroradiologic services; Drip and ship, medical treatment (including intravenous thrombolysis) in a hospital before being transferred to a comprehensive stroke centers for thrombectomy.

<sup>a</sup> Values are expressed as No. (percentage) unless otherwise indicated.

26.5%) and the procedural complication rate was 9.1% ( $n = 19$ ; 95% CI, 5.6%–13.9%). These results are presented in Table 2.

### Predictors of 90-Day Favorable Outcome

Center-adjusted analyses of predictors of favorable outcome are detailed in On-line Table 3. In backward stepwise multivariable regression analysis, age, admission NIHSS score, hypertension, time intervals between onset to imaging and imaging to groin puncture, prestroke mRS ≥1, general anesthesia, and non-M1 MCA occlusion were associated with a decrease in the favorable outcome rate, whereas intravenous thrombolysis was associated with an increase

(Table 3). This prognosis model had good discrimination (median C-statistic, 0.827; range, 0.816–0.838 across imputed datasets).

### Predictors of Successful and Complete Reperfusion

Center-adjusted analyses of predictors of successful and excellent reperfusion outcome are detailed in On-line Tables 4 and 5. A higher ASPECTS (OR per 1-point increase, 1.25; 95% CI, 1.08–1.45) and no current smoking (OR, 0.36; 95% CI, 0.18–0.72) were independently associated with successful reperfusion in backward stepwise multivariate regression analysis (Table 3). This prognosis model had good discrimination (median C-statistic, 0.681; range, 0.672–0.688 across imputed datasets).

For excellent reperfusion, we identified 5 independent predictors: older age, previous antiplatelet medications, lower blood glucose, site of occlusion (with a greater rate of excellent reperfusion for MCA M1 and vertebrobasilar occlusions), and Sofia 6F catheters (Table 3). This prognosis model also had good discrimination (median C-statistic, 0.735; range, 0.725–0.741 across imputed datasets).

### Predictors of First-Pass Effect (mTICI 3 after 1 Pass)

Center-adjusted analyses of predictors of FPE are detailed in On-line Table 6. We identified 3 independent predictors: older age, site of occlusion (with a greater rate of excellent reperfusion after 1 pass for MCA M1 and vertebrobasilar occlusions), and intravenous thrombolysis (Table 3). This prognosis model also showed good discrimination (median C-statistic, 0.795; range, 0.793–0.795 across imputed datasets).

## DISCUSSION

Our study demonstrated a very high efficacy of first-line contact aspiration using the Sofia catheter with 86.1% successful reperfusion (mTICI 2b, 2c/3) and 43% favorable clinical outcome (mRS <3). The FPE rate was high (24.2%). Factors associated with higher recanalization rates were, notably, M1 and vertebrobasilar occlusions and the use of a 6F catheter.

### Clinical Outcomes

As previously described,<sup>1,13</sup> outcome was significantly negatively influenced by age, stroke severity assessed by admission NIHSS score, prestroke mRS ≥1, general anesthesia, ICA terminus and tandem occlusions, and late treatment timeframe. Most interesting, IVT in combination with mechanical thrombectomy is associated with favorable outcome. These predictive factors have already been previously demonstrated with the use of either stent retrievers or the ADAPT technique.

The influence of general anesthesia on clinical outcomes is currently under debate.<sup>14</sup> In our study, general anesthesia was not the first-line option for thrombectomy procedures among most participating centers. This anesthesia regimen was proposed for selected severe cases, thus likely explaining the association between general anesthesia and poorer outcomes in our work.

Despite several studies demonstrating the association between IVT and favorable outcome in cases of stroke treated with thrombectomy,<sup>15</sup> IVT influence is still discussed. Future randomized trials will probably bring answers.

**Table 2: Efficacy and safety outcomes in the overall population and population without rescue therapy (n = 296)<sup>a</sup>**

Outcomes	Overall		Patients without Rescue Therapy	
	Values	95% CI	Values	95% CI
<b>Efficacy outcomes</b>				
Successful reperfusion (mTICI 2b/3)	255/296 (86.1)	81.7–89.9	191/208 (91.8)	87.2–95.2
Near-complete reperfusion (mTICI 2c/3)	157/296 (53.0)	47.4–58.7	128/208 (61.5)	54.6–68.2
Excellent reperfusion (mTICI 3)	122/296 (41.2)	35.5–47.1	104/208 (50.0)	43.0–57.0
FPE (mTICI 3 after first pass)	71/293 (24.2)	19.4–29.6	71/208 (34.1)	27.7–41.0
Early neurologic improvement <sup>b</sup>	133/258 (51.6)	45.4–57.7	109/184 (59.2)	51.8–66.4
Favorable outcome	122/284 (43.0)	37.1–48.9	100/198 (50.5)	43.3–57.7
Groin puncture-to-recanalization time (median) (IQR)	40 (24–65) <sup>c</sup>		30.0 (21.0–50.0) <sup>d</sup>	
No. of passes >2	117/293 (39.9)	34.3–45.8	46/208 (22.1)	16.7–28.4
Rescue therapy	88/296 (29.7)	24.6–35.3		
<b>Safety outcomes</b>				
Procedural complications	28/294 (9.5)	6.4–13.5	19/208 (9.1)	5.6–13.9
Any ICH	115/258 (44.6)	38.4–50.9	79/177 (44.6)	37.2–52.3
PH	31/258 (12.0)	8.3–16.6	22/177 (12.4)	8.0–18.2
sICH	16/258 (6.2)	3.5–9.8	10/177 (5.6)	2.7–10.1
All-cause death (90-day)	65/284 (22.9)	18.1–28.2	40/198 (20.2)	14.8–26.5

**Note:**—ICH indicates intracranial hemorrhage; sICH, symptomatic intracranial hemorrhage.

<sup>a</sup> Values expressed as No./total No. (%) unless otherwise indicated.

<sup>b</sup> Early neurologic improvement is defined as NIHSS score 0–1 at 24 hours or a decrease of  $\geq 4$  points in the NIHSS score at 24 hours. Favorable outcome is defined as a 90-day mRS  $\leq 2$ .

<sup>c</sup> Twenty-six missing data.

<sup>d</sup> Fourteen missing data.

### Angiographic Outcome

We present here the largest population treated with first-line ADAPT using Sofia catheters. Our final rate of favorable mTICI ( $\geq 2b$ ) appears similar to those previously published because authors noted favorable recanalization rates between 86.9% and 94.1% with the Sofia catheter.<sup>8–11</sup> Gory et al<sup>16</sup> reported 89% of mTICI 2b/3 in a meta-analysis of the overall literature dealing with ADAPT using various kinds of DACs. In comparison, reperfusion rates among ADAPT major trials were 92% and 85.4%, respectively, in the COMPASS and ASTER trials. Our results are consistent with these values.

Considering all types of mechanical thrombectomy approaches, these rates are among the best reported. For example, considering stent retrievers for most cases, the Highly Effective Reperfusion Evaluated in Multiple Endovascular Stroke (HERMES) trial meta-analysis revealed 71% successful reperfusion (mTICI 2b/3).<sup>1</sup> Among the stent retriever subgroups of both the COMPASS and ASTER trials, final successful recanalization rates were, respectively, 89% and 83.1%. Of course, the maximalist strategy combining contact aspiration and stent retriever is currently presented as a promising technique. Previous studies reported a rate of 72.4% with the Aspiration-Retriever Technique for Stroke (ARTS) approach.<sup>17</sup> New approaches such as Proximal Balloon Occlusion Together with Direct Thrombus Aspiration during Stent Retriever Thrombectomy (PROTECT<sup>Plus</sup>)<sup>18</sup> and Stent Retriever Assisted Vacuum-Locked Extraction (SAVE) techniques<sup>19</sup> seem to achieve very high revascularization levels. However, these findings can be balanced with the advantages of ADAPT as a first-line approach: ease of use, high effectiveness, and cost-effectiveness.

High-quality revascularization (mTICI 2c/3) is now considered a strong prognostic factor.<sup>20</sup> We found that Sofia distal aspiration alone could achieve mTICI 2c/3 and mTICI 3 results in 53% and 41.2%. These rates are—as other indicators previously reported here—close to recently published data.<sup>5,21</sup>

In our study, rescue therapy using a stent retriever was required in 29.7%. This was a low rate, enhancing the high-efficacy level of aspiration first-pass alone in our experience. In the comparable current literature, rescue therapy after the ADAPT technique was needed in 31%–40%.<sup>6,16,22–24</sup> Lower rescue therapy rates have been published with stent retrievers.<sup>25</sup> However, this has to be questioned because the stent retriever approaches are often already associated with an intermediate catheter able to perform combined aspiration and thus can be seen as a maximalist strategy. Nevertheless, the probable need of a complementary rescue technique seems low.

Most interesting, we also emphasized a higher excellent reperfusion rate (mTICI 3) with a Sofia 6F than Sofia 5F. This strongly suggested a need for the largest diameter DAC possible to reach higher rates of reperfusion. This confirms previously published data.<sup>24,26,27</sup>

Our complication rate is low and in accordance with earlier reports. Moreover, the complication rate included benign events such as vasospasm. In the ASTER trial,<sup>6</sup> the first-line contact aspiration group had a 16.2% complication rate, and the first-line stent retriever ASTER group had a 15.9% complication rate (non-significant difference). Blanc et al<sup>22</sup> also reported a 13.3% rate.

### First-Pass Effect

The FPE has recently been described as a strong prognostic factor of favorable outcome. Zaidat et al<sup>12</sup> reported an FPE rate of 25.1% using stent retrievers exclusively. We report here an FPE rate of 24.2%. M1 and vertebrobasilar occlusions were significant predictors of FPE. These topographies appear to particularly fit with the first-line ADAPT strategy using the Sofia catheter. Predictors of FPE were also older age and intravenous thrombolysis. Zaidat et al found that older age was also associated with the FPE but only in univariate analysis. Most interesting, we found that IVT was 1 remarkable factor associated with a higher prevalence of FPE. This has not been described to date, to our knowledge. In our study, the

**Table 3: Independent predictors of favorable outcome; successful, excellent reperfusion; and first-pass effect<sup>a</sup>**

	OR (95%CI)	P Value <sup>b</sup>
<b>Favorable outcome</b>		
Age	0.72 (0.58–0.91) <sup>b</sup>	.005
Admission NIHSS score	0.86 (0.81–0.91) <sup>c</sup>	<.001
Prestroke mRS $\geq$ 1	0.37 (0.17–0.78)	.009
Intravenous rtPA	2.61 (1.42–4.78)	.002
Site of occlusion		.026
M1 MCA	1.00 (ref)	
M2 MCA	0.81 (0.31–2.09)	.66
T-car	0.65 (0.30–1.41)	.27
Tandem	0.49 (0.21–1.14)	.098
Vertebrobasilar	0.15 (0.05–0.49)	.002
General anesthesia	0.36 (0.17–0.76)	.008
Procedural time (min)		
Onset to imaging	0.87 (0.77–0.97) <sup>d</sup>	.017
Imaging to groin puncture	0.67 (0.52–0.90) <sup>d</sup>	.007
<b>Successful reperfusion</b>		
Current smoking	0.36 (0.18–0.72)	.004
ASPECTS	1.25 (1.08–1.45) <sup>c</sup>	.003
<b>Excellent reperfusion</b>		
Age	1.26 (1.04–1.54)	.018
Antiplatelet drugs	2.31 (1.24–4.32)	.009
Blood glucose (mmol/L)	0.87 (0.77–0.97)	.012
Site of occlusion		<.001
M1 MCA	1.00 (ref)	
M2 MCA	0.86 (0.35–2.14)	.75
T-car	0.38 (0.18–0.79)	.010
Tandem	0.38 (0.16–0.91)	.030
Vertebrobasilar	2.55 (1.11–5.85)	.027
<b>Sofia catheter</b>		
>5F	0.38 (0.17–0.83)	.015
>6F	1.00 (ref)	
<b>First-pass effect</b>		
Age	1.48 (1.16–1.90)	.002
Site of occlusion		<.001
M1 MCA	1.00 (ref)	
M2 MCA	0.75 (0.32–1.75)	
T-car	0.11 (0.03–0.38)	
Tandem	0.13 (0.03–0.60)	
Vertebrobasilar	2.46 (1.07–5.75)	
Intravenous rtPA	2.01 (1.09–3.71)	.024

**Note:**—ref indicates reference; T-Car, occlusion of carotid terminus.

<sup>a</sup> Factors included in multivariate analysis of favorable outcome: age, hta, previous stroke or TIA, systolic BP, admission NIHSS score and ASPECTS, prestroke mRS  $\geq$ 1, intravenous rtPA, general anesthesia, delay in imaging-to-groin puncture, site of occlusion, and the Sofia catheter. Factors included in multivariate model of successful reperfusion: age, current smoking, admission ASPECTS, site of occlusion, intravenous rtPA, etiology, delay in onset to imaging. Factors included in multivariate analysis of excellent reperfusion: age, sex, current smoking, antiplatelet use, glycemia, admission ASPECTS, site of occlusion, intravenous rtPA, and the Sofia catheter. Factors included in multivariate analysis of first-pass effect: age, current smoking, previous stroke or TIA, antiplatelet use, glycemia, admission NIHSS score and ASPECTS, prestroke mRS  $\geq$ 1, site of occlusion, and intravenous rtPA.

<sup>b</sup> Per 10-year increase.

<sup>c</sup> Per 1-point increase.

<sup>d</sup> Per 1-hour increase.

use of a balloon-guide catheter was not significantly associated with FPE, but this could be explained by the rare use of balloon-guide catheters in our population.

Recent publications reported very high rates of FPE.<sup>18,19</sup> Once again, considering our results and literature data, the ADAPT approach, especially with large-bore catheters, has to be considered a reliable front-line technique. In particular, M1 and basilar occlusions are very favorable targets, as demonstrated here.

## Limitations

One limitation of this study is its retrospective nature, which also limits the possibility of harmonizing endovascular procedures among different operators. This can constitute a bias in perioperative data analysis. Nevertheless, this point makes our results very likely to be representative of daily practice in different thrombectomy centers. The absence of core lab analysis might also constitute a limitation. Other potential limitations include differences in study-entry criteria and patient characteristics among the centers that may be a source of bias.

## CONCLUSIONS

The Sofia catheter is an efficient thrombectomy tool, with a good efficacy and safety profile. We demonstrated very high reperfusion rates (mTICI 2b/3 and FPE) with a first-line thrombectomy strategy using Sofia catheters. Further trials comparing different catheters may be useful to appreciate the efficacy and safety differences between these devices.

Disclosures: Bertrand Lapergue—UNRELATED: Consultancy: Stryker; Grants/Grants Pending: research grant from MicroVention for supporting the ETIS Network, research grant for the ASTER 2 trial from Stryker, MicroVention, Penumbra\*; Payment for Lectures Including Service on Speakers Bureaus: Bristol-Myers Squibb, Servier, Boehringer Ingelheim. Xavier Barreau—RELATED: Grant: Bordeaux University Hospital Neuroradiology Unit.\* \*Money paid to the institution.

## REFERENCES

- Goyal M, Menon BK, Van Zwam WH, et al; HERMES collaborators. Endovascular thrombectomy after large-vessel ischaemic stroke: a meta-analysis of individual patient data from five randomised trials. *Lancet* 2016;387:1723–31 CrossRef Medline
- Turk AS, Spiotta A, Frei D, et al. Initial clinical experience with the ADAPT technique: a direct aspiration first pass technique for stroke thrombectomy. *J Neurointerv Surg* 2014;6:231–37 CrossRef Medline
- Turk AS, Frei D, Fiorella D, et al. ADAPT FAST study: a direct aspiration first pass technique for acute stroke thrombectomy. *J Neurointerv Surg* 2014;6:260–64 CrossRef Medline
- Stapleton CJ, Leslie-Mazwi TM, Torok CM, et al. A direct aspiration first-pass technique vs stentriever thrombectomy in emergent large vessel intracranial occlusions. *J Neurosurg* 2018;128:567–74 CrossRef Medline
- Turk AS 3rd, Siddiqui A, Fifi JT, et al. Aspiration thrombectomy versus stent retriever thrombectomy as first-line approach for large vessel occlusion (COMPASS): a multicentre, randomised, open label, blinded outcome, non-inferiority trial. *Lancet* 2019;393:998–1008 CrossRef Medline
- Lapergue B, Blanc R, Gory B, et al; ASTER Trial Investigators. Effect of endovascular contact aspiration vs stent retriever on revascularization in patients with acute ischemic stroke and large vessel occlusion: the ASTER randomized clinical trial. *JAMA* 2017;318:443–52 CrossRef Medline
- Humphries W, Hoit D, Doss VT, et al. Distal aspiration with retrievable stent assisted thrombectomy for the treatment of acute ischemic stroke. *J Neurointerv Surg* 2015;7:90–94 CrossRef Medline
- Stampfl S, Kabbasch C, Muller M, et al. Initial experience with a new distal intermediate and aspiration catheter in the treatment of acute ischemic stroke: clinical safety and efficacy. *J Neurointerv Surg* 2016;8:714–18 CrossRef Medline
- Möhlenbruch MA, Kabbasch C, Kowoll A, et al. Multicenter experience with the new SOFIA Plus catheter as a primary local aspiration catheter for acute stroke thrombectomy. *J Neurointerv Surg* 2017;9:1223–27 CrossRef Medline
- Wong JY, Do HM, Telischak NA, et al. Initial experience with SOFIA as an intermediate catheter in mechanical thrombectomy

- for acute ischemic stroke. *J Neurointerv Surg* 2017;9:1103–06 CrossRef Medline
11. Shallwani H, Shakir HJ, Rangel-Castilla L, et al. **Safety and efficacy of the Sofia (6F) PLUS distal access reperfusion catheter in the endovascular treatment of acute ischemic stroke.** *Clin Neurosurg* 2018;82:312–21 CrossRef Medline
  12. Zaidat OO, Castonguay AC, Linfante I, et al. **First pass effect: a new measure for stroke thrombectomy devices.** *Stroke* 2018;49:660–66 CrossRef Medline
  13. Hungerford JP, Hyer M, Turk AS, et al. **Impact of ASPECT scores and infarct distribution on outcomes among patients undergoing thrombectomy for acute ischemic stroke with the ADAPT technique.** *J Neurointerv Surg* 2017;9:823–29 CrossRef Medline
  14. Sorensen LH, Speiser L, Karabegovic S, et al. **Safety and quality of endovascular therapy under general anesthesia and conscious sedation are comparable: results from the GOLIATH trial.** *J Neurointerv Surg* 2019 Mar 29. [Epub ahead of print] CrossRef Medline
  15. Gariel F, Lapergue B, Bourcier R, et al; ASTER Trial Investigators. **Mechanical thrombectomy outcomes with or without intravenous thrombolysis.** *Stroke* 2018;49:2383–90 CrossRef Medline
  16. Gory B, Armoiry X, Sivan-Hoffmann R, et al. **A direct aspiration first pass technique for acute stroke therapy: a systematic review and meta-analysis.** *Eur J Neurol* 2018;25:284–92 CrossRef Medline
  17. Malisch TW, Zaidat OO, Castonguay C. **Clinical and angiographic outcomes with the combined local aspiration and retriever in the North American Solitaire Stent-Retriever Acute Stroke (NASA) Registry.** *Interv Neurol* 2018;7:26–35 CrossRef Medline
  18. Maegerlein C, Berndt M, Mönch S, et al. **Further development of combined techniques using stent retrievers, aspiration catheters and BGC: the PROTECT<sup>PLUS</sup> technique.** *Clin Neuroradiol* 2018 Nov 9. [Epub ahead of print] CrossRef Medline
  19. Maus V, Henkel S, Riabikin A, et al. **The SAVE technique: large-scale experience for treatment of intracranial large vessel occlusions.** *Clin Neuroradiol* 2018 Jul 19. [Epub ahead of print] CrossRef Medline
  20. Dargazanli C, Fahed R, Blanc R, et al. **Modified Thrombolysis in Cerebral Infarction 2c/Thrombolysis in Cerebral Infarction 3 reperfusion should be the aim of mechanical thrombectomy: insights from the ASTER trial (Contact Aspiration Versus Stent Retriever for Successful Revascularization).** *Stroke* 2018;49:1189–96 CrossRef Medline
  21. Kaschner MG, Rubbert C, Caspers J, et al. **A retrospective single-center case series of direct aspiration thrombectomy as first-line approach in ischemic stroke and review of the literature.** *J Stroke Cerebrovasc Dis* 2019;28:640–48 CrossRef Medline
  22. Blanc R, Redjem H, Ciccio G, et al. **Predictors of the aspiration component success of A Direct Aspiration First Pass Technique (ADAPT) for the endovascular treatment of stroke reperfusion strategy in anterior circulation acute stroke.** *Stroke* 2017;48:1588–93 CrossRef Medline
  23. Schramm P, Navia P, Papa R, et al. **ADAPT technique with ACE68 and ACE64 reperfusion catheters in ischemic stroke treatment: results from the PROMISE study.** *J Neurointerv Surg* 2019;11:226–31 CrossRef Medline
  24. Alawieh A, Chatterjee AR, Vargas J, et al. **Lessons learned over more than 500 stroke thrombectomies using ADAPT with increasing aspiration catheter size.** *Neurosurgery* 2018 Nov 10. [Epub ahead of print] CrossRef Medline
  25. Tsang CO, Cheung IH, Lau KK, et al. **Outcomes of stent retriever versus aspiration-first thrombectomy in ischemic stroke: a systematic review and meta-analysis.** *AJNR Am J Neuroradiol* 2018;39:2070–76 CrossRef Medline
  26. Nikoubashman O, Nikoubashman A, Büsen M, et al. **Necessary catheter diameters for mechanical thrombectomy with ADAPT.** *AJNR Am J Neuroradiol* 2017;38:2277–81 CrossRef Medline
  27. Delgado Almandoz JE, Kayan Y, Wallace AN, et al. **Larger ACE 68 aspiration catheter increases first-pass efficacy of ADAPT technique.** *J Neurointerv Surg* 2019;11:141–46 CrossRef Medline

# Current Hospital Demographics of Subarachnoid Hemorrhage Based on CT Angiography and 3D Rotational Angiography in a Neurosurgical Center

 S.B.T. van Rooij,  R.S. Bechan,  W.J. van Rooij, and  M.E. Sprengers

## ABSTRACT

**BACKGROUND AND PURPOSE:** Aneurysmal subarachnoid hemorrhage is an important cause of mortality and morbidity. Modern hospital demographics are scarce. We evaluated the diagnosis and treatment of patients with SAH in a neurosurgical referral center.

**MATERIALS AND METHODS:** Between March 2013 and April 2015, two hundred eighty-four patients with SAH diagnosed on CT or lumbar puncture were admitted. All patients underwent 64– to 128–detector row CT angiography. Additional imaging was with 3D rotational angiography of all vessels. In patients with aneurysms, characteristics and mode of treatment were recorded.

**RESULTS:** In 197 of 220 patients with an aneurysmal bleeding pattern, we found a cause of the bleeding: One hundred ninety-five patients had a ruptured aneurysm (98%); 1 patient, a micro-AVM; and 1 patient, reversible vasoconstriction syndrome. Of 195 ruptured aneurysms, 6 were dissecting aneurysms and 3 were AVM-associated flow aneurysms. In 23 of 204 patients (11%) with an aneurysmal bleeding pattern and 3D rotational angiography performed, no cause was found. In 8 of 9 patients (89%) with lumbar puncture positive for SAH but CT negative for it, no cause was found. Of 180 patients with a ruptured aneurysm eligible for treatment, 147 (82%) were treated endovascularly and 30 aneurysms (17%) were clipped. Of 204 patients with an aneurysmal bleeding pattern and 3D rotational angiography, 72 (35%) had multiple aneurysms. These 72 patients had, altogether, 117 additional aneurysms, of which 24 (21%) were treated by either coiling or clipping.

**CONCLUSIONS:** This study provides robust data on hospital demographics of SAH in a neurosurgical referral center, based on CTA and 3D rotational angiography of all vessels.

**ABBREVIATION:** 3DRA = 3D rotational angiography

Aneurysmal subarachnoid hemorrhage is an important cause of mortality and continuing morbidity in the population worldwide. The annual incidence of SAH in Western Europe and North America is 6–8 per 100,000 person-years.<sup>1</sup> More than 30% of patients with aneurysmal SAH will die within the first 24 hours, and another 25%–30% will die in the following 4 weeks without some form of intervention.<sup>1</sup> Hospital demographics of SAH have dramatically changed in the past 2 decades. With endovascular techniques, more aneurysms in more patients can be treated than in the era when surgical clipping was the only treatment tech-

nique. Aneurysm diagnosis has immensely improved with acute CTA screening and the implementation of 3D angiographic techniques.<sup>2–4</sup> This results in detection of more and smaller ruptured and (additional) unruptured aneurysms. In this study, we prospectively collected demographic, diagnostic, and treatment data of patients admitted with SAH in a 2-year period in the St Elisabeth Hospital in Tilburg, the Netherlands, a large neurosurgical referral center.

## MATERIALS AND METHODS

### Patient Population

This observational study with prospectively collected data was compliant with institutional privacy policy and approved by the institutional review board. Between March 2013 and April 2015, patients with SAH on native CT scans or with lumbar puncture positive for SAH and who underwent CTA were entered into a data base, as previously described.<sup>3,4</sup> The St. Elisabeth Hospital in Tilburg, the Netherlands, is a large neurosurgical referral center with a recruitment population of 2.5 million and is a Level I trauma center.

Received February 7, 2019; accepted after revision April 4.

From the Department of Radiology (S.B.T.v.R.), Noordwest Ziekenhuisgroep Alkmaar, the Netherlands; Universitair Medisch Centrum Amsterdam (R.S.B.), Vrije Universiteit, Amsterdam, the Netherlands; Algemeen Ziekenhuis Turnhout (W.J.v.R.), Turnhout, Belgium; and Universitair Medisch Centrum Amsterdam (M.E.S.), Academisch Medisch Centrum, Amsterdam, the Netherlands.

Please address correspondence to S.B.T. van Rooij, MD, Department of Radiology, Noordwest Ziekenhuisgroep Alkmaar, Wilhelminalaan 12, 1815JD Alkmaar, the Netherlands; e-mail: s.b.t.rooij@gmail.com

<http://dx.doi.org/10.3174/ajnr.A6060>

Patients were categorized according to medical history and blood distribution on CT as having aneurysmal SAH, perimesencephalic SAH, trauma and SAH, no blood on CT, and a lumbar puncture positive for SAH (xanthochromia). A perimesencephalic bleeding pattern was defined as blood confined to the cisterns around the midbrain in the prepontine, interpeduncular, and ambient cisterns. Patient and aneurysm characteristics and modes of treatment were recorded.

### **CT Angiography**

CTA was performed on 1 of 3 CT scanners: Brilliance iCT 256–detector row, Ingenuity 128–detector row (Philips Healthcare, Best, the Netherlands) and Somatom Definition AS 64–detector row (Siemens, Erlangen, Germany). Volume CT was routinely performed at 130 mA and 100–120 kV(peak). Collimation, rotation time, and pitch were optimized for the individual CT scanner according to recommendations of the manufacturer. A 90-mL dose of iodinated contrast medium (iodixanol, 270 mg of iodine/mL, Visipaque 270; GE Healthcare, Piscataway, New Jersey) was injected at a rate of 4.0 mL/s into an antecubital vein via a 20-ga catheter, followed by 40 mL of saline solution. CT scanning was triggered using a bolus-tracking technique, with the ROI placed in the aortic arch. Image acquisition started 8 seconds after the attenuation reached the predefined threshold of 130–150 HU. The scanning time was approximately 5.0–7.0 seconds. Images were reconstructed with a 0.9- to 1.0-mm section thickness and a 0.45- to 0.5-mm increment. Volume CT dose index and dose-length product were 25.3–26.7 mGy and 475–576 mGy × cm, respectively.

### **3D Rotational Angiography**

Patients with aneurysms diagnosed on CTA or with CTA negative for SAH but an aneurysmal bleeding pattern underwent 3D rotational angiography (3DRA) of all cerebral vessels. Angiography was performed on a biplane angiographic system (Allura Xper FD 20/10; Philips Healthcare). In uncooperative or intubated patients, 3DRA was performed with the patient under general anesthesia. A single 3D rotational angiographic run was acquired of both internal carotid arteries and 1 vertebral artery with a hand injection of 12–20 mL of contrast material. When the contralateral distal vertebral artery was not visualized, an additional 2D biplane run was performed of this vertebral artery. The tube rotation arc was 240° (1 rotation used), with a rotation time of 4.1 seconds. The images were reconstructed in a 256 × 256 matrix. The rotational angiographic data were transferred to an independent workstation (Integris 3DRA Workstation; Philips Healthcare) for instant generation of 3D reformatted images.

### **Analysis of CT Angiography and 3D Rotational Angiography**

CTA data were reformatted on an independent 3D workstation (IntelliSpace Portal; Philips Healthcare). Three neuroradiologists evaluated maximum-intensity-projection, volume-rendered, and multiplanar reformatted images. Source images, postprocessed images, and 3D reconstructions with bone removal were transferred to a PACS.

3DRA reformatted images were reviewed on the workstation

by the first and senior authors in consensus. The presence, location, and size of aneurysms were recorded in a data base. Other vascular disorders that might be responsible for the subarachnoid hemorrhage such as arterial dissections, arteriovenous malformations, Moyamoya phenomenon, or reversible vasospasm syndrome were separately recorded. In patients without an obvious vascular disorder that might be responsible for the SAH, 3DRA was repeated after 1 week.<sup>4</sup>

### **Treatment**

When logistically possible, 3DRA was followed immediately by endovascular treatment, with the patient under general anesthesia. Patients with aneurysms not suitable for coiling (wide-neck anterior circulation, fusiform, vessels arising from the sac) were scheduled for surgery. When logistically possible, good-grade (noncomatose) patients were clipped within 24 hours. In poor-grade patients, the operation was delayed.

### **Statistical Analysis**

Results were expressed with descriptive statistics, and categorical variables, as frequencies or percentages with 95% CIs.

## **RESULTS**

Of 284 patients with SAH, 220 (77%) had an aneurysmal bleeding pattern, 39 (14%) had a perimesencephalic bleeding pattern, 9 (3%) had CT for SAH and a lumbar puncture positive for SAH, and 16 (6%) had a trauma and a subarachnoid hemorrhage.

Of 284 patients, 280 underwent CTA as the first diagnostic technique to detect the cause of the SAH. Four patients with SAH directly proceeded to angiography without CTA. The Figure illustrates the diagnosis and treatment of the study population in a flow chart.

### **Aneurysmal Bleeding Pattern**

Of 220 patients with an aneurysmal bleeding pattern, 16 patients with confirmed aneurysms on CTA (7%) were in moribund clinical condition and died before angiography could be performed.

The remaining 204 patients had 3DRA after CTA. In 29 of 204 patients (14%), the initial 3DRA was negative for SAH and was repeated after 1 week. Repeat 3DRA showed an aneurysm in 6 of these 29 patients: one 8-mm supraclinoid dissecting aneurysm, 2 superior cerebellar artery aneurysms (1 and 2 mm), one 2-mm posterior communicating aneurysm, one 1-mm A1 aneurysm, and 1 vertebral dissection.

In 195 of 220 patients with an aneurysmal bleeding pattern (87%; 95% CI, 84%–92%), at least 1 aneurysm was detected. Seventy-two of 204 patients with 3DRA (35%; 95% CI, 29%–42%) had multiple aneurysms. Forty-three patients had 2 aneurysms, 18 patients had 3 aneurysms, 10 patients had 4 aneurysms, and 1 patient had 5 aneurysms.

Of 220 patients with an aneurysmal bleeding pattern, 184 had saccular aneurysms, 6 had a dissecting aneurysm (1 PICA, 3 vertebral artery, and 2 internal carotid artery aneurysms), and 3 patients had an AVM-related ruptured flow aneurysm.

Of the 25 patients with aneurysmal SAH and no aneurysm, 1 patient (0.5%) had a cervical spinal micro-AVM and 1 patient (0.5%) had a reversible vasoconstriction syndrome. In 23 of 220

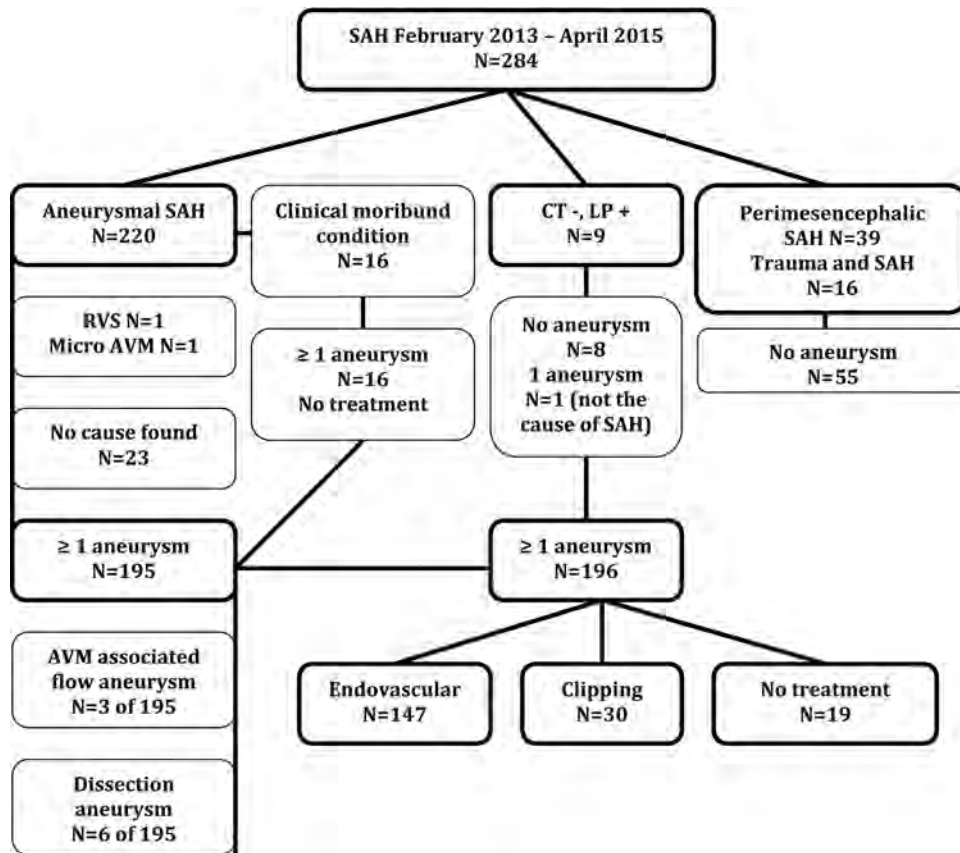


**FIGURE.** Diagnosis and treatment in 284 consecutive patients with SAH. RVS indicates reversible vasospasm syndrome; LP, lumbar puncture.

patients with aneurysmal SAH (10%; 95% CI, 7%–15%), no aneurysm or other vascular disorder was found.

#### **Perimesencephalic Bleeding Pattern**

Of 284 patients, 39 (14%; 95% CI, 10%–18%) had a perimesencephalic bleeding pattern on native CT. Fifteen of 39 underwent 3DRA in addition to CTA. CTA and 3DRA were negative for aneurysms in all 39.

#### **Positive Lumbar Puncture Findings**

Of 284 patients, 9 (3%) had no blood on CT but had a lumbar puncture positive for xanthochromia. All 9 underwent CTA, and 2 patients also had 3DRA. In 1 patient, a 7-mm dysplastic fusiform middle cerebral artery aneurysm was found that was not considered the cause of the SAH.

#### **Trauma and SAH**

Of 284 patients, 16 (6%) had trauma and SAH and an unknown cause and effect. CTA findings were normal in all 16 patients.

#### **Treatment**

**Ruptured Aneurysm Treatment.** Of 180 patients eligible for treatment with a ruptured aneurysm (including 6 dissecting aneurysms), in 147 (82%), this aneurysm was treated endovascularly. Of 141 saccular aneurysms, 115 (82%) were treated with simple coiling; 24 (17%), with balloon- or stent-assisted coiling; and 2 (1%), with an intrasaccular flow disrupter (WEB aneurysm embolization system; Sequent Medical, Aliso Viejo, California).

Of 6 dissecting aneurysms, 3 vertebral dissections and 1 PICA dissection were treated with parent vessel coil occlusion. Of 2 internal carotid artery dissecting aneurysms, 1 was treated with stent-assisted coiling and the other with a flow diverter. Of 3 patients with a ruptured AVM-related flow aneurysm, 2 were treated with parent vessel coil occlusion; and 1, with selective coiling. Of 180 patients with a ruptured aneurysm, 30 aneurysms (17%) were clipped.

#### **Characteristics of Patients with Endovascularly Treated-versus-Clipped Aneurysms**

Patient and aneurysm characteristics of those with endovascularly treated and clipped aneurysms are shown in the Table. Reasons to proceed with an operation instead of endovascular treatment in 30 patients were wide-neck aneurysms in 27, failed coiling procedure in 2, and no endovascular access in 1.

#### **Patients Who Were Not Treated**

Nineteen of 196 patients with a saccular aneurysm (10%) were not treated: Sixteen patients were in a clinically moribund condition, and 3 patients were older than 90 years of age. It was decided not to treat the cervical micro-AVM.

#### **Timing of Treatment**

The mean time between the ictus and endovascular treatment was 1 day (median, 1 day; range, 0–20 days). The mean time between diagnosis and endovascular treatment was 1 day (median, 0 days; range, 0–11 days). Reasons for a delay between ictus and endo-

### Clinical variables at admission of patients with ruptured aneurysms eligible for treatment

	Endovascular (n = 147) (82%)	Surgery (n = 30) (17%)
Age (yr)	Mean, 58; median, 58; range, 27–86	Mean, 58; median, 59; range, 28–84
Sex	106 Female (72%)	23 Female (77%)
HH at admission		
1	54	11
2	22	8
3	33	4
4	21	6
5	17	1
Aneurysm size		
≤3 mm	25	13
4–6 mm	63	9
7–10 mm	39	6
≥10 mm	20	2
Aneurysm location (No.)		
Anterior cerebral artery	61	17
Middle cerebral artery	21	8
Internal carotid artery	43	3
Posterior circulation	22	2

**Note:**—HH indicates Hunt and Hess scale.

vascular treatment were admission or referral from other hospitals several days after the ictus, clinical condition that did not allow angiography directly after admission, or initial negative findings on angiography. Most patients (111 of 146, 76%) were treated within 24 hours after the ictus. The mean time between the ictus and clipping was 10 days (median, 9 days; range, 0–31 days). The mean time between diagnosis of the ruptured aneurysm and clipping was 8 days (median, 8 days; range, 0–30 days).

### Treatment of Additional Aneurysms

Of the 204 patients with an aneurysmal bleeding pattern and 3DRA, 72 (35%) had multiple aneurysms. These 72 patients had, altogether, 117 additional aneurysms, indicating a mean of 1.6 bystander aneurysms next to the index aneurysm. Of these 117 additional aneurysms, 24 (21%) were treated by either coiling or clipping.

## DISCUSSION

In this prospective observational study, we found that in 69% of patients with SAH (195 of 284), a ruptured aneurysm was the cause. This is much lower than in the literature of the early millennium with a ruptured aneurysm as cause of SAH in 85%.<sup>5,6</sup> Our incidence is lower because of zero yield of aneurysms in patients with a perimesencephalic bleeding pattern, with trauma and SAH, and with CT negative/lumbar puncture positive for SAH. Of 220 patients with an aneurysmal bleeding pattern on CT, an aneurysm was found in 195 (89%) and no cause was found in 23 (10%), not even after repeat 3D angiography.

In our study, 39 of 284 patients (14%) had a perimesencephalic bleeding pattern on native CT. CTA was negative for aneurysms in all 39. Fifteen of 39 underwent 3DRA in addition to CTA, all negative for aneurysms. The cause of perimesencephalic hemorrhage is likely not aneurysmal but may be venous, and the patients have no risk of rebleed.<sup>7–9</sup> Cerebral angiography is not needed in patients with perimesencephalic hemorrhage who had negative CTA findings.<sup>10</sup>

Multiple aneurysms were found in 72 of the 204 patients (35.3%) with an aneurysmal bleeding pattern and 3DRA performed. These 72 patients had, altogether, 117 additional aneurysms, indicating a mean of 1.6 bystander aneurysms. These figures are in the same range as in a recent large Swiss study<sup>11</sup> in which multiplicity was found in 474 of 1787 patients (26.5%). Patients with multiple aneurysms had a mean of 1.4 bystander aneurysms in addition to the index aneurysm. In older postmortem and angiographic studies, a prevalence of multiplicity of about 12% was found, substantially less than in the current study.<sup>12</sup> The excellent sensitivity for detecting aneurysms with 3D angiography indicates that multiplicity of intracranial aneurysms is on the order of 1 in 3 instead of 1 in 8 patients as previously believed.

Ruptured aneurysms were treated endovascular in 82%; this proportion is relatively high compared with other reports.<sup>13</sup> Although there have been several studies on changes and trends in the management of SAH since the publication of the International Subarachnoid Aneurysm Trial (ISAT), scarce data exist on the characteristics of patients undergoing surgical treatment.<sup>13–16</sup> Most aneurysms in our population that were referred to surgery were anterior circulation wide-neck aneurysms with vessels coming from the sac. We found that most clipped aneurysms were anterior communicating artery aneurysms; this is in concordance with another study.<sup>14</sup>

AVM-associated flow aneurysms are a rare cause of SAH.<sup>15</sup> In our study, 3 of 195 patients (1.5%) with a ruptured aneurysm had an AVM-associated ruptured flow aneurysm. One AVM was supratentorial, and 2 AVMs were located in the posterior fossa. Posterior fossa AVMs are infrequent, comprising 7%–15% of intracranial AVMs.<sup>15</sup> An infratentorial AVM location is independently associated with hemorrhagic AVM presentation.<sup>16</sup> Dissecting aneurysms are also a rare cause of SAH.<sup>17,18</sup> In our study, they were the cause of SAH in 6 of 195 patients (3%).

In our study, 9 of 284 patients (3%) had CT negative and lumbar puncture positive for SAH. In 1 of 9 patients, an aneurysm was found that was not considered the cause of hemorrhage. Another prospective study found, in 40 of 94 patients (43%), an intracranial aneurysm or dissection.<sup>19</sup> The small patient groups make the comparison invalid.

In our study, 16 of 284 patients (6%) had trauma and SAH and an unknown cause and effect. CTA findings were normal in all 16 patients. In a recent retrospective study, 186 of 617 patients with traumatic SAH underwent CTA. The authors found 8 ruptured aneurysms; these patients all had blood in the subarachnoid cisterns and Sylvian fissures. They found 5 unruptured aneurysms; these patients had only peripheral subarachnoid blood. Their data suggest a more selective approach to screening CTAs in patients with trauma and SAH.<sup>14</sup>

Of note, our results are based on SAH demographics in a neurosurgical referral center and thus cannot be generalized to demographics of SAH in general.

## CONCLUSIONS

Our study provides robust hospital demographic data on SAH based on CTA for screening and 3DRA of all cerebral vessels. The excellent depiction of aneurysms with 3DRA shows a shift of some

data: Aneurysm multiplicity was on the order of 1 in 3 (instead of 1 in 8), and 11% of patients with an aneurysmal bleeding pattern on CT had no aneurysm, not even after repeat 3DRA.

Disclosures: Sanne B.T. van Rooij—UNRELATED: Grant: MicroVention, Comments: support of salary and travel expenses directly related to the study.

## REFERENCES

1. Linn FH, Rinkel GJ, Algra A, et al. **Incidence of subarachnoid hemorrhage: role of region, year, and rate of computed tomography—a meta-analysis.** *Stroke* 1996;27:625–29 CrossRef Medline
2. van Rooij WJ, Sprengers ME, de Gast AN, et al. **3D rotational angiography: the new gold standard in the detection of additional intracranial aneurysms.** *AJNR Am J Neuroradiol* 2008;29:976–79 CrossRef Medline
3. Bechan RS, van Rooij SB, Sprengers ME, et al. **CT-angiography versus 3D rotational angiography in patients with subarachnoid hemorrhage.** *Neuroradiology* 2015;57:1239–46 CrossRef Medline
4. Bechan RS, van Rooij WJ, Peluso JP, et al. **Yield of repeat 3D angiography in patients with aneurysmal-type subarachnoid hemorrhage.** *AJNR Am J Neuroradiol* 2016;37:2299–303 CrossRef Medline
5. van Gijn J, Rinkel GJ. **Subarachnoid haemorrhage: diagnosis, causes and management.** *Brain* 2001;124(Pt 2):249–78 CrossRef Medline
6. Van Gijn J, Kerr RS, Rinkel GJ. **Subarachnoid haemorrhage.** *Lancet* 2007;369:306–18 CrossRef Medline
7. Mensing LA, Vergouwen MD, Laban KG, et al. **Perimesencephalic hemorrhage: a review of epidemiology, risk factors, presumed cause, clinical course, and outcome.** *Stroke* 2018;49:1363–70 CrossRef Medline
8. Rinkel GJ, van Gijn J, Wijdicks EF. **Subarachnoid hemorrhage without detectable aneurysms: a review of the causes.** *Stroke* 1993;24:1403–09 CrossRef Medline
9. van der Schaaf IC, Velthuis BK, Gouw A, et al. **Venous drainage in perimesencephalic haemorrhage.** *Stroke* 2004;35:1614–18 CrossRef Medline
10. Velthuis BK, Rinkel GJ, Ramos LM, et al. **Perimesencephalic hemorrhage: exclusion of vertebrobasilar aneurysms with CT angiography.** *Stroke* 1999;30:1103–09 CrossRef Medline
11. Roethlisberger M, Achermann R, Bawarjan S, et al; Swiss SOS group. **Predictors of occurrence and anatomic distribution of multiple aneurysms in patients with aneurysmal subarachnoid hemorrhage.** *World Neurosurg* 2018;111:e199–205 CrossRef Medline
12. Rinkel GJ, Djibuti M, Algra A, et al. **Prevalence and risk of rupture of intracranial aneurysms: a systematic review.** *Stroke* 1998;29:251–56 CrossRef Medline
13. Qureshi AI, Vazquez G, Tariq N, et al. **Impact of International Subarachnoid Aneurysm Trial results on treatment of ruptured intracranial aneurysms in the United States: clinical article.** *J Neurosurg* 2011;114:834–41 CrossRef Medline
14. Koźba-Gosztyla M, Czapiga B, Jarmundowicz W. **Aneurysmal subarachnoid hemorrhage: who remains for surgical treatment in the post-ISAT era?** *Arch Med Sci* 2015;11:536–43 CrossRef Medline
15. Flett LM, Chandler CS, Giddings D, et al. **Aneurysmal subarachnoid hemorrhage: management strategies and clinical outcomes in a regional neuroscience center.** *AJNR Am J Neuroradiol* 2005;26:367–72 Medline
16. Arnaout OM, Gross BA, Eddleman CS, et al. **Posterior fossa arteriovenous malformations.** *Neurosurg Focus* 2009;26:E12 CrossRef Medline
17. Gonzalez AM, Narata AP, Yilmaz H, et al. **Blood blister-like aneurysms: single center experience and systematic literature review.** *Eur J Radiol* 2014;83:197–205 CrossRef Medline
18. Peluso JP, van Rooij WJ, Sluzewski, et al. **Endovascular treatment of symptomatic intradural vertebral dissecting aneurysms.** *AJNR Am J Neuroradiol* 2008;29:102–06 CrossRef Medline
19. Bakker NA, Groen RJ, Foumani M, et al. **Appreciation of CT-negative, lumbar puncture-positive subarachnoid haemorrhage: risk factors for presence of aneurysms and diagnostic yield of imaging.** *J Neurol Neurosurg Psychiatry* 2014;85:885–88 CrossRef Medline

# Histologic and Biomolecular Similarities in Healing between Aneurysms and Cutaneous Skin Wounds

J.R. Ayers-Ringler, Z. Khashim, Y.-H. Ding, D.F. Kallmes, and R. Kadirvel



## ABSTRACT

**SUMMARY:** The poorly understood mechanisms of aneurysm healing contribute substantially to the pressing medical problem of coiled aneurysm recanalization. Using an established saccular aneurysm model, we developed an animal model system in rabbits to study aneurysm and skin wound healing concurrently in the same animal. We found treated aneurysm healing to be similar to skin wound healing both histologically and in biomarker gene and protein expression, but in a delayed fashion.

**ABBREVIATIONS:** GAPDH = glyceraldehyde phosphate dehydrogenase; H&E = hematoxylin-eosin; SMA1 =  $\alpha$  smooth muscle actin; TGF $\beta$ 1 = transforming growth factor  $\beta$  1; PDGF = platelet derived growth factor; VEGF = vascular endothelial growth factor

Despite wide use and considerable safety of endovascular coiling of intracranial aneurysms, the recurrence rate is high even with second-generation coils,<sup>1</sup> partially due to a dearth of knowledge about healing mechanisms involved.<sup>2</sup> Conversely, cutaneous wound healing is well-established. The 4 distinct-yet-overlapping stages of cutaneous wound healing (hemostasis, inflammation, proliferation, and remodeling) have been thoroughly described.<sup>3</sup> Here we demonstrate that concurrent study, in the same research subjects, of endovascular-versus-cutaneous healing provides insight into deficiencies in the cellular, molecular, and humoral features in aneurysm healing, enabling elucidation of potential targets for improved outcomes.

## MATERIALS AND METHODS

### Aneurysm Creation and Coil Embolization

All procedures were approved by the Institutional Animal Care and Use Committee before study initiation. Elastase-induced saccular aneurysms were created at the origin of the right common carotid artery in 12 female New Zealand white rabbits.<sup>4</sup> At least 3

weeks later, aneurysms were treated with platinum coils. DSA was performed after embolization.

### Cutaneous Ear Wound Creation

Immediately after aneurysm treatment, an ear skin defect was created on the ventral side of 1 ear using a 1-cm stainless steel punch,<sup>5</sup> with removal of skin down to the cartilage. Hemostasis was achieved with pressure, followed by occlusive dressing (TegaDerm; 3M, St. Paul, Minnesota). Ear wounds were assessed visually daily for healing and wound closure rate.

### Follow-Up Imaging and Tissue Harvest

At days 1, 5, 14, and 30 (groups 1–4) following treatment, DSA was performed from a left femoral approach, and the animals were euthanized. The aneurysm, ear wound, and contralateral control tissues were harvested for histology or cut in 2 for biomolecular studies.

### Angiographic Analysis

Aneurysm occlusions at follow-up were rated either stable or progressive, or recanalized compared with posttreatment angiograms using the modified Raymond scale.<sup>6</sup>

### Histologic Analysis

Formalin-fixed aneurysms were evaluated for the degree of neck tissue coverage.<sup>7</sup> Following a modified histologic technique, aneurysms and ear wounds were sectioned and stained with hematoxylin-eosin (H&E) or Masson Trichrome for collagen. A semiquantitative scoring for thrombus organization, neointelialization, inflammation, cellularity, and collagen

Received March 13, 2019; accepted March 19.

From the Department of Radiology, Mayo Clinic, Saint Mary's Hospital, Rochester, Minnesota.

This work was supported by Mayo Clinic Radiology Research and R01 grant number NS076491.

Please address correspondence to Ramanathan Kadirvel, PhD, Mayo Clinic, Department of Radiology, Saint Mary's Hospital, Alfred 9-446CAR, 1216 2nd St SW, Rochester, MN 55902; e-mail: kadir@mayo.edu

Indicates open access to non-subscribers at www.ajnr.org

<http://dx.doi.org/10.3174/ajnr.A6046>

### Genes important in cutaneous wound healing

Wound-Healing Phase	Time	Cell Types	Key Molecules
Inflammation	0 min to 6 days	Platelets, monocytes, neutrophils, macrophages, and T-lymphocytes	PDGF, TGF $\beta$ 1, VEGF, CD86, CD206
Proliferation	24 hr to weeks	Fibroblasts, endothelial cells, keratinocytes	TGF $\beta$ 1, VEGF, PDGF, MMP9, CD86, CD206
Remodeling	4 days to months	Fibroblasts	PDGF, TGF $\beta$ 1, SMA1, CD206

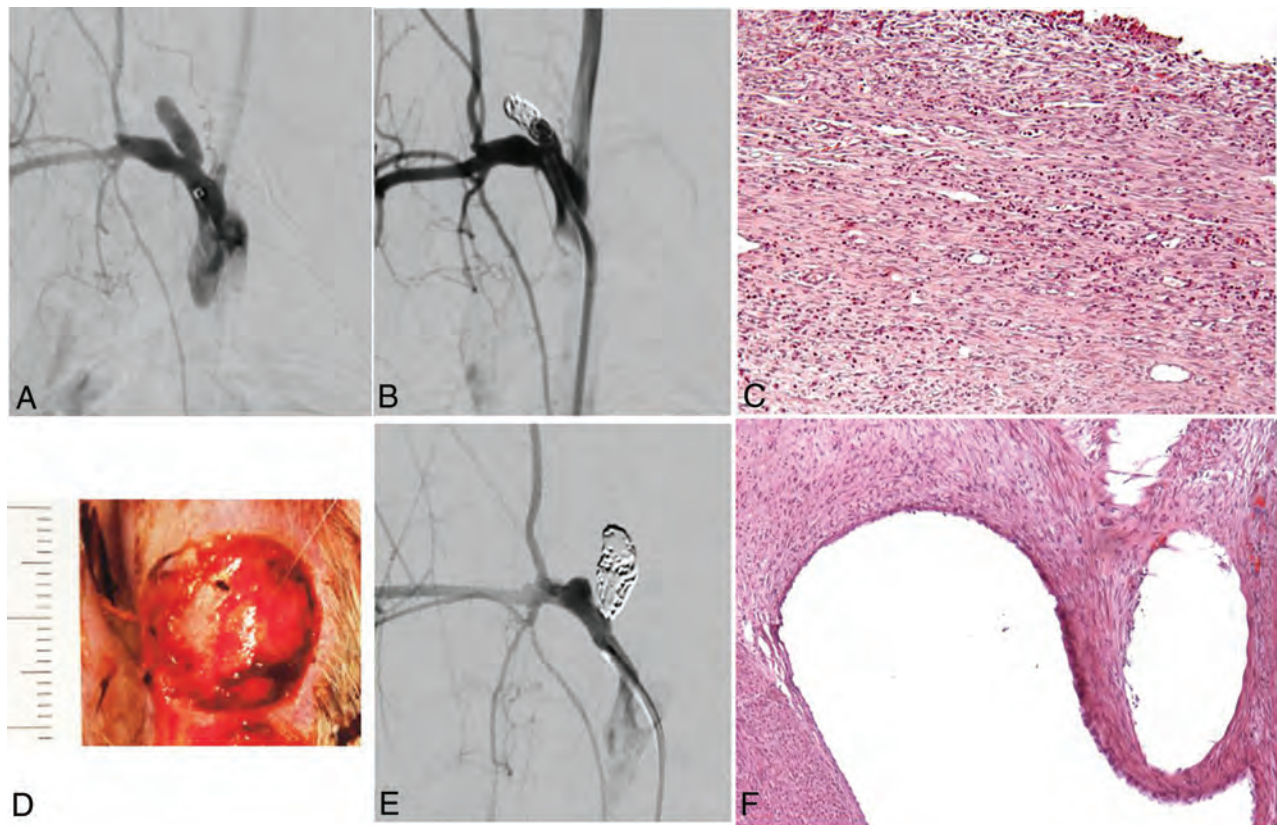


**FIG 1.** Angiograms with H&E-stained tissue sections. Elastase-induced aneurysm (A) on the day of platinum coil embolization and ear wound creation. Angiogram of coiled aneurysm at 14 days (B) with a corresponding ear wound (C, H&E, magnification  $\times 100$ ), macro image of the ear wound on day of sacrifice (D, ruler markings are in centimeters, the smallest ticks in millimeters). Angiogram of 30-day coiled aneurysm (E) with corresponding aneurysm (F, H&E, magnification  $\times 200$ ). Note diffuse, dense myofibroblast (long, spindle-shaped) proliferation in both H&E photomicrographs.

deposition was performed by a blinded reviewer. In addition, an ordinal grading system was used to evaluate histologic healing of aneurysms between groups.

#### RNA Extraction and Expression Analysis by Real-Time Polymerase Chain Reaction

Total RNA was isolated and converted to complementary DNA followed by real-time polymerase chain reaction with SYBR greenER (www.thermofisher.com). Target gene expression (Table) was normalized to *glyceraldehyde phosphate dehydrogenase* (GAPDH) and reported as a fold change relative to control tissues (contralateral tissues) using the  $2^{-\Delta\Delta Ct}$  method.

#### Protein Extraction and Analysis by Sodium Dodecyl Sulfate Polyacrylamide Gel Electrophoresis and Western Blot

Soluble proteins were extracted from tissue samples with RIPA buffer (<https://www.thermofisher.com/order/catalog/product/89900>). Protein separation and western analysis were performed

using a Wes system (ProteinSimple, San Jose, California). Protein expression data were normalized to control proteins (GAPDH or  $\beta$ -actin) using Compass Software (<http://www.compass-software.de/en-us>) and reported as fold change relative to control tissues.

#### Statistical Analysis

Continuous variables were compared using a Student *t* test, and categorical variables were compared using the Fisher exact test.

### RESULTS

#### Aneurysm Angiography

Among the first 3 groups, mean aneurysm neck, width, and height were  $3.3 \pm 1.8$  mm,  $4.0 \pm 1.8$  mm, and  $9.8 \pm 1.6$  mm, respectively. The aneurysms were completely occluded immediately after coil embolization in 11 of 12 cases (92%), the other being incompletely occluded (8%). Two of the 3 aneurysms in the 24-hour

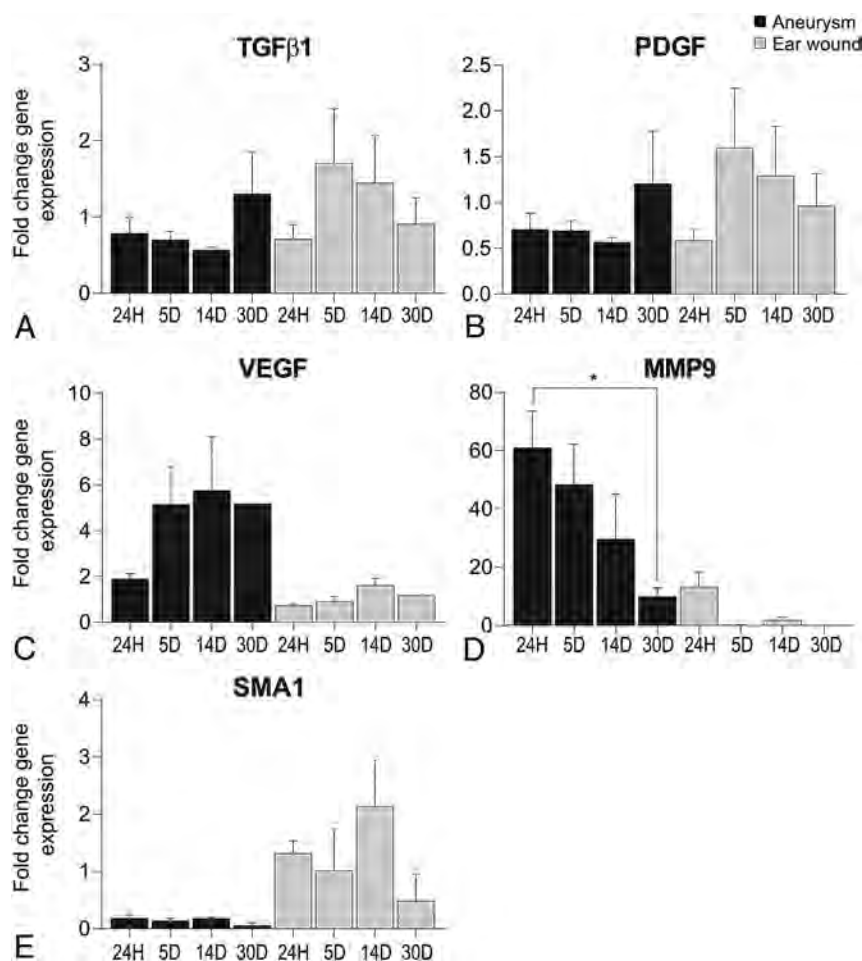


**FIG 2.** Gene expression data from aneurysms and cutaneous ear wounds after 24 hours (24H), 5 days (5D), and 14 days (14D). Data were normalized to *GAPDH* and displayed as a fold change relative to normal tissues (left carotid artery or contralateral ear, respectively) from the same animal ( $P = .0422$  in D) ( $n = 3$  animals, 3 experimental replicates). *PDGF* indicates platelet-derived growth factor; *VEGF*, vascular endothelial growth factor; *MMP9*, matrix metalloproteinase 9; 30D, 30 days.

group, and 1 in the 14-day group showed recanalization at sacrifice. All the other aneurysms (9 of 12) remained completely occluded (75%) (Fig 1).

### Histology

Histologic analysis revealed necrosis and inflammatory cell infiltration in both epidermal and dermal layers of ear wounds at both 24 hours and 5 days, whereas scab formation in the epidermis and diffuse, dense cellular proliferation of myofibroblasts within the dermal layer with minimal inflammatory cells was found by 14 days. Aneurysm features were consistent with previous findings,<sup>8</sup> with sparse myofibroblasts at the periphery of the aneurysm dome by 14 days, increasing dramatically by 30 days (Fig 1D, -F).

### Biomolecules

Inflammatory marker gene expression was elevated at 5 days in ear wounds but reduced/delayed until 30 days in aneurysms (Fig 2A, -B). Protein expression, however, was only 2-fold for transforming growth factor  $\beta 1$  (*TGFβ1*) at 24 hours and 30 days in ear wounds (data not shown). Proliferation marker expressions in

aneurysms were higher compared with ear wounds (Fig 2C, -D) and with inflammatory markers, overall.  $\alpha$  smooth-muscle actin (*SMA1*) remodeling marker expressions were relatively unremarkable, with a small increase at 14 days in ear wounds (Fig 2E). Macrophage analysis showed an overall M1 polarization, with peak CD86 levels at 24 hours in aneurysms and 5 days in ear wounds (data not shown).

### DISCUSSION

Our results reveal similarities and differences in wound-healing mechanisms for these 2 disparate environments. Histologically, skin wounds at 2 weeks resemble aneurysms at 1 month following platinum coil treatment,<sup>8</sup> suggesting a roughly 2-week healing delay in coiled aneurysms relative to skin wounds. Previous studies<sup>8</sup> showed similar findings, supporting this issue of deficient immune cell infiltration and immune-driven healing mechanisms in platinum-coiled aneurysms.<sup>2</sup> The biomolecular profiles reflect this healing delay and confirm an M1 polarization in the macrophage profile, indicating a deficient prohealing phenotype.<sup>9</sup>

### CONCLUSIONS

This novel animal model enabling longitudinal study of platinum-coiled aneurysm healing in parallel with cutaneous wound healing provides an exceptional level of control and will

help determine key signaling events necessary for proper arterial wound healing, promising development of improved treatments.

### ACKNOWLEDGMENTS

We thank Chunfeng Zhao, MD, Praveen Kolumam Parameswaran, and Daiying Dai for essential work done for this article.

Disclosures: David F. Kallmes—UNRELATED: Stock/Stock Options: Superior Medical Experts, Comments: founder/shareholder. Ram Kadirvel—RELATED: Grant: National Institutes of Health, Comments: grant No. NS076491.\* Money paid to the institution.

### REFERENCES

1. Broeders JA, Ahmed Ali U, Molyneux AJ, et al. Bioactive versus bare platinum coils for the endovascular treatment of intracranial aneurysms: systematic review and meta-analysis of randomized clinical trials. *J Neurointerv Surg* 2016;8:898–908 CrossRef Medline
2. Brinjikji W, Kallmes DF, Kadirvel R. Mechanisms of healing in coiled intracranial aneurysms: a review of the literature. *AJNR Am J Neuroradiol* 2015;36:1216–22 CrossRef

3. Baum CL, Arpey C. J. **Normal cutaneous wound healing: clinical correlation with cellular and molecular events.** *Dermatol Surg* 2005;31:674–86; discussion 686 CrossRef Medline
4. Altes TA, Cloft HJ, Short JG, et al. **1999 ARRS Executive Council Award: creation of saccular aneurysms in the rabbit—a model suitable for testing endovascular devices.** *American Roentgen Ray Society. AJR Am J Roentgenol* 2000;174:349–54 CrossRef Medline
5. Houdek MT, Wyles CC, Stalboerger PG, et al. **Collagen and fractionated platelet-rich plasma scaffold for dermal regeneration.** *Plast Reconstr Surg* 2016;137:1498–1506 CrossRef Medline
6. Raymond J, Salazkin I, Georganos S, et al. **Endovascular treatment of experimental wide neck aneurysms: comparison of results using coils or cyanoacrylate with the assistance of an aneurysm neck bridge device.** *AJNR Am J Neuroradiol* 2002;23:1710–16 Medline
7. Dai D, Ding H, Lewis DA, et al. **A proposed ordinal scale for grading histology in elastase-induced, saccular aneurysms.** *AJNR Am J Neuroradiol* 2006;27:132–38 Medline
8. Dai D, Ding YH, Kadirvel R, et al. **A longitudinal immunohistochemical study of the healing of experimental aneurysms after embolization with platinum coils.** *AJNR Am J Neuroradiol* 2006;27:736–41 Medline
9. Hoh BL, Hosaka K, Downes DP, et al. **Monocyte chemotactic protein-1 promotes inflammatory vascular repair of murine carotid aneurysms via a macrophage inflammatory protein-1 $\alpha$  and macrophage inflammatory protein-2-dependent pathway.** *Circulation* 2011;124:2243–52 CrossRef Medline

# An Ultrasonographic Multiparametric Carotid Plaque Risk Index Associated with Cerebrovascular Symptomatology: A Study Comparing Color Doppler Imaging and Contrast-Enhanced Ultrasonography

V. Rafailidis, I. Chrysosgonidis, C. Xerras, E. Grisan, G.-A. Cheimariotis, T. Tegos, D. Rafailidis, P.S. Sidhu, and A. Charitanti-Kouridou

## ABSTRACT

**BACKGROUND AND PURPOSE:** Various ultrasonographic features of carotid plaques have been associated with the occurrence of stroke, highlighting the need for multi-parametric assessment of plaque's vulnerability. Our aim was to compare ultrasonographic multiparametric indices using color Doppler imaging and contrast-enhanced sonography between symptomatic and asymptomatic carotid plaques.

**MATERIALS AND METHODS:** This was a cross-sectional observational study recruiting 54 patients (72.2% male; median age, 61 years) undergoing sonography and contrast-enhanced sonography. Patients were included if a moderately or severely stenotic internal carotid artery plaque was detected, with the plaque being considered symptomatic if it was ipsilateral to a stroke occurring within the last 6 months. A vulnerability index, previously described by Kanber et al, combined the degree of stenosis, gray-scale median, and a quantitative measure of surface irregularities (surface irregularity index) derived from color Doppler imaging and contrast-enhanced ultrasonography, resulting in 2 vulnerability indices, depending on the surface irregularity index used. Mann-Whitney *U* and *t* tests were used to compare variables between groups, and receiver operating characteristic curves were used to compare diagnostic accuracy.

**RESULTS:** Sixty-two plaques were analyzed (50% symptomatic), with a mean degree of stenosis of 68.9%. Symptomatic plaques had a significantly higher degree of stenosis (mean, 74.7% versus 63.1%;  $P < .001$ ), a lower gray-scale median (13 versus 38;  $P = .001$ ), and a higher Kanber vulnerability index based both on color Doppler imaging (median, 61.4 versus 16.5;  $P < .001$ ) and contrast-enhanced ultrasonography (median, 88.6 versus 25.2;  $P < .001$ ). The area under the curve for the detection of symptomatic plaques was 0.772 for the degree of stenosis alone, 0.783 for the vulnerability index–color Doppler imaging, and 0.802 for the vulnerability index–contrast-enhanced ultrasonography, though no statistical significance was achieved.

**CONCLUSIONS:** Symptomatic plaques had a higher degree of stenosis, lower gray-scale median values, and higher values of the Kanber vulnerability index using both color Doppler imaging and contrast-enhanced ultrasonography for plaque surface delineation.

**ABBREVIATIONS:** AUC = area under the curve; CEUS = contrast-enhanced ultrasonography; CDI = color Doppler imaging; DOS = degree of stenosis; GSM = gray-scale median; IQR = interquartile range; ROC = receiver operating characteristic; SII = surface irregularity index; US = ultrasonography; VI = vulnerability index

Carotid atherosclerosis accounts for approximately 10%–15% of all strokes, with thromboembolism from a moderate or severe stenosis representing the underlying mechanism. The degree of internal carotid artery stenosis has long been used as the

primary parameter considered for guiding treatment of patients with carotid disease. Nevertheless, it is now well-established that additional plaque features contribute to the vulnerability of the plaque, a term corresponding to the potential of the plaque for stroke or transient ischemic attack. Such features include the composition and surface morphology of the plaque and can be investigated using any imaging technique, from conventional ultrasonography (US) to noninvasive cross-sectional imaging modalities such as multidetector CT angiography.<sup>1–5</sup> Ultrasonography is valuable for the diagnosis of carotid disease and is the

Received November 12, 2018; accepted after revision March 30, 2019.

From the Department of Radiology (V.R., I.C., A.C.-K.) and First Department of Neurology (C.X., T.T.), AHEPA University General Hospital, Aristotle University of Thessaloniki, Thessaloniki, Greece; Department of Information Engineering (E.G.), University of Padova, Padova, Italy; School of Imaging Sciences and Biomedical Engineering (E.G.), King's College London, London, UK; Laboratory of Computing (G.-A.C.), Medical Informatics and Biomedical-Imaging Technologies, School of Medicine, Aristotle University of Thessaloniki, Thessaloniki, Greece; Department of Radiology (D.R.), "G. Gennimatas" General Hospital of Thessaloniki, Thessaloniki, Greece; and Department of Radiology (P.S.S.), King's College Hospital, London, UK.

V.R. received a scholarship for his PhD studies on "Imaging of the Carotid Vulnerable Plaque with Contrast-Enhanced Ultrasound and Multi-Detector Computed Tomography Angiography" from the Alexander S. Onassis Public Benefit Foundation (grant No. G ZJ 050-2/2015–2016).

Please address correspondence to Vasileios Rafailidis, MD, MSc, PhD, Department of Radiology, AHEPA University General Hospital, Aristotle University of Thessaloniki, Thessaloniki, Greece, St. Kiriakidis 1, P.C. 54636, Thessaloniki, Greece (Hellas); e-mail: billraf@hotmail.com

 Indicates article with supplemental on-line photos.

<http://dx.doi.org/10.3174/ajnr.A6056>

first-line technique with inherent advantages including low cost, repeatability, and high accuracy.<sup>6</sup> Plaque composition can be ultrasonographically evaluated both subjectively and quantitatively using the gray-scale median (GSM) technique, already proved to correlate with neurovascular symptoms and representing a risk factor for stroke.<sup>7-13</sup>

Plaque surface morphology, either in the form of mere irregularities or true ulceration, has also been associated with the occurrence of neurovascular symptoms. Consequently, surface characterization should be an essential part of any imaging examination. Plaque surface can be subjectively classified as smooth, irregular, or ulcerated, but quantitative measures would be more beneficial because they are less operator-dependent and more objective.<sup>2,3,14</sup> There has been an effort to introduce a quantitative measure of surface irregularities, providing some initial promising results.<sup>15,16</sup> In light of these results, it is evident that the introduction and use of a mathematic index combining features of plaque vulnerability are now feasible. Initial reports have already been published by Kanber et al,<sup>17</sup> with encouraging results, indicating that multiparametric indices outperform the degree of stenosis (DOS) alone for the detection of symptomatic plaques. The use of intravenously administered microbubbles acting as ultrasonographic contrast agents has been introduced, and the technique of contrast-enhanced ultrasonography (CEUS) has been investigated in the assessment of carotid disease. CEUS has been shown to improve carotid plaque delineation compared with the color Doppler imaging (CDI) technique, being independent of artifacts such as overwriting, aliasing, and Doppler angle dependency, and could be a valuable alternative to CDI for quantification of surface irregularities.<sup>14,18-20</sup>

The purpose of this study was to investigate the value of a multiparametric ultrasonographic carotid plaque risk index, previously described by Kanber et al,<sup>17</sup> in detecting symptomatic plaques by comparing values between symptomatic and asymptomatic plaques and comparing its diagnostic accuracy with the well-established parameter of DOS. The index investigated is the carotid plaque risk index introduced by Kanber et al, incorporating stenosis, GSM, and a quantitative measure of surface irregularities estimated on the basis of both CDI and CEUS images, known to provide optimal carotid plaque surface delineation. The index will be referred to as the Kanber vulnerability index (VI).

## **MATERIALS AND METHODS**

### ***Patients and Inclusion/Exclusion Criteria***

The institutional ethics review board (Committee of Bioethics and Deontology, School of Medicine, Aristotle University of Thessaloniki) approved this study, and every patient recruited provided written informed consent. Recruitment of patients was performed in a prospective and consecutive pattern from the Radiology and Neurology Department from April 2016 to April 2018 (2 years). Both symptomatic and asymptomatic patients were recruited after being referred for ultrasonography either due to the occurrence of stroke or for unrelated or screening purposes. A patient was considered symptomatic if a stroke had occurred within the past 6-month period, based on the patient's history, clinical examination, or review of radiologic studies. Moreover, an internal carotid artery plaque with moderate (50%–69%) or

severe (70%–99%) stenosis should have been documented on the US examination based on previously reported velocity criteria.<sup>21</sup> A <50% plaque was only included in the study if it was located contralateral to a  $\geq$ 50% plaque. Both carotid systems were analyzed separately in every patient studied. Plaques situated ipsilateral to the stroke were considered symptomatic, while those situated contralateral to the stroke were considered asymptomatic.

Exclusion criteria included a history of allergy or other contraindication to the US contrast agents used, the presence of neurologic diseases mimicking stroke, and a clinical presentation and history of comorbidities that could cause stroke (such as arrhythmias, cardiac anatomic abnormalities, thrombophilia, and immunologic diseases such as antiphospholipid syndrome). In detail, cardiac anatomic conditions that were excluded as potential sources of embolism included the following: left ventricular aneurysm, intracardiac thrombus or myxoma, left ventricular dysfunction or hypokinesis, a patent foramen ovale, a mechanical prosthetic cardiac valve, and valvular dysfunction such as mitral stenosis. Extensively calcified plaques with acoustic shadowing were also excluded from analysis if considered unsuitable for quantification. Namely, the decision to exclude a plaque was made by the 2 observers analyzing the images on the basis of consensus. A plaque was regarded as extensively calcified and was excluded when situated on the near wall (proximal to the probe), thus causing acoustic shadowing hiding the plaque surface even for a small part, if this shadowing was not possible to overcome by changing the probe position and direction of sonography beam. Conversely, when the plaque was located on the distal wall (distal to the probe) and its surface was visible, it was not excluded. The decision to exclude a plaque was made before quantification analysis.

### ***Imaging Technique***

All patients included in the study underwent US and CEUS in both carotid systems. US examinations were performed by an experienced radiologist (9 years of experience) with a Logiq S8 (GE Healthcare, Milwaukee, Wisconsin) with an XDclear technology device and a linear probe (type 9L) with a 3- to 10-MHz bandwidth. B-mode and CDI were used for the routine part of US, including grading of stenosis using the Society of Radiologists in Sonography Consensus velocity criteria<sup>21</sup> and diametric measurements on axial CDI and evaluation of plaque characteristics. For accurate grading of stenosis, the diametric measurements on axial CDI, the peak systolic velocities, and the peak systolic velocity ratios were taken into consideration. If a suitable plaque was detected and the patient met the inclusion criteria, a CEUS examination was performed within 1 week following the conventional US. CEUS was performed with the intravenous administration of 2.4 mL of sulphur hexafluoride microbubbles (SonoVue, Bracco, Milan, Italy) followed by 10 mL of saline and using the contrast-specific mode of the device. The mechanical index was kept to <0.1, and the gain was suitably adjusted to achieve optimal microbubble visualization.

### ***Image Analysis***

Video clips of the affected internal carotid artery in the long axis plane were recorded by the radiologist performing the examination, both on CDI and CEUS. The clips were then reviewed by 2

different radiologists, observers (A and B) who had 11 years of experience and were specifically trained for this study on the use of the software, blinded to the patient's history. The 2 observers chose a single frame of CDI and the CEUS video clip optimally visualizing the carotid plaque surface. Subsequently, 1 observer used the surface irregularities software developed for this study to quantify surface irregularities, while both observers analyzed the images in the first 30 cases for interobserver agreement analysis, being blinded to each other's results.

For the evaluation of the GSM, previously described techniques were used<sup>9,22</sup> based on Adobe Photoshop CS6 (Adobe Systems, San Jose, California). In brief, B-mode images in JPEG format were used, with CDI helping delineate hypoechoic plaques. The same presettings were initially used for the acquisition of B-mode images in all patients. The images were normalized before analysis using linear scaling, by setting the value of zero to the echogenicity of blood and the value of 190 to the adventitia. Once the normalization was complete, a closed ROI was drawn over the plaque, and the echogenicity histogram and GSM value were calculated.

The application used for quantification of surface irregularities in this study was developed on the basis of Matlab, Version R2017b (MathWorks, Natick, Massachusetts) and is able to quantify the surface irregularities of the plaque. The physician using this software manually places successive points on the plaque surface and the outer blood vessel wall, for both the upper and lower vessel wall, depending on the distribution of the plaque. As previously described by Kanber et al,<sup>16,17</sup> a plaque surface irregularity index (SII) is calculated by the computational summation of the angular deviations of the luminal plaque surface from the straight line, divided by the physical length of the plaque surface. The equation used was the following:  $(\varphi_1 + \varphi_2 + \varphi_3 + \varphi_n)/l$ , where  $\varphi$  represents the angle of deviation from the straight line, and  $l$ , the plaque surface length.<sup>16,17</sup> The cosine rule was used for calculating the surface irregularity index as explained in detail in On-line Fig 1. The surface of the plaque is delineated by color Doppler blood flow signals on the CDI and the border of the microbubble column on CEUS.

Given that the US images used by the software were in an appropriately calibrated JPEG format, pixel spacing and length information were available for the software. In detail, the JPEG images were calibrated on the basis of a scale available in all US images and using a calibration tool developed for this software. As a result, the software can measure the required angles by using the cosine rule for the triangles formed by the consecutive points placed by the physician. The SII of the carotid wall with the greater plaque surface irregularities was recorded for analysis because this was considered more clinically relevant for the detection of symptoms. Only 1 measurement of the SII was performed in each plaque and using the single static image chosen in each case. The Kanber vulnerability index was defined as  $(DOS \times SII)/(GSM + 1)$  in concordance with a previous study that introduced this index,<sup>17</sup> and 2 such indices were calculated on the basis of the SII value derived from the CDI or CEUS images (SII-CDI, SII-CEUS, VI-CDI, and VI-CEUS, respectively).

### Statistical Analysis

SPSS, Version 23.0 (IBM, Armonk, New York) was used for statistical analysis. Descriptive statistics included mean and SD for normally distributed variables and median and interquartile

range (IQR) for non-normally distributed variables. The Kolmogorov-Smirnov test was used to test the normal distribution of variables. The intraclass correlation coefficient was used to assess interobserver agreement of the SII. Both observers quantified the SII only for the interobserver agreement analysis in a part of the sample, while the more experienced radiologist quantified the SII in all patients for diagnostic accuracy measures. Mann-Whitney  $U$  and  $t$  tests were used to compare means between groups, depending on the normality of distribution. Receiver operating characteristic (ROC) analysis was used for diagnostic accuracy analysis. Statistical significance level was set at .05. For comparisons between areas under the ROC curves,  $P < .017$  was considered statistically significant (Bonferroni correction for 3 pair-wise comparisons). Comparisons between areas under the ROC curve were performed with MedCalc for Windows (MedCalc Software, Mariakerke, Belgium).

## RESULTS

### Patients

Fifty-four patients (39 males) were recruited prospectively, with 14 patients showing bilateral plaques. The median age was 61 years, and the IQR was 17. In total, 62 plaques (31 symptomatic and 31 asymptomatic) met the inclusion criteria and were studied, while 6 plaques were excluded due to extensive calcification with acoustic shadowing hindering quantitative analysis. The remaining carotid systems had no atherosclerotic lesions detected. The mean DOS was  $68.9\% \pm 12.8\%$ . The median GSM was 22.5 (IQR = 31.5). The median SII-CDI was 10.9 (IQR = 8.6), while the median SII-CEUS was 11.4 (IQR = 10.5). No adverse reaction to the US contrast agent was observed. Median VI-CDI and VI-CEUS were 37.3 and 65.2 (IQR = 34.4 and 91.5), respectively.

### SII Interobserver Agreement

An initial analysis was performed in the first 30 cases to determine the reproducibility and interobserver agreement of the SII by estimating the intraclass correlation coefficient and limits of agreement. The intraclass correlation coefficient for SII-CDI was 0.954 (95% confidence interval, 0.904–0.978), while for SII-CEUS, it was 0.963 (95% CI, 0.923–0.983), both measures indicating very good agreement for the SII parameter, with CEUS providing slightly better agreement. The mean, SD, and lower and upper limits of agreement for SII-CDI and SII-CEUS were  $-1.1$  and  $3.3$ ;  $-7.6$  and  $5.3$ ;  $-0.4$  and  $4.3$ ; and  $-9$  and  $8$ , respectively.

### Comparison of Parameters between Symptomatic and Asymptomatic Plaques

The DOS was found to statistically significantly differ between symptomatic and asymptomatic plaques, based on the  $t$  test ( $P < .001$ ). The Mann-Whitney  $U$  test confirmed statistical significance in the difference of values between asymptomatic and symptomatic plaques for the GSM ( $P = .001$ ), VI-CDI ( $P < .001$ ), VI-CEUS ( $P < .001$ ), but not for SII-CDI alone ( $P = .17$ ) and SII-CEUS, for which a trend toward significance was detected ( $P = .055$ ). The mean and SD values of the previous variables can be found in Table 1. The corresponding boxplots can be found in Fig 1.

### ROC Analysis for the Detection of Symptomatic Plaque

ROC analysis was performed to compare the diagnostic accuracy of the DOS and the Kanber VI, including the SII deriving from both CDI and CEUS for the detection of symptomatic plaque. The areas under the curve (AUCs) with the respective 95% CI are presented in Table 2, while the ROC curves are shown in Fig 2. Screening and optimal and diagnostic cutoff values were defined for the DOS, VI-CDI, and VI-CEUS to achieve superior sensitivity, balanced sensitivity and specificity, and superior specificity, respectively. Screening and optimal and diagnostic cutoff values

were defined for VI (CDI) as 8.6, 17.3, and 104.3, respectively. The respective resulting sensitivity and specificity for the detection of symptomatic plaques were 96.8% and 19.4%, 87.1% and 54.8%, and 35.5% and 96.8%. For VI (CEUS), the cutoff values defined were 7.7 (screening), 29 (optimal), and 134.8 (diagnostic), yielding sensitivity and specificity values of 96.8% and 16.1%, 87.1% and 71%, and 35.5% and 96.8%, respectively. In ROC curve analysis, the areas under the curve of the DOS (area under the curve =  $0.77 \pm 0.06$ ), VI (CDI) (area under the curve =  $0.78 \pm 0.06$ ), and VI (CEUS) (area under the curve =  $0.80 \pm 0.06$ ) were not statistically significantly different ( $P > .017$ ). On the basis of these results, both vulnerability indices achieved a higher area under the curve than the DOS alone for the detection of symptomatic plaques, though no statistical significance was achieved. The greatest area under the curve was achieved when the SII-CEUS was used. Examples of quantitative analysis of an asymptomatic and symptomatic plaque can be found in On-line Figs 2 and 3, respectively.

**Table 1: Descriptive statistics and significance of comparisons between ultrasonography parameters of symptomatic and asymptomatic plaques**

	Asymptomatic		Symptomatic		P Value
	Median	IQR	Median	IQR	
DOS <sup>a</sup>	63.1	11.8	74.7	11.1	<.001 <sup>b</sup>
GSM	38	27	13	19	.001 <sup>b</sup>
SII-CDI	9.5	7.5	12	9.1	.17
SII-CEUS	9.8	6.9	12.9	11	.055
VI-CDI	16.5	29.2	61.4	109.7	<.001 <sup>b</sup>
VI-CEUS	25.2	33.3	88.6	122.1	<.001 <sup>b</sup>

<sup>a</sup> Mean and SD are presented for DOS only (normally distributed variable).

<sup>b</sup> Significant difference.

### DISCUSSION

The present study investigated the value of a previously described multiparametric ultrasonographic risk index (the Kanber carotid

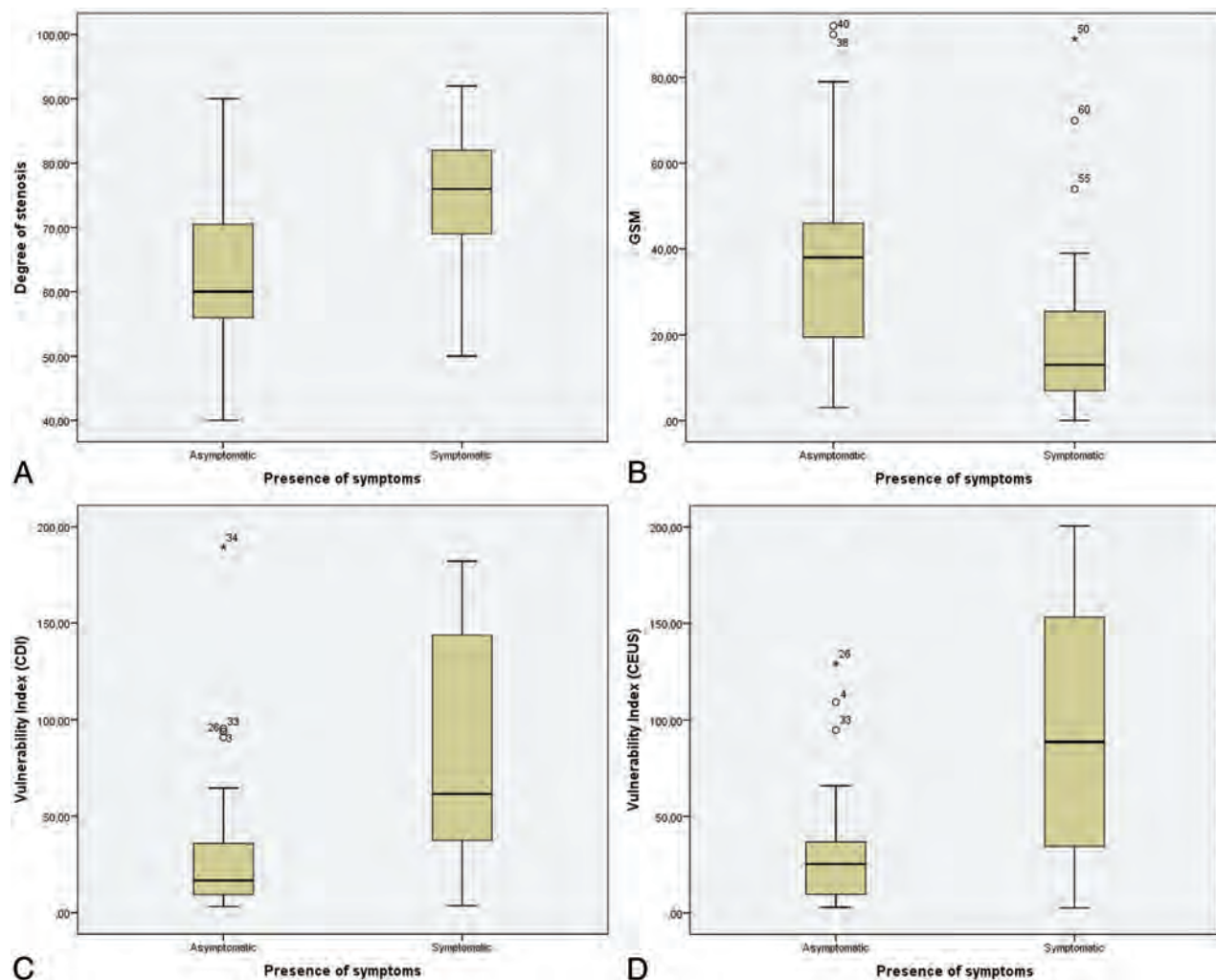


**FIG 1.** Boxplots comparing the degree of stenosis (A), GSM (B), VI-CDI (C), and VI-CEUS (D) between asymptomatic and symptomatic plaques (62 plaques from 54 patients were included).

plaque risk index or VI) for the detection of symptomatic carotid plaques. The VI combined the DOS with the GSM and a quantitative measure of surface irregularities, derived both from CDI and CEUS, because the latter is considered to provide optimal plaque delineation. The study results show that the DOS, GSM, and both VIs significantly differed between asymptomatic and symptomatic plaques. On ROC analysis, both multiparametric VIs had higher areas under the curve than the DOS, with the VI using the SII measured on CEUS achieving the greatest area under the curve for the detection of symptomatic plaques. No statistical significance was reached when comparing ROC curves for potential reasons that will be discussed later.

The concept of carotid vulnerable plaque is currently well-established, with certain imaging features being regarded as risk factors for the occurrence of neurovascular symptoms. Such features include plaque composition and surface morphology, both adequately studied with US.<sup>2,3,14</sup> Consequently, the idea of a multiparametric mathematic index incorporating features of vulnerability with the reference variable of the DOS was introduced, and initial effort was made to conceive and evaluate such indices. Prati et al<sup>23</sup> proposed a VI combining stenosis with subjective measures of surface morphology and plaque composition in the form of echogenicity and texture, achieving an AUC of 0.9, outperforming the accuracy of the Framingham Risk Score alone (0.88) for the prediction of stroke. A later study combined the DOS with an

objective arithmetic variable describing the echogenicity of plaque, concluding that the resulting index was significantly higher in symptomatic patients and had greater prognostic value compared with stenosis or echogenicity alone. This study also determined a cutoff value of 0.36 for optimal discrimination of symptomatic and asymptomatic patients.<sup>24</sup>

In another type of index, termed the “activity index,” the DOS has been combined with the GSM and subjective measures of echogenicity heterogeneity, juxtaluminal echolucent area, and plaque surface interruption. This index was significantly higher in symptomatic plaques, with a cutoff point of 52 being determined for optimal discrimination.<sup>25</sup> The computation of such an index using ultrasonographic images was also made possible with the development of a stand-alone computer-assisted diagnosis software, allowing the physician to readily assess plaque vulnerability in everyday clinical practice.<sup>26</sup> Nicolaides et al<sup>27</sup> have investigated the value of 3 risk-stratification models in a prospective multicenter study of patients with moderate or severe stenosis, concluding that the DOS alone has an AUC of 0.59, while if combined with clinical features or clinical and ultrasonographic features of vulnerability, the AUC is increased to 0.66 and 0.82, respectively. Both the GSM and discrete white areas proved to be independent predictors of ipsilateral cerebral or retinal ischemia.<sup>27</sup>

Despite these promising initial results, a disadvantage of these studies lies in the use of subjective variables, which are limited by lower interobserver agreement and reproducibility and increased operator dependency. The study by Kanber et al<sup>17</sup> suggested a mathematic index exclusively using quantitative variables for DOS, GSM, and surface irregularity. This index was used in the current study, but using different software and manual delineation of the plaque surface and applying both CDI and CEUS techniques for improved plaque surface delineation. This study concluded that the risk index is significantly higher in symptomatic plaques, also being superior in terms of diagnostic accuracy for the detection of symptomatic plaques compared with stenosis alone. The GSM and SII combined with stenosis achieved an AUC of 0.849, outperforming stenosis alone (AUC = 0.771). In keeping with these results, the present study calculated an AUC of 0.772 for stenosis alone, 0.783 for VI-CDI, and 0.802 for VI-CEUS.<sup>17</sup> In our study, the median values of the index in symptomatic (asymptomatic) plaques were 16.5 (61.47) for the CDI technique and 25.2 (88.66) for CEUS, highlighting a greater difference in value in the latter case. These findings confirm the well-established superiority of CEUS to CDI for the delineation of carotid plaque surface free of artifacts and indicate that the CEUS technique provides more clinically significant information regarding surface irregularities.<sup>18-20,28-30</sup> Multiparametric analysis of carotid plaques can

**Table 2: ROC analysis for the detection of symptomatic plaques**

Test Examined	AUC	95% CI	
		Lower	Upper
DOS	0.772	0.653	0.89
VI (CDI)	0.783	0.666	0.899
VI (CEUS)	0.802	0.689	0.916

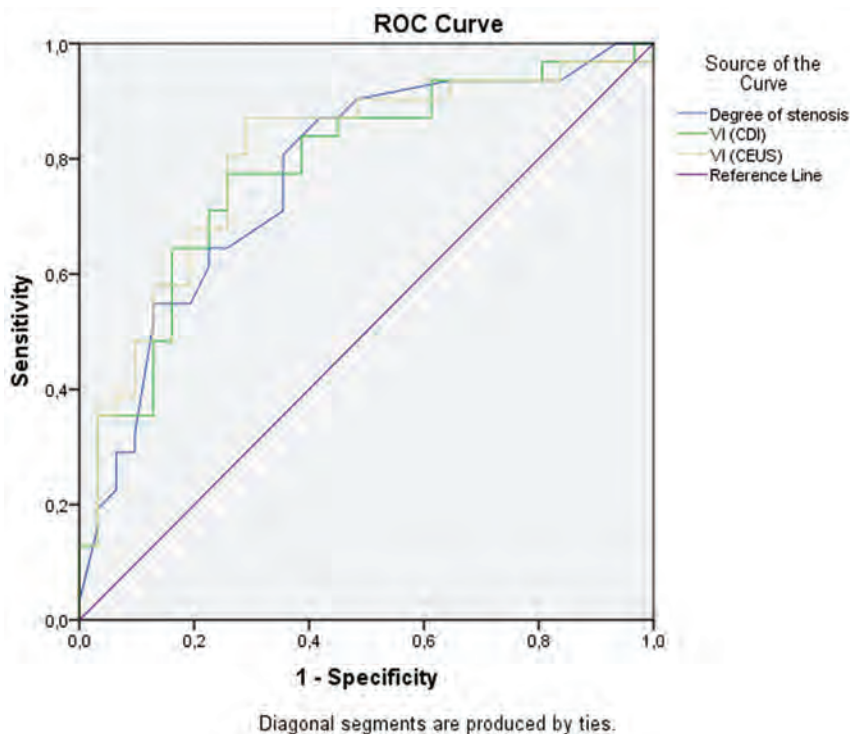


**FIG 2.** ROC curves for the detection of symptomatic plaques by the compared variables.

also be performed through integrated classification systems like the PLAC-RISK score, combining clinical data, the DOS, echogenicity, surface characteristics, and intraplaque neovascularization, to calculate a score with the purpose of suggesting optimal patient management.<sup>31</sup>

The current study has some limitations, including a relatively small number of patients, a potential spectrum bias because only patients with at least 1 plaque with moderate or severe stenosis were recruited, and the 2D nature of the US technique used in this study. It is evident that 3D US could better and more thoroughly characterize plaque echogenicity and irregularities, though this technique is not widely available. The retrospective nature of this study is another limitation because the more vulnerable parts of the plaques may have already been dislodged causing a stroke. Even in this case, the underlying and remaining part of the symptomatic plaque might be expected to have a more irregular surface, and this feature was recorded in the present study. Other limitations of this study include the use of manual delineation of the plaque surface over still frames of carotid plaques, as opposed to the study by Kanber et al<sup>16,17</sup> in which video clips and an automated method of plaque delineation were used. It has been previously found that variables such as the GSM may exhibit dynamic variations throughout the cardiac cycle,<sup>32</sup> thus rendering their quantification more challenging. These along with the smaller number of patients recruited than in the study by Kanber et al may explain no statistical significance being achieved regarding the comparison of areas under the curve. Nevertheless and despite those shortcomings, this study yielded significant differences in the variables examined between symptomatic and asymptomatic plaques and confirmed the pattern of diagnostic accuracy previously reported. Future prospective studies should thus examine some form of multiparametric VI in prospective patient cohorts, validating these initial results in different vascular laboratories and investigating implications for patient management. It would also be very useful to compare symptomatic and asymptomatic patient populations with carotid disease.

On the basis of the currently available literature, factors not included in the present study also contribute to the vulnerability of the plaque. Namely, intraplaque neovascularization and the enhancement of the plaque on delayed-phase CEUS are 2 such factors, with vulnerable plaques having a greater degree of neovascularization.<sup>3</sup> Similarly, late-phase enhancement on CEUS 6 minutes after the administration of microbubbles has been found to be greater in symptomatic plaques, due to the higher degree of inflammation found within these plaques.<sup>33</sup> Studies have shown that symptomatic carotid plaques exhibit diffuse microbubble uptake at their base, something not happening in asymptomatic plaques. The areas showing enhancement on CEUS corresponded to areas with increased numbers of microvessels as demonstrated on immunohistologic staining of endarterectomy specimens.<sup>34</sup>

In a study enrolling 104 patients, 80% of symptomatic patients had a plaque showing enhancement on CEUS, while only 30% of asymptomatic patients had such a plaque, with this difference being significant. On quantitative analysis, the enhanced plaque intensity was significantly higher in symptomatic plaques.<sup>35</sup> Even

when subjectively quantifying plaque enhancement in 2 or 4 levels of classification, this classification significantly correlated with histologically detected neovascularization, intraplaque hemorrhage, and macrophage-rich areas.<sup>36</sup> The presence of neovascularization in patients with symptomatic carotid plaques as detected with CEUS was also significantly associated with the occurrence of microembolic signals in the middle cerebral artery detected by transcranial US. The latter is considered a predictor of future risk of stroke in patients with carotid stenosis.<sup>37</sup> Regarding plaque ulceration, the literature shows that it is an essential feature of plaque vulnerability, being associated with the occurrence of stroke.<sup>14</sup> This entity can be studied ultrasonographically with both the conventional color Doppler technique and CEUS, though improved sensitivity has been found for the latter technique.<sup>14,38</sup> Further investigation of these factors, especially in the setting of a multiparametric index, is important and could have implications for patient management on the grounds of treating plaques deemed more vulnerable with higher priority. Consequently, future studies should also evaluate multiparametric indexes incorporating even more features of vulnerability.

## CONCLUSIONS

This study concluded that symptomatic plaques exhibit a significantly higher degree of stenosis, lower values of the GSM, and higher values of the Kanber vulnerability index, thus confirming previous findings and also further investigating the potential use of CEUS for plaque surface delineation. It is thus evident that the use of multiparametric vulnerability indices is advantageous and should be encouraged and further studied for the detection of symptomatic plaques, even with the use of conventional flow-visualization techniques such as color or power Doppler and not necessarily CEUS. Nevertheless, the examination of the SII with CEUS could be readily incorporated in a CEUS examination protocol performed for intraplaque neovascularization, another well-established feature of vulnerability, to maximize the information provided regarding the vulnerability of plaque.

## ACKNOWLEDGMENTS

We thank Pagkalidou Eirini, MSc, Department of Hygiene and Epidemiology, School of Medicine, Aristotle University of Thessaloniki, Thessaloniki, Greece, for assisting us with statistical analysis performed in this study.

Disclosures: Vasileios Rafailidis—*RELATED: Grant:* Alexander S. Onassis Public Benefit Foundation in Greece, *Comments:* scholarship for PhD studies. Chrysostomos Xerras—*UNRELATED: Employment:* AHEPA University Hospital, *Comments:* resident in the First Department of Neurology. Enrico Grisan—*UNRELATED: Grants/Grants Pending:* Italian Ministry.\* Paul S. Sidhu—*RELATED: Support for Travel to Meetings for the Study or Other Purposes:* Bracco S.p.A, Samsung, *Comments:* travel and lecture fees; *UNRELATED: Consultancy:* ITREAS, *Comments:* consulting for the assessment of venography images in clinical trials; *Payment for Lectures Including Service on Speakers Bureaus:* Philips Healthcare, Hiatchi, Siemens, *Comments:* lecture fees; *Royalties:* Taylor and Francis, owner of Hodder Inc, Thieme AG, *Comments:* book royalties. \*Money paid to the institution.

## REFERENCES

1. Aboyans V, Ricco JB, Bartelink MEL, et al; ESC Scientific Document Group. **2017 ESC Guidelines on the Diagnosis and Treatment of Peripheral Arterial Diseases, in collaboration with the European Society for Vascular Surgery (ESVS): document covering athero-**

- sclerotic disease of extracranial carotid and vertebral, mesenteric, renal, upper and lower extremity arteries—Endorsed by the European Stroke Organization (ESO) The Task Force for the Diagnosis and Treatment of Peripheral Arterial Diseases of the European Society of Cardiology (ESC) and of the European Society for Vascular Surgery (ESVS). *Eur Heart J* 2018;39:763–816 CrossRef Medline
2. Saba L, Yuan C, Hatsukami TS, et al; Vessel Wall Imaging Study Group of the American Society of Neuroradiology. **Carotid artery wall imaging: perspective and guidelines from the ASNR Vessel Wall Imaging Study Group and Expert Consensus Recommendations of the American Society of Neuroradiology.** *AJNR Am J Neuroradiol* 2018;39:E9–31 CrossRef Medline
  3. Saba L, Anzidei M, Marincola BC, et al. **Imaging of the carotid artery vulnerable plaque.** *Cardiovasc Intervent Radiol* 2014;37:572–85 CrossRef Medline
  4. **MRC European Carotid Surgery Trial: interim results for symptomatic patients with severe (70–99%) or with mild (0–29%) carotid stenosis.** European Carotid Surgery Trialists' Collaborative Group. *Lancet* 1991;337:1235–43 CrossRef Medline
  5. Barnett HJ, Taylor DW, Haynes RB, et al; North American Symptomatic Carotid Endarterectomy Trial Collaborators. **Beneficial effect of carotid endarterectomy in symptomatic patients with high-grade carotid stenosis.** *N Engl J Med* 1991;325:445–53 CrossRef Medline
  6. Tahmasebpour HR, Buckley AR, Cooperberg PL, et al. **Sonographic examination of the carotid arteries.** *Radiographics* 2005;25:1561–75 CrossRef Medline
  7. Pedro LM, Pedro MM, Goncalves I, et al. **Computer-assisted carotid plaque analysis: characteristics of plaques associated with cerebrovascular symptoms and cerebral infarction.** *Eur J Vasc Endovasc Surg* 2000;19:118–23 CrossRef Medline
  8. Biasi GM, Sampaolo A, Mingazzini P, et al. **Computer analysis of ultrasonic plaque echolucency in identifying high risk carotid bifurcation lesions.** *Eur J Vasc Endovasc Surg* 1999;17:476–79 CrossRef Medline
  9. Elatrozy T, Nicolaides A, Tegos T, et al. **The objective characterisation of ultrasonic carotid plaque features.** *Eur J Vasc Endovasc Surg* 1998;16:223–30 CrossRef Medline
  10. Grønholdt ML, Nordestgaard BG, Schroeder TV, et al. **Ultrasonic echolucent carotid plaques predict future strokes.** *Circulation* 2001;104:68–73 CrossRef Medline
  11. Tegos TJ, Stavropoulos P, Sabetai MM, et al. **Determinants of carotid plaque instability: echoicity versus heterogeneity.** *Eur J Vasc Endovasc Surg* 2001;22:22–30 CrossRef Medline
  12. Salem MK, Sayers RD, Bown MJ, et al. **Patients with recurrent ischaemic events from carotid artery disease have a large lipid core and low GSM.** *Eur J Vasc Endovasc Surg* 2012;43:147–53 CrossRef Medline
  13. Ruiz-Ares G, Fuentes B, Martinez-Sanchez P, et al. **Utility of the assessment of echogenicity in the identification of symptomatic carotid artery atheroma plaques in ischemic stroke patients.** *Cerebrovasc Dis* 2011;32:535–41 CrossRef Medline
  14. Rafailidis V, Chrysogonidis I, Tegos T, et al. **Imaging of the ulcerated carotid atherosclerotic plaque: a review of the literature.** *Insights Imaging* 2017;8:213–25 CrossRef Medline
  15. Tegos TJ, Kalomiris KJ, Sabetai MM, et al. **Significance of sonographic tissue and surface characteristics of carotid plaques.** *AJNR Am J Neuroradiol* 2001;22:1605–12 Medline
  16. Kanber B, Hartshorne TC, Horsfield MA, et al. **Quantitative assessment of carotid plaque surface irregularities and correlation to cerebrovascular symptoms.** *Cardiovasc Ultrasound* 2013;11:38 CrossRef Medline
  17. Kanber B, Hartshorne TC, Horsfield MA, et al. **A novel ultrasound-based carotid plaque risk index associated with the presence of cerebrovascular symptoms.** *Ultraschall Med* 2015;36:480–86 CrossRef Medline
  18. Rafailidis V, Charitanti A, Tegos T, et al. **Contrast-enhanced ultrasound of the carotid system: a review of the current literature.** *J Ultrasound* 2017;20:97–109 CrossRef Medline
  19. Piscaglia F, Nolsøe C, Dietrich CF, et al. **The EFSUMB Guidelines and Recommendations on the Clinical Practice of Contrast Enhanced Ultrasound (CEUS): update 2011 on non-hepatic applications.** *Ultraschall Med* 2012;33:33–59 CrossRef Medline
  20. Sidhu PS, Cantisani V, Dietrich CF, et al. **The EFSUMB Guidelines and Recommendations for the Clinical Practice of Contrast-Enhanced Ultrasound (CEUS) in Non-Hepatic Applications: Update 2017 (Long Version).** *Ultraschall Med* 2018;39:e2–44 CrossRef Medline
  21. Grant EG, Benson CB, Moneta GL, et al. **Carotid artery stenosis: gray-scale and Doppler US diagnosis—Society of Radiologists in Ultrasound Consensus Conference.** *Radiology* 2003;229:340–46 CrossRef Medline
  22. Sabetai MM, Tegos TJ, Nicolaides AN, et al. **Reproducibility of computer-quantified carotid plaque echogenicity: can we overcome the subjectivity?** *Stroke* 2000;31:2189–96 CrossRef Medline
  23. Prati P, Tosetto A, Casaroli M, et al. **Carotid plaque morphology improves stroke risk prediction: usefulness of a new ultrasonographic score.** *Cerebrovasc Dis* 2011;31:300–04 CrossRef Medline
  24. Momjian-Mayor I, Kuzmanovic I, Momjian S, et al. **Accuracy of a novel risk index combining degree of stenosis of the carotid artery and plaque surface echogenicity.** *Stroke* 2012;43:1260–65 CrossRef Medline
  25. Pedro LM, Fernandes e Fernandes J, Pedro MM, et al. **Ultrasonographic risk score of carotid plaques.** *Eur J Vasc Endovasc Surg* 2002;24:492–98 CrossRef Medline
  26. Afonso D, Seabra J, Suri JS, et al. **A CAD system for atherosclerotic plaque assessment.** *Conf Proc IEEE Eng Med Biol Soc* 2012;2012:1008–11 CrossRef Medline
  27. Nicolaides AN, Kakkos SK, Kyriacou E, et al; Asymptomatic Carotid Stenosis and Risk of Stroke (ACSRS) Study Group. **Asymptomatic internal carotid artery stenosis and cerebrovascular risk stratification.** *J Vasc Surg* 2010;52:1486–96 e1–5 CrossRef Medline
  28. Kono Y, Pinnell SP, Sirlin CB, et al. **Carotid arteries: contrast-enhanced US angiography—preliminary clinical experience.** *Radiology* 2004;230:561–68 CrossRef Medline
  29. Schinkel AF, Kaspar M, Staub D. **Contrast-enhanced ultrasound: clinical applications in patients with atherosclerosis.** *Int J Cardiovasc Imaging* 2016;32:35–48 CrossRef Medline
  30. Staub D, Partovi S, Imfeld S, et al. **Novel applications of contrast-enhanced ultrasound imaging in vascular medicine.** *Vasa* 2013;42:17–31 CrossRef Medline
  31. Eyding J, Geier B, Staub D. **Current strategies and possible perspectives of ultrasonic risk stratification of ischemic stroke in internal carotid artery disease.** *Ultraschall Med* 2011;32:267–73 CrossRef Medline
  32. Kanber B, Hartshorne TC, Horsfield MA, et al. **Dynamic variations in the ultrasound greyscale median of carotid artery plaques.** *Cardiovasc Ultrasound* 2013;11:21 CrossRef Medline
  33. Owen DR, Shalhoub J, Miller S, et al. **Inflammation within carotid atherosclerotic plaque: assessment with late-phase contrast-enhanced US.** *Radiology* 2010;255:638–44 CrossRef Medline
  34. Giannoni MF, Vicenzini E, Citone M, et al. **Contrast carotid ultrasound for the detection of unstable plaques with neoangiogenesis: a pilot study.** *Eur J Vasc Endovasc Surg* 2009;37:722–27 CrossRef Medline
  35. Xiong L, Deng YB, Zhu Y, et al. **Correlation of carotid plaque neovascularization detected by using contrast-enhanced US with clinical symptoms.** *Radiology* 2009;251:583–89 CrossRef Medline
  36. Schmidt C, Fischer T, Rückert RI, et al. **Identification of neovascularization by contrast-enhanced ultrasound to detect unstable carotid stenosis.** *PLoS One* 2017;12:e0175331 CrossRef Medline
  37. Ritter MA, Theismann K, Schmiedel M, et al. **Vascularization of carotid plaque in recently symptomatic patients is associated with the occurrence of transcranial microembolic signals.** *Eur J Neurol* 2013;20:1218–21 CrossRef Medline
  38. Rafailidis V, Chrysogonidis I, Xerras C, et al. **A comparative study of color Doppler imaging and contrast-enhanced ultrasound for the detection of ulceration in patients with carotid atherosclerotic disease.** *Eur Radiol* 2019;29:2137–45 CrossRef Medline

# Dynamic Contrast-Enhanced MRI to Differentiate Parotid Neoplasms Using Golden-Angle Radial Sparse Parallel Imaging

J.L. Mogen, K.T. Block, N.K. Bansal, J.T. Patrie, S. Mukherjee, E. Zan, M. Hagiwara, G.M. Fatterpekar, and S.H. Patel



## ABSTRACT

**BACKGROUND AND PURPOSE:** Conventional imaging frequently shows overlapping features between benign and malignant parotid neoplasms. We investigated dynamic contrast-enhanced MR imaging using golden-angle radial sparse parallel imaging in differentiating parotid neoplasms.

**MATERIALS AND METHODS:** For this retrospective study, 41 consecutive parotid neoplasms were imaged with dynamic contrast-enhanced MR imaging with golden-angle radial sparse parallel imaging using 1-mm in-plane resolution. The temporal resolution was 3.4 seconds for 78.2 seconds and 8.8 seconds for the remaining acquisition. Three readers retrospectively and independently created and classified time-intensity curves as follows: 1) continuous wash-in; 2) rapid wash-in, subsequent plateau; and 3) rapid wash-in with washout. Additionally, time-intensity curve–derived semiquantitative metrics normalized to the ipsilateral common carotid artery were recorded. Diagnostic performance for the prediction of neoplasm type and malignancy was assessed. Subset multivariate analysis ( $n = 32$ ) combined semiquantitative time-intensity curve metrics with ADC values.

**RESULTS:** Independent time-intensity curve classification of the 41 neoplasms produced moderate-to-substantial interreader agreement ( $\kappa = 0.50–0.79$ ). The time-intensity curve classification threshold of  $\geq 2$  predicted malignancy with a positive predictive value of 56.0%–66.7%, and a negative predictive value of 92.0%–100%. The time-intensity curve classification threshold of  $< 2$  predicted pleomorphic adenoma with a positive predictive value of 87.0%–95.0% and a negative predictive value of 76.0%–95.0%. For all readers, type 2 and 3 curves were associated with malignant neoplasms ( $P < .001$ ), and type 1 curves, with pleomorphic adenomas ( $P < .001$ ). Semiquantitative analysis for malignancy prediction yielded an area under the receiver operating characteristic curve of 0.85 (95% CI, 0.73–0.99). Combining time-to-maximum and ADC predicts pleomorphic adenoma better than either metric alone ( $P < .001$ ).

**CONCLUSIONS:** Golden-angle radial sparse parallel MR imaging allows high spatial and temporal resolution permeability characterization of parotid neoplasms, with a high negative predictive value for malignancy prediction. Combining time-to-maximum and ADC improves pleomorphic adenoma prediction compared with either metric alone.

**ABBREVIATIONS:** AUC = area under the curve; DCE = dynamic contrast-enhanced; GRASP = golden-angle radial sparse parallel; NPV = negative predictive value; PPV = positive predictive value; ROC = receiver operating characteristic; SImax = maximum signal intensity; TIC = time-intensity curve; Tmax = time-to-maximum

Parotid neoplasms include a variety of benign and malignant lesions.<sup>1</sup> While most parotid neoplasms are benign pleomorphic adenomas and are often treated with superficial parotidectomy

(or in some instances, conservative monitoring), differentiating such lesions from those considered at high risk for malignancy can be useful for management because malignant parotid neoplasms are more typically scheduled for total parotidectomy with possible facial nerve sacrifice.<sup>2–4</sup> Clinical examination and conventional MR imaging sequences demonstrate considerable overlap among various pathologic entities. Almost all parotid neoplasms demonstrate contrast enhancement and intrinsically low signal on T1WI.<sup>5</sup> While features including irregular/infiltrative margins, heterogeneous signal intensity, and low signal on T2WI correlate with malignant pathology,<sup>2,5</sup> the performance of

Received October 15, 2018; accepted after revision March 31, 2019.

From the Department of Radiology (J.L.M.), Tufts Medical Center, Boston, Massachusetts; Department of Radiology (K.T.B., N.K.B., E.Z., M.H., G.M.F.), New York University Langone Medical Center, New York, New York; Division of Biostatistics and Epidemiology (J.T.P.), University of Virginia, Charlottesville, Virginia; and Department of Radiology and Medical Imaging (S.M., S.H.P.), University of Virginia Health System, Charlottesville, Virginia.

Preliminary results from this subject group previously presented at: American Society of Neuroradiology Annual Meeting and the Foundation of the ASNR Symposium, April 22–27, 2017; Long Beach, California.

Please address correspondence to Sohil H. Patel, MD, Department of Radiology and Medical Imaging, University of Virginia Health System, PO Box 800170, Charlottesville, VA 22908; e-mail: shp4@virginia.edu

Indicates article with supplemental on-line tables.

<http://dx.doi.org/10.3174/ajnr.A6055>

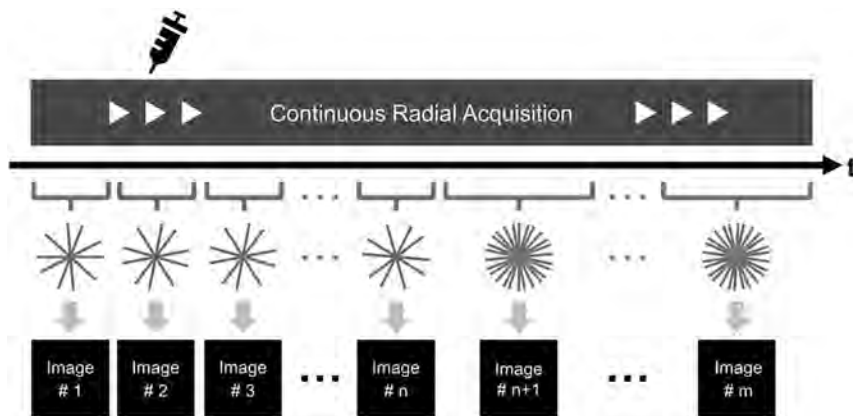


**FIG 1.** GRASP uses a continuous radial stack-of-stars acquisition of  $k$ -space during which the contrast agent is injected (20-second injection delay). Due to use of the golden-angle ordering scheme, an arbitrary number of consecutive frames can be combined into a single image frame and a desired temporal resolution can be thus assigned. Because the  $k$ -space data for each frame are highly undersampled, GRASP uses a compressed-sensing reconstruction with temporal total-variation constraint. Additionally, by combining all acquired frames into a single image frame, one can acquire high-resolution fat-suppressed T1-weighted anatomic images of the entire neck with an excellent signal-to-noise ratio (Figs 2 and 5 for examples).

conventional imaging reported in the literature has been variable. One study evaluating 98 parotid neoplasms found that conventional imaging was only 50% sensitive for the presence of malignancy.<sup>6</sup> Another study provided more encouraging results with a specificity of 95% for pleomorphic adenoma based on a combination of conventional features, though only 21 of the 41 pleomorphic adenomas included in this study met the proposed criteria and the overall diagnostic accuracy was 74.8%.<sup>7</sup> Preoperative biopsy represents a useful diagnostic tool for parotid masses. However, potential limitations include seeding of adjacent tissues after capsular violation, small tissue volumes for pathologic analysis, and procedural risks that include facial nerve injury, sialocele formation, or fistula formation.<sup>2,8,9</sup>

Golden-angle radial sparse parallel (GRASP) MR imaging is a 3D gradient recalled-echo dynamic contrast-enhanced (DCE) MR imaging technique using both compressed sensing and parallel imaging to accelerate data acquisition. GRASP MR imaging uses a radial “spoke-wheel” method of  $k$ -space sampling in the  $xy$  plane according to the golden-angle scheme and Cartesian sampling in the  $z$  axis.<sup>10</sup> Acquiring radial data according to the golden-angle ordering scheme allows dynamic imaging data acquisition as a single continuous scan. Dynamic image reconstruction is achieved by grouping the data into sequential timeframes at a desired temporal resolution (as fast as 2.5 seconds per frame). Iterative image reconstruction with temporal total-variation constraint permits both high temporal and spatial resolution. Thus, GRASP imaging provides both high-spatial-resolution anatomic imaging of a desired imaging volume and also high-temporal-resolution DCE-MR imaging data from the same image acquisition. Prior work in abdominal, breast, and other head and neck applications confirms the excellent image quality, improved fat suppression, and reduced motion and pulsation artifacts of GRASP-derived images compared with conventional anatomic MR imaging techniques, with the additional benefit of concurrently acquired DCE-MR imaging data.<sup>11-17</sup>

The purpose of this study was to investigate the accuracy of qualitative and semiquantitative metrics derived from DCE-MR imaging using GRASP imaging to differentiate parotid neoplasms. Unlike most prior studies, we evaluated semiquantitative metrics normalized for an internal normal reference standard, and we additionally performed comprehensive assessment of interreader reliability of qualitative GRASP-derived DCE analysis, which can be easily integrated into day-to-day workflow. The novel ability of GRASP to provide high-resolution anatomic imaging concurrently with DCE-MR imaging gives a further rationale for investigating GRASP imaging in this context. Finally, the added value of DWI was assessed in a subset cohort.

## MATERIALS AND METHODS

### Patient Selection

This retrospective study of patient data received New York University Langone Medical Center institutional review board approval, and the requirement for informed consent was waived. Health Insurance Portability and Accountability Act-compliant techniques for data management and analysis were used.

From July 2015 through August 2016, DCE-MR imaging using the GRASP technique was performed on 52 consecutive parotid lesions in 48 patients. The patient mean age was 59.8 years with a range of 29–85 years. There were 16 men and 21 women. Eleven patients with 11 parotid lesions were excluded due to the following: a lack of a pathologic diagnosis ( $n = 9$ ), nondiagnostic examination due to poor contrast bolus quality ( $n = 1$ ), and a purely cystic lesion ( $n = 1$ ). A total of 41 parotid lesions in 37 patients were ultimately included. In all cases, the final diagnosis was determined on the basis of histopathologic analysis following surgical resection.

### GRASP DCE-MR Imaging Technique

A detailed description of DCE-MR imaging based on the GRASP technique has been published previously.<sup>10</sup> In brief, the sequence entails a continuous radial  $k$ -space acquisition according to the golden-angle ( $111.25^\circ$ ) scheme to obtain a dynamic acquisition of a desired length, during which a contrast agent is injected (Fig 1). After data acquisition is complete, consecutive spokes are grouped into discrete temporal frames. The number of spokes combined into each frame can be chosen arbitrarily. For a low number of spokes/frame (as needed to achieve high imaging speed), the data are highly undersampled. Therefore, both parallel imaging and compressed sensing are applied in the reconstruction process to obtain artifact-free dynamic images with both high spatial and high temporal resolution (the compressed-sensing implementation uses a temporal total variation constraint). The reconstructed images were then analyzed as described below.

Patients in this study were scanned on both 1.5T and 3T MR imaging units. Dynamic imaging had 144 axial sections at a 2-mm slice thickness. The FOV was 256 × 256 mm at a matrix size of 256 × 256, resulting in a 1-mm in-plane resolution. Anatomic coverage comprised the whole neck from the superior orbit to sternal notch. TR and TE were 4.3 and 2.1 ms, respectively, with a 12° flip angle. Temporal resolution was 3.4 s/frame for the first 78.2 seconds and 8.8 s/frame through the remainder of the examination for a total dynamic acquisition of 240 seconds. A single dose of gadobutrol (0.1 mL/kg, Gadavist; Bayer Schering Pharma, Berlin, Germany) was administered intravenously at a rate of 3 mL/s with an injection delay of 20 seconds relative to the start of the sequence.

### **Qualitative Time-Intensity Curve Classification**

Three readers independently postprocessed and analyzed the DCE-MR imaging data for all 41 parotid neoplasms using the software Olea Sphere 3.0 (Olea Medical, La Ciotat, France). Reader A had 5 years of neuroradiology experience, reader B had 1 year of neuroradiology experience, and reader C was a radiology resident. The readers were blind to the clinical history, pathologic diagnosis, and all prior and subsequent imaging studies. Each reader was instructed to manually create a single ROI that circumscribed the enhancing component of the neoplasm on the axial image judged to contain the largest enhancing area. Vessels and nonenhancing portions of the lesions (eg, cystic components, centrally necrotic components) were excluded from the ROI. Time-intensity curves (TICs) were created from the assigned ROI, and each reader assigned to each TIC 1 of 3 curve classifications: 1) continuously rising, 2) initial rapid wash-in with subsequent plateau, and 3) initial rapid wash-in with subsequent washout (Fig 2).

### **Semiquantitative TIC Analyses**

Semiquantitative analysis was undertaken subsequent to the qualitative analysis by 2 of the readers (A and B) in consensus. At the time of semiquantitative analysis, the 2 readers remained blinded to the clinical history, pathologic diagnosis, and all prior and subsequent imaging studies. An ROI was chosen within the parotid neoplasm to create a TIC, as described above. An additional ROI was chosen within the ipsilateral common carotid artery to serve as an internal reference standard. The common carotid artery was chosen over the external carotid artery or more distal branches due to improved inter- and intraobserver reproducibility of the resulting TICs. TIC metrics including time-to-maximum (T<sub>max</sub>), maximum signal intensity (SI<sub>max</sub>), wash-in slope, washout slope, and area under the curve were calculated for the parotid neoplasm and normalized to (ie, divided by) values obtained from the ipsilateral common carotid artery.

### **Diffusion-Weighted Imaging Data Collection**

A DWI sequence was available in a 32-lesion (28 patient) subset of those enrolled. DWI was performed using EPI with a TR and TE of 7500 and 87 ms, respectively. Matrix size was 128 × 128, slice thickness/gap was 4.0/4.8 mm, and b-values of 0 and 1000 s/mm<sup>2</sup> were obtained. Three gradient directions were used. An ROI was assigned to match the ROI used in the semiquantitative TIC analysis. Mean ADC values were derived from the assigned ROI.

### **Statistical Methods**

Categorical data were summarized by frequencies and percentages, and continuous scaled data were summarized by the mean and SD and the range of the empiric distribution.

**Qualitative TIC Analysis.** Interreader agreement with respect to the TIC classification was evaluated via the unweighted  $\kappa$  statistic. Conventional receiver operating characteristic (ROC) analyses were conducted per reader to determine the ROC associated with malignant parotid neoplasm prediction and pleomorphic adenoma prediction as a function of TIC classification threshold. These categories were chosen on the basis of the frequency of pleomorphic adenoma relative to other parotid neoplasms and the importance of determining the malignant status of a lesion before any intervention. Bivariate associations between each reader's qualitative TIC classifications and the lesion malignant parotid neoplasm status (yes, no) and the lesion pleomorphic adenoma status (yes, no) were evaluated via exact logistic regression. The mid-*P* value method of Clopper and Pearson<sup>18</sup> was used to derive the *P* value of the exact test.

**Semiquantitative TIC Analyses.** Univariate and multivariate relationships between the TIC-derived semiquantitative metrics and the malignant parotid neoplasm status (yes, no) and the pleomorphic adenoma status (yes, no) were evaluated via univariate and multivariate logistic regression, respectively. Conventional ROC analyses were conducted to determine the operator characteristics associated with malignant parotid neoplasms and pleomorphic adenoma prediction as a function of the predicted probabilities derived from the TIC-derived semiquantitative predictor-based logistic regression model.

**Subset Analyses of ADC Values and Semiquantitative TIC-Derived Metrics.** Using the subset data of the 32 parotid neoplasms that underwent a DWI sequence, univariate and multivariate logistic regression analyses were performed to determine whether the ADC values derived from DWI provide additional diagnostic information that is not provided by the TIC-derived semiquantitative metrics. Type III  $\chi^2$  tests were used to test whether the addition of prediction information provided by ADC about malignant parotid neoplasm and pleomorphic adenoma is beyond what would be expected by chance.

**Statistical Software.** The statistical software package SAS, Version 9.4 (SAS Institute, Cary, North Carolina) was used to conduct the qualitative TIC analyses. The statistical software package R, Version 3.4.2 (<http://www.r-project.org>) was used to conduct the semiquantitative TIC analyses and the subset analysis.

## **RESULTS**

The mean patient age was 59.8 ± 14.2 years with a range of 29–85 years. There were 16 men (43.2%) and 21 women (56.8%). There were 27 (65.9%) benign neoplasms (21 pleomorphic adenomas, 4 Warthin tumors, 2 oncocytomas) and 14 (34.1%) malignant neoplasms (2 acinic cell carcinomas, 4 squamous cell carcinomas, 2 adenoid cystic carcinomas, 1 carcinoma ex pleomorphic adenoma, 2 mucoepidermoid carcinomas, 2 salivary duct carcinomas, and 1 spindle cell carcinoma). There was no statistically significant association between patient age or sex and the pathologic diagnosis.

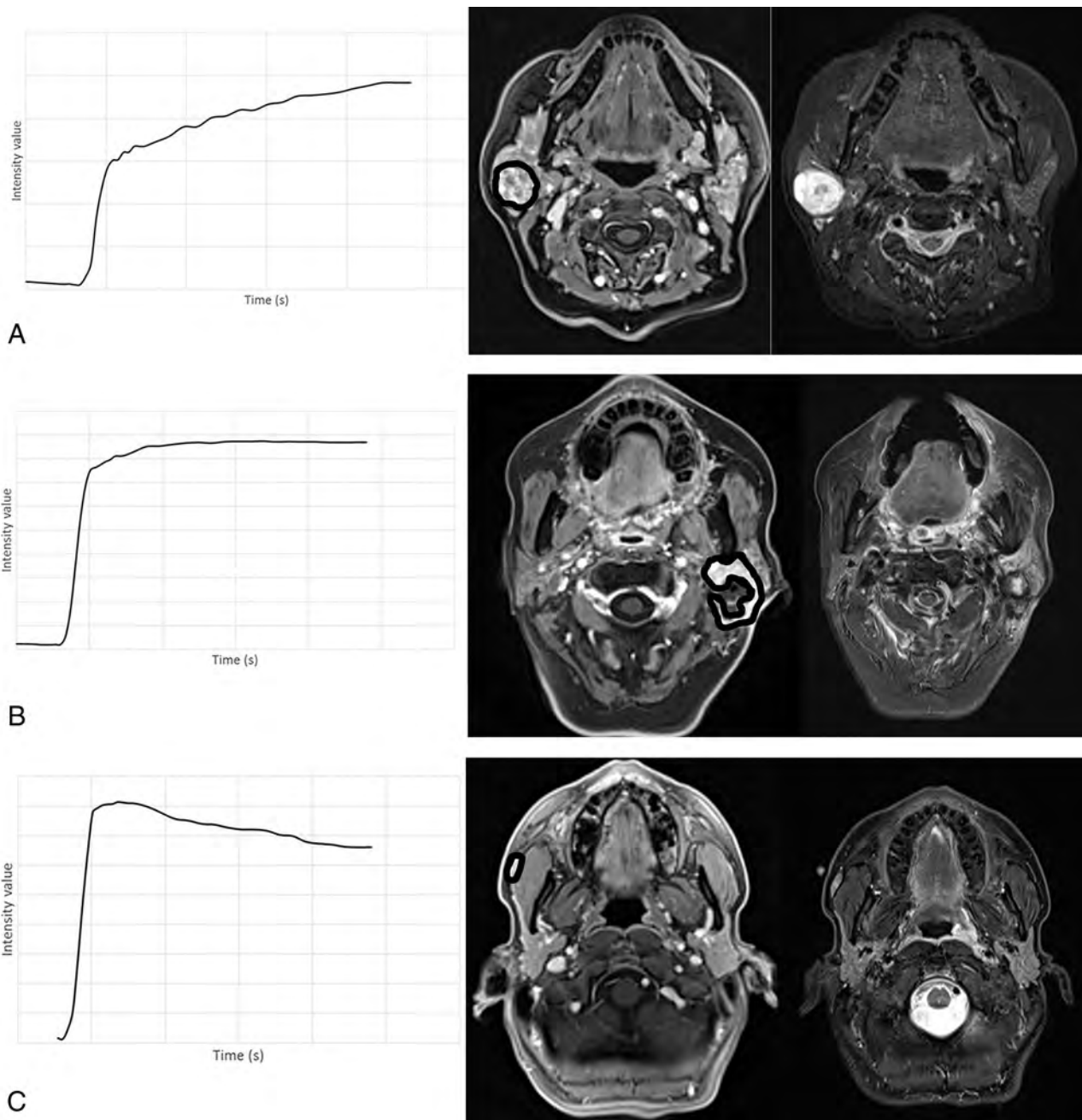


**FIG 2.** Examples of time-intensity curve morphology for each qualitatively applied category with representative axial contrast-enhanced GRASP and axial T2WI demonstrating the lesions and ROIs used for TIC creation. A, Continuous rise in a patient with pleomorphic adenoma. B, Rapid rise with a plateau in a patient with squamous cell carcinoma. C, Wash-in and washout in a patient with myoepithelial carcinoma of the accessory parotid gland. Notice that the GRASP sequence permits high-temporal-resolution dynamic permeability characterization concurrent with high-spatial-resolution fat-suppressed T1-weighted anatomic imaging in a single acquisition.

### Qualitative TIC Analysis

Interreader agreement for the TIC classifications of readers A and B was substantial ( $\kappa = 0.79$ ; 95% CI, 0.63–0.96) and moderate for readers A and C ( $\kappa = 0.54$ ; 95% CI, 0.34–0.73) and readers B and C ( $\kappa = 0.50$ ; 95% CI, 0.30–0.71).

After we combined TIC types 2 and 3, there was a significant association between TIC types 2 and 3 and parotid malignancy for all readers ( $P < .001$  for all). At a TIC classification threshold of  $>1$  (ie, TIC types 2 and 3), the positive predictive value (PPV) for predicting malignancy ranged from 56.0% to 66.7% among readers and the negative predictive value (NPV) for predicting malignancy ranged

from 91.7% to 100%. Among malignant lesions, 92.9% of all reader TIC assignments were type 2 or 3.

After we combined TIC types 2 and 3, there was a significant association between TIC type 1 and pleomorphic adenoma for all readers ( $P < .001$  for all). At a TIC assignment threshold of  $<2$  (ie, TIC type 1), the PPV for predicting pleomorphic adenoma ranged from 87.0% to 95.0% among readers, and the NPV for predicting pleomorphic adenoma ranged from 76.0% to 95.0% among the readers.

The associations between the TIC classification and parotid malignancy and the TIC classification and pleomorphic adenoma

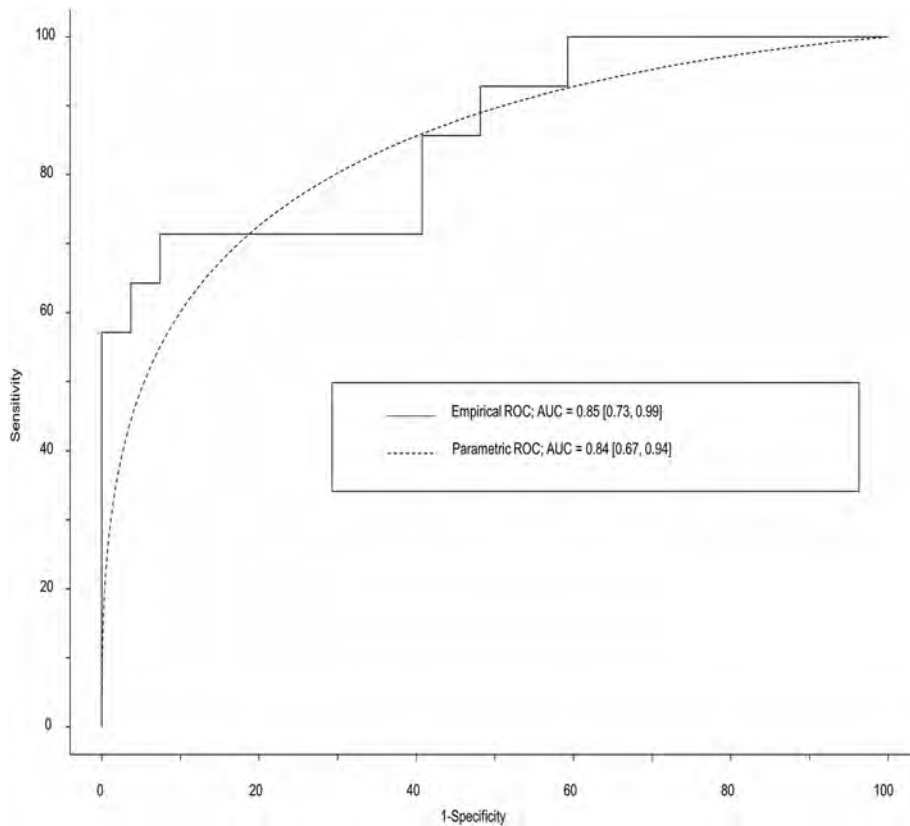


**FIG 3.** Empiric and binormal parametric ROC curves for discrimination of malignant and nonmalignant parotid neoplasms based on Tmax, AUC, washout slope, and SImax.

are summarized in On-line Table 1. Complete summaries of the ROC analyses are provided in On-line Table 2. Figure 2 shows examples of 3 cases.

Among all reader TICs created for Warthin tumors and oncocytomas, 88.9% ( $n = 16$ ) were assigned as type 2 or 3, and 11.1% ( $n = 2$ ), as type 1.

### Semiquantitative TIC Analyses

Univariate logistic regression analyses that examined the bivariate associations between parotid malignancy and the TIC semiquantitative metrics (normalized to the ipsilateral common carotid artery) revealed that Tmax (OR, 7.14; 95% CI, 1.73–29.30;  $P = .007$ ) and wash-in slope (OR, 2.63; 95% CI, 1.07–6.46;  $P = .034$ ) were significantly associated with parotid malignancy. On the basis of type III  $\chi^2$  tests, a multivariate logistic regression analysis identified Tmax ( $P = .018$ ), area under the curve (AUC) ( $P = .030$ ), washout slope ( $P = .031$ ), and SImax ( $P = .048$ ) as unique predictors of parotid malignancy. ROC curves and diagnostic characteristics for discrimination between nonmalignant and malignant parotid neoplasms based on Tmax, AUC, washout slope, and SImax are shown in Fig 3 (and On-line Table 3). The area under the curve for empiric and parametric ROC curves was 0.85 (95% CI, 0.73–0.99) and 0.84 (95% CI, 0.67–0.94), respectively.

Univariate logistic regression analysis that examined the bivariate associations between pleomorphic adenoma and TIC semiquantitative metrics (normalized to the ipsilateral common carotid artery) revealed that Tmax (OR, 27.38; 95% CI, 4.48–167.18;  $P < .001$ ) and wash-in slope (OR, 3.03; 95% CI,

1.13–8.16;  $P = .028$ ) were significantly associated with predicting pleomorphic adenoma. On the basis of type III  $\chi^2$  tests, a multivariate logistic regression analysis identified Tmax ( $P = .024$ ) as the only unique predictor of pleomorphic adenoma. ROC curves and diagnostic characteristics for discrimination of nonpleomorphic adenoma and pleomorphic adenoma based on Tmax are shown in Fig 4 (and On-line Table 4). The area under the curve for empiric and parametric ROC curves was 0.87 (95% CI, 0.73–0.95) and 0.86 (95% CI, 0.73–0.95), respectively.

### Subset Analyses of ADC Values and Semiquantitative TIC-Derived Metrics

A subset of 32 parotid neoplasms underwent a DWI sequence. The odds ratio for the association between ADC and malignancy was 102.39 (95% CI, 2.38–4402.38;  $P = .016$ ). The odds ratio for the association between ADC and pleomorphic adenoma was 71.95 (95% CI, 4.74–1091.38;  $P = .002$ ).

For the determination of parotid malignancy, a logistic regression model combining Tmax, AUC, washout slope, and SImax with ADC could not be created because the covariance matrix of this model is singular. For the determination of parotid malignancy, a logistic regression model that includes both Tmax and ADC is superior to a model based on Tmax alone ( $\chi^2$  statistic, 11.39;  $P < .001$ ), but not superior to a model containing ADC alone ( $\chi^2$  statistic, 0.04;  $P = .846$ ).

For the determination of pleomorphic adenoma, a logistic regression model that includes both Tmax and ADC is superior

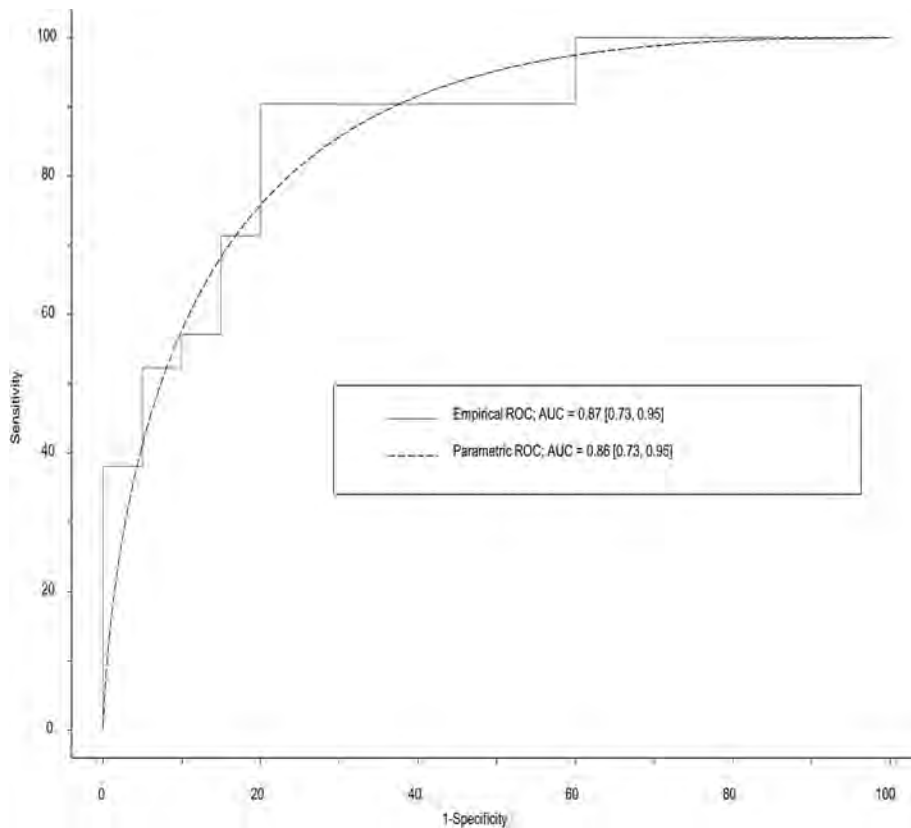


**FIG 4.** Empiric and binormal parametric ROC curves for discrimination between pleomorphic adenomas and nonpleomorphic adenomas based on Tmax.

to both a model containing Tmax alone ( $\chi^2$  statistic, 13.94;  $P < .001$ ) and a model containing ADC alone ( $\chi^2$  statistic, 12.53;  $P < .001$ ).

Figure 5 shows sample cases incorporating GRASP-derived DCE data and ADC data. All raw data from qualitative and semi-quantitative analyses are provided in On-line Table 5.

## DISCUSSION

Our results highlight the technical advantages of GRASP, a sequence that concurrently obtains high spatial resolution and fat-suppressed anatomic imaging of the entire neck as well as permeability information for noninvasive functional characterization of parotid neoplasia. We were able to document the independent processing and interpretation of DCE-MR imaging data in parotid neoplasms by multiple readers, which is a helpful step in attempting to generalize the application of DCE-MR imaging beyond the research setting. To our knowledge, only 1 prior study has evaluated interreader reliability (with 2 readers) for DCE-MR imaging analysis in parotid neoplasms.<sup>1</sup>

The results of our semiquantitative analysis are consistent with previous studies, specifically the findings that pleomorphic adenomas are associated with a relatively long Tmax, while malignant lesions are associated with a shorter Tmax.<sup>1,2,6,8</sup> Multiple Tmax threshold values are reported in the literature for the prediction of pleomorphic adenoma or malignancy, possibly due to differences in the DCE technique, which limits direct comparison of values across studies. Similar to prior analyses, we found that relying on this 1 parameter for the prediction of specific histologic diagnoses

was limited, primarily due to the overlapping TIC features of Warthin tumors and oncocytomas with those of malignant lesions. The most useful way to apply permeability data in clinical practice appears to relate to its high negative predictive value for malignancy. Namely, parotid neoplasms with a long Tmax are unlikely to represent malignant neoplasms. Moreover, our multivariate analysis showed that AUC, washout slope, and SI<sub>max</sub> were also unique predictors of parotid malignancy. Finally, all of our semiquantitative metrics were normalized to an anatomic reference (common carotid artery). Most prior studies did not normalize their data in this fashion. Reference tissue normalization is important because it provides a method to correct for the numerous sources of variability across different patients and scanners.<sup>1,2,6,8,19,20,22-24</sup>

Most interesting, our subset analysis incorporating ADC values showed that a multivariate model combining ADC values with Tmax showed a significantly improved performance for the prediction of pleomorphic adenoma compared with either parameter alone. With respect to malignancy characterization, previous studies have shown that the combined information of neovascularization (shorter Tmax) and higher cellularity (lower ADC) may help to identify parotid malignancies as distinct from benign neoplasms.<sup>20,21</sup> While our results did show that ADC combined with Tmax outperformed Tmax alone when predicting malignancy, our analysis here was limited because we were not able to combine ADC with the full logistic regression model that included Tmax, AUC, washout slope, and SI<sub>max</sub>.

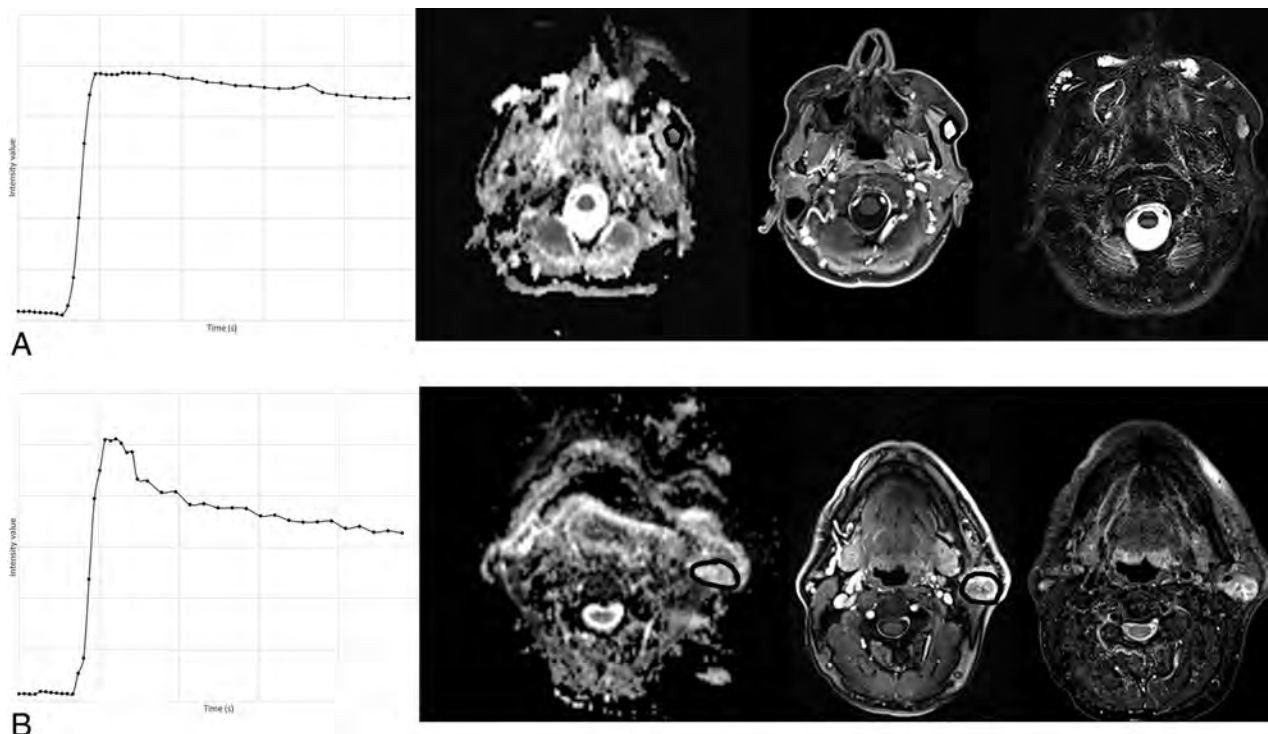


**FIG 5.** Representative examples of TICs, ADC maps, contrast-enhanced GRASP, and T2WI. *A*, Acinic cell carcinoma, displaying a type 2/3 curve TIC and a relatively low ADC of 926, which both favor a malignant neoplasm. *B*, Warthin tumor, displaying a characteristic type 3 TIC in combination with a relatively elevated ADC of 1616. The oncocytomas in our cohort had a similar combination of TIC and ADC features, whereas nearly all pleomorphic adenomas had type 1 TICs in combination with relatively elevated ADC values.

While several of our results support the results of prior literature, the GRASP technique has several key features that represent an improvement over techniques used in prior studies of DCE-MR imaging in parotid neoplasia. Uniquely, GRASP simultaneously provides high-spatial-resolution anatomic T1-weighted images of large anatomic coverage (eg, entire neck) with dynamic high-temporal-resolution permeability imaging of the entire imaging volume. GRASP uses a continuous radial stack-of-stars acquisition of  $k$ -space, and an arbitrary number of consecutive radial spokes can be combined into a single image frame to create DCE imaging of a desired temporal resolution. Additionally, by combining all spokes into a single image frame, one can create high-resolution fat-suppressed anatomic images of the entire neck with an excellent signal-to-noise ratio. Thus, GRASP can be routinely integrated into a parotid gland imaging protocol as a diagnostic anatomic sequence without using examination time solely to obtain permeability information. Although some authors have performed DCE-MR imaging at a similar temporal resolution, the techniques used in those studies were often limited to either a single slice or a smaller portion of the volume of interest at a lower spatial resolution.<sup>6,22,23</sup> Because GRASP acquires high-temporal-resolution permeability imaging for entire neck coverage, it has an added benefit of ensuring that a useful reference standard (such as the common carotid artery) is included in the imaging volume for normalizing imaging metrics. It also removes the possibility of inadvertently excluding portions of parotid neoplasms when selecting the imaging subvolume for DCE acquisition. Finally, a distinct advantage to radial  $k$ -space sampling is its substantially reduced sensitivity to motion arti-

facts. In fact, none of the cases in our study required exclusion due to motion artifacts.<sup>10-12</sup>

One limitation of our study is our cohort size ( $n = 41$ ), and we specifically note here the important 2016 study by Yuan et al,<sup>25</sup> which included DCE imaging in a large cohort of parotid neoplasms. However, despite our smaller patient cohort, we believe our study remains of interest, predominantly due to the application of the GRASP imaging technique as discussed above. Specifically, our GRASP technique enabled entire neck coverage with 2-mm slice thickness (compared with 5 mm in the Yuan study) despite a similar reported temporal resolution. Moreover, Yuan et al did not normalize their DCE metrics using an anatomic reference as we did. Aside from such technical differences, we performed a comprehensive assessment of interreader reliability for independently processing and categorizing the parotid lesion TIC using DCE-MR imaging, whereas Yuan et al used a consensus reading.

Additional limitations of our study include its retrospective design. We undertook qualitative and semiquantitative methods of analysis rather than “quantitative” analysis using baseline T1-mapping that allows determination of parameters such as the volume transfer constant between the extravascular extracellular space and plasma or extravascular extracellular space volume per tissue volume.<sup>26</sup> However, such quantitative techniques are themselves limited by the application of various physiologic assumptions across different patients. We included MR imaging examinations from both 1.5T and 3T scanners and acknowledge that different scanners might yield differing DCE data. Finally, the

GRASP sequence is currently limited to a single vendor and thus not yet available to all MR imaging sites for routine clinical use.

## CONCLUSIONS

GRASP-derived DCE-MR imaging for parotid neoplasms introduces several technical advantages, including the ability to create high-temporal-resolution dynamic data for permeability assessment concurrent with high-spatial-resolution, large-anatomic-coverage, diagnostic imaging of the whole neck. GRASP-derived DCE-MR imaging achieves a high NPV when determining the presence of parotid malignancy and excellent diagnostic performance in predicting pleomorphic adenomas.

Disclosures: Kai Tobias Block—UNRELATED: Patents (Planned, Pending or Issued): New York University GRASP patent, Comments: New York University owns the patent on the GRASP technique of which I am a coinventor. No royalties have been paid.\* Sohil H. Patel—UNRELATED: Grants/Grants Pending: Radiological Society of North America Research Scholar Grant.\* Elcin Zan—UNRELATED: Grants/Grants Pending: Novartis/Advanced Accelerator Applications, Comments: Clinical trial funding is pending.\* \*Money paid to the institution.

## REFERENCES

1. Lechner Goyault J, Riehm S, Neuville A, et al. **Interest of diffusion-weighted and gadolinium-enhanced dynamic MR sequences for the diagnosis of parotid gland tumors.** *J Neuroradiol* 2011;38:77–89 CrossRef Medline
2. Yabuuchi H, Fukuya T, Tajima T, et al. **Salivary gland tumors: diagnostic value of gadolinium-enhanced dynamic MR imaging with histopathologic correlation.** *Radiology* 2003;226:345–54 CrossRef Medline
3. Valentini V, Fabiani F, Perugini M, et al. **Surgical techniques in the treatment of pleomorphic adenoma of the parotid gland: our experience and review of literature.** *J Craniofac Surg* 2001;12:565–68 CrossRef Medline
4. Abdel Razek AA, Samir S, Ashmalla GA. **Characterization of parotid tumors with dynamic susceptibility contrast perfusion-weighted magnetic resonance imaging and diffusion-weighted MR imaging.** *J Comput Assist Tomogr* 2017;41:131–36 CrossRef Medline
5. Yousem DM, Kraut MA, Chalian AA. **Major salivary gland imaging.** *Radiology* 2000;216:19–29 CrossRef Medline
6. Lam PD, Kuribayashi A, Imaizumi A, et al. **Differentiating benign and malignant salivary gland tumours: diagnostic criteria and the accuracy of dynamic contrast-enhanced MRI with high temporal resolution.** *Br J Radiol* 2015;88:20140685 CrossRef Medline
7. Zaghi S, Hendizadeh L, Hung T, et al. **MRI criteria for the diagnosis of pleomorphic adenoma: a validation study.** *Am J Otolaryngol* 2014; 35:713–18 CrossRef Medline
8. Hisatomi M, Asaumi J, Yanagi Y, et al. **Diagnostic value of dynamic contrast-enhanced MRI in the salivary gland tumors.** *Oral Oncol* 2007;43:940–47 CrossRef Medline
9. Haldar S, Sinnott JD, Tekeli KM, et al. **Biopsy of parotid masses: review of current techniques.** *World J Radiol* 2016;8:501–05 CrossRef Medline
10. Feng L, Grimm R, Block TK, et al. **Golden-angle radial sparse parallel MRI: combination of compressed sensing, parallel imaging, and golden-angle radial sampling for fast and flexible dynamic volumetric MRI.** *Magn Reson Med* 2014;72:707–17 CrossRef Medline
11. Chandarana H, Feng L, Block TK, et al. **Free-breathing contrast-enhanced multiphase MRI of the liver using a combination of compressed sensing, parallel imaging, and golden-angle radial sampling.** *Invest Radiol* 2013;48:10–16 CrossRef Medline
12. Rosenkrantz AB, Geppert C, Grimm R, et al. **Dynamic contrast-enhanced MRI of the prostate with high spatiotemporal resolution using compressed sensing, parallel imaging, and continuous golden-angle radial sampling: preliminary experience.** *J Magn Reson Imaging* 2015;41:1365–73 CrossRef Medline
13. Wu X, Raz E, Block TK, et al. **Contrast-enhanced radial 3D fat-suppressed T1-weighted gradient-recalled echo sequence versus conventional fat-suppressed contrast-enhanced T1-weighted studies of the head and neck.** *AJR Am J Roentgenol* 2014;203:883–89 CrossRef Medline
14. Bangiyev L, Raz E, Block TK, et al. **Evaluation of the orbit using contrast-enhanced radial 3D fat-suppressed T1 weighted gradient echo (Radial-VIBE) sequence.** *Br J Radiol* 2015;88:20140863 CrossRef Medline
15. Heacock L, Gao Y, Heller SL, et al. **Comparison of conventional DCE-MRI and a novel golden-angle radial multicoil compressed sensing method for the evaluation of breast lesion conspicuity.** *J Magn Reson Imaging* 2017;45:1746–52 CrossRef Medline
16. Rossi Espagnet MC, Bangiyev L, Haber M, et al. **High-resolution DCE-MRI of the pituitary gland using radial k-space acquisition with compressed sensing reconstruction.** *AJNR Am J Neuroradiol* 2015;36:1444–49 CrossRef Medline
17. Sen R, Sen C, Pack J, et al. **Role of high-resolution dynamic contrast-enhanced MRI with golden-angle radial sparse parallel reconstruction to identify the normal pituitary gland in patients with macroadenomas.** *AJNR Am J Neuroradiol* 2017;38:1117–21 CrossRef Medline
18. Clopper CJ, Pearson ES. **The use of confidence or fiducial limits illustrated in the case of the binomial.** *Biometrika* 1934;26:404 CrossRef
19. Alibek S, Zenk J, Bozzato A, et al. **The value of dynamic MRI studies in parotid tumors.** *Acad Radiol* 2007;14:701–10 CrossRef Medline
20. Yabuuchi H, Matsuo Y, Kamitani T, et al. **Parotid gland tumors: can addition of diffusion-weighted MR imaging to dynamic contrast-enhanced MR imaging improve diagnostic accuracy in characterization?** *Radiology* 2008;249:909–16 CrossRef Medline
21. Barrett T, Brechbiel M, Bernardo M, et al. **MRI of tumor angiogenesis.** *J Magn Reson Imaging* 2007;26:235–49 CrossRef Medline
22. Tao X, Yang G, Wang P, et al. **The value of combining conventional, diffusion-weighted and dynamic contrast-enhanced MR imaging for the diagnosis of parotid gland tumours.** *Dentomaxillofac Radiol* 2017;20160434 CrossRef CrossRef
23. Furukawa M, Parvathaneni U, Maravilla K, et al. **Dynamic contrast-enhanced MR perfusion imaging of head and neck tumors at 3 Tesla.** *Head Neck* 2013;35:923–29 CrossRef Medline
24. Thomas AA, Arevalo-Perez J, Kaley T, et al. **Dynamic contrast enhanced T1 MRI perfusion differentiates pseudoprogression from recurrent glioblastoma.** *J Neurooncol* 2015;125:183–90 CrossRef Medline
25. Yuan Y, Tang W, Tao X. **Parotid gland lesions: separate and combined diagnostic value of conventional MRI, diffusion-weighted imaging and dynamic contrast-enhanced MRI.** *Br J Radiol* 2016;89: 20150912 CrossRef Medline
26. Gaddikeri S, Gaddikeri RS, Tailor T, et al. **Dynamic contrast-enhanced MR imaging in head and neck cancer: techniques and clinical applications.** *AJNR Am J Neuroradiol* 2016;37:588–95 CrossRef Medline

# Localization of Parotid Gland Tumors in Relation to the Intraparotid Facial Nerve on 3D Double-Echo Steady-State with Water Excitation Sequence

H. Fujii, A. Fujita, H. Kanazawa, E. Sung, O. Sakai, and H. Sugimoto

## ABSTRACT

**BACKGROUND AND PURPOSE:** Reliable preoperative facial nerve mapping may help avoid or minimize facial nerve injury during parotid tumor resection. The purpose of this study was to investigate the diagnostic performance of the 3D double-echo steady-state with water excitation sequence in localizing parotid gland tumors through direct visualization of the intraparotid facial nerve in comparison with indirect methods of estimating the facial nerve location.

**MATERIALS AND METHODS:** We retrospectively reviewed 91 parotid gland tumors in 90 patients who underwent surgical resection and preoperative MR imaging, including the 3D double-echo steady-state with water excitation sequence. The tumor locations were categorized as deep or superficial on the basis of direct and 3 indirect methods: the facial nerve line, retromandibular vein, and Utrecht line. Surgical localization was considered the criterion standard. The diagnostic performance for localizing deep lobe lesions using direct and indirect methods was calculated and compared using the McNemar test.

**RESULTS:** Surgical localization confirmed 75 superficial lesions and 16 deep lesions. The interobserver variability of the 3D double-echo steady-state with water excitation sequence was excellent ( $\kappa = 0.870$ ). The diagnostic accuracy, sensitivity, specificity, positive predictive value, and negative predictive value for localizing deep lobe lesions using the 3D double-echo steady-state with water excitation method were 97.8%, 87.5%, 100%, 100%, and 97.4%, respectively. These findings were significantly higher than the facial nerve line in sensitivity, the retromandibular vein in sensitivity, and the Utrecht line in accuracy and specificity ( $P < .05$ ). Overall, the direct method was the most accurate, sensitive, and specific in localizing parotid gland tumors.

**CONCLUSIONS:** We can achieve higher diagnostic performance in localizing parotid gland tumors by directly visualizing the intraparotid facial nerve using the 3D double-echo steady-state with water excitation sequence compared with indirect methods.

**ABBREVIATIONS:** 3D-DESS-WE = 3D double-echo steady-state with water excitation; FNL = facial nerve line; RMV = retromandibular vein; UL = Utrecht line

The facial nerve exits the skull base via the stylomastoid foramen and enters the parotid gland. Within the parotid gland, the intraparotid facial nerve trunk divides into its 2 main branches, the temporofacial and cervicofacial branches, and fur-

ther divides into the temporal, zygomatic, buccal, mandibular, and cervical branches. The intraparotid facial nerve and its branches course predominantly in a single sagittal plane, which separates the superficial and deep lobes of the parotid gland.<sup>1</sup> It is important to know the spatial relationship of the intraparotid facial nerve to a parotid tumor because this information may impact the duration and difficulty of the operation.<sup>2</sup> Several indirect methods to estimate the location of the intraparotid facial nerve have been reported.<sup>3-6</sup> However, the accuracy of indirect methods is variable and can be affected by tumor size, location, and the specific method used. Therefore, direct visualization of the intraparotid facial nerve is desirable.<sup>7</sup> With increasing spatial and contrast resolution of cross-sectional imaging, better visualization of the cranial nerves has become possible.<sup>2,8,9</sup> However, imaging the course of the intraparotid facial nerve still remains a diagnostic challenge due to the fine structure and complex anatomy of the nerve. The 3D double-echo steady-state with water

Received December 17, 2018; accepted after revision April 21, 2019.

From the Department of Radiology (H.F., A.F., H.K., H.S.), Jichi Medical University, School of Medicine, Tochigi, Japan; and Departments of Radiology (E.S., O.S.), Otolaryngology-Head and Neck Surgery (O.S.), and Radiation Oncology (O.S.), Boston Medical Center, Boston University School of Medicine, Boston, Massachusetts.

Paper previously presented, in part, at: Scientific Assembly and Annual Meeting of the Radiological Society of North America, November 27 to December 2, 2016; Chicago, Illinois (Hiroyuki Fujii, Akifumi Fujita, Hidenori Kanazawa, Edward Sung, Osamu Sakai, Hideharu Sugimoto. "Localization of Parotid Gland Tumors in Relation to the Intraparotid Facial Nerve on 3D-Double-Echo Steady-State with Water Excitation Sequence").

Please address correspondence to Hiroyuki Fujii, MD, PhD, Department of Radiology, Jichi Medical University School of Medicine, 3311-1 Yakushiji, Shimotsuke, Tochigi 329-0498, Japan; e-mail: hiroyuki.fujii@jichi.ac.jp

<http://dx.doi.org/10.3174/ajnr.A6078>

excitation (3D-DESS-WE) sequence is a recently introduced MR imaging technique that can delineate the peripheral cranial nerves as high-signal-intensity structures.<sup>10,11</sup> At Jichi Medical University Hospital, this sequence has been added to our standard MR imaging protocol of the salivary glands and has been used routinely to demonstrate the intraparotid facial nerve and salivary ducts within the salivary glands since 2012. The purpose of this study was to investigate the accuracy of the 3D-DESS-WE MR imaging sequence in localizing parotid gland tumors through direct visualization of the intraparotid facial nerve and to compare it with indirect methods of localization.

## MATERIALS AND METHODS

### Patient Population

This retrospective study was approved by our institutional review board, and informed consent was waived. We retrospectively reviewed 107 consecutive patients (53 men and 54 women with a median age of 58 years; range, 19–87 years) with parotid gland lesions who underwent surgical resection and preoperative MR imaging, including the 3D-DESS-WE sequence from October 2012 to March 2018. Two patients with severe motion artifacts, and 15 patients who could not have accurate surgical confirmation of parotid tumor localization (enucleation,  $n = 10$ , and total parotidectomy,  $n = 5$ ) were excluded. Ultimately, 91 parotid gland tumors in 90 patients were included in this study (1 patient had ipsilateral multiple parotid gland tumors).

### MR Imaging and Interpretation

All patients underwent MR imaging with a 3T unit (Magnetom Skyra; Siemens, Erlangen, Germany) using a commercially available 20-channel head and neck coil with our routine neck protocol that included the 3D-DESS-WE sequence. The parameters of the 3D-DESS-WE sequence are as follows: TR/TE = 11/4.21 ms, flip angle = 30°, FOV = 200 × 200 mm, matrix = 384 × 244, effective section thickness = 0.82 mm, number of acquisitions = 1, scan time = 4 minutes 12 seconds. The slab thickness (11.2 cm) of the 3D-DESS-WE sequence is from the skull base to the mandible.

All acquired images were transferred to our clinically used server and evaluated with a PACS system with a 2-megapixel high-resolution liquid crystal display. Two board-certified radiologists (with 21 and 7 years of post training experience in head and neck radiology, respectively) independently evaluated the location of the parotid gland lesions in preoperative MR imaging. The locations of the parotid gland lesions were categorized into the superficial or deep lobe based on direct and 3 indirect methods.

### Direct Method with Visualization of the Intraparotid Facial Nerve on 3D-DESS-WE

The intraparotid facial nerve was identified on the 3D-DESS-WE sequence (Fig 1) using axial source images and multiplanar reconstructions, which were created by radiology technologists. Parotid tumors lateral to the intraparotid facial nerve were defined as being in the superficial lobe (Fig 2), and parotid tumors medial to the intraparotid facial nerve were defined as being in the deep lobe (Fig 3). When peripheral facial nerve branches could not be delineated to determine the tumor location, a plane parallel to the

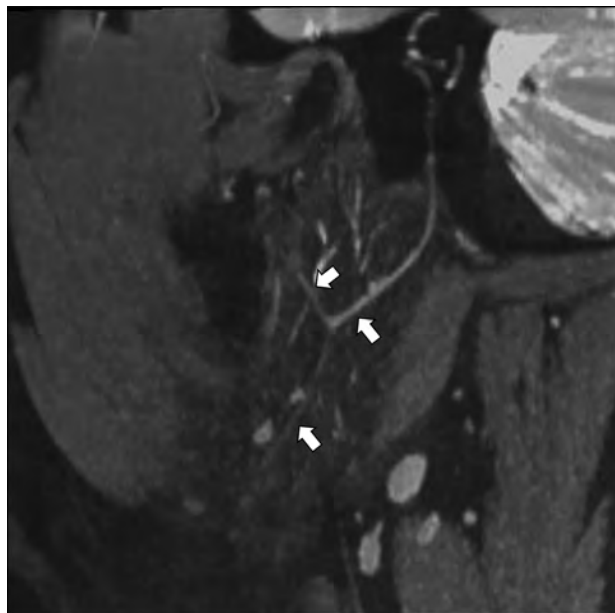


**FIG 1.** Visualization of the intraparotid facial nerve on the 3D-DESS-WE sequence. Reformatted sagittal image of the 3D-DESS-WE sequence clearly shows the intraparotid facial nerve (arrows).

visualized main trunk of the intraparotid facial nerve was used to localize the parotid gland tumor, on the basis of the assumption that the deviation of the facial nerve trunk could determine the tumor location. Tumors totally or with >50% of tumor volume located lateral to the plane were defined as being in the superficial lobe, and tumors totally or with >50% of tumor volume located medial to the plane were defined as being in the deep lobe.

### Indirect Approximation of the Intraparotid Facial Nerve Using the Facial Nerve Line, Retromandibular Vein, and Utrecht Line

The 3 indirect methods were evaluated on axial T2-weighted images (TR/TE, 5000/83 ms) and 3D-T1 volumetric interpolated brain examinations with 2-point Dixon technique images (TR/TE, 6/2.46 ms) after intravenous administration of 0.1 mmol/kg body weight of a gadolinium contrast agent (Fig 4). The facial nerve line (FNL) connects the lateral surface of the posterior belly of the digastric muscle to the lateral surface of the ascending ramus of the mandible. The Utrecht line (UL) connects the most dorsal point observed on the ipsilateral half of a vertebra to the most dorsal point of the retromandibular vein (RMV). Tumors totally or with >50% of tumor volume located lateral to the FNL, UL, or RMV were defined as being in the superficial lobe, and tumors totally or with >50% of tumor volume located medial to the FNL, UL, or RMV were defined as being in the deep lobe.

### Tumor Location Based on Surgical Findings

The spatial relationship of the intraparotid facial nerve to a parotid tumor was confirmed by reviewing the surgical report, which was considered the criterion standard and was used to determine the diagnostic performance of using the direct and indirect methods described above.

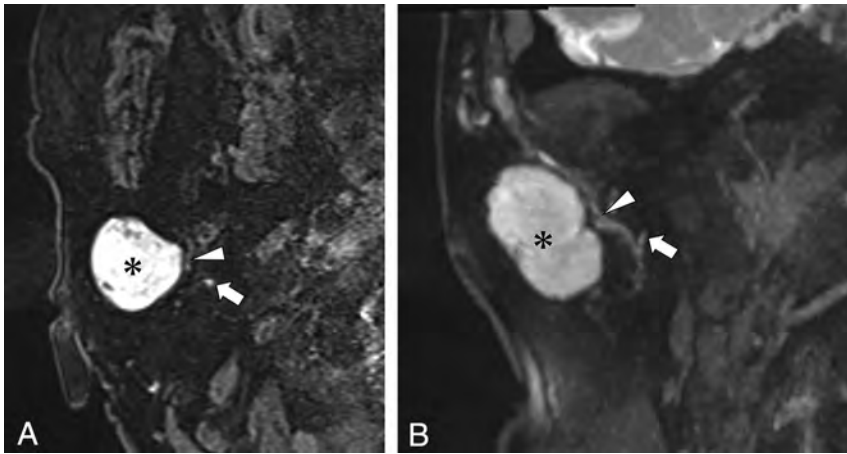


**FIG 2.** A 71-year-old woman with pleomorphic adenoma of the right parotid gland. *A*, Axial source image of the 3D-DESS-WE sequence. *B*, Coronal reformatted image of the 3D-DESS-WE sequence. Axial and reformatted coronal images of the 3D-DESS-WE sequence show the intraparotid facial nerve trunk (*A* and *B*, arrows) and temporofacial trunk (*A* and *B*, arrowheads) coursing medially to the parotid mass (*A* and *B*, asterisk), suggesting localization to the superficial lobe.

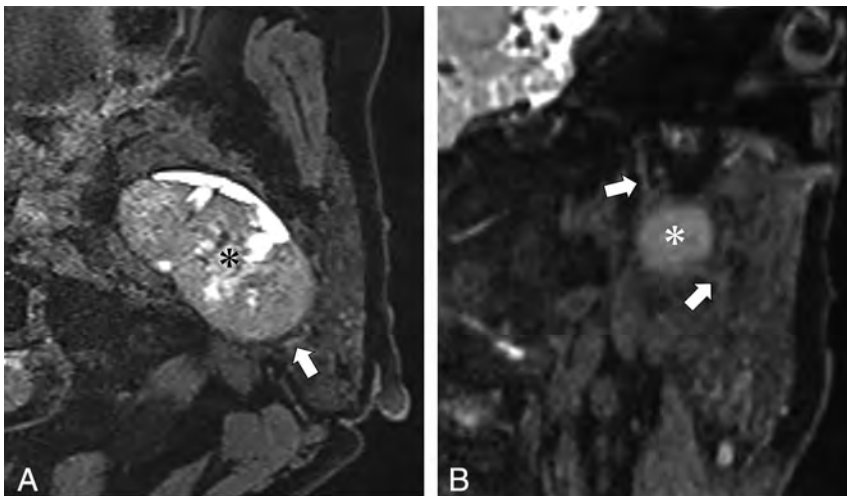


**FIG 3.** A 65-year-old woman with basal cell adenoma of the left parotid gland. *A*, Axial source image of the 3D-DESS-WE sequence. *B*, Coronal reformatted image of the 3D-DESS-WE sequence. Axial and reformatted coronal 3D-DESS-WE images show the intraparotid facial nerve trunk (arrows) coursing lateral to the parotid mass (asterisk), suggesting localization to the deep lobe.

### Statistical Analysis

Two readers independently evaluated the tumor locations using the direct and indirect methods. Inconsistencies were resolved by collaborative review and consensus agreement. The interobserver variability was calculated using  $\kappa$  analysis: poor,  $\kappa \leq 0.2$ ; fair,  $0.2 < \kappa \leq 0.4$ ; moderate,  $0.4 < \kappa \leq 0.6$ ; good,  $0.6 < \kappa \leq 0.8$ ; excellent,  $0.8 < \kappa \leq 1$ . The diagnostic accuracy, sensitivity, specificity, positive predictive value, and negative predictive value for localizing parotid lesions using direct and indirect methods were calculated and compared using the McNemar test. Given the bivariate (superficial-versus-deep) nature of our data, the sensitivity and specificity and the positive and negative predictive values for superficial and deep lobe analyses were the inverse of each other. Therefore, we chose to focus on the analysis for localizing deep lobe lesions. Statistical analyses were performed using Version 3.3.3 of the R statistical and computing software (<http://www.r-project.org/>).

### RESULTS

Surgical findings confirmed 75 lesions localized to the superficial lobe, and 16 lesions localized to the deep lobe. The histologic types and frequencies of parotid lesions are shown in Table 1.

The interobserver variabilities in determining the location of the parotid lesions using direct and indirect methods are shown in Table 2. The interobserver variability of the direct method was excellent (0.870), that of RMV was good (0.706), and those of FNL and UL were moderate (0.587 and 0.471, respectively).

Of the total 91 parotid lesions, 85 lesions could be localized in relation to the intraparotid facial nerve on the 3D-DESS-WE sequence. The remaining 6 lesions were located in the far distal (anterior) part of parotid gland parenchyma, rendering visualization of the intraparotid facial nerve limited on the 3D-DESS-WE sequence. In these cases, we categorized the lesion location using a plane parallel to the visualized main trunk of the intraparotid facial nerve (described in the Materials and Methods section).

The diagnostic accuracy, sensitivity, specificity, positive predictive value, and negative predictive value for surgically confirmed deep lobe lesions using direct and indirect methods are shown in Table 3. Of the 4 methods, the direct method showed the highest accuracy, sensitivity, and negative predictive value for localization of deep lobe parotid gland tumors (97.8%, 87.5%, and 97.4%, respectively). The direct method also showed high specificity and positive predictive value, which were identical to

those of the RMV (100% and 100%, respectively). The accuracy and specificity of the direct method were statistically higher than those of the UL ( $P = .002$  and  $P = .008$ , respectively). The sensitivity of the direct method was statistically higher than that of the FNL and RMV ( $P = .008$  and  $P = .031$ , respectively). Overall, the direct method was the most accurate, sensitive, and specific in localizing parotid gland tumors. Among the indirect methods, the RMV showed the highest accuracy, specificity, positive predictive value, and negative predictive value (91.2%, 100%, 100%, 90.4%, respectively). The FNL showed relatively high specificity but low sensitivity (93.3% and 37.5%, respectively). The UL showed the lowest diagnostic performance among the 4 methods.

### DISCUSSION

Surgery for parotid gland tumors has a relatively high rate of complications, including facial nerve paralysis, salivary fistula, infec-



**FIG 4.** Indirect methods to approximate the intraparotid facial nerve: facial nerve line (solid line), retromandibular vein (dotted circle), and Utrecht line (dotted line).

tion, hematoma, sialocele, and Frey syndrome. Among these, temporary facial nerve paralysis is most frequent.<sup>12</sup> Facial nerve injury mechanisms during parotidectomy include nerve dissection, stretching, compression, ligature entrapment, thermal and electrical injuries, and ischemia.<sup>13</sup> Facial nerve paralysis can cause cosmetic and functional morbidity, ocular complications, diminished quality of life, and medical malpractice litigation.<sup>14,15</sup> Reliable preoperative facial nerve mapping may assist safe and effective tumor resection and provide better information for patients regarding potential risks and morbidity after surgical intervention.

Because it is difficult to visualize the intraparotid facial nerve by routine MR imaging, various indirect methods (such as FNL, RMV, and UL) for approximating the course of the intraparotid facial nerve to aid in localizing parotid gland tumors have been proposed. Several studies have shown high accuracy of the FNL (71.4%–87.5%), though there was low sensitivity for deep lobe lesions (12.5%–50.0%) despite high specificity (98.1%).<sup>3,4,6,16</sup> The RMV has been reported to show relatively high accuracy (63.5%–86.4%) along with high specificity (85.7%–96.2%) and variable sensitivity (29.6%–71%).<sup>5,16,17</sup> Kim et al<sup>16</sup> reported that the UL showed relatively low accuracy (74.8%), low sensitivity (18.5%), and high specificity (89.4%). In this study, the FNL showed low sensitivity and high specificity, and the RMV showed high accuracy and specificity, findings consistent with previous reports. The ULs showed relatively high accuracy and specificity, but they were still the lowest in our study. Among indirect methods, the RMV showed the best diagnostic performance in this study. Our study also showed that the interobserver variability of indirect methods was lower than that of the direct method. In particular, the dorsal points of the FNL (posterior belly of the digastric muscle) and UL (most dorsal point observed on the ipsilateral half of a vertebra) can vary depending on the imaging slice. In some cases, the branch of the external carotid artery was misinterpreted as the RMV. These factors may have led to the lower interobserver variability. Overall, the broad variability of the diagnostic performance for the indirect methods from previous studies as well as our own study suggests that indirect methods are not reliable for accurate surgical planning, with a higher risk of surgical complications related to facial nerve injury.

The 3D-DESS-WE sequence is commonly used in musculoskeletal imaging, but it was recently used for visualization of the intraparotid facial nerve and has been quite successful.<sup>11</sup> The 3D-DESS-WE sequence includes both FISP and reversed fast imaging with steady-state free precession components. The FISP signal intensity provides more anatomic details with tissue contrast dominated by the T1/T2 ratio.<sup>11</sup> The reversed fast imaging with steady-state free precession signal intensity accentuates the signal intensity of the components with a long T2 signal.<sup>18</sup> With 3D-DESS-WE, the facial nerve and its branches can be easily identified because they demonstrate high signal intensity.<sup>11</sup> Another study showed that the 3D-DESS-WE sequence demonstrated excellent visualization of the entire course of the mandibular division of the trigeminal nerve in most patients.<sup>10</sup> Therefore, we routinely use the 3D-DESS-WE sequence to visualize the intraparotid facial nerve for preoperative evaluation. To our knowledge,

**Table 1: Histologic types and frequencies of parotid lesions**

Histologic Types	Surgical Findings		
		Superficial Lobe	Deep Lobe
Benign tumors			
Pleomorphic adenoma	57	44	13
Warthin tumor	15	13	2
Basal cell adenoma	3	2	1
Myoepithelioma	1	1	0
Lymphoepithelial cyst	3	3	0
Reactive lymphadenopathy	1	1	0
Inflammation	1	1	0
Malignant tumors			
Malignant lymphoma	1	1	0
Metastatic tumor	2	2	0
Oncocytic carcinoma	1	1	0
Acinic cell carcinoma	2	2	0
Carcinoma ex pleomorphic adenoma	1	1	0
Basal cell adenocarcinoma	1	1	0
Salivary duct carcinoma	2	2	0
Total	91	75	16

**Table 2: Interobserver variabilities in determining the location of the parotid lesion with direct and indirect methods**

Interobserver Variability	No.	Concordance	$\kappa$
Direct method	91	88	0.870
FNL		81	0.587
RMV		86	0.706
UL		75	0.471

**Table 3: Localization of parotid lesions with imaging and surgical findings and the diagnostic performance of the surgically confirmed deep lobe lesions<sup>a</sup>**

	Surgical Findings		Diagnostic Performance (Deep Lobe Lesions) (%) (95% CI)				
	Deep Lobe	Superficial Lobe	Accuracy	Sensitivity	Specificity	PPV	NPV
1) Direct method							
Deep lobe	14	0	97.8 (91.4–97.8)	87.5 (69.2–87.5)	100 (96.1–100)	100 (79.0–100)	97.4 (93.6–97.4)
Superficial lobe	2	75					
2) FNL							
Deep lobe	6	5	83.5 (76.7–89.7) ( <i>P</i> = .065)	37.5 (18.0–55.0) ( <i>P</i> = .008 <sup>b</sup> )	93.3 (89.2–97.1) ( <i>P</i> = .063)	54.4 (26.2–80.1)	87.5 (83.6–91.0)
Superficial lobe	10	70					
3) RMV							
Deep lobe	8	0	91.2 (84.7–91.2) ( <i>P</i> = .727)	50.0 (31.6–50.0) ( <i>P</i> = .031 <sup>b</sup> )	100 (96.1–100) (NA)	100 (63.2–100)	90.4 (86.8–90.4)
Superficial lobe	8	75					
4) UL							
Deep lobe	8	8	82.4 (74.6–89.5) ( <i>P</i> = .002 <sup>b</sup> )	50 (27.8–70.1) ( <i>P</i> = .070)	89.3 (84.6–93.6) ( <i>P</i> = .008 <sup>b</sup> )	50 (27.8–70.1)	89.3 (84.6–93.6)
Superficial lobe	8	67					

**Note:**—PPV indicates positive predictive value; NPV, negative predictive value; NA, not available.

<sup>a</sup> Statistical analyses (*P* values) were performed comparing the direct method with each indirect method.

<sup>b</sup> Significant difference (*P* < .05).

there have been no previous studies evaluating the 3D-DESS-WE sequence for localizing parotid gland tumors.

In this study, the direct method using the 3D-DESS-WE sequence showed higher accuracy, sensitivity, specificity, positive predictive value, and negative predictive value than indirect methods. Therefore, we found that the 3D-DESS-WE sequence could reliably and accurately depict the intraparotid facial nerve in the presence of parotid gland tumors. However, 2 cases were incorrectly categorized. One lesion was incorrectly categorized to the superficial lobe because a linear high-intensity structure was seen to course medial to the parotid gland tumor, but surgical findings confirmed the presence of a thin branch of the intraparotid facial nerve lying on the surface of the parotid gland tumor, therefore categorizing this as a deep lobe lesion. In another case, the tumor was located in the far distal (anterior) part of parotid gland parenchyma, rendering visualization of the intraparotid facial nerve limited on the 3D-DESS-WE sequence and therefore limiting our ability to localize this lesion. In this case, we categorized the lesion to the superficial lobe based on a plane parallel to the visualized facial nerve trunk. However, surgical findings confirmed the parotid gland tumor localized to the deep lobe.

As mentioned in the Results section, 6 of 91 lesions had to be localized using this method, and this was the only case found to be incorrect. Moreover, this highlights the difficulty in visualizing the intraparotid facial nerve in the far anterior part of the parotid gland because the distal branches of the facial nerve become increasingly thin. However, an isolated injury to a thin, peripheral branch of the facial nerve is less likely to have significant consequences. Nonetheless, our study demonstrated that we could achieve high diagnostic performance in parotid tumor localization using the 3D-DESS-WE sequence with a standard, commercially available head and neck coil. This study showed excellent interobserver variability of 3D-DESS-WE, which was higher than that of the indirect methods. Similarly, a previous study showed that the 3D-DESS-WE sequence enabled uniform detectability of the peripheral branches of the cranial nerve by readers at various training levels.<sup>10</sup>

There are several limitations in this study. First, our study consists of a relatively small number of deep lobe tumors (17.6%) compared with superficial lobe tumors. However, it is well-known that the occurrence of parotid tumors in the deep lobe is

approximately 10%, which was concordant with this study.<sup>19</sup> Furthermore, the number of deep lobe tumors was sufficient to show statistical significance in this study. A second limitation was the disuse of a surface coil, which could achieve better visualization of the intraparotid facial nerve.<sup>20,21</sup> However, we found that using the surface coil was not feasible in routine clinical practice due to its time-consuming and cumbersome application. Despite the lack of a surface coil, this study still demonstrated good diagnostic performance using a standard, commercially available head and neck coil, and the acquisition time of the 3D-DESS-WE sequence was relatively short, maintaining its feasibility for routine clinical practice. A third limitation was a small number of nonfatty parotid glands, which could negatively influence the diagnostic performance. In a patient with a nonfatty parotid gland, it is difficult to trace the course of the intraparotid facial nerve because of low contrast between the nerve and parotid parenchyma. Generally, older patients have more fatty infiltration of the parotid gland. A relatively high median age of the patients was thought to explain the small number of nonfatty parotid glands in this study.

## CONCLUSIONS

Direct visualization of the intraparotid facial nerve using the 3D-DESS-WE sequence demonstrated better diagnostic performance in localizing parotid gland tumors compared with various indirect methods. This technique can be performed without a surface coil and with a relatively short acquisition time and has high interobserver variability. These features make the 3D-DESS-WE sequence feasible for routine clinical practice and could be an integral part of preoperative assessment of parotid gland tumors.

Disclosures: Osamu Sakai—UNRELATED: Consultancy: Boston Imaging Core Lab; Royalties: Gakken Medical Shujunsha Co Ltd, Medical Sciences International Ltd.

## REFERENCES

1. Teresi LM, Kolin E, Lufkin RB, et al. **MR imaging of the intraparotid facial nerve: normal anatomy and pathology.** *AJR Am J Roentgenol* 1987;148:995–1000 CrossRef Medline
2. Takahashi N, Okamoto K, Ohkubo M, et al. **High-resolution magnetic resonance of the extracranial facial nerve and parotid duct: demonstration of the branches of the intraparotid facial nerve and its relation to parotid tumours by MRI with a surface coil.** *Clin Radiol* 2005;60:349–54 CrossRef Medline

3. de Ru JA, van Benthem PP, Hordijk GJ. **The location of parotid gland tumors in relation to the facial nerve on magnetic resonance images and computed tomography scans.** *J Oral Maxillofac Surg* 2002;60:992–94; discussion 995 CrossRef Medline
4. Ariyoshi Y, Shimahara M. **Determining whether a parotid tumor is in the superficial or deep lobe using magnetic resonance imaging.** *J Oral Maxillofac Surg* 1998;56:23–26; discussion 26–27 CrossRef Medline
5. Divi V, Fatt MA, Teknos TN, et al. **Use of cross-sectional imaging in predicting surgical location of parotid neoplasms.** *J Comput Assist Tomogr* 2005;29:315–19 CrossRef Medline
6. Kurabayashi T, Ida M, Ohbayashi N, et al. **Criteria for differentiating superficial from deep lobe tumours of the parotid gland by computed tomography.** *Dentomaxillofac Radiol* 1993;22:81–85 CrossRef Medline
7. Ishibashi M, Fujii S, Kawamoto K, et al. **The ability to identify the intraparotid facial nerve for locating parotid gland lesions in comparison to other indirect landmark methods: evaluation by 3.0 T MR imaging with surface coils.** *Neuroradiology* 2010;52:1037–45 CrossRef Medline
8. Li C, Li Y, Zhang D, et al. **3D-FIESTA MRI at 3 T demonstrating branches of the intraparotid facial nerve, parotid ducts and relation with benign parotid tumours.** *Clin Radiol* 2012;67:1078–82 CrossRef Medline
9. Tsang JC, Yip WH, Lau CS, et al. **Visualization of normal intraparotid facial nerve on MR: BTFE or GRASS?** *Clin Radiol* 2009;64:1115–18 CrossRef Medline
10. Fujii H, Fujita A, Yang A, et al. **Visualization of the peripheral branches of the mandibular division of the trigeminal nerve on 3D double-echo steady-state with water excitation sequence.** *AJNR Am J Neuroradiol* 2015;36:1333–37 CrossRef Medline
11. Qin Y, Zhang J, Li P, et al. **3D double-echo steady-state with water excitation MR imaging of the intraparotid facial nerve at 1.5T: a pilot study.** *AJNR Am J Neuroradiol* 2011;32:1167–72 CrossRef Medline
12. Ruohoalho J, Mäkitie AA, Aro K, et al. **Complications after surgery for benign parotid gland neoplasms: a prospective cohort study.** *Head Neck* 2017;39:170–76 CrossRef Medline
13. Eisele DW, Wang SJ, Orloff LA. **Electrophysiologic facial nerve monitoring during parotidectomy.** *Head Neck* 2010;32:399–405 CrossRef Medline
14. Lydiatt DD. **Medical malpractice and facial nerve paralysis.** *Arch Otolaryngol Head Neck Surg* 2003;129:50–53 CrossRef Medline
15. Ryzenman JM, Pensak ML, Tew JM Jr. **Facial paralysis and surgical rehabilitation: a quality of life analysis in a cohort of 1,595 patients after acoustic neuroma surgery.** *Otol Neurotol* 2005;26:516–21; discussion 21 CrossRef Medline
16. Kim JY, Yang HC, Lee S, et al. **Effectiveness of anatomic criteria for predicting parotid tumour location.** *Clin Otolaryngol* 2016;41:154–59 CrossRef Medline
17. Imaizumi A, Kuribayashi A, Okochi K, et al. **Differentiation between superficial and deep lobe parotid tumors by magnetic resonance imaging: usefulness of the parotid duct criterion.** *Acta Radiol* 2009;50:806–11 CrossRef Medline
18. Zhang Z, Meng Q, Chen Y, et al. **3-T imaging of the cranial nerves using three-dimensional reversed FISP with diffusion-weighted MR sequence.** *J Magn Reson Imaging* 2008;27:454–58 CrossRef Medline
19. Harney MS, Murphy C, Hone S, et al. **A histological comparison of deep and superficial lobe pleomorphic adenomas of the parotid gland.** *Head Neck* 2003;25:649–53 CrossRef Medline
20. Chu J, Zhou Z, Hong G, et al. **High-resolution MRI of the intraparotid facial nerve based on a microsurface coil and a 3D reversed fast imaging with steady-state precession DWI sequence at 3T.** *AJNR Am J Neuroradiol* 2013;34:1643–48 CrossRef Medline
21. Zhao Y, Yang B. **Value of visualization of the intraparotid facial nerve and parotid duct using a micro surface coil and three-dimensional reversed fast imaging with steady-state precession and diffusion-weighted imaging sequence.** *J Craniofac Surg* 2018;29:e754–57 CrossRef Medline

# Evaluating the Utility of a Postprocessing Algorithm for MRI Evaluation of Optic Neuritis

L. Stunkel, A. Sharma, M.S. Parsons, A. Salter, and G.P. Van Stavern

## ABSTRACT

**BACKGROUND AND PURPOSE:** MR imaging is useful for the detection and/or confirmation of optic neuritis. The objective of this study was to determine whether a postprocessing algorithm selectively increases the contrast-to-noise ratio of abnormal optic nerves in optic neuritis, facilitating this diagnosis on MR imaging.

**MATERIALS AND METHODS:** In this retrospective case-control study, coronal FLAIR images and coronal contrast-enhanced T1WI from 44 patients (31 eyes with clinically confirmed optic neuritis and 28 control eyes) underwent processing using a proprietary postprocessing algorithm designed to detect and visually highlight regions of contiguous increases in signal intensity by increasing the signal intensities of regions that exceeded a predetermined threshold. For quantitative evaluation of the effect on image processing, the contrast-to-noise ratio of equivalent ROIs and the contrast-to-noise ratio between optic nerves and normal-appearing white matter were measured on baseline and processed images. The effect of image-processing on diagnostic performance was evaluated by masked reviews of baseline and processed images by 6 readers with varying experience levels.

**RESULTS:** In abnormal nerves, processing resulted in an increase in the median contrast-to-noise ratio from 17.8 to 85.0 ( $P < .001$ ) on FLAIR and from 19.4 to 93.7 ( $P < .001$ ) on contrast-enhanced images. The contrast-to-noise ratio for control optic nerves was not affected by processing ( $P = 0.13$ ). Image processing had a beneficial effect on radiologists' diagnostic performance, with an improvement in sensitivities for 5/6 readers and relatively unchanged specificities. Interobserver agreement improved following processing.

**CONCLUSIONS:** Processing resulted in a selective increase in the contrast-to-noise ratio for diseased nerves and corresponding improvement in the detection of optic neuritis on MR imaging by radiologists.

**ABBREVIATIONS:** CIE = correlative image enhancement; CNR = contrast-to-noise ratio

Optic neuritis is an acute-to-subacute, demyelinating optic neuropathy, typically occurring in young women<sup>1,2</sup> in association with multiple sclerosis.<sup>1,3-5</sup> It presents with changes in visual acuity, eye pain, a relative afferent pupillary defect, and sometimes optic disc swelling.<sup>1,2,5-10</sup> While the diagnosis can often be made clinically, misdiagnosis is common, reported in almost 60% of referrals in 1 study.<sup>11</sup> MR imaging can help solidify the clinical diagnosis, especially in atypical cases.<sup>7</sup> In addition,

with increasing recognition of subclinical optic neuropathy in patients with multiple sclerosis,<sup>12</sup> the use of MR imaging to detect optic neuritis-related nerve abnormalities might become even more important.

Challenges of MR imaging of the optic nerve include its small size, heterogeneity of the surrounding orbital tissue, and artifacts related to eye movements or the presence of surrounding orbital fat.<sup>13-19</sup> The optic nerve signal is best compared with normal white matter in the brain.<sup>20</sup> However, the lack of proximity of the optic nerve to the white matter and different intensities of surrounding structures make this comparison difficult. Despite these challenges, some previous studies have reported sensitivities in the detection of optic neuritis by neuroradiologists ranging from 75.7% on noncontrast MR imaging<sup>21</sup> to 94% on contrast-enhanced MR imaging.<sup>22</sup> Improving the conspicuity of optic nerve abnormalities on MR imaging may help improve the detection of optic neuritis, particularly to minimize the need for intravenous contrast, detect subclinical disease, or improve the sensitivity in communities where scans are interpreted by general radiologists.

Received November 29, 2018; accepted after revision March 31, 2019.

From the Department of Neurology (L.S.), Mallinckrodt Institute of Radiology (A. Sharma, M.S.P.), Division of Biostatistics (A. Salter), and Department of Ophthalmology and Visual Sciences (G.P.V.S.), Washington University in St. Louis School of Medicine, St. Louis, Missouri.

Data previously presented at: North American Neuro-Ophthalmology Society Annual Meeting, March 3–8, 2018; Waikoloa Village, Hawaii; and the American Academy of Neurology Annual Meeting, April 21–27, 2018; Los Angeles, California.

Please address correspondence to Gregory P. Van Stavern, MD, Washington University School of Medicine, Department of Ophthalmology and Visual Sciences, 660 S Euclid Ave, Campus Box 8096, St. Louis, MO 63110; e-mail: vanstavern@wustl.edu

<http://dx.doi.org/10.3174/ajnr.A6057>

**Table 1: Technical parameters for the coronal FLAIR and coronal contrast-enhanced T1WI used in the study**

Parameter	FLAIR	Contrast-Enhanced T1WI
Slice thickness (mm)	3–4	3–4
TR (ms)	9000–10,000	400–800
TE (ms)	74–102	10–20
TI (ms)	2500	NA
FOV (mm)	200–220 × 166–186	180–220 × 170–200
Matrix	256–512 × 192–384	226–512 × 288–512
Fat saturation	Yes	Yes
Contrast material used	NA	Omniscan, <sup>a</sup> MultiHance, <sup>b</sup> Dotarem <sup>c</sup>

**Note:**—NA indicates not applicable.

<sup>a</sup> Gadodiamide; GE Healthcare, Piscataway, New Jersey.

<sup>b</sup> Gadobenate dimeglumine; Bracco Diagnostics, Princeton, New Jersey.

<sup>c</sup> Gadoterate meglumine, Guerbet, Aulnay-sous-Bois, France.

Correlative image enhancement (CIE) is a proprietary image postprocessing algorithm based on the correlative properties of contiguous pixels designed to increase the conspicuity of details of interest on existing CT and MR imaging scans.<sup>23</sup> It has been previously shown to improve the contrast-to-noise ratio (CNR) between diseased and normal brain tissue in brain infarction and mesial temporal sclerosis.<sup>24,25</sup> The objective of this study was to test whether image processing of existing MR imaging scans with CIE can be used to improve detection of optic neuritis by selectively improving the CNR of diseased optic nerves.

## MATERIALS AND METHODS

Institutional review board approval was obtained.

### Cases and Controls

This was a retrospective study of 44 patients (31 women, 13 men; mean age, 43.0 ± 14.2 years) who had undergone orbital MR imaging including coronal fat-saturated FLAIR and coronal fat-saturated contrast-enhanced T1-weighted imaging (Table 1) for clinical suspicion of optic neuritis on 1.5T MR imaging scanners at our institution between January 2014 and October 2016. Of these, 31 eyes diagnosed with optic neuritis based on clinical evaluation were included as cases and 28 eyes found not to have any clinical evidence for optic neuritis or optic neuropathy served as controls. Twenty-nine asymptomatic eyes in patients with unilateral optic neuritis were excluded because they could be affected by subclinical disease. Coronal FLAIR images were available for 28 cases and 28 control eyes. Coronal contrast-enhanced images were available for 28 cases and 18 control eyes.

### Image Processing

For each patient, the entire set of coronal FLAIR and contrast-enhanced MR images in a DICOM format was de-identified and transferred to an OsiriX Lite workstation (<https://www.macupdate.com/app/mac/14362/osirix-lite>). A masked investigator processed these images using the CIE algorithm with a custom-built plug-in. The algorithm required manual placement of an ROI within normal-appearing white matter. If the signal intensity of a contiguous set of pixels exceeded the intensity of the normal appearing white matter by a predetermined threshold, the algo-

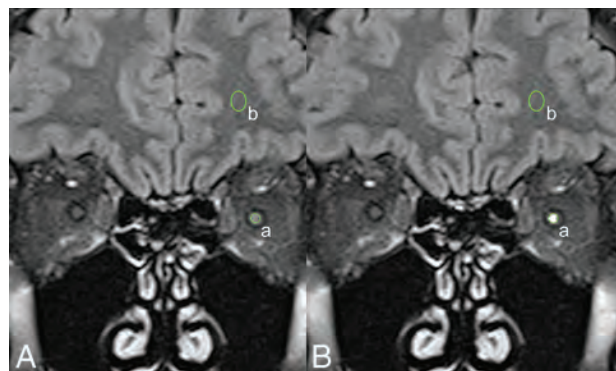


**FIG 1.** Measurement of the CNR between the optic nerve and ipsilateral white matter. Baseline (A) and processed (B) coronal FLAIR images show equivalent placement of ROIs to measure signal intensities of the optic nerve (a) and the ipsilateral white matter (b). The SD of the intensity in air around the head (c, not shown) was used as a measure of noise. CNR was defined as (a – b) / c. In this patient with left optic neuritis, processing resulted in an increase of the left optic nerve signal intensity from 355 at baseline to 754 after processing. Other measurements were unaffected by processing.

gorithm markedly increased the signal intensity of those pixels. The processed images were saved as a new DICOM file.

### Contrast-to-Noise Ratio Calculations

Using an ROI tool inbuilt in OsiriX Lite, we measured the signal intensities of each optic nerve ( $SI^{on}$ ), and the ipsilateral normal-appearing white matter ( $SI^{wm}$ ) for both baseline and processed images at equivalent locations (Fig 1). For optic nerves with obvious signal abnormality, the ROI was placed in the region of abnormal signal. Otherwise, the optic nerve was sampled in its retrobulbar portion on an image that allowed its best visualization free from partial volume averaging effects. The SD of the signal intensity of air in the image was similarly recorded as a measure of noise. These measurements were then used to calculate the CNR for both FLAIR and contrast-enhanced images using the following formula:  $CNR = (SI^{on} - SI^{wm})/Noise$ .

### Masked Image Review

Six masked readers, including 2 radiology residents, 2 neuroradiology fellows, and 2 attending neuroradiologists, reviewed baseline and processed images separately in OsiriX Lite. Readers rated optic nerve signal intensity (on FLAIR images) and the presence of contrast enhancement (on contrast-enhanced images) within the optic nerve on a 5-point Likert scale, ranging from 1 (definitely normal) to 5 (definitely abnormal). For subsequent analysis to calculate the diagnostic performance of each reader, ratings of 4 (probably abnormal) or 5 were taken as an abnormal test result, while ratings of ≤3 (possibly normal) were taken as a normal test result. The baseline-versus-processed status of the images was not revealed to the readers. However, readers were asked to comment on whether they saw markedly high signal in the optic nerves and whether this influenced their interpretation of the image.

### Statistical Analysis

Descriptive statistics were used to summarize the imaging metrics. Continuous variables were summarized using means and SDs and median (25th percentile, 75th percentile). A paired *t* test

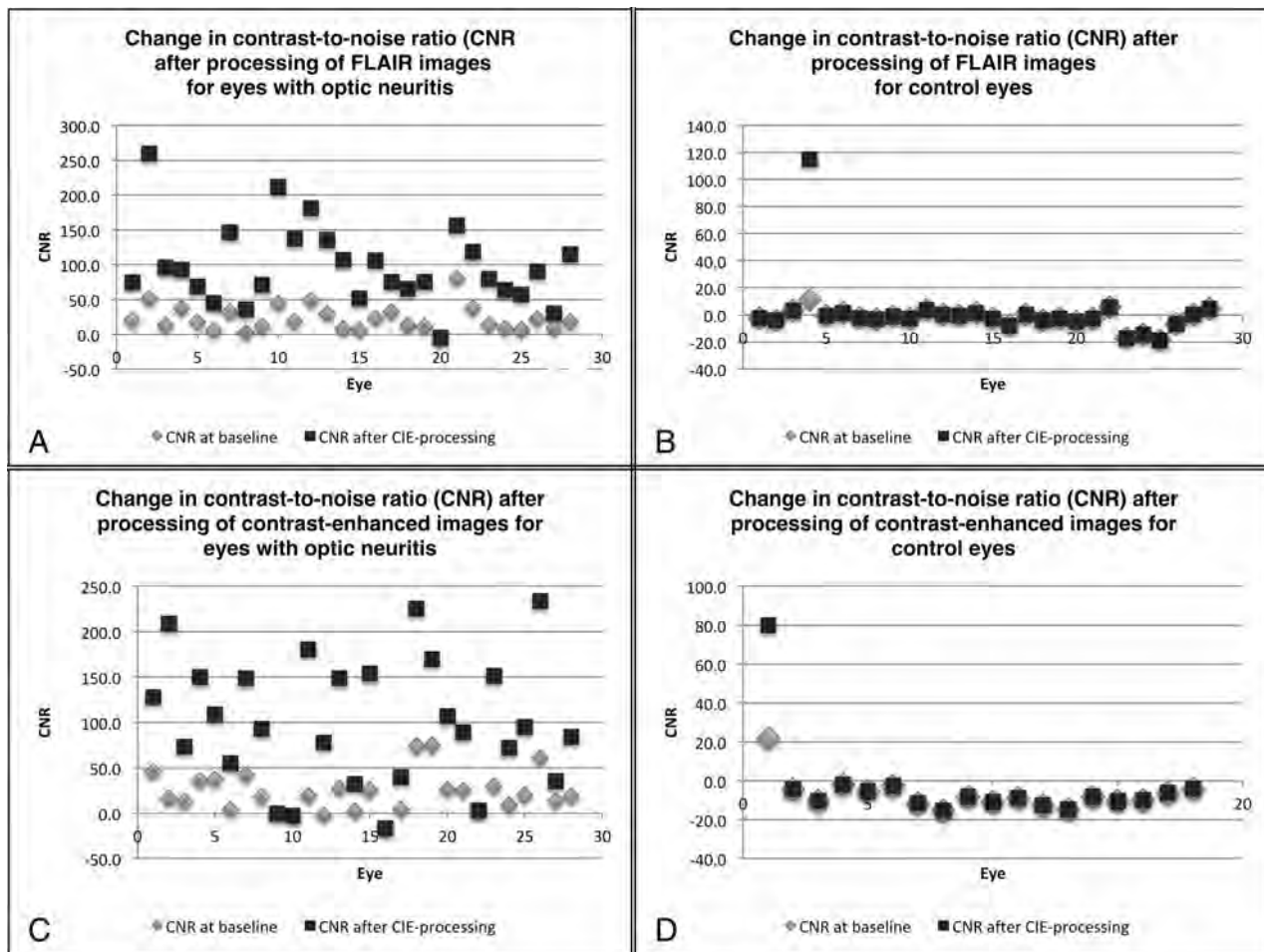


**FIG 2.** The effect of image processing on the CNR for optic nerves with and without optic neuritis. Scatterplots show the contrast-to-noise ratio of the optic nerve for the baseline images and the postprocessed images in both eyes with optic neuritis and control eyes.

or a signed rank test was used to evaluate differences between baseline and processed images in the optic nerve and control groups. The median of the ratings across all readers was identified for both baseline and processed images, and the difference in the median (processed-baseline image) was computed and compared using a paired *t* test or signed rank test, to assess improvement in the confidence of categorizing the optic nerve using signal intensity and enhancement. Sensitivity, specificity, positive predictive value, negative predictive value, and diagnostic accuracy were calculated for each reader and were also averaged for all readers. Improvements in diagnostic performances in cases versus controls were compared between the baseline and processed image within a group using a McNemar test.

Interobserver reliability was computed using a model-based measure of agreement, which is robust to the underlying disease prevalence,<sup>26</sup> and 95% confidence intervals were obtained from 1000 bootstrapped samples. The pair-wise  $\kappa$  for each pair of readers with similar experience levels (the pair of radiology residents, the pair of neuroradiology fellows, etc.) was also compared using the Cohen and weighted  $\kappa$ . A *P* value of .05 was considered statistically significant. Statistical analyses were conducted in SAS, Version 9.4 (SAS Institute, Cary, North Carolina) and R statistical and computing software (Version 1.0.136; <http://www.r-project.org/>).

## RESULTS

### Effect of Processing on the CNR

For FLAIR images of eyes with optic neuritis, processing resulted in a statistically significant increase in the median (25th to 75th) CNR from 17.8 (8.9–32.3) to 85.0 (64.8–127.2) ( $P < .001$ ), with an increased CNR seen in 27/28 eyes (Figs 2A and 3). CNRs for control eyes were not significantly affected ( $P = .625$ ), with a CNR increase noted only in 1/28 control eyes (Fig 2B). For contrast-enhanced images of eyes with optic neuritis, processing resulted in an increase in the median (25th to 75th) CNR from 19.35 (4.0–32.8) to 93.7 (47.2–150.6) ( $P < .001$ ), with an increased CNR seen in 24/28 eyes (Figs 2C and 3). The CNR for control eyes was not significantly affected ( $P = 0.13$ ), with the CNR increase noted in only 1/18 control eyes (Fig 2D).

### Effect of Processing on Confidence Ratings

For FLAIR images, there was a statistically significant increase in the median confidence rating for processed images of eyes with optic neuritis ( $P < .001$ ). For control eyes, processing did not result in any significant change in the median confidence rating on FLAIR images ( $P = 0.08$ ). Processing did not result in any significant change ( $P = .54$ ) in average confidence ratings for eyes with optic neuritis for contrast-enhanced images.

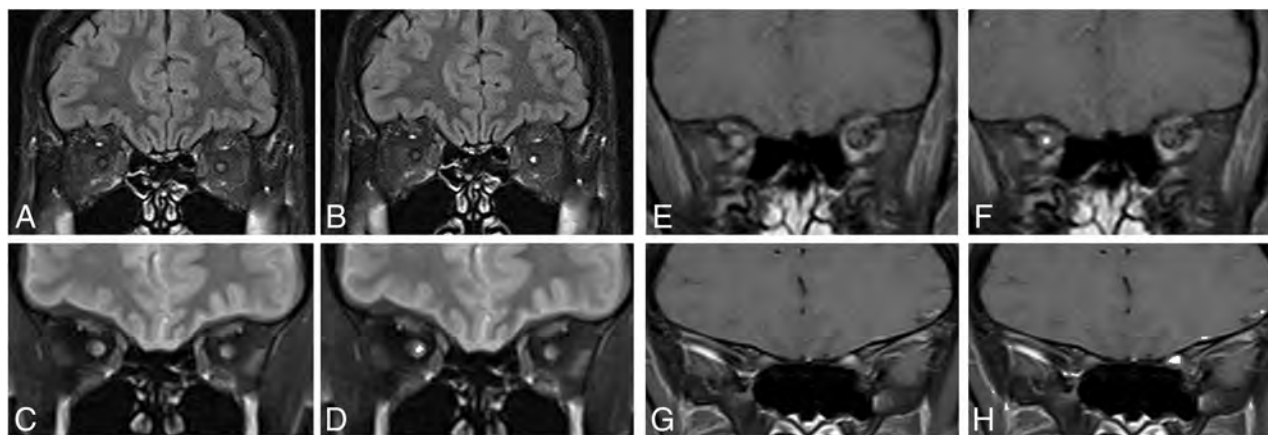


**FIG 3.** Examples highlighting the effect of processing on FLAIR and contrast-enhanced TWI in patients with optic neuritis. A, Baseline FLAIR image of a patient with left-sided optic neuritis. B, Processed version of the same FLAIR image (from A) of a patient with left-sided optic neuritis. C, Baseline FLAIR image of a patient with right-sided optic neuritis. D, Processed version of the same FLAIR image (from C) of a patient with right-sided optic neuritis. E, Baseline contrast-enhanced image of a patient with right-sided optic neuritis. F, Processed version of the same contrast-enhanced image (from E) of a patient with right-sided optic neuritis. G, Baseline contrast-enhanced image of a patient with left-sided optic neuritis. H, Processed version of the same contrast-enhanced image (from G) of a patient with left-sided optic neuritis.

**Table 2: Effect of image processing on sensitivity and specificity for detection of optic neuritis on FLAIR and contrast-enhanced TWI by 6 masked readers including 2 radiology residents (readers 1, 2), 2 neuroradiology fellows (readers 3, 4), and 2 attending neuroradiologists (readers 5, 6)**

Reader	1	2	3	4	5	6	Average
Sensitivity for baseline FLAIR image	18/28 64%	16/28 57%	19/28 68%	27/28 96%	19/28 68%	21/28 75%	71.4 ± 13.6
Sensitivity for processed FLAIR image	26/28 93%	26/28 93%	26/28 93%	27/28 96%	27/28 96%	27/28 96%	94.6 ± 2.0
Specificity for baseline FLAIR image	28/28 100%	28/28 100%	26/28 93%	20/28 71%	26/28 93%	27/28 96%	92.3 ± 10.7
Specificity for processed FLAIR image	26/28 93%	25/28 89%	26/28 93%	24/28 86%	26/28 93%	27/28 96%	91.7 ± 3.7
<i>P</i> value <sup>a</sup>	<.001	<.001	.02	.02	.01	.01	
Sensitivity for baseline contrast-enhanced image	17/28 61%	18/28 64%	20/28 71%	25/28 89%	19/28 68%	22/28 79%	72.0 ± 10.5
Sensitivity for processed contrast-enhanced image	22/28 79%	20/28 71%	21/28 75%	23/28 82%	24/28 86%	22/28 79%	78.6 ± 5.1
Specificity for baseline contrast-enhanced image	18/18 100%	18/18 100%	18/18 100%	13/18 72%	17/18 94%	18/18 100%	94.4 ± 11.1
Specificity for processed contrast-enhanced image	18/18 100%	18/18 100%	18/18 100%	17/18 94%	17/18 94%	18/18 100%	98.1 ± 2.9
<i>P</i> value <sup>a</sup>	<.001	<.001	.002	.12	.01	.003	

<sup>a</sup>*P* value for improvement of diagnostic performance in the optic neuritis eyes compared with the control eyes.

### Effect of Processing on Diagnostic Performance of Readers

For FLAIR images, the average sensitivity for the detection of optic neuritis for all readers increased from 71.4% ± 13.6% on baseline images to 94.6% ± 2.0% on processed images. Sensitivity improved for 5 readers and remained unaffected for the sixth (Table 2). Accordingly, the McNemar test revealed a significant increase in the number of additional detections of optic neuritis by 5/6 readers (*P* ranging from .01 to <.01 for individual readers). The average specificity did not change with image processing (Table 2), with individual specificities unaffected for 3 readers, decreased for 2 readers, and improved for 1 reader after processing (Table 2). The positive predictive value was relatively unaffected (92.3% at baseline and 92.0% after processing), but the negative predictive value improved from 77.8% ± 9% to 94.5% ± 1.9% following processing. The average accuracy for the detection of optic neuritis increased from 0.83 ± 0.03 for baseline images to 0.93 ± 0.02 for processed images.

For contrast-enhanced images, the sensitivity for the detection of enhancement in eyes with optic neuritis increased from 72.0% ± 10.5% to 78.6% ± 5.1% after processing, with improved sensitivities in 4/6 readers (Table 2). The McNemar test indicated a significant increase in the detection of enhancement for 2 readers (*P* = .025). The average specificity did not significantly change with image processing (Table 2). The positive predictive value changed from 96.4 ± 6.7 to 98.6 ± 2.1, and the negative predictive value, from 69.5 ± 7.3 to 74.9 ± 4.1. The average accuracy for the detection of optic neuritis increased from 0.81 ± 0.04 to 0.86 ± 0.02 with processing.

### Effect of Processing on Interobserver Agreement

Interobserver agreement in the categorization of optic nerves into abnormal or normal categories on FLAIR images improved following processing (Fleiss  $\kappa$  = 0.59 for baseline images and 0.91 for processed images). The pair-wise  $\kappa$  for readers with similar expe-

rience improved from 0.48 for the radiology residents, 0.46 for the neuroradiology fellows, and 0.55 for the neuroradiology attendings, and for baseline images to 0.76, 0.71, and 0.82, respectively, for processed images.

Interobserver agreement in the categorization of optic nerves into enhancing or nonenhancing categories improved following processing (Fleiss  $\kappa$  improving from 0.63 for baseline images to 0.83 for processed images). The pair-wise  $\kappa$  for readers with similar experience improved from 0.85 for the radiology residents, 0.62 for the neuroradiology fellows, and 0.78 for the neuroradiology attendings, and for baseline images to 0.90, 0.69, and 0.88, respectively, for processed images.

## DISCUSSION

Our results indicate that this algorithm can improve the sensitivity for the detection of optic neuritis on MR imaging by readers with varied training and experience levels, without a detrimental effect on specificity. Our quantitative assessment validated this benefit by demonstrating a selectively increased CNR of diseased optic nerves while affecting only a small proportion of controls. Eyes affected by optic neuritis can be expected to have higher average signal intensity on T2-weighted images such as FLAIR.<sup>27,28</sup> By exaggerating the signal differences between the diseased optic nerve and the normal white matter, this algorithm makes these underlying differences more easily recognizable.

McKinney et al<sup>21</sup> reported 75.7%–77.3% sensitivity and 90.5%–93.5% specificity in the detection of optic neuritis on FLAIR images. While the average sensitivity (71.4%) and specificity (94.6%) of readers for baseline FLAIR images in our study was comparable, sensitivity achieved after processing (94.6%) was substantially higher. This improved sensitivity on noncontrast MR imaging may help obviate a contrast-enhanced study in the detection of optic neuritis, thereby minimizing cost and scanning time.

Previous studies have suggested that contrast-enhanced T1-weighted images may be more sensitive than noncontrast sequences, with reported sensitivities of 89.5%<sup>21</sup> and 94%.<sup>22</sup> In our study, the average baseline sensitivity for the detection of acute optic neuritis on contrast-enhanced sequences was lower (72%), even for expert neuroradiologists (75%, readers 5 and 6; Table 2). The reason for this difference is unclear. While it may result from underlying technical differences, it is possible that it simply reflects a different patient population. Additionally, image processing was also helpful in improving the sensitivity for contrast-enhanced images.

Many previous studies have assessed different pulse sequences, including fat-suppression techniques (STIR and spectral presaturation with inversion recovery), fluid-suppression techniques (FLAIR), artifact-minimizing techniques (fast spin-echo with fat suppression), combined fat- and fluid-suppression techniques (spectral presaturation with inversion recovery–FLAIR and XETA [Cube; GE Healthcare, Milwaukee, Wisconsin] FLAIR), and diffusion-weighted imaging in the detection of optic neuritis.<sup>13–15,29</sup> It is not feasible for us to test the effect of postprocessing on images acquired by all these different techniques.

In prior studies, interobserver reliability in identifying optic nerve abnormalities has varied depending on the type of se-

quences being studied, with the  $\kappa$  reported from 0.60 to 0.96.<sup>18,27</sup> For readers with similar experience, the baseline  $\kappa$  in our study ranged from 0.60 to 0.85. Postprocessing improved the interobserver reliability, with  $\kappa$  for postprocessed FLAIR images ranging from 0.69 to 0.90. This result may prove beneficial in settings where the images are interpreted by less experienced readers. An improvement in the Fleiss  $\kappa$  also indicated improved agreement among readers of varying experience. Interobserver agreement for the detection of contrast enhancement remained low for controls, even after processing. This outcome is possibly due to the exaggeration of high signal in vasculature in close proximity to the optic nerves that could be misinterpreted as optic nerve enhancement by some readers.

While our study was restricted to acute optic neuritis, it is possible that improved detection of underlying signal alterations in optic nerve signal intensity may make this processing beneficial for the detection of other causes of optic neuropathy, including patients with remote optic neuritis. In patients being assessed for multiple sclerosis, such image processing may help uncover underlying optic nerve abnormalities that are otherwise not captured on routine clinical assessment or routine MR imaging.<sup>30,31</sup>

By using patients who underwent imaging due to concern for optic neuritis but were found to have no clinical evidence of optic neuritis and by incorporating a large number of masked reviewers with a range of training experience, our study tries to overcome some of the limitations of prior studies, which include restriction of controls to the contralateral eye in symptomatic patients and only 1 or 2 subspecialist reviewers.<sup>13–15,18,21,22,27,32</sup>

Some limitations of our study are worth mentioning. Optic neuritis is a clinical diagnosis, and MR imaging is not always required for the diagnosis. Thus, there may be a selection bias toward atypical presentations in the patients who underwent MR imaging. Patients with other types of optic neuropathy were excluded, preventing evaluation of whether the algorithm can distinguish optic neuritis from other forms of optic neuropathy; this exclusion may affect the generalizability of the specificity results. The control patients were those who presented with visual or ocular symptoms but were found not to have optic neuropathies; there were no asymptomatic controls. Finally, this study was limited to coronal FLAIR sequences obtained at a single institution. It remains to be seen whether the incremental benefit seen in our study would hold for scans performed on higher field strength scanners with potentially higher baseline sensitivity.

## CONCLUSIONS

The described postprocessing algorithm increased the CNR between diseased optic nerves and normal white matter for eyes with optic neuritis on both FLAIR and contrast-enhanced images. This result translated into an improved sensitivity, negative predictive value, diagnostic accuracy, and interobserver reliability for the detection of optic neuritis by readers with varied training and experience levels.

## ACKNOWLEDGMENTS

We thank the following physicians for participating as masked observers: Devin Vaswani, MD; Ben Strand, MD; Albert Sohn, MD; Jason Carmichael, MD; Hilary Orłowski, MD.

Disclosures: Aseem Sharma—*RELATED: Other:* Correlative Enhancement LLC, *Comments:* The algorithms used in this study were coined by me. I hold the intellectual property rights to these patented algorithms. I have founded a company (Correlative Enhancement LLC) with the aim of future commercialization of this intellectual property. I am the sole proprietor of the company, and since the inception of the company until now (including the time during which I processed the images for this study), in a company that has not received funding from any external source. While I used the algorithms to process the images for this study, I did not participate in image review, image analysis, or the subsequent statistical analysis; *UNRELATED: Consultancy:* Biomedical Systems, *Comments:* As a consultant, I serve as an independent reviewer for imaging studies performed for research by third parties; *Patents (Planned, Pending or Issued):* "Method for Medical Image Analysis and Manipulation," US patent No. 9,846,937, December 19, 2017; *Stock/Stock Options:* GE Healthcare, *Comments:* I own publicly traded GE Healthcare stocks (current value of \$10–15,000) in a company that makes imaging equipment among other things. Amber Salter—*UNRELATED: Consultancy:* Circulation Cardiovascular Imaging journal.

## REFERENCES

1. **The clinical profile of optic neuritis: experience of the optic neuritis treatment trial—Optic Neuritis Study Group.** *Arch Ophthalmol* 1991;109:1673–78 CrossRef Medline
2. Rizzo JF 3rd, Lessell S. **Optic neuritis and ischemic optic neuropathy: overlapping clinical profiles.** *Arch Ophthalmol* 1991; 109:1668–72 CrossRef Medline
3. Beck RW, Cleary PA, Trobe JD, et al. **The effect of corticosteroids for acute optic neuritis on the subsequent development of multiple sclerosis: the Optic Neuritis Study Group.** *N Engl J Med* 1993;329: 1764–69 CrossRef Medline
4. Beck RW, Trobe JD, Moke PS, et al; Optic Neuritis Study Group. **High- and low-risk profiles for the development of multiple sclerosis within 10 years after optic neuritis: experience of the optic neuritis treatment trial.** *Arch Ophthalmol* 2003;121:944–49 CrossRef Medline
5. Bee, YS, Lin MC, Wang CC, et al. **Optic neuritis: clinical analysis of 27 cases.** *Kaohsiung J Med Sci* 2003;19:105–12 CrossRef Medline
6. Balcer LJ. **Clinical practice: optic neuritis.** *N Engl J Med* 2006;354: 1273–80 CrossRef Medline
7. Toosy AT, Mason DF, Miller DH. **Optic neuritis.** *Lancet Neurol* 2014; 13:83–99 CrossRef Medline
8. Hoorbakht H, Bagherkashi F. **Optic neuritis, its differential diagnosis and management.** *Open Ophthalmol J* 2012;6:65–72 CrossRef Medline
9. Keltner JL, Johnson CA, Spurr JO, et al; Optic Neuritis Study Group. **Baseline visual field profile of optic neuritis: the experience of the optic neuritis treatment trial.** *Arch Ophthalmol* 1993;111:231–34 CrossRef Medline
10. Fang JP, Donahue SP, Lin RH. **Global visual field involvement in acute unilateral optic neuritis.** *Am J Ophthalmol* 1999;128:554–65 CrossRef Medline
11. Stunkel L, Kung NH, Wilson B, et al. **Incidence and causes of over-diagnosis of optic neuritis.** *JAMA Ophthalmol* 2018;136:76–81 CrossRef Medline
12. Galetta SL, Balcer LJ. **The optic nerve should be included as one of the typical CNS regions for establishing dissemination in space when diagnosing MS: yes.** *Mult Scler* 2018;24:121–22 CrossRef Medline
13. Miller DH, Johnson G, McDonald WI, et al. **Detection of optic nerve lesions in optic neuritis with magnetic resonance imaging.** *Lancet* 1986;1:1490–91 Medline
14. Aiken AH, Mukherjee P, Green AJ, et al. **MR imaging of optic neuropathy with extended echo-train acquisition fluid-attenuated inversion recovery.** *AJNR Am J Neuroradiol* 2011;32:301–05 CrossRef Medline
15. Gass A, Barker GJ, MacManus D, et al. **High resolution magnetic resonance imaging of the anterior visual pathway in patients with optic neuropathies using fast spin echo and phased array local coils.** *J Neurol Neurosurg Psychiatry* 1995;58:562–69 CrossRef Medline
16. Hanawa T, Mizota A. **Quantitative evaluation of signal intensity of magnetic resonance images in optic neuritis.** *Open Ophthalmol J* 2007;6:1:1–3 Medline
17. Hoch MJ, Bruno MT, Shepherd TM. **Advanced MRI of the optic nerve.** *J Neuroophthalmol* 2017;37:187–196 CrossRef Medline
18. Hodel J, Outteryck O, Bocher AL, et al. **Comparison of 3D double inversion recovery and 2D STIR FLAIR MR sequences for the imaging of optic neuritis: pilot study.** *Eur Radiol* 2014;24:3069–75 CrossRef Medline
19. Rocca MA, Hickman SJ, Bö L, et al. **Imaging the optic nerve in multiple sclerosis.** *Mult Scler* 2005;11:537–41 CrossRef Medline
20. Onodera M, Yama N, Hashimoto M, et al. **The signal intensity ratio of the optic nerve to ipsilateral frontal white matter is of value in the diagnosis of acute optic neuritis.** *Eur Radiol* 2016;26:2640–45 CrossRef Medline
21. McKinney AM, Lohman BD, Sarikaya B, et al. **Accuracy of routine fat-suppressed FLAIR and diffusion-weighted images in detecting clinically evident acute optic neuritis.** *Acta Radiol* 2013;54:455–61 CrossRef Medline
22. Kupersmith MJ, Alban T, Zeiffer B, et al. **Contrast-enhanced MRI in acute optic neuritis: relationship to visual performance.** *Brain* 2002; 125:812–22 CrossRef Medline
23. Sharma A, Sharma A. **Method for medical image analysis and manipulation.** US patent 9, December 18, 2017;846:937
24. Madaelil TP, Sharma A, Hildebolt C, et al. **Using correlative properties of neighboring pixels to improve gray-white differentiation in pediatric head CT images.** *AJNR Am J Neuroradiol* 2018;39:577–82 CrossRef Medline
25. Parsons MS, Sharma A, Hildebolt C. **Using correlative properties of neighboring pixels to enhance contrast-to-noise ratio of abnormal hippocampus in patients with intractable epilepsy and mesial temporal sclerosis.** *Acad Radiol* 2019;26:e1–e8 CrossRef Medline
26. Nelson KP, Edwards D. **Measures of agreement between many raters for ordinal classifications.** *Stat Med* 2015;34:3116–32 CrossRef Medline
27. Jackson A, Sheppard S, Laitt RD, et al. **Optic neuritis: MR imaging with combined fat- and water-suppression techniques.** *Radiology* 1998;206:57–63 CrossRef Medline
28. Harrigan RL, Smith AK, Mawnd LA, et al. **Short term reproducibility of a high contrast 3-D isotropic optic nerve imaging sequence in healthy controls.** *Proc SPIE Int Soc Opt Eng* 2016;9783 CrossRef Medline
29. Tian Y, Wang J, Li M, et al. **Comparison of field-of-view optimized and constrained undistorted single-shot diffusion-weighted imaging and conventional diffusion-weighted imaging of optic nerve and chiasma at 3T.** *Neuroradiology* 2018;60:903–12 CrossRef Medline
30. Sartoretti T, Sartoretti E, Rauch S, et al. **How common is signal-intensity increase in optic nerve segments on 3D double inversion recovery sequences in visually asymptomatic patients with multiple sclerosis?** *AJNR Am J Neuroradiol* 2017;38:1748–53 CrossRef Medline
31. Boegel KH, Tyan AE, Iyer VR, et al. **Utility of coronal contrast-enhanced fat-suppressed FLAIR in the evaluation of optic neuropathy and atrophy.** *Eur J Radiol Open* 2017;4:13–18 CrossRef Medline
32. Lu P, Sha Y, Wan H, et al. **Role of coronal high-resolution diffusion-weighted imaging in acute optic neuritis: a comparison with axial orientation.** *Neuroradiology* 2017;59:737–45 CrossRef Medline

# A Scoring System for Prediction of Cervical Lymph Node Metastasis in Patients with Head and Neck Squamous Cell Carcinoma

M.S. Chung, Y.J. Choi, S.O. Kim, Y.S. Lee, J.Y. Hong, J.H. Lee, and J.H. Baek



## ABSTRACT

**BACKGROUND AND PURPOSE:** An accurate and comprehensive assessment of lymph node metastasis in patients with head and neck squamous cell cancer is crucial in daily practice. This study constructed a predictive model with a risk scoring system based on CT characteristics of lymph nodes and tumors for patients with head and neck squamous cell carcinoma to stratify the risk of lymph node metastasis.

**MATERIALS AND METHODS:** Data included 476 cervical lymph nodes from 191 patients with head and neck squamous cell carcinoma from a historical cohort. We analyzed preoperative CT images of lymph nodes, including diameter, ratio of long-to-short axis diameter, necrosis, conglomeration, infiltration to adjacent soft tissue, laterality and T-stage of the primary tumor. The reference standard comprised pathologic results. Multivariable logistic regression analysis was performed to develop the risk scoring system. Internal validation was performed with 1000-iteration bootstrapping.

**RESULTS:** Shortest axial diameter, ratio of long-to-short axis diameter, necrosis, and T-stage were used to develop a 9-point risk scoring system. The risk of malignancy ranged from 7.3% to 99.8%, which was positively associated with increased scores. Areas under the curve of the risk scoring systems were 0.886 (95% CI, 0.881–0.920) and 0.879 (95% CI, 0.845–0.914) in internal validation. The Hosmer–Lemeshow goodness-of-fit test indicated that the risk scoring system was well-calibrated ( $P = .160$ ).

**CONCLUSIONS:** We developed a comprehensive and simple risk scoring system using CT characteristics in patients with head and neck squamous cell carcinoma to stratify the risk of lymph node metastasis. It could facilitate decision-making in daily practice.

**ABBREVIATIONS:** AUC = area under the curve; HNSCC = head and neck squamous cell carcinoma; L/S = long-to-short axis

The presence of lymph node metastasis has a great impact on the treatment and prognosis in patients with head and neck squamous cell carcinoma (HNSCC).<sup>1</sup> Solitary lymph node metastasis from HNSCC has a 5-year survival rate of 50%; additional contralateral lymph node metastasis reduces survival to 33%. Detection of lymph node metastasis by imaging is more accurate

than by clinical examination; thus, performing preoperative CT or MR imaging in the initial work-up for HNSCC has become routine.<sup>1</sup>

Imaging assessment of lymph node metastasis in the head and neck can be challenging for the radiologist because there are multiple cervical levels to review and variable suggested criteria for metastatic lymph nodes. Furthermore, multiple image features of lymph nodes (including diameters, shapes, and presence of necrosis), combinations of those features, and characteristics of primary tumor (such as T-stage or location) should be considered to determine the possibility of metastasis in daily practice.<sup>1–5</sup> In particular, there is greater difficulty in cases that show both benign and probable abnormal features. Therefore, a comprehensive and systematic approach, based on a combination of previously proposed criteria, is needed to maximize the benefits of preoperative CT.

Furthermore, additional image evaluation and pathologic confirmations are not possible in all cases (eg, deep locations, including retropharyngeal or upper mediastinal lymph nodes);

Received November 1, 2018; accepted after revision April 13, 2019.

From the Department of Radiology (M.S.C.), Chung-Ang University Hospital, Chung-Ang University College of Medicine, Seoul, Republic of Korea; and Departments of Radiology and Research Institute of Radiology (Y.J.C., J.H.L., J.H.B.), Clinical Epidemiology and Biostatistics (S.O.K.), Otolaryngology (Y.S.L.), and Oncology (J.Y.H.), Asan Medical Center, University of Ulsan College of Medicine, Seoul, Republic of Korea.

Paper previously presented at: Symposium Neuroradiologicum, March 19–23, 2018; Taipei, Taiwan.

Please address correspondence to Young Jun Choi, MD, PhD, Department of Radiology and Research Institute of Radiology, University of Ulsan College of Medicine, Asan Medical Center, 86 Asanbyeongwon-Gil, Songpa-Gu, Seoul 138-736, Republic of Korea; e-mail: jehee23@gmail.com

Indicates article with supplemental on-line table.

<http://dx.doi.org/10.3174/ajnr.A6066>

these increase medical costs and procedure-related complications.<sup>6,7</sup> MR imaging also may provide an option for the diagnosis of lymph node metastasis due to its higher spatial resolution and advanced techniques, such as diffusion-weighted imaging, whereas the real added value of MR imaging combined with other imaging modalities remains controversial despite high costs.<sup>8,9</sup> PET/CT is known to have potential diagnostic and prognostic roles in patients with HNSCC,<sup>10-14</sup> and PET/CT has achieved approximately 21% sensitivity improvement in the diagnosis of nodal metastasis per-neck-level compared with conventional images.<sup>15</sup> However, considering false-positive results caused by inflammatory conditions and false-negative results due to small size, necrosis, or cystic change of metastatic lymph nodes using PET/CT, a proper diagnostic approach based on the conventional image findings should be essential.<sup>10,16</sup>

Accordingly, a practical and comprehensive prediction model that uses variable CT findings could be useful for assessing the presence of lymph node metastasis in patients with HNSCC in daily practice and might maximize the efficiency of CT by enhancing the understanding of variable CT features. A risk scoring system estimates the probability of the presence/occurrence of a particular event, based on multiple predictors, to facilitate individual diagnostic and therapeutic decision-making.<sup>17</sup> Therefore, this study aimed to develop a simple prediction model using a risk scoring system in patients with HNSCC, based on CT findings, to stratify the risk of lymph node metastasis.

## MATERIALS AND METHODS

This retrospective study was approved by our institutional review board at Asan Medical Center, and informed consent was waived for data evaluation. The methods and reporting of results are in accordance with the Transparent Reporting of a Multivariable Prediction Model for Individual Prognosis or Diagnosis statement,<sup>18</sup> the Strengthening the Reporting of Observational Studies in Epidemiology statement,<sup>19</sup> and the statistical methods for prediction models.<sup>17</sup>

### Study Population

The study population was obtained from a historical cohort of consecutive patients who were newly diagnosed with HNSCC and underwent pretreatment contrast-enhanced neck CT at our large (2700 beds) academic tertiary referral hospital between July 2010 and December 2013. The eligibility criteria were as follows: 1) Patients had newly diagnosed HNSCC; 2) patients underwent a neck CT examination before the treatment of HNSCC; 3) patients underwent lymph node dissection, and the presence of lymph node metastasis was pathologically confirmed at each cervical level; 4) the shortest axial diameter of the lymph node on CT was  $\geq 5$  mm; and 5) patients were older than 20 years of age. Exclusion criteria included the following: 1) Patients underwent definite radiation or concurrent chemoradiation therapy; 2) patients underwent radiation therapy and/or chemotherapy before lymph node neck dissection; 3) CT scan slice thickness was  $> 3$  mm; 4) CT scans were without coronal reconstruction; and 5) CT scans had severe metal- or motion-related artifacts, making tumor boundary delineation difficult. We also retrospectively col-

lected patients' demographic and clinical data by review of electronic medical records; these data included age, sex, location of the mass, and surgical and chemoradiotherapy history.

### Image Acquisition

All patients underwent CT examinations on one of several commercially available CT systems, with the multidetector capability ranging from 64 to 128 channels. The techniques and parameters varied depending on the system used. However, most examinations were performed with a 128-channel CT scanner (Somatom Definition Flash; Siemens Medical Solutions, Erlangen, Germany), and typical imaging parameters were as follows: 120 kV, 200 effective mAs, axial scan mode, 22-cm display FOV, 50-cm large-body scan FOV, pitch of 1, gantry rotation time of 0.5 seconds, detector collimation of  $128 \times 0.6$  mm, and 3-mm axial and coronal reconstructed slice thickness with a soft-tissue algorithm reconstruction. Real-time automatic tube current modulation software (CARE Dose4D; Siemens) was applied to regulate the tube current in accordance with the patient's anatomic structures. Scan coverage was from the upper margin of the frontal sinus to the top of the aortic arch. Acquisition of CT images began 70 seconds after the injection of 140 mL of intravenous iopamidol (Isovue-370; Bracco, Princeton, New Jersey) at a rate of 2.5 mL/s. A PACS system was used for the review and analysis of all radiologic images.

### Image Analysis

All CT images were independently reviewed by 2 neuroradiologists, with 5 and 12 years of head and neck oncology imaging experience, respectively. Before evaluation, the 2 neuroradiologists completed a training session with 10 patients to help them reach a consensus regarding the measurement of the diameter and imaging findings of the lymph nodes.

We analyzed possible predictors of lymph node metastasis on preoperative CT images as follows: lymph node diameter (shortest and longest axial diameter and longest coronal diameter)<sup>3</sup>; the long-to-short axis (L/S) ratio<sup>2,5,20</sup>; presence of necrosis<sup>3,21</sup>; conglomeration of lymph nodes, infiltration to adjacent soft tissue, laterality to the primary tumor (ipsilateral versus contralateral); and T-stage of primary tumor, following the *AJCC Cancer Staging Manual*, eighth edition. The largest diameters of each node in the axial and coronal planes were measured and defined as the longest diameter.<sup>5</sup> The largest diameter perpendicular to the longest axial diameter was measured and defined as the shortest axial diameter.<sup>5</sup> Slices for the measurement of the diameter of the lymph nodes were independently selected by each observer, and electronic calipers on the PACS system were used for such measurements. The L/S ratio was calculated by using the longest axial diameter/shortest axial diameter.<sup>5</sup> The presence of necrosis was defined as central low density with irregular or rim-like enhancement of residual lymphatic tissue.<sup>21,22</sup> The degree of necrosis was classified as none, present, or cystic (demonstrating a rim-like thin enhancing or imperceptible wall with  $> 90\%$  of central low density) by visual analysis.<sup>1</sup> Infiltration to adjacent soft tissue was defined as poorly defined nodal margins or soft-tissue infiltration or stranding of the muscles or fat in the neck.<sup>22</sup>

**Table 1: Univariable and multivariable regression models of lymph node metastasis**

Variable	Univariable Analysis			Multivariable Analysis		
	OR	95% CI	P Value	OR	95% CI	P Value
T-stage						
1	Reference			Reference		
2	1.13	0.68–1.89	.64	0.97	0.46–2.06	.93
3 or 4	1.59	0.98–2.59	.06	1.86	0.95–3.77	.07
Shortest axial diameter (cm)	41.29	18.09–94.27	<.001	6.69	2.95–17.31	<.001
Longest axial diameter (cm)	6.59	4.12–10.56	<.001			
L/S ratio	0.07	0.03–0.14	<.001	0.50	0.22–1.10	.09
Longest longitudinal diameter (cm)	4.87	3.36–7.08	<.001			
Conglomeration <sup>a</sup>	9.73	3.66–25.84	<.001			
Necrosis						
No	Reference			Reference		
Present	38.99	17.81–85.37	<.001	15.21	6.97–36.60	<.001
Cystic	82.25	24.88–271.89	<.001	21.76	7.51–84.63	<.001
Infiltration <sup>a</sup>	75.54	10.26–556.09	<.001			
Laterality to primary tumor (ipsilateral vs contralateral) <sup>a</sup>	2.27	1.37–3.75	<.001			

<sup>a</sup> The reference standard in this study comprised no conglomeration, no infiltration, and no contralateral location to the primary tumor.

### Statistical Analysis

For the development of a risk scoring system for the discrimination of lymph node metastasis, pathologic results after lymph node dissection were used as a reference standard for the presence or absence of metastasis of lymph nodes. Univariable and multivariable logistic regression analysis was performed to estimate the risk of metastasis associated with CT findings and pathologic results. Variable selection for the multivariable model was achieved by iterative backward elimination in 1000-iteration bootstrap resampling. A 50% relative frequency of selection was the criterion for inclusion in the final model.

A simple scoring system was developed using the penalized maximum likelihood estimates of the covariates in models that followed the method of Sullivan et al.<sup>23</sup> After selecting a base value of each variable, we used regression coefficients as weights and distance from the base value to generate each point value (On-line Table). Score 1 was defined as the effect of a 5-mm increase in the minimal axial diameter of the lymph node. To prove the power of discrimination of the risk scoring system, we calculated the area under the curve (AUC) of the receiver operating characteristic curve. The Hosmer–Lemeshow goodness-of-fit statistic was used to evaluate the agreement between the observed and expected number of metastatic lymph nodes across all strata, based on the probabilities of malignancy estimated from the prediction model. Internal validation was performed using the bootstrap validation algorithm.<sup>24,25</sup> Bootstrap resampling began by fitting the logistic model in a bootstrap sample of the same number of nodules as the original sample ( $n = 476$ ), which was drawn with replacement from the original sample. The optimism-corrected performance for internal validation was calculated as the AUC of the receiver operating characteristic curve with 1000 repetitions. The apparent performance represented the performance in the original sample. The performance in each bootstrap sample represents the apparent performance of the bootstrap model, and the test performance represents the performance of the bootstrap model in the original sample. The difference between these performances is an estimate of the optimism. The optimism performance is subtracted from the apparent performance to estimate the internally validated performance: Optimism-Corrected Performance =

Apparent Performance – Average (Bootstrap Performance – Test Performance).<sup>24–26</sup> All statistical analyses were performed using SPSS, Version 22.0 (IBM, Armonk, New York) and R, Version 3.0.2 (www.r-project.org), with rms and pROC packages. A 2-sided  $P$  value < .05 was considered statistically significant.

### RESULTS

This study included 476 lymph nodes from 191 patients (142 men, 49 women; mean age,  $61.8 \pm 13.0$  years; range, 28–91 years). Metastatic lymph nodes were present in 38% (181/476) of lymph nodes. Location of the primary tumor was the oral cavity in 48.2% (92/191), oropharynx in 23.0% (44/191), and larynx in 28.8% (55/191). The T-stage of the primary tumor was stage 1 in 25.7% (49/191), stage 2 in 33.5% (64/191), stage 3 in 29.3% (56/191), and stage 4 in 11.5% (22/191).

By multivariate logistic regression analysis, the shortest axial diameter of the lymph node and necrosis of the lymph node demonstrated significant differences between benign and metastatic lymph nodes. Necrosis of the lymph node showed the highest odds ratio of >15 (Table 1).

A 9-point risk scoring system was developed using the results of multivariable analysis (Table 2, On-line Table, and Fig 1). The T-stage of the primary tumor, shortest axial diameter, L/S ratio, and necrosis of the lymph node were assigned to one or more points, according to their  $\beta$  (regression coefficient) values in the development of the risk scoring system. The presence of necrosis in the lymph nodes, regardless of the extent of necrosis (ie, present versus cystic), and the shortest axial diameter of >2 cm showed relatively high scores in this system: 3 points and 4 points, respectively. Table 2 also shows the risk of metastasis according to the risk scoring system. If a lymph node had a score of zero, the risk of metastasis was <7.0%. Furthermore, the risk of metastasis continuously increased when the risk score increased, with 9 points achieving the highest value of 100% of the estimated probability of metastasis.

The AUC of the risk scoring system was 0.886, with a 95% CI, 0.881–0.920 (Fig 2). The sensitivity and specificity of the risk scoring system were 74.0% (95% CI, 67.2%–79.9%) and 95.3% (95% CI, 92.2%–97.2%) using the cutoff value of 3 points. The optimism-corrected performance was good (AUC = 0.879; 94% CI, 0.845–

0.914). The Hosmer–Lemeshow goodness-of-fit test indicated that the prediction model and scoring system were well-calibrated ( $P = .160$ ). The calibration plot showed good agreement between the predicted and actual risks of lymph node metastasis (Fig 3).

## DISCUSSION

In the present study, we developed a simple 9-point risk scoring system using CT characteristics of lymph nodes and tumors for HNSCC to stratify the risk of cervical lymph node metastasis. This scoring system demonstrated an excellent predictive accuracy, with an AUC of 0.89 in interval validation by 1000-repetition bootstrapping. The presence of necrosis, regardless of the extent of necrosis, and shortest axial diameter of lymph nodes of  $>2$  cm demonstrated relatively higher scores in this risk scoring system, which could be useful for estimating the risk of malignancy of lymph nodes in routine practice.

**Table 2: Risk scoring system for lymph node metastasis in patients with newly diagnosed HNSCC**

Image Findings	Score
T-stage	
1 or 2	0
3 or 4	1
Shortest axial diameter (cm)	
$<1$	0
1–2	1
$\geq 2$	4
L/S ratio	
$<1.5$	1
$\geq 1.5$	0
Necrosis	
No	0
Yes	3
Total score	9
Risk classification by total risk score <sup>a</sup>	
0–1: low risk ( $\leq 17\%$ of metastasis)	
2–4: intermediate risk ( $17\% \sim 78\%$ of metastasis)	
5–9: high risk ( $\geq 78\%$ of metastasis)	

<sup>a</sup> Estimated metastases for the each score in the risk groups were as follows: low-risk group (score zero, 7% and score one, 17%), intermediate-risk group (score two, 35%; score three, 58%; and score four, 78%), and high-risk group (score five, 90%; score six, 96%; score seven, 98%; score eight, 99%; and score nine, 100%).



**FIG 1.** Example of lymph node scoring. CT images show a 71-year-old man with right hypopharyngeal cancer (asterisk, A) in the lymph node at left cervical level 1 (arrow) and right cervical level 2 (arrowhead). Zero points for left cervical level 1 suggest benign lymph nodes (B), whereas 5 points for right cervical level 2 lymph node are calculated following the scoring system (0 points for stage 2 [T-stage], 1 point for 1.5 cm of shortest axial diameter, 1 point for 1.25 of long-to-short ratio, and 3 points for the cystic necrosis, C). The left cervical level 1 lymph node was classified as a benign lymph node, and the surgical specimen confirmed it as a benign lymph node. The lymph node in the right cervical level 2 was classified as high risk for the metastasis, and the surgical specimen proved it as a metastatic lymph node.

Risk scoring systems have been used to stratify the risk of lymph node metastasis in various organs, such as esophageal cancer, gastric cancer, melanoma, endometrial cancers, and thyroid cancer.<sup>27–33</sup> Similar to these tumors, the existence and extent of lymph node metastasis change the extent of lymph node dissection and therapeutic plans in patients with HNSCC; consequently, accurate decisions for lymph node metastasis are crucial. However, almost all pre-existing modalities have variable diagnostic accuracy (sensitivities range from 14% to 80% for CT and from 29% to 85% for MR imaging; specificities range from 80% to 100% for both CT and MR imaging) for detecting node metastases in HNSCC.<sup>2,3,6,8,34</sup> Our prediction model, which provides risk scores for the evaluation of lymph nodes, may provide objective evidence for diagnosis and might contribute to reduced interobserver variability.

PET/CT is known to have an advantage in staging the nodal status of HNSCC.<sup>10–15</sup> A recent meta-analysis reported that the sensitivity, specificity, and AUC of PET/CT were 84% (95% CI, 71%–87%), 96% (95% CI, 94%–97%), and 0.97 (95% CI, 0.95–0.98) with per-neck-level data.<sup>15</sup> PET/CT showed the improvement of per-neck-level sensitivity by 21% over conventional imaging.<sup>15</sup> The sensitivity, specificity, and AUC of our scoring system are slightly lower than those of PET/CT and similar to those of conventional CT.

However, our risk scoring system may apply to several clinically complex circumstances for radiologists. First, there are several cases in which it is technically impossible to perform ultrasonography and biopsy. Although ultrasonography and ultrasonography-guided biopsy are very powerful techniques for the assessment of indeterminate lymph nodes in patients with cancer, technical limitations exist in deep lymph nodes, such as retropharyngeal, mediastinal, and lower level 6 lymph nodes, as well as in situations that involve poor patient conditions or low patient compliance.<sup>6,7</sup> Second, a risk scoring system could provide a more targeted review for radiologists in an additional imaging study. Rather than focusing on high-score (definite malignant) or low-score (definite benign) lymph nodes, the additional evaluation should focus on lymph nodes with intermediate risk scores. Fur-

thermore, our risk scoring system integrates variable pre-existing CT criteria for lymph node metastasis and primary tumors in HNSCC. Given these advantages, our risk scoring system could enhance the efficiency of preoperative CT by supporting reasonable decision-making based on estimated malignancy.

Our present study had several limitations of note. First, some selection bias could have been introduced because our study was performed at a single center with a small number of patients. Further validation studies with larger populations are warranted. Second, we did not evaluate the potential for interobserver variability in interpretations of CT images between radiologists. However, the radiologists who participated in the study had  $>5$  years of clinical experience

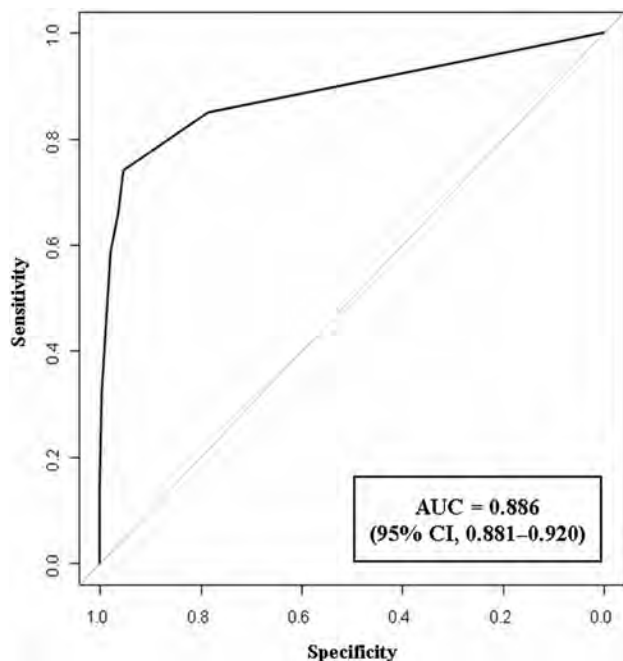


**FIG 2.** Performance of prediction model.

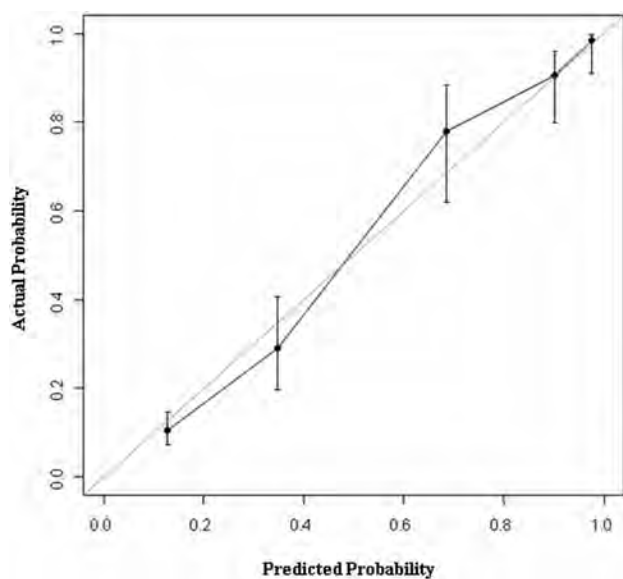


**FIG 3.** Calibration plot. The calibration plot shows good agreement between the predicted risk and actual risk of lymph node metastasis.

in head and neck oncology imaging, and both had completed an image training session to perform more reproducible and accurate image analysis within the parameters of the study protocol. Third, we focused on the development of the prediction model and did not perform external validation. However, as we previously described, our risk scoring system might be helpful, at least in several clinically complicated circumstances. The clinical implications of our study should be validated in further analyses. Fourth, we enrolled the patients who underwent a curative operation because we used pathologic specimens after neck dissection as a reference standard to match image findings in each lymph node. Therefore, some degree of selection bias was also included because we did not include patients who were treated with definite

radiation therapy or concurrent chemoradiotherapy. Finally, we focused on the image findings of enhanced neck CT, without correlation of the results of other modalities. As we previously described, many studies suggest the potential diagnostic and prognostic roles of PET/CT in patients with HNSCC,<sup>10,11,13,14</sup> and some countries and referral centers routinely perform PET/CT for the initial work-up. Further studies may reveal whether adding this scoring system to the results of PET/CT could improve the sensitivity and specificity of determining neck nodal disease.

## CONCLUSIONS

A simple 9-point risk scoring system using CT characteristics of lymph nodes and tumors for HNSCC could be feasible to stratify the risk of cervical lymph node metastasis with high diagnostic accuracy. This comprehensive and practical risk scoring system, based on various CT features, could be helpful for decision-making regarding the possibility of lymph node metastasis in patients with HNSCC in daily practice.

Disclosures: Jung Hwan Baek—UNRELATED: Consultancy: RF Medical and StarMed since 2017.

## REFERENCES

1. Hoang JK, Vanka J, Ludwig BJ, et al. **Evaluation of cervical lymph nodes in head and neck cancer with CT and MRI: tips, traps, and a systematic approach.** *AJR Am J Roentgenol* 2013;200:W17–25 CrossRef Medline
2. Castelijns JA, van den Brekel MW. **Imaging of lymphadenopathy in the neck.** *Eur Radiol* 2002;12:727–38 CrossRef Medline
3. Som PM. **Detection of metastasis in cervical lymph nodes: CT and MR criteria and differential diagnosis.** *AJR Am J Roentgenol* 1992; 158:961–69 CrossRef Medline
4. Som PM, Curtin HD, Mancuso AA. **Imaging-based nodal classification for evaluation of neck metastatic adenopathy.** *AJR Am J Roentgenol* 2000;174:837–44 CrossRef Medline
5. Steinkamp HJ, Cornehl M, Hosten N, et al. **Cervical lymphadenopathy: ratio of long- to short-axis diameter as a predictor of malignancy.** *Br J Radiol* 1995;68:266–70 CrossRef Medline
6. Suh CH, Baek JH, Choi YJ, et al. **Performance of CT in the preoperative diagnosis of cervical lymph node metastasis in patients with papillary thyroid cancer: a systematic review and meta-analysis.** *AJNR Am J Neuroradiol* 2017;38:154–61 CrossRef Medline
7. Kim E, Park JS, Son KR, et al. **Preoperative diagnosis of cervical metastatic lymph nodes in papillary thyroid carcinoma: comparison of ultrasound, computed tomography, and combined ultrasound with computed tomography.** *Thyroid* 2008;18:411–18 CrossRef Medline
8. Wu LM, Xu JR, Liu MJ, et al. **Value of magnetic resonance imaging for nodal staging in patients with head and neck squamous cell carcinoma: a meta-analysis.** *Acad Radiol* 2012;19:331–40 CrossRef Medline
9. King AD, Chow KK, Yu KH, et al. **Head and neck squamous cell carcinoma: diagnostic performance of diffusion-weighted MR imaging for the prediction of treatment response.** *Radiology* 2013;266: 531–38 CrossRef Medline
10. Plaxton NA, Brandon DC, Corey AS, et al. **Characteristics and limitations of FDG PET/CT for imaging of squamous cell carcinoma of the head and neck: a comprehensive review of anatomy, metastatic pathways, and image findings.** *AJR Am J Roentgenol* 2015;205: W519–31 CrossRef Medline
11. Al-Ibraheem A, Buck A, Krause BJ, et al. **Clinical applications of FDG PET and PET/CT in head and neck cancer.** *J Oncol* 2009;2009:208725 CrossRef Medline
12. Yongkui L, Jian L, Wanghan, et al. **18FDG-PET/CT for the detection of regional nodal metastasis in patients with primary head and neck**

- cancer before treatment: a meta-analysis. *Surg Oncol* 2013;22:e11–16 CrossRef Medline
13. Castaldi P, Leccisotti L, Bussu F, et al. **Role of (18)F-FDG PET-CT in head and neck squamous cell carcinoma.** *Acta Otorhinolaryngol Ital* 2013;33:1–8 Medline
  14. Mak D, Corry J, Lau E, et al. **Role of FDG-PET/CT in staging and follow-up of head and neck squamous cell carcinoma.** *QJ Nucl Med Mol Imaging* 2011;55:487–99 Medline
  15. Sun R, Tang X, Yang Y, et al. **(18)FDG-PET/CT for the detection of regional nodal metastasis in patients with head and neck cancer: a meta-analysis.** *Oral Oncol* 2015;51:314–20 CrossRef Medline
  16. Saindane AM. **Pitfalls in the staging of cervical lymph node metastasis.** *Neuroimaging Clin N Am* 2013;23:147–66 CrossRef Medline
  17. Han K, Song K, Choi BW. **How to develop, validate, and compare clinical prediction models involving radiological parameters: study design and statistical methods.** *Korean J Radiol* 2016;17:339–50 CrossRef Medline
  18. Moons KM, Altman DG, Reitsma JB, et al. **Transparent Reporting of a Multivariable Prediction Model for Individual Prognosis or Diagnosis (TRIPOD): explanation and elaboration.** *Ann Intern Med* 2015;162:W1–73 CrossRef Medline
  19. von Elm E, Altman DG, Egger M, et al; STROBE Initiative. **Strengthening the Reporting of Observational Studies in Epidemiology (STROBE) statement: guidelines for reporting observational studies.** *BMJ* 2007;335:806–08 CrossRef Medline
  20. Bruneton JN, Balu-Maestro C, Marcy PY, et al. **Very high frequency (13 MHz) ultrasonographic examination of the normal neck: detection of normal lymph nodes and thyroid nodules.** *J Ultrasound Med* 1994;13:87–90 CrossRef Medline
  21. van den Brekel MW, Stel HV, Castelijns JA, et al. **Cervical lymph node metastasis: assessment of radiologic criteria.** *Radiology* 1990;177:379–84 CrossRef Medline
  22. Gor DM, Langer JE, Loevner LA. **Imaging of cervical lymph nodes in head and neck cancer: the basics.** *Radiol Clin North Am* 2006;44:101–10, viii Medline
  23. Sullivan LM, Massaro JM, D'Agostino RB Sr. **Presentation of multivariate data for clinical use: the Framingham Study risk score functions.** *Stat Med* 2004;23:1631–60 CrossRef Medline
  24. Steyerberg EW, Harrell FE Jr, Borsboom GJ, et al. **Internal validation of predictive models: efficiency of some procedures for logistic regression analysis.** *J Clin Epidemiol* 2001;54:774–81 CrossRef Medline
  25. Harrell FE Jr, Lee KL, Mark DB. **Multivariable prognostic models: issues in developing models, evaluating assumptions and adequacy, and measuring and reducing errors.** *Stat Med* 1996;15:361–87 CrossRef Medline
  26. Efron B. **Estimating the Error Rate of a Prediction Rule: Improvement on Cross-Validation.** *J Am Stat Assoc* 1983;382:316–31
  27. Lee L, Ronellenfitsch U, Hofstetter WL, et al. **Predicting lymph node metastases in early esophageal adenocarcinoma using a simple scoring system.** *J Am Coll Surg* 2013;217:191–99 CrossRef Medline
  28. Leers JM, DeMeester SR, Oezcelik A, et al. **The prevalence of lymph node metastases in patients with T1 esophageal adenocarcinoma a retrospective review of esophagectomy specimens.** *Ann Surg* 2011;253:271–78 CrossRef Medline
  29. Koskas M, Fournier M, Vanderstraeten A, et al. **Evaluation of models to predict lymph node metastasis in endometrial cancer: a multi-centre study.** *Eur J Cancer* 2016;61:52–60 CrossRef Medline
  30. Imai K, Kato H, Katayama K, et al. **A preoperative risk-scoring system to predict lymph node metastasis in endometrial cancer and stratify patients for lymphadenectomy.** *Gynecol Oncol* 2016;142:273–77 CrossRef Medline
  31. Jeong JJ, Lee YS, Lee SC, et al. **A scoring system for prediction of lateral neck node metastasis from papillary thyroid cancer.** *J Korean Med Sci* 2011;26:996–1000 CrossRef Medline
  32. Murali R, Desilva C, Thompson JF, et al. **Non-Sentinel Node Risk Score (N-SNORE): a scoring system for accurately stratifying risk of non-sentinel node positivity in patients with cutaneous melanoma with positive sentinel lymph nodes.** *J Clin Oncol* 2010;28:4441–49 CrossRef Medline
  33. Tran TB, Worhunsky DJ, Squires MH, et al. **Clinicopathologic score predicting lymph node metastasis in T1 gastric cancer.** *Surgery* 2018;163:889–93 CrossRef Medline
  34. Ashraf M, Biswas J, Jha J, et al. **Clinical utility and prospective comparison of ultrasonography and computed tomography imaging in staging of neck metastases in head and neck squamous cell cancer in an Indian setup.** *Int J Clin Oncol* 2011;16:686–93 CrossRef Medline

# Readout-Segmented Echo-Planar DWI for the Detection of Cholesteatomas: Correlation with Surgical Validation

N. Fischer, V.H. Schartinger, D. Dejaco, J. Schmutzhard, H. Riechelmann, M. Plaikner, and B. Henninger



## ABSTRACT

**BACKGROUND AND PURPOSE:** MR imaging has become an important tool for the detection of cholesteatomas of the middle ear. Various diffusion-weighted imaging sequences are available and have shown promising results. This study aimed to evaluate readout-segmented echo-planar DWI for the detection of cholesteatoma and compare the results with surgical validation.

**MATERIALS AND METHODS:** Fifty patients with chronic otitis media (24 females and 26 males; range, 12–76 years of age; mean age, 41 years) who underwent MR imaging before an operation of the middle ear (1–169 days) were included. The MR imaging protocol consisted of axial and coronal readout-segmented echo-planar DWI with b-values of 0 and 1000 s/mm<sup>2</sup> and 3-mm slice thickness. The readout-segmented echo-planar diffusion-weighted images were fused with standard T2-weighted sequences for better anatomic assignment. The results of the MR imaging evaluation were correlated with the results from the operation.

**RESULTS:** Readout-segmented echo-planar DWI detected 22 of the 25 cases of surgically proved cholesteatoma. It has an accuracy of 92% (95% confidence interval, 80.8%–97.8%), a sensitivity of 88%, a specificity of 96%, a positive predictive value of 96%, and a negative predictive value of 89%. In 1 case, a positive finding for cholesteatoma with readout-segmented echo-planar DWI could not be proved by histology, and in 3 cases, histology yielded a cholesteatoma that was not detected with MR imaging.

**CONCLUSIONS:** Readout-segmented echo-planar DWI is a promising and reliable MR imaging sequence for the detection and exclusion of cholesteatoma.

**ABBREVIATION:** RESOLVE = readout-segmented echo-planar

Cholesteatoma is defined as a mass of keratinizing squamous epithelium in the tympanic cavity, mastoid cells, and the subepithelial connective tissue that can lead to an inflammatory reaction by the progressive accumulation of keratin debris and bone resorption.<sup>1–3</sup> Cholesteatoma can only be cured by surgical removal of the entire mass.<sup>4</sup> Depending on the surgical technique, the prevalence of residual or recurrent cholesteatoma is as high as 25%.<sup>4–7</sup>

The detection of cholesteatoma in patients who have undergone a middle ear operation is often difficult due to the grafts used, and regrowing squamous epithelium in the back of the middle ear or mastoid can remain symptomless for a long time. A high-resolution CT scan, which is the basic method for imaging the nonoperated middle ear, cannot reliably distinguish residual or recurrent disease

from postoperative changes such as fluid, fibrous tissue, or granulations.<sup>8,9</sup> Temporal bone CT scans have low specificity (48%) and sensitivity (43%) for residual or recurrent cholesteatoma.<sup>9</sup> Thus, second-look surgery is a standard for the diagnosis of recurrent and residual cholesteatoma. However, it is associated with anesthesia and surgical risks. In approximately one-third of planned second-look procedures, a residual cholesteatoma can be found.<sup>10</sup> In well-reconstructed middle ears with normal postoperative clinical findings and good postoperative auditory results, a second-look procedure could be avoided in two-thirds of cases.

As an alternative to second-look surgery, MR imaging has become an important tool for the detection of cholesteatoma of the middle ear. Various DWI sequences are available and have shown considerable improvement in the diagnosis of cholesteatoma, providing a variation of the conventional MR imaging sequences that use the principles of molecular diffusion or Brownian motion to generate contrast. In certain pathologic conditions, the molecular diffusion, which refers to the random movement of water molecules, is restricted. The keratin debris in cholesteatomas restricts water diffusion and produces a high signal intensity. Mu-

Received December 6, 2018; accepted after revision April 21, 2019.

From the Departments of Otorhinolaryngology (N.F., V.H.S., D.D., J.S., H.R.) and Radiology (M.P., B.H.), Medical University of Innsbruck, Innsbruck, Austria.

Please address correspondence to Volker H. Schartinger, MD, Department of Otorhinolaryngology, Medical University of Innsbruck, Anichstraße 35, 6020 Innsbruck, Austria; e-mail: Volker.Schartinger@i-med.ac.at

<http://dx.doi.org/10.3174/ajnr.A6079>

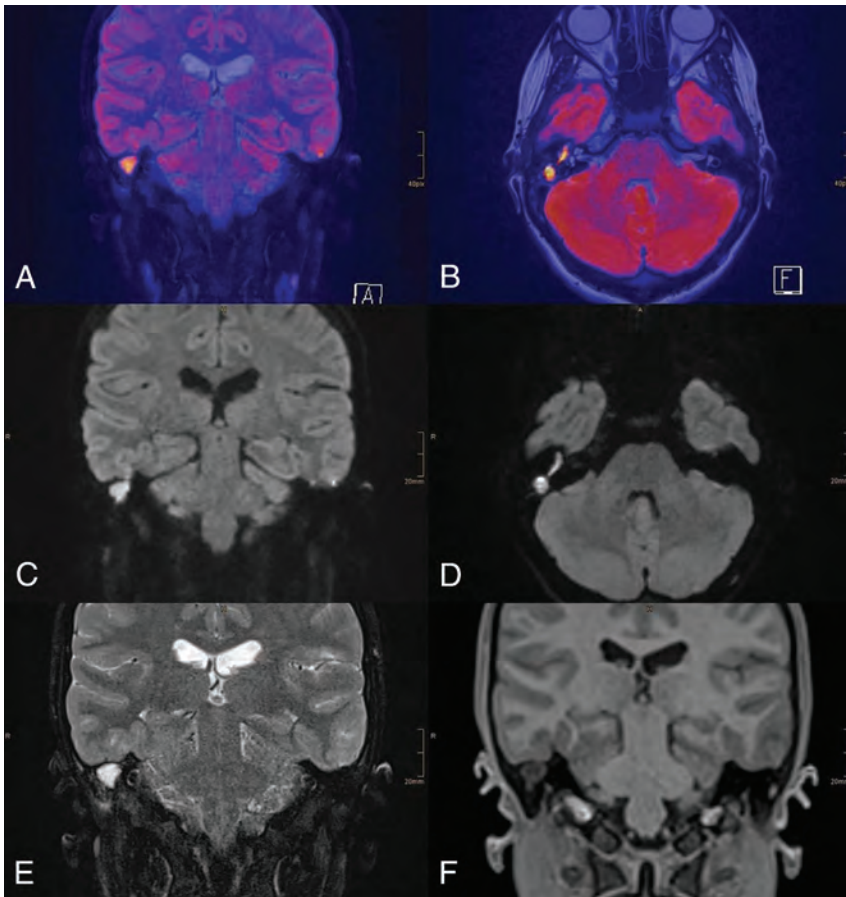


**FIG 1.** A 13-year-old female patient with chronic otitis media on the right side. RESOLVE-DWI shows a large hyperintense lesion on the right side. A and B, Colored fused images of RESOLVE-DWI ( $b=1000$ ) and T2-weighted images. C and D, RESOLVE-DWI in coronal and axial orientations ( $b=1000$ ). T2-weighted image (E) shows a well-delineated T2 hyperintense lesion. T1-weighted image (F) shows no sign of hyperintensity. The cholesteatoma was proved intraoperatively.

cosal edema, fibrosis, and scar or granulation tissue produce a hypointense signal. DWI techniques can be divided basically into EPI-based and non-EPI-based techniques.<sup>11</sup> Whereas EPI-DWI consists of single-shot spin-echo pulse sequences, the non-EPI-DWI consists of either single-shot turbo-spin or multishot turbo-spin sequences. Due to different artifacts that can be generated during the acquisition of DWI, such as ghosting, motion, or susceptibility artifacts, non-EPI-DWI is recommended to avoid false-positive results.<sup>11,12</sup>

Readout-segmented echo-planar (RESOLVE)-DWI is a relatively new alternative technique for obtaining diffusion-weighted images with high quality, delivering sharp images at high spatial resolution and reduced slice thickness. RESOLVE-DWI uses the same diffusion preparation as single-shot EPI. The  $k$ -space trajectory is divided into multiple segments in the readout direction, so that the echo spacing is reduced compared with single-shot EPI-DWI; this feature reduces image blurring due to long echo-trains and susceptibility artifacts. Further distortion artifacts are minimized. Usually 2 spin-echoes are acquired to reduce potential phase artifacts, and the second echo is used to generate 2D navigator data for phase correction.<sup>11,13</sup>

Our purpose was to evaluate RESOLVE-DWI for the detection of cholesteatomas compared with the criterion standard intraoperative and histopathologic findings.

## MATERIALS AND METHODS

### Study Overview

In a retrospective study at a single academic center, we analyzed patients with chronic otitis media who had undergone an operation at the Department of Otorhinolaryngology of the Medical University of Innsbruck and underwent MR imaging before the operation from November 2015 to March 2018.

A data base search was initially performed to identify all patients who had undergone a middle ear operation because of chronic otitis media. Only data of patients who underwent MR imaging before the operation were included in the study. Operative reports and histopathologic results were available for all patients. The institutional review board of the Medical University of Innsbruck approved the study (approval number: 1215/2018). Informed consent was not obtained because the data were collected retrospectively and all imaging data were pseudonymized.

### Imaging Technique

MR imaging was performed with a 1.5T scanner (Magnetom Avanto-fit; Siemens Healthineers, Erlangen, Germany). The MR imaging protocol consisted of axial and coronal RESOLVE-DWI with  $b$ -values of 0 and 1000  $s/mm^2$  and a 3-mm slice thickness (19 acquired slices with each sequence). The acquisition time for each sequence was 3 minutes 1 second. In addition, T2-weighted images in coronal and axial orientations and T1-weighted images with fat saturation in an axial orientation were acquired. RESOLVE-diffusion-weighted images were fused with standard T2-weighted sequences for better anatomic assignment using the software provided by the vendor. DWI was further translated into a color-coded image for better visualization.

MR images were evaluated by 2 experienced radiologists (B.H. with 12 years and M.P. with 8 years of experience in reading head and neck MR images) on the basis of standard diagnostic criteria for cholesteatoma<sup>11</sup> with DWI. Examiners were blinded to the results of the operation and histopathology; a final decision on the presence of a cholesteatoma was made in consensus. The main diagnostic criterion for cholesteatoma on DWI is lesion hyperintensity, compared with the signal intensity of brain, on  $b=0$   $s/mm^2$  images that persists or increases on high  $b$ -value (800–1000  $s/mm^2$ ) images.<sup>14,15</sup> The so-called “T2 shine through” effect is also observed in cholesteatomas; therefore, ADC values were not integrated into our evaluation.<sup>11</sup> Further analysis included reviewing T1-weighted images with fat saturation and T2-weighted images considering known pitfalls (Fig 1).<sup>16</sup> The color-encoded images were not included in the evaluation procedure.

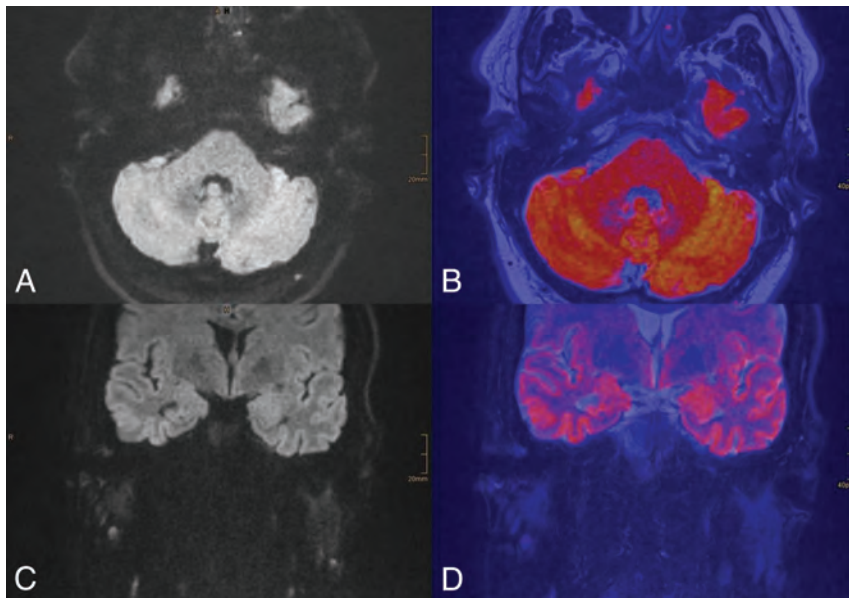


**FIG 2.** A 52-year-old male patient with suspected cholesteatoma on the right side. MR imaging with RESOLVE-DWI shows no sign of hyperintense signal on the right side (axial and coronal RESOLVE-DWI, A and C, and colored fused images with T2-weighted images, B and D). There were no findings on T1-weighted and T2-weighted images. Intraoperatively, a 4-mm cholesteatoma directly adherent to the malleus was detected. The small size of the lesion probably explained the false-negative results with RESOLVE-DWI.

#### Accuracy data for the detection of cholesteatomas using MRI with RESOLVE-DWI

Parameter	Value (%) (95% CI)
All operations	
Sensitivity	88% (68.8%–97.5%)
Specificity	96% (79.7%–99.9%)
PPV	0.96 (0.76–0.99)
NPV	0.89 (0.73–0.96)
Accuracy	92% (80.8%–97.8%)
Primary operation	
Sensitivity	83% (55.2%–95.3%)
Specificity	100% (75.8%–100%)
PPV	1.00
NPV	0.86 (0.63–0.96)
Revision operation	
Sensitivity	92% (64.6%–98.5%)
Specificity	93% (68.5%–98.7%)
PPV	0.92 (0.63–0.99)
NPV	0.93 (0.66–0.99)

**Note.**—NPV indicates negative predictive value; PPV, positive predictive value.

#### Surgical Validation

The diagnosis of cholesteatoma was made on the basis of the intraoperative presence of keratinizing squamous epithelium and debris in the middle ear and/or mastoid and pathohistologic examination of the removed tissue. Microsurgical techniques with the patient under general anesthesia were used in all patients.

#### Data Analysis

Numeric data were reported as mean  $\pm$  SD or mean and 95% confidence interval, and categoric data were reported as frequencies and percentages. True-positives, false-positives, true-negatives, and false-negatives were calculated from the findings on RESOLVE-DWI and surgical findings. On the basis of these data, standard diagnostic parameters were calculated. Interobserver agreement of the 2 radiologists' measurements was assessed using

the Cohen  $\kappa$ . Statistical analysis was performed using SPSS software, Version 24 (IBM, Armonk, New York).

#### RESULTS

In this study, 50 MR images (cases) of 47 patients were analyzed. Three patients underwent 2 operations. The patients were 12–76 years of age at the operation (mean age, 41 years). Twenty-four (48%) cases were female, and 26 (52%) cases were male. In 24 (48%) cases, it was the first ear operation, and in 26 (52%) cases, revision surgery was performed. The interval between imaging and the operation was 0–169 days, with a mean interval of 54 days.

The overall rate of interobserver agreement was 92% with a Cohen  $\kappa$  value of  $0.84 \pm 0.075$ . In 25/50 cases (50%), a cholesteatoma was detected intraoperatively, and in 22/25, there was a positive finding of surgically validated cholesteatoma on RESOLVE-DWI. In 3/25, there was no hyperintense signal on RESOLVE-DWI despite the surgical and pathohistologic proof of cholesteatoma (Fig 2).

In 1/23 cases, a positive finding for cholesteatoma with RESOLVE-DWI could not be proved intraoperatively. RESOLVE-DWI was therefore true-positive in 22/50, true-negative in 24/50, false-positive in 1 case, and false-negative in 3/50 cases. In 46/50 cases (92%), the radiologic and intraoperative evaluations concurred. The sensitivity for detecting cholesteatoma with RESOLVE-DWI was 88% (95% CI, 68.8%–97.5%), the specificity was 96% (95% CI, 79.7%–99.9%), the positive predictive value was 0.96 (95% CI, 0.76–0.99), and the negative predictive value was 0.89 (95% CI, 0.73–0.96). The diagnostic accuracy was 92% (95% CI, 80.8%–97.8%).

In 12/24 (50%) patients who had undergone an intervention on the affected ear for the first time, a cholesteatoma was detected intraoperatively. In 10/12 (83%) cases, there was a positive finding of surgically validated cholesteatoma on RESOLVE-DWI. In the 12 surgically negative cases, the RESOLVE-DWI also showed a negative result. The sensitivity for detecting cholesteatoma with RESOLVE-DWI in unoperated ears was 83% (95% CI, 55.2%–95.3%), the specificity was 100% (95% CI, 75.8%–100%), the positive predictive value was 1.00, and the negative predictive value was 0.86 (95% CI, 0.63–0.96).

In 12/26 (46.2%) cases with revision surgery, a cholesteatoma was diagnosed histologically, and in 11/12 (92%) cases, there was a positive finding of surgically validated cholesteatoma on RESOLVE-DWI. In 13/14 (93%) cases in whom no cholesteatoma was found, the MR imaging also showed a negative result. The sensitivity for detecting residual cholesteatoma with RESOLVE-DWI was 92% (95% CI, 64.6%–98.5%), the specificity was 93% (95% CI, 68.5%–98.7%), the positive predictive value was 0.92 (95% CI, 0.63–0.99), and the negative predictive value was 0.93 (95% CI, 0.66–0.99). A summary of the results is shown in the Table.

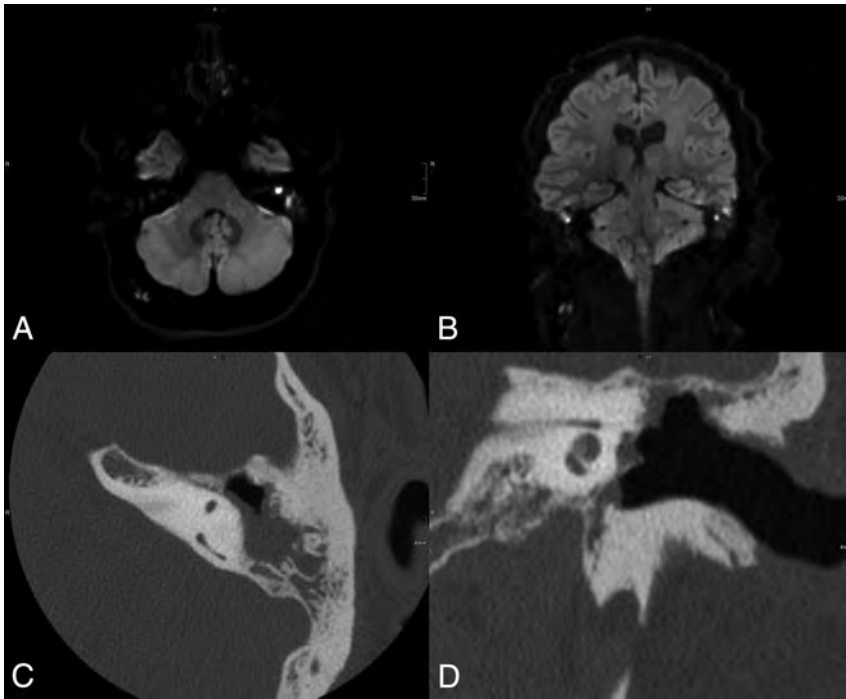


**FIG 3.** A 31-year-old male patient with suspected recurrent cholesteatoma on both sides. MR imaging with RESOLVE-DWI showed a hyperintense lesion on both sides highly suspicious for cholesteatoma (A and B). The patient underwent an operation of the left ear after the MR imaging. Intraoperatively, there was no sign of recurrent cholesteatoma. The reason for the false-positive MR imaging findings was probably detected wax accumulation in the open mastoid cavity. Axial (C) and coronal (D) CT scans show the radical cavity.

## DISCUSSION

RESOLVE-DWI is a new technique for the diagnosis of cholesteatoma.<sup>11</sup> So far, only a few studies have evaluated this new approach and found promising results.<sup>17-19</sup> This study evaluated RESOLVE-DWI for the detection of cholesteatoma and compared the results with surgical validation.

Pooled sensitivity of non-EPI DWI for the detection of residual and recurrent cholesteatomas in a recent meta-analysis was 91% with a specificity of 92%.<sup>20</sup> In our study, RESOLVE-DWI reached a sensitivity of 88% and a specificity of 96%. Therefore, in general, both sequences provide comparable results concerning the detection of cholesteatoma. In 1 patient, a positive finding for cholesteatoma with RESOLVE-DWI could not be proved intraoperatively. The reason for the high signal intensity was a wax accumulation in the open mastoid cavity (Fig 3). Lingam et al. also mentioned wax as a reason for false-positive cases: It can produce high signal changes on the  $b=1000$  images and low signal and values on the ADC map.<sup>21</sup> Thus, it is important that the open mastoid cavity be cleaned before imaging and the surgeon be aware that wax can lead to a false-positive result.

The study by Yamashita et al<sup>22</sup> evaluated a multishot EPI sequence for the diagnosis of cholesteatoma and compared the results with a single-shot EPI sequence. They found that multishot EPI improved the accuracy of diagnosis but had no correlation with intraoperative findings or histology. Our RESOLVE sequence differs from the sequence of the Yamashita study group because it is based on a different approach using the same diffusion preparation as single-shot EPI and dividing the  $k$ -space trajectory into multiple segments. Potential phase artifacts are

duced by acquiring 2 spin-echoes, with the second echo used to generate 2D navigator data for phase correction. Algin et al<sup>17</sup> used a similar approach with a readout-segmented echo-planar imaging-based technique and compared this sequence with single-shot EPI. Compared with our study, the specificity was lower, at only 78% (96% in our study); the sensitivity was slightly higher at 100%. In their study, no correlation with intraoperative findings or histology was available in patients with negative findings on MR imaging. Furthermore, they used 3T, which is, in our opinion, the worst choice for cholesteatomas due to the greater susceptibility at higher field strengths.

In 3 of 25 patients, the surgically validated cholesteatoma could not be detected with RESOLVE-DWI. The images were re-analyzed postoperatively. In 1 case, blood components (due to methemoglobin) in the middle ear, detected with T1-weighted images, caused artifacts, which led to a false-negative result because this was not considered a cholesteatoma. In the other 2 cases, the reason for the false-negative results remained unclear. We assume that these cholesteatomas could not be detected with 3-mm slice thickness RESOLVE-DWI due to their small size.

We did not encounter any relevant artifacts with RESOLVE-DWI that had an influence on radiologic diagnoses in any of our cases. All recognized artifacts could be anatomically clearly assigned to the adjacent brain, which, in turn, was facilitated by the image fusion. Non-EPI-DWI is known to provide less image distortion and artifacts than other DWI techniques.<sup>23</sup> Nevertheless, the acquisition time for non-EPI-DWI and EPI-DWI can be quite different. We found acquisition times between 3 and 6 minutes for 1  $b$ -value with non-EPI-DWI in the literature,<sup>21</sup> and some studies did not indicate the acquisition time.<sup>12,24-26</sup> Therefore, comparison between different sequences is always difficult. As with sequences used in other studies, many parameters such as slice thickness, number of slices, and FOV must be taken into account. Our RESOLVE-DWI takes 3:01 minutes for 1 orientation with 19 slices, 2  $b$ -values, and a slice thickness of 3 mm. In total, our protocol with 2 orientations for RESOLVE-DWI takes <20 minutes, including T1- and T2-weighted sequences, and delivers images with a sufficient SNR ratio. The non-EPI HASTE sequence that is provided by the manufacturer on our scanner takes much longer, with >5 minutes and the same slice thickness and number of images as in our RESOLVE-DWI. The acquisition would also be possible with a smaller number of slices, especially coronal slices. This could further reduce the scanning time.

The limitations of this study include a slice thickness of 3 mm instead of 2 mm, which is already used in some studies. Two-

millimeter slices are possible with the RESOLVE-DWI, but keeping the SNR at such a high level would result in a much longer scanning time. Furthermore, we performed no direct comparison with other DWI techniques such as non-EPI-DWI, but this should definitely be considered for future studies with emphasis on a correlation with histopathology. Because of the retrospective character of our study, the size of the intraoperatively found cholesteatomas was not documented and could not be further evaluated. This feature could have explained the false-negative results.

The results of this study support RESOLVE-DWI having high sensitivity and specificity for detecting cholesteatomas. Sinus tympani disease and incus erosion are associated with higher rates of cholesteatoma recurrence; thus, in these cases, a second-look operation should be considered.<sup>27</sup> In asymptomatic patients with normal postoperative clinical findings and good hearing results, a postoperative follow-up with RESOLVE-DWI can be recommended to reduce the number of avoidable second-look procedures.<sup>28</sup> RESOLVE-DWI remains a promising alternative to non-EPI-DWI.

## CONCLUSIONS

RESOLVE-DWI is highly sensitive and specific in identifying residual and recurrent cholesteatomas.

Disclosures: All authors declare that there are no conflict of interest related to the subject matter or material discussed in this article.

## REFERENCES

1. Yung M, Tono T, Olszewska E, et al. **EAONO/JOS Joint Consensus Statements on the Definitions, Classification and Staging of Middle Ear Cholesteatoma.** *J Int Adv Otol* 2017;13:1–8 CrossRef Medline
2. Si Y, Chen YB, Chen SJ, et al. **TLR4 drives the pathogenesis of acquired cholesteatoma by promoting local inflammation and bone destruction.** *Sci Rep* 2015;5:16683 CrossRef Medline
3. Xie S, Wang X, Ren J, et al. **The role of bone resorption in the etiopathogenesis of acquired middle ear cholesteatoma.** *Eur Arch Otorhinolaryngol* 2017;274:2071–78 CrossRef Medline
4. Kuo CL, Shiao AS, Yung M, et al. **Updates and knowledge gaps in cholesteatoma research.** *Biomed Res Int* 2015;2015:854024 CrossRef Medline
5. Syms MJ, Luxford WM. **Management of cholesteatoma: status of the canal wall.** *Laryngoscope* 2003;113:443–48 CrossRef Medline
6. Westerberg J, Mäki-Torkko E, Harder H. **Cholesteatoma surgery with the canal wall up technique combined with mastoid obliteration: results from primary surgery in 230 consecutive cases.** *Acta Otolaryngol* 2018;138:452–57 CrossRef Medline
7. Haginomori S, Takamaki A, Nonaka R, et al. **Residual cholesteatoma: incidence and localization in canal wall down tympanoplasty with soft-wall reconstruction.** *Arch Otolaryngol Head Neck Surg* 2008;134:652–57 CrossRef Medline
8. Corrales CE, Blevins NH. **Imaging for evaluation of cholesteatoma: current concepts and future directions.** *Curr Opin Otolaryngol Head Neck Surg* 2013;21:461–67 CrossRef Medline
9. Tierney PA, Pracy P, Blaney SP, et al. **An assessment of the value of the preoperative computed tomography scans prior to otoscopic ‘second look’ in intact canal wall mastoid surgery.** *Clin Otolaryngol Allied Sci* 1999;24:274–76 CrossRef Medline
10. Keeler JA, Kaylie DM. **Cholesteatoma: is a second stage necessary?** *Laryngoscope* 2016;126:1499–500 CrossRef Medline
11. Henninger B, Kremser C. **Diffusion weighted imaging for the detection and evaluation of cholesteatoma.** *World J Radiol* 2017;9:217–22 CrossRef Medline
12. De Foer B, Vercruyse JP, Pilet B, et al. **Single-shot, turbo spin-echo, diffusion-weighted imaging versus spin-echo-planar, diffusion-weighted imaging in the detection of acquired middle ear cholesteatoma.** *AJNR Am J Neuroradiol* 2006;27:1480–82 Medline
13. Porter DA, Heidemann RM. **High resolution diffusion-weighted imaging using readout-segmented echo-planar imaging, parallel imaging and a two-dimensional navigator-based reacquisition.** *Magn Reson Med* 2009;62:468–75 CrossRef Medline
14. Lingam RK, Connor SE, Casselman JW, et al. **MRI in otology: applications in cholesteatoma and Meniere’s disease.** *Clin Radiol* 2018;73:35–44 CrossRef Medline
15. Más-Estellés F, Mateos-Fernández M, Carrascosa-Bisquert B, et al. **Contemporary non-echo-planar diffusion-weighted imaging of middle ear cholesteatomas.** *Radiographics* 2012;32:1197–213 CrossRef Medline
16. Fukuda A, Morita S, Harada T, et al. **Value of T1-weighted magnetic resonance imaging in cholesteatoma detection.** *Otol Neurotol* 2017;38:1440–44 CrossRef Medline
17. Algin O, Aydin H, Ozmen E, et al. **Detection of cholesteatoma: high-resolution DWI using RS-EPI and parallel imaging at 3 Tesla.** *J Neuroradiol* 2017;44:388–94 CrossRef Medline
18. Azuma T, Kodama T, Yano T, et al. **Optimal imaging parameters for readout-segmented EPI of the temporal bone.** *Magn Reson Med Sci* 2015;14:145–52 CrossRef Medline
19. Holdsworth SJ, Skare S, Newbould RD, et al. **Readout-segmented EPI for rapid high resolution diffusion imaging at 3 T.** *Eur J Radiol* 2008;65:36–46 CrossRef Medline
20. Lingam RK, Bassett P. **A meta-analysis on the diagnostic performance of non-echo-planar diffusion-weighted imaging in detecting middle ear cholesteatoma: 10 years on.** *Otol Neurotol* 2017;38:521–28 CrossRef Medline
21. Lingam RK, Nash R, Majithia A, et al. **Non-echo-planar diffusion weighted imaging in the detection of post-operative middle ear cholesteatoma: navigating beyond the pitfalls to find the pearl.** *Insights Imaging* 2016;7:669–78 CrossRef Medline
22. Yamashita K, Yoshiura T, Hiwatashi A, et al. **Detection of middle ear cholesteatoma by diffusion-weighted MR imaging: multishot echo-planar imaging compared with single-shot echo-planar imaging.** *AJNR Am J Neuroradiol* 2011;32:1915–18 CrossRef Medline
23. Castle JT. **Cholesteatoma pearls: practical points and update.** *Head Neck Pathol* 2018;12:419–29 CrossRef Medline
24. Steens S, Venderink W, Kunst D, et al. **Repeated postoperative follow-up diffusion-weighted magnetic resonance imaging to detect residual or recurrent cholesteatoma.** *Otol Neurotol* 2016;37:356–61 CrossRef Medline
25. Cimsit NC, Cimsit C, Baysal B, et al. **Diffusion-weighted MR imaging in postoperative follow-up: reliability for detection of recurrent cholesteatoma.** *Eur J Radiol* 2010;74:121–23 CrossRef Medline
26. Wong PY, Lingam RK, Pal S, et al. **Monitoring progression of 12 cases of non-operated middle ear cholesteatoma with non-echo-planar diffusion weighted magnetic resonance imaging: our experience.** *Otol Neurotol* 2016;37:1573–76 CrossRef Medline
27. McRackan TR, Abdellatif WM, Wanna GB, et al. **Evaluation of second look procedures for pediatric cholesteatomas.** *Otolaryngol Head Neck Surg* 2011;145:154–60 CrossRef Medline
28. Garrido L, Cenjor C, Montoya J, et al. **Diagnostic capacity of non-echo planar diffusion-weighted MRI in the detection of primary and recurrent cholesteatoma.** *Acta Otorrinolaringol Esp* 2015;66:199–204 CrossRef Medline

# Radiologic and Pathologic Features of the Transmantle Sign in Focal Cortical Dysplasia: The T1 Signal Is Useful for Differentiating Subtypes

Yukio Kimura, A. Shioya, Y. Saito, Y. Oitani, Y. Shigemoto, E. Morimoto, F. Suzuki, N. Ikegaya, Yuiko Kimura, K. Iijima, Y. Takayama, M. Iwasaki, M. Sasaki, and N. Sato



## ABSTRACT

**BACKGROUND AND PURPOSE:** The transmantle sign is a characteristic MR imaging finding often seen in focal cortical dysplasia type IIb. The transmantle sign is typically hyperintense on T2WI and FLAIR and hypointense on T1WI. However, in some cases, it shows T1 high signal. We evaluated the imaging and pathologic findings to identify the causes of the T1 high signal in the transmantle sign.

**MATERIALS AND METHODS:** We retrospectively reviewed the preoperative imaging data of 141 consecutive patients with histologically proved focal cortical dysplasia. We selected 25 patients with focal cortical dysplasia with the transmantle sign and divided them into groups based on the pathologic focal cortical dysplasia subtype and T1 signal of the transmantle sign. We evaluated the clinical, radiologic, and pathologic findings, including the number of balloon cells and dysmorphic neurons and the severity of gliosis or calcifications and compared them among the groups.

**RESULTS:** Nine of the 25 patients had a T1-high-signal transmantle sign; the other 16 patients did not. All 9 patients with a T1-high-signal transmantle sign were diagnosed as type IIb (group A). Of the 16 patients with no T1-high-signal transmantle sign, 13 were diagnosed as having type IIb (group B), and the other 3 patients, as type IIa (group C). The number of balloon cells was significantly higher in group A than in the other groups, but there were no differences regarding dysmorphic neurons, the severity of gliosis, or calcifications.

**CONCLUSIONS:** Approximately 6% (9/141) of this patient series had a T1-high-signal transmantle sign, and all were type IIb. The signal may reflect a rich density of balloon cells. This finding could support the differentiation of subtypes, especially type IIb.

**ABBREVIATIONS:** FCD = focal cortical dysplasia; ILAE = International League Against Epilepsy; KB = Klüver-Barrera; TMS = transmantle sign

Focal cortical dysplasia (FCD) is a localized cerebral cortical malformation frequently associated with drug-resistant focal epilepsy.<sup>1</sup> It is critical to identify the epileptogenic focus when planning surgery. The pathologic features of FCD range from

mild cortical dyslamination to more severe forms.<sup>2</sup> The typical MR imaging features of FCD include gray-white matter blurring, cortical thickening, white matter hypointensities on T1WI and increased signal intensity on T2WI and FLAIR images, and localized brain atrophy.<sup>1,3,4</sup> However, it is sometimes difficult to detect such FCD features when the signal intensity is mild or the abnormality is slight.

We recently treated several patients with FCD who showed the transmantle sign (TMS), which exhibits high signal intensity not only on T2WI and FLAIR but also on T1WI. These T1-high-signal areas matched the areas of the TMS, TMS is characterized by abnormal signal intensity expanding from the deep white matter to the surface and is a distinctive MR imaging finding of type IIb FCD.<sup>1,5-7</sup> To the best of our knowledge, only 1 study has reported such atypical signal intensity,<sup>8</sup> and no study has examined the etiology of these signal abnormalities. We performed the present study to evaluate the signal intensity of the TMS and its correlation with pathologic findings in patients with FCD.

Received February 3, 2019; accepted after revision March 27.

From the Department of Radiology (Yukio K., Y. Shigemoto, E.M., F.S., N.S.), National Center Hospital, National Center of Neurology and Psychiatry, Kodaira, Tokyo, Japan; Departments of Pathology and Laboratory Medicine (A.S., Y. Saito), Child Neurology (Y.O., M.S.), and Neurosurgery (N.I., Yuiko K., K.I., Y.T., M.I.), National Center of Neurology and Psychiatry, Kodaira, Tokyo, Japan; Department of Neurology (A.S.), Mito Kyodo General Hospital, University of Tsukuba, Tsukuba, Ibaraki, Japan; Department of Pediatrics (Y.O.), Tokyo Women's Medical University Medical Center East, Tokyo, Japan; and Department of Neurosurgery (N.I.), Yokohama City University, Yokohama, Kanagawa, Japan.

This work was funded by a grant from the Japan Society for the Promotion of Science (KAKENHI grant No. 17K10423).

Please address correspondence to Noriko Sato, MD, Department of Radiology, National Center of Neurology and Psychiatry, 4-1-1 Ogawa-Higashi, Kodaira, Tokyo 187-8551, Japan; e-mail: snoriko@ncnp.go.jp

Indicates open access to non-subscribers at [www.ajnr.org](http://www.ajnr.org)

Indicates article with supplemental on-line table.

<http://dx.doi.org/10.3174/ajnr.A6067>

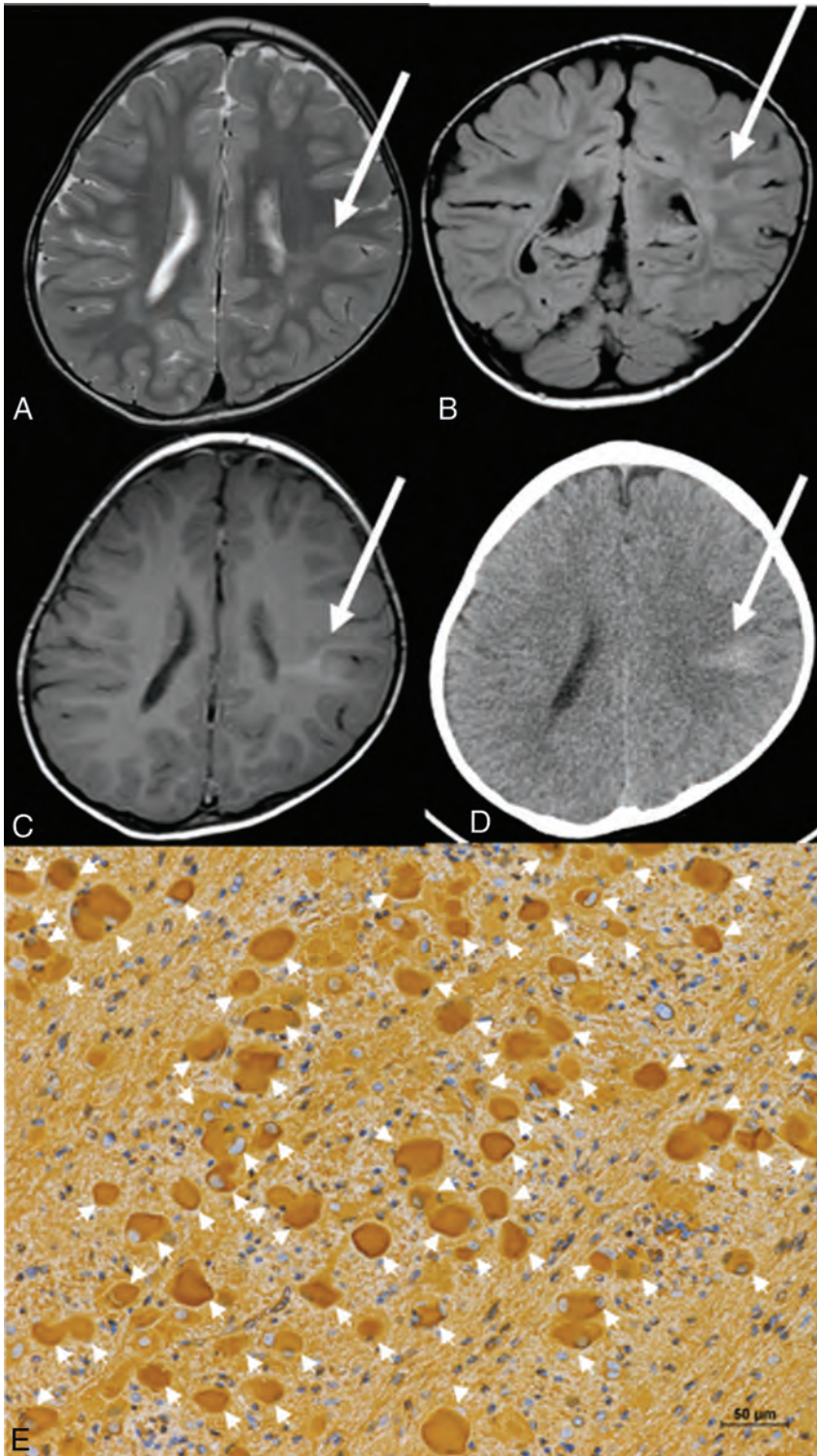


**FIG 1.** Case 1, in group A. Axial T2WI (A), coronal FLAIR (B), axial T1WI (C), and CT (D). T2WI and FLAIR images obtained at 23 months of age demonstrate a focal hyperintensity area from the bottom of the sulcus to the lateral ventricle, which represents the transmantle sign of FCD in the left parietal lobe (arrows, A and B). The T1WI also shows hyperintensity in the same area (arrow, C). The CT image shows high density (arrow, D). E, Photomicrograph shows many balloon cells (arrowheads), stained with vimentin (magnification  $\times 200$ ). Scale bars: 50  $\mu\text{m}$ .

## MATERIALS AND METHODS

### Patients

We retrospectively reviewed the preoperative MR imaging data of 141 consecutive patients with histologically proved FCD who under-

went an operation for refractory epilepsy between March 2008 and January 2018 at the National Center of Neurology and Psychiatry, Tokyo, Japan. All enrolled patients were diagnosed on the basis of the histologic classification system proposed by the International League Against Epilepsy (ILAE).<sup>9</sup> There were 25 cases of FCD with TMS; 22 cases were type IIb and the other 3 cases were type IIa. The TMS was identified by the following definition: “a markedly hyperintense funnel shaped subcortical zone tapering toward the lateral ventricle was the characteristic finding on FLAIR MR imaging.”<sup>10</sup> The present retrospective study was approved by the institutional review board at the National Center of Neurology and Psychiatry Hospital, and the need for patient informed consent was waived.

We investigated clinical data including sex, age at operation, age at the onset of seizure, seizure frequency, surgery site, and postoperative seizure outcome in the 25 patients with FCD with TMS. Postoperative seizure outcome was determined at the patient’s last follow-up ( $\geq 12$  months) using the ILAE criteria.<sup>11</sup> For statistical analysis, ILAE outcomes 1 and 2 (seizure freedom or only auras since surgery) were regarded as a good outcome, and ILAE outcomes 3–6, as a poor outcome.

### Imaging Analysis

All patients underwent MR imaging in a 1.5T (Magnetom Symphony; Siemens, Erlangen, Germany) or 3T (Achieva, Philips Healthcare, Best, the Netherlands, or Magnetom Verio, Siemens) system with a standard head coil. Sequences included routine structural images: axial T1WI, axial T2WI, and FLAIR images. Spin-echo T1WI was acquired with the following parameters: TR/TE/NEX = 600–613 ms/9.4–15 ms/1, matrix = 201–230  $\times$  183–256, FOV = 25 cm, section thickness = 3–5 mm. Turbo spin-echo T2WI was performed with the following parameters: TR/TE/NEX = 3800–5000 ms/80–95 ms/1–2, matrix = 291–365  $\times$  368–512, FOV = 25 cm, section thickness = 3–5 mm. FLAIR images were acquired with the following parameters: TR/TE/NEX = 9000–12,000 ms/101–120 ms/2500–2700 ms/1, matrix = 179–202  $\times$  256–320, FOV = 25 cm, section thickness = 3–5 mm. Axial and coronal FLAIR images were obtained using the same parameters.

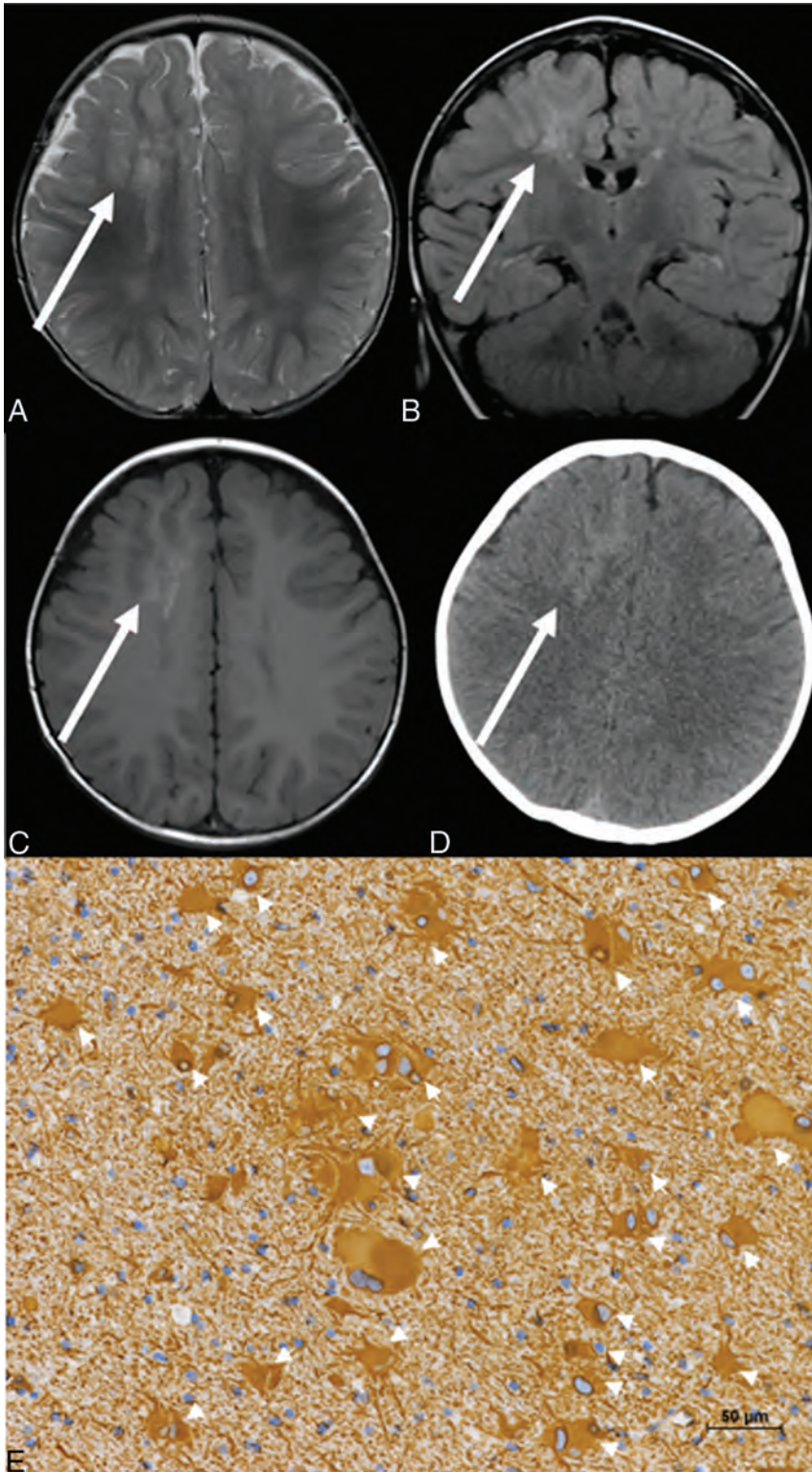


**FIG 2.** Case 2, in group A. Axial T2WI (A), coronal FLAIR (B), axial T1WI (C), and CT (D). T2WI and FLAIR images obtained at 13 months of age demonstrate focal hyperintensity in the white matter of the right frontal lobe, representing the TMS (arrows, A and B). The T1WI also shows hyperintensity in the same area (arrow, C). The CT scan shows high density (arrow, D). E, Photomicrograph shows many balloon cells observed (arrowheads), and they are stained with vimentin (magnification  $\times 200$ ). Scale bars: 50  $\mu\text{m}$ .

Two neuroradiologists (Yukio Kimura and Yoko Shigemoto with 14 and 10 years of experience in neuroradiology, respectively) independently evaluated all images to assess the signal in-

tensity of the TMS on T1WI, T2WI, and FLAIR images and the density on CT. The differences in evaluations were resolved by consensus.

### Pathologic Methods

All specimens were diagnosed by experienced neuropathologists. For all patients, 4% paraformaldehyde-fixed paraffin-embedded tissues of the resection specimens were available. All the examined resected tissues were treated identically, grossly inspected, and measured. After representative small sections were fixed in glutaraldehyde or frozen, the remaining sections were fixed in 4% paraformaldehyde. The specimens were cut to obtain representative tissue slices perpendicular to the cortical surface. The specimens were cut into evaluable sections; 6- $\mu\text{m}$ -thick serial sections were stained with antibodies to vimentin or anti-neurofilament H nonphosphorylated antibody (SMI-32), as well as routine hematoxylin-eosin and Klüver-Barrera (KB) stains. One neuropathologist (A.S.) counted the number of balloon cells and dysmorphic neurons of each case in the FOV with the greatest number at  $\times 200$  magnification in the TMS areas using vimentin and SMI-32 stains, respectively, in addition to the KB stain. The severity of gliosis was classified into normal, mild, moderate, and severe. The degree of calcification in the same areas was classified into absence, slight presence, and presence.

### Statistical Analysis

We divided the patients into groups based on their pathologic FCD subtype and the T1 signal of the TMS. We compared the groups' ages at the onset of seizure, severity of gliosis, and number of balloon cells and dysmorphic neurons using nonparametric tests, ie, the Kruskal-Wallis or Mann-Whitney *U* test. Regarding the postoperative seizure outcomes, we analyzed the categorical variables using the  $\chi^2$  test. A *P* value  $< .05$  was considered significant. All statistical analyses were performed with SPSS, Version 25.0 software (IBM, Armonk, New York).

## RESULTS

The details of the clinical demographics and radiologic and pathologic findings of the 25 patients with FCD with the TMS are

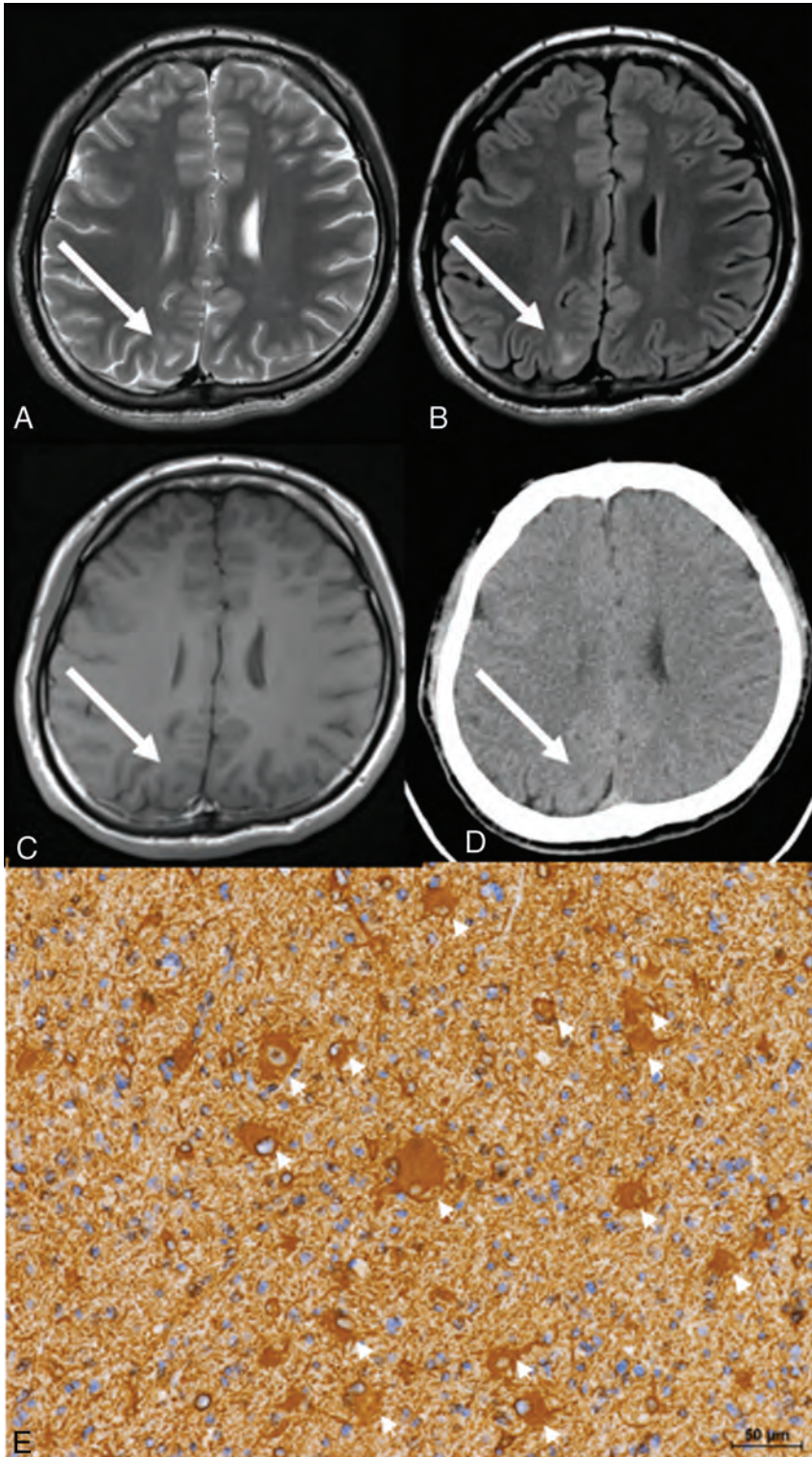


**FIG 3.** Case 17, in group B. Axial T2WI (A), axial FLAIR (B), axial T1WI (C), and CT (D). T2WI and FLAIR images obtained at 23 years of age demonstrate focal hyperintensity in the subcortical area extending to the ventricle of the right abnormal parietal gyrus, indicating the TMS (arrows, A and B). T1WI shows low intensity in the same area (arrow, C). CT shows low density (arrow, D). E, Photomicrograph shows a few balloon cells (arrowheads), stained with vimentin (magnification  $\times 200$ ). Scale bars: 50  $\mu\text{m}$ .

summarized in the On-line Table. We divided the patients into 3 groups based on their pathologic FCD subtype and the T1 signal of the TMS. Nine of the 25 patients had T1-high-signal

TMS, and the other 16 patients had no T1-high-signal TMS. All 9 patients with T1-high-signal TMS had been diagnosed with FCD type IIb (group A: 3 boys and 6 girls; median age, 7 years; mean age,  $6.6 \pm 5.9$  years) (Figs 1 and 2). Among the 16 patients with no T1-high-signal TMS, 13 patients had been diagnosed with FCD type IIb (group B: 8 males and 5 females; median age, 21 years; mean age,  $21.7 \pm 14.1$  years) (Fig 3) and the other 3 patients had been diagnosed with FCD type IIa (group C: 3 girls; median age, 15 years; mean age,  $13.3 \pm 8.6$  years). There were no patients with FCD type IIa with T1-high-signal TMS.

Among the 3 groups, there were no significant differences in the age at seizure onset ( $P = .24$ ) or the seizure outcomes ( $P = .54$ ). In group A, 8 patients had good postoperative seizure outcomes (ILAE class 1: seven patients, and class 2: one patient), and the remaining (ninth) patient had a poor outcome (ILAE class 5). In group B, 10 patients had good outcomes (ILAE class 1: nine patients, and class 2: one patient) and the other 3 patients had poor outcomes (ILAE class 5). All 3 patients in group C had good outcomes (ILAE class 1).

On the T2WI and FLAIR imaging, all patients showed hyperintensity in the TMS. On CT, high density was observed in the TMS in all 9 patients of group A. The hyperintense areas on T1WI matched the areas of high density on CT scans. Among the patients in groups B and C, though areas of slightly high density in the TMS were observed on CT in 5 patients, their densities were lower than those in the group A.

Our pathologic analysis revealed significantly more balloon cells in group A compared with group B with both KB ( $P = .007$ ) and vimentin ( $P = .011$ ) stains (Fig 4), but there was no significant difference concerning dysmorphic neurons among the 3 groups in KB ( $P = .69$ ) and SMI-32 ( $P = .52$ ) stains (Fig 5). There was no significant difference in the severity of gliosis among the 3 groups ( $P = .93$ ). Microcalcification was observed in 4 patients

in group A, but in 3 of the 4 patients, the microcalcification was imperceptible. Microcalcifications were absent in groups B and C.

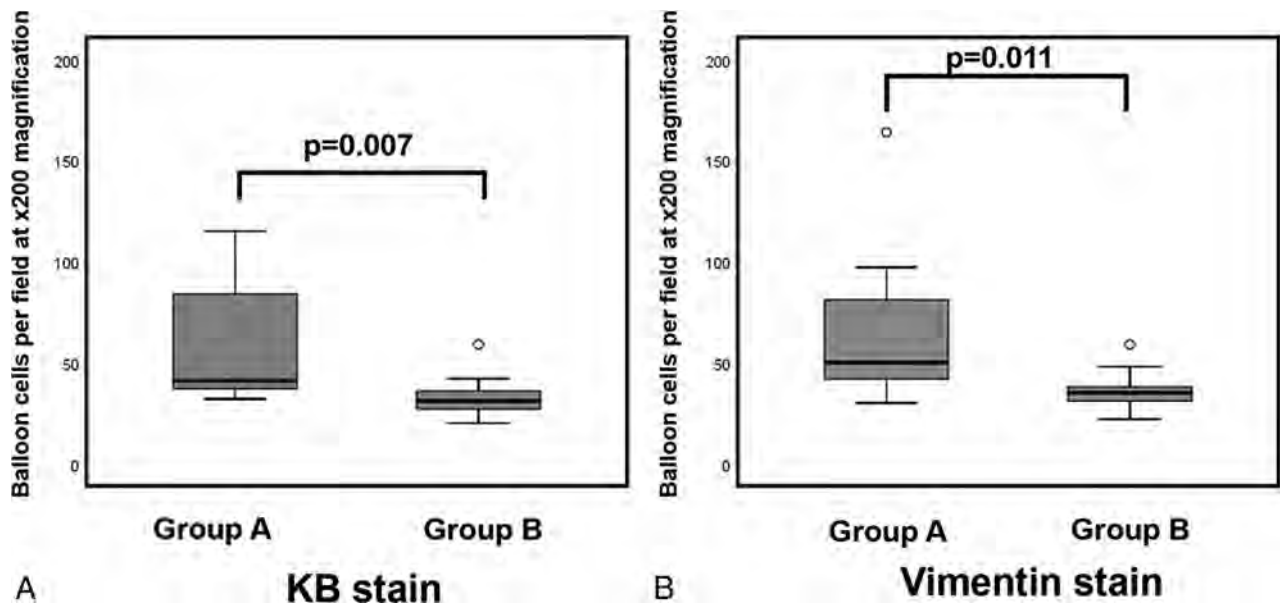


**FIG 4.** The greatest number of cells counted in the FOV at  $\times 200$  magnification. Group differences in the number of balloon cells with KB (A) and vimentin (B) stains. The *boxplot* shows the minimum, first quartile, median, third quartile, and maximum. Outliers are shown as *small circles*. The number of balloon cells is significantly higher in group A versus group B in both stains. There were no balloon cells in group C (data not shown).

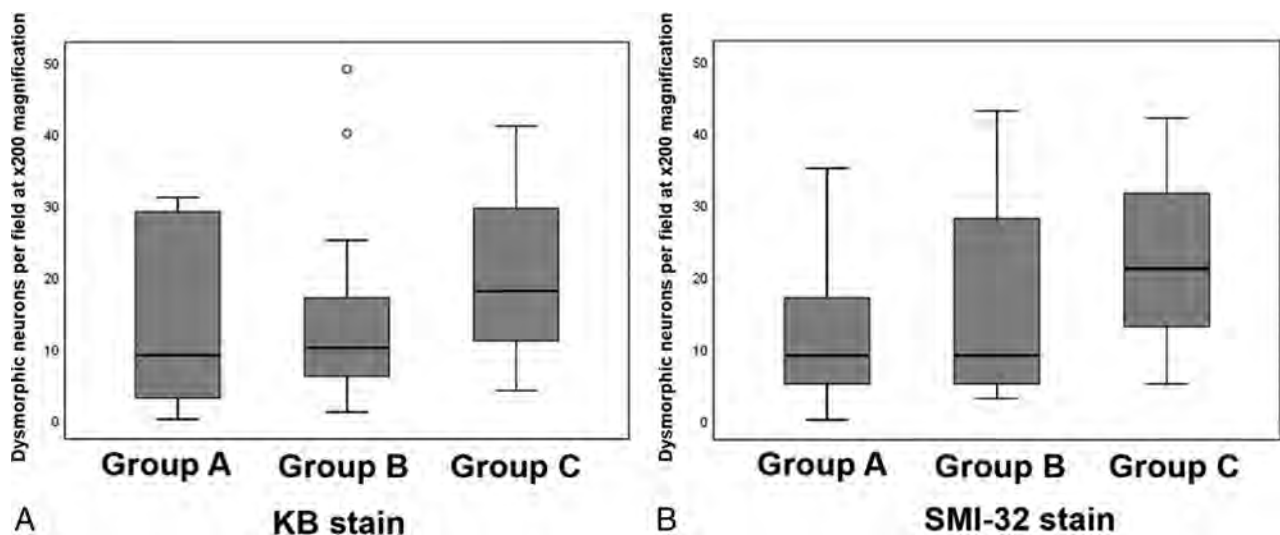


**FIG 5.** The greatest number of cells counted in the FOV at  $\times 200$  magnification. Group differences in the number of dysmorphic neurons in KB (A) and SMI-32 (B) stains. The *boxplot* shows the minimum, first quartile, median, third quartile, and maximum. Outliers are shown as *small circles*. No significant difference in the cell numbers is shown by both stains.

## DISCUSSION

We reviewed the clinical, radiologic, and pathologic findings in a series of patients with T1 high signal in the TMS. To the best of our knowledge, this is the first attempt to identify the etiology of the T1 high signal of the TMS by investigating the imaging and pathologic findings. The results of our analysis demonstrated that there were significantly more balloon cells in the T1-high-signal group than the non-T1-high-signal group, but no evidence of differences regarding dysmorphic neurons, the severity of gliosis, or calcifications. We therefore speculate the following: 1) The density of the balloon cells may be associated with the T1 high signal, and 2) our findings could help diagnose the FCD subtype, more specifically FCD type IIb.

According to the current ILAE classification system,<sup>9</sup> the pathology of FCD is classified into 3 types: Type I has isolated cor-

tical dyslamination, type II has dysmorphic neurons with or without balloon cells in addition to cortical dyslamination, and type III occurs alongside another lesion (eg, hippocampal sclerosis, tumors, or vascular malformations).<sup>5,9</sup> The histopathologic hallmark of type IIb FCD is the presence of balloon cells, which have an enlarged cell body with eosinophilic cytoplasm and are present in all layers but tend to concentrate in the upper layers and white matter.<sup>12,13</sup> Several studies indicate that balloon cells are not epileptogenic.<sup>14,15</sup> Although the exact role of balloon cells remains obscure, several studies have found evidence of an increase in the mechanisms leading to glutamate clearance in areas containing balloon cells, thus reducing the spread of epileptogenic activity.<sup>16,17</sup> Balloon cells could play a protective and/or antiepileptic role.<sup>12</sup>

The TMS is the main radiologic landmark of FCD type II, but it is more frequently detected in patients with type IIb than type IIa and is the only MR imaging feature that can be used to accurately identify type IIb.<sup>1,5-7</sup> The etiology of the signal changes in the TMS is thought to be some combination of gliosis, hypomyelination or dysmyelination, neuronal heterotopia, and balloon cells,<sup>6,11</sup> though an exact correlation has yet to be verified. The TMS is typically hyperintense on T2WI and FLAIR and hypointense on T1WI.<sup>18</sup> However, some patients have shown T1 high signal. Our present pathologic study reveals that there are more balloon cells in the T1-high-signal group, but there are no significant between-group differences in the number of dysmorphic neurons or the severity of gliosis. Our results suggest that the density of the balloon cells may be associated with the T1 high signal. In addition, there was no T1 high signal in the other types of FCD. The T1 high signal in the TMS may thus be regarded as evidence of type IIb.

Eltze et al<sup>19</sup> reported patients with FCD who had shown T1 hyperintensity during the first year of their lives, but it was difficult to identify them by the process of myelination. The degree of myelination may be an additional factor to evaluate the MR imaging signal intensity of FCD in infants. In our study, only 1 patient was younger than 1 year of age (case 9 in group 1). However, she had undergone an operation at 5 months, and we could not observe the signal changing appearances.

Compared with other FCDs without the TMS, the presence of the TMS indicated a high likelihood of a seizure-free outcome.<sup>20,21</sup> Detecting these lesions during a preoperative examination is important for surgical decision-making and improving postoperative outcomes.<sup>1,22,23</sup> If the preoperative MR imaging indicates type IIb, a favorable prognosis can be expected after surgery.

Several research groups have reported the hyperintensity of FCD and cortical tubers of tuberous sclerosis on T1-weighted images with magnetization transfer contrast.<sup>8,24-26</sup> Although Kadom et al<sup>8</sup> did not describe the type of FCD, these T1 hyperintensities with magnetization transfer contrast may reflect the presence of balloon cells. The cortical tubers also show MR imaging findings, known as the radially oriented white matter band, that are similar to the TMS of FCD type IIb.<sup>27-29</sup> Magnetization transfer contrast is a technique for improving image contrast in MR imaging, based on the difference in magnetic field-induced frequencies between mobile free water protons and macromolecular bound protons.<sup>26,30</sup> Pinto Gama et al<sup>25</sup> noted that the density of cells and calcium deposition may also play a role by causing shortening of the water T1, leading to a decrease in the effectiveness of signal suppression by magnetization transfer contrast. However, in the present study, there were few cases with sparse calcifications in the pathologic findings, and the association between high density on CT and calcifications was weak. We therefore suspect that the high density on CT was due not to calcification but rather to a high cell concentration, especially of the balloon cells themselves. In addition, even in cases without calcifications in pathologic findings, T1 high signal was observed, and we consider that calcifications were not necessarily associated with T1 high signal in our patients.

This study has some limitations. First, the sample size of T1-high-signal FCD cases was small (9 patients). However, we were

able to detect significant relationships with the balloon cell concentration. Many cases should be examined to test this result. Second, the internal structure of the balloon cell has not been clarified. Further pathologic studies are needed to validate this information.

## CONCLUSIONS

Some cases of FCD type IIb have T1 high signal in the TMS. The density of balloon cells may be associated with this phenomenon, and this information would be useful for differentiating FCD subtypes and contributing to the diagnosis of FCD and its subtypes, especially type IIb.

Disclosures: Yukio Kimura—RELATED: Grant: The Japan Society for the Promotion of Science (KAKENHI grant No. 17K10423)\* \*Money paid to the institution.

## REFERENCES

- Colombo N, Tassi L, Deleo F, et al. **Focal cortical dysplasia type IIa and IIb: MRI aspects in 118 cases proven by histopathology.** *Neuroradiology* 2012;54:1065–77 CrossRef Medline
- Palmini A, Najm I, Avanzini G, et al. **Terminology and classification of the cortical dysplasias.** *Neurology* 2004;62(6 Suppl 3):S2–8 Medline
- Lerner JT, Salamon N, Hauptman JS, et al. **Assessment and surgical outcomes for mild type I and severe type II cortical dysplasia: a critical review and the UCLA experience.** *Epilepsia* 2009;50:1310–35 CrossRef Medline
- Colombo N, Salamon N, Raybaud C, et al. **Imaging of malformations of cortical development.** *Epileptic Disord* 2009;11:194–205 Medline
- Adler S, Lorio S, Jacques TS, et al. **Towards in vivo focal cortical dysplasia phenotyping using quantitative MRI.** *Neuroimage Clin* 2017;15:95–105 CrossRef Medline
- Mühlebner A, Coras R, Kobow K, et al. **Neuropathologic measurements in focal cortical dysplasias: validation of the ILAE 2011 classification system and diagnostic implications for MRI.** *Acta Neuropathol* 2012;123:259–72 CrossRef Medline
- Kim DW, Kim S, Park SH, et al. **Comparison of MRI features and surgical outcome among the subtypes of focal cortical dysplasia.** *Seizure* 2012;21:789–94 CrossRef Medline
- Kadom N, Trofimova A, Vezina GL. **Utility of magnetization transfer T1 imaging in children with seizures.** *AJNR Am J Neuroradiol* 2013;34:895–98 CrossRef Medline
- Blümcke I, Mühlebner A. **Neuropathological work-up of focal cortical dysplasias using the new ILAE consensus classification system: practical guideline article invited by the Euro-CNS Research Committee.** *Clin Neuropathol* 2011;30:164–77 CrossRef Medline
- Urbach H, Scheffler B, Heinrichsmeier T, et al. **Focal cortical dysplasia of Taylor's balloon cell type: a clinicopathological entity with characteristic neuroimaging and histopathological features, and favorable postsurgical outcome.** *Epilepsia* 2002;43:33–40 Medline
- Wieser HG, Blume WT, Fish D, et al; Commission on Neurosurgery of the International League Against Epilepsy (ILAE). **ILAE Commission Report: proposal for a new classification of outcome with respect to epileptic seizures following epilepsy surgery.** *Epilepsia* 2001;42:282–86 Medline
- Leach JL, Greiner HM, Miles L, et al. **Imaging spectrum of cortical dysplasia in children.** *Semin Roentgenol* 2014;49:99–111 CrossRef Medline
- Abdijadid S, Mathern GW, Levine MS, et al. **Basic mechanisms of epileptogenesis in pediatric cortical dysplasia.** *CNS Neurosci Ther* 2015;21:92–103 CrossRef Medline
- Cepeda C, André VM, Vinters HV, et al. **Are cytomegalic neurons and balloon cells generators of epileptic activity in pediatric cortical dysplasia?** *Epilepsia* 2005;46:82–88 CrossRef Medline
- Marusic P, Najm IM, Ying Z, et al. **Focal cortical dysplasias in elo-**

- quent cortex: functional characteristics and correlation with MRI and histopathologic changes. *Epilepsia* 2002;43:27–32 Medline
16. Gonzalez-Martinez JA, Ying Z, Prayson R, et al. **Glutamate clearance mechanisms in resected cortical dysplasia.** *J Neurosurg* 2011;114:1195–202 CrossRef Medline
  17. Boonyapisit K, Najm I, Klem G, et al. **Epileptogenicity of focal malformations due to abnormal cortical development: direct electrocorticographic-histopathologic correlations.** *Epilepsia* 2003;44:69–76 Medline
  18. Mellerio C, Labeyrie MA, Chassoux F, et al. **Optimizing MR imaging detection of type 2 focal cortical dysplasia: best criteria for clinical practice.** *AJNR Am J Neuroradiol* 2012;33:1932–38 CrossRef Medline
  19. Eltze CM, Chong WK, Bhatte S, et al. **Taylor-type focal cortical dysplasia in infants: some MRI lesions almost disappear with maturation of myelination.** *Epilepsia* 2005;46:1988–92 CrossRef Medline
  20. Yao K, Mei X, Liu X, et al. **Clinical characteristics, pathological features and surgical outcomes of focal cortical dysplasia (FCD) type II: correlation with pathological subtypes.** *Neurol Sci* 2014;35:1519–26 CrossRef Medline
  21. Wang DD, Deans AE, Barkovich AJ, et al. **Transmantle sign in focal cortical dysplasia: a unique radiological entity with excellent prognosis for seizure control.** *J Neurosurg* 2013;118:337–44 CrossRef Medline
  22. Berg AT, Vickrey BG, Langfitt JT, et al; Multicenter Study of Epilepsy Surgery. **The multicenter study of epilepsy surgery: recruitment and selection for surgery.** *Epilepsia* 2003;44:1425–33 Medline
  23. Bien CG, Szinay M, Wagner J, et al. **Characteristics and surgical outcomes of patients with refractory magnetic resonance imaging-negative epilepsies.** *Arch Neurol* 2009;66:1491–99 CrossRef Medline
  24. Rugg-Gunn FJ, Eriksson SH, Boulby PA, et al. **Magnetization transfer imaging in focal epilepsy.** *Neurology* 2003;60:1638–45 CrossRef Medline
  25. Pinto Gama HP, da Rocha AJ, Braga FT, et al. **Comparative analysis of MR sequences to detect structural brain lesions in tuberous sclerosis.** *Pediatr Radiol* 2006;36:119–25 CrossRef Medline
  26. Girard N, Zimmerman RA, Schnur RE, et al. **Magnetization transfer in the investigation of patients with tuberous sclerosis.** *Neuroradiology* 1997;39:523–28 CrossRef Medline
  27. Kokkinos V, Kallifatidis A, Kapsalaki EZ, et al. **Thin isotropic FLAIR MR images at 1.5T increase the yield of focal cortical dysplasia transmantle sign detection in frontal lobe epilepsy.** *Epilepsy Res* 2017;132:1–7 CrossRef Medline
  28. Soares BP, Porter SG, Saindane AM, et al. **Utility of double inversion recovery MRI in paediatric epilepsy.** *Br J Radiol* 2016;89:20150325 CrossRef Medline
  29. Yagishita A, Arai N. **Cortical tubers without other stigmata of tuberous sclerosis: imaging and pathological findings.** *Neuroradiology* 1999;41:428–32 CrossRef Medline
  30. Wolff SD, Balaban RS. **Magnetization transfer contrast (MTC) and tissue water proton relaxation in vivo.** *Magn Reson Med* 1989;10:135–44 CrossRef Medline

# Radiation Dose and Image Quality in Pediatric Neck CT

S.V. Tipnis, W.J. Rieter, D. Patel, S.T. Stalcup, M.G. Matheus, and M.V. Spampinato

## ABSTRACT

**BACKGROUND AND PURPOSE:** Optimization of pediatric neck CT protocols is of critical importance in order to maintain good diagnostic image quality while reducing the radiation burden. Our aim was to evaluate the image quality of pediatric neck CT studies before and after the implementation of a low radiation dose protocol.

**MATERIALS AND METHODS:** We retrospectively reviewed 179 pediatric neck CT studies, 75 before and 104 after the implementation of low-dose protocols, performed in children 0–16 years of age. The 2 cohorts were divided into 3 age groups, 0–4, 5–9, and 10–16 years. The signal-to-noise ratio was calculated using the axial image through the true vocal folds. Three neuroradiologists assessed the image quality of the same CT scan using a 5-point scoring system. We compared the CT dose index volume, dose-length product, image-quality ratings, and SNR of studies conducted at baseline and with low-dose protocols.

**RESULTS:** Image-quality ratings were lower in the low-dose than in the baseline cohort in children 10–16 years of age, but not in children 0–4 and 5–9 years of age. The SNR was lower in the low-dose cohort than in the baseline cohort in children 0–4 and 10–16 years of age, but not in children 5–9 years of age. Despite the decrease in image-quality scores in older children, 97% of the studies (73/75) in the baseline cohort and 96% of studies (100/104) in the low-dose cohort were considered of sufficient image quality.

**CONCLUSIONS:** Images acquired with the low-dose CT protocols were deemed to be of sufficient quality for making a clinical diagnosis. Our initial results suggest that there may be an opportunity for further radiation dose reduction without compromising diagnostic image quality using iterative reconstruction algorithms.

**ABBREVIATIONS:** CTDI<sub>vol</sub> = CT dose index volume; DLP = dose-length product

Pediatric CT volume has rapidly increased in the United States since the introduction of helical and multidetector CT, which allow fast image acquisition and a decreased need for moderate sedation.<sup>1–5</sup> Because of the smaller size of the patients and higher radiation sensitivity, pediatric CT poses some unique challenges in terms of achieving diagnostic-quality images with the least possible radiation burden to the patients.<sup>4,6–12</sup> Optimization of a pediatric neck CT protocol is of utmost importance because in this study, the thyroid gland, one of the most radiosensitive organs, is

directly exposed to the x-ray beam.<sup>13–15</sup> Thus, it is critical that the examination be clinically indicated, with a high benefit-to-risk ratio. All CT examinations should be optimized to yield diagnostic images at the lowest possible radiation dose, following the principle of as low as reasonably achievable (ALARA).

We conducted a departmental quality-improvement project to optimize pediatric neck CT protocols. The goal of this study was to minimize the radiation exposure to patients while maintaining the required diagnostic image quality. This was done by reviewing and scoring baseline scans acquired with unoptimized CT protocols; applying appropriate dose-reduction criteria including age-stratification to optimize the image acquisition; and finally reviewing and scoring the images in the follow-up cohort to confirm their diagnostic value.

## MATERIALS AND METHODS

This study was approved by the institutional review board with a waiver of informed consent. The patient population included a baseline cohort and a follow-up cohort that underwent neck

Received December 19, 2018; accepted after revision April 18, 2019.

From the Department of Radiology and Radiological Science (S.V.T., W.J.R., D.P., S.T.S., M.G.M., M.V.S.) and Center for Biomedical Imaging (M.V.S.), Medical University of South Carolina, Charleston, South Carolina.

Paper previously presented at: American Society of Neuroradiology Annual Meeting and the Foundation of the ASNR Symposium, June 2–7, 2018; Vancouver, British Columbia, Canada.

Please address correspondence to Maria Vittoria Spampinato, MD, Department of Radiology and Radiological Science, Medical University of South Carolina, 96 Jonathan Lucas, MSC 323, Charleston, SC 29425; e-mail: spampin@musc.edu; @mvspampinato

<http://dx.doi.org/10.3174/ajnr.A6073>

**Table 1: Total number of patients and distribution of patient age and sex in the 3 age groups of the study**

Group	0–4 yr	5–9 yr	10–16 yr	0–16 yr
Baseline cohort				
♂	10	11	20	41
♀	7	7	20	34
Total (No.)	17	18	40	75
Follow-up cohort				
♂	17	17	21	55
♀	8	9	32	49
Total (No.)	25	26	53	104

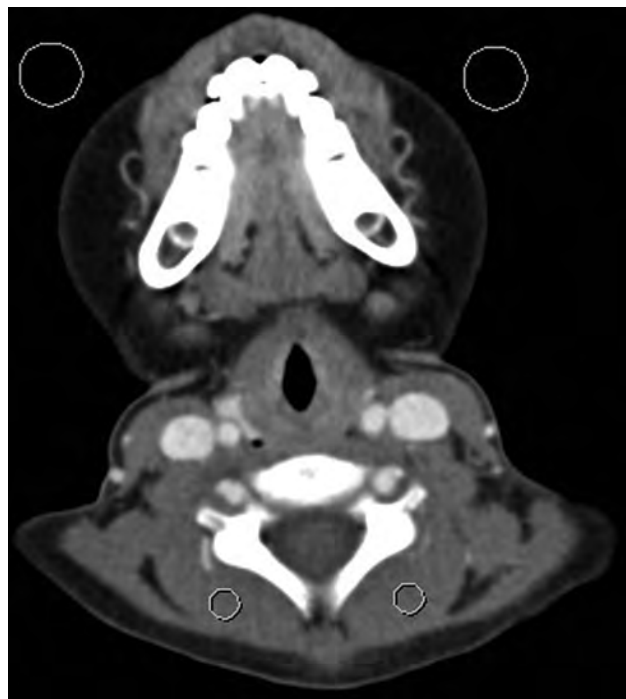


**FIG 1.** Representative CT image of a 6-year-old boy at the level of the vocal cords for assessment of the signal-to-noise ratio. Background noise was estimated as the average SD in Hounsfield units of 2 ROIs drawn over the air anterior to the patient (*large circles*). Signal was estimated as the average attenuation in Hounsfield units of 2 ROIs drawn over the paraspinal musculature (*small circles*).

CT examinations before and after the implementation of optimized, age-specific, pediatric neck CT protocols at our institution.

### Patient Population

Both the baseline and the follow-up cohorts in the study were identified by searching the PACS. Because of the differences in the body habitus of the patient population between 0 and 16 years of age, we thought it necessary to divide each cohort into 3 age groups to make a proper comparison. Accordingly, the study compared the examinations between the 2 cohorts in 3 distinct subgroups of 0–4, 5–9, and 10–16 years of age. We used the age-classification scheme for pediatric CT protocols proposed by Paolicchi et al.<sup>16</sup> We changed the age range for the older age group from 10–14 years to 10–16 years because at our institution, we use pediatric neck CT protocols in patients 16 years of age or younger.

For the baseline cohort, we retrospectively reviewed all neck CT examinations acquired at our institution in patients 16 years

**Table 2: Interpretation of the subjective image-quality scores for the individual, prelabeled CT image slices at the level of the vocal cords**

Score	Comment
1	Image quality very poor (significant noise and/or artifacts, study uninterpretable)
2	Image quality poor (noise and/or artifacts, can only answer broad clinical questions)
3	Image quality adequate (some noise and/or artifacts, but study interpretable)
4	Above-average image quality (minimal noise and/or artifacts)
5	Excellent image quality (imperceptible noise and free of artifacts)

of age or younger between May 2013 and April 2014. Scans acquired as part of radiation planning, studies for which the radiation dose summary sheet was not available on the PACS, those conducted without the use of automatic tube current modulation, and those with significant artifacts due to motion or hardware were excluded from the study. Thus, a total of 75 pediatric neck CT examinations were included in the baseline cohort. For the follow-up cohort, we retrospectively reviewed all neck CT examinations acquired at our institution in patients 16 years of age or younger between February 2016 and January 2017 using the modified, reduced-dose, and age-specific acquisition protocols. With the same exclusion criteria used for the baseline cohort, we selected a total of 104 pediatric neck CT examinations for the follow-up cohort. Table 1 shows the distribution of patients in the 2 cohorts and the 3 age groups.

### Image Acquisition

All neck CT examinations were helical acquisitions from the forehead to the thoracic inlet and were acquired with tube current modulation on multidetector CT scanners (Somatom Sensation 64, Somatom Definition 64, or Somatom Definition Flash; Siemens, Erlangen, Germany). The scans were obtained using the manufacturer-provided automatic tube current modulation algorithms (CARE Dose4D; Siemens), with a pitch of 0.8–1.2 depending on the scanner, and using a display FOV ranging from 13 to 25 cm. Scans were obtained following administration of a non-ionic iodinated contrast agent (2 mL/kg of body weight) and following a 90-second delay from the start of the contrast injection. Demographic data (age and sex) were obtained for each patient. Acquisition parameters, including the kilovolt, milliamperes-seconds, and CT dose index volume ( $CTDI_{vol}$ ) (corresponding to a 32-cm acrylic dosimetry phantom) were obtained from dose-report sheets imported into the PACS. Note that the vendor software uses the 32-cm phantom for all head and neck scans by default while using the 16-cm phantom for the head scans. We believe that the inclusion of the shoulder region in the scans is the primary reason for using the 32-cm phantom for the head and neck scans, as opposed to the 16-cm phantom (which is used in the head scans alone).

Subjective and quantitative image-quality assessment (described in detail the following 2 sections) was conducted by 3 board-certified neuroradiologists for the baseline cohort. Most studies (97%) in the baseline cohort were deemed of diagnostic quality by the reviewers. On the basis of these data, we adjusted

**Table 3: Median values of the scan parameters, signal-to-noise ratio, image-quality scores, estimated effective dose, and the percentage difference for the 2 cohorts**

Parameter	0–4 yr			5–9 yr			10–16 yr		
	I	II	% Diff	I	II	% Diff	I	II	% Diff
Tube current (mAs)	150	128	–15	182	162	–11	266	165	–38
CTDI <sub>vol</sub> (mGy)	7.4	4.4	–41	8.6	5.5	–36	20	7	–67
Scan length (cm)	17.6	17.8	1	20.3	21	5	26	27	1
DLP (mGy-cm)	125	77	–38	175	132	–24	522	240	–54
ED (mSv)	2.1	1.2	–40	2.2	1.7	–21	9.7	4.4	–55
SNR	16.4	13.4	–18	13.4	16.3	22	20.2	16.2	–20
IQ	3.67	4.00	9	4.00	4.00	0	4.33	4.00	–8

**Note:**—IQ indicates image quality; ED, effective dose; Diff, difference; I, baseline; II, follow-up.

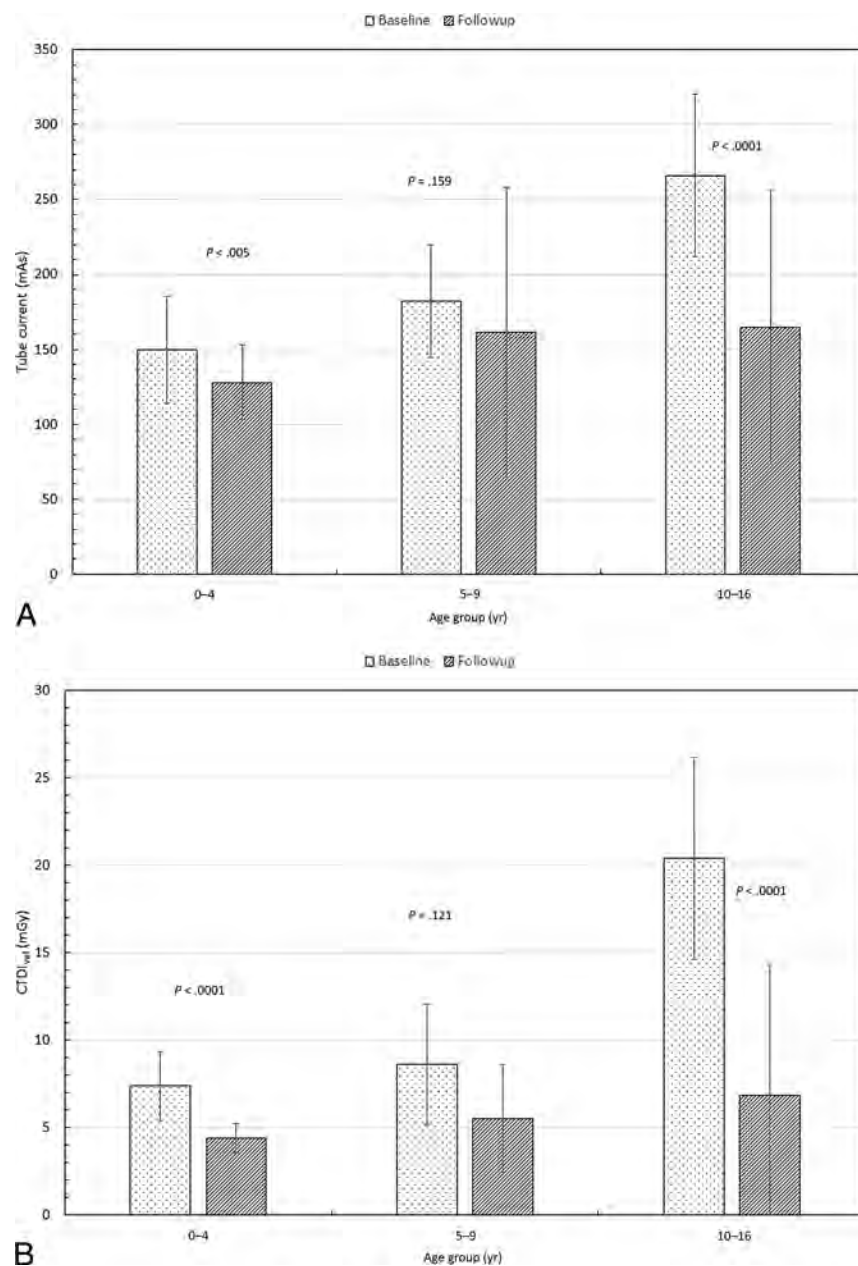


**FIG 2.** Comparison of the median values of tube current (milliampere-seconds) (A), radiation output of scanner (CTDI<sub>vol</sub>) (B), and scan length between the 2 cohorts (C). Also shown are P values from an unpaired *t* test.

the target CTDI<sub>vol</sub> to lower values for the follow-up cohort. Accordingly, the target CTDI<sub>vol</sub> values for the follow-up cohort were set at 6, 8, and 15 mGy for the 0–4, 5–9, and 10–16 age groups,

respectively, by adjusting the reference milliampere-seconds for the examination protocols. These values corresponded to the first-quartile CTDI<sub>vol</sub> for each age group from the baseline cohort. Our rationale for this choice was that the first quartile (25th percentile) of the CTDI<sub>vol</sub> represents a reasonable compromise between radiation dose and diagnostic quality.

### Subjective Assessment of Image Quality

From each neck CT examination, 1 image at the level of the true vocal cords was selected for evaluation (Fig 1). Three board-certified neuroradiology attending physicians subjectively assessed the image quality of each selected image. For the follow-up cohort, the same 3 board-certified neuroradiologists assessed the image quality of each selected image. Readers were shown the complete image set on a standard reading room workstation in a randomized manner and were blinded to patient demographics, study indications, and protocol parameters during the rating process. Readers were allowed to change window and level settings as in routine image interpretation and were instructed to assign an integer score ranging from 1 to 5 using the rating system depicted in Table 2. Scores were based on diagnostic-quality parameters such as image noise, intrinsic artifacts, and contrast among tissues. Scores of  $\geq 3$  were considered of sufficient quality for clinical diagnosis. Subjective image-quality interrater agreement among the 3 readers was assessed with the intraclass correlation coefficient using the Statistical Package for the Social Sciences software (Version 22; IBM, Armonk, New York). The intraclass correlation coefficient was interpreted as follows: 0–0.2, poor agreement; 0.3–0.4, fair agreement; 0.5–0.6, moderate agreement; 0.7–0.8, strong agreement; and  $>0.8$ , almost perfect agreement.

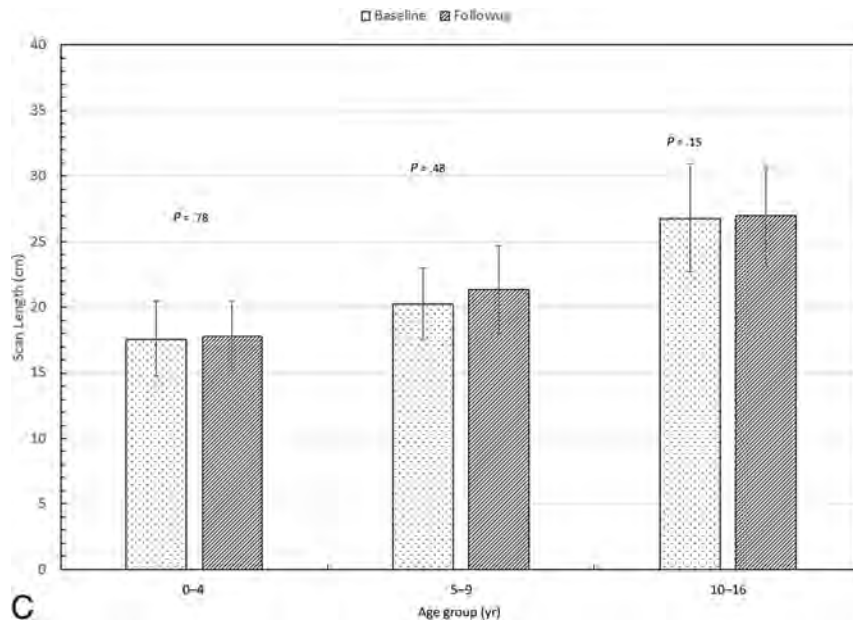


FIG 2. Continued.

### Quantitative Assessment of Image Quality

For each patient in the study group, a quantitative assessment of image quality was performed by measuring the image background noise (BN) and calculating the signal-to-noise ratio. The BN was defined as the average SD in Hounsfield units of 2 ROIs measuring  $\sim 1.0 \text{ cm}^2$  drawn over the air anterior to the patient (Fig 1) on the neck CT image obtained at the level of the true vocal cord.<sup>17,18</sup> Image signal ( $M_{\text{HU}}$ ) was defined as the average attenuation of 2 ROIs measuring  $\sim 0.5 \text{ cm}^2$  drawn over the paraspinous musculature. The SNR was then calculated as

$$\text{SNR} = M_{\text{HU}} / \text{BN}.$$

We believe that the SNR is a more reproducible metric than the contrast-to-noise ratio in pediatric neck CT due to a lack of consistency across subjects with respect to pathology, fat content, and the degree of contrast opacification in the internal jugular vein.

### Effective Dose

Finally, to estimate the effective dose for the patient cohort, we used the data published by Deak et al<sup>19</sup> in the following manner: This publication lists the age-specific “k” conversion factors for neck CT examinations for neonates; 1, 5, 10 years of age; and adults. The authors used mathematically defined phantoms with the most recent International Commission on Radiological Protection Publication 103 tissue-weighting factors and Monte Carlo simulations to estimate organ and effective doses from multislice CT examinations. We used a polynomial fit and interpolated these data to estimate the appropriate k value for the median age for each of our groups because the article has conversion factors specified only for neonates; children 1, 5, and 10 years of age; and adults. Note that we did not use the factors to estimate doses for individual patients, but only for a “median” patient of each age group/cohort in the study.

## RESULTS

Subjective image-quality interrater agreement was assessed for the baseline cohort as well as for the follow-up cohort. There was strong agreement among the 3 neuroradiology attending physicians for the baseline cohort (intraclass correlation coefficient = 0.769; 95% confidence interval, 0.676–0.839;  $P < .001$ ) and for the follow-up cohort (intraclass correlation coefficient = 0.695; 95% confidence interval, 0.567–0.790;  $P < .001$ ). Scores of all the readers were averaged for each CT image in the baseline cohort and the follow-up cohort.

Table 3 shows the median values of milliampereseconds,  $\text{CTDI}_{\text{vol}}$ , scan length, dose-length product (DLP), effective dose, SNR, and image quality by age groups for the baseline and follow-up patient cohorts. Also shown is the percentage difference among the values

of these parameters between the 2 cohorts. For convenience, these values are also depicted graphically in Figs 2–4, with  $P$  values from an unpaired  $t$  test to examine the significance of the difference between the 2 cohorts. Error bars in the figures represent 1 SD. Ninety-seven percent of the studies (73/75) in the baseline cohort and 96% (100/104) in the follow-up cohort were considered of sufficient image quality.

Tube current,  $\text{CTDI}_{\text{vol}}$ , and DLP were significantly lower in the follow-up cohort than in the baseline cohort in children 0–4 and 10–16 years of age, but not in children 5–9 years of age (Figs 2 and 3). Scan length did not differ between the baseline and follow-up cohorts in any age group (Fig 2). The SNR was lower in the low-dose than in the baseline cohort in children 0–4 and 10–16 years of age, but not in children 5–9 years of age (Fig 4). Image-quality ratings for all 3 age groups did not show major differences; they were lower in the follow-up cohort than in the baseline cohort in children 10–16 years of age, slightly higher in children 0–4 years of age, and with no significant difference for those 5–9 years of age (Fig 4). Despite the decrease in image-quality scores in older children, in the follow-up patient cohort, 96% of the studies were considered of sufficient image quality (average image quality,  $\geq 3$ ). Comparison of the effective doses before and after the implementation of low-dose protocols demonstrates 40%, 21%, and 55% reduction respectively in children 0–4, 5–9, and 10–16 years of age (Fig 3).

## DISCUSSION

In this study, we used the information obtained from the baseline cohort to implement age-specific pediatric neck CT protocols standardized across all scanners and facilities at our institution. Because most studies in the baseline sample were deemed of diagnostic quality by the reviewers, we decided to implement lower dose protocols using the first quartile  $\text{CTDI}_{\text{vol}}$  for each age group

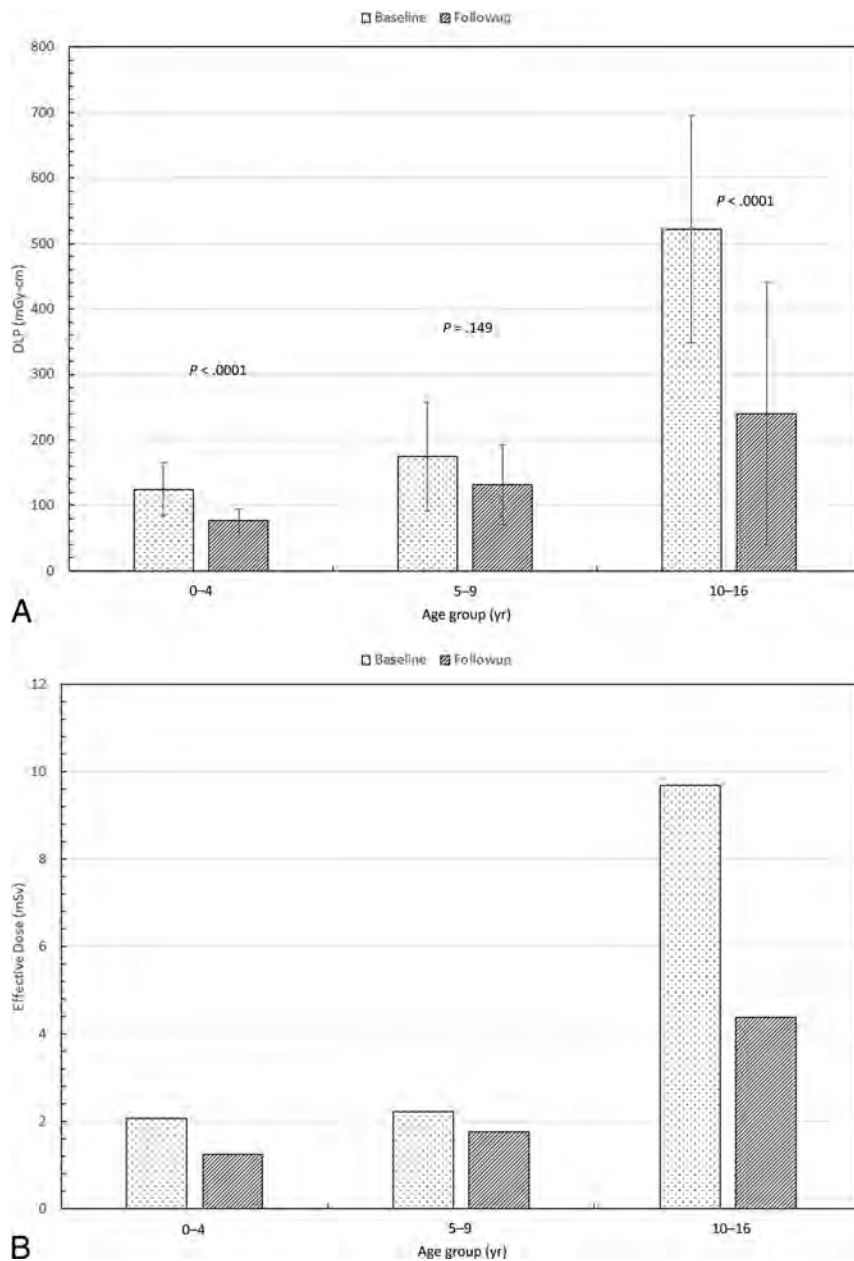


**FIG 3.** Comparison of the median values of the dose-length product (A) and estimated effective dose (B) between the 2 cohorts. Also shown are the *P* values from an unpaired *t* test.

as a reference. Our rationale for this choice was that the first quartile (25th percentile) of the  $CTDI_{vol}$  for each age group represents a reasonable compromise between the radiation dose and diagnostic quality for pediatric neck CT.

Data in Table 3 indicate that the median values of the tube current and  $CTDI_{vol}$  increased from the youngest to the oldest age groups. This increase is to be expected and is a reflection of the use of automatic tube current modulation, which increases the radiation output to compensate for the increased patient size.<sup>13,20</sup> For the baseline cohort, the median tube current varied by a factor of  $\sim 1.8$  (150–266 mAs), while the  $CTDI_{vol}$  increased by a factor of  $\sim 3$  (7–20 mGy) from the youngest to the oldest age group. For the follow-up cohort, these parameters varied by a factor of  $\sim 1.3$  (128–165 mAs) and 1.6 (4.4–7 mGy), respectively.

Figure 2A, -B shows a comparison of median values of the tube current and  $CTDI_{vol}$  between the 2 cohorts. While the DLP dropped only moderately for the 2 youngest cohorts, there was a significant drop in the DLP for the oldest age group. The reduction in the median  $CTDI_{vol}$  for the follow-up cohort was far more dramatic,  $\sim 40\%$ – $65\%$ . Figure 2C shows the median scan length for the 3 age groups. Note that there was no significant difference in the scan length between the baseline and follow-up cohorts for any of the age groups. This is important because these data reflect no attempt being made to “shorten” the length of the CT scan and risk missing clinically significant findings to simply reduce the dose.

Table 3 shows that the median scan length increased monotonically from  $\sim 17$  to 27 cm across the 3 age groups for both cohorts. For the baseline cohort, the DLP changed from 125 to 175 mGy-cm (a factor of  $\sim 1.4$ ) between the 0–4 and the 5–9 age groups. However, there is a sharp rise in the DLP from 175 to 522 mGy-cm (a factor of  $\sim 3$ ) between the 5–9 and the 10–16 age groups. One reason could be that the patients in the 0–4 and the 5–9 age groups were scanned at 80 or 100 kV, while the 10- to 16-year groups were scanned at 120 kV.<sup>21</sup>

For the follow-up cohort, the DLP changed from 77 to 132 mGy-cm (a factor of  $\sim 1.7$ ) between the 0–4 and 5–9 age groups. However, the DLP rose from 132 to 240 mGy-cm (a factor of  $\sim 1.8$ ) between the 5–9 and the 10–16 age groups. This finding is in contrast to the increase in DLP by a factor of 3 in the baseline cohort. We believe this difference to be the result of better coaching

and re-education of the technologists, resulting in many of the scans ( $\sim 35\%$ ) in this cohort being obtained at 100 kV.

Figure 4 shows that the median SNR and the image-quality scores were approximately the same (within 1 SD) across all age groups. The SNR not changing much is to be expected because larger patients were automatically scanned with higher kilovolt and/or tube currents to compensate for their size. Despite slight differences in the image-quality scores between the baseline and the follow-up cohorts for all 3 age groups, the median scores were well above 3 (making the scans diagnostically acceptable).

The estimated effective dose was reduced by 40%, 21%, and 55% for the follow-up protocol compared with the baseline (Table 3). The estimated effective doses did not change much between the 2 youngest age groups (2.1–2.2 mSv for baseline and 1.2–1.7 mSv for the

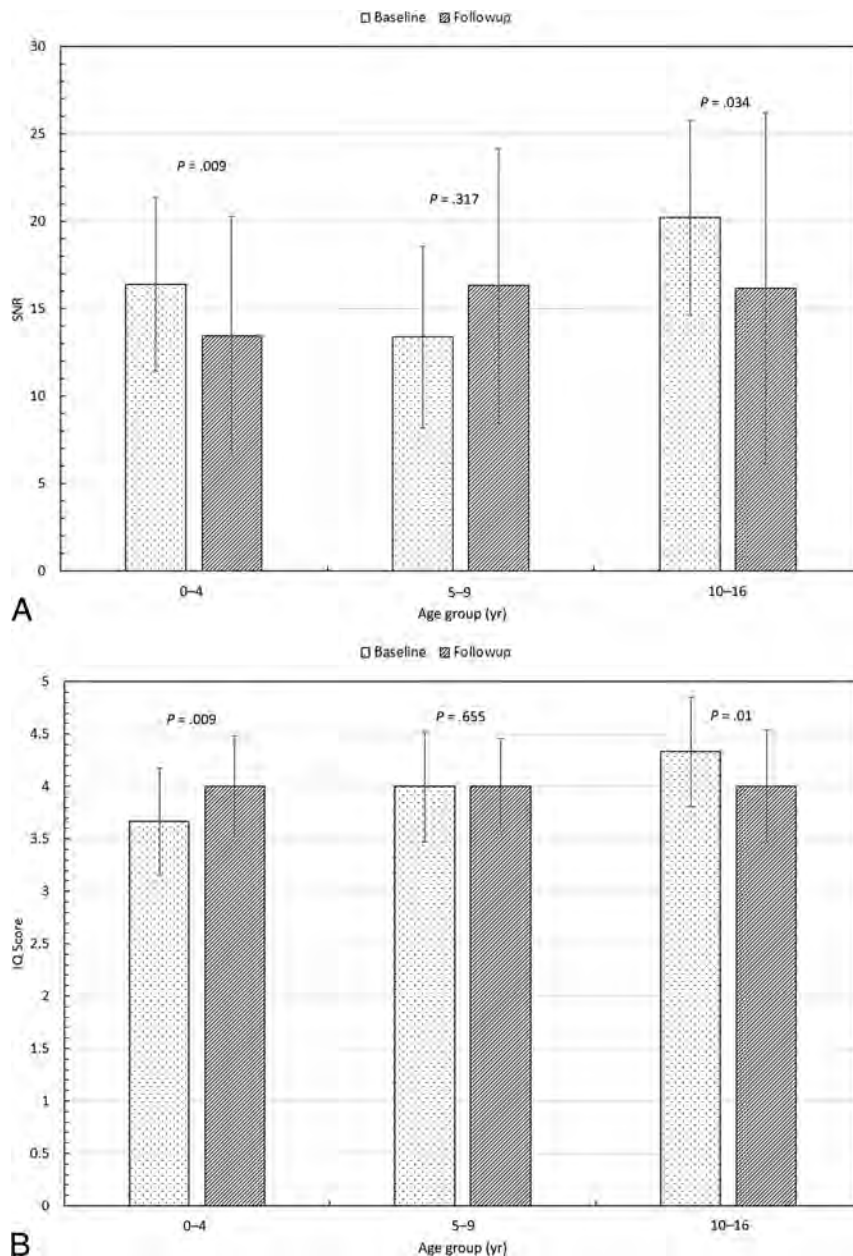


**FIG 4.** Comparison of the median values of the signal-to-noise ratio (A) and image-quality score (B) between the 2 cohorts. Also shown are the *P* values from an unpaired *t* test.

follow-up). However, the effective dose increased quite substantially when one looks at the oldest age groups. For the baseline cohort, the effective dose increased by a factor of  $\sim 5$  (2.1–9.7 mSv) from the youngest to the oldest group. For the follow-up cohort, there was a similar increase by a factor of  $\sim 4$  (1.2–4.4 mSv). We did not use the *k* conversion factors to estimate the effective dose for individual patients.<sup>22</sup> Rather, as explained before, we used only the median value of the DLP and age for each subgroup for the estimation of the effective dose. While this makes the estimate somewhat broad, we believe it is still a good way of comparing the radiation risks between the 2 cohorts.

This study has certain limitations. First, all examinations were conducted on 64- and 128-slice Siemens scanners. Thus, the results may not necessarily be readily transferable to examinations conducted on scanners by other manufacturers. Second, all image

reconstruction was performed using filtered back-projection algorithms. At the time of the study (2013–2016), we had not switched to iterative reconstruction, which is now routinely used on all our scanners. However, iterative reconstruction has its own challenges: Depending on what “level” of mixing one uses, the texture of the image can be vastly different between even identical scanners. With the use of newer, iterative reconstruction algorithms, it may be possible to reduce the radiation dose even further. Last, the effective doses listed in this study are fairly broad estimates, and individual patient doses could easily vary by up to a factor of  $\geq 2$  depending on the body habitus. Thus, caution must be used in interpreting these results. However, we believe that this is a fair way of estimating effective doses from clinical scans for a “standard” patient, to design appropriate CT protocols.

## CONCLUSIONS

The main inference to be drawn from this study is that even in a large clinical practice, with a well-reasoned choice of target  $CTDI_{vol}$  and using techniques such as automatic tube current modulation, it is possible to optimize the amount of radiation used for performing CT examinations without compromising on the diagnostic image quality. While this is important for patients of all age groups, it is of particular importance for pediatric patients due to their increased radiation risk.

Disclosures: M. Vittoria Spampinato—UNRELATED; Grants/Grants: Bracco.\* \*Money paid to the institution.

## REFERENCES

1. Broder J, Fordham LA, Warshauer DM. **Increasing utilization of computed tomography in the pediatric emergency department, 2000–2006.** *Emerg Radiol* 2007;14:227–32 CrossRef Medline
2. Markel TA, Kumar R, Koontz NA, et al. **The utility of computed tomography as a screening tool for the evaluation of pediatric blunt chest trauma.** *J Trauma* 2009;67:23–28 CrossRef Medline
3. Blackwell CD, Gorelick M, Holmes JF, et al. **Pediatric head trauma: changes in use of computed tomography in emergency departments in the United States over time.** *Ann Emerg Med* 2007;49:320–24 CrossRef Medline
4. Brenner DJ, Hall EJ. **Computed tomography—an increasing source of radiation exposure.** *N Engl J Med* 2007;357:2277–84 CrossRef Medline
5. Shahi V, Brinjikji W, Cloft HJ, et al. **Trends in CT utilization for pediatric fall patients in US emergency departments.** *Acad Radiol* 2015;22:898–903 CrossRef Medline

6. Brenner D, Elliston C, Hall E, et al. **Estimated risks of radiation-induced fatal cancer from pediatric CT.** *AJR Am J Roentgenol* 2001;176:289–96 CrossRef Medline
7. UNSCEAR 2013 Report. Sources, Effects and Risks of Ionizing Radiation. 2013. [http://www.unscear.org/docs/reports/2013/13-85418\\_Report\\_2013\\_Annex\\_A.pdf](http://www.unscear.org/docs/reports/2013/13-85418_Report_2013_Annex_A.pdf). Accessed January 15, 2017
8. Brenner DJ. **Estimating cancer risks from pediatric CT: going from the qualitative to the quantitative.** *Pediatr Radiol* 2002;32:228–31; discussion 242–44 CrossRef Medline
9. Mettler FA Jr, Wiest PW, Locken JA, et al. **CT scanning: patterns of use and dose.** *J Radiol Prot* 2000;20:353–59 CrossRef Medline
10. Zacharias C, Alessio AM, Otto RK, et al. **Pediatric CT: strategies to lower radiation dose.** *AJR Am J Roentgenol* 2013;200:950–56 CrossRef Medline
11. Berrington de Gonzalez A, Mahesh M, Kim KP, et al. **Projected cancer risks from computed tomographic scans performed in the United States in 2007.** *Arch Intern Med* 2009;169:2071–77 CrossRef Medline
12. Miglioretti DL, Johnson E, Williams A, et al. **The use of computed tomography in pediatrics and the associated radiation exposure and estimated cancer risk.** *JAMA Pediatr* 2013;167:700–07 CrossRef Medline
13. Spampinato MV, Tipnis S, Tavernier J, et al. **Thyroid doses and risk to paediatric patients undergoing neck CT examinations.** *Eur Radiol* 2015;25:1883–90 CrossRef Medline
14. Yamauchi-Kawaura C, Fujii K, Aoyama T, et al. **Radiation dose evaluation in head and neck MDCT examinations with a 6-year-old child anthropomorphic phantom.** *Pediatr Radiol* 2010;40:1206–14 CrossRef Medline
15. Huda W, Spampinato MV, Tipnis SV, et al. **Computation of thyroid doses and carcinogenic radiation risks to patients undergoing neck CT examinations.** *Radiat Prot Dosimetry* 2013;156:436–44 CrossRef Medline
16. Paolicchi F, Faggioni L, Bastiani L, et al. **Optimizing the balance between radiation dose and image quality in pediatric head CT: findings before and after intensive radiologic staff training.** *AJR Am J Roentgenol* 2014;202:1309–15 CrossRef Medline
17. Scholtz JE, Kaup M, Kraft J, et al. **Objective and subjective image quality of primary and recurrent squamous cell carcinoma on head and neck low-tube-voltage 80-kVp computed tomography.** *Neuroradiology* 2015;57:645–51 CrossRef Medline
18. Gaddikeri S, Andre JB, Benjert J, et al. **Impact of model-based iterative reconstruction on image quality of contrast-enhanced neck CT.** *AJNR Am J Neuroradiol* 2015;36:391–96 CrossRef Medline
19. Deak PD, Smal Y, Kalender WA. **Multisection CT protocols: sex- and age-specific conversion factors used to determine effective dose from dose-length product.** *Radiology* 2010;257:158–66 CrossRef Medline
20. Kalra MK, Maher MM, Toth TL, et al. **Techniques and applications of automatic tube current modulation for CT.** *Radiology* 2004;233:649–57 CrossRef Medline
21. Yu L, Bruesewitz MR, Thomas KB, et al. **Optimal tube potential for radiation dose reduction in pediatric CT: principles, clinical implementations, and pitfalls.** *Radiographics* 2011;31:835–48 CrossRef Medline
22. **The 2007 Recommendations of the International Commission on Radiological Protection: ICRP Publication 103.** *Ann ICRP* 2007;37:1–332 CrossRef Medline

# Deep Learning–Based Automatic Segmentation of Lumbosacral Nerves on CT for Spinal Intervention: A Translational Study

G. Fan, H. Liu, Z. Wu, Y. Li, C. Feng, D. Wang, J. Luo, W.M. Wells III, and S. He



## ABSTRACT

**BACKGROUND AND PURPOSE:** 3D reconstruction of a targeted area (“safe” triangle and Kambin triangle) may benefit the viability assessment of transforaminal epidural steroid injection, especially at the L5/S1 level. However, manual segmentation of lumbosacral nerves for 3D reconstruction is time-consuming. The aim of this study was to investigate the feasibility of deep learning–based segmentation of lumbosacral nerves on CT and the reconstruction of the safe triangle and Kambin triangle.

**MATERIALS AND METHODS:** A total of 50 cases of spinal CT were manually labeled for lumbosacral nerves and bones using Slicer 4.8. The ratio of training/validation/testing was 32:8:10. A 3D U-Net was adopted to build the model SPINECT for automatic segmentations of lumbosacral structures. The Dice score, pixel accuracy, and Intersection over Union were computed to assess the segmentation performance of SPINECT. The areas of Kambin and safe triangles were measured to validate the 3D reconstruction.

**RESULTS:** The results revealed successful segmentation of lumbosacral bone and nerve on CT. The average pixel accuracy for bone was 0.940, and for nerve, 0.918. The average Intersection over Union for bone was 0.897 and for nerve, 0.827. The Dice score for bone was 0.945, and for nerve, it was 0.905. There were no significant differences in the quantified Kambin triangle or safe triangle between manually segmented images and automatically segmented images ( $P > .05$ ).

**CONCLUSIONS:** Deep learning–based automatic segmentation of lumbosacral structures (nerves and bone) on routine CT is feasible, and SPINECT-based 3D reconstruction of safe and Kambin triangles is also validated.

**ABBREVIATIONS:** ESI = epidural steroid injection; IoU = Intersection over Union; tESI = transforaminal epidural steroid injection

Low back pain with a radicular component is a common ailment in many clinics and is a leading cause of disability and adds a great burden to health care costs globally.<sup>1,2</sup> It is difficult to

detect the specific etiology, but the pain is usually caused by inflammation of nerves due to mechanical compression or chemical irritation.<sup>3</sup> Lumbar degenerative disease, including spinal stenosis and lumbar disc herniation, is a main culprit of low back pain and radicular symptoms. Before spinal surgery, epidural steroid injection (ESI) is an interventional option for the management of low back and radicular pain.<sup>4,5</sup> Transforaminal epidural steroid injection (tESI) is a well-validated technique with merits of large distributions of injectate and superior short-term pain relief compared with an interlaminar or caudal approach.<sup>6,7</sup> Typically, tESI is conducted via a “safe” triangle, while others prefer via a Kambin triangle because the safe triangle has been found to sometimes not be safe.<sup>8</sup> The Kambin triangle is defined as an anatomic triangle with the nerve root (hypotenuse), traversing nerve root and/or facet joint (height), and superior border of a lower vertebra (base) as its components.<sup>9</sup> The safe triangle is defined as the lower margin of the pedicle (base), the lateral border of the vertebral body (height), and the outer border of the exiting nerve (hypotenuse).<sup>10</sup> Because the 2 triangles are 3D, the targeted area of tESI is variable from different views or even totally concealed by bony

Received January 14, 2019; accepted after revision April 16.

From the Orthopedic Department, Shanghai Tenth People's Hospital (G.F., C.F., D.W., S.H.), Tongji University School of Medicine, Shanghai, China; Department of Spine Surgery (G.F.), Third Affiliated Hospital of Sun Yatsen University, Guangzhou, China; Surgical Planning Lab (G.F., J.L., W.M.W.), Radiology Department, Brigham and Women's Hospital, Harvard Medical School, Boston, Massachusetts; Spinal Pain Research Institute of Tongji University (H.L., C.F., D.W., S.H.), Shanghai, China; School of Data and Computer Science (Z.W.), Sun Yat-sen University, Guangzhou, China; Shanghai Jiao Tong University School of Medicine (Y.L.), Shanghai, China; and Graduate School of Frontier Sciences (J.L.), University of Tokyo, Tokyo, Japan. G. Fan and H. Liu contributed equally to the study.

This work is supported by the China Scholarship Council (201706260169), Shanghai Hospital Development Center (16CR3017A), and National Institutes of Health grant P41EB015898 (W.M.W.).

Please address correspondence to Shisheng He, MD, and Guoxin Fan, MD, 301 Yanchang Rd, Shanghai 200072, China; e-mail: tjhss7418@tongji.edu.cn, gfan@tongji.edu.cn

Indicates open access to non-subscribers at www.ajnr.org

Indicates article with supplemental on-line appendix and table.

<http://dx.doi.org/10.3174/ajnr.A6070>

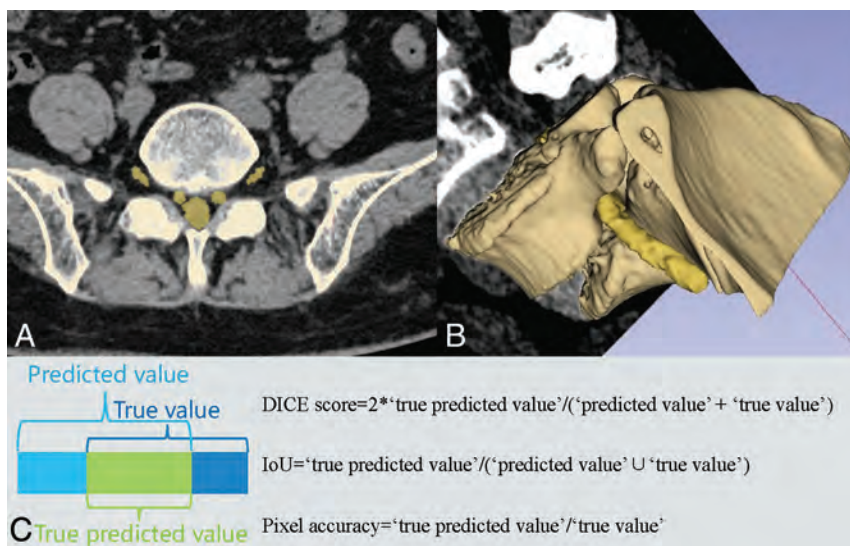


**FIG 1.** Manual segmentation and 3D reconstruction on Slicer. *A*, manual labels. *B*, 3D reconstruction with a coronal image. *C*, Illustrations of the Dice score, Intersection-over-Union, and pixel accuracy.

structures such as a high iliac crest, enlarged transverse process, and facet joint, especially at the L5/S1 level.<sup>10-12</sup> An increased area of the safe triangle and Kambin triangle should lead to more frequent successful outcomes of tESI.<sup>10</sup> Complications of tESI such as intravascular injection and nerve root injury cause serious problems.<sup>13,14</sup>

X-ray fluoroscopy is the criterion standard to guide tESI.<sup>15</sup> The bony landmark “Scotty dog” is identified to estimate the targeted area to present larger areas of the safe triangle or Kambin triangle. The C-arm machine is usually tilted to a certain angle to conduct an oblique fluoroscopy to identify the Scotty dog.<sup>16</sup> However, x-ray fluoroscopy is incapable of providing information about soft tissues and localizing the needle tip in a real-time manner. Thus, CT fluoroscopy is introduced to guide the tESI because it can quickly and safely localize needles and minimize the risk of nerve injury.<sup>17</sup> Usually, an initial CT scan with good image quality is obtained for viability assessment of the tESI, during which an ideal needle trajectory is planned on a single axial CT slice.<sup>18</sup> Then, a CT fluoroscopy technique is used to guide the needle advancement on a single CT slice during which soft tissue is poorly presented on images.<sup>18</sup> Therefore, a larger targeted area of needle advancement should reduce the risk of injuring the neurovascular structure. However, the CT plane is incapable of directly and quickly identifying an accessible trajectory targeting the largest safe or Kambin triangle, and sometimes the CT plane presents no accessible pathway on all axial slices. Instead, 3D construction of the safe or Kambin triangle may benefit the viability assessment of the tESI. Free manipulation of the 3D model will quickly identify an oblique needle pathway targeting the large safe triangle or Kambin triangle. However, manual segmentation of lumbosacral nerves for 3D reconstruction is time-consuming.

Recently, deep learning has gained substantial attention in the field of radiology.<sup>19-22</sup> Deep learning algorithms can learn from large amounts of data using neural networks, frequently

convolutional neural networks.<sup>23</sup> Although convolutional neural networks were proposed decades ago, it is only in the past 7 years that deep learning has achieved great success due to massive available data, increased processing power, and rapid development of algorithms.<sup>23</sup> The U-Net (<https://lmb.informatik.uni-freiburg.de/people/ronneber/u-net/>) is a kind of convolutional neural network that was developed for biomedical image segmentation by Ronneberger et al<sup>24</sup> in 2015, and it has many applications in the segmentation of 2D images. In 2016, the same group developed a 3D U-Net ([https://www.researchgate.net/publication/304226155\\_3D\\_U-Net\\_Learning\\_Dense\\_Volumetric\\_Segmentation\\_from\\_Sparse\\_Annotation](https://www.researchgate.net/publication/304226155_3D_U-Net_Learning_Dense_Volumetric_Segmentation_from_Sparse_Annotation)) for volumetric segmentation as an extension architecture of the U-Net.<sup>25</sup> Many

studies have validated the segmentation performance of the 3D U-Net for volumetric medical images.<sup>26-28</sup> To the best of our knowledge, no studies are available on achieving automatic segmentation of lumbosacral nerves on CT. The aim of this study was to investigate the feasibility of automatically segmenting lumbosacral structures (nerves and bone) on CT with the 3D U-Net and the reconstruction of the safe and Kambin triangles.

## MATERIALS AND METHODS

This retrospective study was Health Insurance Portability and Accountability Act-compliant and approved by the institutional ethical committee of Shanghai Tenth People’s Hospital before data extraction. A total of 50 patients with thin-layer CT covering the lumbosacral level from Shanghai Tenth People’s Hospital were included in this study. All algorithms were developed and tested using Keras (Version 2.1.1 with tensorflow\_backend.py; <http://pydoc.net/Keras/2.1.2/keras.preprocessing.image/>) in a personal computer (graphics processing unit: a Nvidia GeForce 1080Ti, <https://www.nvidia.com/en-us/geforce/products/10series/geforce-gtx-1080-ti/>, with 4 GB of memory and a 3.5-GHz Intel Core i7-4790 CPU with 8 GB of memory).

### Manual Annotations

All data were manually segmented with Slicer 4.8 (<http://www.slicer.org>).<sup>29</sup> Lumbosacral nerves and bones were meticulously segmented and labeled (Fig 1A, -B). A spine surgeon who is an expert in reading lumbar CT and had systematic training in Slicer manually segmented the nerves and bones. Then the segmented images were reviewed by an interventional radiologist and pain physician, both of whom are experts in CT-guided epidural steroid injection. Any disagreements of segmentation were solved by the 3 doctors voting. These manual annotations were regarded as the ground truth.

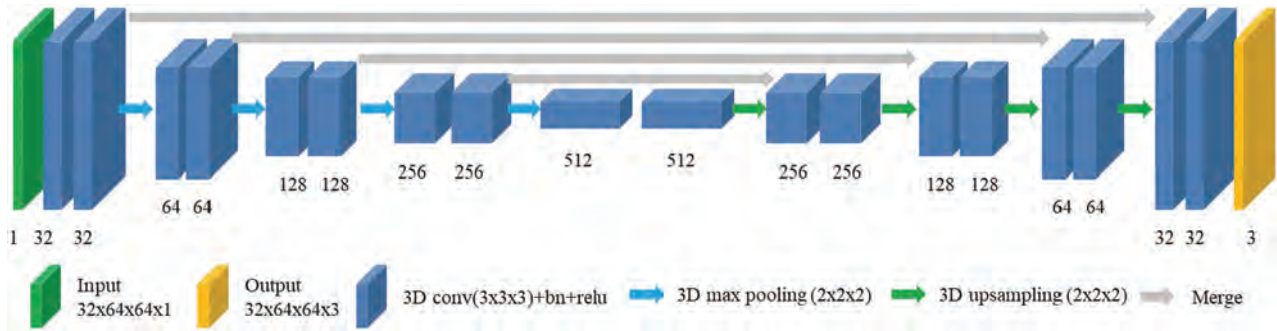


FIG 2. Schematic of the network architecture.

Table 1: Overview of the combined algorithm

Algorithm 1: Combined Algorithm
<b>Require:</b> $X$ : CT volume, shape = $D \times H \times W$
<b>Require:</b> $x_i = X(L_i)$ , ( $i=1, \dots, k$ ): CT voxel patch
<b>Require:</b> $y_i = M(x_i)$ : $y_i$ is the output of the last layer (softmax activation function) of the model $M$ , $y_i$ has 1 more dimension than $x_i$ , and this dimension has 3 channels. Each channel refers to the probability of the corresponding voxel belonging to background or bone or nerve, respectively.
1) <b>Initialize:</b> $Y \leftarrow 0$
2) <b>For</b> $x_i \in X, (i = 1, \dots, k)$ <b>do</b>
3) $Y(L_i, \cdot) + = y_i$
4) <b>End for</b>
5) $S \leftarrow \arg \max(Y, \text{axis} = -1)$ (find the channel with the largest value in the last dimension)
6) <b>Return</b> $S$ (the automatic mask)

**Note:**— $M$  indicates the model (network);  $L$ , location of the CT voxel patch  $x$  at the CT volume  $X$ ;  $Y$ , summed probability; max, maximum.

### Data Preprocessing and Segmentation Assessment

All thin-layer CT scans were preprocessed using the following steps: resampling, cropping, and intensity normalization (Online Appendix). Pixel accuracy, Intersection over Union (IoU), and the Dice score were used to assess the segmentation performance of lumbosacral structures (Fig 1C). The functions of these 3 indicators are as follows:

$$\text{Dice Score} = 2 \times \text{True Predicted Voxels} / (\text{Predicted Voxels} + \text{True Voxels})$$

$$\text{IoU} = \text{True Predicted Voxels} / (\text{Predicted Voxels} \cup \text{True Voxels})$$

$$\text{Pixel Accuracy} = \text{True Predicted Voxels} / \text{True Voxels}.$$

Because the Dice score is the most common indicator in computer vision,<sup>30</sup> the current study adopted it as the primary index to assess the segmentation performance.

### Network Architecture

The 3D U-Net was adopted for multiclass segmentation of lumbosacral structures (Fig 2). The adopted network consists of 2 parts, the encoder and the decoder parts. The encoder part performs data analysis and feature-representation learning from the input data, and the decoder part generates segmentation results. There are also 4 shortcut connections (concatenations) between layers of equal resolution in the encoder and decoder paths. The last layer of the model is a  $1 \times 1 \times 1$  convolutional layer followed by a softmax layer (<https://www.mathworks.com/help/deeplearning/ref/nnet.cnn.layer.softmaxlayer.html>), with 3 output channels. The input of the model is  $32 \times 64 \times 64$  voxel patches of CT. The output is the corre-

sponding probability mask, and its shape is  $32 \times 64 \times 64 \times 3$ . The whole architecture has 22,581,411 parameters. The developed model is named SPINECT because it aims to automatically segment multiple structures solely on the basis of spinal CT.

### Training

During the training phase, a number of minibatch CT and manual labeling masks are randomly selected from the training dataset, and the image data are subjected to the standardization processing and the augmentation operation. As a result, the training data input to each training iteration is different, and this feature improves the generalization ability of the model. The convolutional layer parameters of 3D U-Net are initialized by the method of He et al.<sup>31</sup> The size of the patch (depth  $\times$  height  $\times$  width) input to the 3D U-Net during training is  $32 \times 64 \times 64$  (unit: voxel); the minibatch is 4, which is optimized by the Adam optimization algorithm<sup>32</sup>; and the learning rate is  $5e-4$ . We selected the Adam optimization algorithm instead of stochastic gradient descent for training the deep learning network because it was straightforward to implement and computationally efficient.

### Five-Fold Validation

During model training, 1 validation was performed every 100 training iterations. Specifically, 6 cases were randomly selected from the validation dataset for standard processing. The standard processing included several sequential steps: 1) Set the voxel size to 1 mm by the nearest interpolation method, and 2) standardization. Then, we added random noise plus random horizontal and vertical flipping to augment the selected cases. A sliding window of  $20 \times 40 \times 40$  was used to traverse the data with stride =  $(20 \times 40 \times 40)$  to obtain the patch. The patch is input to the current model; then the model generates the corresponding probability mask. Finally, the automatic segmented mask is obtained with a combined algorithm (Table 1). The Dice score of each voxel class is obtained with comparison of the automatic segmented mask and the manually labeled mask. If the average of the Dice score is greater than the prior best Dice score by the current iteration, the current model parameters will be saved. We use a combined algorithm in which the patch-based CNN is applied at a sequence of patches of the data, and the resulting label probabilities are summed according to their voxel location. Subsequently, the labels are established by the probabilities.

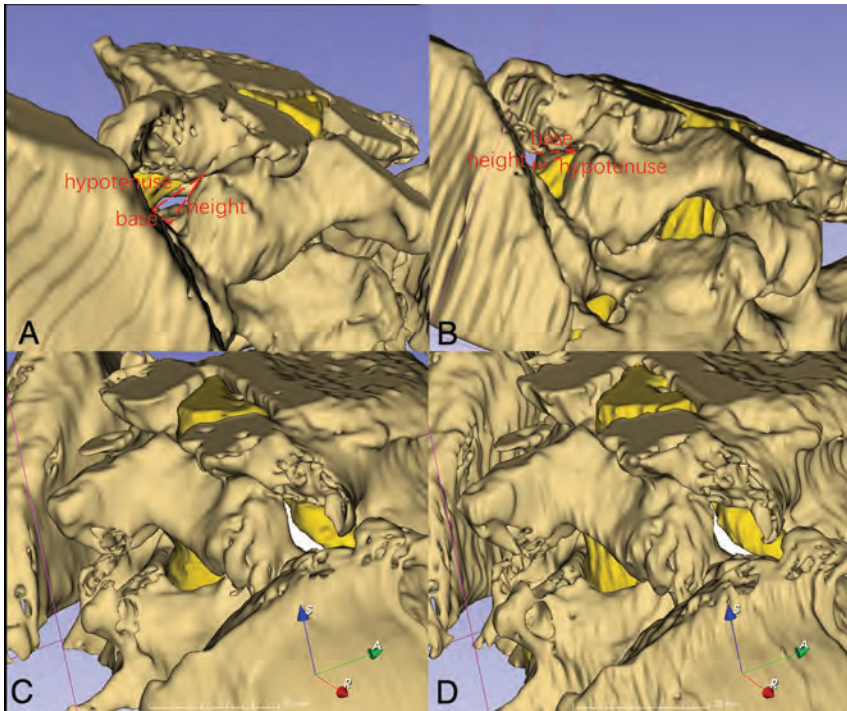


**FIG 3.** Measurement of safe and Kambin triangles. *A*, Schematics of the Kambin triangle. *B*, Schematics of the safe triangle. *C*, Measurement of the Kambin triangle on a manually segmented image. *D*, Measurement of the safe triangle on automatically segmented images.

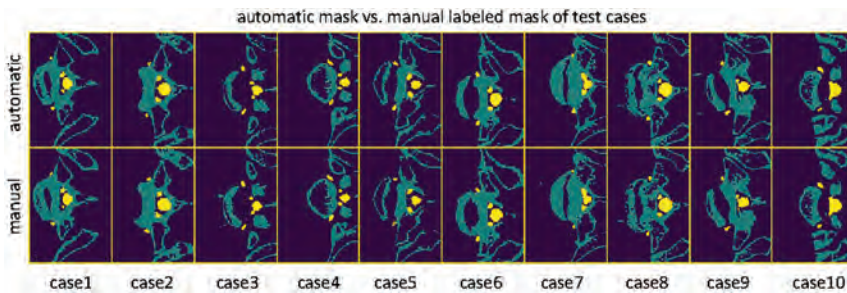


**FIG 4.** Automatic and manually labeled masks.

**Table 2: Segmentation accuracy in 10 testing cases<sup>a</sup>**

Structures	Pixel Accuracy (%)	IoU (%)	Dice Score (%)
Bones	94.05 ± 6.68 (82.0–99.9)	89.73 ± 4.32 (82.0–95.2)	94.54 ± 2.43 (90.1–97.5)
Nerves	91.43 ± 3.48 (85.3–94.4)	82.71 ± 3.25 (76.3–87.4)	90.51 ± 1.94 (86.6–93.2)

<sup>a</sup> Data are means and percentages unless otherwise noted.

### Testing

The ratio of training, validation, and testing of the 50 cases from our local dataset is 32:8:10. A total of 10 cases randomly selected from the local dataset were tested on SPINECT. To validate the robustness of our trained model, we also conducted cross-dataset testing on 10 cases from an on-line imaging dataset (SpineWeb; <http://spineweb.digitalimaginggroup.ca/>).<sup>33</sup> Pixel accuracy, IoU, and the Dice score were used to assess the segmentation performance of lumbosacral structures.

### Radiographic Evaluation

To compare the difference between manually segmented masks and automatically generated masks, we present a random slice

from each case. In addition, 3D rendering of manual masks before preprocessing, post-preprocessing masks, automatically generated masks, as well as smoothed 3D rendering of automatically generated masks (smoothing method: median; Kernel size: 1.5 mm) are also presented. To further investigate the segmentation performance of SPINECT, we measured both Kambin and safe triangles at the L5/S1 level on both sides on manually segmented and automatically segmented images (Fig 3). First, the Kambin triangle and safe triangle were visualized on Slicer with 3D rendering of manually and automatically segmented labels. Then, the Kambin triangle and safe triangle were set with the same angles between manually and automatically segmented images. Screenshots were obtained and imported into Image J software (Version 1.8.0\_112; National Institutes of Health, Bethesda, Maryland) for area measurements of the Kambin and safe triangles. Two independent observers measured the area of the 2 triangles from manually and automatically segmented images. One month later, one of the observers measured the area of the 2 triangles again. The intraclass correlation coefficient was calculated to assess test-retest reliability and interobserver reliability of multiple measurements.

### Statistical Analysis

The generated labels from SPINECT were used to generate the 3D rendering of bones and nerves on Slicer. After testing the normal distribution (Shapiro-Wilk test), we used a paired Student *t* test to detect statistically significant differences of the safe and Kambin triangles between manually segmented images and automatically segmented images. All continuous data are presented as mean ± SD, and a *P* value <.05 is a statistically significant difference.

### RESULTS

Testing results revealed that SPINECT could achieve successful segmentation of multiple structures (bones and nerves) on CT (Fig 4). Quantitative segmentation accuracy is shown in Table 2. The average pixel accuracy for the bones was 0.940, and for the nerves, 0.918. The average IoU for the bones was 0.897, and for the nerves, it was 0.827. The Dice score for the bones was 0.945, and for the nerves, it was 0.905. In each validation fold, it took about 4 hours 35 minutes to finish the training of the segmentation net. After training, SPINECT requires a total RAM space of 305.384 MB, and it takes about 3.1 seconds (Nvidia GeForce 1080Ti) to complete an automatic segmentation on a single case (On-line

**Table 3: Segmentation accuracy in 10 testing cases from the open dataset<sup>a</sup>**

Structures	Pixel Accuracy (%)	IoU (%)	Dice Score (%)
Bones	99.62 ± 0.35 (99.3–99.9)	81.40 ± 11.33 (60.5–93.3)	89.34 ± 7.28 (75.42–96.5)
Nerves	87.74 ± 4.82 (79.4–93.1)	80.64 ± 3.31 (75.5–82.9)	89.25 ± 2.00 (88.1–93.4)

<sup>a</sup>Data are means and percentages unless otherwise noted.

**Table 4: Measured area of the safe and Kambin triangles<sup>a</sup>**

Area (mm <sup>2</sup> )	Manual Images	Automatic Images	P Value
Kambin triangle	37.80 ± 20.90 (15.11–87.51)	36.41 ± 19.27 (11.46–78.63)	.302
Safe triangle	8.69 ± 2.24 (6.04–13.27)	8.56 ± 3.25 (3.18–17.91)	.792

<sup>a</sup>Data are means and percentages unless otherwise noted.

**Table 5: Test-retest reliability and interobserver reliability of multiple measurements**

Intraclass Correlation Coefficient	Test-Retest Reliability	Interobserver Reliability
3D rendering of manual segmentation		
Kambin triangle	0.983	0.984
Safe triangle	0.881	0.922
3D rendering of automatic segmentation		
Kambin triangle	0.988	0.982
Safe triangle	0.977	0.959

Table). In total, it took about 13 seconds to process 1 set of CT data (from data uploading and data preprocessing to semantic segmentation) with a graphics processing unit (Nvidia GeForce 1080Ti), which is far less than the 30 minutes for manual segmentation. Besides, the segmentation performance of 10 cases from SpineWeb was similar to that of our testing dataset (Table 3).

More important, there were no significant differences in the measured area of the safe or Kambin triangle between manual images and automatic images (Table 4). The area of Kambin triangle was 37.80 ± 20.90 mm<sup>2</sup> on manual images and 36.41 ± 19.27 mm<sup>2</sup> on automatic images ( $P = .302$ ). The area of the safe triangle was 8.69 ± 2.24 mm<sup>2</sup> on manual images and 8.56 ± 3.25 mm<sup>2</sup> on automatic images ( $P = .792$ ). The reliability test revealed strong test-retest reliability and interobserver reliability of multiple measurements (Table 5). As in Fig 5, 3D rendering of automatic masks was similar to that of post-preprocess masks, and 3D rendering of manual masks was similar to that of smoothed automatic masks. Moreover, dura compression was clearly present in the four 3D rendered images.

## DISCUSSION

Knowledge of bony and neurovascular anatomy of the spinal foramen is essential when performing tESI.<sup>34</sup> However, the Kambin or safe triangle has never been visualized before tESI. Thin-layer CT has great potential for reconstructing the safe and Kambin triangles, whereas manual segmentation of nerve roots is time-consuming. The current study has validated the feasibility of automatically segmenting lumbosacral structures (nerves and bone) on CT through deep learning and the 3D reconstruction of Kambin and safe triangles. To the best of our knowledge, this is the first study automatically segmenting lumbosacral nerves on CT through deep learning.

Reconstruction of the safe or Kambin triangle may benefit the

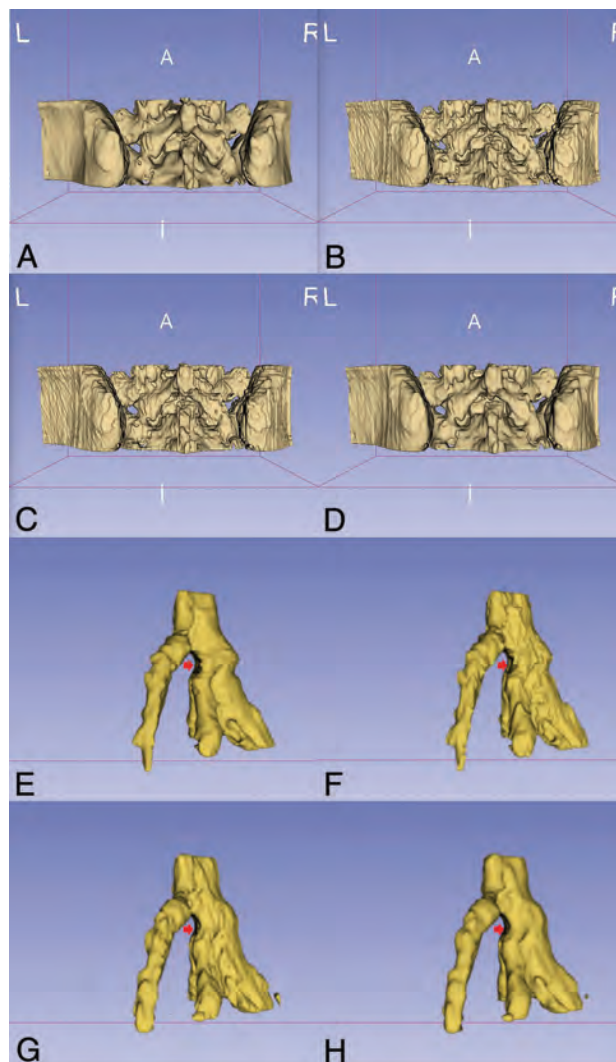


**FIG 5.** 3D rendering of automatic masks and manually labeled masks of bones and nerves. A, 3D rendering of manual masks before preprocessing. B, 3D rendering of post-preprocessed masks. C, 3D rendering of automatically generated masks. D, Smoothed 3D rendering of automatically generated masks. E, 3D rendering of manual masks before preprocessing (arrow indicates the compressed dura). F, 3D rendering of post-preprocessed masks (arrow indicates the compressed dura). G, 3D rendering of automatically generated masks (arrow indicates the compressed dura). H, Smoothed 3D rendering of automatically generated masks (arrow indicates the compressed dura).

viability assessment of tESI, especially at the L5/S1 level. Ideally, the needle trajectory is planned on an axial plane of conventional CT slices.<sup>10</sup> However, trajectory planning could be difficult at the L5/S1 level in some cases due to the bony obstacles such as the iliac crest, facet joint, and transverse process (Fig 6). In that case, an accessible pathway could be found in an oblique perspective. However, operators may fail to quickly identify an oblique trajectory targeting the largest safe or Kambin triangle, even if the CT gantry can be tentatively angled caudally or cranially. Another option is to change the targeted area (eg, from the safe to the Kambin triangle) for trajectory planning.<sup>35</sup> Nevertheless, axial CT slices are still incapable of presenting a large safe or Kambin triangle directly and quickly. Thus, 3D reconstruction of the safe or Kambin triangle may facilitate the viability assessment of tESI because it can quickly provide the specific perspective with a large

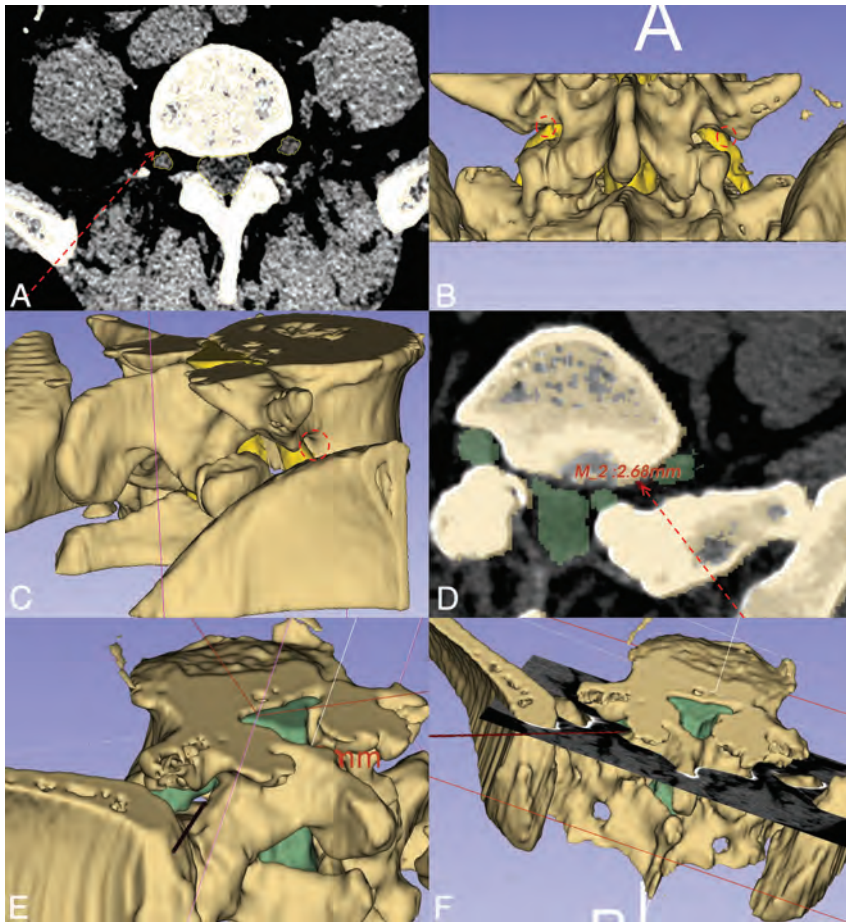


**FIG 6.** 3D model-based viability assessment of a transforaminal epidural steroid injection. *A*, Inaccessible trajectory to the safe triangle on an axial CT slice. *B*, Minimal space of the safe triangle on the posterior 3D model. *C*, Accessible oblique trajectory to the safe triangle on the 3D model. *D*, Inaccessible trajectory to the Kambin triangle on axial CT slice. *E*, Accessible trajectory on the 3D model. *F*, Oblique trajectory-guided nonaxial CT plane.

targeted area. Ra and Min<sup>10</sup> tried to identify an optimal angle of a nonaxial needle path with the largest area of the safe triangle for x-ray fluoroscopic guidance, but others thought a specific needle path is dictated by specific patient anatomy and cannot be consistently predicted using a constant angle. With free manipulation of 3D-rendering models, an oblique needle path could be planned when a large area of the safe triangle or Kambin triangle is presented (Fig 6*C*, *-E*). Our study also quantified the area of the safe or Kambin triangle, which might also help assess the viability of specific approaches. The area of the safe triangle ranged from 4 to 18 mm<sup>2</sup> in our series, which is similar to that in the previous study.<sup>10</sup> The area of the Kambin triangle at the L5/S1 level ranged from 10 to 84 mm<sup>2</sup> in our series, which is smaller than the results from other studies<sup>36,37</sup> because others removed the facet joint for measurement. More important, the measurements of triangles in our study confirmed no significant differences between manually segmented images and automatically segmented images, which validates the 3D reconstruction based on SPINECT in medical indicators.

Nerve segmentation is essential for visualizing the safe and Kambin triangles because the exiting nerve root is the hypotenuse of the 2 triangles. Physicians usually recognize the Scotty dog to estimate the location of the safe and Kambin triangles under the

guidance of x-ray fluoroscopy because the exiting nerve root has not yet been outlined. Moreover, only after multiple attempted punctures will contrast be injected to show the epidural and perineural flow, which may finally outline the nerve root sheath and epidural flow. Thus, x-ray fluoroscopy fails to demonstrate the detailed location of the exiting nerve root before punctures. The main advantage of CT is that it is good at precisely locating the needle placement using 3D imaging of soft tissues and osseous anatomy.<sup>38</sup> Moreover, CT fluoroscopy is also capable of demonstrating real-time contrast flow. Nevertheless, nerve segmentation is not yet available on the current CT workstations for ESI. Diffusion tensor imaging or the MR neurography technique may be useful to enhance the spinal nerves for diagnosis and surgical planning.<sup>37,39</sup> However, DTI or MR neurography scanning can be lengthy and costly and is not practical for ESI. In this current study, however, we have achieved automatic and precise segmentation of lumbosacral nerves on routine CT and successfully visualized the safe and Kambin triangles with segmented bones and nerves.

As more medical imaging datasets are created by medical experts, the application of deep learning in radiology is growing because of its excellent performance

in recognition and segmentation. While bony structures are easily identified in intraoperative practice, deep learning may enable rapid recognition and precise segmentation of important soft tissue. Moreover, all paraspinous structures (eg, nerves, vessels, discs, muscles, ligaments) may also play an important role in procedure planning, spinal navigation, and even robotic surgery in the near future. The current study has shown that thin-layer CT is a good candidate for segmenting nerves, which discloses the substantial potential of CT in segmenting spinal soft tissue. Moreover, the performance of SPINECT further supports the findings of other similar studies using U-Net and its variants for semantic segmentation of biomedical images.<sup>40,41</sup> We adopted the 3D U-Net instead of the 2D U-Net because 3D U-Net can adopt the information between slices of the CT volume. However, the U-Net has limitations of class imbalance and decreased segmentation accuracy. Because the voxels of background, bone, and nerve are quite different, small structure (nerve) tends to have a lower Dice score compared with large structures (bone and background) in semantic segmentation. Thus, we adopted the weighted softmax cross-entropy loss function, and the outcomes seemed to be acceptable. Feng et al<sup>42</sup> used the U-Net to segment the spinal cord on thoracic CT with a Dice score of 0.89, which is

similar to our study with a Dice score of 0.905 for lumbosacral nerves. Novikov et al<sup>43</sup> segmented bones on CT on the basis of the U-Net with a Dice score of 0.95, which is similar to our study with a Dice score of 0.945 for lumbosacral bones. Furthermore, SPINECT segments lumbosacral nerves and bones in about 13 seconds, which is much shorter than the 30 minutes needed for manual segmentation. In summary, the developed model has the potential to be adopted in the workflow of spinal interventions and minimally invasive spine surgery.

The current study has limitations. First, this pilot study only conducted segmentation on the L5/S1 level because it is one of the most difficult levels for spinal intervention and even for minimally invasive spine surgery. SPINECT will be developed and tested on more levels (eg, L3/L4, L4/L5) and different spinal regions (eg, thoracic, cervical) in the near future. Second, although small vessels surrounding the foramen are critical for tESI, we did not segment pertinent vessels because they were not clear on non-contrast CT. However, semantic segmentation of multiple structures (eg, discs, large vessels, muscles, ligaments) will be integrated into SPINECT. Third, while the subject number and segmentation accuracy are acceptable, more cases may be needed for the accuracy to be further improved. Last, the automatic location of CT planes through deep learning may also help physicians in planning ESIs, and a large observational study exploring its feasibility is also on the way.

## CONCLUSIONS

Deep learning with a 3D U-Net can effectively segment spinal nerves and bones from routine CT. The results of this study suggest that our proposed SPINECT can be used to segment spinal nerves on CT seemingly within near-human expert performance, which is reliable for reconstructing Kambin and safe triangles for tESI.

## ACKNOWLEDGMENTS

We thank our colleagues (Tie Y, Jagadeesan J, Mehrtash A, Zhou H, Kapur T, Kikinis R) in Brigham and Women's Hospital for professional comments and suggestions. We also appreciate the revision contribution by Xiaofei Guan from the Burke Neurologic Institute.

Disclosures: William M. Wells—RELATED: Grant: National Institutes of Health, Comments: P41\*; UNRELATED: Employment: Brigham and Women's Hospital, Massachusetts Institute of Technology; Grants/Grants Pending: National Institutes of Health, Comments: P41, R01s.\* Shisheng He—RELATED: Grant: Shanghai Shenkang Hospital Development Center.\* \*Money paid to the institution.

## REFERENCES

- Mokdad AH, Ballesteros K, Echko M, et al; US Burden of Disease Collaborators. **The state of US Health, 1990–2016: burden of diseases, injuries, and risk factors among US states.** *JAMA* 2018;319:1444–72 CrossRef Medline
- Buchbinder R, van Tulder M, Oberg B, et al; Lancet Low Back Pain Series Working Group. **Low back pain: a call for action.** *Lancet* 2018;391:2384–88 CrossRef Medline
- Iannuccilli JD, Prince EA, Soares GM. **Interventional spine procedures for management of chronic low back pain—a primer.** *Semin Intervent Radiol* 2013;30:307–17 CrossRef Medline
- ÖKmen K, ÖKmen BM. **The efficacy of interlaminar epidural steroid administration in multilevel intervertebral disc disease with chronic low back pain: a randomized, blinded, prospective study.** *Spine J* 2017;17:168–74 CrossRef Medline
- Cohen SP, Hanling S, Bicket MC, et al. **Epidural steroid injections compared with gabapentin for lumbosacral radicular pain: multicenter randomized double blind comparative efficacy study.** *BMJ* 2015;350:h1748 CrossRef Medline
- Lee JH, Shin KH, Bahk SJ, et al. **Comparison of clinical efficacy of transforaminal and caudal epidural steroid injection in lumbar and lumbosacral disc herniation: a systematic review and meta-analysis.** *Spine J* 2018;18:2343–53 CrossRef Medline
- Wei G, Liang J, Chen B, et al. **Comparison of transforaminal versus interlaminar epidural steroid injection in low back pain with lumbosacral radicular pain: a meta-analysis of the literature.** *Int Orthop* 2016;40:2533–45 CrossRef Medline
- Glaser SE, Shah RV. **Root cause analysis of paraplegia following transforaminal epidural steroid injections: the ‘unsafe’ triangle.** *Pain Physician* 2010;13:237–44 Medline
- Tumialán LM, Madhavan K, Godzik J, et al. **The history of and controversy over Kambin’s triangle: a historical analysis of the lumbar transforaminal corridor for endoscopic and surgical approaches.** *World Neurosurg* 2019;123:402–08 CrossRef Medline
- Ra IH, Min WK. **Optimal angle of needle insertion for fluoroscopy-guided transforaminal epidural injection of L5.** *Pain Pract* 2015;15:393–99 CrossRef Medline
- Surange PN. S1 Transforaminal: Technique and Troubleshooting. 2016. [https://www.researchgate.net/publication/303324602\\_S1\\_Transforaminal\\_Technique\\_and\\_Troubleshooting](https://www.researchgate.net/publication/303324602_S1_Transforaminal_Technique_and_Troubleshooting). Accessed January 1, 2016
- Chen X, Cheng J, Gu X, et al. **Development of preoperative planning software for transforaminal endoscopic surgery and the guidance for clinical applications.** *Int J Comput Assist Radiol Surg* 2016;11:613–20 CrossRef Medline
- Boswell MV, Trescot AM, Datta S, et al; American Society of Interventional Pain Physicians. **Interventional techniques: evidence-based practice guidelines in the management of chronic spinal pain.** *Pain Physician* 2007;10:7–111 Medline
- Wilkinson I, Cohen SP. **Epidural steroids for spinal pain and radiculopathy: a narrative, evidence-based review.** *Curr Opin Anaesthesiol* 2013;26:562–72 CrossRef Medline
- Kim WJ, Shin HY, Yoo SH, et al. **Comparison of epidural spreading patterns and clinical outcomes of transforaminal epidural steroid injection with high-volume injectate via the subpedicular versus the retrodiscal approach.** *Pain Physician* 2018;21:269–78 Medline
- Park KD, Lee J, Jee H, et al. **Kambin triangle versus the supraneural approach for the treatment of lumbar radicular pain.** *Am J Phys Med Rehabil* 2012;91:1039–50 CrossRef Medline
- Fenster AJ, Fernandes K, Brook AL, et al. **The safety of CT-guided epidural steroid injections in an older patient cohort.** *Pain Physician* 2016;19:E1139–46 Medline
- Timpone VM, Hirsch JA, Gilligan CJ, et al. **Computed tomography guidance for spinal intervention: basics of technique, pearls, and avoiding pitfalls.** *Pain Physician* 2013;16:369–77 Medline
- Han Z, Wei B, Leung S, et al. **Automated pathogenesis-based diagnosis of lumbar neural foraminal stenosis via deep multiscale multitask learning.** *Neuroinformatics* 2018;16:325–37 CrossRef Medline
- Pesteie M, Lessoway V, Abolmaesumi P, et al. **Automatic localization of the needle target for ultrasound-guided epidural injections.** *IEEE Trans Med Imaging* 2018;37:81–92 CrossRef Medline
- Yasaka K, Akai H, Abe O, et al. **Deep learning with convolutional neural network for differentiation of liver masses at dynamic contrast-enhanced CT: a preliminary study.** *Radiology* 2018;286:887–96 CrossRef Medline
- Lu JT, Pedemonte S, Bizzo B, et al. **DeepSPINE: automated lumbar vertebral segmentation, disc-level designation, and spinal stenosis grading using deep learning.** 2018. <https://arxiv.org/abs/1807.10215>. Accessed July 26, 2018
- Mazurowski MA, Buda M, Saha A, et al. **Deep learning in radiology: an overview of the concepts and a survey of the state of the art.** *J Magn Reson Imaging* 2019;49:939–94 CrossRef Medline

24. Ronneberger O, Fischer P, Brox T. U-Net: convolutional networks for biomedical image segmentation. 2015. <https://arxiv.org/abs/1505.04597>. Accessed November 18, 2015
25. Ö Çiçek, Abdulkadir A, Lienkamp SS, et al. 3D U-Net: learning dense volumetric segmentation from sparse annotation. 2016. <https://arxiv.org/abs/1606.06650>. Accessed October 2, 2016
26. Wang C, Macgillivray T, Macnaught G, et al. A two-stage 3D U-Net framework for multi-class segmentation on full resolution image. 2018. <https://arxiv.org/pdf/1804.04341.pdf>. Accessed April 12, 2018
27. Huang Q, Sun J, Ding H, et al. **Robust liver vessel extraction using 3D U-Net with variant dice loss function.** *Comput Biol Med* 2018; 101:153–62 CrossRef Medline
28. Funke J, Tschopp FD, Grisaitis W, et al. **Large scale image segmentation with structured loss based deep learning for connectome reconstruction.** *IEEE Trans Pattern Anal Mach Intel* 2018 May 24. [Epub ahead of print] CrossRef Medline
29. Fedorov A, Beichel R, Kalpathy-Cramer J, et al. **3D Slicer as an image computing platform for the Quantitative Imaging Network.** *Magn Reson Imaging* 2012;30:1323–41 CrossRef Medline
30. Zou KH, Warfield SK, Bharatha A, et al. **Statistical validation of image segmentation quality based on a spatial overlap index.** *Acad Radiol* 2004;11:178–89 CrossRef Medline
31. He K, Zhang X, Ren S, et al. **Delving deep into rectifiers: surpassing human-level performance on ImageNet classification.** 2015. <https://arxiv.org/abs/1502.01852>. Accessed February 6, 2015
32. Kingma DP, Ba J. Adam: a method for stochastic optimization. *Computer Science* 2014. <https://arxiv.org/abs/1412.6980>. Accessed December 22, 2014
33. Cai Y, Osman S, Sharma M, et al. **Multi-modality vertebra recognition in arbitrary views using 3D deformable hierarchical model.** *IEEE Trans Med Imaging* 2015;34:1676–93 CrossRef Medline
34. Mandell JC, Czuczman GJ, Gaviola GC, et al. **The lumbar neural foramen and transforaminal epidural steroid injections: an anatomic review with key safety considerations in planning the percutaneous approach.** *AJR Am J Roentgenol* 2017;209:W1–10 CrossRef Medline
35. Kim C, Choi HE, Kang S. **Contrast spreading patterns in retrodiscal transforaminal epidural steroid injection.** *Ann Rehabil Med* 2012; 36:474–79 CrossRef Medline
36. Hardenbrook M, Lombardo S, Wilson MC, et al. **The anatomic rationale for transforaminal endoscopic interbody fusion: a cadaveric analysis.** *Neurosurg Focus* 2016;40:E12 CrossRef Medline
37. Guan X, Gu X, Zhang L, et al. **Morphometric analysis of the working zone for posterolateral endoscopic lumbar discectomy based on magnetic resonance neurography.** *J Spinal Disord Tech* 2015;28: E78–84 CrossRef Medline
38. Mandell JC, Czuczman GJ, Gaviola GC, et al. **The lumbar neural foramen and transforaminal epidural steroid injections: an anatomic review with key safety considerations in planning the percutaneous approach.** *AJR Am J Roentgenol* 2017;209:W26–35 CrossRef Medline
39. Guan X, Fan G, Wu X et al. **Diffusion tensor imaging studies of cervical spondylotic myelopathy: a systemic review and meta-analysis.** *PLoS One* 2015;10:e0117707 CrossRef Medline
40. Janssens R, Zeng G, Zheng G. Fully automatic segmentation of lumbar vertebrae from CT images using cascaded 3D fully convolutional networks. 2018. [https://www.researchgate.net/publication/325516176\\_Fully\\_automatic\\_segmentation\\_of\\_lumbar\\_vertebrae\\_from\\_CT\\_images\\_using\\_cascaded\\_3D\\_fully\\_convolutional\\_networks](https://www.researchgate.net/publication/325516176_Fully_automatic_segmentation_of_lumbar_vertebrae_from_CT_images_using_cascaded_3D_fully_convolutional_networks). Accessed December 5, 2017
41. Dong H, Liu F, Yang G, et al. Automatic brain tumor detection and segmentation using U-Net based fully convolutional networks. 2017. [https://www.researchgate.net/publication/318168153\\_Automatic\\_Brain\\_Tumor\\_Detection\\_and\\_Segmentation\\_Using\\_U-Net\\_Based\\_Fully\\_Convolutional\\_Networks](https://www.researchgate.net/publication/318168153_Automatic_Brain_Tumor_Detection_and_Segmentation_Using_U-Net_Based_Fully_Convolutional_Networks). Accessed June 22, 2017
42. Feng X, Qing K, Tustison NJ, et al. **Deep convolutional neural network for segmentation of thoracic organs-at-risk using cropped 3D images.** *Med Phys* 2019 Mar 4. [Epub ahead of print] CrossRef Medline
43. Novikov AA, Major D, Wimmer M, et al. **Deep sequential segmentation of organs in volumetric medical scans.** *IEEE Trans Med Imaging* 2018 Nov 16. [Epub ahead of print] CrossRef Medline

## Vessel Wall Imaging of Unruptured Intracranial Aneurysms: Ready for Prime Time? Not so Fast!

There are differing viewpoints on the utility of vessel wall imaging (VWI) assessment of unruptured aneurysms within the neuroradiology community. Many authors, including us, have interpreted their data to indicate it offers clinical value. This enthusiasm undoubtedly arises from a sincere viewpoint that the current literature assessing it is compelling enough to positively impact patient care. Vessel wall imaging of intracranial aneurysms is already being used at dozens, if not hundreds, of institutions across the world and may seem ready for prime time. However, despite our initial optimism, we have now concluded that radiologists and clinicians should exercise some caution in their interpretation of the utility of aneurysm wall enhancement (AWE) in the evaluation of intracranial aneurysms as well as some judiciousness when interpreting the existing data.

First, the evaluation of the sensitivity and specificity of AWE in detecting unstable aneurysms is severely limited because to date, there have been few longitudinal studies demonstrating the presence of AWE prior to an unruptured aneurysm growing or rupturing. None of these longitudinal studies have enough follow-up data to reliably assess the natural history of unruptured intracranial aneurysms. Demonstrating that aneurysms that have recently grown, become symptomatic, or ruptured have wall enhancement and concluding that AWE is thus a generalizable biomarker to predict aneurysm instability is a logical fallacy. What came first? The enhancement or the instability? The chicken or the egg? Furthermore, these categories of unstable aneurysms can all be detected with other clinical or radiologic methods, whereas unruptured aneurysms without these features are the group in which VWI might have the greatest potential to impact management. Thus, few meaningful conclusions on the clinical utility of AWE in unruptured aneurysms can be made until we have longitudinal studies comparing the natural history of unruptured aneurysms with or without wall enhancement.

Our group has also purported that AWE is a reliable biomarker of aneurysm instability. For example, we recently published a meta-analysis finding that AWE is sensitive (95%), but not highly specific (62.7%), for unstable aneurysms with a high negative predictive value.<sup>1</sup> The numbers are correct in context, but to analyze the available data, we had to group several definitions of wall enhancement

(circumferential, partial, thick, strong, and so forth) and several definitions of unstable (growing, changing, symptomatic, ruptured, and so forth). Subsequent articles have continued to use similar methods, and the associated limitations have become clear. Any thorough reader of the AWE literature is likely frustrated by the variability of the study designs of prior investigations (Table). Furthermore, the inclusion of ruptured aneurysms and grouping of these aneurysms with “other unstable” is not necessarily helpful. Specifically, the mechanism of enhancement in ruptured aneurysms is likely different and may reflect the ruptured status itself rather than that of any inflammatory precursor condition. Overall, standardization of definitions and logical inclusion criteria would allow fair comparison between study findings.

In addition to all the variability in study design, definitions, and outcomes, one should consider that there are so many confounding variables in our analysis of AWE and aneurysm natural history. In 1 study by the group in Utrecht, there was a more-or-less linear correlation between aneurysm size and the prevalence of wall enhancement.<sup>2</sup> While this association has been inconsistently demonstrated, it seems to be a recurring theme in the AWE literature. If there is truly a correlation of AWE to size, then the added value of VWI to size alone may be diminished because aneurysm size is already a well-established risk factor for future growth and rupture.

Furthermore, we do not even really know what AWE really means. Although some data correlating AWE to inflammation on histopathology are emerging from clinical data and a rabbit study, mechanisms beyond wall inflammation, including slow flow near the wall (particularly in larger aneurysms), vasa vasorum, thrombotic lining, and increased permeability due to endothelial dysfunction, remain possible alternate or additional etiologies.<sup>3,4</sup> Additionally, the histology of vulnerable aneurysm walls has been shown to be variable, including some aneurysms with extremely thin hypocellular walls and others with thickened walls. Additional correlation of VWI findings to various histologic aneurysm wall patterns would be useful.

The existing studies are meritorious and lay solid groundwork for initial assessment of this topic, but many questions remain. These include the optimal methods of AWE assessment, long-term diagnostic accuracy in asymptomatic unchanging aneurysms, the added value of VWI luminal size and morphologic data alone, and a more complete understanding of the pathogenic mechanism. Given the high morbidity and mortality of an aneurysm rupture, the proce-

**Major clinical studies characterizing saccular aneurysm wall enhancement on VWI**

Study <sup>a</sup>	Aneurysm Categories (Type, Any Enhancement Present) (No.)	Pattern of AWE	Degree of AWE <sup>b</sup>	AWE Association with Size (Range) (mm)	Histopathologic Correlation
Marouk et al. <i>Neurosurgery</i> 2013;72:492–96	Ruptured (5/5) <sup>c</sup> Unruptured (0/3) Total = 8	Thick	Not assessed	Not assessed (2–8)	No
Edjlali et al. <i>Stroke</i> 2014;45:3704–06	Ruptured (16/17) Changing (5/5) Symptomatic (6/9) Other (22/77) Total = 108	CAWE	Not assessed	No correlation to size of entire cohort (4–8)	No
Nagahata et al. <i>Clin Neuroradiol</i> 2014;26:277–83	Ruptured (60/61) Unruptured (15/83) Total = 144	1) CAWE/PAWE grouped 2) Focal	1) Strong 2) Faint 3) Absent Not assessed	No correlation to size in the unruptured cohort (1–18)	No
Liu et al. <i>Interv Neuroradiol</i> 2016;22:501–05	Unruptured (33/61) Total = 61	Present or absent	Not assessed	AWE likelihood increased with size (only 12% of those <7 mm) (2.9–30.5)	No
Omodaka et al. <i>AJNR Am J Neuroradiol</i> 2016;37:1262–66	Ruptured (28) Unruptured (76) Total = 104 (signal intensity cutoff values rather than absolute numbers determined)	1) Circumferential signal intensity 2) Focal enhancement of bleb in some cases	Assessed as a signal intensity ratio	Not reported (>2 and <12)	No
Hu et al. <i>Neuroradiology</i> 2016; 58:979–85	Ruptured (6/6)	Partial or CAWE	Not assessed	No relationship of AWE to size found	Reported for 2 aneurysms (1 giant symptomatic and 1 ruptured) demonstrating inflammatory mediators
Fu et al. <i>Clin Neuroradiol</i> 2017 [Epub ahead of print]	Symptomatic (4/4) Growing (1/1) Other (4/19) Total = 30	CAWE	Not assessed	Mean size = 11 ± 11.7	No
Wang. <i>J Neurointerven Surg</i> 2018;10:566–70	Symptomatic (16/23) Asymptomatic (6/22) Total = 45	CAWE	Not assessed	AWE not correlated to size in entire cohort Mean size = 7.8 ± 4.5 for symptomatic aneurysms	No
Edjlali et al. <i>Radiology</i> 2018;289:181–87	Ruptured (19/19) Unruptured (64/87) Total = 106	1) CAWE 2) PAWE	(Quantitative signal intensity analysis)	Not assessed (Unruptured 7.29 ± 6.60) (Ruptured mean size = 8.4 ± 4.8 for asymptomatic aneurysms)	No
	Ruptured (23/26) Symptomatic or growing/ changing (22/31) Other (106/276) Total = 333	1) Focal thick 2) Thin CAWE 3) Thick CAWE	Not assessed	Correlation to size not assessed Median size (5–6)	No

Continued on next page

**Continued**

Study <sup>a</sup>	Aneurysm Categories (Type, Any Enhancement Present) (No.)	Pattern of AWE	Degree of AWE <sup>b</sup>	AWE Association with Size (Range) (mm)	Histopathologic Correlation
Lv et al. <i>Neurosurgery</i> 2018 [Epub ahead of print]	Unruptured (82/140) Total = 140	Present or absent	Not assessed	Positive association with size (1.7–36.0)	No
Lv et al. <i>World Neurosurg</i> 2018:e338–43	Unruptured (16/30) Total = 30	Present or absent	Not assessed	Positive association with size (2.5–15.9)	No
Omodaka et al. <i>Neurosurgery</i> 2018;82:638–44	Ruptured (26) <sup>c</sup>	Circumferential signal intensity	Signal intensity ratio of ruptured to unruptured aneurysms	Results adjusted for size, but not formally assessed	No
Backes et al. <i>Neurosurgery</i> 2018;83:719–25	Unruptured (26/89) Total = 89	Present or absent	Not assessed	Ruptured (2.7–11.8) Unruptured (2.0–11.4)	No
Wang et al. <i>J Neuroradiol</i> 2019;46:25–28	Unruptured (65/88) Total = 88	Present or absent	Not assessed	Positive association with size (≤7)	No
Larsen et al. <i>AJNR Am J Neuroradiol</i> 2018;39:1617–21	Unruptured (6/13)	None/faint vs strong	None/faint vs strong	3.6–7.9 Enhancement present in 4/4 aneurysms ≥10 mm but absent in 7/9 <10 mm	Inflammatory mediators, neovascularization and vasa vasorum variably present in aneurysms with strong AWE; absent in those without AWE
Shimonaga et al. <i>Stroke</i> 2018;49:2516–19	Total = 13 Unruptured (5/6)	Present or absent	Not assessed	(4–17) Not assessed	Thickening of the wall with vasa vasorum, inflammatory mediators (n = 5); thin vessel wall with a few macrophages with 3 others with walls not visible on 1.5T VWI
	Total = 6 (additional aneurysms had walls not discernable on VWI)			(5.3–9.0)	

**Note:**—CAWE indicates circumferential aneurysm wall enhancement; PAWE, partial aneurysm wall enhancement.

<sup>a</sup> Reports do not account for any aneurysm with duplicate reports in instances of 2 publications by the same institution/author.

<sup>b</sup> Not assessed beyond binary present/absent.

<sup>c</sup> All patients had at least 1 ruptured aneurysm.

dural risks with treatment, and the high prevalence of “stable” aneurysms, a very high diagnostic accuracy is necessary for any novel imaging modalities to improve on existing clinical prognostic factors that have been studied in longitudinal multicenter prospective clinical trials. Additional methods to help stratify aneurysms into stable and unstable categories are needed. Continued evaluation of VWI for this purpose may be very useful to better define the potential value for such risk stratification. Given the limitations of the existing literature on VWI, determinations regarding its clinical utility and its added value over standard clinical and radiographic risk factor predictors are premature.

## REFERENCES

1. Texakalidis P, Hilditch CA, Lehman V, et al. **Vessel wall imaging of intracranial aneurysms: systematic review and meta-analysis.** *World Neurosurg* 2018;117:453–58.e1 CrossRef Medline
2. Backes D, Hendrikse J, van der Schaaf I, et al. **Determinants of gadolinium-enhancement of the aneurysm wall in unruptured intracranial aneurysms.** *Neurosurgery* 2018;83:719–25 CrossRef Medline
3. Wang G, Xia, C, Liu J, et al. **The relationship of arterial wall enhancement ratio on MRI with the degree of inflammation in a rabbit aneurysm model: a pilot study.** *Acad Radiol* 2018 Dec 17. [Epub ahead of print] CrossRef Medline
4. Vakil P, Ansari SA, Cantrell CG, et al. **Quantifying intracranial aneurysm wall permeability for risk assessment using dynamic contrast-enhanced MRI: a pilot study.** *AJNR Am J Neuroradiol* 2015;36:953–59 CrossRef Medline

✉ V.T. Lehman

Department of Radiology

✉ W. Brinjikji

Departments of Radiology and Neurosurgery  
Mayo Clinic College of Graduate Medical Education  
Rochester, Minnesota

## Patients with High-Grade Gliomas and Café-au-Lait Macules: Is Neurofibromatosis Type 1 the Only Diagnosis?

We read with great interest the publication “High-Grade Gliomas in Children with Neurofibromatosis Type 1: Literature Review and Illustrative Cases” by Spyris et al.<sup>1</sup> As discussed by the authors, high-grade gliomas in children may be associated with neurofibromatosis type 1 (NF-1). However, several other cancer predisposition syndromes, including constitutional mismatch repair deficiency (CMMRD), also increase the risk of childhood high-grade glioma. Most important, not only does the spectrum of CMMRD-associated malignancies overlap that reported for NF-1 but patients with CMMRD frequently also show nonmalignant features of NF-1.<sup>2</sup> This phenotypic overlap between NF-1 and CMMRD challenges the clinical diagnosis of NF-1 in a patient with pediatric high-grade glioma and, overall, our current knowledge on associations between NF-1 and rare childhood malignancies.<sup>3</sup>

Because patients with CMMRD-associated high-grade gliomas may benefit from immunotherapy with anti-programmed cell death protein 1 drugs,<sup>4</sup> it is key to explore extensively the underlying genetic disease by molecular genetic diagnosis. Distinction between CMMRD and NF-1 in this setting also has implications for further cancer surveillance of the patient, recurrence risk in siblings, and Lynch syndrome–associated cancer risks in the extended family.

In this respect, the cases presented by Spyris et al<sup>1</sup> are illustrative of the diagnostic challenge that may occur in this setting. The article reports 5 patients with a brain tumor who were “diagnosed with NF-1 in accordance with the diagnostic criteria.” Considering that the message of the article is to raise awareness of the occurrence of high-grade glioma in children with NF-1, we would be very interested in a description of the phenotype and family history of these children and what NF-1 criteria were used to state the clinical diagnosis of NF-1. It would also be of interest to know whether focal abnormal signal intensities (FASIs), a very common finding in children with NF-1, were present. None of the reported patients had visible FASIs on the MRIs presented in the figures. Three patients (patients 1, 2, and 4) had malignant tumors molecularly consistent with diffuse midline *H3K27M*-mutated gliomas, which have not been described in children with NF-1.<sup>5,6</sup> “Skin spots,” presumably café-au-lait macules, were explicitly re-

ported only for patient 4. Even the tumors most typically associated with NF-1 (ie, optic pathway glioma and pilocytic astrocytoma) as diagnosed in patients 3 and 5 have been described in CMMRD.<sup>3</sup> Taken together, the diagnosis of NF-1 is questionable in at least some of the patients. Considering the impact of the diagnosis of the underlying genetic disease on the treatment of affected patients, it would be of major importance to genetically confirm the diagnosis of NF-1 in these 5 patients.

To conclude, we strongly recommend that in all children with high-grade gliomas and a phenotype reminiscent of NF-1, this diagnosis should be confirmed as the underlying disease by identification of a clearly pathogenic germline *NF1* mutation. In the absence of this confirmation, CMMRD should be excluded by mutation analysis of the *MMR* genes and/or by immunohistochemistry showing the expression of all 4 MMR proteins in the tumor or by appropriate molecular and functional assays.<sup>3</sup> A correct diagnosis in these children will be important to adapt the therapeutic strategy, surveillance, and genetic counseling as stated in recent consensus papers. A definite genetic diagnosis of NF-1 and exclusion of CMMRD in future patients are necessary to substantiate the reported association of NF-1 with childhood high-grade gliomas because this is currently largely based on patients diagnosed only on clinical criteria (for review see Wimmer et al<sup>3</sup>) and, therefore, challenged by our current knowledge of the phenotypic overlap between CMMRD and NF-1.

Disclosures: Eric Legius—UNRELATED: Grants/Grants Pending: University of Leuven. Comments: I applied for a new grant at the University of Leuven for studying behavior in a genetic mouse model. I received a grant from the University of Leuven for studying autistic behavior in a mouse model.\* \*Money paid to the institution.

### REFERENCES

1. Spyris CD, Castellino RC, Schniederjan MJ, et al. **High-grade gliomas in children with neurofibromatosis type 1: literature review and illustrative cases.** *AJNR Am J Neuroradiol* 2019;40:366–69 CrossRef Medline
2. Wimmer K, Kratz CP, Vasen HF, et al; EU-Consortium Care for CMMRD (C4CMMRD). **Diagnostic criteria for constitutional mismatch repair deficiency syndrome: suggestions of the European consortium “care for CMMRD” (C4CMMRD).** *J Med Genet* 2014;51:355–65 CrossRef Medline
3. Wimmer K, Rosenbaum T, Messiaen L. **Connections between constitutional mismatch repair deficiency syndrome and neurofibromatosis type 1.** *Clin Genet* 2017;91:507–19 CrossRef Medline

4. Bouff t E, Tabori U, Bartels U. **Paediatric ependymomas: should we avoid radiotherapy?** *Lancet Oncol* 2007;8:665–66 CrossRef Medline
5. Mackay A, Burford A, Carvalho D, et al. **Integrated molecular meta-analysis of 1,000 pediatric high-grade and diffuse intrinsic pontine glioma.** *Cancer Cell* 2017;32:520–37.e5 CrossRef Medline
6. D’Angelo F, Ceccarelli M, Tala, et al. **The molecular landscape of glioma in patients with neurofibromatosis 1.** *Nat Med* 2019;25:176–87 CrossRef Medline

● **L. Guerrini-Rousseau**

Department of Pediatric and Adolescents Oncology  
Gustave Roussy Cancer Center  
Paris-Saclay University  
Villejuif, France

● **M. Suerink**

Department of Clinical Genetics  
Leiden University Medical Centre  
Leiden, the Netherlands

● **J. Grill**

Department of Pediatric and Adolescents Oncology  
Gustave Roussy Cancer Center  
Paris-Saclay University  
Villejuif, France

● **E. Legius**

Department of Human Genetics  
University Hospital Leuven and KU Leuven  
Leuven, Belgium

● **K. Wimmer**

Division of Human Genetics  
Medical University Innsbruck  
Innsbruck, Austria

● **L. Brugi res**

Department of Pediatric and Adolescents Oncology  
Gustave Roussy Cancer Center  
Paris-Saclay University  
Villejuif, France

**REPLY:**

We appreciate that Guerrini-Rousseau and colleagues are raising awareness for constitutional mismatch repair deficiency (CMMRD) syndrome and its phenotypical overlap with neurofibromatosis type 1 (NF-1). All 5 patients described in our article met clinical criteria for NF-1 (Table). None of the patients reported had confirmatory genetic testing; for children who meet the clinical criteria, genetic testing is not typically obtained.

CMMRD is rare (200 patients reported), and our patients had none of the other diagnostic criteria of CMMRD.<sup>1</sup> Café au lait spots are common (up to 97%) in CMMRD, but the other clinical manifestations of NF-1 are much less frequent.<sup>2</sup> Focal abnormal signal intensities have also been reported in CMMRD.

<http://dx.doi.org/10.3174/ajnr.A6062>

**REFERENCES**

1. Wimmer K, Kratz CP, Vasen HF, et al; EU-Consortium Care for CMMRD (C4CMMRD). **Diagnostic criteria for constitutional mismatch repair deficiency syndrome: suggestions of the European consortium ‘care for CMMRD’ (C4CMMRD).** *J Med Genet* 2014;51:355–65 CrossRef Medline
2. Wimmer K, Rosenbaum T, Messiaen L. **Connections between constitutional mismatch repair deficiency syndrome and neurofibromatosis type 1.** *Clin Genet* 2017;91:507–19 CrossRef Medline
3. Friedman JM. Neurofibromatosis 1. October 2, 1998, updated May 17, 2018. GeneReviews® [Internet]. <https://www.ncbi.nlm.nih.gov/books/NBK1109/>. Accessed April 21, 2019

**N. Kadom**

Departments of Radiology and Pediatrics

**R.C. Castellino**

Department of Pediatrics and Aflac Cancer & Blood Disorders Center  
Children’s Healthcare of Atlanta  
Atlanta, Georgia

**D.S. Wolf**

Department of Pediatrics, Division of Child Neurology  
Emory University School of Medicine  
Atlanta, Georgia

**For a diagnosis of NF-1, at least 2 of the diagnostic criteria should be present<sup>3</sup>**

NF-1 Diagnostic Criteria	Patient 1	Patient 2	Patient 3	Patient 4	Patient 5
Six or more café au lait macules >5 mm in greatest diameter in prepubertal individuals and >15 mm in greatest diameter in postpubertal individuals	Yes	Yes	Yes	Yes	Yes
Two or more neurofibromas of any type or 1 plexiform neurofibroma		Yes			
Freckling in the axillary or inguinal regions	Yes	Yes	Yes	Yes	Yes
Optic glioma			Yes		Yes
Two or more Lisch nodules (iris hamartomas)	Yes	Yes			Yes
A distinctive osseous lesion such as sphenoid dysplasia or tibial pseudarthrosis					
A first-degree relative (parent, sibling, or offspring) with NF-1 as defined by the above criteria	Yes	Yes	Unknown (adopted)		
MRI findings: focal abnormal signal intensities	Yes	Yes	Yes	Yes	Yes

The authors of “Disorder in Pixel-Level Edge Directions on T1WI Is Associated with the Degree of Radiation Necrosis in Primary and Metastatic Brain Tumors: Preliminary Findings” (*AJNR Am J Neuroradiol* 2019;40:412–17; <https://doi.org/10.3174/ajnr.A5958>) reported missing references 19–21, which were cited in the text but do not appear in the “References” section. The references are provided below in the same order. The Journal regrets this error.

#### REFERENCES

19. Chaddad A, Tanougast C. **Extracted magnetic resonance texture features discriminate between phenotypes and are associated with overall survival in glioblastoma multiforme patients.** *Med Biol Eng Comput* 2016;54:1707–18 CrossRef Medline
20. Rathore S, Akbari H, Doshi J, et al. **Radiomic signature of infiltration in peritumoral edema predicts subsequent recurrence in glioblastoma: implications for personalized radiotherapy planning.** *J Med Imaging (Bellingham)* 2018;5:021219 CrossRef Medline
21. Ismail M, Hill V, Statsevych V, et al. **Shape features of the lesion habitat to differentiate brain tumor progression from pseudoprogression on routine multiparametric MRI: a multisite study.** *AJNR Am J Neuroradiol* 2018;39:2187–93 CrossRef Medline

<http://dx.doi.org/10.3174/ajnr.A6069>